Molecular Mechanisms of Cholangiocarcinoma-Cholangiocyte Cell Interactions *in vitro*



Gemma Jane Owen
Green Templeton College
University of Oxford

A thesis submitted for the degree of
Doctor of Philosophy
Trinity Term 2023

Table of Contents

Acknowledgements 5
Abstract 6
COVID-19 Discrepancies 7
List of Tables and Figures 8
List of abbreviations 0

1 INTRODUCTION 2

1.1 Cholangiocarcinoma 2
1.1.1 Anatomy of CCA 2
1.1.2 Tumour classification 4
1.1.3 Incidence and Epidemiology 5
1.1.4 Risk Factors 5
1.1.5 Clinical Presentation & Diagnosis 6
1.1.6 Treatment & Prognosis 8
1.2 CCA Tumour Microenvironment 13
1.2.1 Pathological relevance of Paracrine Signalling in CCA 14
1.2.2 Epithelial-mesenchymal transition 15
1.2.3 Inflammation 17
1.2.4 Immune Response 17
1.2.5 Chemoresistance 18
1.3 Cell-cell interactions in CCA 18
1.3.1 Cholangiocytes 19
1.4 Molecular Phenotype 21
1.4.1 Genomic component of CCA 21
1.4.2 Epigenetic component of CCA 21
1.4.3 Metabolic component of CCA 22

2 RESEARCH AIMS AND OBJECTIVES 24

3 MATERIALS AND METHODS 25

3.1 Cell lines and culture 25
3.2 Indirect Co-Culture 25
3.3 Western Blot 26
3.3.1 Protein extraction 26
3.3.2 Protein Quantification 27
3.3.3 Gel Preparation 28
3.3.4 Protein Separation 28
3.3.5 Protein Visualisation 28
3.3.6 Image Analysis 30
3.4 Nucleic Acid Work 30
3.4.1 RNA extraction 30
3.4.2 Generation of cDNA 30
3.4.3 Quantitative Polymerase Chain Reaction (qPCR) 31
3.4.4 Silencing of gene expression using silencing RNA (siRNA) 33
3.4.5 siRNA Sequences 33
3.5 Cell Viability 34
3.5.1 Cell Counting Kit-8 (CCK8) 34
3.6 Cell Proliferation 35
3.7 Cell Migration 35
3.8 Flow Cytometry 36
3.8.1 Apoptosis 36
3.8.2 Cell Cycle 36
3.9 Metabolomics 37
3.9.1 Exogenous metabolites 41
3.10 RNA-sequencing 42

3.11 Integration of metabolomic and transcriptomic analyses 44
3.12 TCGA Analysis 46
3.13 ATP Assay 49
3.14 Cytokine Expression Analysis 49
3.15 Epigenetic Inhibitor Screen 52
3.15.1 Epigenetic Inhibitor Panel 52
3.15.2 CyQuant 52
3.15.3 Generation of IC50 curves 53
3.16 Statistical Analysis 55

4 RESULTS CHAPTER 1 – FUNCTIONAL EVALUATION OF INDIRECT CHOLANGIOCYTE-CHOLANGIOCARCINOMA INTERACTIONS 56

4.1 Introduction 56
4.2 Model Selection 58
4.2.1 CCA Cell Phenotypes 58
4.2.2 CCA cell proliferation is attenuated by nutrient restricted culture media 60
4.3 Cholangiocyte viability is improved by co-culture 63
4.3.1 Conditioned media from CC-SW1 cells boosts MMNK1 cholangiocyte viability 63
4.3.2 Co-Culture with CC-SW1 cells boosts cholangiocyte viability 64
4.4 Co-Culture reduces CC-SW1 migration 67
4.4.1 Co-culture reduces the proportion of migratory CC-SW1 cells 67
4.4.2 Co-culture reduces EMT protein and gene expression 69
4.5 Co-culture increases cholangiocyte, and restricts CCA cell cycle progression 73
4.6 Co-culture triggers a reduction cholangiocyte apoptosis 75
4.6.1 Co-culture triggers a downregulation in apoptotic protein expression 82
4.7 Heat inactivation of culture media highlights the proportional importance of proteins and metabolic components 83
4.7.1 Heat inactivated conditioned media reduces cholangiocyte and CCA cell viability 83
4.7.2 Heat inactivated conditioned media has no effect on cholangiocyte or CCA apoptosis 85
4.8 Human primary cholangiocytes validate indirect co-culture with CCA 90
4.8.1 NHC3 cell proliferation is attenuated by culture media 90
4.8.2 NHC3 cell viability is not attenuated by co-culture with CC-SW1 cells 91
4.8.3 Co-culture triggers an increase in NHC3 cell migration 92
4.8.4 NHC3 cell apoptosis is not affected by co-culture with CC-SW1 cells 94
4.9 Summary 95
4.10 Discussion 98

5 RESULTS CHAPTER 2 - DELINEATING THE INTERCELLULAR CROSSTALK BETWEEN CHOLANGIOCYTES AND CHOLANGIOCARCINOMA CELLS 104

5.1 Introduction 104
5.2 Metabolic Compartment 109
5.2.1 Basal metabolite concentrations of cholangiocyte and cholangiocarcinoma cells 109
5.2.2 Co-Culture Alters Metabolic Profile of Cellular Compartments 116
5.2.3 6 hours of co-culture increase glycolytic intermediates in cholangiocytes 116
5.2.4 24 hours of co-culture reduces pentose phosphate pathway and glycolytic intermediates in cholangiocytes, with an increase in nucleoside mono- and diphosphates 122
5.2.5 48 hours of co-culture reduces aspartate and glutamate concentration, with an increase in choline and creatine concentration 128
5.3 Validation of cholangiocyte metabolite concentration 135
5.3.1 Exogenous asparagine increased cholangiocyte viability and migration 135
5.3.2 Exogenous choline decreased cholangiocyte viability, with no effect on apoptosis or migration 139
5.3.3 Exogenous creatine improves cholangiocyte viability and ATP availability 144
5.3.4 Summary 155
5.4 Changes to the cholangiocarcinoma metabolome during indirect co-culture 156
5.4.1 6 hours of co-culture decreased nucleoside mono-, di-, and triphosphate concentration in cholangiocarcinoma cells 156

5.4.2 24 hours of co-culture increased 2-oxoisopentanote and decreased glutamine concentrations in cholangiocarcinoma cells *162*
5.4.3 48 hours of co-culture increased 2-oxoisopentanote, and decreased glutamine/glutamate concentrations in cholangiocarcinoma cells *167*
5.5 Validation of cholangiocarcinoma metabolite concentration 173
5.5.1 Exogenous 2-Oxoisopentanoate reduces CCA cell viability *173*
5.5.2 Summary *181*
5.6 Cytokine-Mediated Crosstalk 182
5.6.1 Indirect co-culture triggers a reciprocal shift in cytokine secretion *182*
5.6.2 Changes to the cholangiocyte secretome during indirect co-culture *182*
5.6.3 Changes to the cholangiocarcinoma secretome during indirect co-culture *185*
5.6.4 Summary *188*
5.7 Discussion 189

6 RESULTS CHAPTER 3 – INTERPRETING THE TRANSCRIPTOMIC ALTERATIONS DUE TO INDIRECT CELL-CELL COMMUNICATION 193

6.1 Introduction 193
6.2 Genomic differences between cholangiocyte and cholangiocarcinoma cells 195
6.2.1 Application of the DESeq2 model *196*
6.2.2 Differential gene expression *200*
6.2.3 Gene Set Enrichment Analysis *202*
6.3 Genomic alterations in cholangiocytes due to co-culture 206
6.3.1 Transcriptomic analysis *206*
6.3.2 Application of the DESeq2 model *206*
6.3.3 Differential Gene Expression *209*
6.3.4 Gene Set Enrichment Analysis *211*
6.4 Validation of cholangiocyte genomic alterations 218
6.4.1 Validation of RNAseq data *218*
6.4.2 siRNA knockdown of HSPA8 ..... *222*
6.5 Validation of Cytokine Secretion 231
6.6 Integrating cholangiocyte metabolomic and genomic data 234
6.6.1 Joint-Pathway Analysis highlights increased TCA cycle *234*
6.6.2 Evaluation of metabolic-associated genes *236*
6.7 Genomic alterations in cholangiocarcinoma cells due to co-culture 250
6.7.1 Transcriptomic analysis *250*
6.7.2 Application of the DESeq2 model *250*
6.7.3 Differential Gene Expression *253*
6.7.4 Gene Set Enrichment Analysis *255*
6.8 Validation of cholangiocarcinoma genomic alterations 263
6.8.1 Validation of RNAseq *263*
6.8.2 Validation of Cytokine Expression *265*
6.9 Integrating cholangiocyte metabolomic and genomic data 268
6.9.1 Joint-Pathway Analysis highlights increased TCA cycle *268*
6.9.2 Evaluation of metabolic-associated genes *270*
6.9.3 Exogenous 2-Oxoisopentanoate Modulated CC-SW1 Gene Expression *273*
6.10 TCGA Genomic Validation 275
6.10.1 Introduction *275*
6.10.2 CCA vs Normal Tissue Differential Gene Analysis *275*
6.10.3 Metabolic Gene Set Enrichment Analysis *278*
6.10.4 TCGA validation of target genes *281*
6.11 Discussion 287

7 RESULTS CHAPTER 4 – EVALUATION AND INHIBITION OF THE EPIGENOME DURING CO-CULTURE 292

7.1 INTRODUCTION 292
7.2 5-FLUOROURACIL RESISTANCE IN CCA CELL LINES 294
7.3 EPIGENETIC INHIBITOR PANEL 296
7.4 ANALYSIS OF UNC0642 AND SGC-3027 298
7.5 EFFECT OF CO-CULTURE ON UNC0642 AND SGC-3027 EFFICACY 300
7.6 EVALUATION OF EPIGENOME-ASSOCIATED GENES 301
7.6.1 EHMT1, EHMT2, and PRMT7 transcriptomic data 301
7.6.2 EHMT1, EHMT2, and PRMT7 TCGA data 302
7.7 SUMMARY 304
7.8 DISCUSSION 305

8 OVERALL DISCUSSION 311

8.1 CONCLUSION 311
8.2 STUDY LIMITATIONS 321
8.3 POTENTIAL FUTURE WORK 326
8.4 CLOSING REMARKS 330

REFERENCES 331

Acknowledgements

I want to express my deepest and most sincere gratitude to my supervisors Prof David Kerr and Dr Shijie Cai. I am also deeply thankful to all members of the Kerr-Cai group, both past and present who helped me navigate the complexities of research.

This DPhil project would not have been possible without the contribution from our collaborators, and I would personally like to thank Dr Kaori Igarashi, Prof Tomoyoshi Soga, Dr Kevin Rue-Albrecht, Prof Jesús Bañales, and Prof David Sims for their contributions. Likewise I want to express my gratitude to the AMMF for their continued academic and financial support, and I hope their impactful work continues to shape the field of cholangiocarcinoma for patients far into the future. Moreover, I would like to extend my sincere thanks to Prof Alison Banham for her time spent proofreading the thesis, Dr Amanda Anderson for her encouragement and (often daily) support in the lab, Prof Marella de Bruijn for always fighting my corner, and Dr Mark Coldwell for his endless enthusiasm.

I cannot emphasize enough how thankful I am for my parents, whose sacrifices, encouragement, and resilience has shaped me into the person I am today. Dad, whether running a company, or completing an Ironman, you inspire me to strive for excellence in every aspect of my life and my work. Mum, your strength and determination is astounding, you have sacrificed so much, I am proud to be your daughter. Caz, your presence in my life has brought warmth, support, and an extra dose of love in the form of my brother Josh. To my sister Els, whose presence in my life has been a grounding force, keeping me humble, I'm immensely proud of everything you have achieved. Nanny, your endless love and unwavering faith in my abilities has been my driving force, and I am profoundly grateful for your belief in me.

A big thank you to my Oxford friends Becky, Nicole, Ellie, and Max who will likely run the world one day, and to my home friends (Hayley, Georgia, Molly, Faye, and Roz), who have stuck by my side no matter what. I could not have undertaken this DPhil journey without the support of my best friend Rachel Roberts, my newfound big brother Aik Seng, and Euan, who believed in me even when I doubted myself. I am deeply and eternally grateful to everyone who has inspired and impacted my life, especially to all the teachers and mentors who encouraged me to be here. This achievement is not mine alone, but the achievement of every individual that has shaped my life. Thank you from the bottom of my heart.

Finally, I dedicate this thesis to my biggest cheerleaders, Grandad and Nanny Jill, I know without a shadow of a doubt that I have made you proud.

Abstract

Cholangiocarcinoma is a highly aggressive cancer originating within the biliary tract. Whilst the role of the tumour microenvironment in CCA progression is well established, the function of surrounding cholangiocytes on CCA behaviour is often overlooked. Specifically, the effect of paracrine communication between cholangiocytes and cholangiocarcinoma cells has not been investigated previously. In this study, we provide evidence that cholangiocyte cells are a crucial paracrine modulator that influences the permissive or restrictive state to CCA progression.

Indirect co-culture of cholangiocarcinoma cells with cholangiocyte cells causes a significant decrease in CCA cell viability, migratory behaviour, and cell cycle progression, associated with a demonstratable switch in the gene and protein expression of the EMT markers E-cadherin, Slug, Snail, and Vimentin. Moreover, co-culture triggered a metabolic shift in CCA cells, with enhanced branched chain amino acid (BCAA) metabolism, as well as a transcriptomic shift resulting in increased cytokine signalling gene expression, recapitulated in the secretome.

In turn, cholangiocytes respond to this interaction with CCA cells, undergoing changes resulting in a growth advantage. Cholangiocytes experience an increase in creatine metabolism and ATP availability, linking to improved cell viability, increased cell cycle progression and reduced apoptosis, in conjunction with a reduction in gene and protein expression of p53 and apoptotic pathways.

Moreover, a high-throughput screen of epigenetic inhibitors successfully identified two targets, UNC0642 and SGC3027, for further development against CCA. More crucially, although effective against our CCA cell lines, co-culture with cholangiocytes caused a significant increase in IC50 value for these epigenetic inhibitors, implicating cholangiocyte cells in CCA chemoresistance.

We hypothesise the metabolic and genomic alterations triggered by this interaction contributes to CCA survival, invasiveness, and chemoresistance in the later stages of CCA development. Overall, our findings highlight the importance of cholangiocyte cells in modulating cholangiocarcinoma cells, impacting the development, progression, and treatment of cholangiocarcinoma.

COVID-19 Discrepancies

The global COVID-19 pandemic had a profound and far-reaching impact on my project, disrupting its course in several crucial ways. Principally, the closure of University facilities to non-Covid-19 research led to a cessation of my experiments from the 24th March 2020 till the 3rd September 2020.

The sudden shift to remote working and the closure of the research facilities severely hampered my ability to gather critical data and progress the project. The loss of 6 months of experimental work has been detrimental to my project, with a 6 month set back in all functional and molecular experiments. Unfortunately, this has led to the validation of our findings in our cohort of patient samples (24 matched CCA and normal tissue samples) being uncompleted. Due to this 6 month delay, we were unable to begin experiments using the hepatocyte cell line H69 as a model for late stage CCA development, and with more time would have expanded the experimental work in the extrahepatic cell line SNU-1196 and primary human cholangiocyte cell line NHC3.

Additionally, the pandemic caused significant disruptions to the supply chain, making it challenging to procure necessary materials and equipment, further impeding progress once the research spaces reopened. Moreover, the emotional and psychological toll of the pandemic, coupled with the need to juggle personal caring responsibilities, significantly affected the advancement of the project, with an additional period of time away from the bench side January till May 2021.

In summary, the pandemic's unforeseen challenges had a substantial impact on my project, necessitating adjustments to my experimental plan, increased resilience, and a re-evaluation of my timelines and research priorities. Despite this, in the period of time since the pandemic I believe I have acquired a good general knowledge in the field of cholangiocarcinoma, and that this project does indeed form a significant and substantial contribution to the field.

List of Tables and Figures

Table 1 - List of primary and secondary antibodies used in this study 29
Table 2 - List of qPCR primers used in this study 32
Table 3 - List of siRNA sequences used in this study. 33
Table 4 - Table of exogenous metabolites 41
Table 5 - Table of Metabolic Gene Sets 46
Table 6 - List of SGC epigenetic probes and targets 54
Table 7 - Table showing phenotypic and genotypic differences in CCA cell lines 59

Introduction

Figure 1:1 - Structure of the biliary tree……17
Figure 1:2 - CCA tumour morphology……18
Figure 1:3 - Key molecular pathways and respective small molecule inhibitors in CCA……29
Figure 1:4 - The molecular processes behind the epithelial-mesenchymal transition……37

Materials & Methods

Figure 3:1 - Indirect co-culture model of cholangiocarcinoma and cholangiocyte cells……40
Figure 3:2 - Workflow of integrating metabolomic and RNA-sequencing analysis……59
Figure 3:3 - Cytokine assay analysis……65

Results Chapter 1 – Functional Evaluation of Indirect Cholangiocyte-Cholangiocarcinoma Interactions

Figure 4:1 - Treatment media affects CCA and cholangiocyte proliferation over 48 hours...76
Figure 4:2 - Conditioned media affects cholangiocyte and CCA cell viability……77
Figure 4:3 - Culture media effects co-culture mediated improvements to MMNK1 cell viability……79
Figure 4:4 - Indirect co-culture boosts MMK1 cholangiocyte viability, whilst reducing CCA cell viability……80
Figure 4:5 - Co-culture reduces the proportion of migratory CC-SW1 cells ……82
Figure 4:6 - Co-culture reduces EMT protein expression in CC-SW1 cells……83
Figure 4:7 - qPCR housekeeping gene validation and selection……85
Figure 4:8 - Co-culture reduces EMT gene expression in CC-SW1 cells ……86
Figure 4:9 - Co-culture increases the proportion of MMNK1 cells in the G2M cell cycle phase……87
Figure 4:10 - Co-culture increases the proportion of CC-SW1 cells in S phase……88
Figure 4:11 - Co-culture with CC-SW1 triggers a reduction in the proportion of apoptotic MMNK1 cells……90
Figure 4:12 - Co-culture with CC-LP1 triggers a reduction in the proportion of apoptotic MMNK1 cells……91
Figure 4:13 - Co-culture with SNU-1079 has no effect on the proportion of apoptotic MMNK1 cells……92
Figure 4:14 - Co-culture with SNU-1196 has no effect on the proportion of apoptotic MMNK1 cells……93
Figure 4:15 - Co-culture with MMNK1 cholangiocytes has no effect on the proportion of apoptotic CC-SW1 cells……94
Figure 4:16 - Co-culture with MMNK1 cholangiocytes has no effect on the proportion of apoptotic CC-LP1 cells……95
Figure 4:17 - Co-culture reduces apoptotic protein expression in MMNK1 cells……96
Figure 4:18 - Heat inactivated conditioned media reduces cholangiocyte and CCA cell viability……98
Figure 4:19 - Heat inactivated conditioned has no effect on the proportion of apoptotic MMNK1 cholangiocytes……100
Figure 4:20 - Heat inactivated conditioned has no effect on the proportion of apoptotic CC-SW1 cells……102
Figure 4:21 - Treatment media affects human primary cholangiocyte cell NHC3 proliferation over 48 hours ……104

Figure 4:22 - Co-culture has no effect on NHC3 cholangiocyte viability.....105
Figure 4:23 - Co-culture increases the proportion of migratory NHC3 and CC-SW1 cells....107
Figure 4:24 - Co-culture with CC-SW1 cells has no effect on the proportion of apoptotic NHC3 cholangiocyte cells.....108

Results Chapter 2 – Delineating Intercellular Crosstalk Between Cholangiocytes and CCA

Figure 5:1 - Normalisation and clustering of MMNK1 and CC-SW1 metabolomic samples in monoculture at 48 hours.....125
Figure 5:2 - Heatmap of differentially expressed metabolites in CC-SW1 cells compared to MMNK1 cholangiocytes 126
Figure 5:3 - Differentially expressed metabolites in CC-SW1 cells compared to MMNK1 cells after 48 hours.....127
Figure 5:4 - Basally enriched metabolic pathways in CC-SW1 cells.....128
Figure 5:5 - Dendrogram and Scores Plot for the metabolic profiling of MMNK1 cells after 6 hours of mono- and co-culture.....131
Figure 5:6 - Heatmap of differentially expressed metabolites in MMNK1 cholangiocytes after 6 hours of indirect co-culture.....132
Figure 5:7 - Differentially expressed metabolites in MMNK1 cells after 6 hours of indirect co-culture.....133
Figure 5:8 - Enriched metabolic pathways in MMNK1 cholangiocytes after 6 hours of co-culture with CC-SW1 cells.....134
Figure 5:9 - Dendrogram and Scores Plot for the metabolic profiling of MMNK1 cells after 24 hours of mono- and co-culture.....137
Figure 5:10 - Heatmap of differentially expressed metabolites in MMNK1 cholangiocytes after 24 hours of indirect co-culture.....138
Figure 5:11 - Differentially expressed metabolites in MMNK1 cells after 24 hours of indirect co-culture with CC-SW1 cells.....139
Figure 5:12 - Enriched metabolic pathways in MMNK1 cholangiocytes after 24 hours of indirect co-culture with CC-SW1 cells.....140
Figure 5:13 - Dendrogram and Scores Plot for the metabolic profiling of MMNK1 cells after 48 hours of mono- and co culture.....143
Figure 5:14 - Heatmap of differentially expressed metabolites in MMNK1 cholangiocytes after 48 hours of indirect co-culture.....144
Figure 5:15 - Differentially expressed metabolites in MMNK1 cells after 48 hours of indirect co-culture with CC-SW1 cells.....145
Figure 5:16 - Flux of differentially expressed metabolites in MMNK1 cholangiocytes across 48 hours.....146
Figure 5:17 - Enriched metabolic pathways in MMNK1 cells after 48 hours of indirect co-culture with CC-SW1 cells.....147
Figure 5:18 - Aspartate/asparagine ratio in MMNK1 cells across 48 hours.....149
Figure 5:19 - Exogenous asparagine increases MMNK1 cell viability.....150
Figure 5:20 - Exogenous asparagine increases MMNK1 cell migration.....151
Figure 5:21 - Exogenous choline decreases MMNK1 cell viability.....153
Figure 5:22 - Exogenous choline has no effect on MMNK1 cell migration 154
Figure 5:23 - Exogenous choline has no effect on the proportion of apoptotic or viable MMNK1 cells.....155
Figure 5:24 - Exogenous creatine increases MMNK1 cell viability.....158

Figure 5:25 - Exogenous creatine has no effect on the proportion of apoptotic or viable MMNK1 cells.....159
Figure 5:26 - Exogenous cyclocreatine decreases MMNK1 cell viability.....161
Figure 5:27 - Exogenous cyclocreatine has no effect on the proportion of apoptotic or viable MMNK1 cells.....162
Figure 5:28 – Dual exogenous doses of creatine and choline have no effect on MMNK1 cell viability.....164
Figure 5:29 - Indirect co-culture with CCA cells increase the concentration of available ATP in MMNK1 cells.....165
Figure 5:30 - Exogenous creatine increases the concentration of cellular ATP in MMNK1 cells.....167
Figure 5:31 - Dendrogram and Scores Plot for the metabolic profiling of CC-SW1 cells after 6 hours of mono- and co-culture.....171
Figure 5:32 - Heatmap of differentially expressed metabolites in CC-SW1 cells after 6 hours of indirect co-culture 172
Figure 5:33 - Differentially expressed metabolites in CC-SW1 cells after 6 hours of indirect co-culture with MMNK1 cells.....173
Figure 5:34 - Enriched metabolic pathways in CC-SW1 cells after 6 hours of indirect co-culture with MMNK1 cholangiocytes.....174
Figure 5:35 - Dendrogram and Scores Plot for the metabolic profiling of CC-SW1 cells after 24 hours of mono- and co-culture.....176
Figure 5:36 - Heatmap of differentially expressed metabolites in CC-SW1 cells after 24 hours of indirect co-culture..... 177
Figure 5:37 - Differentially expressed metabolites in CC-SW1 cells after 24 hours of indirect co-culture with MMNK1 cells.....178
Figure 5:38 - Enriched metabolic pathways in CC-SW1 cells after 24 hours of indirect co-culture with MMNK1 cholangiocytes.....179
Figure 5:39 - Dendrogram and Scores Plot for the metabolic profiling of CC-SW1 cells after 48 hours of mono- and co-culture.....182
Figure 5:40 - Heatmap of differentially expressed metabolites in CC-SW1 cells after 48 hours of indirect co-culture.....183
Figure 5:41 - Differentially expressed metabolites in CC-SW1 cells after 48 hours of indirect co-culture with MMNK1 cells.....184
Figure 5:42 - 2-oxoisopentanoate concentration in CC-SW1 cells during co- culture.....185
Figure 5:43 - Enriched metabolic pathways in CC-SW1 cells after 48 hours of co-culture...185
Figure 5:44 - Flux in 2-oxoisopentanoate and valine concentration in CC-SW1 cells over 48 hours.....187
Figure 5:45 - Exogenous 2-oxoisopentanoate reduces CC-SW1 cell viability.....189
Figure 5:46 - Exogenous 2-oxoisopentanoate has no effect on the proportion of apoptotic or viable CC-SW1 cells.....190
Figure 5:47 - Exogenous 2-oxoisopentanoate has divergent effects on CCA cell proliferation.....193
Figure 5:48 - Evaluation of cytokine expression in MMNK1 cells in mono- and co-culture with CC-SW1 cells.....196
Figure 5:49 - Quantification of differentially expressed cytokines in MMNK1 cells after indirect co-culture with CC-SW1 cells.....197

Figure 5:50 - Evaluation of cytokine expression in CC-SW1 cells in mono- and co-culture with MMNK1 cells.....199
Figure 5:51 - Quantification of differentially expressed cytokines in CC-SW1 cells after indirect co-culture with MMNK1 cells.....200

Results Chapter 3 – Interpreting the Genomic Alterations due to Indirect Cell-Cell Communication

Figure 6:1 - Normalisation and clustering of MMNK1 and CC-SW1 gene expression data from RNA-seq in.....211
Figure 6:2 - Differential gene expression analysis of MMNK1 and CC-SW1 gene expression at 48 hours.....213
Figure 6:3 - Histogram comparing enriched gene expression pathways in CC-SW1 and MMNK1 cells.....217
Figure 6:4 - Normalisation of RNA-sequencing data from MMNK1 cells.....220
Figure 6:5 - Differential gene expression analysis of MMNK1 cholangiocytes after 48 hours of co-culture with CC-SW1 cells.....222
Figure 6:6 - Histogram comparing enriched gene expression pathways in MMNK1 cholangiocytes after 48 hours of co-culture 225
Figure 6:7 - Heat Map depicting the top 100 most differentially expressed genes in MMNK1 cholangiocytes.....226
Figure 6:8 - Histogram of the KEGG pathways differentially expressed in MMNK1 cells after 48 hours of co-culture during.....227
Figure 6:9 - Enrichment plots demonstrating positive gene set correlations in MMNK1 cholangiocytes.....228
Figure 6:10 - Enrichment plots demonstrating negative gene set correlations in MMNK1 cholangiocytes.....229
Figure 6:11 - qPCR validation of RNAseq gene expression in MMNK1 cholangiocytes.....231
Figure 6:12 - qPCR validation of RNAseq gene expression exclusive to MMNK1 cholangiocytes.....232
Figure 6:13 - Validation of HSPA8, TXNIP, and TXN protein expression.....233
Figure 6:14 - Impact of HSPA8 knockdown on target protein expression in MMNK1 cholangiocytes.....235
Figure 6:15 - Knockdown of *HSPA8* leads to a reduction in cell cycle progression, irrecoverable by co-culture.....239
Figure 6:16 - Knockdown of *HSPA8* leads to an increase in apoptosis, recoverable by co-culture.....242
Figure 6:17 - RNA Validation of co-culture mediated alterations to MMNK1 cytokine expression during co-culture.....245
Figure 6:18 - Integrating MMNK1 metabolomic and RNAseq data.....247
Figure 6:19 - Schematic of the asparagine metabolic pathways.....249
Figure 6:20 - Gene expression of ASNS in co-culture.....250
Figure 6:21 - Protein expression of ASNS in co-culture.....251
Figure 6:22 - Exogenous asparagine reduces ASNS protein expression 252
Figure 6:23 - Schematic of the choline metabolism.....253
Figure 6:24 - Evaluation of choline metabolism gene expression via RNA-seq.....254
Figure 6:25 - Co-culture increases the gene expression for choline metabolism.....255
Figure 6:26 - Co-culture decreases CHKα protein expression.....256

Figure 6:27 - Exogenous choline decreases CHKα protein expression.....257
Figure 6:28 - Schematic of the creatine metabolic pathway.....258
Figure 6:29 - RNAseq evaluation of creatine metabolism gene expression.....259
Figure 6:30 - Exogenous creatine reduces *EXTL1* and *IDO1* gene expression.....261
Figure 6:31 - Normalisation of CC-SW1 gene expression data from RNA-sequencing.....264
Figure 6:32 - Differential gene expression analysis of CC-SW1 after 48 hours of co-culture with MMNK1 cholangiocytes.....266
Figure 6:33 - Histogram of enriched Hallmark Gene Pathways in CC-SW1 cells after 48 hours of co-culture.....270
Figure 6:34 - Heat Map depicting the top 100 most differentially expressed genes in CC-SW1 cells.....271
Figure 6:35 - Histogram of enriched KEGG pathways in CC-SW1 cells after 48 hours of co-culture 272
Figure 6:36 - Enrichment plots demonstrating positive gene set correlations in CC-SW1 cells.....273
Figure 6:37 - Enrichment plots demonstrating positive gene set correlations in CC-SW1 cells.....274
Figure 6:38 - qPCR validation of RNAseq gene expression in CC-SW1 cells.....276
Figure 6:39 - RNA Validation of co-culture mediated alterations to CC-SW1 cytokine expression during co-culture.....279
Figure 6:40 - Integrating CC-SW1 metabolomic and RNAseq data.....281
Figure 6:41 - Schematic of 2-oxoisopentanoate metabolic pathways.....283
Figure 6:42 - Evaluation of 2-oxoisopentanoate metabolism using gene expression data from RNAseq.....284
Figure 6:43 - Exogenous 2-oxoisopentanoate increases target gene expression in CC-SW1 cells.....286
Figure 6:44 - Principle Component Analysis of The Cancer Genome Atlas (TCGA) data.....287
Figure 6:45 - Differential gene expression analysis of CCA vs normal tissue.....289
Figure 6:46 - Metabolic Gene Set Analysis of TCGA RNA-seq data classified by KEGG pathways.....291
Figure 6:47 - Table of gene expression data from The Cancer Genome Atlas (TCGA) in CCA tumour samples for our genes of interest.....293
Figure 6:48 - Table of gene expression data from The Cancer Genome Atlas (TCGA) in CCA tumour samples for our metabolic genes of interest.....297

Results Chapter 4 – Evaluation and Inhibition of the Epigenome during Co-Culture
Figure 7:1 - CCA cell resistance to 5-Fluorouracil.....307
Figure 7:2 - Epigenetic inhibitor screen in CCA cells.....309
Figure 7:3 - The effect of the epigenetic inhibitors UNC0642 and SGC3027 on iCCA cell viability.....311
Figure 7:4 - The effect of co-culturing CC-SW1 cells with MMNK1 cholangiocytes on epigenetic inhibitor efficacy.....312
Figure 7:5 - Relative mRNA gene expression of EHMT1, EHMT2, and PRTM7 in MMNK1 and CC-SW1 cells.....315
Figure 7:6 - Relative mRNA gene expression of EHMT1, EHMT2, and PRTM7 in TCGA tumour samples.....316

List of abbreviations

Abbreviation	Definition
AML	Acute Myeloid Leukaemia
APS	Ammonium Persulfate
AURKA	Aurora Kinase A
BSA	Bovine Serum Albumin
CAF	Cancer Associated Fibroblast
CCA	Cholangiocarcinoma
CFI	Complement Factor I
CK-7	Cytokeratin-7
CK-19	Cytokeratin-19
CTGF	Connective Tissue Growth Factor
DGE	Differential Gene Expression
DNMT	DNA Methyltransferase
DRC	Ductular Reactive Cholangiocytes
eCCA	Extrahepatic Cholangiocarcinoma
ECM	Extracellular Matrix
EGF	Epidermal Growth Factor
EMT	Epithelial-Mesenchymal Transition
EpCAM	Epithelial Cell Adhesion Molecule
EXTL1	Exostosin Like Glycosyltransferase 1
EZH2	Enhance of Zeste Homolog 2
FAP	Fibroblast Activation Protein Alpha
FBS	Foetal Bovine Serum
FGFR	Fibroblast Growth Factor Receptor
FSP-1	Fibroblast Specific Protein
GSEA	Gene Set Enrichment Analysis
HDAC	Histone Deacetylase
HGF	Hepatocyte Growth Factor
HMT	Histone Methyltransferase
HPLC	High-Performance Liquid Chromatography
HSPA8	Heat Shock Protein Family A [Hsp70] Member 8
iCCA	Intrahepatic Cholangiocarcinoma
IDH	Isocitrate Dehydrogenase
IDO1	Indoleamine 2,3-Dioxygenase 1
KCNK3	Potassium Two Pore Domain Channel Subfamily K Member 3
KL	Klotho
LBP	Lipopolysaccharide Binding Protein
LPS	Lipopolysaccharide
MCP-1	Monocyte Chemoattractant Protein-1 (Chemokine Ligand 2, CCL2)
MET	Mesenchymal-Epithelial Transition
MGAT3	1,4-Mannosyl-Glycoprotein 4- Beta-N-Acetylglucosaminyltransferase
MSEA	Metabolic Set Enrichment Analysis
NGS	Next-Generation Sequencing
NPPB	Natriuretic Peptide B

PCA	Principal Component Analysis
PDX	Patient-Derived Xenograft
PHGDH	Phosphoglycerate Dehydrogenase
PI	Propidium Iodide
PIGF	Placental Growth Factor
PSC	Primary Sclerosing Cholangitis
Rb	Retinoblastoma
RNA-seq	RNA-Sequencing
SASP	Senescence-Associated Secretory Phenotype
SAM	S-Adenosyl Methionine
SDS-PAGE	Sodium Sodecyl Sulfate–Polyacrylamide Gel Electrophoresis
SOCS-3	Suppressor Of Cytokine Signalling 3
SOX9	Sex-Determining Region Y-Box 9
SPRR2A	Small Proline Rich Protein 2A
TAM	Tumour Associated Macrophage
TEMED	Tetramethylethylenediamine
TNF-α	Tumour Necrotic Factor Alpha
TXN	Thioredoxin
TXNIP	Thioredoxin Interacting Protein
VEGF	Vascular Endothelial Growth Factor

1 Introduction

1.1 Cholangiocarcinoma

Cholangiocarcinoma (CCA) is a rare, malignant cancer occurring in the biliary tract, and constitutes the second most common primary hepatobiliary malignancy, after hepatocellular carcinoma (HCC)(1). Prognosis for patients diagnosed with CCA is very poor, primarily due to early metastatic propensity, and elevated resistance to conventional chemotherapeutics.

1.1.1 Anatomy of CCA

The biliary tract is a network of interconnected tubular structures that play a crucial role in the production, transportation, and storage of bile (Figure 1:1). Bile is a digestive fluid produced by the liver, which is used to aid the digestion and absorption of fats in the small intestine. Bile is transported through the bile ducts for storage in the gallbladder, and is secreted into the duodenum of the small intestine via the distal bile ducts passing through the pancreas.

Bile is secreted through Ampulla of Vater, a small opening located where the common bile duct and the pancreatic duct meet, which is controlled by the Sphincter of Oddi, a muscular valve that controls the flow of bile and pancreatic secretions into the small intestine.

The intrahepatic and extrahepatic bile ducts are lined by hyper-specialised epithelial cells called cholangiocytes. From the small to large bile ducts, cholangiocytes acquire a greater degree of differentiation, and CCA's occurring in the small and large ducts often display different histological morphology (2).

CCA's are divided into intrahepatic cholangiocarcinoma (iCCA) for tumours occurring within the bile ducts inside the liver, and extrahepatic cholangiocarcinoma (eCCA) for tumours occurring in the bile ducts located outside the liver, and include the common hepatic duct and the common bile duct (Figure 1:1). The common hepatic duct receives bile from the intrahepatic ducts, while the common bile duct carries bile from the liver to the small intestine. eCCA can be further subdivided into perihilar cholangiocarcinoma (pCCA) for tumours occurring at the junction where the left and right bile ducts merge outside the liver (also known as Klatskin tumours), and distal cholangiocarcinoma (dCCA) for tumours occurring in the distal bile ducts, away from the liver or adjacent to the pancreas (3).

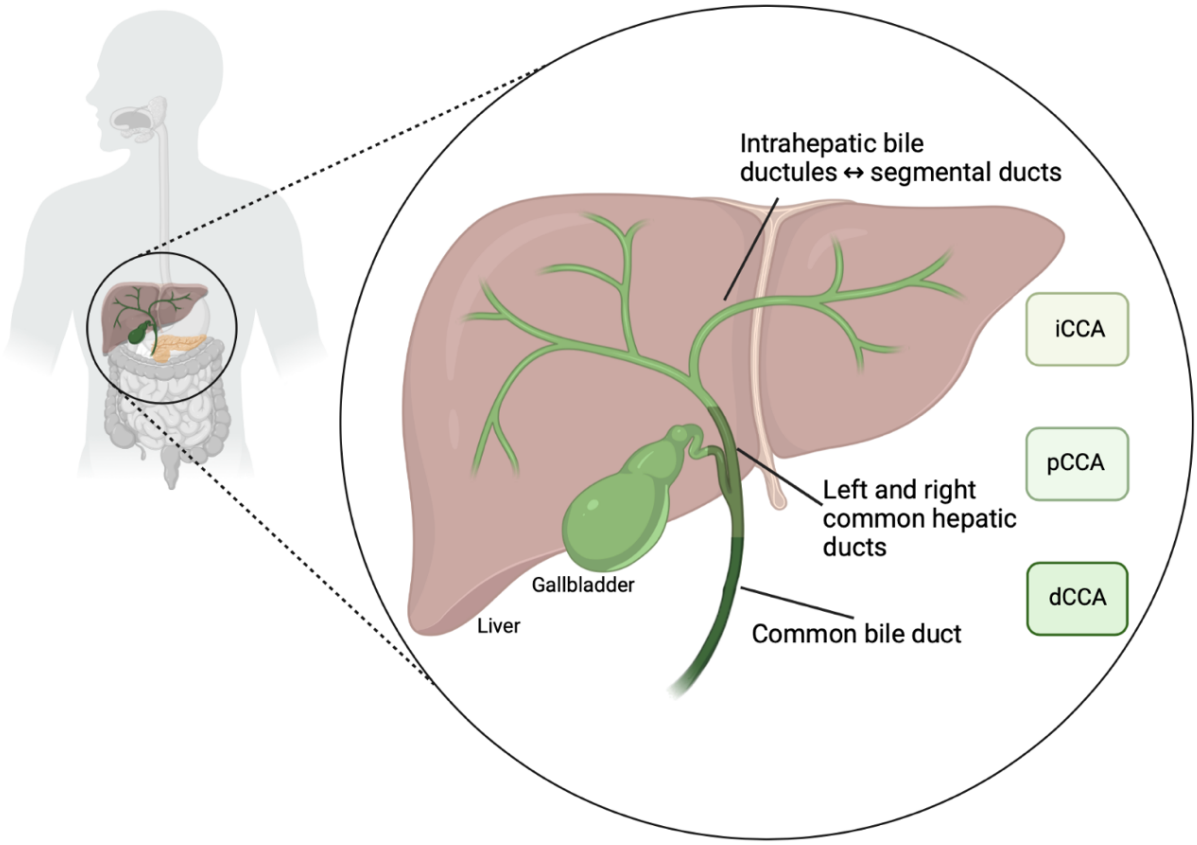


Figure 1:1 – Structure of the biliary tree. *CCA's are classified according to anatomical location, either intrahepatic (iCCA) or extrahepatic (eCCA), which can be further subdivided into perihilar (pCCA), and distal (dCCA). Adapted from "Cholangiocarcinoma" P.J. Brindley. Nat Rev Dis Primers 7, 65 (2021). https://doi.org/10.1038/s41572-021-00300-2.*

1.1.2 Tumour classification

As well as anatomical classification, CCA's are further classified by gross morphology classification and histological classification. There are 3 primary morphological classifications: mass-forming, whereby the tumour forms a distinct mass or nodular lesion; intraductal, whereby the tumour grows within the bile ducts, commonly causing biliary obstruction; and periductal-infiltrating, whereby the tumour infiltrates the walls of the bile ducts themselves, without forming a distinct mass (Figure 1:2).

Likewise, there are also 3 primary histological classifications: well-differentiated CCA, in which the tumour cells phenotype closely resembles that of normal bile duct cells; moderately differentiated CCA, in which only some of the tumour cells resemble the normal bile duct phenotype; and poorly differentiated CCA, in which tumour cells have marked abnormalities and show little resemblance to the phenotype of normal bile duct cells.

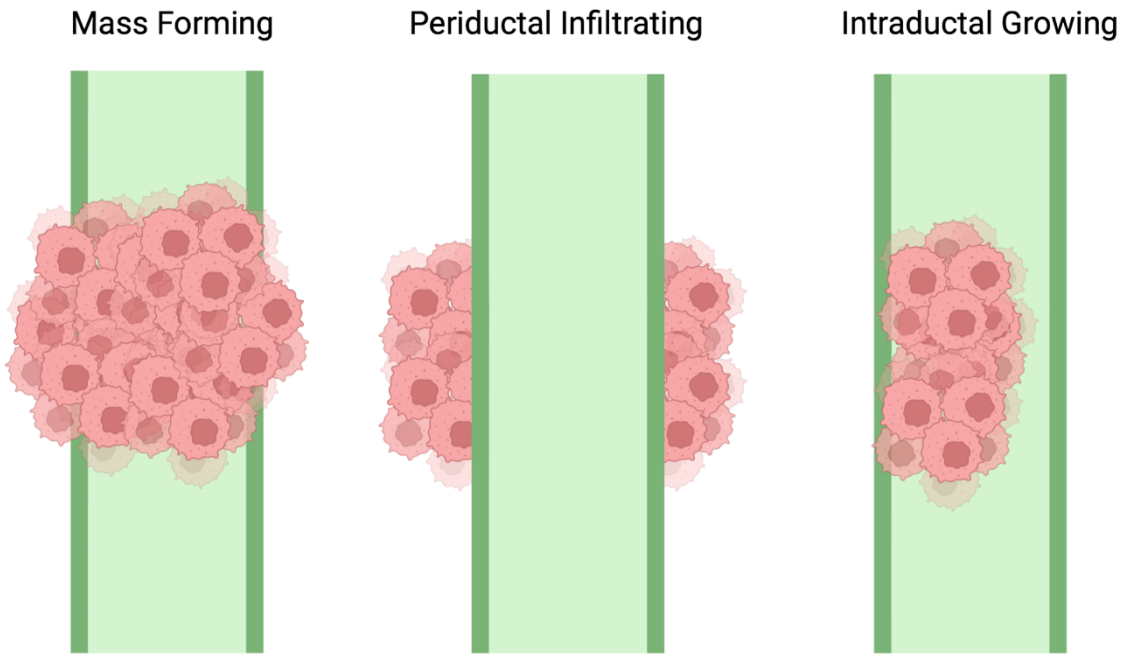


Figure 1:2 *- CCA tumour morphology. There are 3 primary growth patterns that iCCA follows: mass-forming, periductal infiltrating, and intraductal growing. Adapted from J. Banales. Cholangiocarcinoma: current knowledge and future perspectives consensus statement from the European Network for the Study of Cholangiocarcinoma (ENS-CCA). Nat Rev Gastroenterol Hepatol 13, 261–280 (2016). https://doi.org/10.1038/nrgastro.2016.51.*

1.1.3 Incidence and Epidemiology

In the UK and Europe, a cancer is classified as rare if less than 6 in 100,000 people are diagnosed each year (4). CCA is therefore classified as a rare cancer, as the incidence in the UK and Europe is around 0.3–3.5 cases per 100,000 people, although evidence (5), suggests this is increasing.

CCA is more commonly diagnosed in individuals over the age of 60, and is more common in males, with a male to female dominance of 1.2-1.5 : 1.0 (6). Interestingly there is also evidence to show that female patients with CCA have better prognosis than male patients with CCA, although the cause for this is unknown.

CCA is highly prevalent in South East Asia due to infection with endogenous liver flukes, whilst cases in the West are typically spontaneous. The highest incidence of CCA is centralised on South East Asia, specifically Northeast Thailand, which exhibits the highest CCA rate in the world, where CCA accounts for 90% of hepatobiliary cancers (7). In the past 10 years, the incidence of CCA has been increasing globally (8). In Europe, the incidence of iCCA is rising whilst the rate of eCCA is falling, except in Denmark, Norway and the Czech Republic where the reverse is true (9). Not only this, but the mortality of CCA is also increasing worldwide (10).

1.1.4 Risk Factors

The pathophysiological mechanism behind most cholangiopathies including cholangiocarcinogenesis is primarily attributed to chronic inflammation. Patients with the chronic inflammatory condition Primary Sclerosing Cholangitis (PSC) have a significantly increased risk of developing CCA, as well as those with cholelithiasis (gallstones). Likewise, metabolic conditions such as non-alcoholic fatty liver disease (NAFLD), and type 2 diabetes

also contribute to the risk of CCA in the West, as well as risk factors also associated with an increased risk of HCC, such as liver cirrhosis, and chronic hepatitis B or C infection. The radioactive contrast agent thorotrast has also been linked to an increased risk of CCA due its carcinogenic properties, however usage for medical imaging ceased in the 1950's (1,11).

The unusually high incidence of CCA in South EA is due to the parasitic infection by the liver flukes *Opisthorchis viverrini* and *Clonorchis sinensis* which are endemic to the region (12). Both flukes are currently identified as group 1 biological carcinogens by the International Agency Research on Cancer (IARC)(13). *O. viverrini* and *C. sinesis* infections lead to a 5-fold risk of CCA (7). These liver flukes infect their human host after consumption of freshwater fish infected with the parasite larvae. Unfortunately, current public health measures to reduce the consumption of these fish have been unsuccessful, and despite anti-helminthic treatment, 10% of individuals infected develop CCA (14). Likewise, genome sequencing has identified a distinct genomic profile of liver-fluke associated CCA, with an overall higher mutational rate (median 4,700 versus 3,143 somatic mutations per tumor) including mutations in SMAD4 and TP53 as well as ERBB2 amplifications (15). Further whole-genome sequencing is required to elucidate the full genetic component contributing to CCA development.

1.1.5 Clinical Presentation & Diagnosis

British Society of Gastroenterology first published guidelines for the diagnosis and treatment of CCA in 2002 (16), which was updated in 2012 (17) as the clinical presentation of CCA can vary depending on the location, stage, and extent of the tumour. However, there are several common clinical manifestations associated with CCA, including jaundice,

abdominal pain, nausea and generalised malaise. CCA is difficult to diagnose initially, due to appearing as a generalised mass on the liver, which can lead to misdiagnosis and delays in effective treatment.

Patients with suspected CCA will undergo multiple tests to confirm the diagnosis. Typically this involves imaging the bile ducts, alongside a blood test, and histological investigation. Most commonly, magnetic resonance imaging (MRI) is used to diagnose CCA, alongside magnetic resonance cholangiopancreatography (MRCP) which uses radio waves. Endoscopic Retrograde Cholangiopancreatography (ERCP) uses x-rays, to allow for stenting to rectify bile duct obstruction and brush cytology to enable biopsy collection. Often percutaneous transhepatic cholangiography (PTC), a contrast X-ray, is used if ERCP fails. An abdominal ultrasound or Endoscopic Ultrasound Scan (EUS) can also be used to guide a biopsy. Typically, advanced/inoperable CCA is diagnosed using cytological confirmation, using either a EUS-guided or a percutaneous, US or CT guided biopsy using Fine Needle Aspiration (FNA). However, there is a general movement away from FNA due to the risk of tumour seeding along the needle tract (18). As with most solid tumours, a Positron Emission Tomography (PET) scan can be used to identify whether the cancer has metastasized to elsewhere in the body. PET scans can be combined with CT scans to produce more detailed images (PET-CT) and utilises a radioactive tracer.

Blood tests evaluating liver function (Liver Function Tests, LFTs) and bilirubin (jaundice) are used, as well as serum CA19-9 (Carbohydrate Antigen 19-9) (>129 U/ml) and CEA (Carcinoembryonic Antigen), although not specific to CCA, can be elevated. There is a key need to identify CCA-specific biomarkers, for both earlier and more accurate detection.

1.1.6 Treatment & Prognosis

Treatment of CCA depends on several factors, including anatomical location and stage of the tumour, overall health of the patient, and individual treatment preferences.

1.1.6.1 Surgical Intervention

Currently, the only curative therapy for CCA is surgical resection. However, most patients present with symptoms only once cancer has progressed sufficiently to block the duct, leading to symptoms such as jaundice, which is often late stage. Consequently, surgical intervention is limited. There is some evidence to suggest lymphadenectomy, the surgical removal of lymph nodes, can significantly improves prognosis. Some CCA patients have a stent inserted, to improve bile drainage, and reduce symptoms like jaundice. There is also some evidence supporting the use of radiotherapy in CCA (5,17).

1.1.6.2 Liver Transplantation

Liver transplantation has traditionally been considered to be contraindicated with CCA. However this remains controversial, with evidence from the Mayo Clinic utilising neoadjuvant chemoradiotherapy suggesting liver transplantation may prove beneficial, as well as the ongoing phase III TRANSPHIL trial (NCT02232932).

1.1.6.3 Chemotherapy

Chemotherapy is the primary treatment for patients with metastatic or locally-advanced stage biliary tract cancer.

The standard first-line systemic therapy for advanced CCA is a combination of cisplatin and gemcitabine, after the landmark ABC-02 trial which demonstrated superior median

progression-free survival (PFS) (8.0 vs. 5.0 months), and overall survival (11.7 vs. 8.1 months) with the combined chemotherapeutics, compared to gemcitabine alone (19). Alternative second-line treatments include capecitabine, fluorouracil, oxaliplatin, FOLFOX (leucovorin calcium (folinic acid), fluorouracil, and oxaliplatin) or a combination of the above. Neoadjuvant chemotherapy of gemcitabine and cisplatin can be used to successfully trigger the down-staging of a tumour, permitting surgical intervention and improved prognosis (17,20). Likewise adjuvant chemotherapy of capecitabine is often used post-operatively for 6 months.

1.1.6.4 Targeted Therapies

In July 2021, NICE (National Institute for Health and Care Excellence), the department responsible for the use of health technologies and clinical practice in the UK, approved the first targeted therapy for CCA, pemigatinib (21). This was a breakthrough for the CCA community, as prior to that point, and the commencement of this research project, no targeted therapy existed for CCA.

1.1.6.4.1 FGFR

Pemigatinib, is an oral, selective protein kinase inhibitor targeting FGFR (Fibroblast Growth Factor Receptor) 1, 2, and 3 (Figure 1:3) and is indicated for CCA patients with a fibroblast growth factor receptor 2 (FGFR2) fusion or rearrangement. This receptor tyrosine kinase is crucial for its role in cell signalling pathways involved in the growth, development, and maintenance of various tissues, including epithelial tissues. The FIGHT-202 trial recruited 146 patients with FGF/FGFR alterations previously treated with at least one systemic therapy (22). Of these, 107 patients with FGFR2 gene rearrangements/fusions had an overall

response rate (ORR) of 35.5% , with 2.8% achieving a complete response and 32.7% achieving partial response. Interestingly, only the patients with the FGFR2 gene rearrangements/fusions responded to Pemigatinib treatment, not those with other FGF/FGFR alterations (22).

Since then, four FGFR inhibitors have been developed specifically for CCA including Derazantinib, Infigratinib, Erdafitinib, and Futibatinib, the latter of which was approved by the FDA in the US in September 2022 and as of writing, is yet to be approved by NICE in the UK.

1.1.6.4.2 EGFR

The Human Epidermal Receptor (HER) family include epidermal growth factor receptor (EGFR) and human epidermal growth factor receptor 2 (HER2), constitute growth factor receptors responsible for the intracellular transmission of growth factor signalling. HER2 has been well established for its role in tumorigenesis (23), and HER2 mutant tumours have been targeted by a combination of pertuzumab, trastuzumab, and neratinib (Figure 1:3). Zanidatamab has yet to be formally approved by the FDA or NICE, although the results from the Phase II clinical trial released in January 2023 showed promise in gastro-oesophageal cancer (24).

1.1.6.4.3 IDH1/2

Tumour profiling studies have shown that ~40% of biliary tract cancers contain potentially actionable mutations, and of these, isocitrate dehydrogenase (IDH) 1/2 mutations constitute the largest proportion (10%) (25). IDH1/2 enzymes catalyse the catabolism of isocitrate to α-ketoglutarate, and therefore function as metabolic regulators. However,

mutated IDH further catabolises α-ketoglutarate to 2-hydroxyglutarate, which functions as a on oncometabolite, promoting CCA growth. Ivosidenib is an oral, small-molecule inhibitor of mutant IDH1, and was approved by the FDA for CCA in August 2021 (Figure 1:3). The IDH1 mutant inhibitors NCT02381886, NCT02481154, NCT03684811 are currently under investigation in clinical trials.

1.1.6.4.4 BRAF

BRAF mutations occur in 1−3% of iCCA cases (26). BRAF is a kinase with mitogenic properties, promoting cell proliferation and survival. Much like in colorectal cancer, CCA tumours containing the BRAF V600E codon mutation have seen little benefit from treatment with BRAF inhibitors likely due to EGFR pathway circumvention. The dual application of the BRAF inhibitor Dabrafenib with the MEK inhibitor Trametinib has been suggested to counter this issue (27)(Figure 1:3).

1.1.6.4.5 Immune Checkpoint Inhibitors

Typically CCA is considered “immune-cold” due to immune evasion, but there is growing evidence to suggest immune checkpoint inhibitors, such as anti-PD-1 (pembrolizumab or nivolumab), anti-PD-L1 (durvalumab), and anti-CTLA-4 (ipilimumab or tremelimumab) therapies are beneficial for CCA patients (28)(Figure 1:3).

However, the obstacle facing the development and implementation of molecular therapies for CCA is still the heterogenous nature of CCA, as well as the high prevalence of chemoresistance (18). Therefore, it is imperative more work is conducted in order to

elucidate the molecular mechanisms responsible for aggressive, malignant and resistant development of CCA, to expose novel, targetable vulnerabilities.

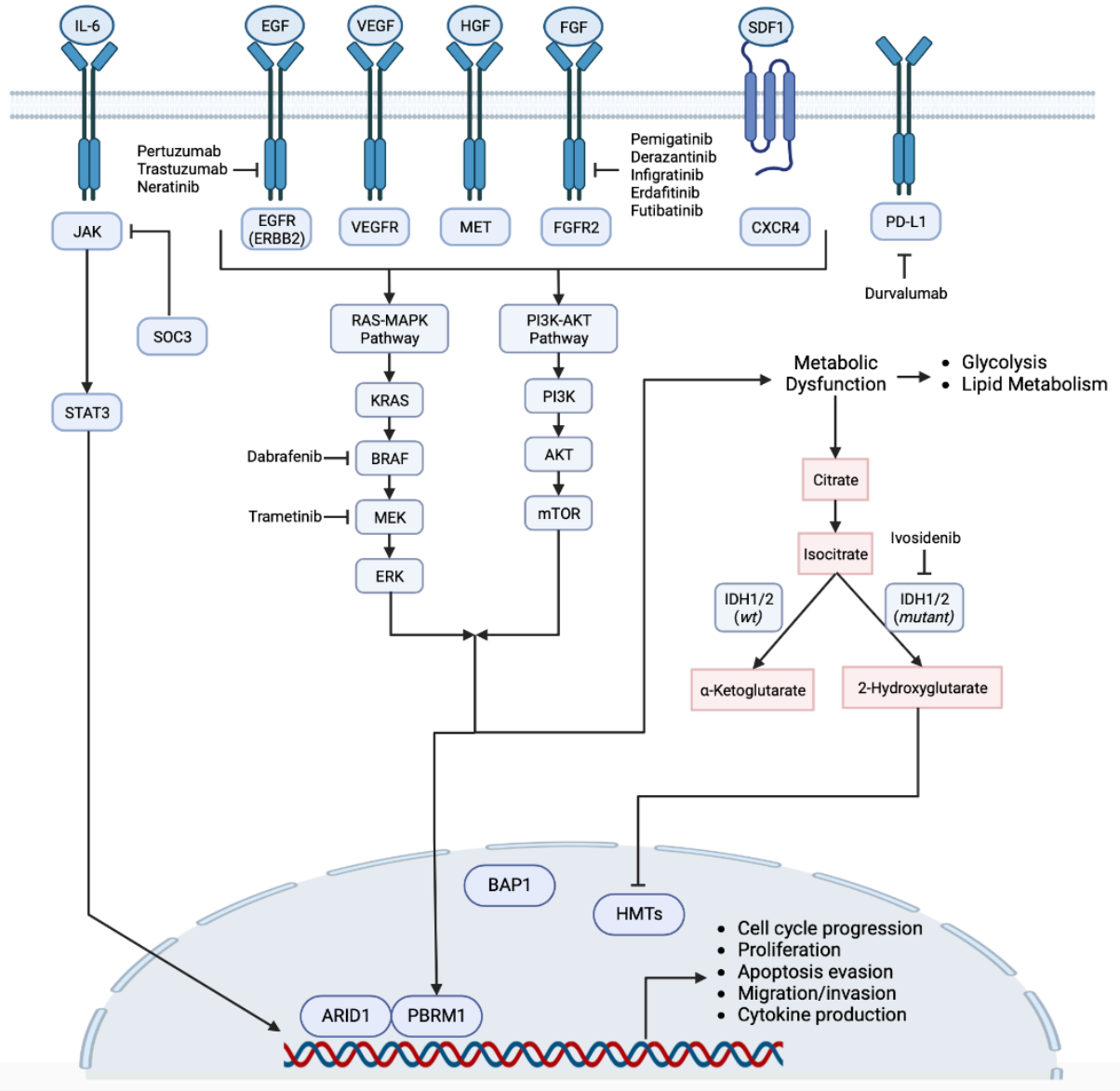


Figure 1:3 *- Key molecular pathways and their respective small molecule inhibitors in CCA development. Adapted from J. Banales. Cholangiocarcinoma 2020: the next horizon in mechanisms and management. Nat Rev Gastroenterol Hepatol 17, 557–588 (2020). https://doi.org/10.1038/s41575-020-0310-z.*

1.2 CCA Tumour Microenvironment

The tumour microenvironment (TME) is currently recognized as a considerable driving force behind the emergence of the hallmarks of cancer. The TME itself is a complex mix of ECM, inflammatory immune cells, vasculature, and activated fibroblasts. One of the distinguishable features of CCA is the presence of a desmoplastic stroma; the increased deposition of collagens present in the ECM. The interaction between CCA cells and the tumour stroma has been proven to be crucial in the tumorigenesis process (29,30) and CCA cells have been shown to secrete a multitude of factors to enable cellular cross talk with surrounding fibroblasts, hepatic cells, inflammatory cells, and endothelial cells. Previous genomic profiling of CCA-associated stromal cells highlighted gene expression changes in metabolism, cell cycle, signalling, and ECM secretion, which correlated with poor clinical prognosis (31).

Often overlooked is the impact of neighbouring cholangiocyte cells, the non-transformed, non-cancerous epithelial cells at the boundary surrounding the tumour, on the TME. One of the first interactions cancer cells experience during tumorigenesis is between themselves and the normal, non-cancerous neighbours. A mutual paracrine communication occurs between the cholangiocytes and the CCA cells in this environment. These normal cells undergo concurrent changes with cancer cells that affect initiation, progression, and metastasis of cancer development. Ultimately, the interaction triggers distinct reciprocal changes in both compartments, leading to modulation of the environment in both a restrictive and permissive manner depending on time.

1.2.1 Pathological relevance of Paracrine Signalling in CCA

Indirect cellular communication encompasses two main forms: soluble chemical signal communication and extracellular matrix-mediated communication. Soluble chemical signals facilitate paracrine and autocrine communication, allowing the transmission of signalling molecules between cells through extracellular vesicles. On the other hand, extracellular matrix-mediated communication primarily involves the establishment of interaction links between cells and the extracellular matrix (30).

CCA cells can secrete paracrine factors that promote their own growth, survival, and invasive capabilities. These factors, such as growth factors, cytokines, and chemokines, can stimulate the proliferation of nearby cancer cells and induce angiogenesis, facilitating the formation of new blood vessels to supply glucose and oxygen to the tumour. This signalling can also mediate surrounding cells, in turn causing the increased secretion of chemokines, cytokines, growth factors, and matrix metalloproteinases which further contributes to the tumour aggressiveness (32).

We hypothesise that CCA cells trigger the remodelling of the tumour stroma via paracrine signalling, for the recruitment and activation of surrounding cholangiocytes; which in turn leads to chronic inflammation and the recruitment of other inflammatory and mesenchymal cell types to promote the long term survival of the tumour. We wish to investigate the molecular and functional changes during this early interaction between cholangiocytes and CCA cells, which occurs prior to the cholangiocyte transition from gatekeeper of tissue homeostasis to the developer of the cancer niche, in line with CCA development and progression.

1.2.2 Epithelial-mesenchymal transition

Prior to the degradation of the basement membrane, the basal lamina is a barrier to tumour growth and migration. In the early stages of tumour development, only the neighbouring non-cancerous cells can obstruct or support the tumour growth. When the cholangiocytes and surrounding immune cells lose the homeostatic battle, the true aggressiveness of the cancer is revealed, with the invasion-metastasis cascade activated and actively supported by the surrounding stroma.

One mechanism for increased cell mobility and invasive capabilities is Epithelial-Mesenchymal Transition (EMT). EMT allows cells to develop a more migratory phenotype, increasing their invasive propensity. EMT is controlled by a group of master transcription factors: SNAIL, SLUG, TWIST1/2 and ZEB1/2 (Figure 1:4). These transcription factors repress the expression of epithelial genes (E-cadherin, Cytokeratin 19) whilst inducing the expression of mesenchymal genes (N-cadherin, Vimentin, MMP's) leading to a reduction in cell-cell adhesion and apical-basal polarisation.

EMT gene expression in CCA cells correlates with poor prognosis (29). CCA cells express high levels of N-cadherin, Vimentin with concurrent low expression levels of E-cadherin and CK19, with an elongated morphology (33). EMT is often triggered by factors in the tumour microenvironment, for example EGF is produced by malignant cholangiocytes, as well as TNF-α which is often derived from TAMs and promotes SNAIL, ZEB2, and MMP-9 expression (34). Crucially, EMT facilitated by paracrine factors released by neighbouring cells can lead to the enhanced metastatic spread of CCA.

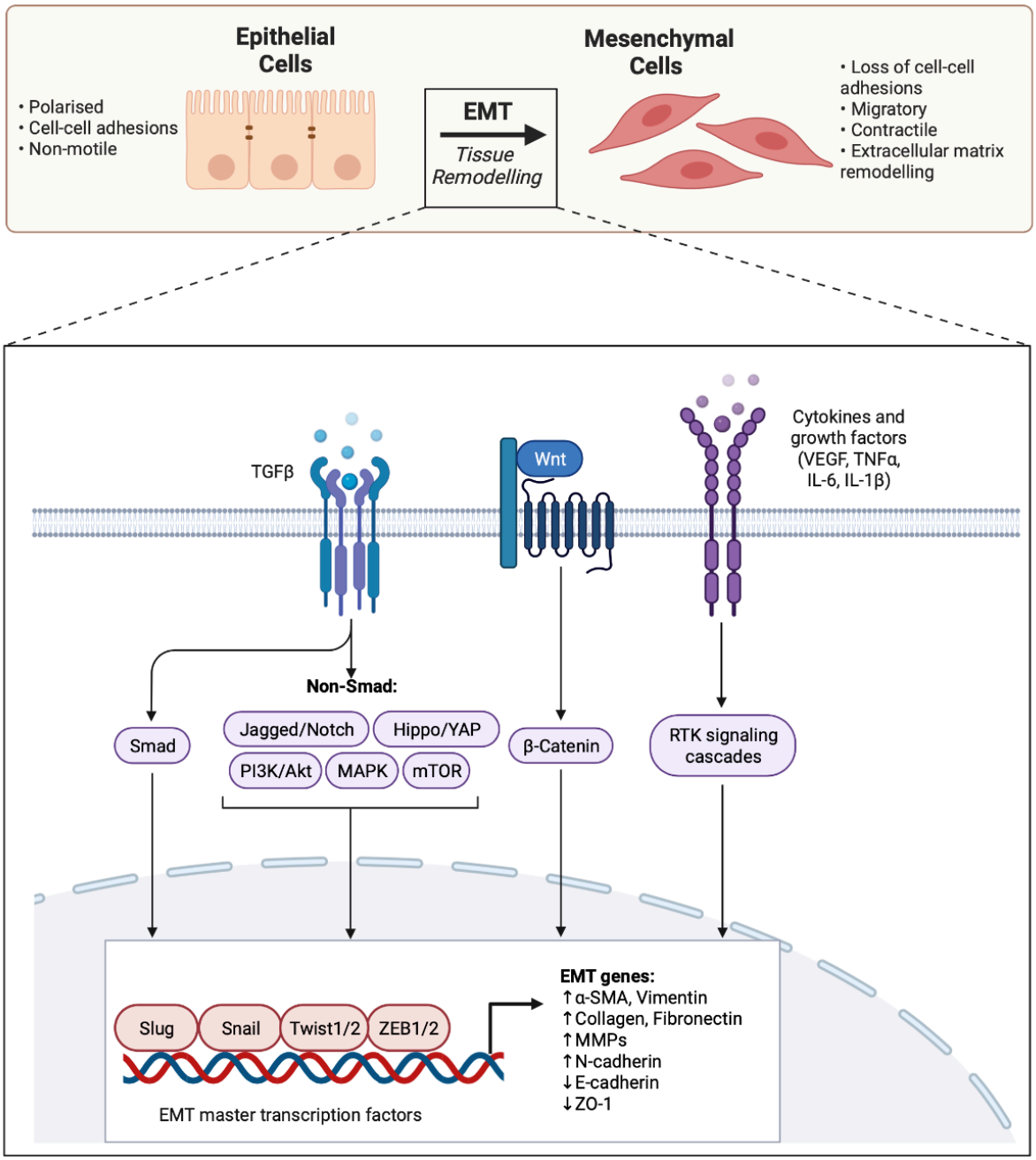


Figure 1:4 *- The molecular processes behind the epithelial-mesenchymal transition. Adapted from AS. Ng. Novel therapeutic strategies: targeting epithelial– mesenchymal transition in colorectal cancer. Lancet Oncol 22, 358-68 (2021). https://doi.org/10.1016/S1470-2045(21)00343-0*

1.2.3 Inflammation

The connection between proliferation and inflammation is a process that has been conserved throughout evolution, because inflammatory cascades that are transient or self-limited can assist in regeneration responses (35). However, chronic inflammation has been identified as a key driver for CCA tumorigenesis. The persistent 'unhealing wound' triggers inflammatory and epithelial cells, leading to a TME enriched with cytokines and growth factors (36). High levels of the inflammatory cytokines IL-6, CCL2, and MCP1 have been identified in the CCA TME (37). These pro-inflammatory cytokines lead to increased oxidative stress via NOS generation, as well as triggering cell proliferation and inhibition of apoptosis. What's more, the lack of ability to eliminate dysfunctional cells further contributes to the accumulation of somatic mutations (38), which are potentially conducive to tumorigenesis, and the heterogenous tumour.

The interleukin IL-6 is pro-oncogenic and mitogenic for cholangiocyte cells (39), and is secreted by numerous cell types including epithelial cells, stromal cells (e.g., fibroblasts, monocytes, macrophages), and normal cholangiocytes. IL-6 signal transduction occurs via the JAK/STAT3 pathway, triggering the expression of the anti-apoptosis protein MCL-1, further contributing to oncogenic progression (40).

1.2.4 Immune Response

Paracrine signalling can also impact the immune response within the tumour microenvironment. The chemokines PDGF, CCL2, CSF1, and VEGF are continually secreted by malignant cholangiocytes, and can trigger fibroblast migration, monocyte migration, as well as lymphangiogenesis. In turn, this reactive tumour microenvironment can trigger

fibroblasts and monocytes to differentiate into cancer-associated fibroblasts (CAFs) and tumour-associated macrophages (TAMs) respectively, which uses further paracrine signalling to support the malignant development of the tumour (41,42). Moreover, the presence of TAM's and regulatory T cells (Tregs), can contribute to chemoresistance and tumour growth via the secretion of cytokines and growth factors that promote CCA cell survival, and suppress anti-tumour immune responses respectively (29,30).

1.2.5 Chemoresistance

CCA often displays resistance to standard chemotherapeutics. Paracrine signalling can influence the tumour microenvironment to modulate drug delivery and response, contributing to therapeutic resistance in CCA (1,5,43). Likewise, CCA is characterized by extensive fibrosis which forms a physical barrier impeding drug penetration into the tumour cells, limiting the effectiveness of chemotherapy. Additionally, the activated CAF's within the stroma further produce factors that promote chemoresistance, supporting CCA survival (41).

1.3 Cell-cell interactions in CCA

CCA cells interact with neighbouring liver cells, endothelial cells, immune cells, stromal cells, fibroblasts, as well as cholangiocyte cells during the development and progression of CCA. Two primary types of stromal cells are considered to contribute to CCA growth, Cancer-Associated Fibroblasts (CAFs)(44) and Tumour Associated Macrophages (TAMs). CAF's are activated via TGF-B, FGF, and PDGF secretion by TAMs(1). Signalling molecules like SDF1, Il-1b, EGF, Notch 3, and Hedgehog are secreted by activated CAFs, which further supports the invasion and proliferation of CCA(29). Cholangiocytes are also intimately associated with

other cells within the tumour niche, including HSCs and macrophages, as well as the extracellular matrix.

1.3.1 Cholangiocytes

Cholangiocytes are the epithelial cells that line the biliary tract (Figure 1:2). With distinct apical and basolateral plasma membrane domains, cholangiocytes utilise multiple solute transporters to adjust the composition of bile. The impact of non-transformed neighbouring cholangiocytes on the progression of CCA development has not previously been evaluated.

The increased expression of oestrogen receptor alpha (ERα) has been highlighted in cholangiocytes(45), culminating in enhanced cell growth, as well as dopamine, serotonin, histamine, and leptin(46). Currently, there is controversy over the origin of CCA cells, whether this be cholangiocytes, hepatocytes, or stem cells.

A small subset of immature cholangiocytes have the capacity to differentiate into hepatocyte cells, during a process called the ductular reaction (DR), which occurs after chronic liver damage (47). These cholangiocytes can actually support regeneration of the liver parenchyma when hepatocyte proliferation is impaired (48). The ductular reaction occurs during a persistent inflammatory response, or extensive acute tissue damage, leading to ineffective repair, angiogenesis, aberrant bile duct proliferation and tissue fibrosis (49). This reactive reaction occurs in response to both endogenous and exogenous insults (50). Morphogenic signals such as Wnt/β-catenin, Hedgehog, YAP/Hippo, Notch, TWEAK, and Fn14 have been shown to trigger the ductular reaction (51).

Activated cholangiocytes are typified by increased proliferation and pro-fibrotic and pro-inflammatory secretions (52). These hyper-proliferative cholangiocytes exhibit an altered secretory profile, with increased TNF-a, IL-6, MCP1, PDGF, VEGF secretion, highlighting the pro-inflammatory behaviour. In mice, depletion of cIAP1 and cIAP2 in cholangiocyte cells resulted in the non-canonical activation of NF-κB and induction of the fibroinflammatory biliary phenotype (53). Likewise, depletion of cIAP1 and cIAP2 has been identified in cholangiocytes from patients with PSC, a condition with similar proinflammatory profile (54).

Alternatively, some cholangiocytes can acquire a hypersecretory state, known as the senescence-associated secretory phenotype (SASP). This phenomenon attenuates tissue homeostasis and maintains senesce behaviours via the secretion of growth factors, cytokines, chemokines, and protease enzymes. The senescent phenotype is typified by irreversible cell cycle withdrawal (55). We also see up-regulation of antiapoptotic pathways in conjunction with altered gene expression, enhanced cytokine and growth factor secretion, and metabolic dysfunction (55). Senescent cholangiocytes have also been shown to activate and trigger the migration of the monocytic cell line THP-1 via conditioned media alone. This effect was not triggered by normal cholangiocytes, and illustrates the secretion of monocyte-attractant chemokines by these senescent cholangiocytes, and this process was ablated by blocking the key cholangiocyte SASP cytokines IL-6, IL-8, and MCP1 (49,56).

Both ductular reactive (DR) cholangiocytes and senescent cholangiocytes (SASP) are involved in chronic liver diseases (57,58). The ductular reactive cholangiocytes actually have a similar secretory profile to these SASP-associated cholangiocytes. This SASP phenotype

and cholangiocyte senescence can promote activation and propagation of myofibroblasts, contributing to the tissue fibrosis. Increased expression of EMT markers including Vimentin, Snail and MMP2, and decreased expression of E-cadherin are seen in reactive cholangiocytes. Both these compartments contribute to tissue disease progression through fibroinflammatory behaviour (46).

1.4 Molecular Phenotype

1.4.1 Genomic component of CCA

Mutations in classical proto-oncogenes such as KRAS, EGFR, FGFR2, ERBB2, MET, and IDH1/2 as well tumour suppressor genes like TP53, SMAD4, ARID1A, PBRM1, and BAP1 have been identified in CCA (59,60). Tumour location and aetiology contribute to the specific oncogenetic mutations in CCA. Mutation in KRAS and ERBB2 are more prevalent in eCCA, compared to FGFR2, MET, IDH1/2, ARID1A, PBRM1, and BAP1 mutations which are more prevalent in iCCA (59,60) . Likewise, liver-fluke associated CCA exhibits a vastly different molecular profile to spontaneous cases. TP53 mutations occur more frequently in liver fluke-related CCA, whereas mutations in IDH1/2 and BAP1 are more likely in spontaneous CCA (61). As mentioned previously, chromosomal translocations involving the FGFR2 gene are identified in around 15% of iCCA cases(62), whilst IDH mutations occur in 4% of cases (5). Likewise, aberrant activation of both the Notch and Hedgehog pathways (Figure 1:3) have been reported in cholangiocarcinogenesis (5).

1.4.2 Epigenetic component of CCA

Epigenetic alterations within CCA cells have been shown to have a crucial part in CCA development, as well as epigenetic alterations caused by the tumour reactive stroma (63).

Epigenetic silencing via promoter hypermethylation in tumour suppressor genes such as SOCS3, CDKN2A, APC, and RASSF1 has been repeatedly identified in CCA (64). SOC3 acts a negative-feedback regulator of the JAK/STAT3 axis, and as such the reduction in SOC3 expression via epigenetic silencing contributes to atypical IL-6 signalling in CCA (65). BRCA1 associated protein (BAP)1 is a nuclear deubiquitylating enzyme, responsible for the attenuation of ubiquitination on histone 2A, thereby modulating chromatin structure and gene expression (66).

Moreover, accumulation of the onco-metabolite 2-hydroxyglutarate in IDH mutant CCA leads to aberrant epigenetic modifications due to impaired function of DNA methyltransferase (DNMT) and histone methyltransferase (HMT) enzymes (67). Likewise, mutant IDH1/2 has been shown to inhibit expression of the master regulator of hepatocytic differentiation hepatocyte nuclear factor 4α (HNF4a), in HPC-derived iCCA (67).

1.4.3 Metabolic component of CCA

CCA displays distinct altered cellular metabolism and energetics compared to cholangiocyte cells, such as impaired mitochondrial function, decreased oxidative phosphorylation (OXPHOS), and increased reliance on glycolysis (68). Increased glycolysis leads to a metabolic shift to promote the production of lactate, and glucose metabolism is further altered to upregulate glucose transporters such as GLUT1, and key glycolytic enzymes to ensure a continuous supply of glucose for ATP production. Moreover, mitochondrial dysfunction causes increased production of reactive oxygen species (ROS). CCA cells also exhibit altered amino acid metabolism, through upregulation of amino acid transporters and enzymes involved in amino acid metabolism to support protein synthesis, energy production, and redox balance (69–71). Oncogenic signalling pathways, such as the MAPK

and PI3K/AKT pathways, can drive metabolic reprogramming in CCA cells, which regulates glucose metabolism, lipid metabolism, and other metabolic processes (1). Ultimately, the altered cellular metabolism in CCA cells contributes to tumour growth, survival, and progression. Targeting metabolic pathways involved in altered metabolism in CCA, such as glycolysis or lipid metabolism, holds promise as a potential therapeutic avenue.

2 Research aims and objectives

In brief, we wish to uncover the molecular pathways, signalling cascades, and cellular processes triggered by cholangiocyte paracrine signalling that contribute to CCA development. A deeper understanding of the underlying mechanisms driving CCA development, progression, and invasion is crucial, as the insights discussed here could provide a springboard for the development of potential therapeutic targets and as such, more effective treatment strategies.

This study aimed to:

1. Investigate the reciprocal effects of non-cancerous cholangiocytes on CCA cells *in vitro*
2. Identify the molecular mechanisms regulating the interaction, with a focus on the shift in metabolism and gene expression
3. Evaluate the impact of cholangiocytes on CCA sensitivity to epigenetic inhibitors

3 Materials and Methods

3.1 Cell lines and culture

Intrahepatic human cholangiocarcinoma (iCCA) cell lines CC-SW1 (72), CC-LP1 (72), and SNU1079 (73) and extrahepatic human cholangiocarcinoma (eCCA) cell line SNU1196 (73), were kindly provided by Professor Stuart Forbes, Director of the Institute for Regeneration and Repair and Centre for Regenerative Medicine, University of Edinburgh. The immortalised human cholangiocyte cell line MMNK1 (74) was purchased from Sekisui XenoTech, Japan. The primary human cholangiocyte cell line NHC3 was kindly provided by Professor Jesus Bañales, Head of the Liver Diseases Group at the Biodonostia Health Research Institute, Spain.

All non-primary cell lines were cultured in high-glucose Dulbecco's Modified Eagle Medium (DMEM, Gibco), supplemented with 10% (v/v) foetal bovine serum (FBS, Sigma) and 1% L-glutamine (v/v) (Gibco)(denoted as Complete culture media), and maintained at 37°C in the presence of 5% CO_2. Cells were passaged regularly at 70-90% confluency in a T75 growth flask. Sterile phosphate buffered saline (PBS, Oxoid) was used to wash cells before detachment with Trypsin (Lonza).

The primary human cholangiocyte cell line NHC3 was cultured in DMEM/F12 supplemented as per the directions of Prof. Bañales, in a T75 growth flask coated with thin collagen prior to passaging of the cell lines(75).

3.2 Indirect Co-Culture

Co-culture experiments utilised transwell inserts (Figure 3:1) with a 0.4 µM pore size (Sarstedt, #83.3930.040, #83.3931.040, and #83.3933.040). Cells were seeded on the

primary plate and within the insert at the appropriate seeing density for the required investigation (as below) and incubated overnight in high-glucose (4.5 g/L) DMEM supplemented with 10% FBS before media was removed, and cells washed with PBS. Cells were then treated with low-glucose (1 g/L) DMEM supplemented with 0.1% (v/v) Bovine Serum Albumin (BSA, ThermoFisher)(denoted as Experimental culture media), and inserts added into the wells on the primary plate for 48 hours at 37°C in the presence of 5% CO_2. As required by the experiment, low-glucose DMEM supplemented with 5% FBS (v/v) is denoted as Half culture media.

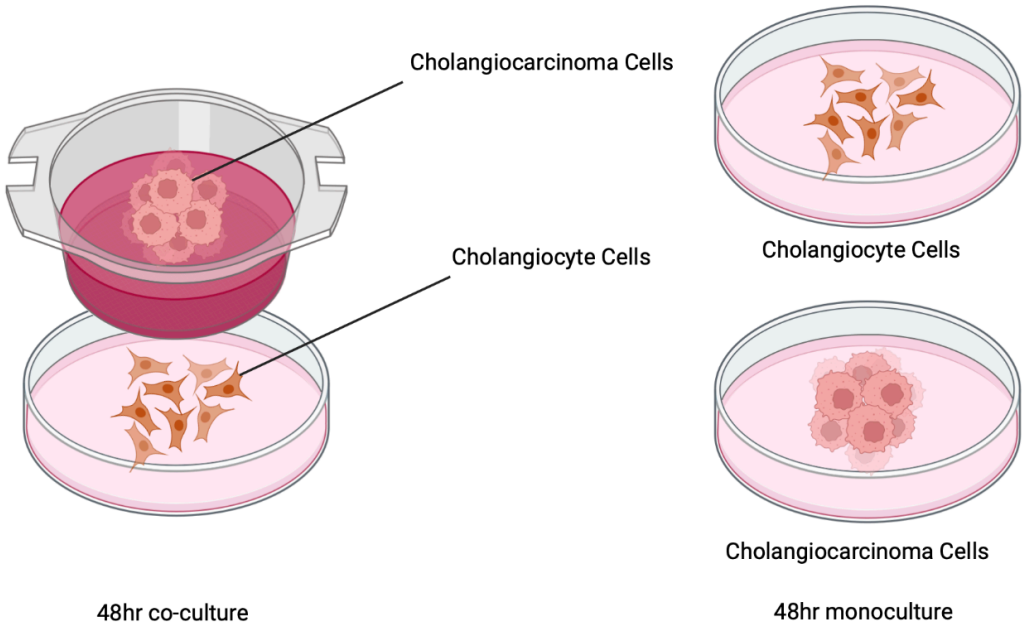


Figure 3:1 *- Indirect co-culture model of cholangiocarcinoma and cholangiocyte cells.*

3.3 Western Blot

3.3.1 Protein extraction

Cells were seeded at $1x10^6$ cells/well in 1.5 ml of high-glucose DMEM supplemented with 10% FBS and incubated overnight, before the addition of low-glucose DMEM supplemented with 0.1% BSA. After 48 hours, inserts were transferred into a secondary plate and all media

was aspirated from both plates. Cells were washed in 1 ml of cold PBS prior to the addition of 500 µL of 1X Trypsin, and incubated for an additional 10 minutes. 500 µL of high-glucose DMEM supplemented with 10% FBS was used to stop the reaction, and the cell solution was transferred into labelled Eppendorf's. Cells were pelleted via centrifugation at 18000 x *g* for 5 minutes. Supernatant was discarded and 30 µL of 1X RIPA Lysis Buffer, prepared from 10X stock RIPA Lysis and Extraction Buffer (Thermo Scientific) with Milli-Q water, supplemented with Pierce Protease and Phosphatase Inhibitor (Thermo Scientific, 1 tablet per 10 ml), was added to each sample. Samples were left to rotate at 4°C for 2 hours, before lysates were centrifuged at 10000 x *g* for 5 minutes to remove cellular debris. Lysate supernatant were transferred to fresh, labelled Eppendorf's for quantification and normalisation of protein concentration.

3.3.2 Protein Quantification

A Bradford Assay (Bio-Rad) was used to calculate protein concentration. 1 µL of each sample and each BSA standard was plated in triplicate on a 96-well plate (Sarstedt). 1x Bio-Rad reagent was added to 4X deionised H_2O and 100 µL of solution added to each well. Absorbance readings were taken at 595 nm using the Tecan Sunrise Microplate Reader. BSA Standard Curve was plotted using Microsoft Excel, and sample protein concentrations calculated. 10 µL of 4X Sample Buffer (Bio-Rad, 1610747)(Lamelli, 1970) was added to each sample, and protein concentrations were normalised to a constant concentration using 1X Sample Buffer. Samples were then boiled at 100°C for 5 minutes, before being centrifuged at 10000 x *g* for 1 minute and either ran using SDS-PAGE or frozen at -20 °C.

3.3.3 Gel Preparation

Samples were separated by size using sodium dodecyl sulphate polyacrylamide gel electrophoresis (SDS-PAGE). All gels for SDS-PAGE were prepared in house using a 10% resolving gel and 5% stacking gel. Solution for the preparation of 10% resolving gels: 6.3 mL H_2O, 5.3 mL 30% Acrylamide Mix, 4 mL 1.5 M Tris (pH 8.8), 160 µL 10% SDS, 160 µL 10% Ammonium Persulfate (APS), and 16 µL tetramethylethylenediamine (TEMED). Solution for the preparation of 5% stacking gel: 3.4 mL H2O, 830 µL 30% Acrylamide Mix, 630 µL 1.0 M Tris (pH 6.8), 50 µL 10% SDS, 50 µL 10% Ammonium Persulfate, an 5 µL TEMED.

3.3.4 Protein Separation

SDS-PAGE gels were added to cassettes and placed in a tank topped with 1X Running Buffer (BioRad). 5 µl of Amersham ECL Rainbow Marker was added to the first well in each gel. After normalisation, 15-20 µg of sample protein was added to the wells. Gels were run at 100 V for 1 hr, followed by 130 V for an additional hour, or until fully resolved. Proteins were transferred onto PVDF membranes that had been soaked in methanol and equilibrated with 1X Transfer Buffer (BioRad), using the Bio-Rad Wet Blot system (Whatman) topped up with 1X Transfer Buffer. Proteins were allowed to transfer from gel to membranes at 100 V for 130 minutes. Membranes were removed and blocked in 5% milk in PBS-Tween 0.1%, or 5% BSA in TBS-Tween 0.1% for one hour at room temperature.

3.3.5 Protein Visualisation

After blocking, membranes were incubated in the Primary Antibody overnight on a gentle rocker at 4°C. Primary Antibodies are found in Table 1. Membranes were then washed for 5 minutes, three times, in PBS-Tween 0.1%, or TBS-Tween 0.1%, as appropriate, before

incubation with the secondary horse radish peroxidise (HRP)-conjugated antibody for 1 hour on a gentle rocker at room temperature. Membranes were then washed (as above) prior to the addition of the ECL chemiluminescent reagent (GE Healthcare). ECL reagent was prepared according to the manufacturer's instructions; briefly 200 µL Reagent A to 200 µl Reagent B of the visualisation solution. Each membrane was imaged using the G:BOX imaging system (Syngene).

Table 1 - List of primary and secondary antibodies used in this study

Target	Expected mW / kDa	Dilution	Source	Company
Primary antibodies				
ASNS	64	1:1000	Mouse	Santa Cruz (sc-376151)
Aurora A/AIK	48	1:1000	Rabbit	Cell Signaling Technology (1G4)
β-actin	42	1:1000	Rabbit	Cell Signaling Technology (D6A8)
Bax	20	1:1000	Rabbit	Cell Signaling Technology (2772)
Caspase-3	17/19/35	1:100	Rabbit	Cell Signaling Technology (9662)
Caspase-8	18/43/57	1:1000	Mouse	Cell Signaling Technology (IC12)
CHKα	50	1:500	Rabbit	Proteintech (13520-1-AP)
E-cadherin	135	1:1000	Mouse	Cell Signaling Technology (4A2)
KCNK3	43	1:500	Rabbit	GeneTex (GTX132622)
p21 Waf1/Cip 1	21	1:2000	Mouse	Cell Signaling Technology (DCS60)
p44/42 MAPK	42/44	1:2000	Mouse	Cell Signaling Technology (L34F12)
p53	53	1:1000	Rabbit	Cell Signaling Technology (9282S)
Phospho-p44/42 MAPK	42/44	1:1000	Rabbit	Cell Signaling Technology (9101)
Phospho-Rb	110	1:1000	Rabbit	Cell Signaling Technology (D20B12)
Puma	23	1:1000	Rabbit	Cell Signaling Technology (4976)
Rb	110	1:2000	Mouse	Cell Signaling Technology (4H1)
Slug	30	1:1000	Rabbit	Cell Signaling Technology (9585S)
Thioredoxin 1	12	1:1000	Rabbit	Cell Signaling Technology (C63C6)
TXNIP	55	1:1000	Rabbit	Cell Signaling Technology (D5F3E)
Vimentin	57	1:1000	Rabbit	Cell Signaling Technology (D21H3)
Secondary antibodies				
Anti-Rabbit conjugated to HRP	-	1:10000	Goat	Dako (P0448)
Anti-Mouse conjugated to HRP	-	1:10000	Goat	Dako (P0447)

3.3.6 Image Analysis

Densitometry was conducted on each protein band using Fiji/ImageJ. Data was plotted as mean protein expression ± SEM using GraphPad Prism (Version 9.5.0), with significance denoted as *P<0.05.

3.4 Nucleic Acid Work

3.4.1 RNA extraction

RNA was extracted using the Zymo Research Direct-zol RNA Miniprep kit as per the manufactures instructions. Briefly, cells were washed with 1x PBS prior to extraction. 100 µL of TRI Reagent was added directly to each well and lysed for 5 minutes at room temperature. 100 µL of 100% ethanol was added to each well, and 200 µL of the solution was transferred to labelled Zymo-Spin IICR Columns in a Collection Tube. Samples were centrifuge at 10000 x *g* for 1 minute. Columns were transferred into new collection tubes and flow-through discarded. Twice, 400 µL Direct-zol RNA PreWash was added to the columns before being centrifuged and flow-through discarded. 700 µL of RNA Wash Buffer was added to each column and centrifuged for 2 minutes. Columns were transferred to labelled Eppendorf's before the addition of 50 µL of DNase/RNase-Free, followed by centrifugation to elute RNA. Eluted RNA was quantified using the Thermo Scientific NanoDrop ND-1000 UV-Vis Spectrophotometer (NanoDrop Technologies) measuring absorbance at 260 nm.

3.4.2 Generation of cDNA

Reverse transcription was performed using the High-Capacity cDNA Reverse Transcription Kit (Applied Biosystems) to synthesise cDNA from eluted RNA as per the manufacturer's

instructions. A 20 µL reaction volume was used, with 1 ng of RNA normalised using nuclease-free H_2O toa total volume 10 µL, plus the addition of 2 µL 10X RT Buffer, 0.8 µL 25X dNTP Mix (100 mM), 2 µl 10X RT Random Primers, 1 µL MultiScribe Reverse Transcriptase, and 4.2 µL nuclease-free H2O. The thermal cycler LabCycler (SensoQuest) was set according to the following protocol: 25°C for 10 minutes, 37°C for 120 minutes, 85°C for 5 minutes, finishing at 4°C. Final cDNA concentration was validated using the Thermo Scientific NanoDrop ND-1000 UV-Vis Spectrophotometer.

3.4.3 Quantitative Polymerase Chain Reaction (qPCR)

qPCR was performed using the SensiFAST SYBR No-ROX kit (Bioline) as per the manufacturer's specifications, using the QuantStudio 1 Real-Time PCR System (Applied Biosystems). In brief, a 20 µL reaction was used, with 0.5 µL Forward Primers, 0.5 µL Reverse Primers, 10 µL SYBR Green, 8 µL RNAse/DNase free H2O, an 1 µL of cDNA at a concentration of 200 ng/µl. Primer sequences are found in Table 2. Forward and reverse primers were prepared in RNAase-free water, to a concentration of 10 µM. *β-actin* was used as the housekeeping gene. PCR efficiency of both amplicons was confirmed to be between 90 and 110%, and visualisation of the melt curve after the amplification was used to to check for primer dimers or genomic contamination of the samples. Analysis was performed using the ΔΔCT method where raw CT values were normalised to monoculture, followed by normalisation to control gene expression (*β-actin*). These were converted into fold change gene expression, as below:

ΔCT = CT(Co-Culture) – CT(Monoculture)

ΔΔCT = ΔCT (target gene) – ΔCT (control gene)

Fold enrichment = 2-ΔΔCT

Results shown are means of three independent experiments, run in triplicate with standard error shown. Significance was determined using a Student's T-test, denoted as *P<0.05.

Table 2 - List of qPCR primers used in this study

qPCR Primer	Forward primer sequence 5'-3'	Reverse primer sequence 5'-3'
β-actin	ATTGGCAATGAGCGGTTC	GGATGCCACAGGACTCCAT
β2M	TGCTGTCTCCATGTTTGATGTATCT	TCTCTGCTCCCCACCTCTAAGT-3
GAPDH	AGCCACATCGCTCAGACAC	GCCCAATACGACCAAATCC
ASNS	GAGTCAGACCTTTGTTTAAAGCA	GGAGTGCTTCAATGTAACAAGAC
AURKA	GGAATATGCACCACTTGGAACA	TAAGACAGGGCATTTGCCAAT
CDH1	CCCGCCTTATGATTCTCTGCTCGTG	TCCGTACATGTCAGCCAGCTTCTTG
CFI	GGCAGAAATGCTGGAGAGTGTC	ACCACCTCGATGCCAAAGACCA
CHKA	GAAAGTGCTCCTGCGGCTGTATG	CGGCTCGGGATGAACTGCTC
CHKB	CCGAGGAGCTGAGGGTTTACC	GCGAAAACATGGAGCATCCTGAG
CHT1	ATCCCAGCCATACTCAAT	CAGAAACTGACCAAGACCA
CTL1	CCTTGTTCCACGTAGCTGGCAA	GCCTTGCTCATTCTGAACAGGAC
CTL2	TTCTGGTGCTGGGCTACGGAAT	TCTGAAAGCCGAGGTCCACCAA
CTL3	TCCTTGGCCTGTGTATCCTCGCA	ACACCGCAGACAAACAACAATCCCA
CTL4	TGCTGATGCTCATCTTCCTGCG	GGACAAAGGTGACCAGTGGGTA
CTL5	CTGCTGAAGGAAGGAAGCAAAGCCA	AGGTACCCCCGATGTCGCCAA
CXCL1	GTTGGATTTGTCACTGTTCAGC	CCCAAGAAGAACATCAAAGTGTG
CXCL2	GGGCAGAAAGCTTGTCTCAA	GCTTCCTCCTTCCTCTGGT
CXCL3	TCCCCCATGGTTCAGAAAATC	GGTGCTCCCCTTGTTCAGTATC
EXTL1	CTTCCTGCTTGCTGGCAGCAGA	AGGAGGTGAAACAACGGCATCTTC
FAP	AGGAAGATTGGGAAAAGAGAGGTTAG	GAGAGATTCATGGGTCTCCCAAC
HIF1A	CAGCTATTTGCGTGTGAGGA	TGTGCTTTCATGTCATCTTCAA
HSPA8	ACTCCAAGCTATGTCGCCTTT	TGGCATCAAAAACTGTGTTGGT
IDO1	CCCTGTGATAAACTGTGGTCACT	CCACAGTTGTTCAGTAGAAGTTAACATTG
IL-6	CCTGAAGAACGGGAAGC	GACTGGGCAATTTTATGATG
KCNK3	TCATCGTGTGCACCTTCACC	CGTTACCGATGGTGGTGATGA
KL	TGTGTGAAGTTACTCGTGTGTCAAA	GCAGGTACTCCGAAGTCTGT
LBP	GTGAAGCAGATCGAGAGCAAG	CGTGGCTGAGAAGTCAACTACTA
MGAT3	GAACAATGCCCCGGTCAC	GCCTCTCCAGCATCTTGGT
NPPB	CACAGGTGTCTGGAAGTCCC	TAATGCCGCCTCAGCACTTT
Slug	GAGCATTTGCAGACAGGTCA	ACAGCAGCCAGATTCCTCAT
Snail	AACTTCTCAGCATCGATGAC	TTGTAGGAGTGTCGGTTCTTAAG
SPRR2	AGTGCCAGCAGAAATATCCTCC	GGATATTTGGCTCACCTCGTTC
TXN	GTGAAGCAGATCGAGAGAAG	CGTGGCTGAGAAGTCAACTACTA
TXNIP	TGTGTGAAGTTACTCGTGTCAAA	GCAGGTACTCCGAAGTCTGT
VEGFA	CTACGTCCACCATGCCAAGT	CCACTTCGTGATGATTCTGC
Vimentin	AACTTCTCAGCATCCGATGAC	TTGTAGGAGTGTCGGTTGTTAAG

3.4.4 Silencing of gene expression using silencing RNA (siRNA)

Transfection of small interfering RNA (siRNA) was performed using Lipofectamine RNAiMAX (Invitrogen) according to the manufacturer's instructions.

For siRNA reversed transfection, siRNA was prepared in two parts for a 5 µM stock. Tube A consisted of 1 ml OptiMEM plus 30 µl RNAiMAX. Tube B consisted of 1 ml OptiMEM plus 10 µM siRNA, incubated at room temperature for 5 minutes. Tubes A and B were mixed together for a final volume of 2 ml, and incubated at room temperature for 20 minutes.

Cells were resuspended in 5 ml of serum free DMEM for a cell count of $2x10^6$ cells in a 10 cm dish with a final volume of 10 ml. The transfection mix was added dropwise to dishes pre-seeded with cells, with serum-free OptiMEM. The total concentration of siRNA was 25 nM per dish. After 4 hours, an additional 5 ml of high glucose DMEM supplemented with 10% FBS was added to the dish. The cells were incubated at 37°C in the presence of 5% CO_2 overnight, and media replaced by fresh high-glucose DMEM supplemented with 10% (v/v) FBS the following day. Cells were then seeded and harvested as necessary, with silencing checked using qPCR, and Western blotting.

3.4.5 siRNA Sequences

Table 3 - List of siRNA sequences used in this study.

siRNA mediated gene silencing	**Company**
ON-TARGETplus Non-targeting Pool	Dharmacon (D-001810-10-05)
ON-TARGETplus Human HSPA8 siRNA	Dharmacon (L-017609-00-0005)

3.5 Cell Viability

3.5.1 Cell Counting Kit-8 (CCK8)

The Cell Counting Kit-8 (CCK8) was used to determine cell viability post co-culture, media treatment, and drug treatment as per the manufacturer's instructions. Cells were seeded into 96-well plates (Sarstedt) at 3000 cells/well in triplicate. Plates were incubated at 37°C, 5% CO_2 overnight prior to being washed with 1X PBS. 100 µL treatment media was added, and plates incubated for 48 hours. The CCK8 reagent (Sigma-Aldrich) contains the highly water-soluble tetrazolium salt (WST-8), which when reduced by cellular dehydrogenases forms the orange product formazan. By measuring the absorbance of the final solution, the number of viable cells can be determined by the intensity of the orange colour. 10 µL of the CCK8 reagent was added to each well, and incubated for 2 hours. Absorbance readings were taken at 450 nm using the Tecan Sunrise Microplate Reader. Background absorbance readings were subtracted, and absorbances were normalised to control wells. Percentage cell viability was calculated according to the following formula:

Cell Viability (%) = (O.D (Treatmet) – O.D (Background) / Average O.D (Control)) x 100

Data are plotted as mean cell viability ± SEM using GraphPad Prism (Version 9.5.0), with significance denoted as *P<0.05.

3.6 Cell Proliferation

Cell proliferation was measured using the imaging-based IncuCyte Live-Cell Analysis System (Sartorius). Cells were seeded in triplicate into 96-well plates (Sarstedt) at 3000 cells/well (low confluency). Plates were incubated at 37°C, 5% CO_2 overnight prior to media aspiration and treatment as denoted by the experiment. Plates were incubated in- and imaged using the IncuCyte SX1 Live-Cell Analysis System (Sartorius). 4 images per well were taken every 6 hours, across 48 hours. Images were analysed using the IncuCyte Basic Analysis Software (Sartorius) and cell proliferation curves plotted using GraphPad Prism. Data are plotted as percentage confluency (%) ± SEM, with significance denoted as *P<0.05.

3.7 Cell Migration

Crystal violet staining was used for the evaluation of migration and invasion. Cells were plated at $1.5x10^5$ cells/well in 12-well plates (Sarstedt) or 12-well plate transwell inserts pore size 8 µM (Sarstedt), and incubated overnight at 37°C, 5% CO_2. The following day, 1.5 ml of low glucose DMEM supplemented with 5% FBS (v/v) was added to the 12-well plate, whilst 500 µL of low glucose DMEM supplemented 0% FBS was added to the transwell inserts. Inserts were added to the plates and incubated for 48 hours at 37°C, 5% CO_2. Media was aspirated and wells and inserts washed with 1X PBS. Cells were fixed using 500 µL acetic acid/methanol for 5 minutes. The acetic acid/methanol was removed before the addition of crystal violet for 30 minutes at RTP. Inserts were washed thoroughly with fresh H_2O and allowed to dry overnight before being mounted on microscopy slides. Slides were imaged using a the Olympus BX51 microscope (Olympus), with 5 images taken per insert. Images were quantified using batch processing in Fiji/ImageJ (Fiji). Data were plotted in GraphPad Prism as fold change number of migratory cells ± SEM, with significance denoted as *P<0.05.

3.8 Flow Cytometry

3.8.1 Apoptosis

The proportion of apoptotic cells was assessed using the BD Biosciences FITC Annexin V Apoptosis Detection Kit I. $3x10^4$ cells were seeded in a 12-well plate and incubated for 48 hours before being harvested. Media from each well was transferred into a 15 ml Falcon Tube. Wells were washed using 1X PBS which was transferred into the appropriate 15 ml Falcon Tube. Cells were harvested using 500 µL 1X trypsin for 10 minutes at 37°C, 5% CO_2, before the reaction was stopped using 500 µL full media. 300 µL of the cell solution was transferred into the correct 15 ml Falcon Tube, whilst 700 µL was saved for Cell Cycle analysis (see below). Samples were centrifuged at 300 x *g* for 5 minutes, and supernatant aspirated. Cells were resuspended in 100 µL 1X Binding Buffer plus 2 µL FITC-Annexin V (BD Biosciences) and incubated in the dark, at room temperature for 15 minutes. An additional 400 µL of 1X Binding Buffer was added to each sample, before samples were transferred into labelled Flow Cytometry tubes. 5 µL of Propidium Iodide (PI) (BD Biosciences) was added to each tube and vortexed. Samples were run and analysed using the BD FACSCalibur Flow Cytometer (BD Biosciences), and quantified using FlowJo 10.7.1 (FlowJo LLC). Data are plotted as percentage apoptotic or viable cells (%) ± SEM, with significance denoted as *P<0.05.

3.8.2 Cell Cycle

The proportion of cells in each stage of the cell cycle (G1, S, and G2M) was assessed using staining with Propidium Iodide (BD Biosciences). $3x10^4$ cells were seeded in a 12-well plate (Sarstedt) and incubated for 48 hours before being harvested as above. 700 µL of the cell solution was transferred into Eppendorf's, to which 300 µL of 100% ethanol was added (70%

EtOH v/v). Samples were mixed gently and incubated at 4°C overnight. Samples were pelleted via centrifugation at 300G for 5 minutes, and supernatant aspirated. Samples were washed 3X using cold 1X PBS. 50 µl of 100 µg/ml RNAseA stock was added to each sample, plus 200 µl PI from a 50 µg/ml stock solution. Samples were transferred into labelled Flow Cytometry tubes, analysed using the BD FACSCalibur Flow Cytometer (BD Biosciences), and quantified using FlowJo 10.7.1. Data are plotted percentage number of cells (%) ± SEM, with significance denoted as *P<0.05.

3.9 Metabolomics

We used a large scale metabolomic analysis to evaluate the change in intracellular metabolite concentration after 6, 24, and 48 hours of co-culture.

Cells were plated at $1.0x10^6$ cells/well in 6-well plates or 6-well plate Transwell Inserts (Sarstedt), pore size 0.4 µM, in high-glucose DMEM supplemented with 10% FBS (v/v) and incubated overnight at 37°C, 5% CO_2. The following morning, media was aspirated and cells washed in 1X PBS, before the addition of 1 ml low-glucose DMEM supplemented with 0.1% BSA (v/v) to each insert and each well with an insert, and 2 ml to wells without inserts. Cells were incubated for 6, 24, and 48 hours at 37°C, 5% CO_2 before being harvested.

During harvesting, media from each well was extracted and stored in low-binding Eppendorf's at -80°C for future analysis. To harvest intracellular metabolites, cells were first washed gently x2 with 2 mL of 5% Mannitol. 1 ml of methanol (MeOH) plus the first Internal Standards (IS) 25 µM of L-methionine sulfone, MES (Morpholino-ethanesulfonic acid), and CSA (D-Camphor-10-sulfonic acid) were then added to each well and left to rest at room temperature for 10 minutes. Sample supernatant was transferred into labelled Eppendorf's and stored at -80°C before being sent to our collaborators for analysis.

Samples were analysed using capillary electrophoresis time-of-flight mass spectrometry (CE-TOFMS) by collaborators Dr Kaori Saitoh and Dr Tomoyoshi Soga from the Institute for Advanced Biosciences, Keio University(76). Briefly, the MeOH solution containing cells and each of internal standards and transferred it to a new tube before the addition and vortex of 400 µL of $CHCl_3$ (cholorform) and 200 µL of Milli-Q water.

The tubes were centrifuged at 10,000 G for 3 minutes at 4 °C. Proteins were removed by centrifugally filtering the aqueous layer through a 5-kDa filter, before centrifuging snd concentrating the filtrate. The filtrate was then dissolved in the second IS's; 25 µL of 3-Aminopyrrolidine (200 µM) and Trimesate aqueous solution (200 µM), before being measured via CE-TOFMS. Prior to CE-MS/MS analysis, the sample solution for Cation was diluted 10 times with Milli-Q water.

Four metabolite standard solutions (STD) were generated: Anion 114 STD at 50 µM, Cation 114 STD at 20 µM, Anion All STD at 20 µM, and Cation All STD at 20 µM, whereby 114 constitutes compounds of basal metabolic pathways, and All contains all cationic/anionic compounds available in the Keio laboratory as of 2020. The standard solutions were analysed at the beginning of each sequence.

The concentration for each metabolite in MeOH suspension was calculated using the equation below, using the Internal Standards and metabolite standard solutions (STD).

$$\textbf{Concentration of MeOH suspention}(\mu\mathbf{M}) = \frac{\text{Peak Area[sample]}}{\text{IS Peak Area[sample]}} \Big/ \frac{\text{Peak Area[STD]}}{\text{IS Peak Area[STD]}} \times \text{STDConc. [STD]} \times \frac{\text{IS Conc. [suspension]}}{\text{IS Conc. [STD]}}$$

The data were analysed and quantified using an in-house software in the Keio laboratory (Master Hands-2.18.0.2), which developed particularly for CE-MS-based metabolomic data

analysis. We received the metabolite concentration data from the Keio laboratory, and proceeded to conduct metabolite enrichment and metabolic pathway analysis using MetaboAnalyst 5.0.

Metabolites were analysed using Metabolomic Data Analysis with MetaboAnalyst 5.0. Data was read and raw data processed, before row-wise normalization using a constant sum with no data transformation. Row-wise normalization via a constant sum was used normalize each metabolite (row) to allow comparisons between metabolites, using a normalisation factor calculated from the number of metabolites analysed, whilst nonlinear conversions of the data such as log or power transformations were not applied. Data was scaled via Pareto Scaling (mean-centred and divided by the square root of the standard deviation of each variable). The uploaded data file consisted of a data matrix composed of 12 samples by 491 metabolic compounds. Only metabolites sets containing at least 4 entries were used. 1 empty feature was detected and excluded, whilst 383 features with a constant or single value (0) across the samples were found and deleted.

Hierarchical clustering of the monoculture and coculture samples using Euclidean distance and Ward clustering were conducted at each time point and plotted as a dendrogram. Euclidean distance is the straight line distance between two 2D point, in this case referring to the proximity of sample clusters, whilst the Ward clustering algorithm aims to minimise the within-cluster variance (77).

Likewise, we used a PCA plot to demonstrate strong patterns from our large and complex datasets. It is a way of mathematically combining pairs of metabolite comparisons, whereby PC1 is in essence, a line through the data which explains the most variation between our 12

samples. PC2 is the second line that meets PC1 perpendicularly at the centre of our data and describes the second most variation in the data. As a general rule of thumb, PC1 should account for 80% of the variation in the data. PCA and score plots are a visual representation of the causes of variation between mono- and co-culture samples at each time point.

Differential metabolite expression was conducted using fold change analysis and Student's T-Test. Fold change metabolite concentration was calculated as the ratio between the monoculture and co-culture group means (CC/NT) pre-normalization. The goal of fold change analysis is to compare the absolute values of change between our group means. Our significant threshold parameter was set to a Fold Change in concentration >2/<-2 (FC= 2 or -2) and a P-value<0.01. The fold change in concentration of metabolites were plotted as a heatmap, to demonstrate the metabolic profile of each compartment during co-culture.

Metabolite Set Enrichment Analysis (MESA) (78,79) is directly comparable to GSEA in transcriptomic analyses, and is a way of identifying biologically meaningful patterns which are significantly enriched in quantitative metabolomic data. Quantitative enrichment analysis uses a linear model to estimate a Q-statistic for each metabolite. In our case, this describes the correlation between metabolite set concentrations and cell type. The Q statistic for a metabolite set is the average of the Q statistics for each metabolite in the set. In the MESA analysis for MMNK1 and CC-SW1 cells after 48 hours of mono-culture, the size of the circles in each metabolite set represents the Enrichment Ratio and the colour represents the P-value, with red being more significant, and yellow less significant.

3.9.1 Exogenous metabolites

Exogenous concentrations of metabolites identified in the metabolomic analysis were used to assess biological relevance. Details of each metabolic compound are listed in Table 4.

Table 4 - Table of exogenous metabolites

Compound	**Company (Product Code)**
2-Oxoisopentanoate (3-Methyl-2-oxobutanoic acid)	Fisher Scientific (AC189720010)
L-Asparagine	Sigma-Aldrich (A4159)
Choline Chloride	Sigma-Aldrich (C7527)
Creatine	Santa Cruz (SC-214774)
L-Valine	Sigma-Aldrich (V0500)

3.10 RNA-sequencing

Transcriptomic changes during co-culture were evaluated via bulk RNA-sequencing.

Cells were plated in triplicate at $1.0x10^6$ cells/well in 6-well plates or 6-well plate Transwell Inserts, pore size 0.4 µM, and incubated overnight at 37°C, 5% CO_2. The following morning, media was aspirated and cells washed in 1X PBS, before the addition of 1 ml low glucose DMEM supplemented with 0.1% BSA (v/v) to each insert and each well with an insert, and 2 ml to wells without inserts. Cells were incubated for 48 hours at 37°C, 5% CO_2 before being harvested. RNA was extracted using the Qiagen RNeasy Mini, as per the manufacturer's instructions. Briefly, cells were lysed with 350 µL of RNeasy Mini Lysis Buffer, before the addition of 70% ethanol, and transfer to a RNA binding column. Columns were centrifuged, washed and the incubated with DNAse for 15 minutes at RTP. RNA was eluted in RNAse-free water and stored at -80°C. Quality Control (QC) of the eluted RNA was conducted using the Agilent Bioanalyzer High Sensitivity RNA Analysis Kit (Agilent) in combination with the Agilent 2100 Bioanalyzer Instrument (Agilent).

RNA samples were analysed by BGI Tech Solutions, Hong Kong. The raw data was filtered to remove adapter sequences and low-quality sequences, using SOAPnuke software developed by BGI. Reads were interpreted by our collaborators Dr David Sims and Dr Kevin Rue-Albrecht, in the Computational Genomics Group, MRC Weatherall Institute of Molecular Medicine, University of Oxford. Briefly, quality control checks for FASTQ reads were completed using the QC FastQC software package (MultiQC). HISAT2 is an alignment program used for mapping DNA and RNA sequencing reads to reference genomes.

Principal Component Analysis (PCA) quantifies the similarity between samples and identifies the highly expressed genes in each sample prior to comparing them. PCA transforms a set of

correlated variables (in our case, gene expression) into a new set of uncorrelated variables called principal components. These components are linear combinations of the original variables and are sorted based on the amount of variation they capture in the data. The first principal component accounts for the largest amount of variation, followed by the second, third, and so on. Replicates of singular conditions should therefore cluster closely on the PCA, whilst we should see a clear separation between clusters of monoculture and co-culture samples provided there are significant differences in gene expression. A scree plot is used as a graphical representation of the variance explained by each principal component in the PCA. The loading scores determine which genes have the largest effect on where samples are plotted on the PCA plot, as such positive loading scores push the coculture samples to the right side of the graph, and negative loading scores push the monoculture samples to the left side of the graph. A Gene-wise Dispersion Estimate (GWE) plot was plotted as a graphical representation of the dispersion estimates for each gene in the differential gene expression analysis. A curve was fitted to dispersion estimates for each gene, representing the relationship between the mean expression and dispersion estimates, when assuming a reasonable estimation of dispersion across all genes (shown in red) plotting the expected dispersion for each with a given expression (mean count).

Differential expression analysis was performed with RStudio DESeq2 Bioconductor package (Version 3.17). An adjusted P-value of 0.05 was chosen as the threshold for significantly differentially expressed genes. Gene counts were filtered to keep only genes at least 10 reads total (cpm>=0.2) in at least 4 of the 6 samples.

Gene Set Enrichment Analysis (GSEA) was conducted using the GSEA tool by the Broad Institute using the Hallmark Pathway gene database (version 2022.1, h.all.v2022.1.Hs.symbols.gmt) and the KEGG database (version 2022.1, c2.cp.kegg.v2022.1.Hs.symbols.gmt). GSEA utilizes gene ontology terms to classify gene functions and assigns weights to pathways by considering both the number of genes affected within a specific pathway, in combination with the fold change of up- or down-regulation to provide a more comprehensive evaluation of the impact of a particular treatment on cellular biology. The Fast Gene Set Enrichment Analysis (FGSEA) algorithm was set with 1000 permutations, with an False Discovery Rate (FDR) of 25%, and genes with a $q<0.05$ were considered significant. Normalised enrichment score from GSEA using the Hallmark database was plotted, with significantly enriched pathways shown in blue and non-significant pathways shown in red. The KEGG database was used to plot ranked gene list correlation, and highlight the enriched gene set and top enriched genes.

3.11 Integration of metabolomic and transcriptomic analyses

Changes to metabolite concentration identified via Metabolomic analysis (see Section 3.9) and differential gene expression as identified via RNA-sequencing (see Section 3:10) were integrated as shown in the workflow in Figure 3:2.

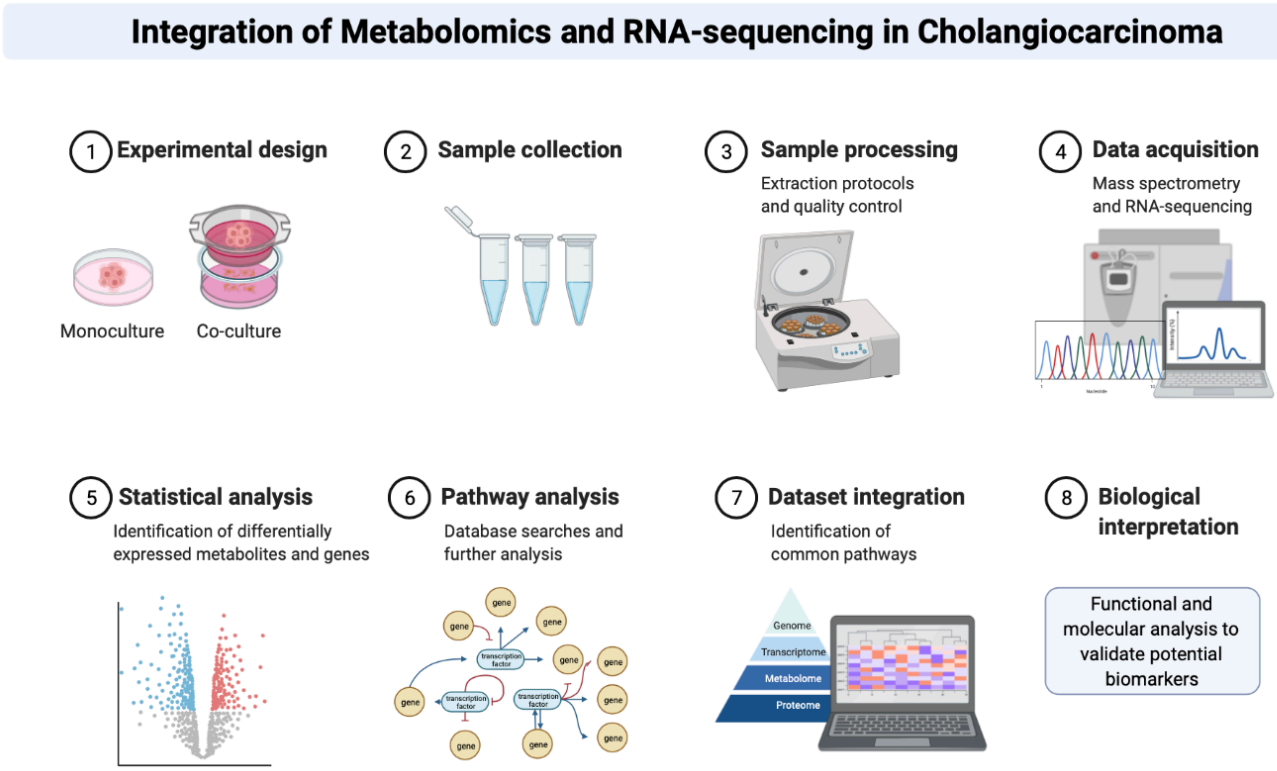


Figure 3:2 - Workflow of integrating metabolomic and RNA-sequencing analysis for the interpretation of secretory factors during indirect co-culture of CCA with cholangiocytes.

3.12 TCGA Analysis

Evaluation of target gene expression in patient CCA tumour samples was conducted using RNA sequencing data from the Cancer Genome Atlas (TCGA) PanCancer Atlas project (chol_tcga_pan_can_atlas_2018). The data consisted of 9 normal and 36 tumour samples. The R package, *DESeq2* (Bioconductor, Version 3.17) , was used to integrate the normal and CCA expression profiles to perform differential expression gene analysis. Data was filtered keep only rows (genes) that have at least 10 reads total. The threshold for differential expression analysis was set as FDR=0.05.

2752 genes encoding known human metabolic enzymes and transporters were classified into metabolic gene sets according to the Kyoto Encyclopaedia of Genes and Genomes (KEGG) (80–83). The list of genes in each gene set is shown in Table 5. These metabolic gene set criteria were applied to the data, and each set ranked based on median Log2FoldChange gene expression CCA tumours vs normal tissue. Data were plotted as median Log2FoldChange gene expression (red) and individual Log2FoldChange gene expression (black) using GraphPad Prism.

Table 5 - Table of Metabolic Gene Sets

Metabolic Gene Set	Number of Genes
ABC Transporter	46
Amino Acid	38
Aminosugar	22
Anaerobic Glycolysis	6
ATPase	5
B12	4
BCAAs	10
BH4	4
Bile Acid	6
Carbohydrate Storage	13
Cholesterol	16

CoA	17
Cofactor	25
Complex I	49
Complex II	4
Complex III	11
Complex IV	27
Creatine	8
Cysteine	9
Detox	48
Fatty Acid	139
Folate	12
Glutamate	11
Glutathione	34
Glycan	156
Glycan Anchor	25
Glycan Degradation	48
Glycan Sulphate	28
Glycine	7
Glycolysis	41
Glyoxylate	5
Heparin Sulphate	25
Histidine	7
Hormone	37
Inositol Phosphate	58
Ion Transport	405
Ketone Bodies	4
Krebs	26
Lysine	4
Membrane Lipid	124
Methionine	8
Mevalonate	8
Multipurpose	118
NAD	19
Neurotransmitter	16
Nucleotide	63
Nucleotide Sugar	3
Other	48
Other Transport	26
Pentose Phosphate	10
Pigment	4
Polyamine	11
Porphyrin	13

Proline	6
Propanoate	4
Proton Transport	49
Purine	41
Pyrimidine	28
Reactive Oxygen	6
Redox	68
Serine	3
Signalling	50
Small Molecule Transport	358
Sphingolipid	31
Sphingosine	9
Steroid	64
Sugar	42
Sulphate	22
Tryptophan	9
Tyrosine	9
Ubiquinone	13
Urea	7
Vitamin A	17
Vitamin B6	4
Xylulose	2

3.13 ATP Assay

Intracellular ATP concentration was evaluated using the CellTiter-Glo Luminescent Cell Viability Assay (Promega). Cells were seeded in triplicate, in high-glucose DMEM supplemented with 10% FBS (v/v) in 96-well plates (Sarstedt) at 3000 cells/well. Plates were incubated at 37°C, 5% CO_2 overnight prior to treatment for 48 hours. The Promega CellTiter-Glo Luminescent Cell Viability Assay was conducted as per the manufacturer's instructions. In brief, after 48 hours of incubation, 100µl of CellTiter-Glo Reagent was added to each well, which was mixed on an orbital shaker for 2 minutes to induce cell lysis. A standard curve was created using serial dilutions of ATP (Thermo Scientific Chemicals, L14522.03). The microplate was then incubated at RTP for 10 minutes to stabilize the luminescent signal. Luminescence was measured with the SpectraMax i3x (Molecular Devices) and sample ATP concentrations derived from luminescence readings and the standard curve. Data were plotted as mean ATP concentration ± SEM in GraphPad Prism(Version 9.5.0). Significance is denoted by *P<0.05.

3.14 Cytokine Expression Analysis

We used the C-Series Human Cytokine Antibody Array C3 (RayBio) to simultaneously screen for the relative protein expression and patterns of 42 cytokines and, growth factors, with high specificity and sensitivity. As little as 4 pg/ml of MCP-1 can be detected using the C-Series Array (RayBio), with a greater range of detection (25 to 250,000 pg/ml) than ELISA. Negative Control Spots with buffer printed (no antibodies) were used to measure the baseline responses, to determine the level of non-specific binding of the samples, highlighting specificity.

Supernatant was extracted from the previously conducted metabolomics experiment (see above). In brief, 1x10^6 cells were plated in low glucose DMEM supplemented with 0.1% BSA in 6-well plates in the following format: MMNK1 monoculture, CC-SW1 monoculture, and the co-culture system of MMNK1 and CC-SW1. After 48 hours of incubation, culture media was extracted, and cells harvested. Fresh, low-glucose DMEM supplemented with 0.1% BSA was used as control medium. The AAH-CYT-3-4, 4 Sample Kit was used, with 1x membrane each for media from MMNK1, CC-SW1, co-culture, and the control.

The array was performed as per the manufacturer's instructions, but in brief: membranes were blocked in 2 ml of Blocking Buffer and incubated on a gentle rocker for 30 minutes at RTP. The blocking buffer was aspirated and 1 ml of undiluted sample was added to each well, and incubated for 2 hours on a gentle rocker at RTP. Sample was aspirated prior to washing three times with 2 ml of Wash Buffer 1 for 5 minutes at RTP on a gentle rocker, followed by washing twice 2 ml of Wash Buffer 2 for 5 minutes at RTP on a gentle rocker. Membranes were then incubated with 1 mL Biotinylated Detection Antibody Cocktail for 2 hours, before washing as above. Membranes were then incubated with 2 mL of HRP-Conjugated Streptavidin for 2 hours at RTP, and washed as above. For detection of chemiluminescence, membranes were transferred to the provided plastic sheet, and edges blotted with blotting paper to remove excess wash buffer. 1 mL of Detection Buffer C was added to 1 mL of Detection Buffer D, prior to the addition of 500 µL Detection Buffer solution added to each membrane and incubated for 2 minutes at RTP. Membranes were imaged using the G:BOX imaging system (Syngene).

Densitometry and analysis was conducted with Protein Array Analyzer macro (http://rsb.info.nih.gov/ij/macros/toolsets/ProteinArrayAnalyzer.txt) (84) in ImageJ

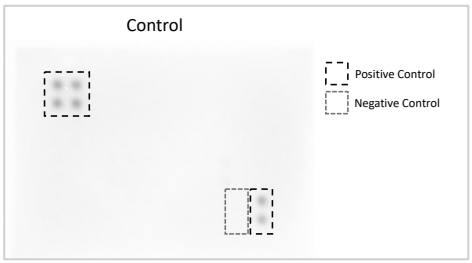
software (NIH), as shown in Figure 3:3. Briefly, arrays were normalised using the Positive Control Spots, as the concentration of biotinylated antibody on each Positive Control Spot was consistent between arrays (wells C1L1,C2L1,C1L1,and C2L2 in Figure 3:3). The Negative Control Spots (wells C11L7, and C11L8 in Figure 1) contain no biotinylated antibody, and were used for background subtraction. Intensity values were normalised according to the following equation:

Normalised Intensity Value = (Intensity Value - (Negative Controls))/ Positive Controls

A

	A	B	C	D	E	F	G	H	I	J	K	L
1	POS	POS	NEG	NEG	CXCL5	GCSF	GM-CSF	GRO	CXCL1	CCL1	IL-1a	Il-1b
2	POS	POS	NEG	NEG	CXCL5	GCSF	GM-CSF	GRO	CXCL1	CCL1	IL-1a	Il-1b
3	IL-2	IL-3	IL-4	IL-5	IL-6	IL-7	IL-8	IL-10	IL-12	IL-13	Il-15	IFNY
4	IL-2	IL-3	IL-4	IL-5	IL-6	IL-7	IL-8	IL-10	IL-12	IL-13	Il-15	IFNY
5	MCP-1	MCP-2	MCP-3	M-CSF	CCL22	CXCL9	MIP-1	CCL5	SCF	SDF-1	CCL17	TGFB
6	MCP-1	MCP-2	MCP-3	M-CSF	CCL22	CXCL9	MIP-1	CCL5	SCF	SDF-1	CCL17	TGFB
7	TNF-a	TNF-b	EGF	IGF-1	Angiogenin	OSM	TPO	VEGF-A	PDGF	Leptin	NEG	POS
8	TNF-a	TNF-b	EGF	IGF-1	Angiogenin	OSM	TPO	VEGF-A	PDGF	Leptin	NEG	POS

B



C

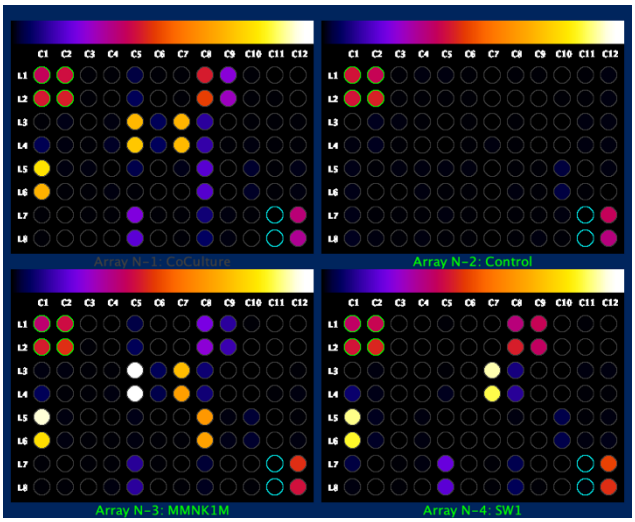


Figure 3:3 – Cytokine assay analysis. A) Cytokine Array Map. B) Protein Array Analyzer image of the Normalised Master Cytokine Array prior to quantification. C) ECL image of the Control Media blot, with Positive Control Spots delineated by black rectangles, and Negative Control Spots delineated by grey rectangles on the cytokine array membrane

Each cytokine/growth factor was assessed in duplicate. Background expression from media was subtracted from Normalised Intensity Values, and Normalised Cytokine Expression

calculated as a ratio of expression between monoculture:co-culture. Data are shown as mean of duplicates of Normalised Cytokine Expression ± SEM and plotted using GraphPad Prism (Version 9.5.0). Significance is denoted by *P<0.05.

3.15 Epigenetic Inhibitor Screen

3.15.1 Epigenetic Inhibitor Panel

We used high throughput screening of cell viability to assess efficacy and selectivity of epigenomic inhibition on CCA. We obtained a panel of 63 epigenetic inhibitors from the Structural Genomics Consortium, (https://www.thesgc.org/chemical-probes) and used a control of DMSO resulting in a total of 64 compounds (see Table 3). We screened 4 CCA cell lines (CC-SW1, CC-LP1, SNU1079, SNU1196) and non-tumour cholangiocyte cell line (MMNK1) as a control, using a set concentration of 10 µM for each compound in 200 µM high-glucose DMEM supplemented with 10% FBS (v/v).

3.15.2 CyQuant

The CyQUANT Cell Direct Cell Proliferation Assay (Invitrogen) was used as per the manufactures instructions for the evaluation of cell viability post-epigenetic inhibition. Cells were seeded into 96-well plates at 10000 cells/well. Triplicate plates were seeded for each cell line. Plates were incubated at 37°C, 5% CO_2 overnight prior to washing with 1X PBS, drug treatment for 48 hours. Plates were frozen at -80°C for 48 hours.

To determine cell viability, plates were thawed and allowed to equilibrate to RTP before the addition of 200 µL CyQUANT GR dye/cell-lysis buffer. The concentrated cell lysis buffer stock solution (Component B) was diluted 20-fold in distilled water, and the CyQUANT GR stock solution (Component A) was diluted 400-fold into the 1X cell-lysis buffer. Each microplate

required the generation of 20 mL of CyQUANT GR working solution as follows: 1 mL of 20X cell lysis buffer stock, 19 mL of nuclease-free distilled water, and 50 µL CyQUANT GR stock solution.

A solution of 10^6 cells of each cell line in CyQUANT GR dye/cell-lysis buffer was used to generate a dilution series ranging 50 to 50,000 cells per well for each cell line, in the spare wells of the microplate. 4 replicates of each standard, and a set of replicates without cells as a control, were prepared. Plates were incubated in the dark for 2 minutes before fluorescence readings taken using the SpectraMax i3x (Molecular Devices). A reference standard curve was created using the cell dilution series, in order to convert sample fluorescence values into cell number. Fold change cell viability was determined by the following equation:

Cell Viability = Cell number (Drug Treatment) / Cell number (DMSO Control)

Data are plotted as a heatmap of mean cell viability using GraphPad Prism (Version 9.5.0). Statistical analysis was conducted using a Student's T-Test, with significance denoted as *P<0.05. CCA cell viability of <60% was chosen as the threshold for compound efficacy, in additional to the cholangiocyte cell viability threshold of >80%, to highlight compounds that selectively killed CCA cells.

3.15.3 Generation of IC50 curves

IC50 values for the compounds UNC0642 (Tocris, 5132) and SGC3027 (MedChemExpress, HY-112445) were generated in monoculture and co-culture calculated using a CCK8 cell viability assay (see above). Inhibitors were tested in a concentration range of 0 – 20 µM in

200 µM high-glucose DMEM supplemented with 10% FBS (v/v). Data were plotted as mean cell viability (%) and a nonlinear regression curve calculated using GraphPad Prism (Version 9.5.0) in order to calculate IC50.

Table 6 - List of SGC epigenetic probes and targets

Compound	Target
(+)-JQ1	BET
A 196	SUV420H1/H2
A 366	G9a
A 395	EED
A-485	CREBBP. EP300
BAY 299	BRPF2/TAF1
BAY 598	SMYD2
BAY 6035	SMYD3
BAY-850	ATAD2A
BAZ2-ICR	BAZ2A/B
BI 9321	NSD3
BI 9564	BRD9
DMSO	-
GSK 2801	BAZ2A/B
GSK 343	EZH2
GSK 591	PRMT5
GSK 6853	BRPF1B
GSK 864	IDH1 Mutant
GSK J4	JMJ3, UTX, JARDI1B
GSK LSD1	LSD1
GSK-J1	JMJ3, UTX
GSK4027	SMARCA2/4, PB1, PCAF, GCN5
GSK484	PAD4
GSK8814	ATAD2A/B
I-BRD9	BRD9
I-CBP 112	CBP, EP300
IOX1	2OG
IOX2	2OG
L-Moses	GCN5/PCAF
LLY 283	PRMT5
LLY-507	SMYD2
LP99	BRD9/7
MRK 740	PRDM9
MS 023	PRMT1

MS049	PRMT4/6
NI 57	BRPF1/2/3
NVS CECR2-1	CERC2
NVS-BPTF-1	BPTF
NVS-MLLT-1	MLLT1/3
OF 1	BRPF1/2/3
OICR 9429	WDR5
PFI 3	SMARCA2/4, PB1
PFI-1	BET
PFI-2	SETD7
PFI-4	BRPF1B
PFI-5	SMYD2
PFI-6	MLLT1/3
SGC 0946	DOT1L
SGC 3027	PRMT7
SGC 707	PRMT3
SGC-CBP30	CBP, EP300
SGC-iMLLT1	MLLT1/3
SGC6870	PRMT6
TP 064	PRMT4
TP 472	BRD9/7
TP238	CERC2/BPTF
UNC 0642	G9a/GLP
UNC 1215	L3MBTL3
UNC 1999	EZH2, EZH1
UNC0638	G9a/GLP
UNC6934	NSD2
VinSpinIn	SPIN family
WM-1119	KAT6A

3.16 Statistical Analysis

The data are expressed as mean ± SEM unless stated otherwise. Statistical analysis was performed using a Student's t-test or by one-way ANOVA if more than 1 comparison, with a P-value <0.05 considered significant. Graphs were plotted using GraphPad Prism Version 9.5.0. Significance is denoted as: * $P \leq 0.05$, ** $P \leq 0.01$, *** $P \leq 0.001$, **** $P \leq 0.0001$.

4 Results Chapter 1 – Functional Evaluation of Indirect Cholangiocyte- Cholangiocarcinoma Interactions

4.1 Introduction

Paracrine signalling is a critical mechanism by which cells communicate with each other. It involves the secretion of signalling molecules from one cell that then act on nearby target cells, influencing their behaviour and function. Tumour cells in particular can secrete paracrine factors that promote angiogenesis, immune evasion, and metastasis, shaping the tumour microenvironment and facilitating disease progression(30). Paracrine signalling also impacts the phenotypic behaviour of the surrounding non-transformed epithelial neighbours, and in turn tumour cells themselves are acted upon by paracrine signals secreted by these “normal” neighbours(46).

During the development of CCA, surrounding “normal” cholangiocytes interact with CCA cells in both a direct and an indirect fashion(46). As well as interactions with CCA cells, the paracrine secretion of growth factors and peptides by cholangiocyte cells mediates extensive cross-talk with other cells, such as hepatocytes, stellate cells, stem cells, and myofibroblasts, as well as endothelial cells, inflammatory cells, and immune cells. As such, cholangiocytes can also modulate the tumour microenvironment, and hence CCA progression.

We hypothesise that CCA cells may trigger the remodelling of the tumour stroma to promote CCA progression, through the recruitment and activation of surrounding cholangiocytes.

By comparing the gene expression, protein expression, and epigenetic modifications of CCA cells grown in monoculture, to their counterparts in co-culture with cholangiocytes, we aim to study the impact of non-tumorous cholangiocyte interactions on CCA progression. Using data generated by our model system, we aim to evaluate the reciprocal effects on biological function in order to understand the underlying mechanisms that regulate this interaction. In turn, this understanding has the potential to contribute to the investigation and the development of novel biomarkers, to be used for early detection, diagnosis, and monitoring of cancer, as well as for predicting treatment response and patient outcomes.

Co-culture models provide a controlled and accessible platform to mimic *in vivo* interactions. They provide a more representative view of cancer progression than just 2D monoculture models alone, mimic *in vivo* interactions without the difficult separation of cells found in direct culture models, or additional complexity of animal models. Moreover, co-culture models permit the systematic evaluation of the *in vivo* environment, one factor at a time, permitting the interpretation of the contribution each compartment plays during the reciprocal modulation of cell behaviour. We have therefore established an indirect co-culture model between cholangiocytes and CCA cell lines to imitate the early onset of CCA development, in order to evaluate the contribution of paracrine signalling from each compartment on phenotypic behaviour of the reciprocal cell line.

In this study, we sought to deconstruct the functional phenotypic changes that occur in each cellular compartment as a result of the indirect crosstalk between CCA cells and cholangiocytes. Specifically, we aimed to classify functional alterations to both CCA and cholangiocyte phenotypes. To this end, we utilized a panel of cellular assays to evaluate

changes to proliferation, viability, apoptosis, and cell cycle behaviours in CCA and cholangiocytes after indirect co-culture.

4.2 Model Selection

4.2.1 Cholangiocyte Phenotype

For the present study, we utilised the immortalised cholangiocyte cell line MMNK1 as our 'normal' cholangiocyte cell line. Immortalized cell lines constitute cells that have been genetically modified to proliferate indefinitely. The cell line MMNK1 was generated via a process serial transfection, firstly, epithelial-like cells from human foetal liver tissue were immortalised using the SV40 T-Antigen, generating OUMS-21 cells (which, although not immortal, are used to study HCC)(85). These cells were subsequently immortalised using hTERT and MMNK1 selected via GFP-positive selection, and express cholangiocyte markers such as cytokeratin (CK)-7 and -19, and exhibit cholangiogenic tubule formation (74) confirming their cholangiocyte behaviour. As MMNK1 is not a CCA cell line, it is not classified as intrahepatic or extrahepatic, and though MMNK1 is used in the field as a 'normal' cholangiocyte cell line (86–88), the use of a primary cell line is considerably more representative, and is further discussed in Study Limitations.

4.2.2 CCA Cell Phenotypes

We accessed four CCA cell lines, three of which were intrahepatic CCA cell lines CC-SW1, CC-LP1, SNU-1079, and one extrahepatic CCA cell line, SNU-1196 (72,73). It is vital to separate research into iCCA and eCCA, as each type of CCA is so distinct, both genetically and phenotypically. (74)(74)We utilised immortalised cell lines as opposed to primary cells to conduct our initial analyses, due to the lack of availability of CCA tissue. CCA is currently

classified as a rare cancer (89), meaning the incidence in the UK is relatively low and as such it is less commonly encountered in clinical settings. The limited number of cases therefore makes it more difficult to obtain a sufficient number of tissue samples for research purposes. Moreover, a distinct advantage of cell lines is the availability and reproducibility they provide.

All cell lines are epithelial by nature, forming regular structures when confluent. Of the CCA cell lines, the intrahepatic cell line CC- SW1 displays a doubling time and cell morphology most similar to MMNK1 cells. Comparatively, the extrahepatic cell line SNU-1196 displays a doubling time considerable longer than MMNK1, as well as a cell morphology that is most different to MMNK1 cells or the other CCA cell lines. The intrahepatic cell line CC-LP1 is the smallest, with a much rounder morphology. The intrahepatic cell line SNU-1079 has a more mesenchymal morphology compared to the other CCA cell lines. Table 7 outlines some of the phenotypic and genomic differences between the CCA cell lines.

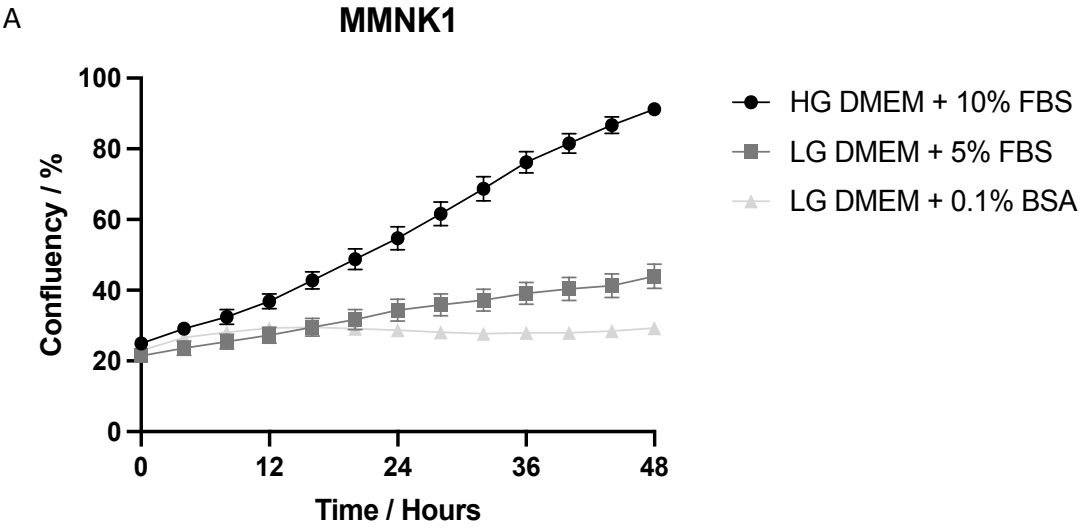
Table 7 - Table showing phenotypic and genotypic differences in CCA cell lines

	CC-SW1 (72)	**CC-LP1** (72)	**SNU-1079** (73)	**SNU-1196** (73)
CCA Subtype	Intrahepatic	Intrahepatic	Intrahepatic	Extrahepatic
Doubling Time	24hr	48hr	24hr	72hr
Year Established	1992	1992	2002	2002
Cell Morphology	Compact, small, and polygonal	Compact, small, and polygonal	Pleomorphic	Spindle to polygonal
Mutational Burden	-	-	p15 & p16 Homozygous Deletion, IDH1mutation	p15 & p16 Homozygous Deletion, p53 missense mutation
Drug Response	-	-	Dasatinib Sensitivity	Gemcitabine Resistant

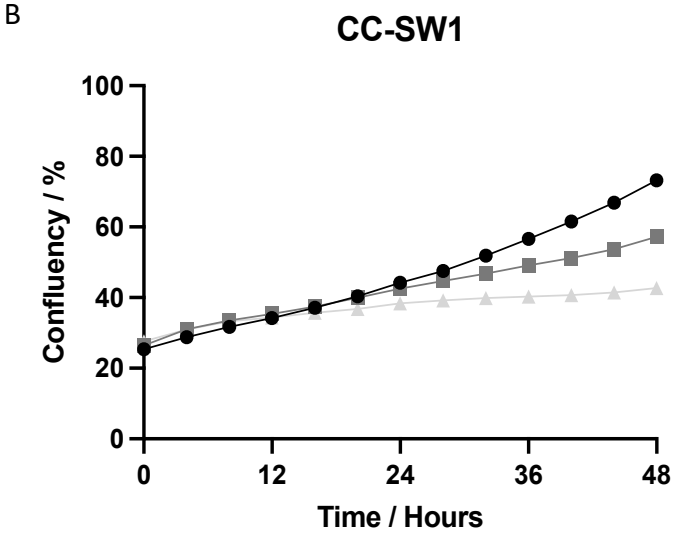
4.2.3 CCA cell proliferation is attenuated by nutrient restricted culture media

Firstly, we used an IncuCyte to assess cell proliferation of our cholangiocyte (MMNK1) and CCA cell lines. This was used to select the most appropriate CCA cell lines with which to conduct our initial experiments, as well as the most appropriate culture media. Three culture media were tested: High Glucose DMEM supplemented with 10% FBS, Low Glucose DMEM supplemented with 5% FBS, and Low Glucose DMEM supplemented with 0.1% BSA. Figure 4:1 shows the growth curves for each cell line. MMNK1 cells proliferated the fastest, reaching 91.23% confluency after 48 hours in Complete Media (Figure 4:1). This was reduced to 43.92% in Half Media and 29.32% in Experimental Media (Figure 4:1). CC-SW1 was the CCA cell line with the fastest proliferation rate, reaching 73.19% confluency after 48 hours in Complete Media, 57.18% confluency in Half Media, and 42.74% in Experimental Media (Figure 4:1). CC-LP1 cells reached 61.73%, 57.75%, and 62.48% confluency in Complete, Half, and Experimental Media respectively (Figure 4:1). SNU-1079 cells reached 57.26%, 64.59%, and 48.32% confluency in Complete, Half, and Experimental Media respectively (Figure 4:1). SNU-1196 cells had the slowest proliferation rate out of our CCA cells, reaching 54.91%, 53.39%, and 45.47% confluency in Complete, Half, and Experimental Media respectively (Figure 4:1). As MMNK1 cells were used as our 'normal' cholangiocyte cell line, we required a CCA cell line with a similar proliferation rate, to allow experiments to be conducted over the same period which resulted in sufficient cell growth. As CC-SW1 demonstrated a proliferation rate most similar to MMNK1 cells, and good phenotypic separation in varying culture medium whereby lowering richness of growth medium reduced proliferation, (72,74) we selected CC-SW1 as our primary CCA line of interest for further analysis.

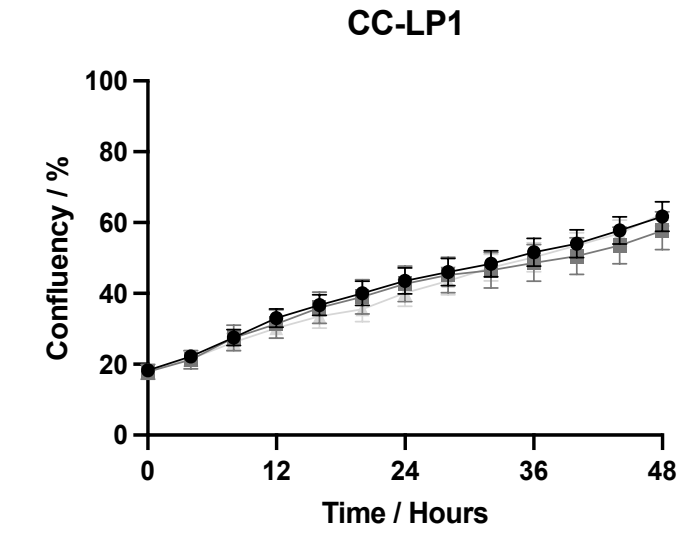
A


MMNK1
Confluency / %
Time / Hours
HG DMEM + 10% FBS
LG DMEM + 5% FBS
LG DMEM + 0.1% BSA

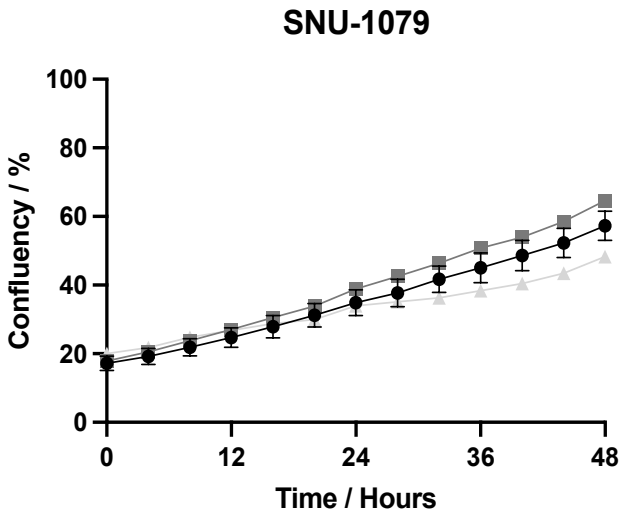
B


CC-SW1
Confluency / %
Time / Hours

C


CC-LP1
Confluency / %
Time / Hours

D



E

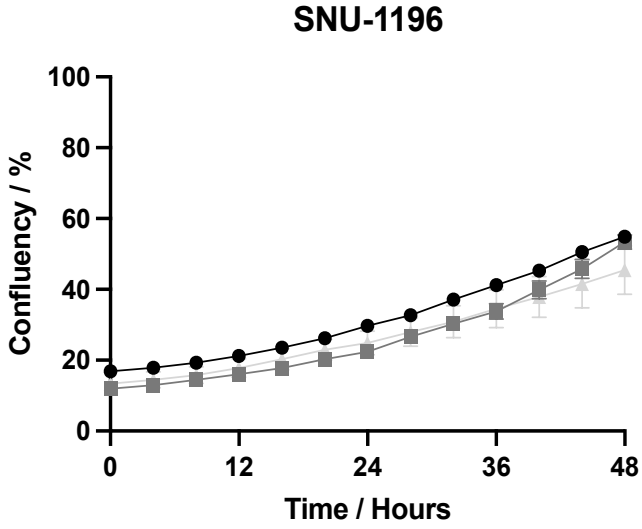


Figure 4:1 – Treatment media affects CCA and cholangiocyte proliferation over 48 hours. *Growth curves for cells cultured over 48 hours with High Glucose DMEM supplemented with 10% FBS, Low Glucose DMEM supplemented with 5% FBS, and Low Glucose DMEM supplemented with 0.1% BSA. A) MMNK1 cells, B) CC-SW1 cells, C) CC-LP1 cells, D) SNU-1079 cells, and E) SNU-1196 cells. Data are plotted as mean confluency (%) ± SEM. (n=3)*

It should be noted that it is unusual that the 'normal' cell line (MMNK1) proliferates faster than the cancer cell line (CC-SW1) as in Figure 4:1. However, as different cell lines, they will have inherently different proliferation rates due to differing genetic backgrounds, and as such one explanation for this rapid proliferation is the immortalization process. Despite this, we consider MMNK1 to constitute a valid cholangiocyte line.

4.3 Cholangiocyte viability is improved by co-culture

4.3.1 Conditioned media from CC-SW1 cells boosts MMNK1 cholangiocyte viability

Conditioned media from each cell line was applied to the reciprocal cell line, after centrifugation at 18000 x *g* to assess the impact of soluble secreted factors on CCA and cholangiocyte cell viability. The cell viability assay revealed a small but significant increase in MMNK1 cell viability with CC-SW1 conditioned media (Figure 4:2)(P=0.03), with no change to CC-SW1 cell viability with MMNK1 conditioned media (Figure 4:2)(P=0.7). As seen in in Figure 4:2, the effect of conditioned media was negligible, and the decsion was made to move towards an indirect co-culture system to gain a larger separation in phenotypic changes and more accurately uncover the indirect reciprocal action of each cell line.

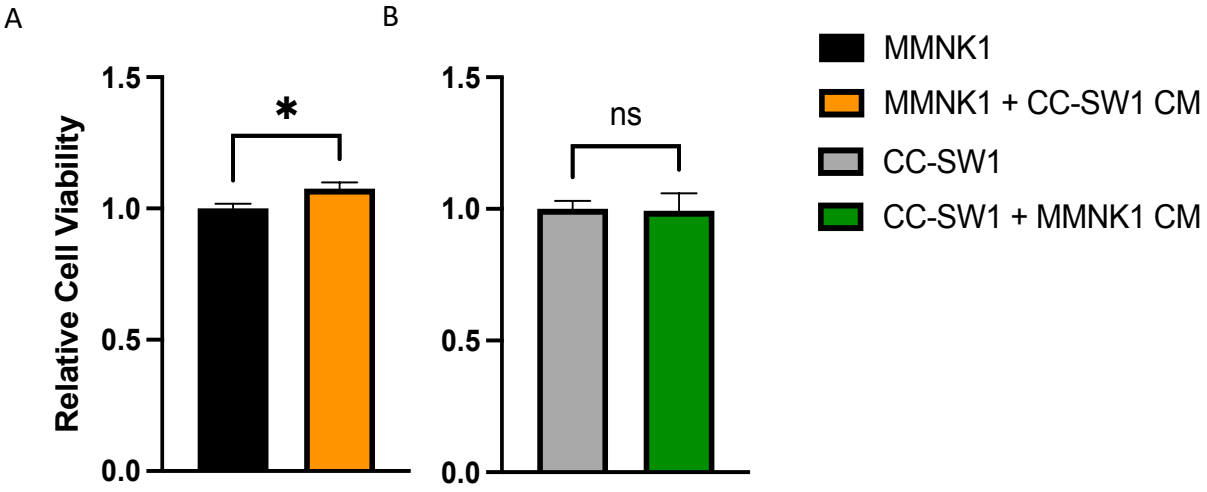


***Figure 4:2 – Conditioned media affects cholangiocyte and CCA cell viability**. A) Relative cell viability of MMNK1 cells treated with CC-SW1 conditioned media for 48 hours. B) Relative cell viability of CC-SW1 cells treated with MMNK1 conditioned media for 48 hours. Data plotted as mean cell viability ± SEM(n=3). *P<0.05. (n=3)*

4.3.2 Co-Culture with CC-SW1 cells boosts cholangiocyte viability

The cell viability assay was repeated, this time using the indirect co-culture system, rather than conditioned media, in order to evaluate the contribution of continually produced secretory factors, as opposed to finite levels in conditioned media. Firstly, we assessed the effect of culture medium on MMNK1 cell viability when grown in the indirect co-culture system. The transwell inserts containing CC-SW1 cells were removed prior to the addition of the CCK8 reagent. Figure 4:3 shows how co-culture increased MMNK1 cell viability when cultured in High Glucose DMEM supplemented with 10% FBS (P=0.0046) or Low Glucose DMEM supplemented with 0.1% BSA (P=0.0001) but not Low Glucose DMEM supplemented with 5% FBS. From this, we concluded Low Glucose DMEM supplemented with 0.1% BSA would be the most suitable Experimental Media.

This Experimental Media was chosen in order to imitate the harsh tumour microenvironment. We required cells to be under stress via starvation, in order to mimic the nutrient depletion and environmental stresses of a harsh tumour microenvironment, whilst allowing for clear phenotypic separation due changes as a direct result of the indirect co-culture system. Our criteria for cellular stress was based on a reduction in proliferation rate. Whilst also using a low concentration to stress cells, unlike FBS, BSA is non-stimulatory, further contributing to the stressed environment.

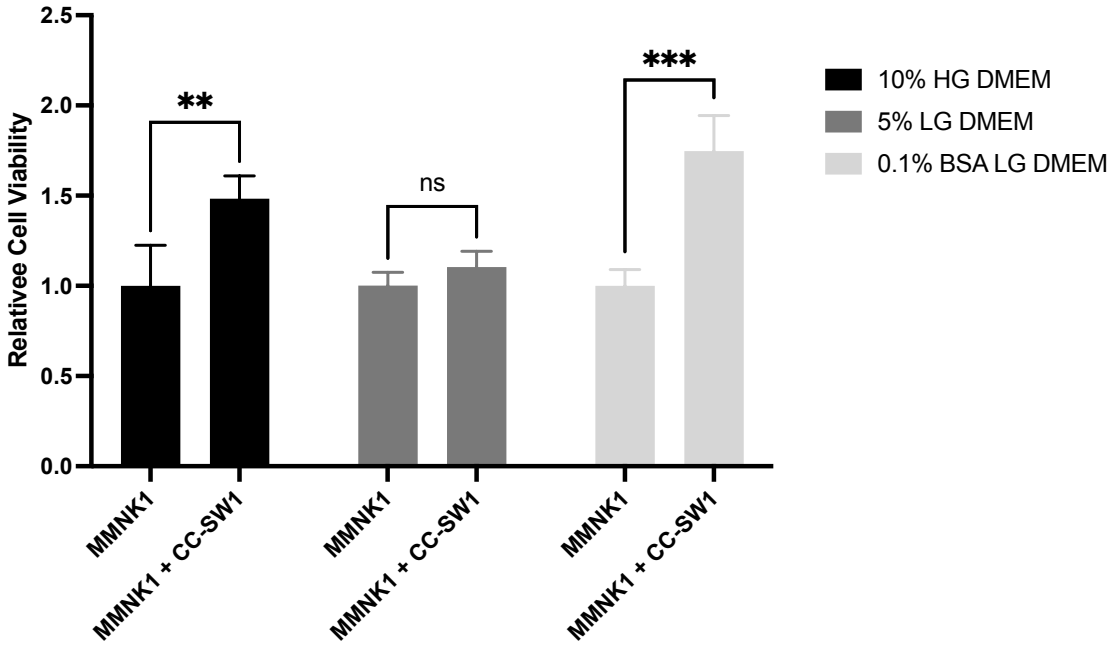


Figure 4:3 – Culture media affects indirect co-culture mediated improvements in MMNK1 cholangiocyte viability*. Relative cell viability of MMNK1 cells in a 1:1 indirect co-culture with CC-SW1 cells cultured over 48-hours, with High-Glucose DMEM supplemented with 10% FBS (Complete culture media), Low-Glucose DMEM supplemented with 5% FBS (Half culture media), and Low Glucose DMEM supplemented with 0.1% BSA (Experimental culture media). Data plotted as mean cell viability ± SEM(n=3). **P<0.01, ***P<0.001.*

Next, we confirmed that culturing MMNK1 cells in Low Glucose DMEM supplemented with 0.1% BSA in the indirect co-culture system with CC-SW1 cells caused a statistically significant increase in MMNK1 cell viability (P=0.0057) (Figure 4:4), which is a similar trend to the data seen in Figure 4:2. Dissimilar to Figure 4:2 however, we found that CC-SW1 cells in the indirect co-culture system experienced a statistically significant decrease in cell viability (P=0.0068) (Figure 4:4).

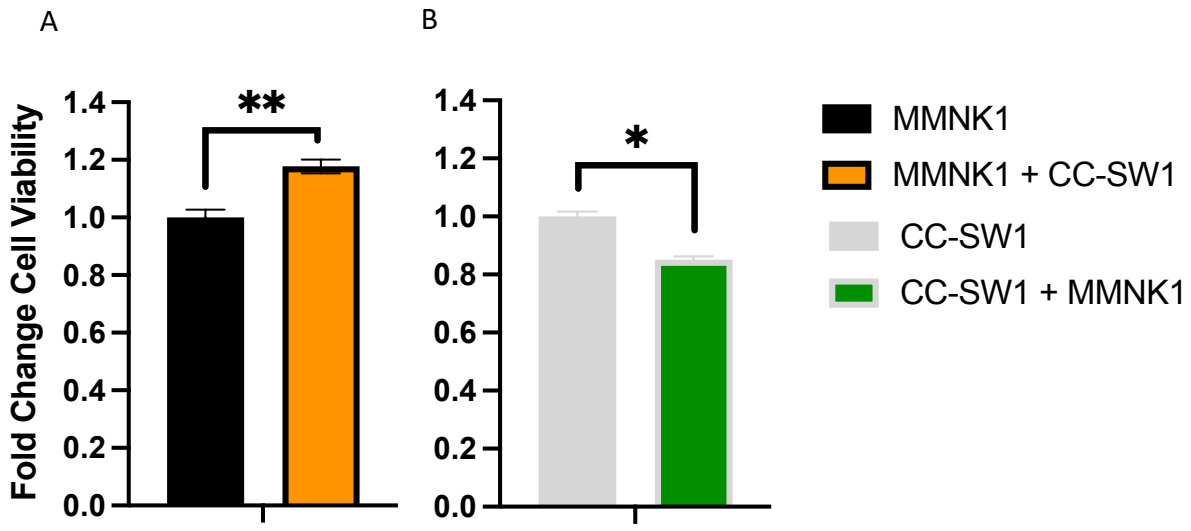


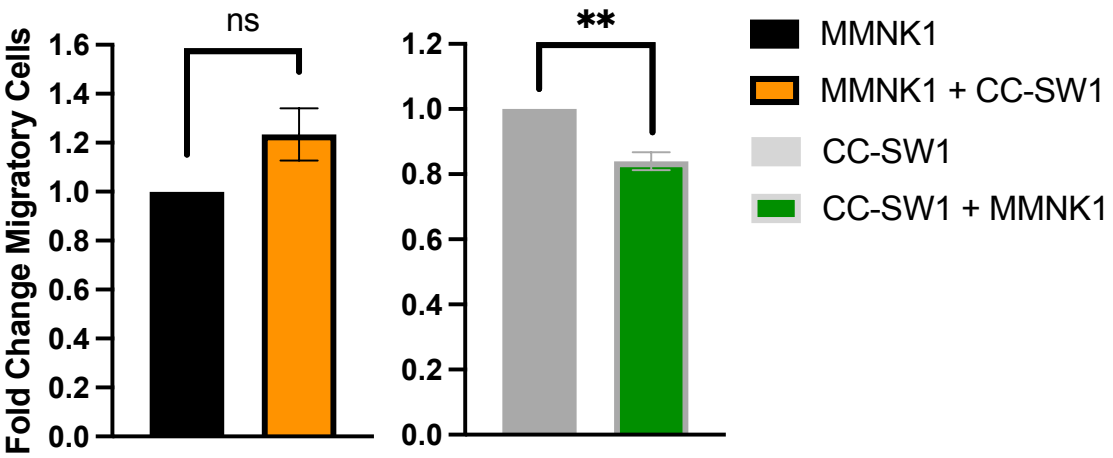
Figure 4:4 - Indirect co-culture boosts MMK1 cholangiocyte viability, whilst reducing CCA cell viability*. Fold change in cell viability of MMNK1 cells during co-culture with CC-SW1 cells, and fold change in CC-SW1 cell viability during co-culture with MMNK1 cholangiocytes. Data plotted as mean fold change in cell viability ± SEM(n=3). *P<0.05,**P<0.01.*

4.4 Co-Culture reduces CC-SW1 migration

4.4.1 Co-culture reduces the proportion of migratory CC-SW1 cells

A transwell migration assay was used to assess changes to the migratory properties of each cell line in the co-culture system. Cells are stained with crystal violet (purple), as seen in Figure 4:5. There was no change to the proportion of migratory MMNK1 cells (P=0.1) (Figure 4:5) whilst indirect co-culture decreased the number of migratory CC-SW1 cells (P=0.02) (Figure 4:5). Figure 4:5 shows representative images of the transwell system, with no significant difference in the proportion of migratory MMNK1 cells, and a distinct decrease in the proportion of migratory CC-SW1 cells.

A



B

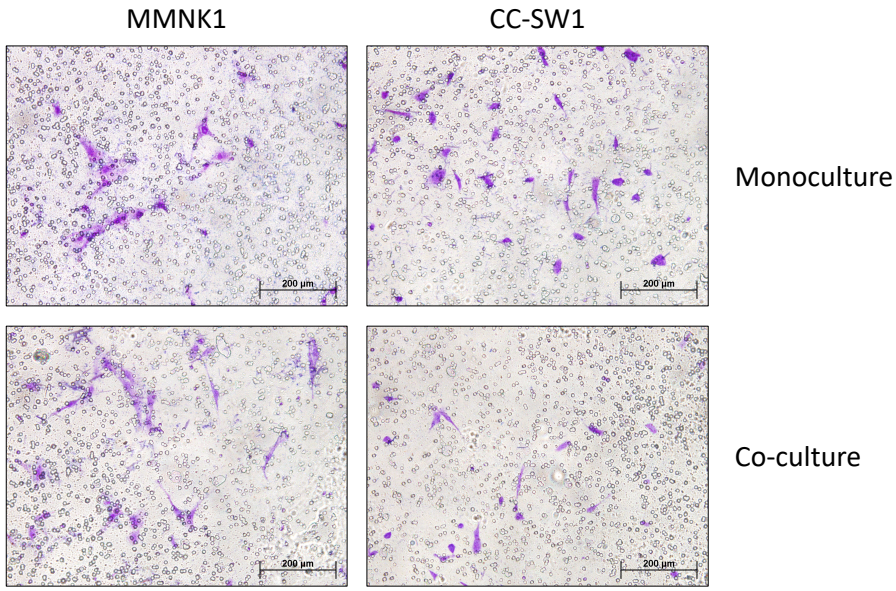


Figure 4:5 – Co-culture reduces the proportion of migratory CC-SW1 cells*. A) Fold change in proportion of transwell migratory MMNK1 cholangiocytes and CC-SW1cells during co-culture. B) Representative microscope images of MMNK1 cholangiocytes and CC-SW1 cells grown in monoculture and co-culture. Data plotted as fold migratory cells ± SEM (n=3). **P<0.01.*

4.4.2 Co-culture reduces EMT protein and gene expression

We selected CC-SW1 for molecular analysis of motile behaviours, specifically EMT protein expression due to the changes in its migratory behaviours illustrated in Figure 4:6. Western blotting confirmed inhibition of expression of the EMT proteins Vimentin (Figure 4:6) (P=0.0045) and Slug (Figure 7A and C) (P=0.0001), with concurrent increase in the expression of the epithelial marker E-cadherin (Figure 4:6) (P=0.0204).

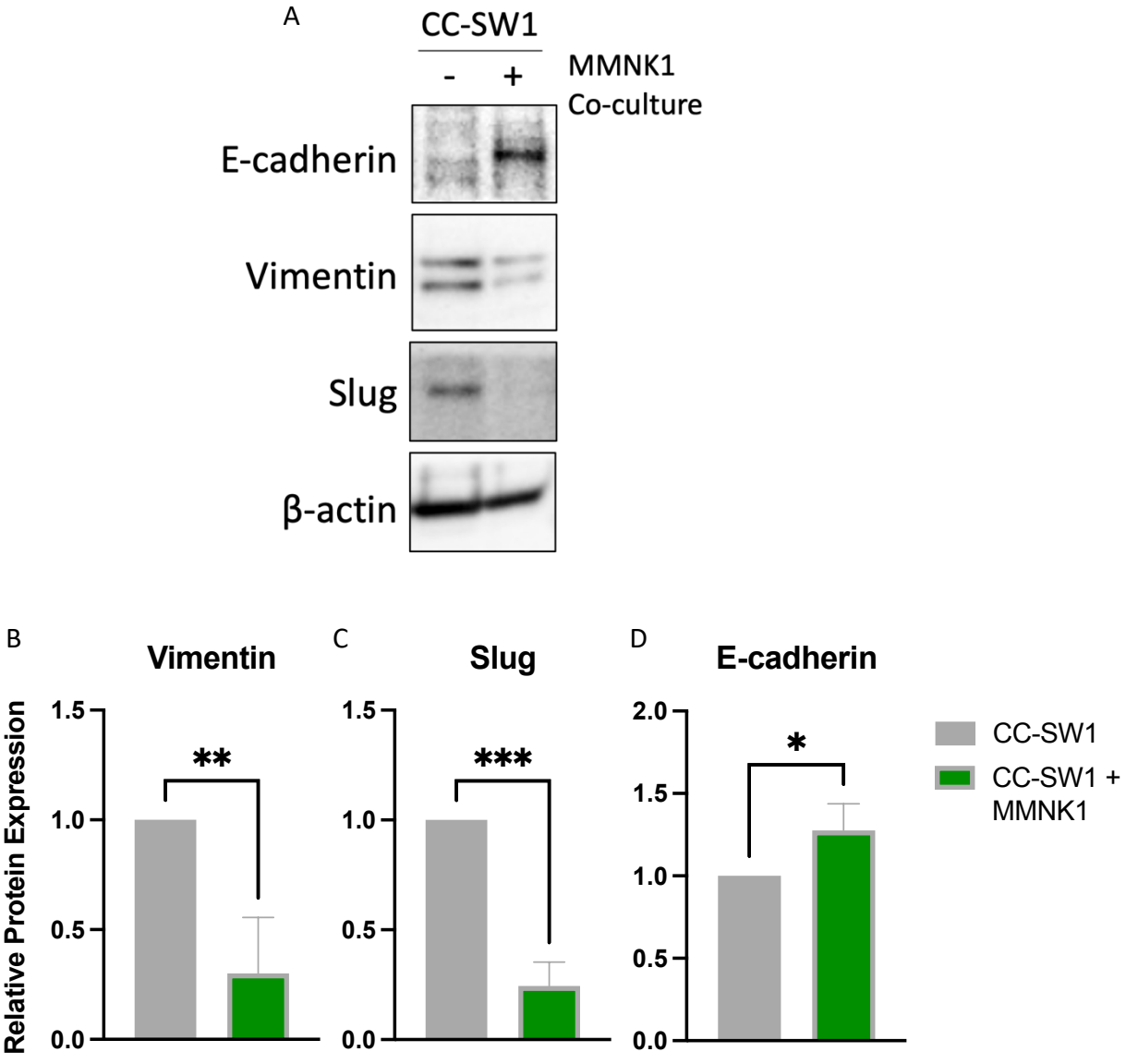
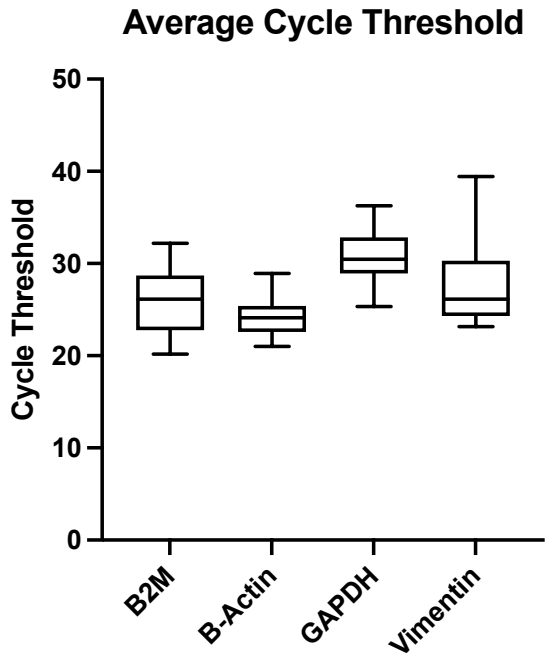


***Figure 4:6 – Co-culture reduces EMT protein expression in CC-SW1 cells**. A) Immunoblotting revealed a significant decrease in the relative protein expression of B) Vimentin, and V) Slug, with a concurrent increase in D) E-cadherin protein expression. Data plotted as mean relative protein expression cells ± SEM (n=3). *P<0.05, **P<0.01, ***P<0.001.*

In order to assess gene expression levels, we first conducted a study to select an appropriate housekeeping gene to normalise our expression data. Figure 4:7A shows the average cycle threshold for 3 potential housekeeping genes, whilst Figure 4:7B shows the variability in the ΔCT values for each housekeeping gene when compared to our gene of interest (*Vimentin*). *β-actin* had the smallest variation in cycle threshold (Figure 4:7A) averaging 26.07 cycles, as well as the smallest variation in ΔCT compared to *Vimentin* (Figure 4:7B) averaging 2.93, and as such was selected as the most appropriate housekeeping gene for all future qPCR work.

A



B

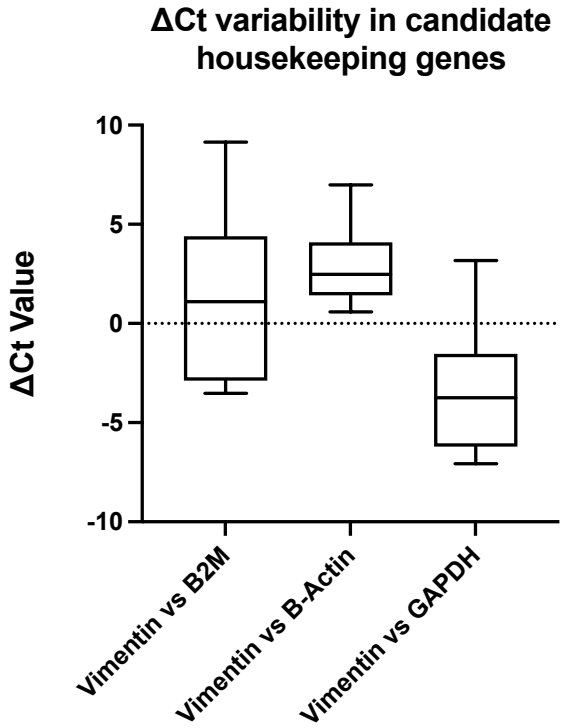


Figure 4:7 – qPCR housekeeping gene validation and selection*. A) Average cycle threshold for amplification of the housekeeping genes* B2M, B-actin, GAPDH*, contrasted to gene of interest, Vimentin. Data plotted as mean cycle threshold ± SEM (n=3). B) The ΔCt variability in candidate housekeeping genes compared to the gene of interest, Vimentin. Data plotted as mean ΔCt ± SEM (n=3).*

A qPCR analysis of *Vimentin, Slug,* and *Snail* gene expression was then conducted (Figure 4:8), and illustrated a significant decrease in gene expression with P-values of 0.0245, 0.0001, and 0.0043 respectively. Likewise qPCR showed an increase in the gene expression of *CDH1*, (P=0.0367) which encodes E-Cadherin (Figure 4:8).

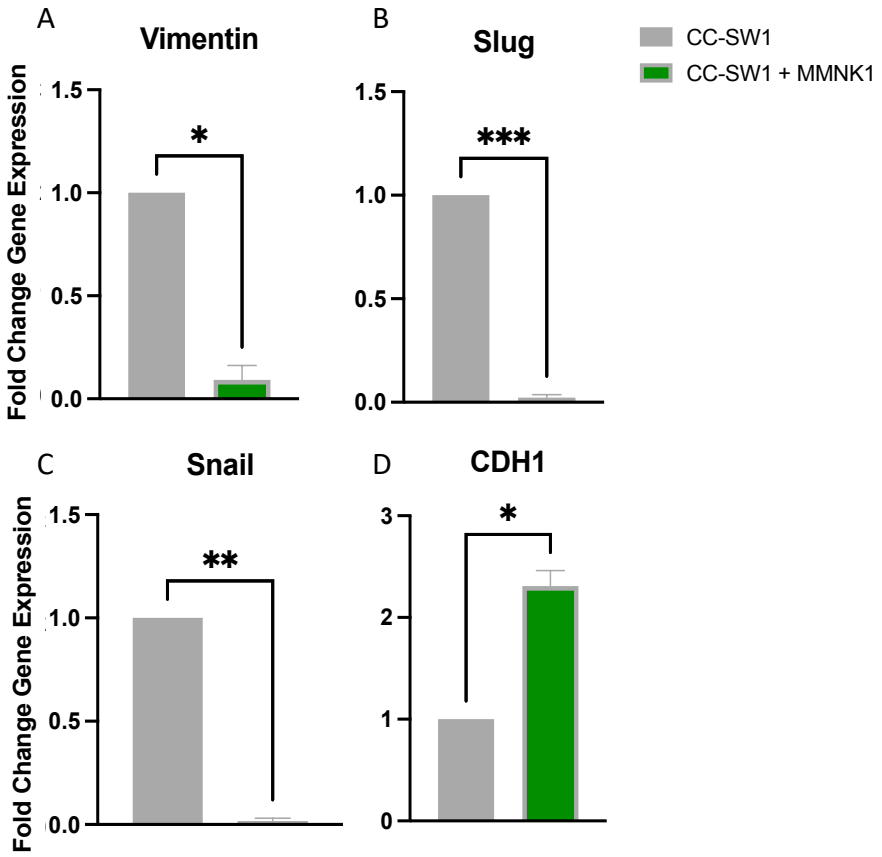


Figure 4:8 - ***Co-culture reduces EMT gene expression in CC-SW1 cells****. Evaluation of CC-SW1 gene expression via qPCR revealed a significant decrease in gene expression of A)* Vimentin*, B)* Slug*, and C)* Snail*, with a concurrent increase in D)* CDH1 *(E-cadherin) gene expression. Data plotted as mean fold change gene expression ± SEM(n=3). *P<0.05, **P<0.01, ***P<0.001.*

4.5 Co-culture increases cholangiocyte, and restricts CCA cell cycle progression

We used Flow Cytometry to compare the proportion of cells in each phase of the cell cycle during co-culture. Figure 4:9 shows an increase in the proportion of MMNK1 cells in the G2M phase during co-culture (P= 0.0341), with no changes to the G1 or S phases.

Figure 4:10 shows a decrease in the proportion of CC-SW1 cells in S phase during co-culture (P=0.0460), with no changes to the G1 or G2M phases.

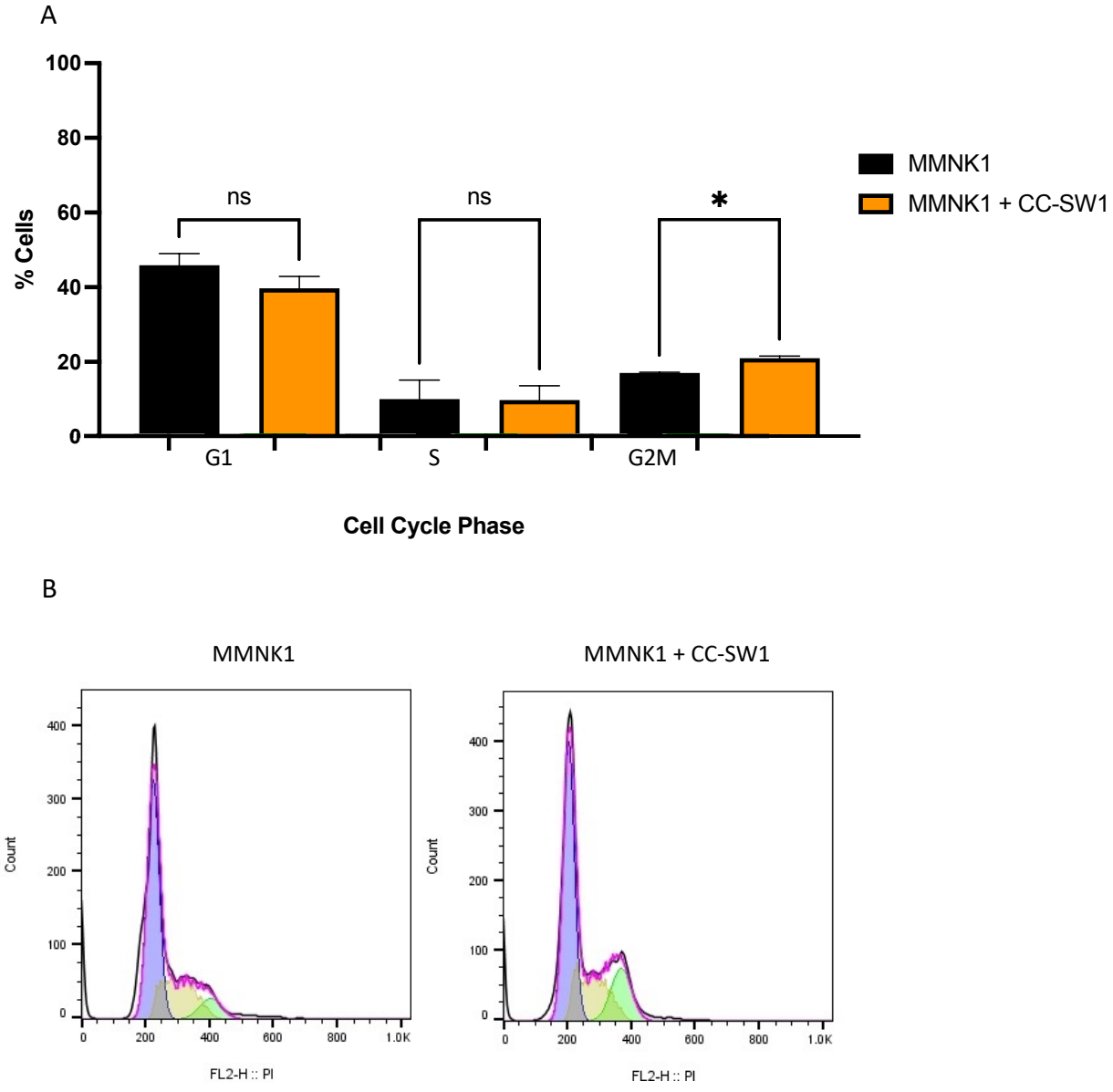


***Figure 4:9 – Co-culture increases the proportion of MMNK1 cells in the G2M cell cycle phase**. A) The percentage of MMNK1 cells in the G1, S, and G2M phase of the cell cycle when cultured in mono- and co-culture. Data plotted as mean percentage of cells (%) ± SEM (n=3). *P<0.05. B) Representative FlowJo plot of the FACS gating for MMNK1 cells in each phase of the cycle, when cultured in mono- and co-culture.*

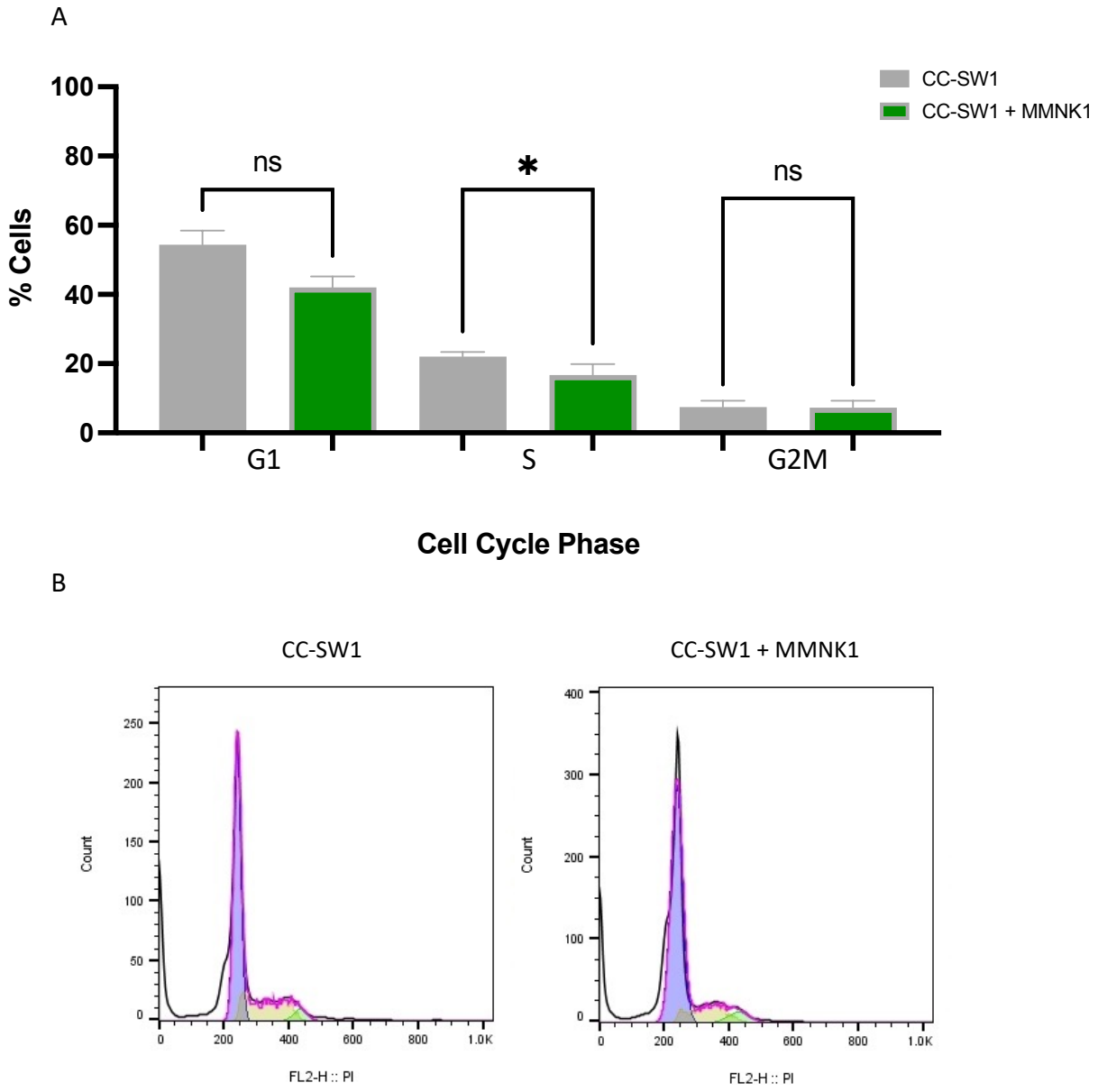


Figure 4:10 – Co-culture increases the proportion of CC-SW1 cells in S phase*. A) The percentage of CC-SW1 cells in the G1, S, and G2M phase of the cell cycle when cultured in mono- and co-culture. Data plotted as mean percentage of cells (%)± SEM (n=3). *P<0.05. B) Representative FlowJo plot of the FACS gating for CC-SW1 cells in each phase of the cycle, when cultured in mono- and co-culture.*

4.6 Co-culture triggers a reduction cholangiocyte apoptosis

Flow cytometry (FACS) analysis was used to assess the proportion of cells in early and late apoptosis via the presence of phosphatidylserine (PS) on the cell surface, as assayed by Annexin V staining, and the cell permeability DNA-binding dye propidium iodide (PI). PS is only present on the cell surface when a cell is undergoing apoptosis. Likewise PI, is excluded from viable cells and can only penetrate the cell membranes of dead or dying cells, thus only binding to the DNA of cells in the later stages of apoptosis. The cells in the upper left quadrant (Q1) indicate Annexin-negative/PI-positive, necrotic cells. Cells in the upper right quadrant (Q2) indicate Annexin-positive/PI-positive, late apoptotic cells. Cells in the lower right quadrant (Q3) indicate Annexin V-positive, early apoptotic cells. The cells in the lower left quadrant (Q4) indicate Annexin-negative/PI-negative, viable cells.

Flow cytometric analysis of Annexin V and PI-staining demonstrated a reduction in early apoptotic (Figure 4:11, Q3) and late apoptotic (Figure 4:11, Q2) MMNK1 cells during indirect co-culture with CC-SW1 cells (P=0.05)(Figure 4:11).

We expanded the study to include the other CCA cell lines CC-LP1, SNU-1079, and SNU-1196, to evaluate whether the change in apoptosis was commonly observed across multiple CCA cell lines. There was also a reduction in apoptosis (late apoptosis) in MMNK1 cells when in co-culture with CC-LP1 cells (P=0.04)(Figure 4:12). There was no significant difference in the proportion of apoptotic MMNK1 cells when cultured with SNU-1079 (Figure 4:13) or SNU-1196 (Figure 4:14) cells. Conversely there was no change in the proportion of apoptotic CC-SW1 (Figure 4:15) or CC-LP1 (Figure 4:16) cells during co-culture with MMNK1 cells (P=0.1 and 0.4 respectively).

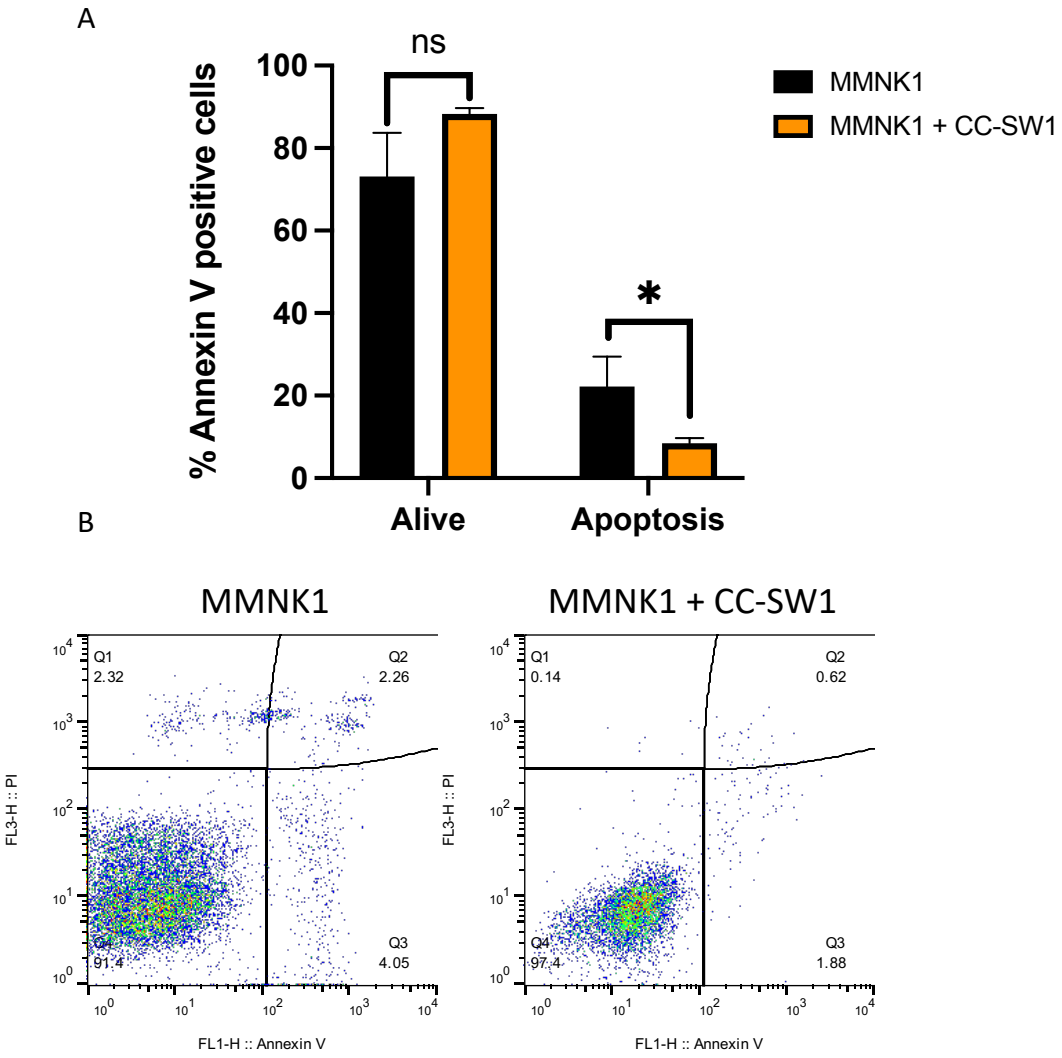


Figure 4:11 – Co-culture with CC-SW1 triggers a reduction in the proportion of apoptotic MMNK1 cells. *A) Flow cytometry quantification of the proportion of apoptotic and alive MMNK1 cells in mono- and co-culture with CC-SW1. Data plotted as mean percentage of Annexin V positive cells ± SEM, (n=5). *P<0.05. B) Representative FlowJo plot with quadrant separation of Annexin V and PI positively stained MMNK1 cells.*

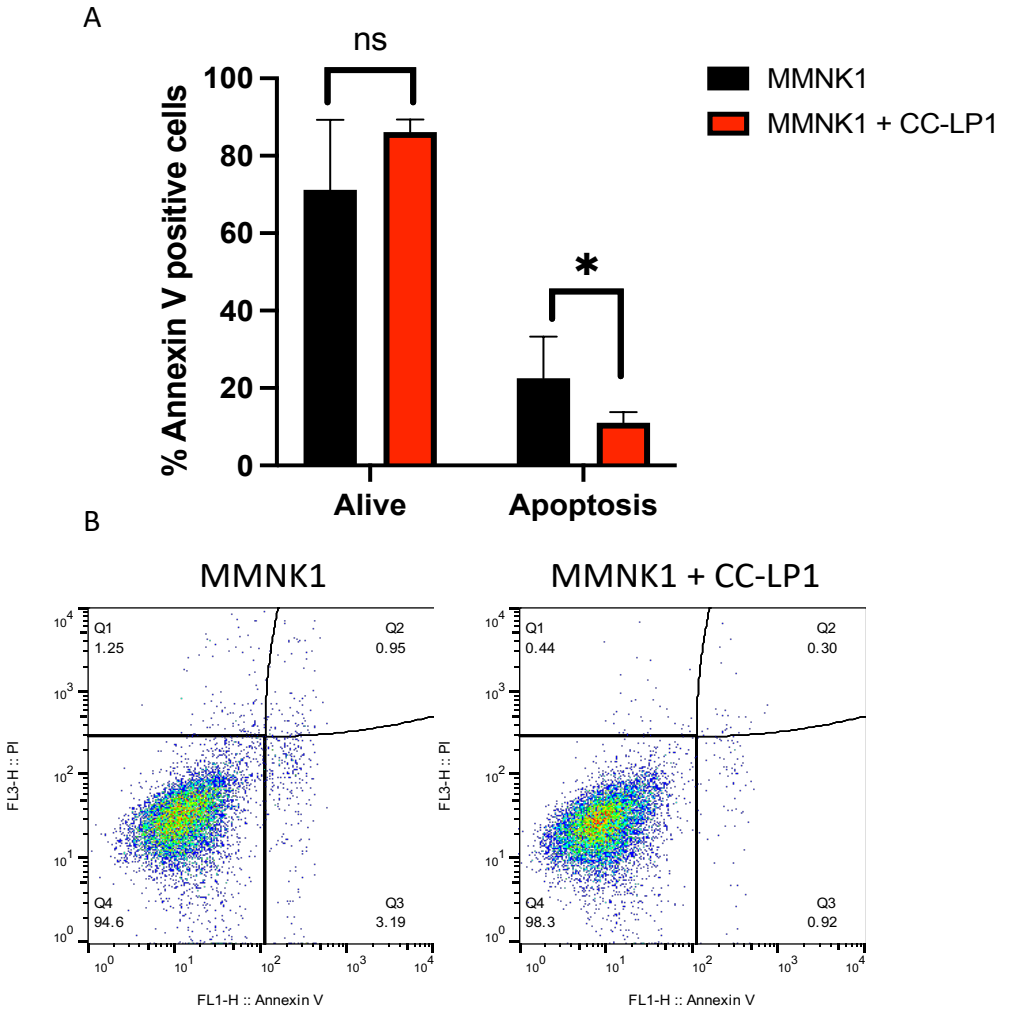


Figure 4:12 – Co-culture with CC-LP1 triggers a reduction in the proportion of apoptotic MMNK1 cells. *A) Flow cytometry quantification of the proportion of apoptotic and alive MMNK1 cells in mono- and co-culture with CC-LP1 cells. Data plotted as mean percentage of Annexin V positive cells ± SEM, (n=5). *P<0.05. B) Representative FlowJo plot with quadrant separation of Annexin V and PI positively stained MMNK1 cells.*

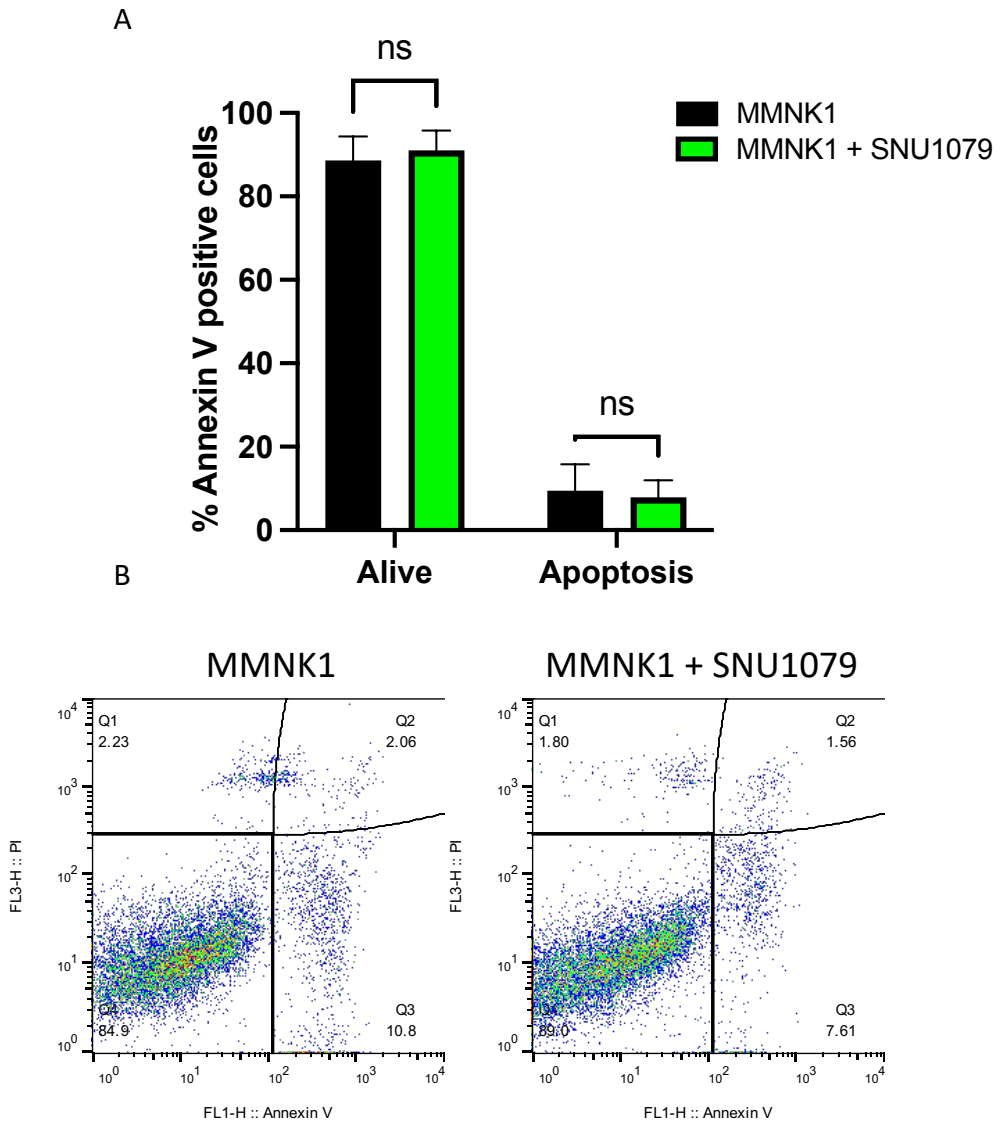


Figure 4:13 – Co-culture with SNU-1079 has no effect on the proportion of apoptotic MMNK1 cells. *A) Flow cytometry quantification of the proportion of apoptotic and alive MMNK1 cells in mono- and co-culture with SNU-1079. Data plotted as mean percentage of Annexin V positive cells ± SEM, (n=3). *P<0.05. B) Representative FlowJo plot with quadrant separation of Annexin V and PI positively stained MMNK1 cells.*

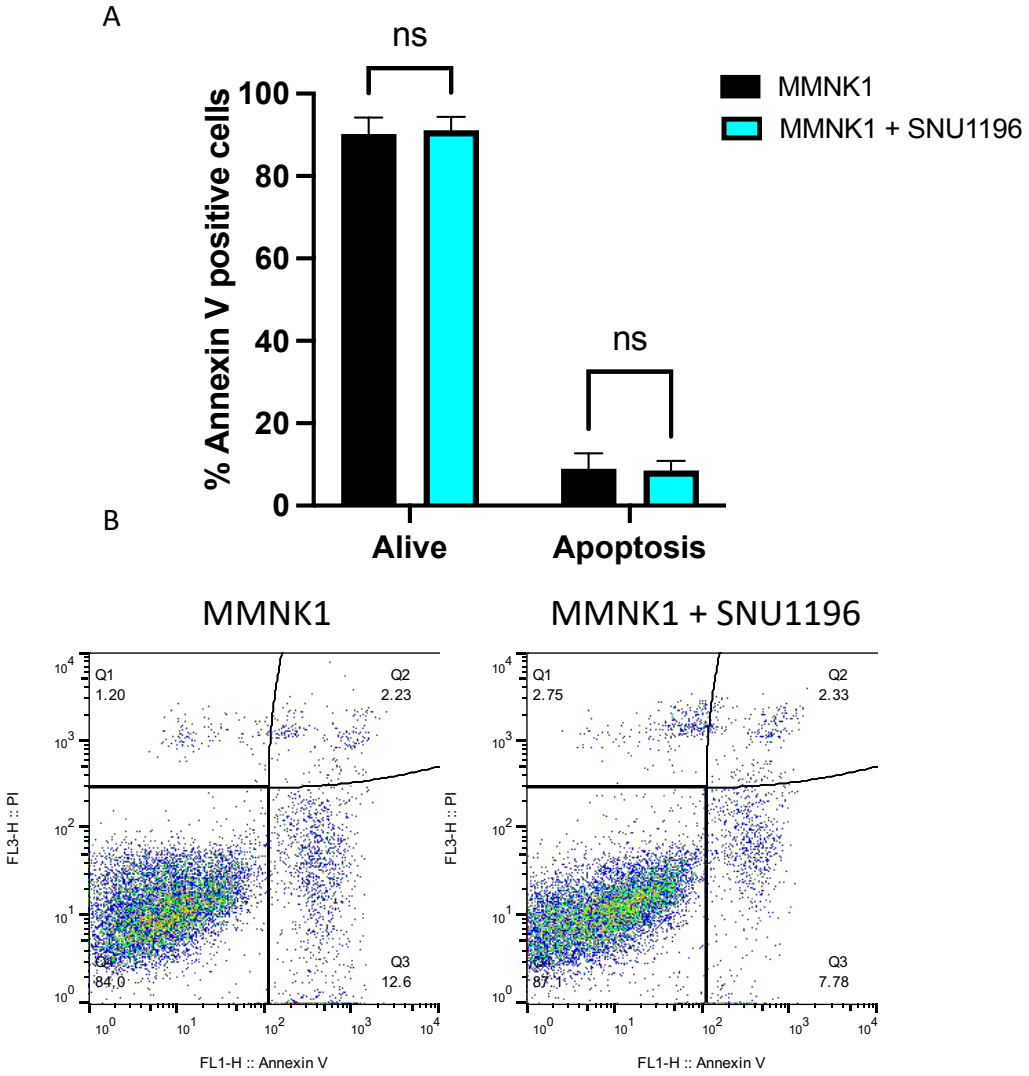


Figure 4:14 – Co-culture with SNU-1196 has no effect on the proportion of apoptotic MMNK1 cells. *A) Flow cytometry quantification of the proportion of apoptotic and alive MMNK1 cells in mono- and co-culture with SNU-1196. Data plotted as mean percentage of Annexin V positive cells ± SEM, (n=3). *P<0.05. B) Representative FlowJo plot with quadrant separation of Annexin V and PI positively stained MMNK1 cells*

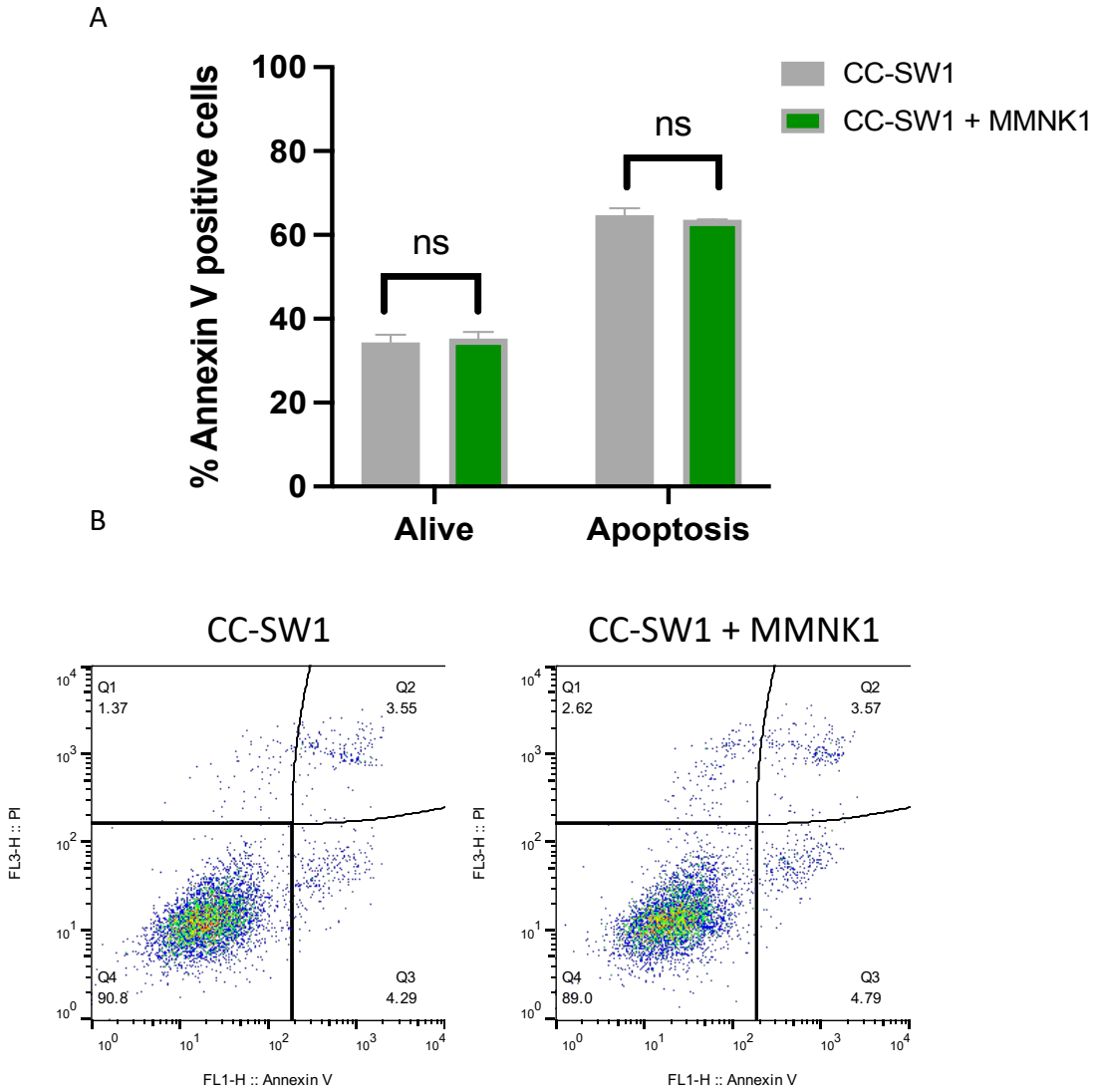


Figure 4:15 - Co-culture with MMNK1 cholangiocytes has no effect on the proportion of apoptotic CC-SW1 cells. *A) Flow cytometry quantification of the proportion of apoptotic and alive CC-SW1 cells in mono- and co-culture with MMNK1 cholangiocyte cells. Data plotted as mean percentage of Annexin V positive cells ± SEM, (n=5). *P<0.05. B) Representative FlowJo plot with quadrant separation of Annexin V and PI positively stained CC-SW1 cells.*

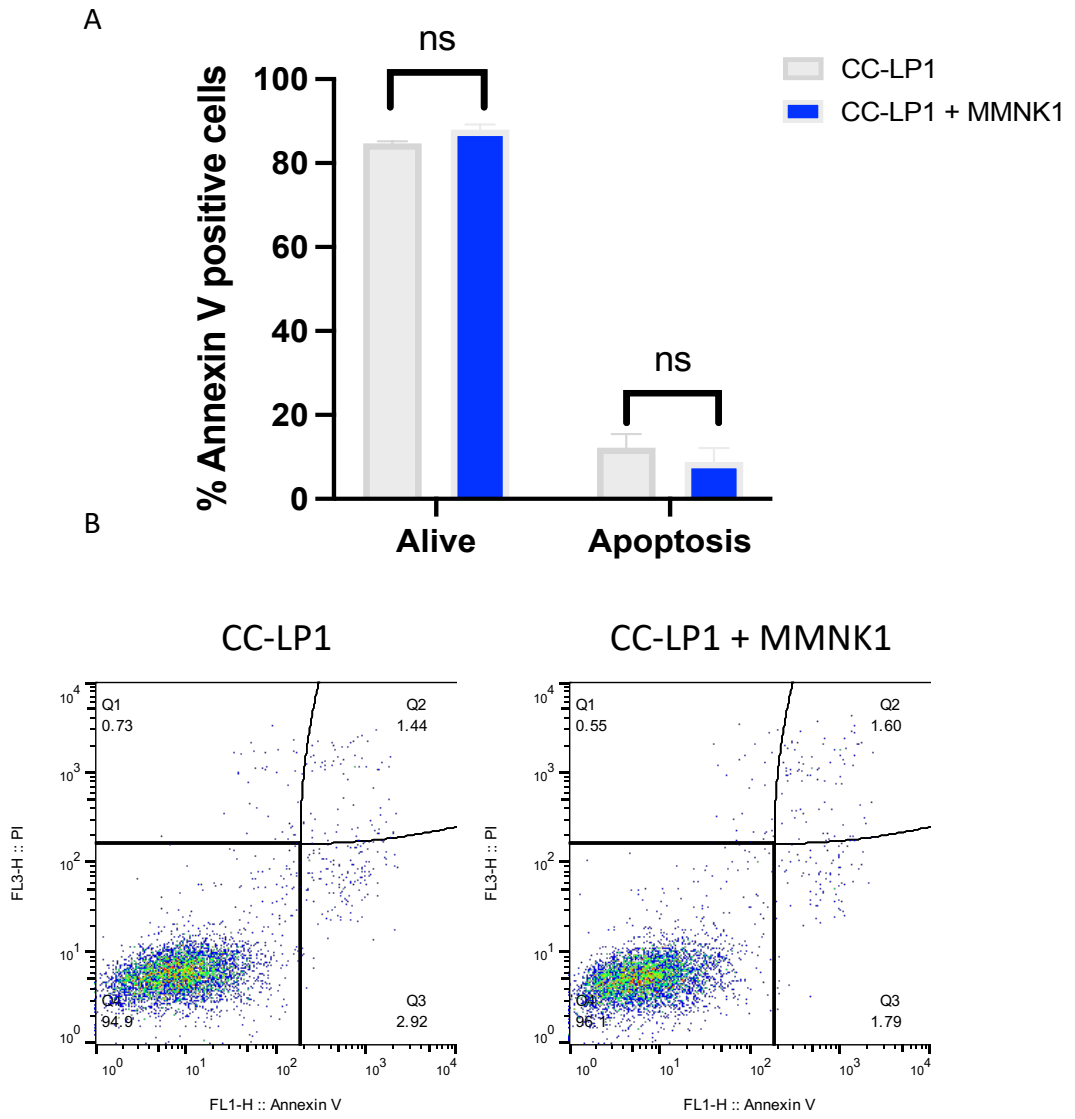


Figure 4:16 - Co-culture with MMNK1 cholangiocytes has no effect on the proportion of apoptotic CC-LP1 cells. *A) Flow cytometry quantification of the proportion of apoptotic and alive CC-LP1 cells in mono- and co-culture with MMNK1 cholangiocyte cells. Data plotted as mean percentage of Annexin V positive cells ± SEM, (n=4). *P<0.05. B) Representative FlowJo plot with quadrant separation of Annexin V and PI positively stained CC-LP1 cells.*

4.6.1 Co-culture triggers a downregulation in apoptotic protein expression

Due to the reduction in apoptosis illustrated in Figure 4:11, we conducted molecular analyses on MMNK1 cells after co-culture with CC-SW1 cells. Immunoblotting analysis (Figure 4:17A) revealed a decrease in p53, BAX, Caspase-3, and Caspase-8 protein expression in MMNK1 cells (P=0.008, 0.03, 0.012, and 0.001 respectively) after co-culture (Figure 4:17B).

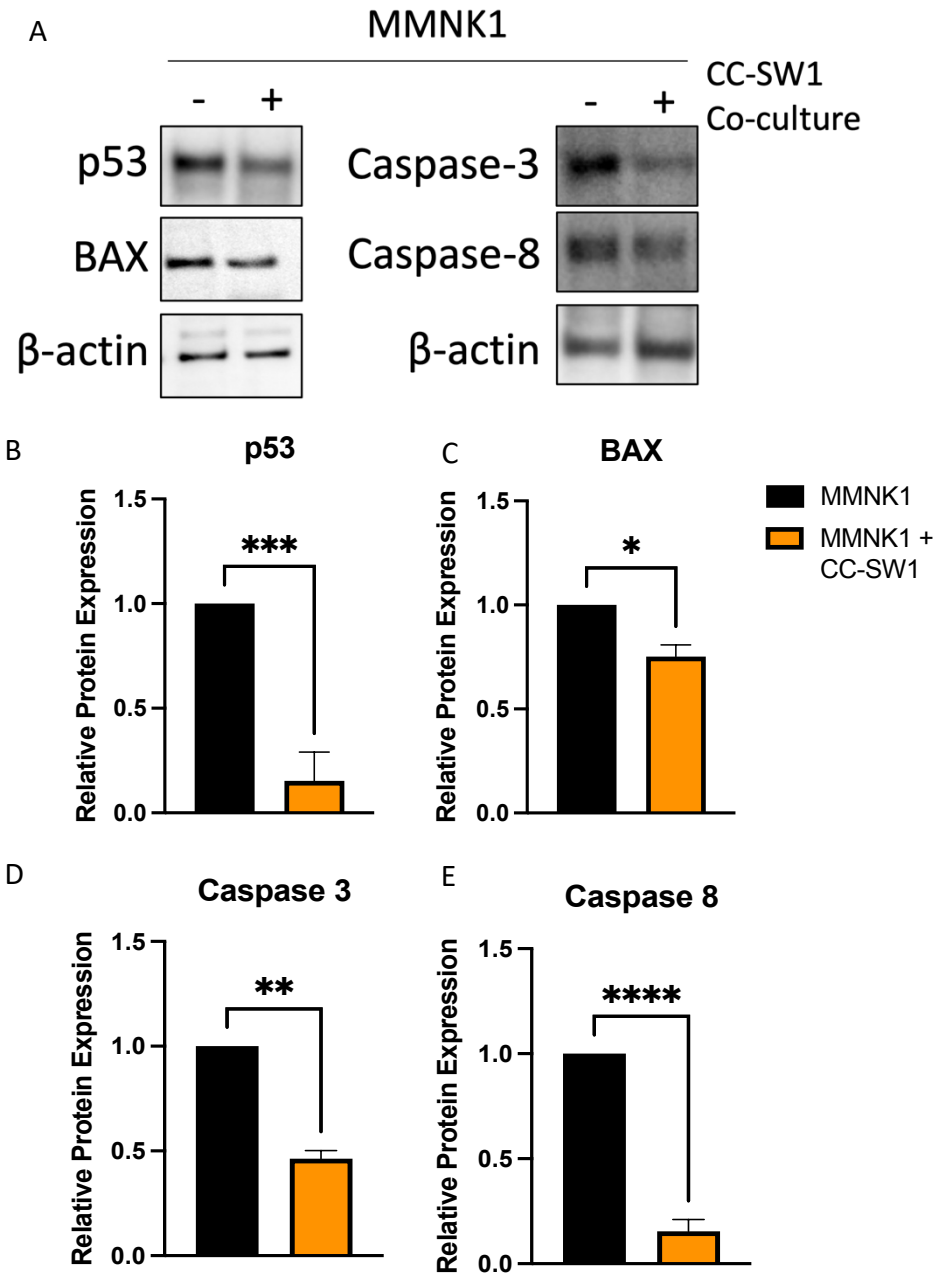


Figure 4:17 - Co-culture reduces apoptotic protein expression in MMNK1 cells. *A) Immunoblotting revealed a significant decrease in the relative protein expression of B) p53, C) BAX, D) Caspase-3, and E) Caspase-8. Data plotted as mean relative protein expression cells ± SEM(n=3). *P<0.05, **P<0.01, ***P<0.001, ****P<0.0001.*

4.7 Heat inactivation of culture media highlights the proportional importance of proteins and metabolic components

To deduce whether the changes in MMNK1 and CC-SW1 cell viability were due to a protein or metabolite based effect, we heat inactivated the conditioned culture media from each cell line, at 90°C for 30 minutes, and reassessed its capability to induce functional changes.

4.7.1 Heat inactivated conditioned media reduces cholangiocyte and CCA cell viability

There was a significant decrease in MMNK1 cell viability when cultured in the Experimental Media (low glucose DMEM supplemented with 0.1% BSA) after heat inactivation (Figure 4:18A)($P<0.0001$), as well as after culturing in conditioned media from CC-SW1 cells that had been heat inactivated (Figure 4:18A)($P=0.0027$). There was a small significant increase in MMNK1 cell viability when cultured in conditioned media from MMNK1 cells that had been heat inactivated (Figure 4:18A).

There was a significant decrease in CC-SW1 cell viability when cultured in the Experimental Media (low glucose DMEM supplemented with 0.1% BSA) after heat inactivation (Figure 4:18B)($P=0.0346$). There was no significant change in CC-SW1 cell viability when cultured in conditioned media from either MMNK1 or CC-SW1 cells that had been heat inactivated (Figure 4:18B).

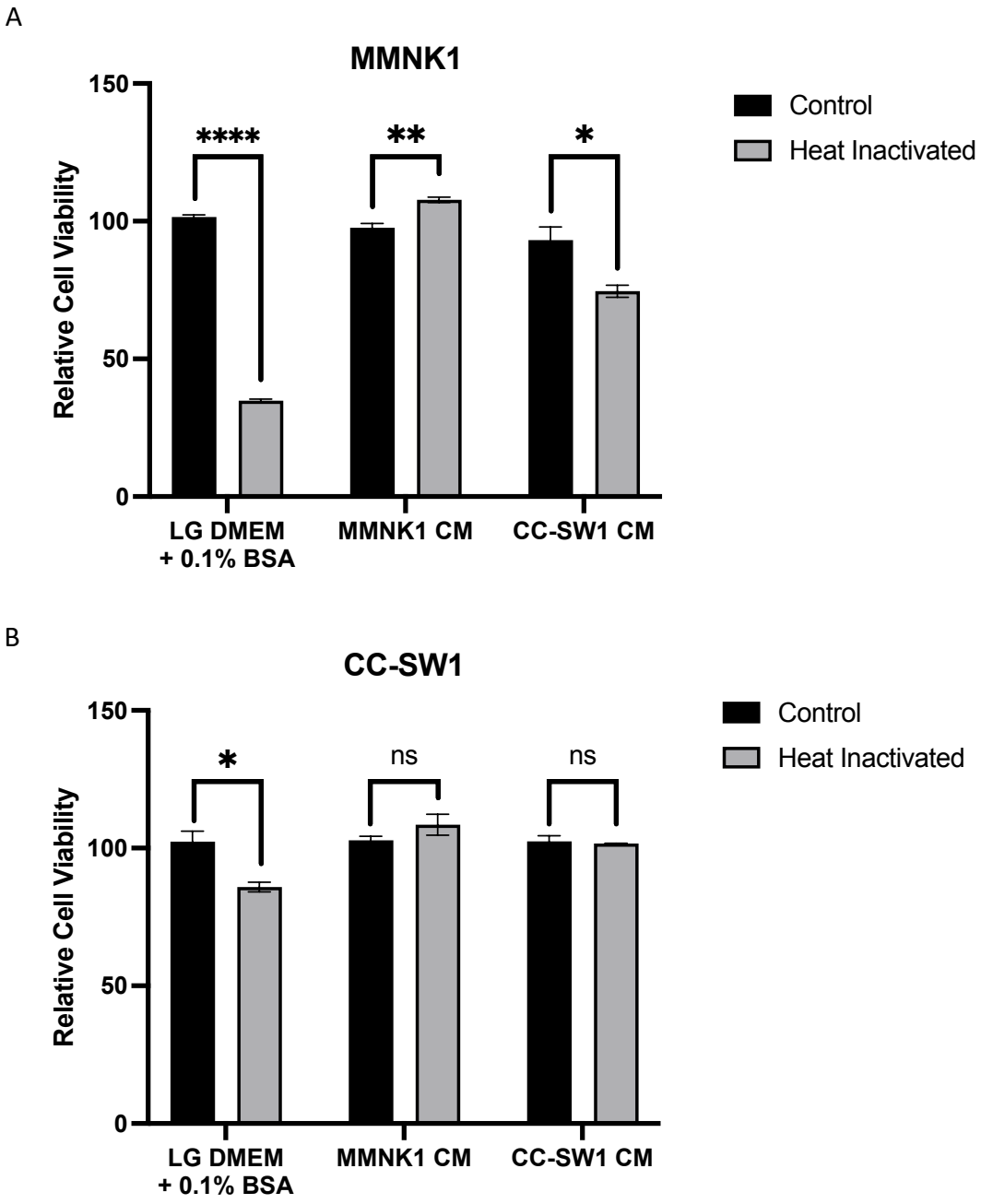
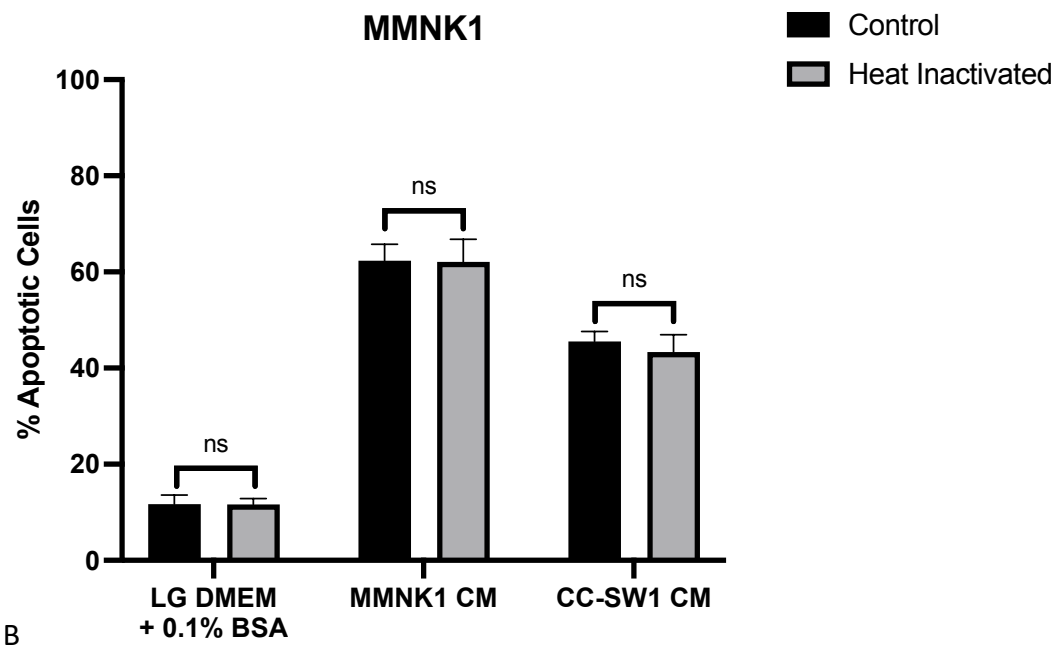


Figure 4:18 – Heat inactivated conditioned media reduces cholangiocyte and CCA cell viability. *Conditioned media was extracted from MMNK1 and CC-SW1 cells, with half of each volume inactivated at 90°C for 30 minutes. A) MMNK1 cell viability was assessed when cultured in raw or heat inactivated versions of fresh low-glucose DMEM supplemented with 0.1% BSA, conditioned media extracted from MMNK1 cells, and conditioned media extracted from CC-SW1 cells. Heat inactivated low-glucose DMEM supplemented with 0.1% BSA reduced MMNK1 cell viability, as did heat inactivated conditioned media from CC-SW1 cells. There was a significant increase in MMNK1 cell viability when treated with MMNK1 conditioned media that had been heat inactivated. B) CC-SW1 cell viability was assessed when cultured in raw or heat inactivated versions of fresh low-glucose DMEM supplemented with 0.1% BSA, conditioned media extracted from MMNK1 cells, and conditioned media extracted from CC-SW1 cells. Heat inactivated conditioned media from CC-SW1 cells caused a significant reduction in CC-SW1 cell viability compared to CC-SW1 conditioned media that had not been heat inactivated. Data plotted as mean change in cell viability ± SEM(n=3). *P<0.05, **P<0.01, ***P<0.001, ****P<0.0001*

4.7.2 Heat inactivated conditioned media has no effect on cholangiocyte or CCA apoptosis

Flow cytometry was used to determine the proportion of apoptotic MMNK1 and CC-SW1 cells following treatment with control or heat inactivated media. We found no significant difference in the number of apoptotic or viable MMNK1 (Figure 4:19) or CC-SW1 cells (Figure 4:20) when treated with control or heat inactivated media.

A



B

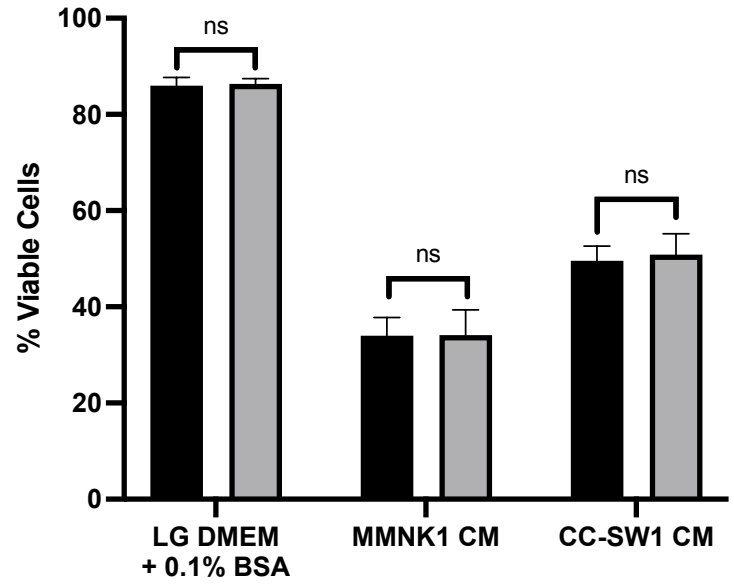
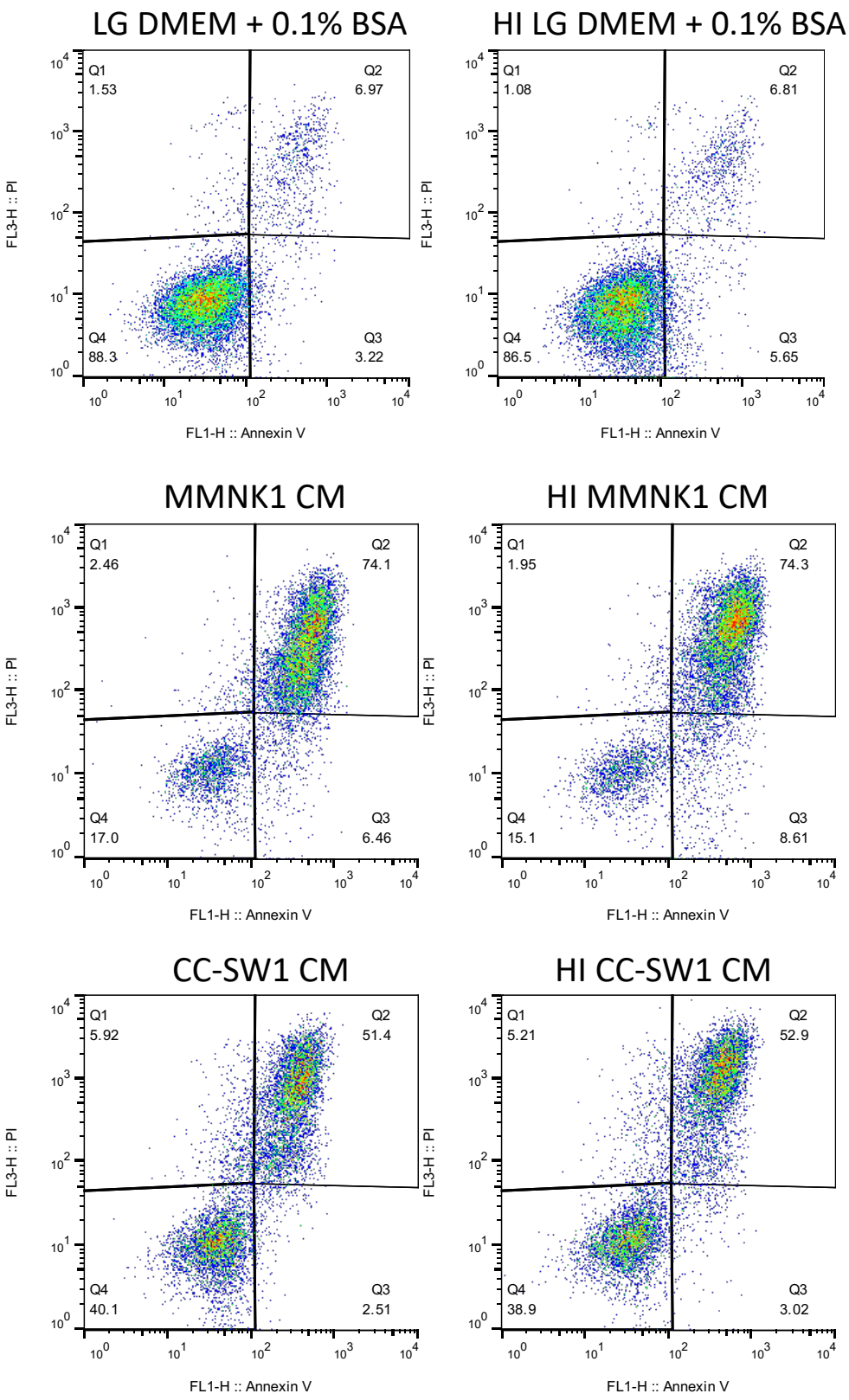


Figure 4:19 - Heat inactivated conditioned has no effect on the proportion of apoptotic MMNK1 cholangiocytes. *Conditioned media was extracted from MMNK1 and CC-SW1 cells, with half of each volume inactivated at 90°C for 30 minutes. Flow cytometry was conducted to quantify the proportion of A) apoptotic, and B) alive MMNK1 cells after treatment with raw and heat inactivated media. Heat inactivation of each media had no statistically significant impact on cell viability. C) Representative FlowJo plot with quadrant separation of Annexin V and PI positively stained MMNK1 cells.(n=3).*

C


LG DMEM + 0.1% BSA
Q1
1.53
Q2
6.97
Q4
88.3
Q3
3.22
HI LG DMEM + 0.1% BSA
Q1
1.08
Q2
6.81
Q4
86.5
Q3
5.65
MMNK1 CM
Q1
2.46
Q2
74.1
Q4
17.0
Q3
6.46
HI MMNK1 CM
Q1
1.95
Q2
74.3
Q4
15.1
Q3
8.61
CC-SW1 CM
Q1
5.92
Q2
51.4
Q4
40.1
Q3
2.51
HI CC-SW1 CM
Q1
5.21
Q2
52.9
Q4
38.9
Q3
3.02
FL3-H :: PI
FL1-H :: Annexin V

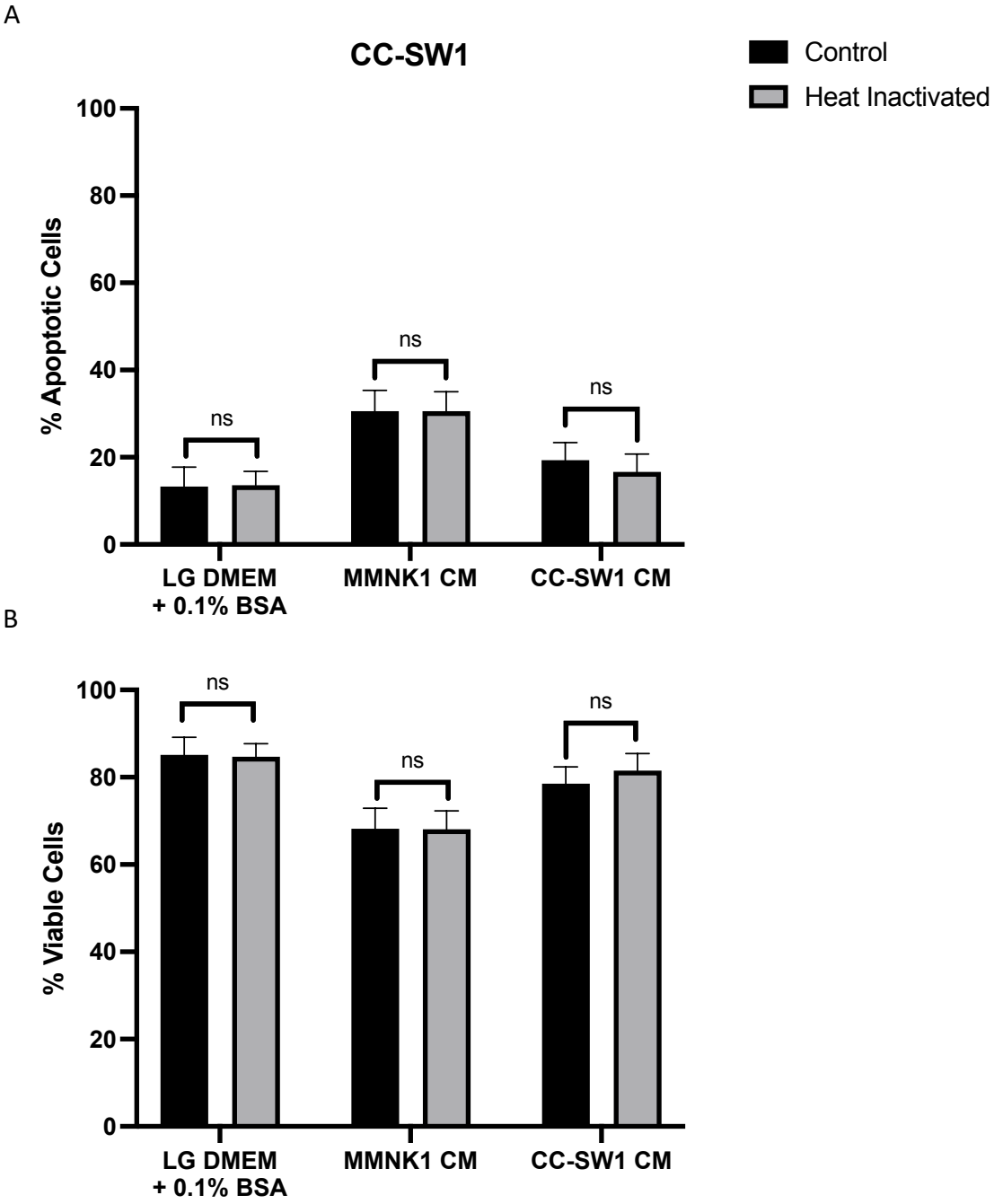
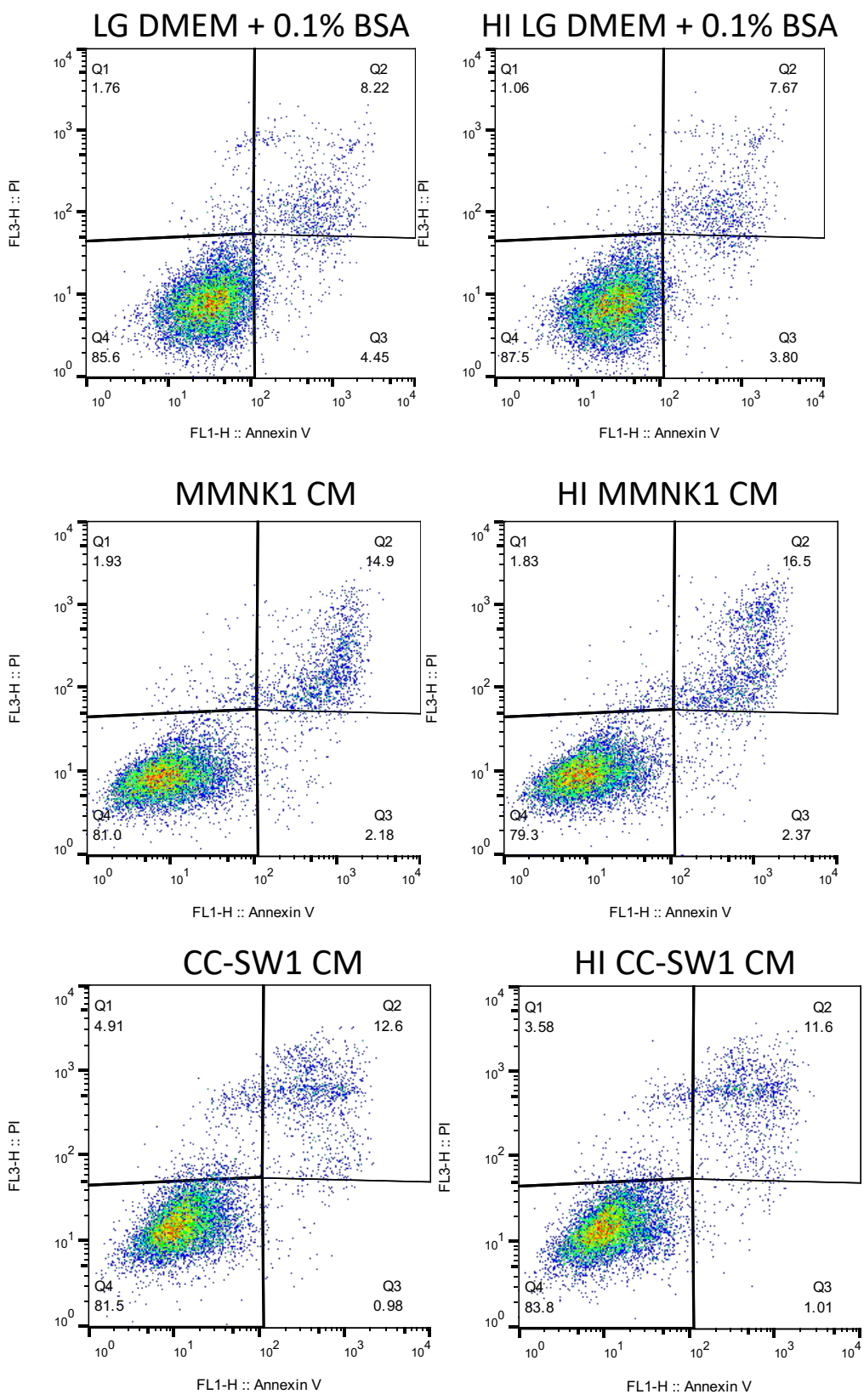


Figure 4:20 - Heat inactivated conditioned has no effect on the proportion of apoptotic CC-SW1 cells*. Conditioned media was extracted from MMNK1 and CC-SW1 cells, with half of each volume inactivated at 90°C for 30 minutes. Flow cytometry was conducted to quantify the proportion of A) apoptotic, and B) alive CC-SW1 cells after treatment with raw and heat inactivated media. Heat inactivation of each media had no statistically significant impact on cell viability. C) Representative FlowJo plot with quadrant separation of Annexin V and PI positively stained CC-SW1 cells.(n=3).*

C


LG DMEM + 0.1% BSA
Q1
1.76
Q2
8.22
Q4
85.6
Q3
4.45
HI LG DMEM + 0.1% BSA
Q1
1.06
Q2
7.67
Q4
87.5
Q3
3.80
MMNK1 CM
Q1
1.93
Q2
14.9
Q4
81.0
Q3
2.18
HI MMNK1 CM
Q1
1.83
Q2
16.5
Q4
79.3
Q3
2.37
CC-SW1 CM
Q1
4.91
Q2
12.6
Q4
81.5
Q3
0.98
HI CC-SW1 CM
Q1
3.58
Q2
11.6
Q4
83.8
Q3
1.01
FL3-H :: PI
FL1-H :: Annexin V

4.8 Human primary cholangiocytes validate indirect co-culture with CCA

We extended the study to confirm the biological relevance of the phenotypic and functional changes to CCA cell lines by testing whether similar changes were observed in primary cholangiocyte cells. Therefore we utilised the human primary cholangiocyte line NHC3 to validate the relevance of our model.

4.8.1 NHC3 cell proliferation is attenuated by culture media

Firstly we assessed NHC3 cell proliferation using our standard treatment media, standard culture media, or the NHC3 specific culture media. When cultured in the NHC3 specified media, cells reached a confluency of 44.30% after 48 hours, which increased to 50.36% in Complete Media, but was reduced to 28.96% in our Experimental Media (Figure 4:21).

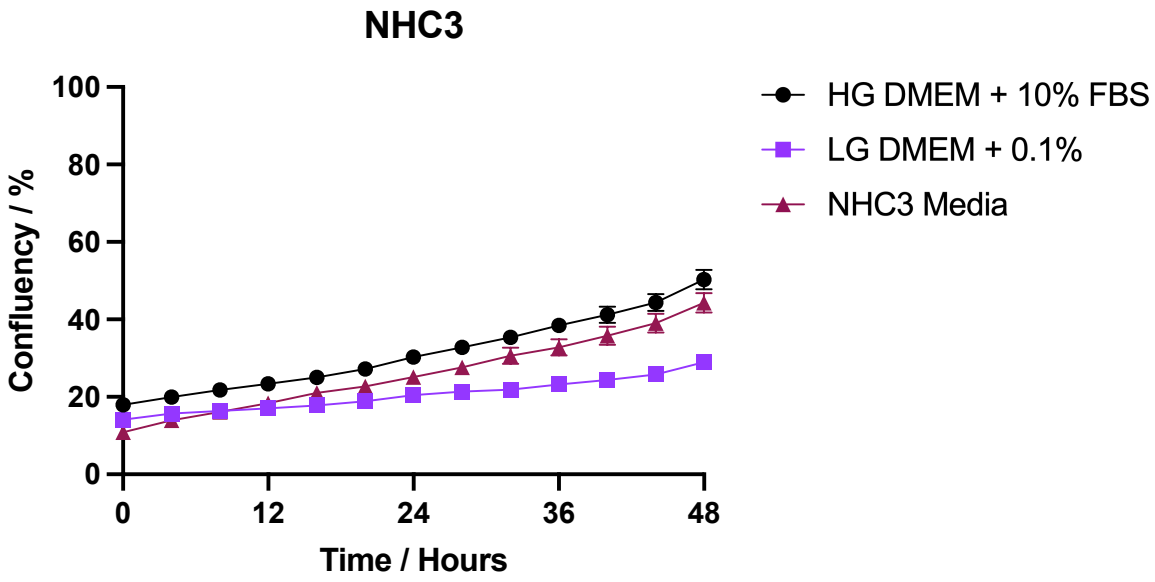


Figure 4:21 – Treatment media affects human primary cholangiocyte cell NHC3 proliferation over 48 hours. *Growth curve for NHC3 cells cultured over 48 hours with High Glucose DMEM supplemented with 10% FBS, Low Glucose DMEM supplemented with 0.1% BSA, and NHC3 proprietary media. Data are plotted as mean confluency (%) ± SEM.(n=6).*

4.8.2 NHC3 cell viability is not attenuated by co-culture with CC-SW1 cells

Next we investigated cell viability using NHC3 and CC-SW1 in our indirect co-culture system. We found no significant difference in cell viability of NHC3 cells (Figure 4:22A) or CC-SW1 cells (Figure 4:22B) in co-culture.

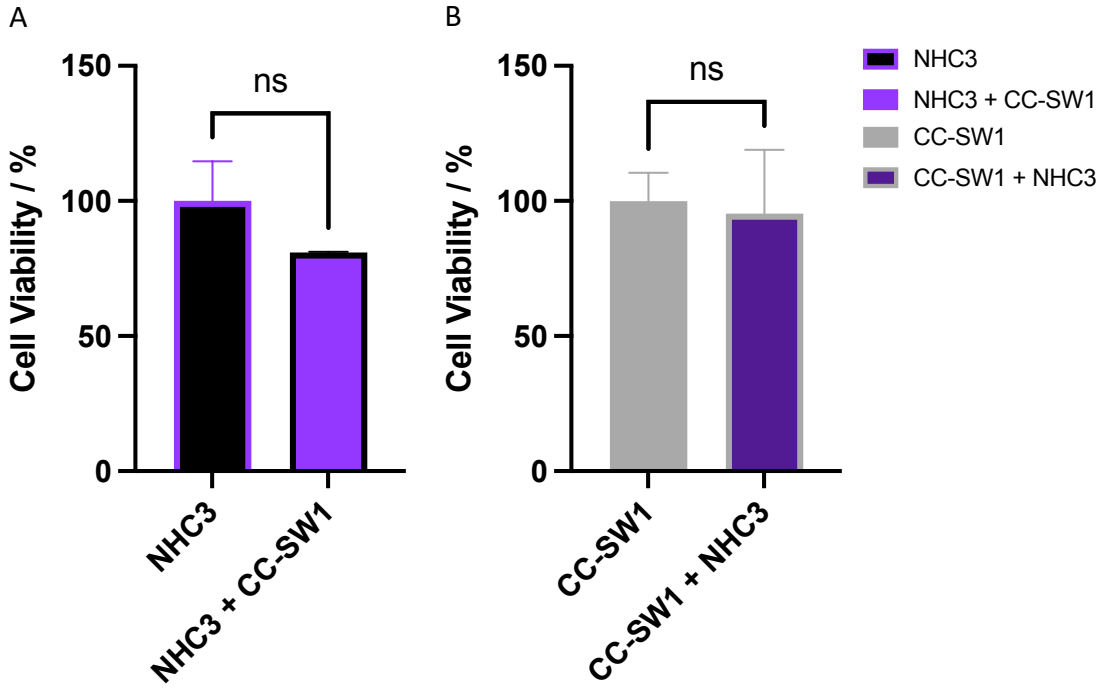


Figure 4:22 – Co-culture has no effect on NHC3 cholangiocyte viability. *A) Relative cell viability of NHC3 cells in co-culture with CC-SW1 cells. B) Relative cell viability of CC-SW1 cells in co-culture with MMNK1 cells. Data plotted as mean cell viability ± SEM(n=3). *P<0.05.*

4.8.3 Co-culture triggers an increase in NHC3 cell migration

A transwell migration assay was used to assess changes to the migratory properties of each cell line in the co-culture system. There was significant increase in the proportion of migratory NHC3 cells ($P=0.0043$) (Figure 4:23A) as well as an increase in the proportion of migratory CC-SW1 cells ($P<0.0001$) (Figure 4:23B). Figure 4:23 shows representative images of the transwell system, with increased migratory NHC3 and CC-SW1 cells during co-culture.

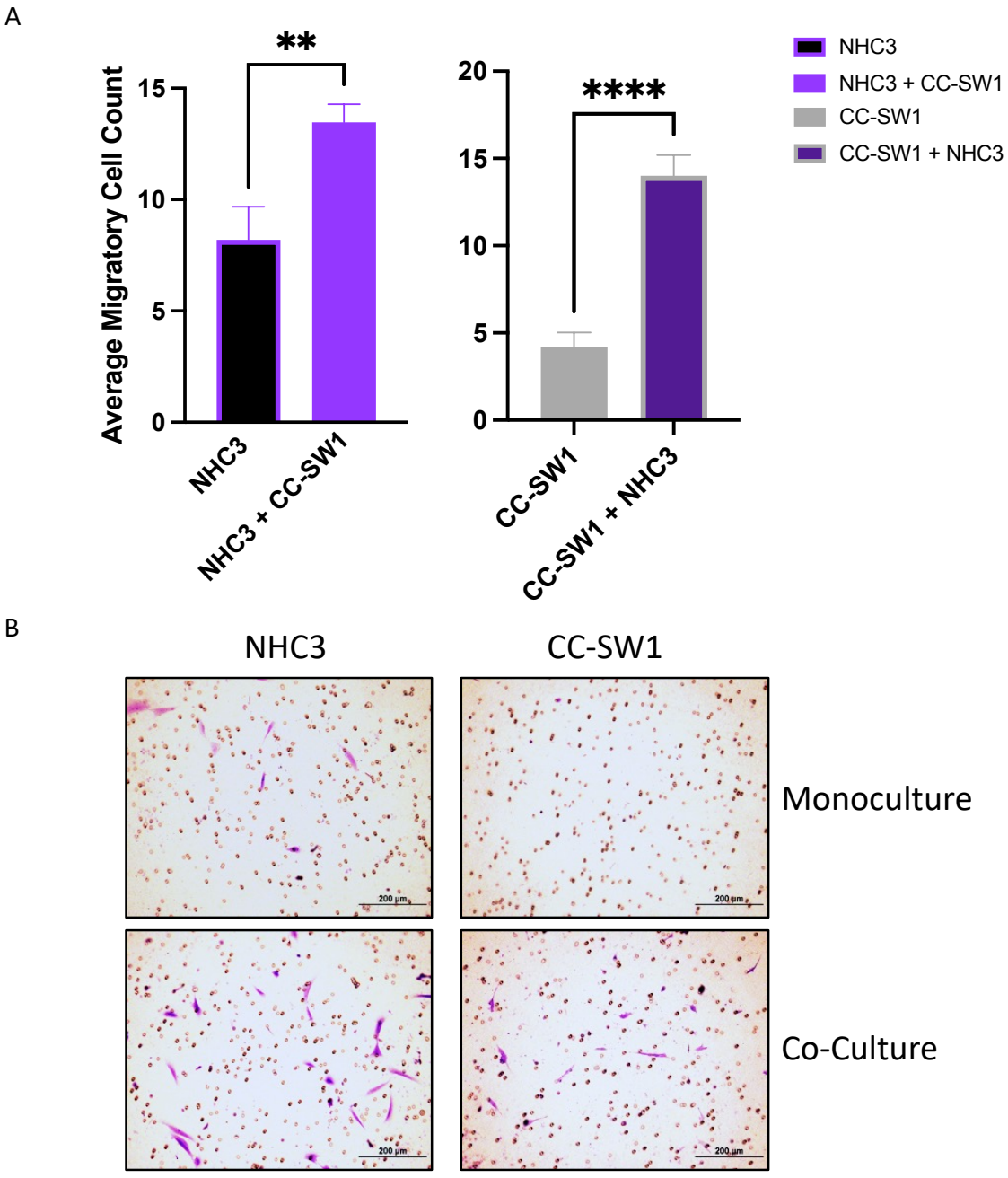


Figure 4:23 – Co-culture increases the proportion of migratory NHC3 and CC-SW1 cells*. A) Fold change in proportion of transwell migratory NHC3 cholangiocytes, and CC-SW1cells during co-culture. B) Representative microscope images of NHC3 cholangiocytes and CC-SW1 cells grown in monoculture and co-culture. Data plotted as average migratory cells ± SEM(n=3). *P<0.05, **P<0.01, ***P<0.001, ****P<0.0001.*

4.8.4 NHC3 cell apoptosis is not affected by co-culture with CC-SW1 cells

Flow cytometry (FACS) analysis demonstrated no significant change in the proportion of apoptotic and viable NHC3 cells during indirect co-culture with CC-SW1 cells (Figure 4:24).

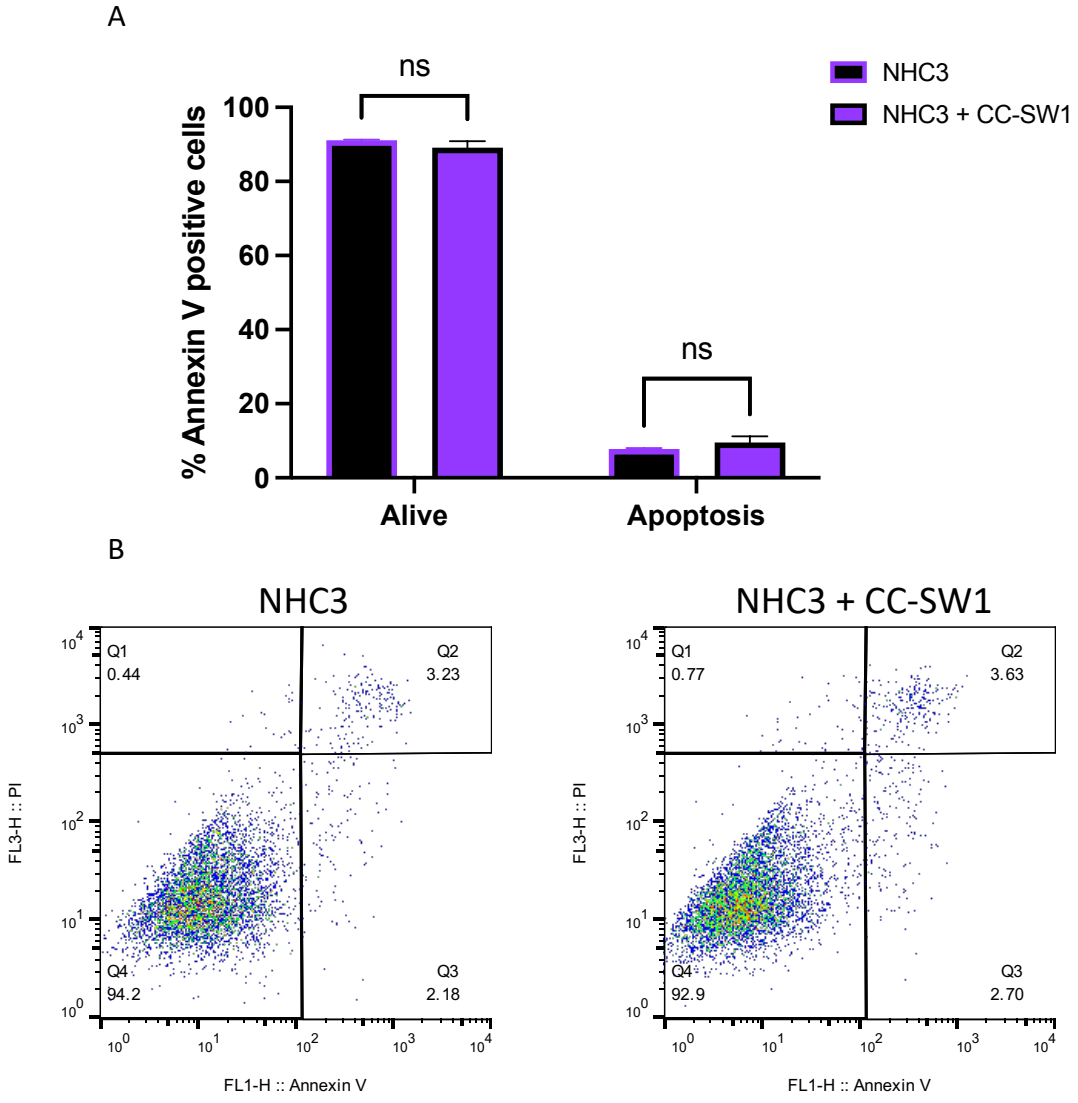


Figure 4:24 – Co-culture with CC-SW1 cells has no effect on the proportion of apoptotic NHC3 cholangiocyte cells. *A) Flow cytometry quantification of the proportion of apoptotic and alive NHC3 cells in mono- and co-culture with CC-SW1 cells. Data plotted as mean percentage of Annexin V positive cells ± SEM, (n=3). *P<0.05. B) Representative FlowJo plot with quadrant separation of Annexin V and PI positively stained NHC3 cells.*

4.9 Summary

The improvement in MMNK1 cell viability after treatment with CC-SW1 conditioned media (Figure 4:2) is much smaller than during indirect co-culture (Figure 4:4). Similarly, there was no change to CC-SW1 cell viability with MMNK1 conditioned media alone (Figure 4:2), however there was a significant decrease in cell viability during indirect co-culture (Figure 4:4). We hypothesise that this is due to the fact that conditioned media contains a limited quantity of secreted factors, with a finite capacity to induce a response, whereas indirect co-culture allows continued production and secretion of the secreted factors leading to a greater degree/sustainment of functional changes. Improved cell viability was observed when MMNK1 cells were cocultured with CC-SW1 cells in both the Complete and the Experimental media (Figure 4:3), leading us to propose that there is a secreted factor produced by CC-SW1 cells which does indeed improve MMNK1 cell viability whilst a secretory factor from MMNK1 cells reduced CC-SW1 cell viability.

There was no change in the mobility of the MMNK1 cells under co-culture (Figure 4:5), which is to be expected as MMNK1 are not typically migratory cells, unlike CCA cells. Indirect co-culture decreased the number of migratory CC-SW1 cells (Figure 4:5). This is likely explained by reduction in EMT protein and gene expression. Specifically, molecular analysis revealed a decrease in Vimentin and Slug expression, with an increase expression in the epithelial marker E-cadherin (Figures 4:6). Likewise we saw a reduction in the gene expression of the EMT markers *Vimentin, Slug,* and *Snail* (Figure 4:6) and an increase in the gene expression of *CDH1* (E-cadherin) (Figure 4:6). Together, this suggests indirect co-culture with MMNK1 inhibits EMT in CC-SW1 cells, triggering a phenotype more characteristic of Mesenchymal-Epithelial Transition (MET).

The flow cytometry data in Figure 4:9 demonstrated an increase in the proportion of MMNK1 cells in the G2M phase, compared to a non-significant reduction in G1 phase (Figure 4:9) which we have interpreted as increased rate of progression through the cell cycle, whilst the flow cytometry data in Figure 4:10 shows a decrease in the proportion of CC-SW1 cells in the S phase (Figure 4:10) which we have interpreted as cell cycle arrest. Taken together, the data suggests co-culture triggered a concurrent increase in the number of MMK1 cells progressing through the cell cycle, whilst inhibiting CC-SW1 cell cycle progression. However a change in cell number would need to be evaluated, as determined via another measure (such as a cell count assay, Promega's CellTiterGlo) concurrent with these proportional changes in order to take finite conclusions about the effect of indirect co-culture on cell cycle.

As well as apoptosis, programmed cell death includes pyroptosis, necroptosis and autophagy. These cell death processes can interact with each other through interconnected and overlapping signalling pathways. As such, autophagy usually precedes apoptosis, and necrosis is triggered when apoptotic cells are not cleared rapidly (90). Therefore we chose to investigate the centralised system of apoptotic cell death, using expression of classical apoptotic markers such as Bax, Caspase-3, and Caspase-8. We saw a reduction in apoptosis when MMNK1 cells were co-cultured with CC-SW1 cells (Figure 4:11), and molecular analysis revealed a concurrent decrease in p53, BAX, Caspase-3, and Caspase-8 protein expression (Figure 4:17). Yet there was no change to the proportion of apoptotic CC-SW1 cells (Figure 4:15).

To begin to untangle whether the stimulatory and inhibitory secreted factors are protein-based, we used heat inactivation to assess cell viability and apoptosis. We saw a reduction in MMNK1 cell viability when treated with heat inactivated Experimental Media as well as heat inactivated conditioned media from CC-SW1 cells (Figure 4:18). This suggested that the protein component in CC-SW1 plays a significant role in the increase in MMNK1 cell viability, as this is lost after heat inactivation when we see a decline in cell viability.

We do not see this decline in cell viability when CC-SW1 cells are treated with conditioned media from CC-SW1 cells that had been heat inactivated, suggesting a protective or compensatory mechanism in CC-SW1 cells. No changes in cell viability were detected in CC-SW1 cells were treated with MMNK1 heat inactivated conditioned media, and an increase in MMNK1 cell viability, suggesting a non-protein component is the more important secretory factor in the MMNK1 media. In cell culture, albumins like BSA are used to bind and deliver molecules to cells, including among other molecules: fatty acids, mixed disulphides such as cysteine or glutathione (protecting them from oxidation and improving their availability), pyridoxal (preventing the reaction with and destruction of amino acids), metals such as zinc, iron, and copper (preventing the engagement of these metals in redox reactions and hence the formation of free radicals), metabolites, and amino acids (91). Denaturation of BSA has been shown to occur in the range of 51.9-81.0°C (92), and we hypothesis that the heat inactivation of our media causes the loss of albumin, and hence a reduction in the transport of these crucial growth molecules and antioxidant compounds into cells, limiting cell viability.

We found no significant difference in the number of apoptotic MMNK1 (Figure 4:19) or CC-SW1 cells (Figure 4:20) when treated with heat inactivated media vs non heat inactivated media, suggesting the change to apoptosis when in the co-culture system is reliant on a non-protein component.

NHC3 cells behaved differently to MMNK1 cells in our co-culture system. Firstly, we found no significant difference in cell viability of NHC3 cells (Figure 4:22) or CC-SW1 cells (Figure 4:22) in co-culture. Secondly, there was significant increase in the proportion of migratory NHC3 cells (Figure 4:23) as well as an increase in the proportion of migratory CC-SW1 cells (Figure 4:23). Moreover, there was no significant change in the proportion of apoptotic and alive NHC3 cells during indirect co-culture with CC-SW1 cells (Figure 4:24). Whilst it appears that co-culture confers MMNK1 cells a growth advantage and inhibits CCA, it seems that the picture is more complex with NHC3 cells, with co-culture making them more migratory.

In summary, indirect co-culture with CC-SW1 CCA cells confers MMNK1 cholangiocytes a growth advantage; with improved viability, cell cycle progression, and inhibition of apoptosis, involving a reduction in p53 and apoptotic protein expression. This is in combination with CC-SW1 cell inhibition; reduced cell viability, cell cycle progression, and migration, involving a reduction in EMT protein and gene expression.

4.10 Discussion

The pathogenic mechanisms behind the development of cholangiopathies like CCA remain relatively unknown. Here we demonstrate how indirect co-culture with CCA cells led to a growth advantage in cholangiocyte cells, concurrent with a reduction in cell cycle

progression and migratory behaviour in the CCA cells. This dual behaviour is indicative of inherent cholangiocyte biology frequently identified in PSC (49).

Firstly, the enhanced proliferation, and apoptotic inhibition in our cholangiocytes is indicative of a “reactive cholangiocyte” phenotype. Cholangiocyte proliferation can be induced in multiple ways including in response to bile acids, acetylcholine, oestrogen, hepatocyte growth factor (HGF), and IL-6 (46). Likewise, Il-6 signalling can be induced in an autocrine loop that can be initiated by proinflammatory cytokines like TNF-α, and bacterial products such as lipopolysaccharide (LPS)(93). Continuous signalling stimulating the proliferation of cholangiocytes, can result in the formation of reactive cholangiocytes.

Reactive cholangiocytes are thought to play a key role in the triggering of biliary fibrosis (52), and the transformation into the reactive cholangiocyte phenotype has been suggested as the initial cholangiocyte response to exogenous and endogenous insults (50,94), although this remains controversial. Proliferating cholangiocytes often display increased secretion of pro-inflammatory cytokines and growth factors, which act in both a paracrine and autocrine manner to promote biliary remodelling and immune regulation, factors that both affect tumorigenesis (95). These include proinflammatory and chemotactic cytokines TNF-α, IL-1, IL-6, IL-8, MCP-1, and IFN-γ. It has been shown that during the activation process, reactive cholangiocytes experience a loss in their epithelial phenotype, increasing their ability to migrate and to produce ECM components such as collagen. This is characterised by a downregulation in the expression of E-cadherin, Cytokeratin-7 (CK-7), and Cytokeratin-19 (CK-19), and the promotion of a mesenchymal phenotype through the expression of fibroblast-specific markers like fibroblast specific protein-1 (FSP-1) and Vimentin(41).

However the expression of the DRC markers CK-7 and CK-19, as well as Epithelial Cell Adhesion Molecule (EpCAM), and Sex-Determining Region Y-Box 9 (SOX9), are not exclusive to DRC's; in-fact are expressed by normal and, occasionally, senescent cholangiocytes (49). Similarly to a study conducted by Phukhum et al, (96) the protein level of E-cadherin in MMNK1 cholangiocytes was problematic to detect.

Myofibroblasts have a mesenchymal phenotype with an enhanced propensity for migration, as well as the ability to secrete cytokines and collagen, and modulate the immune response which is similar to that of reactive cholangiocytes (30). Whether cholangiocytes function as myofibroblasts or reactive cholangiocytes is currently controversial (97), as there is considerable overlap between the behaviour, phenotype, and marker expression of reactive cholangiocytes and myofibroblasts, and as such further work is needed. Hedgehog ligands secreted by myofibroblasts can actually activate Hedgehog signalling in reactive cholangiocytes, promoting EMT(98,99). Stem-like features, such as invasive and resistant properties, are also conferred during EMT (100), driven by transcription factors such as ZEB1 (101). ZEB1 also regulates CTGF, HGF, and IL-6 expression, and IL-6 expression has been linked to increased resistance to 5-FU *in vitro* (102). The primary source of myofibroblasts in CCA originate from portal fibroblasts, however whether EMT triggers the cholangiocytes or hepatocytes to become myofibroblasts remains a matter of controversy (103). Epithelial-mesenchymal interactions contribute significantly to tumorigenesis, and it is thought the myofibroblasts interact with reactive cholangiocytes via shared ligand-receptor pathways (104).

Previous work has indicated that nitric oxide can inhibit cholangiocyte apoptosis via mitochondrial interruption, downstream of cytochrome C release (105), suggesting a role

for ROS production and control in MMNK1 cells in co-culture, whilst the inhibition of apoptosis may trigger cholangiocyte hyperplasia, facilitating the malignant transformation of cholangiocyte cells. Reactive cholangiocytes express adhesion molecules that regulate interactions between cells and the extracellular matrix (ECM). They can also restrict growth of differentiated epithelial phenotypes.

When evaluating CCA cell behaviour, we observed cell cycle withdrawal, and migration inhibition, contrasting the proliferative ability of the cholangiocyte compartment. Interestingly, previous research has shown that a subpopulation of damaged cholangiocytes can acquire a senescent phenotype, characterized by irreversible cell cycle withdrawal, altered gene expression, mitochondrial dysfunction, increased cytokine secretion, and up-regulation of anti-apoptotic pathways (55). Multiple cell stressors can trigger this cellular senescence though activation of the p53 and p16INK4a tumour suppressor pathways, including DNA damage and chromatin remodelling, strong mitogenic signals, repeated cell division and telomere shortening(106). The senescence-associated secretory phenotype (SASP) is a hypersecretory state, typified by the increased secretion of cytokines, chemokines, growth factors, proteases, and extracellular matrix factors, which can reinforce senescence and attenuate tissue homeostasis(50). Both senescent cholangiocytes and reactive cells have very similar secretory profiles, further contributing to the fibro-inflammatory process and potentially CCA progression. We hypothesise that co-culture with cholangiocyte cells trigger a similar SASP-like state in our CCA cells, and that a crucial development of CCA is the escape from the ‘irreversible’ cell cycle withdrawal.

Ductular reactive cholangiocytes and senescent cholangiocytes can modify the tumour microenvironment in similar ways, via the secretion of cytokines, chemokines, and growth factors, ultimately triggering chronic inflammation. Previous research has shown that co-culture of the CCA cell lines KKU-055 and KKU-213A with CAFs caused a 1.5- and 1.9-fold increase in cell viability (107) suggesting 2D co-cultures do modulate CCA effectively *in vitro*, supporting the use of our model, however more work is needed to validate the same phenotype in 3D (96).

We show here support for the hypothesis that cholangiocyte cells actively participate in cholangiocarcinogenesis through a transformation into reactive cholangiocytes, similar to that seen in the ductular reaction. We hypothesise that aberrant proliferation and senescence represent dual fates to cholangiocytes during CCA development, and show here the potential tumorigenic roles of these reactive proliferative and senescent cholangiocyte subpopulations.

Furthermore, heat inactivation of the conditioned media from CC-SW1 cells led to a reduction in MMNK1 cholangiocyte viability (Figure 4:19A), suggesting the loss of the protein growth factors secreted by CC-SW1 caused a reduction in MMNK1 cell viability. Interestingly, heat inactivation of the conditioned media from both MMNK1 and CC-SW1 cells had no effect on CC-SW1 cell viability, compared to a reduction in CC-SW1 cell viability with heat inactivation of the control media (Figure 4:19B), suggesting a compensatory metabolic component in the conditioned medias was enough to sustain CC-SW1 cell viability (Figure 4:19B). Therefore we hypothesise that the indirect co-culture triggers a metabolic shift leading to a change in metabolite expression, which then triggers a change in growth

factor expression via modulation of gene expression, which leads to functional phenotypic changes noted in this chapter. As such, investigating both the metabolic and growth factor component of the co-culture system was imperative.

5 Results Chapter 2 - Delineating the Intercellular Crosstalk Between Cholangiocytes and Cholangiocarcinoma Cells

5.1 Introduction

As identified in Chapter 1, indirect co-culture triggers time-dependent functional alterations including cell viability, migration, cell cycle, and apoptosis, in both CCA and normal bile epithelium. Due to the nature of the indirect transwell system, these alterations are likely to be due to soluble, diffusible factors that mediate a form of crosstalk between the cellular compartments, as opposed to signalling via direct cell-cell contacts.

Every cell has a unique secretome that serves specific functions, and they can take the form of metabolites, cytokines, chemokines, ions, vesicles, DNA or even RNA. Specifically, metabolites are produced by a variety of metabolic cellular processes, including energy production, pyrimidine and purine biosynthesis, and amino acid cycling, whilst cytokines, chemokines, and hormones can stimulate cell proliferation, differentiation, and cell cycle progression. These factors facilitate paracrine and autocrine communication, allowing the transmission of signalling molecules between cells. Broadly speaking, we can refer to these soluble, secretory factors in terms of two sets of components: the metabolic, and the growth factor components.

The ability of cancer cells to adapt and thrive in nutrient-deficient conditions while maximizing cell growth, survival, proliferation, and metastasis is often attributed to metabolic plasticity. Tumour development exerts numerous effects on metabolism, encompassing both the reconfiguration of intracellular metabolic pathways to facilitate aberrant proliferation, adaptation to the nutrient starved tumour microenvironment, as

well as triggering alterations in the metabolism of normal tissue. Moreover, multiple factors, including tumour hypoxia, stromal composition, and immune cell infiltration significantly influence the metabolic characteristics of cancer cells. Likewise, both genetic and epigenetic changes can confer vital survival advantages to cancer cells in nutrient-deprived environments, triggering metabolic reprograming.

Increased glucose consumption by tumours is one of the earliest and most recognized metabolic alterations. Aberrant glucose metabolism was identified by Otto Warburg in 1956 (108), denoting the phenomena whereby tumour cells predominantly convert pyruvate to lactate via glycolysis, even in the presence of abundant oxygen, permitting glycolytic intermediates to fuel secondary pathways and fulfil the metabolic requirements of rapidly proliferating cancer cells (109). This is primarily regulated by HIF-1a and c-MYC transcription factors, as well as the PI3K-Akt-mTOR pathway, and the activation of oncogenes and inactivation of tumour suppressor genes. A “reverse” Warburg effect has also been identified, whereby tumour cells induce oxidative stress in surrounding stromal fibroblasts, triggering the production of lactate via aerobic glycolysis. This lactate is then exported, recaptured by the tumour, and converted back to pyruvate, and enters the TCA cycle to fuel oxidative phosphorylation, highlighting the importance of the tumour stroma in influencing tumour metabolism (68). Disrupted cellular energetics was added as an emerging Hallmark of Cancer by Douglas Hanahan and Robert Weinberg in 2011, further supporting the importance of metabolism in cancer development (110).

Recent research has demonstrated that cell metabolism plays a particularly important role in CCA development. The cell metabolism enzymes isocitrate dehydrogenase (IDH) 1 and 2

are located in the cytoplasm and mitochondria, respectively, and trigger the decarboxylation of isocitrate to α-ketoglutarate. Mutations in IDH1/2 result in the pathogenic accumulation of the oncometabolite 2-hydoxyglutarate (2-HG), promoting tumorigenesis. The FDA approval of ivosidenib in 2021 was a breakthrough for the 15%-20% of iCCA patients with mutations in the *IDH1* and *IDH2* genes (111). Likewise, serum and urine 2-HG levels have been evaluated as a marker for disease progression and therapeutic response in IDH-mutant acute myeloid leukaemia (AML) (112), further highlighting the clinical potential for novel metabolic markers in cancer development.

Both lipid and glucose metabolism have been implicated in iCCA development (113), whilst a decrease in glucose, citrate, and glycerol 3-phosphate concentration coupled with an increase in pyruvate, as well as a switch from mitochondrial respiration to cytosolic aerobic glycolysis (114,115) indicative of metabolic remodelling has been detected by metabolomic analysis in the livers of HCC patients.

In the clinic, biofluids such as plasma and urine are readily accessible, making metabolomics a powerful tool to potentially identify cancer biomarkers and drivers of CCA tumorigenesis. Specifically, the detection of metabolites altered during the very early stage of CCA development would provide a crucial step forward in disease detection.

We hypothesise that the indirect interaction between CCA and cholangiocytes results in detectable changes to metabolite concentration. These metabolic changes regulate cell behaviour in the tumour environment, and thereby control the dynamic growth or suppression of each cell line during CCA development and progression. We further hypothesise that the changes in metabolite concentration will permit the identification of a novel metabolite biomarker for highlighting the progression and development of CCA, which

can be taken forwards for validation in patient samples. At the time of the study, very little metabolomic data had been published on CCA.

Whilst tumours are considered to be initiated by oncogenic mutations and sustained by metabolic plasticity, growth factors are the major regulators of all subsequent steps in tumour progression, including clonal expansion, angiogenesis, invasion of basement membranes, and metastatic dissemination (116). The importance of growth factors and their receptors systems have been described in multiple cancers, and the therapeutic targeting of these receptor pathways including those downstream of EGF, IGF, and HGF have been attempted in tumour patients (117). The EGF-family of peptide growth factors and corresponding receptor EGFR play a pivotal role in the pathogenesis and progression of various carcinomas (117) and whilst preclinical studies of EGFR inhibition in CCA have been promising, the use of anti-EGFR therapy in the clinic for the treatment of CCA has been disappointing (118). Fibroblast growth factor receptor (FGFR) gene fusions have also been reported in CCA, with *FGFR2* gene fusions detected in around 15% of iCCA patients (119). In addition, an increase in FGF/FGFR signalling has been identified as a secondary resistance mechanism to targeted therapies (120). Placental growth factor (PlGF), a member of the vascular endothelial growth factor (VEGF) family, enhances VEGF-driven responses (121), activates stromal cells, promotes angiogenesis, inflammatory and stromal cell recruitment and metastatic progression (122), as well as transmitting pro-survival and pro-migration signals to cancer cells via Nrp1 in GI cancer (123). PIGF is highly expressed in iCCA and is associated with poor prognosis (124). Blocking PlGF leads to changes in the tumour microenvironment, including an enrichment of less active cancer-associated fibroblasts characterized by heightened gene transcription relating to the Akt pathway, hypoxia, and

glycolysis, decreasing metastatic dissemination, enhancing sensitivity to chemotherapy, and increasing survival in mice with iCCA (124).

The inflammation-associated cytokine interleukin-6 (IL-6) is considered to be one of the primary drivers of CCA, with elevated levels detected in the blood and bile of CCA patients (125). IL-6 is a mitogenic cytokine that functions via an autocrine mechanism to enhance CCA growth through altered gene expression. Oncogenic KRAS mutations have been shown to promote IL-6 expression in CCA cells (126). Moreover, IL-6 overexpression has been shown to epigenetically modulate the expression of growth-regulatory pathways, such as EGFR, further contributing to CCA growth (127).

We hypothesise that the indirect interaction between CCA and cholangiocytes triggers reciprocal, detectable changes to growth factor expression. The alteration in growth factor expression modulates cell fate during indirect co-culture, increasing migratory, cell cycle, and anti-apoptotic behaviour in the cell lines. We further hypothesise that the identification of growth factor switch will provide a molecular 'early warning sign', occurring during the early onset of CCA development, prior to the progression of the invasive, aggressive CCA, as well as a potentially novel therapeutic target, for the treatment of CCA.

In this study, we sought to parse out the secretome that mediate the indirect crosstalk between CCA cells and cholangiocytes in terms of both the metabolic compartment, and the growth factor compartment. Specifically, we aimed to identify specific factor(s) responsible for eliciting the functional alterations to cellular phenotypes as discussed in the previous chapter. To this end, we utilized large scale metabolomics to evaluate the change in concentration of intracellular metabolites in CC-SW1 and MMNK1 cells after 6, 24, and 48

hours of indirect co-culture, using low glucose DMEM supplemented with 0.1% BSA to mimic the nutrient sparse tumour microenvironment. Moreover, we evaluated the supernatant from the co-culture at 48 hours to simultaneously screen for the relative expression and pattern of 42 cytokines and growth factors using a Human Cytokine Array Assay.

5.2 Metabolic Compartment

5.2.1 Basal metabolite concentrations of cholangiocyte and cholangiocarcinoma cells

Given that indirect coculture was able to elicit phenotypic changes to cellular compartments, we reasoned that it is essential to explore the basal metabolite modifications to both CCA and cholangiocyte cells when grown in a nutrient deficient microenvironment. As such, we performed metabolomic analysis on both cellular compartments to understand their individual metabolic profiles. We evaluated the concentration of each metabolite in CC-SW1 and MMNK1 cells when cultured in monoculture for 48 hours, in low-glucose DMEM supplemented with 0.1% BSA (v/v), to illustrate the baseline metabolic differences between the CCA and cholangiocyte cells.

A total 102 metabolites were processed, with the hierarchical clustering of the samples shown in the dendrogram in Figure 5:1A. This represents the degree of separation between CCA and cholangiocyte samples mathematically, using the unique expression of metabolite concentrations. The hierarchical clustering shows unclear separation of MMNK1 and CC-SW1 samples, primarily due to the inclusion of CC-SW1 sample 6 in the MMNK1 cluster. The MMNK1 sample 4 is also clustered away from the other cholangiocyte samples, but not as to cluster it within the CC-SW1 cluster. This shows the metabolic differences in MMNK1 and CC-SW1 cells in mono-culture after 48 hours occur on a spectrum; with the MMNK1 sample 6 and CC-SW1 sample 5 at the polar ends of the spectrum, whilst CC-SW1 sample 6

and MMNK1 sample 4 occur closer to the middle of the spectrum, showing similarity in metabolite expression. However, it should be noted that biological separation between the two compartments is still very clear (Figure 5:1B) as PCA separation demonstrated that the variation between the CC-SW1 and MMNK1 samples along PC1 is much greater than the intrasample variation along PC2, suggesting a clear biological separation, thus suggesting that their metabolic profiles are biologically different as denoted in the heatmap (Figure 5:2).

We further resolved the differences between the two cellular compartments by performing a fold change analysis (where Fold Change >2/<-2) and a Student's T-Test (where $P<0.01$) (Figure 5:3A). 24 metabolites were found to be significant, where 11 metabolites had a fold change >2 and $P<0.01$, and 13 metabolites with a fold change in concentration <-2 and $P<0.01$. Details of these significant metabolites can be found in Figure 5:3B. Interestingly, there were significantly lower concentrations of the TCA intermediates citrate, isocitrate, cis-aconitate, as well as the nucleoside and nucleotide mono-, di-, and triphosphates UMP, UDP, dTMP, dTTP, cofactor NADPH, UDP-glucuronate, phosphoserine, alpha-aminoadipate, glycolytic intermediate PEP, and BCKA 2-oxoisopentanoate in CC-SW1 cells after 48 hours, compared to MMNK1 cells.

The concentrations of the amino acids glutamine, proline, serine, beta-alanine, and arginine, the energetic intermediates creatine, choline, and carnitine, as well as concentrations of UDP-N-acetylglucosamine, N-acetylglutamate, 3-hydroxy-3-methylglutarate, were significantly higher in CC-SW1 cells after 48 hours, compared to MMNK1 cells. Notably, we observed that creatine concentration was significantly enriched in CC-SW1 cells, with the greatest fold change difference in concentration compared to MMNK1 cells.

The volcano plot in Figure 5:4 is a concise visualization of the enriched metabolic pathways in CC-SW1 cells compared to MMNK1 cholangiocytes, as identified by metabolic pathway enrichment analysis. This allows us to identify pathways that are both statistically significant and biologically meaningful in the context of the metabolomic dataset. To that end, some of the enriched metabolic pathways which satisfy the most stringent criteria for significance and impact, are indicated by black arrows and annotated (Figure 5:4). This includes purine metabolism, pyrimidine metabolism, and amino sugar/nucleotide sugar metabolism, pathways which are central to a cell's ability to replicate DNA and synthesize RNA during growth and division, as well as the energy production pathways of the TCA cycle and glutamate metabolism.

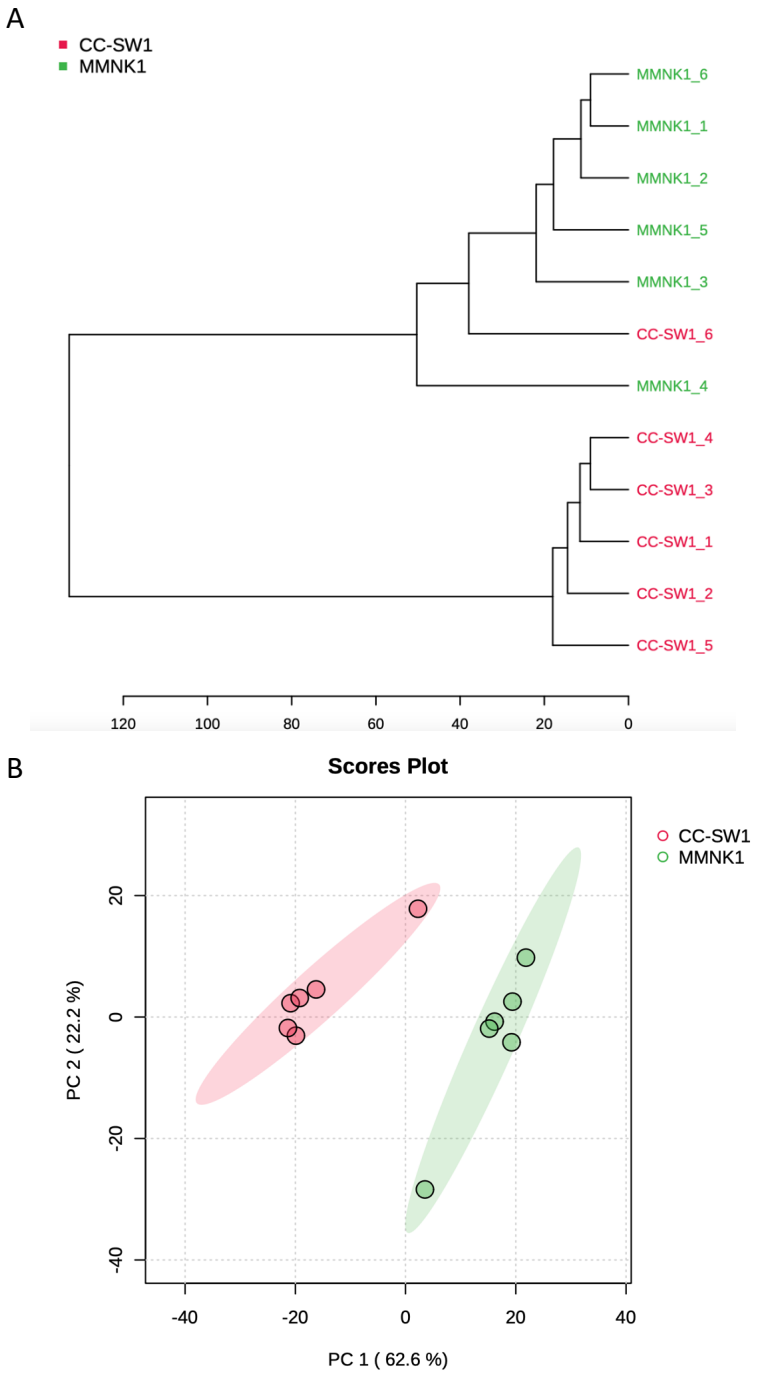


Figure 5:1 - Normalisation and clustering of MMNK1 and CC-SW1 metabolomic samples in monoculture at 48 hours*. The metabolic profile of MMNK1 cholangiocytes (green) and CC-SW1 cells (red) were evaluated after 48 hours of monoculture. A) Dendrogram illustrates hierarchical clustering of samples based on Euclidean distances calculated from concentration profiles. Samples with similar profiles are grouped together, as indicated by the branches, whilst vertical lines represent the distance at which clusters merge, identifying sample clusters and subgroups. B) Scores plot represents the complete 48 hour metabolic dataset in a two-dimensional space, generated through the principal component analysis (PCA). Each point on the plot corresponds to a sample. Samples that cluster closely together share similar metabolic profiles, while those farther apart along PC1 exhibit distinct metabolic differences, aiding the visualisation of biological variation between the MMNK1 and CC-SW1 metabolic profiles.*

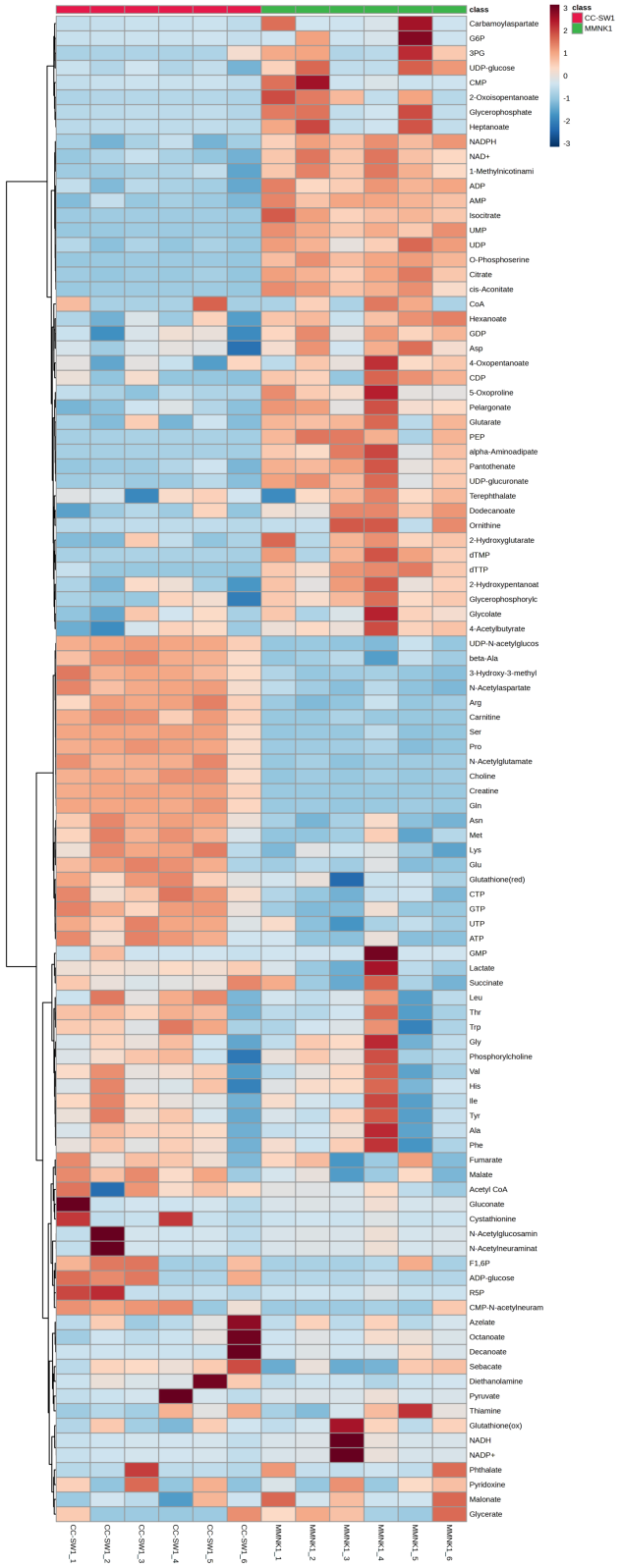
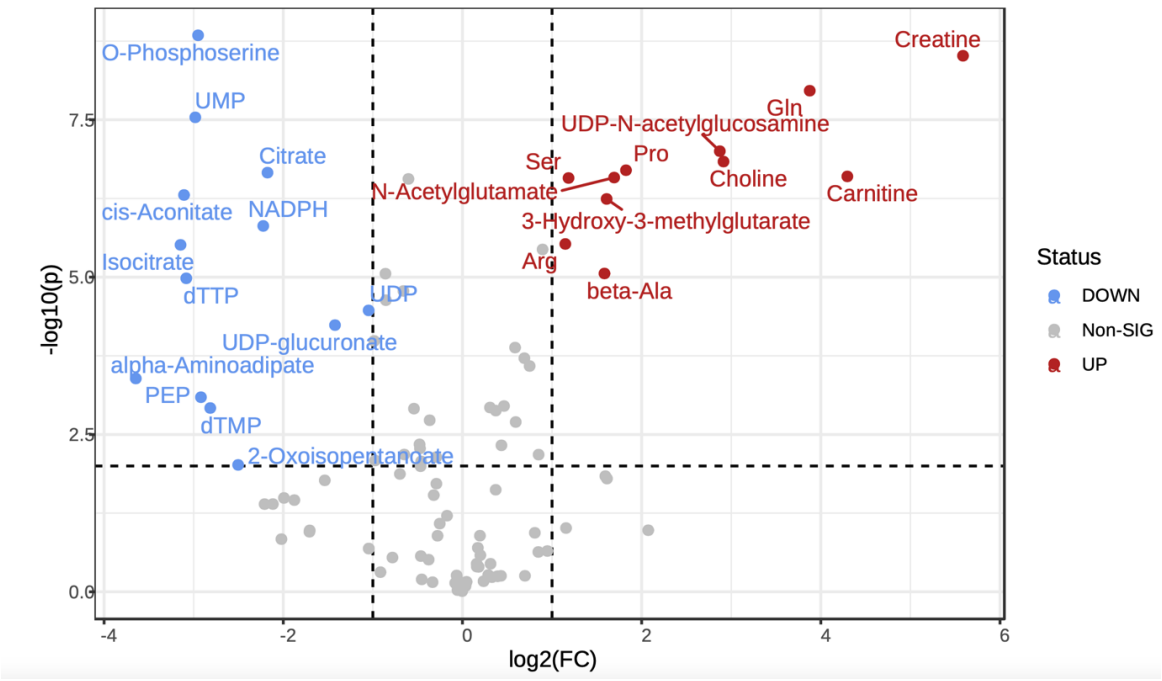


Figure 5:2 – Heatmap of differentially expressed metabolites in CC-SW1 cells compared to MMNK1 cholangiocytes*. The relative expression of each metabolite (rows) was evaluated in CC-SW1 cells and MMNK1 cholangiocytes after 48 hours of monoculture. Metabolites which are more highly expressed are shown in red, whilst metabolites which are reduced in concentration are shown in blue. Each column represents a sample, MMNK1 in green and CC-SW1 in red.*

A



B

Table 4: Important features identified by volcano plot

	Compounds	FC	log2(FC)	raw.pval	-log10(p)
1	O-Phosphoserine	0.12931	-2.9511	1.4397e-09	8.8417
2	Creatine	48.07	5.5871	3.0432e-09	8.5167
3	Gln	14.685	3.8762	1.0927e-08	7.9615
4	UMP	0.12655	-2.9822	2.8949e-08	7.5384
5	UDP-N-acetylglucosamine	7.3235	2.8725	9.9799e-08	7.0009
6	Choline	7.536	2.9138	1.4604e-07	6.8355
7	Pro	3.5438	1.8253	2.004e-07	6.6981
8	Citrate	0.22124	-2.1763	2.1881e-07	6.6599
9	Carnitine	19.645	4.2961	2.5116e-07	6.6
10	N-Acetylglutamate	3.2341	1.6934	2.6182e-07	6.582
11	Ser	2.2721	1.184	2.6618e-07	6.5748
12	cis-Aconitate	0.11599	-3.1079	4.9553e-07	6.3049
13	3-Hydroxy-3-methylglutarate	3.0511	1.6093	5.726e-07	6.2421
14	NADPH	0.21409	-2.2237	1.5365e-06	5.8135
15	Arg	2.2164	1.1482	2.9726e-06	5.5269
16	Isocitrate	0.11289	-3.147	3.0712e-06	5.5127
17	beta-Ala	3.0003	1.5851	8.7464e-06	5.0582
18	dTTP	0.11802	-3.0829	1.0434e-05	4.9816
19	UDP	0.48386	-1.0473	3.3722e-05	4.4721
20	UDP-glucuronate	0.37305	-1.4226	5.7751e-05	4.2384
21	alpha-Aminoadipate	0.079876	-3.6461	0.00040739	3.39
22	PEP	0.13223	-2.9188	0.00080829	3.0924
23	dTMP	0.1421	-2.8151	0.0012002	2.9207
24	2-Oxoisopentanoate	0.17631	-2.5038	0.0096055	2.0175

Figure 5:3 – Differentially expressed metabolites in CC-SW1 cells compared to MMNK1 cells after 48 hours. *A) Volcano plot depicting the results of the differential expression analysis for intracellular metabolites in CC-SW1 and MMNK1 cells after 48 hours of monoculture. Each point on the plot represents a metabolite, with its position indicating both statistical significance and fold-change in expression. The dashed horizontal line represents the predefined threshold for significance of -log10(P-value) >2, equating to a raw P-value < 0.01. The dashed vertical lines represents the predefined thresholds for fold change, log_2fold change <1 and log_2fold change >1, equating to a raw fold change <-2 and >2 respectively. Metabolites falling above the upper threshold line (red) are considered significantly upregulated, whilst those below the lower threshold line (blue) are significantly downregulated. B) 24 metabolites are differentially expressed between CC-SW1 and MMNK1 cells after 48 hours of monoculture.*

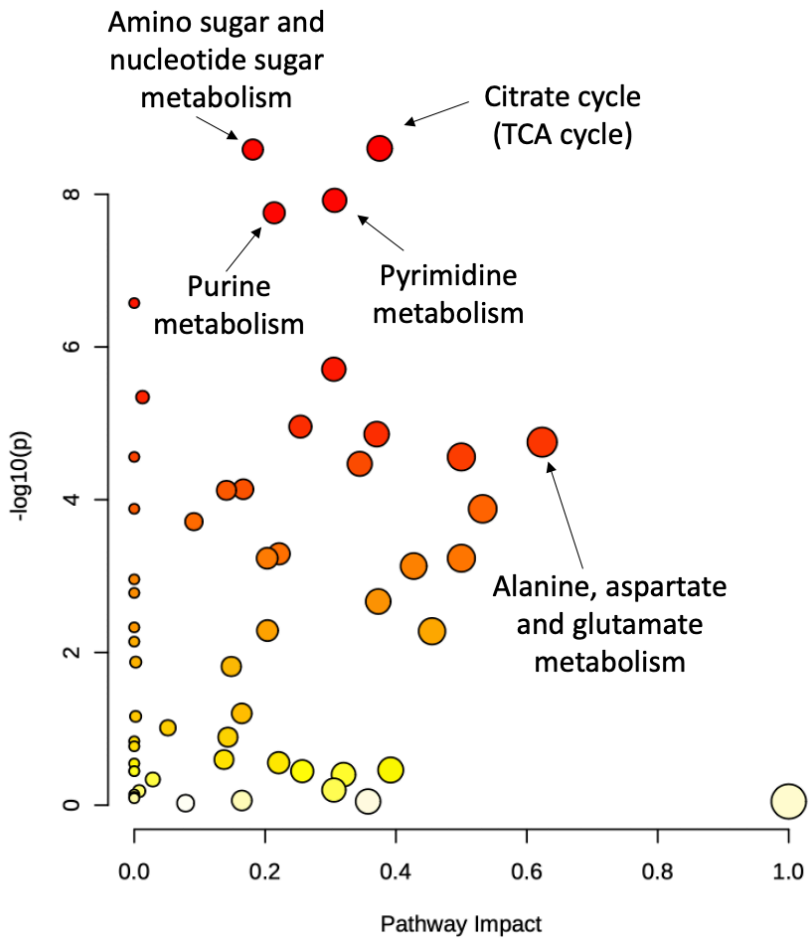


Figure 5:4 – Basally enriched metabolic pathways in CC-SW1 cells*. Volcano plot depicting enriched metabolic pathways in CC-SW1 cells compared to MMNK1 cells when grown in monoculture for 48 hours, as identified by metabolic pathway enrichment analysis. Each point on the plot corresponds to a metabolic pathway, and its position conveys both the pathway impact, which reflects the cumulative influence of metabolite changes within each pathway as a measure of biological relevance, and the pathway significance. A subset of enriched metabolic pathways meeting the highest significance, and highest impact criteria are marked with black arrows and labelled, to provide a subset of the most relevant pathways in the analysis. In CC-SW1, these pathways include purine, pyrimidine, and amino sugar/nucleotide sugar metabolism, as well as the TCA cycle, and alanine/aspartate/glutamate metabolism.*

5.2.2 Co-Culture Alters Metabolic Profile of Cellular Compartments

After establishing the individual metabolic profiles of CCA and cholangiocytes, we proceeded to evaluate the concentration of intracellular metabolites in MMNK1 cells following indirect co-culture with CC-SW1 cells. We performed the metabolomics analysis at 6, 24, and 48 hours, to evaluate the early, intermediate, and late metabolic changes that occurred during coculture. For all timepoints, we performed hierarchical clustering and PCA analysis to understand the biological distances and relevance between the two compartments.

We evaluated the concentration of intracellular metabolites in MMNK1 cells when in monoculture or co-culture with CC-SW1 cells for 6, 24, and 48 hours.

5.2.3 6 hours of co-culture increase glycolytic intermediates in cholangiocytes

It should be noted that during early coculture, there was weak separation between the two compartments (Figure 5:5A), suggesting that there were little biological differences to tell them apart mathematically.

PCA can be used to demonstrate strong patterns from large and complex datasets. Each point represents all metabolite expression values from one sample, ergo we end up with 12 points on each plot, six for monoculture and six for co-culture samples. It is a way of mathematically combining pairs of metabolite comparisons. PC1 is in essence, a line through the data which explains the most variation between our 12 samples. PC2 is the second line that meets PC1 perpendicularly at the centre of our data and describes the second most variation in the data. As a general rule of thumb, PC1 should account for 80% of the variation in the data. Figure 5:4B is a score plot of PC1 and PC2 for the 6 hours samples.

From this we can see that the variation in the co-culture samples along PC1 have a much great variation than the monoculture samples in PC2, and much like the Euclidean clustering in Figure 5:5A, Figure 5:5B shows that the separation between the mono- and co-culture samples is weak. As denoted in the heatmap showing relative expression of metabolites (rows) in each sample (columns) in Figure 5:6, there were variations occurring within and between samples, thus explaining the inability to separate them clearly at this timepoint. We subsequently used the expression of each metabolite to conduct statistical analysis.

Using the threshold of a Fold Change >2/<-2 and P<0.01, only 2 metabolites emerge. As shown in the volcano plot in Figure 5:7A, DHAP and 3PG concentrations reduced significantly during co-culture, with raw Fold Change and P-value for both metabolites shown in Figure 5:7B.

Using a Metabolic Pathway enrichment analysis, we investigated the weight of each metabolite on its respective metabolic pathway. The volcano plot in Figure 5:8 highlights the metabolic pathways enriched in cholangiocyte cells after 6 hours of co-culture. Phenylalanine/tyrosine/tryptophan biosynthesis had the largest Pathway Impact, followed by alanine/aspartate/glutamate metabolism, and glycine/serine/threonine metabolism.

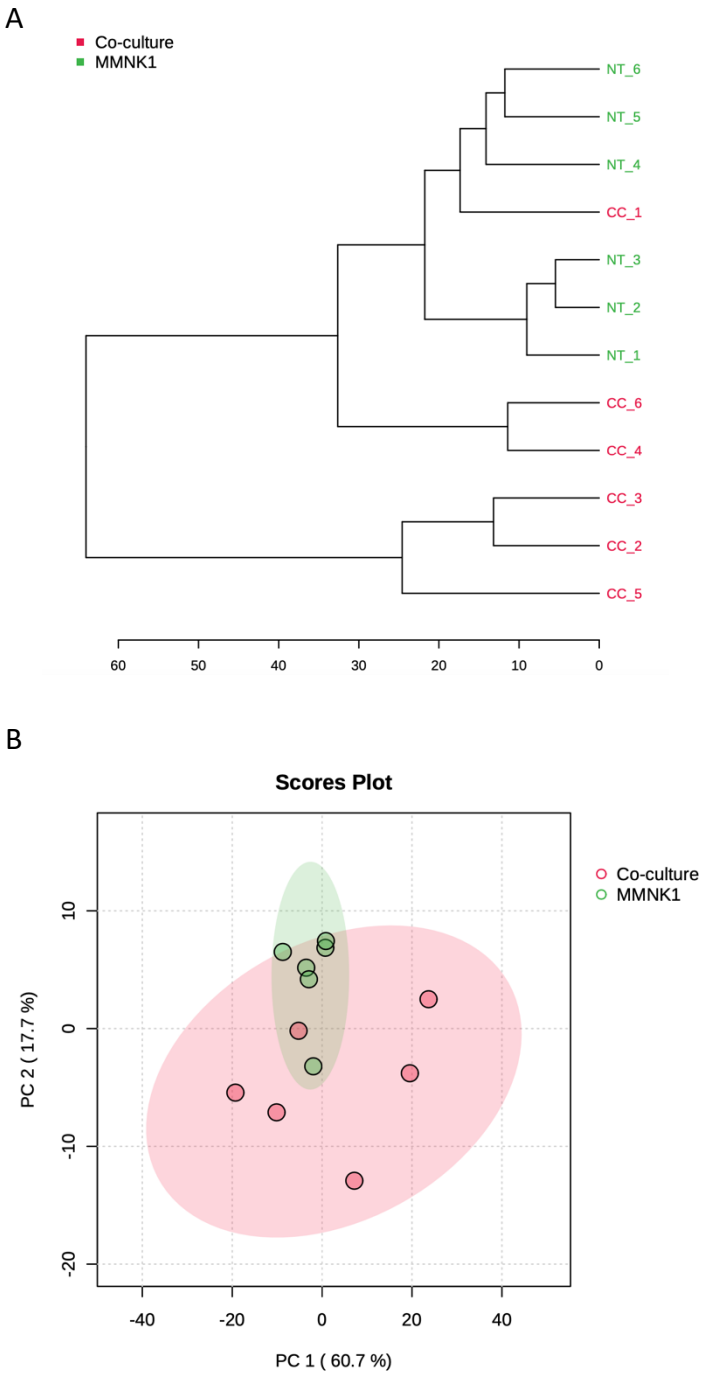


Figure 5:5 - Dendrogram and Scores Plot for the metabolic profiling of MMNK1 cells after 6 hours of mono- and co-culture. *Normalisation and clustering was conducted on the metabolic profiles of MMNK1 cholangiocytes after 6 hours of mono- (green) and co-culture (red) with CC-SW1 cells. A) Dendrogram illustrates hierarchical clustering of samples based on Euclidean distances calculated from concentration profiles. Samples with similar profiles are grouped together, as indicated by the branches, whilst vertical lines represent the distance at which clusters merge, identifying sample clusters and subgroups. B) Scores plot represents the complete 6 hour metabolic dataset in a two-dimensional space, generated through the principal component analysis (PCA). Each point on the plot corresponds to a sample. MMNK1 monoculture samples cluster closely together along PC1, whilst co-culture samples are both overlapping and spread farther apart along PC1, suggesting a spectrum of variation in the metabolite profile of MMNK1 cells after 6 hours of co-culture.*

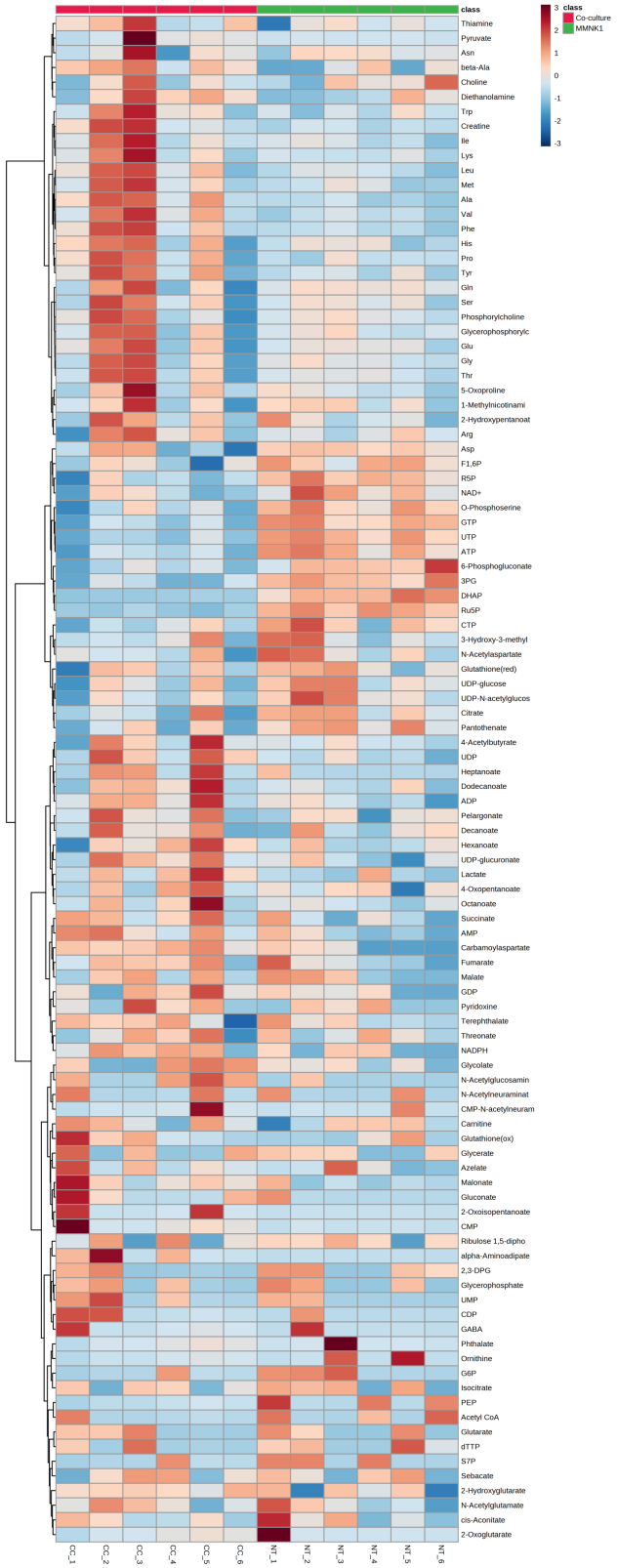
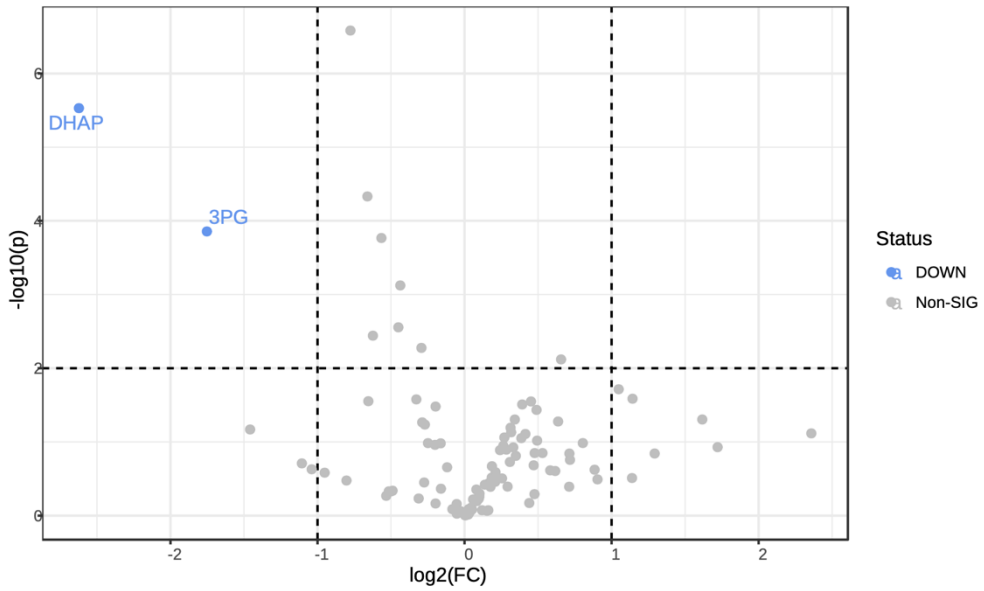


Figure 5:6 – Heatmap of differentially expressed metabolites in MMNK1 cholangiocytes after 6 hours of indirect co-culture*. The relative expression of each metabolite (rows) in MMNK1 cholangiocytes after 6 hours of monoculture, or co-culture with CC-SW1 cells. Metabolites which are more highly expressed are shown in red, whilst metabolites which are reduced in concentration are shown in blue. Each column represents a sample, monoculture in green and co-culture in red.*

A



B

Table 4: Important features identified by volcano plot

	Compounds	FC	log2(FC)	raw.pval	-log10(p)
1	DHAP	0.16237	-2.6227	2.9508e-06	5.5301
2	3PG	0.2968	-1.7524	0.00013943	3.8556

Figure 5:7 - Differentially expressed metabolites in MMNK1 cells after 6 hours of indirect co-culture with CC-SW1 cells. *A) Volcano plot depicting the results of the differential expression analysis for intracellular metabolites in MMNK1 cholangiocytes after 6 hours of indirect co-culture with CC-SW1 cells. Each point on the plot represents a metabolite, with its position indicating both statistical significance and fold-change in expression. The dashed horizontal line represents the predefined threshold for significance of -log10(P-value) >2, equating to a raw P-value < 0.01. The dashed vertical lines represents the predefined thresholds for fold change, log_2fold change <1 and log_2fold change >1, equating to a raw fold change <-2 and >2 respectively. Metabolites falling above the upper threshold line (red) are considered significantly upregulated, whilst those below the lower threshold line (blue) are significantly downregulated. B) Only 2 metabolites are differentially expressed in MMNK1 cholangiocytes after 6 hours of co-culture, DHAP and 3PG.*

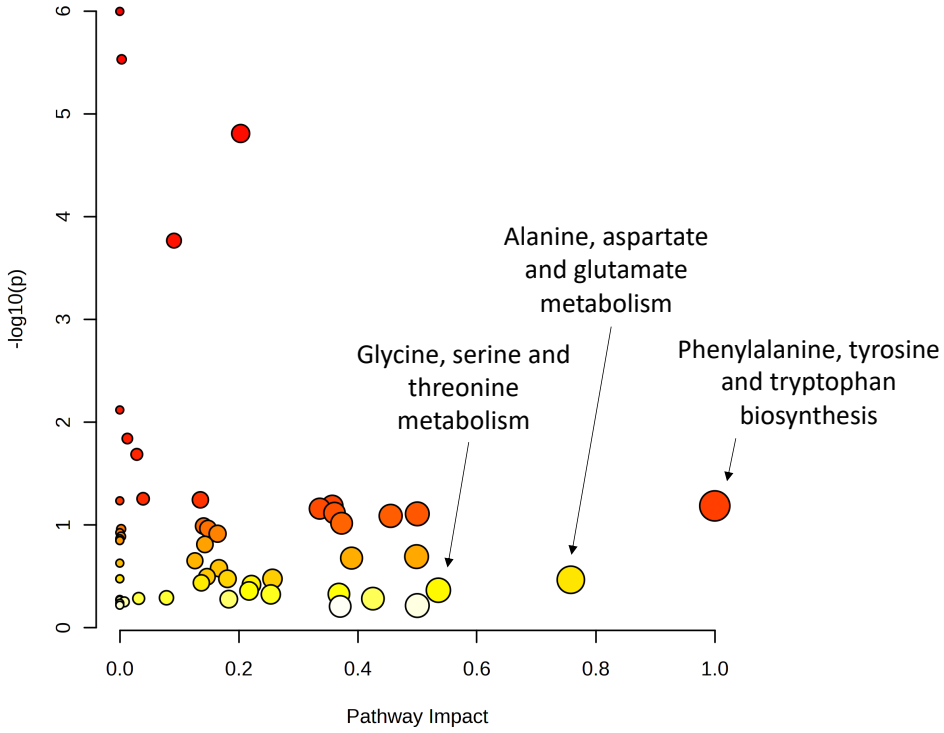


Figure 5:8 – Enriched metabolic pathways in MMNK1 cholangiocytes after 6 hours of indirect co-culture with CC-SW1 cells. *Volcano plot depicting enriched metabolic pathways in MMNK1 cholangiocytes after 6 hours of indirect co-culture with CC-SW1 cells, compared to MMNK1 cells cultured in monoculture, as identified by metabolic pathway enrichment analysis. Each point on the plot corresponds to a metabolic pathway, and its position conveys both the pathway impact, which reflects the cumulative influence of metabolite changes within each pathway as a measure of biological relevance, and the pathway significance. A subset of enriched metabolic pathways meeting the highest significance, and highest impact criteria are marked with black arrows and labelled, to highlight the most relevant pathways in the analysis. In MMNK1 cells after 6 hours of indirect co-culture, these pathways included glycine/serine/threonine metabolism, phenylalanine/tyrosine/tryptophan biosynthesis, and alanine/aspartate/glutamate metabolism.*

5.2.4 24 hours of co-culture reduces pentose phosphate pathway and glycolytic intermediates in cholangiocytes, with an increase in nucleoside mono- and diphosphates

Unlike at 6 hours, there was clear separation of the two compartments after 24 hours (Figure 5:9A), suggesting multiple biological differences, allowing clear mathematically separation and clustering. This is reiterated by the distinct clusters in the score plot (Figure 5:9B) where the monoculture samples along PC1 have a much greater variation than the co-culture samples in PC2. Similar to the Euclidean clustering in Figure 5:9A, Figure 5:9B shows clear separation between the mono- and co-culture samples.

As denoted in the heatmap showing relative expression of metabolites (rows) in each sample (columns) in Figure 5:10, there is a greater change in metabolite concentration at 24 hours compared to 6 hours. However, whilst the overall profile of each compartment was more consistent, there was some variation occurring within and between samples, explaining the low mathematical power of PC1 (44.3%) suggesting an explanation for the biological differences.

We subsequently used the expression of each metabolite to conduct statistical analysis, using the threshold of a Fold Change >2/<-2 and $P<0.01$. When these data are taken together as in the volcano plot in Figure 5:11A, we can see 22 metabolites emerge, 7 metabolites with a fold change in concentration >2 and $P<0.01$, and 15 metabolites with a fold change in concentration <-2 and $P<0.01$ (Figure 5:11A). The fold changes and P-values for the 22 metabolites are listed in Figure 5:11B.

Using a Metabolic Pathway enrichment analysis, we investigated the weight of each metabolite on its respective metabolic pathway. The volcano plot in Figure 5:12 shows the metabolic pathways enriched in cholangiocyte cells after 24 hours of co-culture. We see a shift from 6 to 24 hours in our pathway analysis, with the significance of the glycine/serine/threonine as well as the alanine/aspartate/glutamate metabolic pathways increasing, as well as the emergence of the pentose phosphate pathway, and the glutamine/glutamate metabolic pathways.

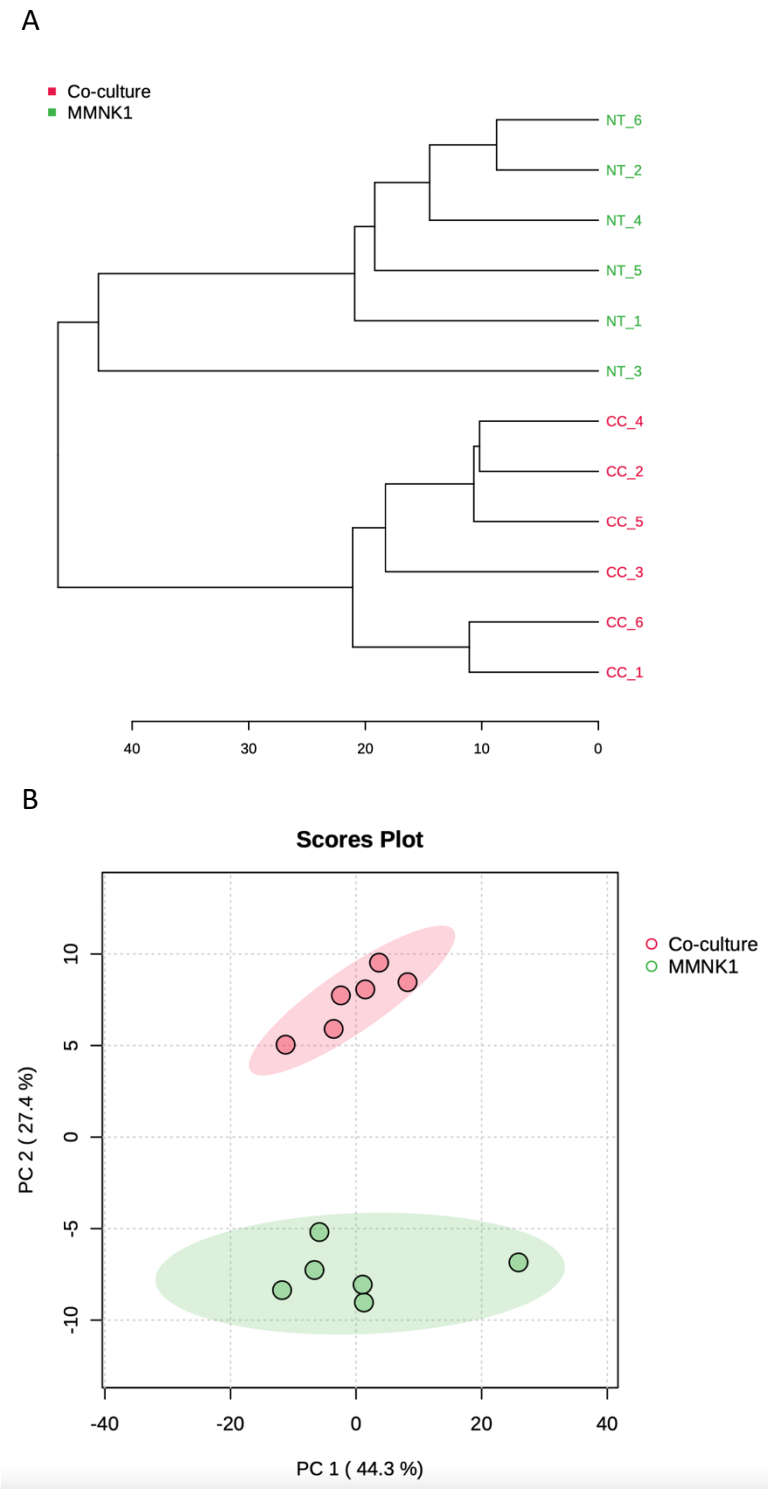


Figure 5:9 - Dendrogram and Scores Plot for the metabolic profiling of MMNK1 cells after 24 hours of mono- and co-culture. *Normalisation and clustering was conducted on the metabolic profiles of MMNK1 cholangiocytes after 24 hours of mono- (green) and co-culture (red) with CC-SW1 cells. A) Dendrogram illustrates hierarchical clustering of samples based on Euclidean distances calculated from concentration profiles. Samples with similar profiles are grouped together, as indicated by the branches, whilst vertical lines represent the distance at which clusters merge, identifying sample clusters and subgroups. B) Scores plot represents the complete 24 hour metabolic dataset in a two-dimensional space, generated through the principal component analysis (PCA). Each point on the plot corresponds to a sample. MMNK1 co-culture samples are clustered away from monoculture samples along PC2, suggesting co-culture mediated biological variation in metabolite profile after 24 hours.*

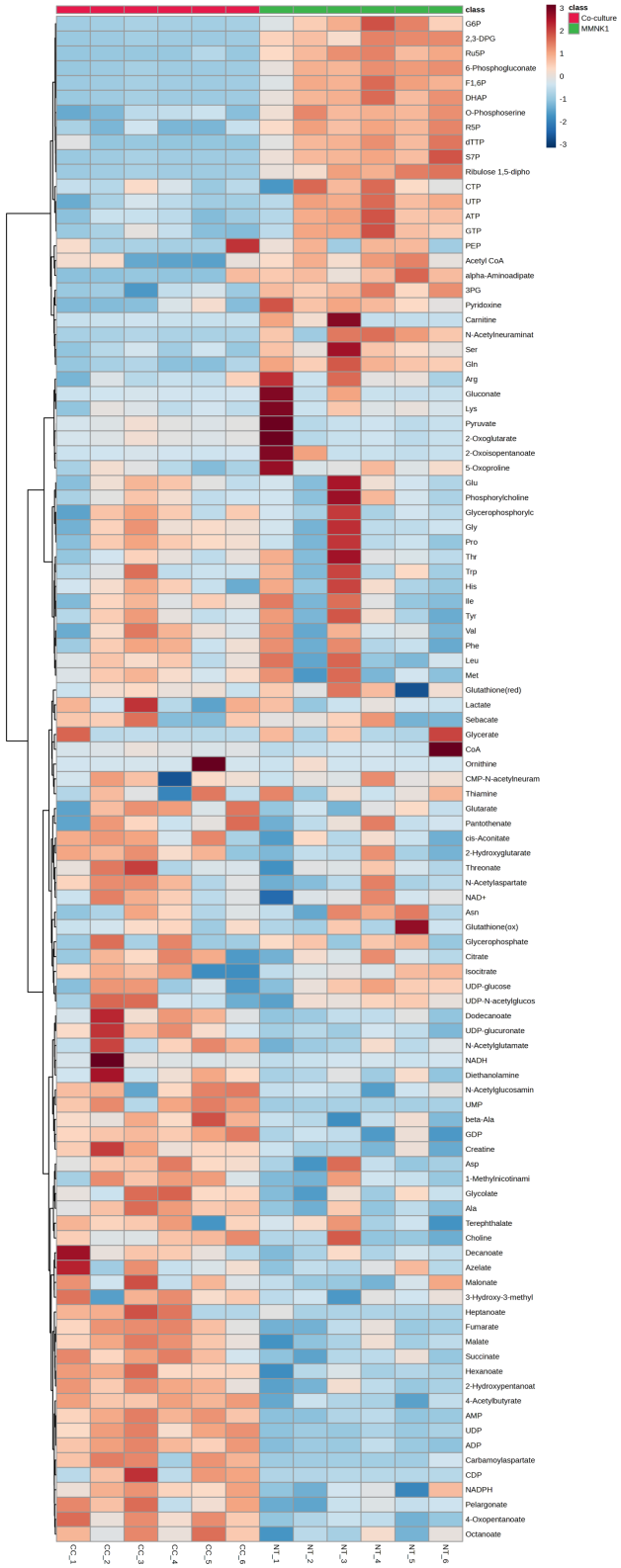
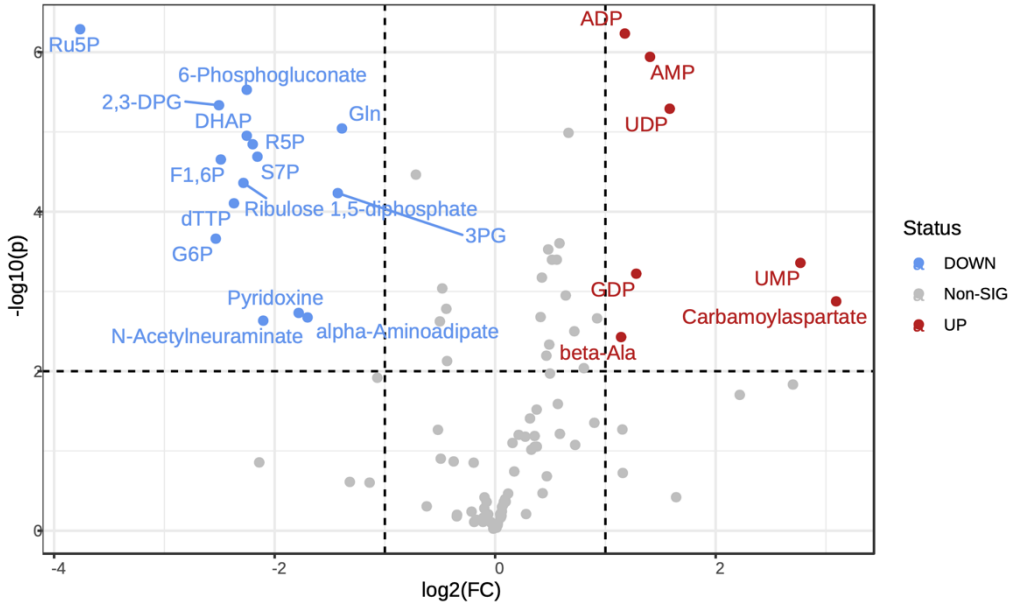


Figure 5:10 – Heatmap of differentially expressed metabolites in MMNK1 cholangiocytes after 24 hours of indirect co-culture. *The relative expression of each metabolite (rows) in MMNK1 cholangiocytes after 24 hours of monoculture, or co-culture with CC-SW1 cells. Metabolites which are more highly expressed are shown in red, whilst metabolites which are reduced in concentration are shown in blue. Each column represents a sample, monoculture in green and co-culture in red.*

A



B

Table 4: Important features identified by volcano plot

	Compounds	FC	log2(FC)	raw.pval	-log10(p)
1	Ru5P	0.073598	-3.7642	5.1527e-07	6.288
2	ADP	2.2597	1.1761	5.8366e-07	6.2338
3	AMP	2.6468	1.4043	1.1447e-06	5.9413
4	6-Phosphogluconate	0.20977	-2.2531	2.9595e-06	5.5288
5	2,3-DPG	0.17614	-2.5052	4.6264e-06	5.3348
6	UDP	2.9959	1.583	5.1172e-06	5.291
7	Gln	0.3818	-1.3891	9.0395e-06	5.0439
8	DHAP	0.20979	-2.253	1.117e-05	4.9519
9	R5P	0.21776	-2.1992	1.4258e-05	4.8459
10	S7P	0.22431	-2.1564	2.0429e-05	4.6897
11	F1,6P	0.17821	-2.4883	2.2149e-05	4.6546
12	Ribulose 1,5-diphosphate	0.20543	-2.2833	4.3559e-05	4.3609
13	3PG	0.37191	-1.427	5.8472e-05	4.233
14	dTTP	0.19356	-2.3691	7.8435e-05	4.1055
15	G6P	0.17265	-2.5341	0.00021792	3.6617
16	UMP	6.8122	2.7681	0.00043835	3.3582
17	GDP	2.4274	1.2794	0.00059884	3.2227
18	Carbamoylaspartate	8.5332	3.0931	0.001331	2.8758
19	Pyridoxine	0.29069	-1.7824	0.0018579	2.731
20	alpha-Aminoadipate	0.3074	-1.7018	0.0021171	2.6743
21	N-Acetylneuraminate	0.23264	-2.1038	0.0023235	2.6339
22	beta-Ala	2.2072	1.1422	0.0037325	2.428

Figure 5:11 - Differentially expressed metabolites in MMNK1 cells after 24 hours of indirect co-culture with CC-SW1 cells. *A) Volcano plot depicting the results of the differential expression analysis for intracellular metabolites in MMNK1 cholangiocytes after 24 hours of indirect co-culture with CC-SW1 cells. Each point on the plot represents a metabolite, with its position indicating both statistical significance and fold-change in expression. The dashed horizontal line represents the predefined threshold for significance of -log10(P-value) >2, equating to a raw P-value < 0.01. The dashed vertical lines represents the predefined thresholds for fold change, log_2fold change <1 and log_2fold change >1, equating to a raw fold change <-2 and >2 respectively. Metabolites falling above the upper threshold line (red) are considered significantly upregulated, whilst those below the lower threshold line (blue) are significantly downregulated. B) 22 metabolites are differentially expressed in MMNK1 cholangiocytes after 24 hours of co-culture.*

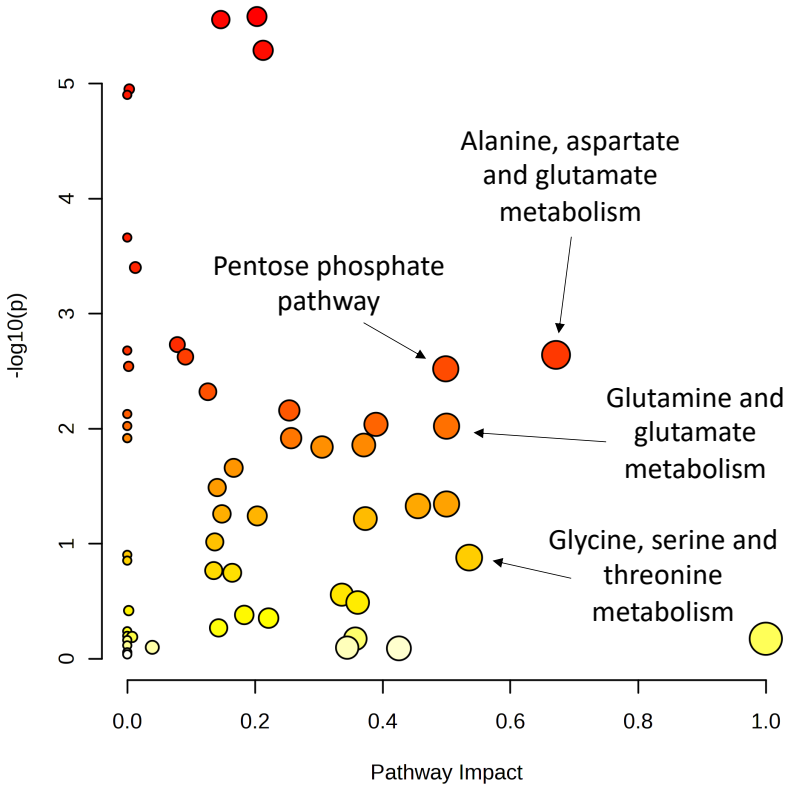


Figure 5:12 - Enriched metabolic pathways in MMNK1 cholangiocytes after 24 hours of indirect co-culture with CC-SW1 cells. *Volcano plot depicting enriched metabolic pathways in MMNK1 cholangiocytes after 24 hours of indirect co-culture with CC-SW1 cells, compared to MMNK1 cells cultured in monoculture, as identified by metabolic pathway enrichment analysis. Each point on the plot corresponds to a metabolic pathway, and its position conveys both the pathway impact, which reflects the cumulative influence of metabolite changes within each pathway as a measure of biological relevance, and the pathway significance. A subset of enriched metabolic pathways meeting the highest significance, and highest impact criteria are marked with black arrows and labelled, to highlight the most relevant pathways in the analysis. In MMNK1 cells after 24 hours of indirect co-culture, these pathways included glycine/serine/threonine metabolism, glutamine/glutamate metabolism, the pentose-phosphate pathway, and alanine/aspartate/glutamate metabolism.*

5.2.5 48 hours of co-culture reduces aspartate and glutamate concentration, with an increase in choline and creatine concentration

In agreement with the trend in improved hierarchical clustering after 24 hours, hierarchical clustering for samples after 48 hours of indirect co-culture showed distinct separation between monoculture and the co-culture samples (Figure 5:13A). This is recapitulated in the PCA (Figure 5:13B) to a greater degree than at 24 hours. This suggests a time dependent change in metabolite concentration mediated by co-culture, with more significant changes to metabolite concentrations at 48 hours, as denoted by the heatmap in Figure 5:14, permitting greater mathematical segregation of each compartment. Due to this, 48 hours was selected at the optimal time for metabolite evaluation due to significant mathematical separation of the compartments.

We further resolved the differences between the two cellular compartments by performing a fold change analysis and Student's t-test to identify metabolites with a fold change >2/<-2 $P<0.01$ (Figure 5:15A). Using this threshold, only 7 metabolites emerge; 2 metabolites with a fold change in concentration >2 (creatine and choline) and 5 metabolites with a fold change in concentration<-2 (aspartate, glutamine, UDP-glucose, acetyl CoA, and dTTP). Figure 5:15B lists the fold changes and P-values for these 7 metabolites. The flux in choline, aspartate, and creatine concentration in MMNK1 cells during co-culture over 48-hours is shown in Figures 5:16A, B, and C respectively. The concentrations of choline and creatine during co-culture appear to be sustained over time (Figure 5:16A and 5:16C).

The glycine/serine/threonine, alanine/aspartate/glutamate, and glutamine/glutamate metabolic pathways were sufficiently enriched after 24 hours of co-culture, which was recapitulated after 48-hours, with an increase in pathway significance (Figure 5:17). The alanine, aspartate, and glutamate metabolic pathway experienced the greatest pathway impact, as well as the most significant enrichment after 48 hours of co-culture.

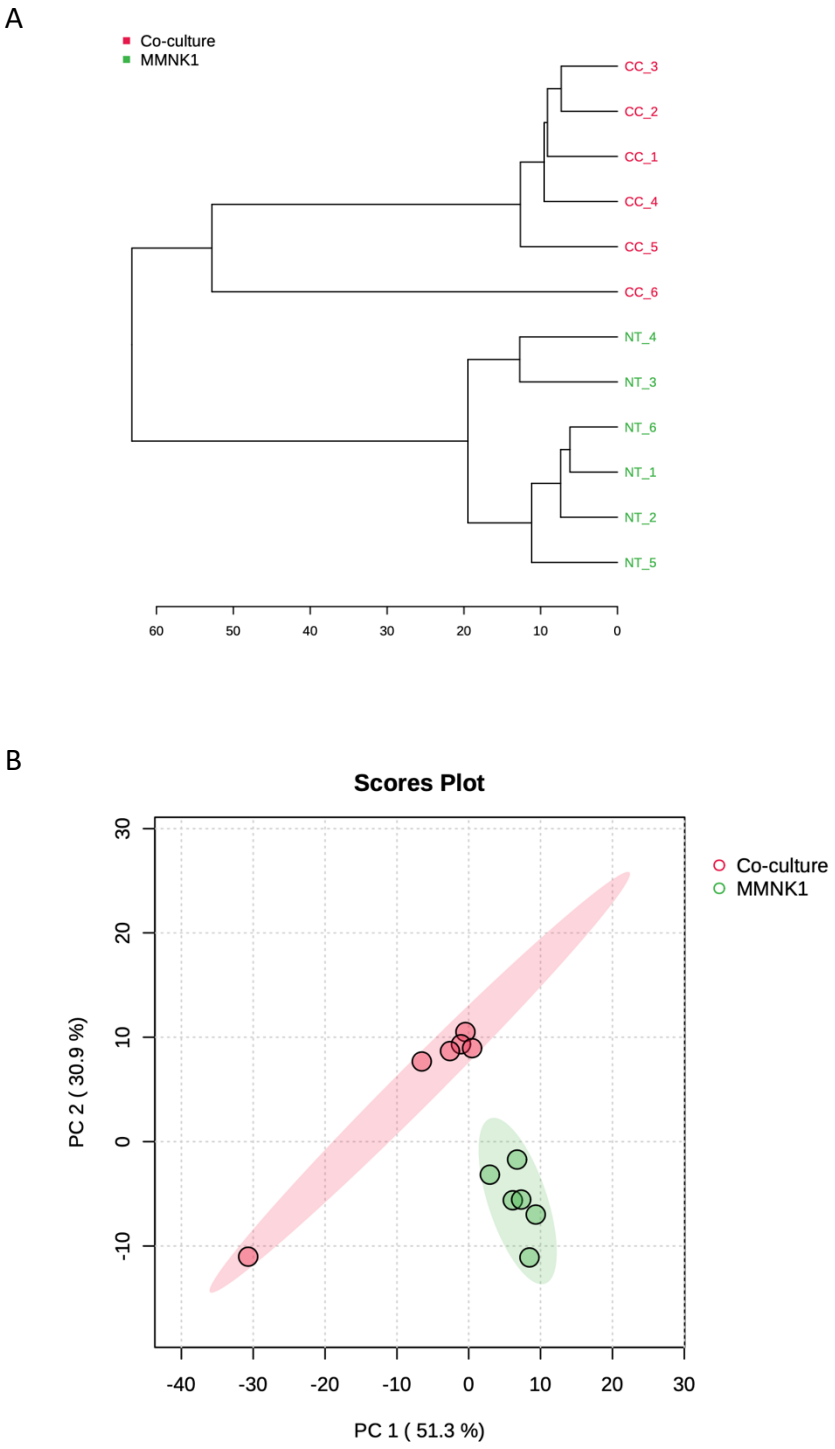


Figure 5:13 - Dendrogram and Scores Plot for the metabolic profiling of MMNK1 cells after 48 hours of mono- and co-culture. *Normalisation and clustering was conducted on the metabolic profiles of MMNK1 cholangiocytes after 48 hours of mono- (green) and co-culture (red) with CC-SW1 cells. A) Dendrogram illustrates hierarchical clustering of samples based on Euclidean distances calculated from concentration profiles. Samples with similar profiles are grouped together, as indicated by the branches, whilst vertical lines represent the distance at which clusters merge, identifying sample clusters and subgroups. B) Scores plot represents the complete 48 hour metabolic dataset in a two-dimensional space, generated through the principal component analysis (PCA). Each point on the plot corresponds to a sample. MMNK1 co-culture samples are clustered away from monoculture samples along PC1 and PC2, suggesting distinct co-culture mediated biological variation in metabolite profile after 48 hours.*

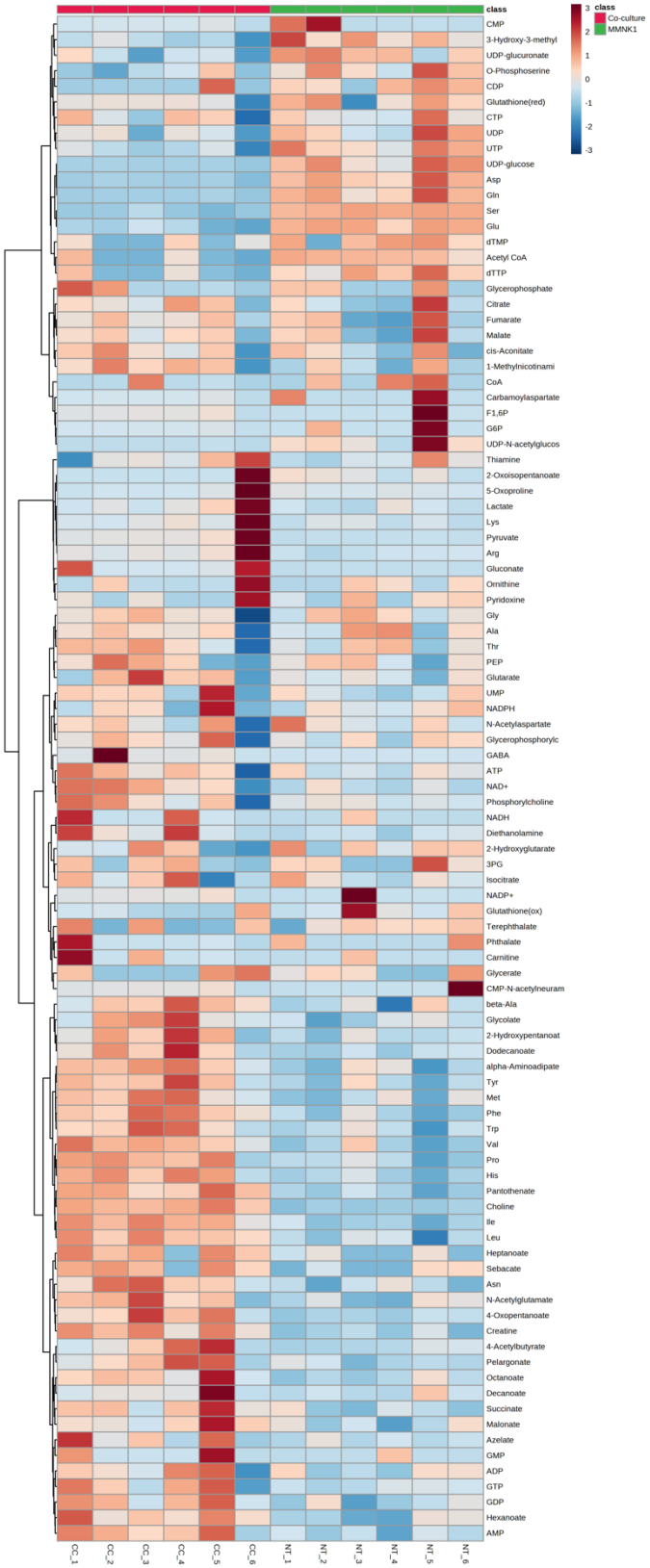
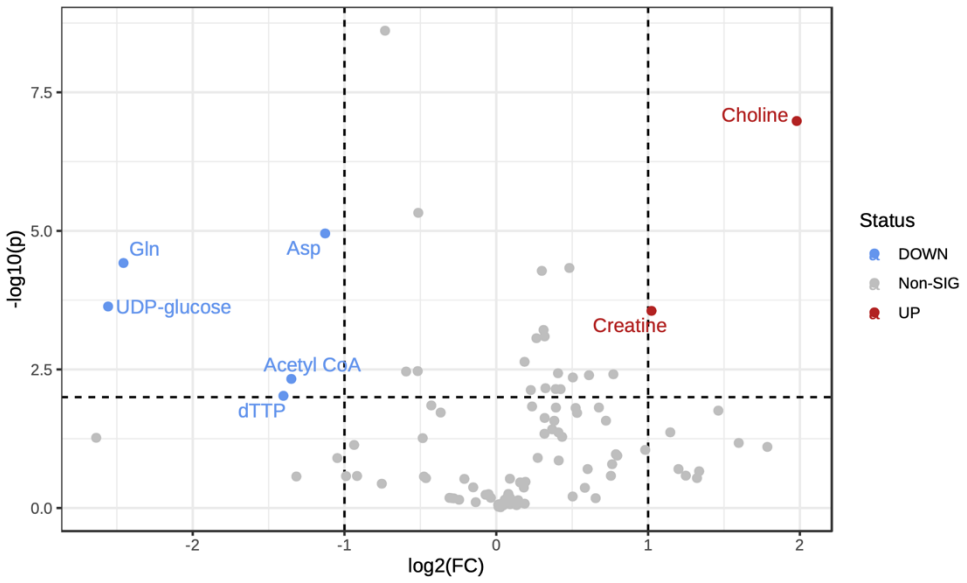


Figure 5:14 – Heatmap of differentially expressed metabolites in MMNK1 cholangiocytes after 48 hours of indirect co-culture. *The relative expression of each metabolite (rows) in MMNK1 cholangiocytes after 48 hours of monoculture, or co-culture with CC-SW1 cells. Metabolites which are more highly expressed are shown in red, whilst metabolites which are reduced in concentration are shown in blue. Each column represents a sample, monoculture in green and co-culture in red.*

A



B

Table 4: Important features identified by volcano plot

	Compounds	FC	log2(FC)	raw.pval	-log10(p)
1	Choline	3.9433	1.9794	1.0408e-07	6.9826
2	Asp	0.45781	-1.1272	1.1119e-05	4.9539
3	Gln	0.18223	-2.4562	3.798e-05	4.4205
4	UDP-glucose	0.16986	-2.5576	0.00023131	3.6358
5	Creatine	2.031	1.0222	0.00027739	3.5569
6	Acetyl CoA	0.39213	-1.3506	0.0046857	2.3292
7	dTTP	0.37825	-1.4026	0.0094695	2.0237

Figure 5:15 - Differentially expressed metabolites in MMNK1 cells after 48 hours of indirect co-culture with CC-SW1 cells. *A) Volcano plot depicting the results of the differential expression analysis for intracellular metabolites in MMNK1 cholangiocytes after 48 hours of indirect co-culture with CC-SW1 cells. Each point on the plot represents a metabolite, with its position indicating both statistical significance and fold-change in expression. The dashed horizontal line represents the predefined threshold for significance of -log10(P-value) >2, equating to a raw P-value < 0.01. The dashed vertical lines represents the predefined thresholds for fold change, log_2fold change <1 and log_2fold change >1, equating to a raw fold change <-2 and >2 respectively. Metabolites falling above the upper threshold line (red) are considered significantly upregulated, whilst those below the lower threshold line (blue) are significantly downregulated. B) 7 metabolites are differentially expressed in MMNK1 cholangiocytes after 48 hours of co-culture.*

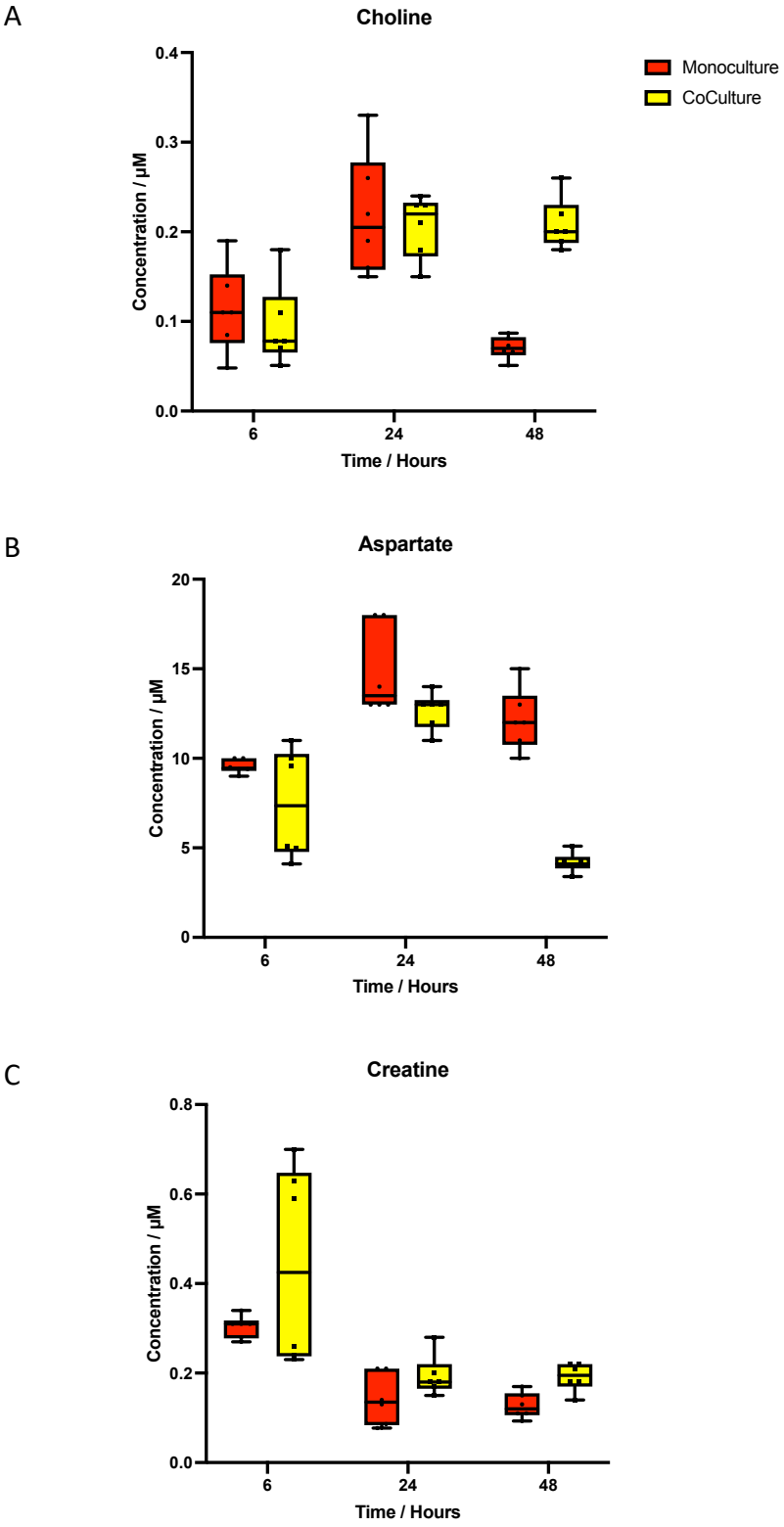


Figure 5:16 - Flux of differentially expressed metabolites in MMNK1 cholangiocytes across 48 hours. *The concentration of the metabolites of interest as reported by the metabolomic analysis are displayed as a series of bar graphs. Concentrations for MMNK1 cells in monoculture are shown in red, whilst concentrations for MMNK1 cells in indirect co-culture with CC-SW1 cells are shown in yellow, at 6, 24, and 48 hours of culture. A) Choline. B) Aspartate. C) Creatine.*

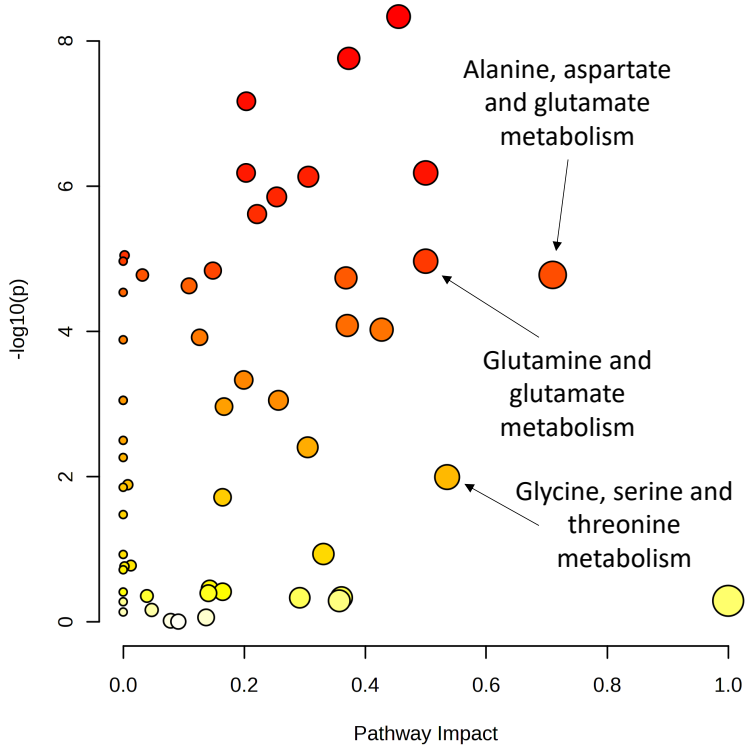


Figure 5:17 - Enriched metabolic pathways in MMNK1 cholangiocytes after 48 hours of indirect co-culture with CC-SW1 cells. *Volcano plot depicting enriched metabolic pathways in MMNK1 cholangiocytes after 48 hours of indirect co-culture with CC-SW1 cells, compared to MMNK1 cells cultured in monoculture, as identified by metabolic pathway enrichment analysis. Each point on the plot corresponds to a metabolic pathway, and its position conveys both the pathway impact, which reflects the cumulative influence of metabolite changes within each pathway as a measure of biological relevance, and the pathway significance. A subset of enriched metabolic pathways meeting the highest significance, and highest impact criteria are marked with black arrows and labelled, to highlight the most relevant pathways in the analysis. In MMNK1 cells after 48 hours of indirect co-culture, these pathways included glycine/serine/threonine metabolism, glutamine/glutamate metabolism, and alanine/aspartate/glutamate metabolism.*

5.3 Validation of cholangiocyte metabolite concentration

Through the timepoint metabolomic analysis, we observed many transient changes across the timepoints. However, we placed our focus on 3 metabolites for their unique observations across the timepoints. Firstly, aspartate was chosen as the differences between monoculture and coculture widened along with time. Secondly, choline was shown to accumulate significantly by 48 hours. Lastly, creatine was enriched at the earliest timepoint assessed, and this enrichment was sustained through till 48 hours.

After analysing the concentration of metabolite detected in the metabolomics, we selected exogenous doses that represented physiological levels of the metabolite, exogenous doses close to optimal effectivity as identified in current literature, and one extremely high dose for investigation. Specific concentrations are listed for each metabolite investigated.

5.3.1 Exogenous asparagine increased cholangiocyte viability and migration

Aspartate and asparagine play crucial roles in cellular metabolism, protein synthesis, and nucleotide biosynthesis. In particular, aspartate has been highlighted as a limiting factor for cancer cell growth (128,129). Aspartate is transamidated by asparagine synthetase (ASNS) to form asparagine, whilst aspartate transaminase (AST) catalyses the interconversion of aspartate and α-ketoglutarate to oxaloacetate and glutamate. In the reverse reaction, asparagine is hydrolysed to aspartate by asparaginase.

The metabolomics analysis identified a Fold Change of 0.46 in aspartate concentration ($P<0.0001$) in MMNK1 cells after 48-hours of co-culture (Figure 5:15B). Likewise there was a significant ($P<0.0001$) difference in the aspartate/asparagine ratio at 48 hours during co-culture (Figure 5:18).

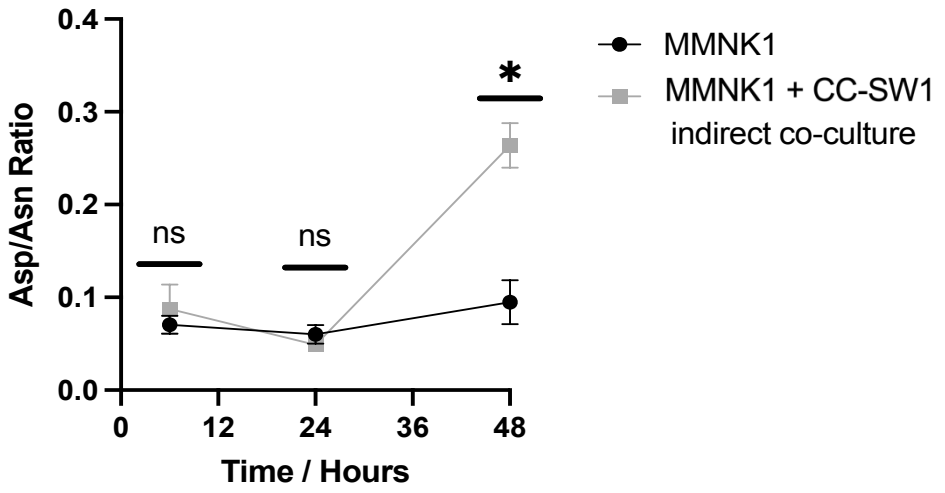


Figure 5:18 – Aspartate/asparagine ratio in MMNK1 cells across 48 hours. *The ratio of aspartate (asp) to asparagine (asn) concentration was calculated for MMNK1 cholangiocytes cultured alone (black), and in indirect co-culture with CC-SW1 cells (grey) at 6, 24, and 48 hours. There was a significant increase in asp/asn ratio in co-cultured cells after 48 hours (*P<0.05), compared to monocultured cells.*

We hypothesised that the reduction in aspartate concentration was due to increased shuttling of aspartate towards asparagine formation to meet the increased demand for asparagine, and that the functional changes identified were due to increased asparagine metabolism. Therefore, we elected to investigate whether exogenous doses of asparagine could mimic the phenotypic changes seen in cholangiocyte cells during co-culture.

In general, the concentration of asparagine in the blood plasma of a healthy individual typically ranges from approximately 0.03 to 0.06 mM (130), whilst we reported a concentration of 0.012 mM in MMNK1 cells after 48 hours of co-culture. Previous research has demonstrated the proliferative benefit of 0.1 mM of exogenous asparagine (131,132). We therefore selected 3 doses of exogenous asparagine, one close to physiological levels (0.01 mM), one close to optimal dosing (0.10 mM), and one extremely high dose (1.00 mM) for investigation. Exogenous asparagine had no effect on MMNK1 cell viability at 0.01 and

0.10 mM (P=0.7415, and 0.9590 respectively) but increased MMNK1 cell viability at 1.00 mM (P=0.0422)(Figure 5:19).

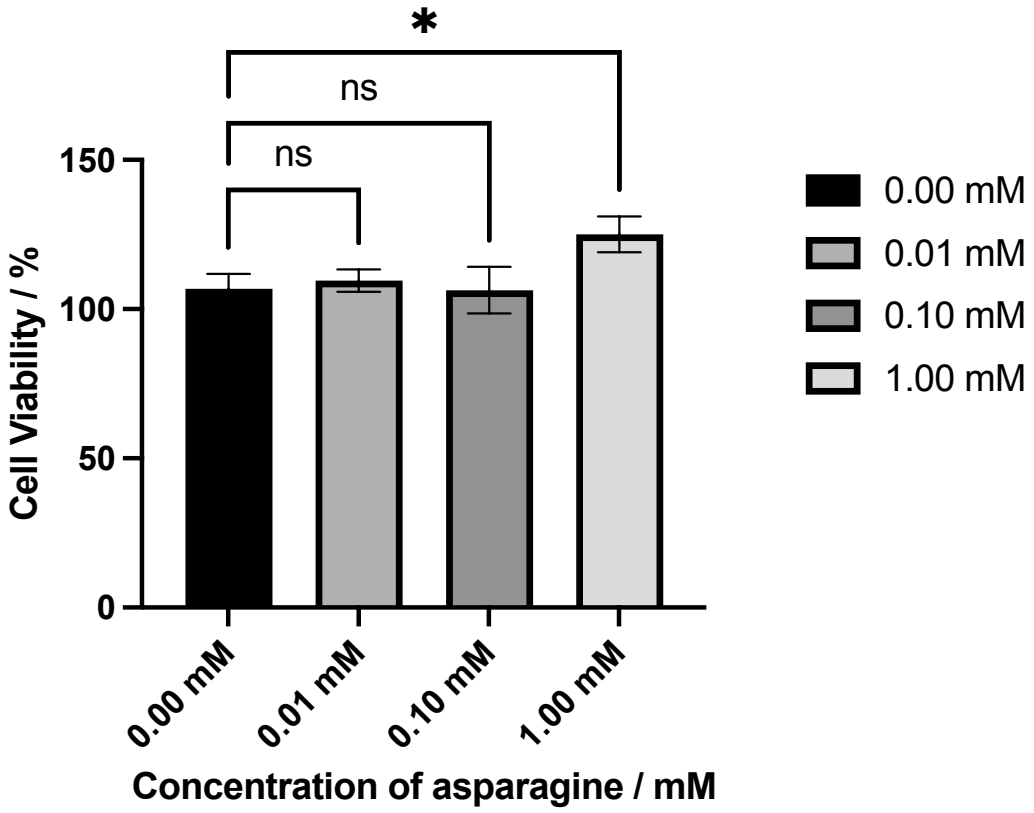


Figure 5:19 - Exogenous asparagine increases MMNK1 cell viability*. MMNK1 cells were treated with exogenous doses of 0.01, 0.10, and 1.00 mM of asparagine and cultured for 48 hours in low glucose DMEM supplemented with 0.1% BSA. Cell viability was evaluated via CCK8 colorimetric analysis. 1.00 mM of asparagine significantly increased MMNK1 cholangiocyte viability (*P<0.05)(n=4).*

Exogenous doses of asparagine caused a dose-response like increase in MMNK1 cell migration (P=0.456 at 0.01 mM, and P=0.1505 at 0.10 mM) which was statistically significant at 1.00mM (P=0.0108)(Figure 5:20).

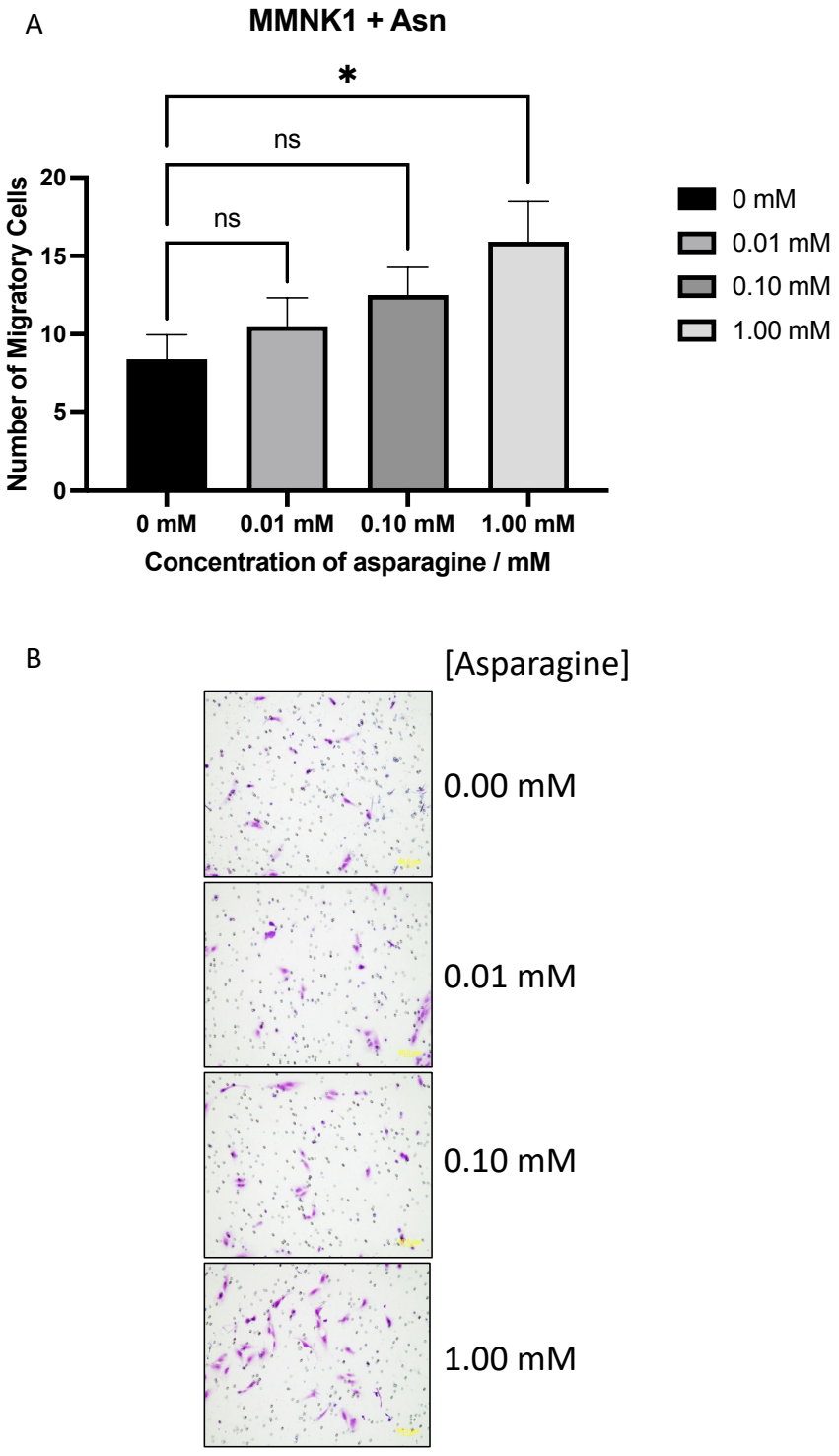


Figure 5:20 – Exogenous asparagine increases MMNK1 cell migration. *A) MMNK1 cells were treated with exogenous doses of 0.01, 0.10, and 1.00 mM of asparagine and cultured for 48 hours in low glucose DMEM supplemented with 0% FBS in the top chamber, and 5% FBS in the bottom chamber of a transwell system. Cell migration was evaluated via crystal violet staining, imaged using light microscopy and analysed via Fiji/ImageJ analysis. 1.00 mM of asparagine significantly increased the proportion of migratory MMNK1 cholangiocytes (*P<0.05)(n=4). B) Representative microscopy images of migratory MMNK1 cholangiocytes following treatment with 0.01, 0.10, and 1.00 mM of exogenous asparagine for 48 hours.*

5.3.2 Exogenous choline decreased cholangiocyte viability, with no effect on apoptosis or migration

Choline is the precursor of phosphatidylcholine, a major component of biological membranes, making choline essential for cell division and growth. The metabolomics analysis identified that choline concentration increased by 3.9 fold ($P<0.0001$) in MMNK1 cells after co-culture for 48-hours (Figure 5:16A).

We hypothesised that the increase in choline concentration was to fulfil the lipid membrane requirements for the increased proliferation identified in our cholangiocytes during co-culture. Therefore, we selected to investigate whether exogenous doses of choline could recapitulate the phenotypic changes in MMNK1 cholangiocytes during co-culture. Typically, plasma choline concentrations range from 7 – 20 µM (133,134) whilst we reported a concentration of 0.21 µM in MMNK1 cells after 48 hours of co-culture. We therefore selected 3 doses of exogenous choline, one close to our reported concentration (2 µM), one close physiological levels (20 µM), and one extremely high dose (40 µM) to recapitulate the effect of co-culture.

Exogenous choline had a negative effect on MMNK1 cell viability, with 2, 20, and 40 µM of choline causing a statistically significant decrease in viability ($P=0.023$, 0.0031, and <0.0001 respectively)(Figure 5:21). Exogenous choline had no effect on the amount of migratory MMNK1 cells ($P=0.1680$, 0.2496, and 0.6500 respectively)(Figure 5:22).

Exogenous choline had no effect on the proportion of alive ($P=0.4389$, 0.3950, 0.9678, and 0.6880 respectively)(Figure 5:23A) and apoptotic ($P=0.4782$, 0.7858, 0.8580, and 0.8724 respectively)(Figure 5:23B) MMNK1 cells as determined by flow cytometry.

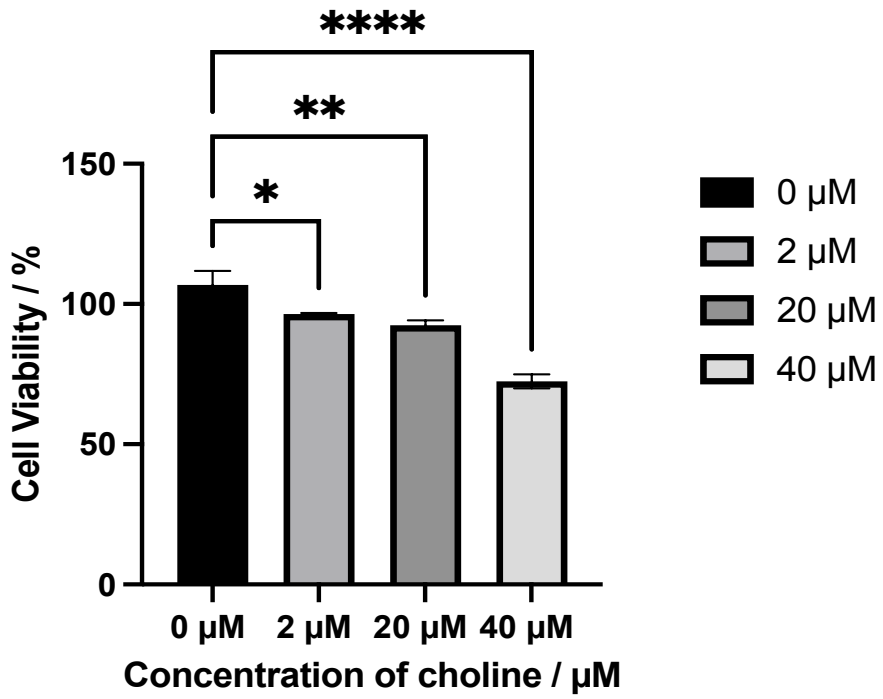


Figure 5:21 - Exogenous choline decreases MMNK1 cell viability*. MMNK1 cells were treated with exogenous doses of 2, 20, and 40 µM of choline and cultured for 48 hours in low glucose DMEM supplemented with 0.1% BSA. Cell viability was evaluated via CCK8 colorimetric analysis. Exogenous doses of 2, 20, and 40 µM of choline significantly decreased MMNK1 cholangiocyte viability (*P<0.05, **P<0.01, ****P<0.0001)(n=3).*

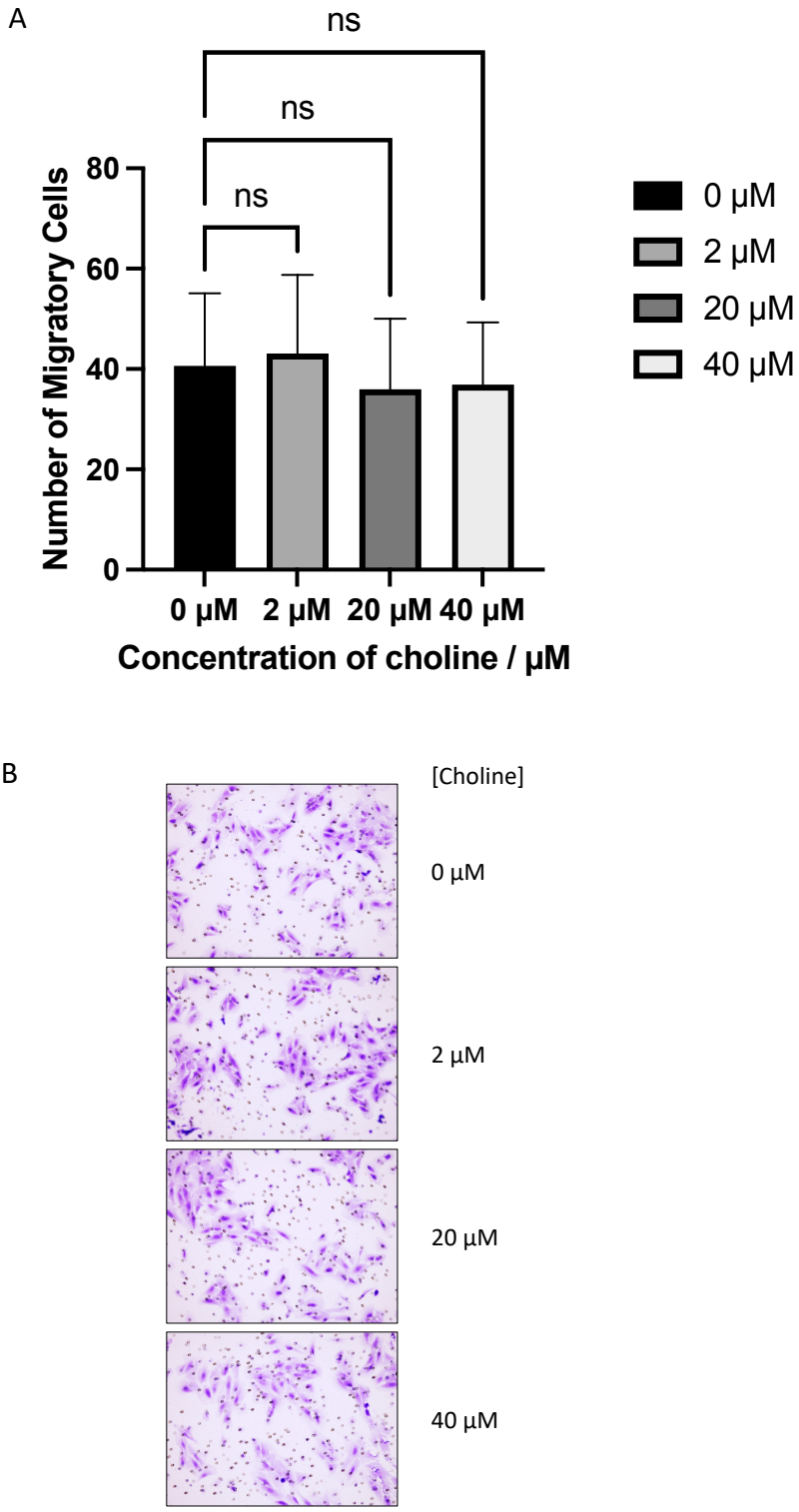


Figure 5:22 – Exogenous choline has no effect on MMNK1 cell migration*. MMNK1 cells were treated with exogenous doses of 2, 20, and 40 µM of choline and cultured for 48 hours in low glucose DMEM supplemented with 0% FBS in the top chamber, and 5% FBS in the bottom chamber of a transwell system. Cell migration was evaluated via crystal violet staining, imaged using light microscopy and analysed via Fiji/ImageJ analysis. Exogenous doses of choline had no significant effect on the proportion of migratory MMNK1 cholangiocytes (ns, P>0.05)(n=3). B) Representative microscopy images of migratory MMNK1 cholangiocytes following treatment with 2, 20, and 40 µM of exogenous choline for 48 hours.*

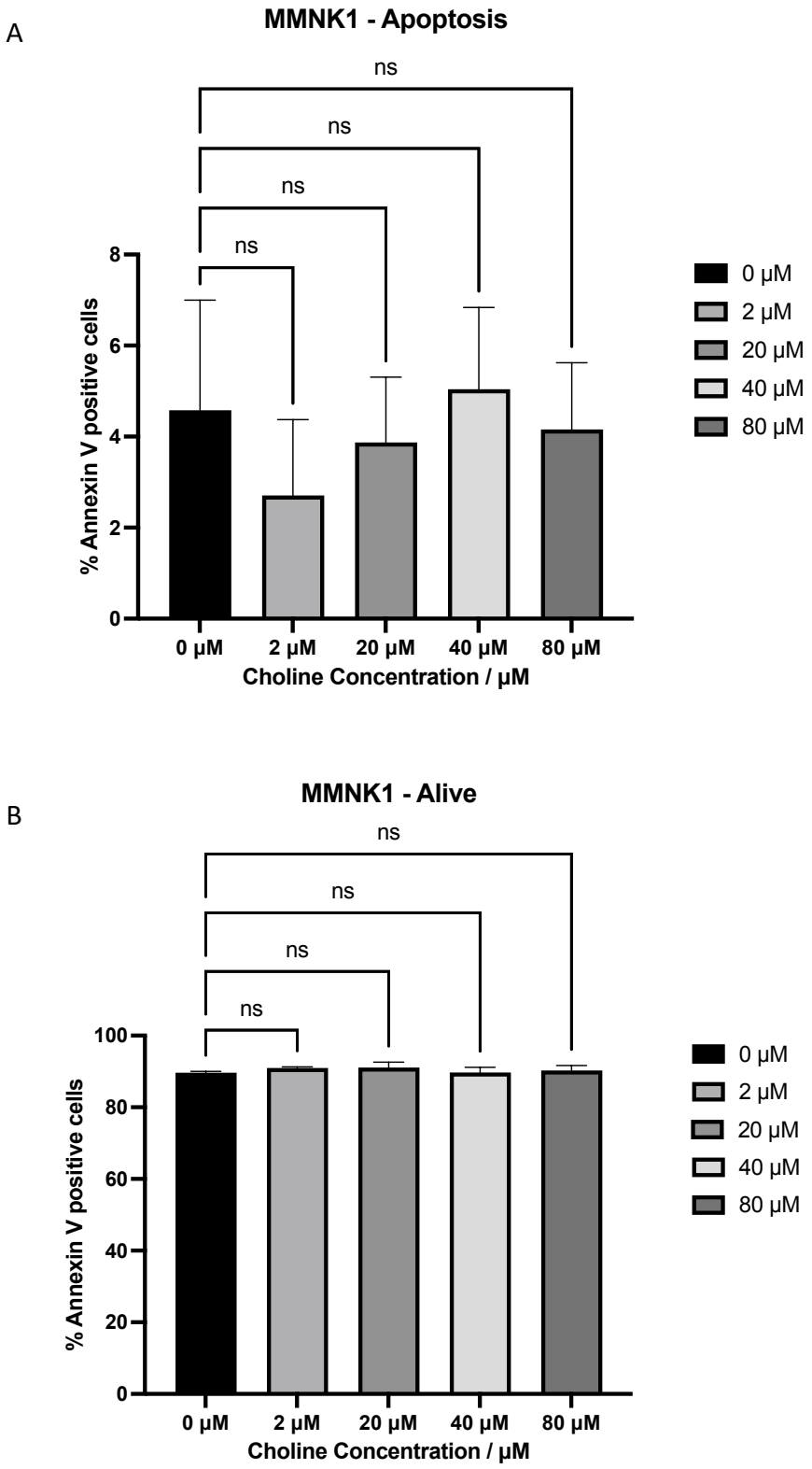
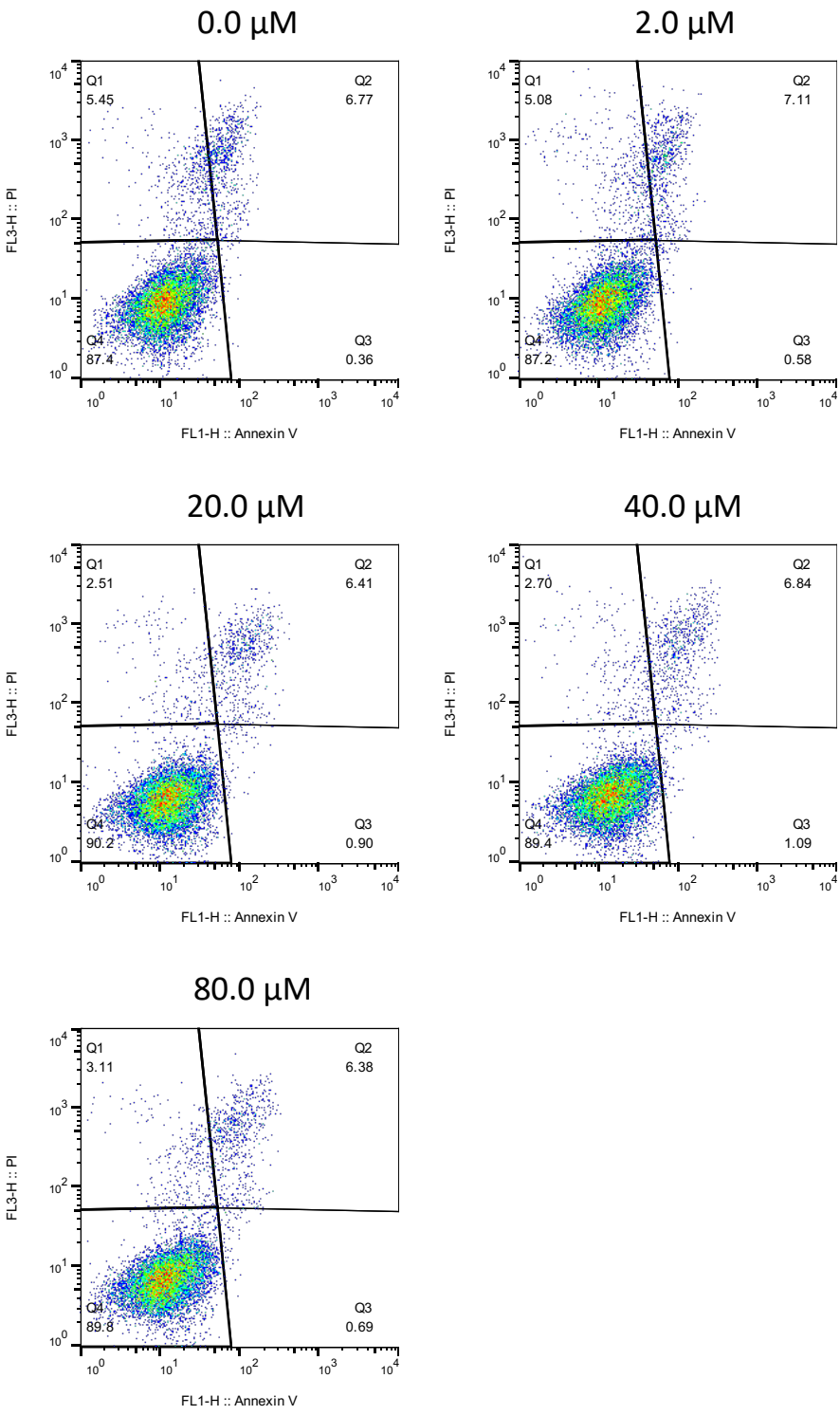


Figure 5:23 – Exogenous choline has no effect on the proportion of apoptotic or viable MMNK1 cells*. MMNK1 cells were treated with 2, 20, and 40 µM of exogenous choline and cultured in low glucoses DMEM supplemented with 0.1% BSA for 48 hours. Cells were stained with propidium iodide and annexin V prior to flow cytometry, to evaluate the proportion of A) apoptotic, and B) viable cells, after treatment with exogenous choline. Quadrants from the flow cytometry analysis are shown in C). Exogenous choline had no effect on the proportion of apoptotic or viable MMNK1 cholangiocytes.*

C


0.0 µM
Q1
5.45
Q2
6.77
Q4
87.4
Q3
0.36
2.0 µM
Q1
5.08
Q2
7.11
Q4
87.2
Q3
0.58
20.0 µM
Q1
2.51
Q2
6.41
Q4
90.2
Q3
0.90
40.0 µM
Q1
2.70
Q2
6.84
Q4
89.4
Q3
1.09
80.0 µM
Q1
3.11
Q2
6.38
Q4
89.8
Q3
0.69
FL3-H :: PI
FL1-H :: Annexin V

5.3.3 Exogenous creatine improves cholangiocyte viability and ATP availability

Creatine plays a crucial role in cellular energy metabolism, acting as a store of energy in the form of phosphocreatine (PCr). During periods of high energy demand, PCr donates its phosphate group to ADP to generate ATP which can be readily utilized as an immediate energy source by the cells. The *de novo* synthesis of cellular creatine requires glycine and arginine.

The metabolomics analysis identified the concentration of creatine increased by 2.0 fold (P=0.0002) in MMNK1 cells during co-culture at 48-hours (Figure 5:16C). We therefore chose to investigate whether this metabolite was the fuel behind the functional and molecular changes to the MMNK1 phenotype during co-culture.

The average concentration of creatine in skeletal muscle is approximately 40 mM (135,136) whilst we reported a concentration of 0.19 µM in MMNK1 cells after 48 hours of co-culture. We therefore selected a range of exogenous creatine: 0.25, 0.50, 1.00, 2.50, and 5.00 mM, covering our reported concentration, approximate physiological levels, and extremely high doses to recapitulate the effect of co-culture.

An exogenous creatine dose of 2.50 mM and 5.00 mM caused a statistically significant increase in MMNK1 cell viability (P=0.0219 and 0.0373 respectively)(Figure 5:24).

Exogenous creatine doses of 1.00, 2.50 mM, and 5.00 mM caused a non-significant reduction in the proportion of apoptotic MMNK1 cells (P= 0.5474, 0.6861, and 0.4710)(Figure 5:25A) with no change to the proportion of viable MMNK1 cells (P=0.6703, 0.7386, and 0.6117)(Figure 5:25B).

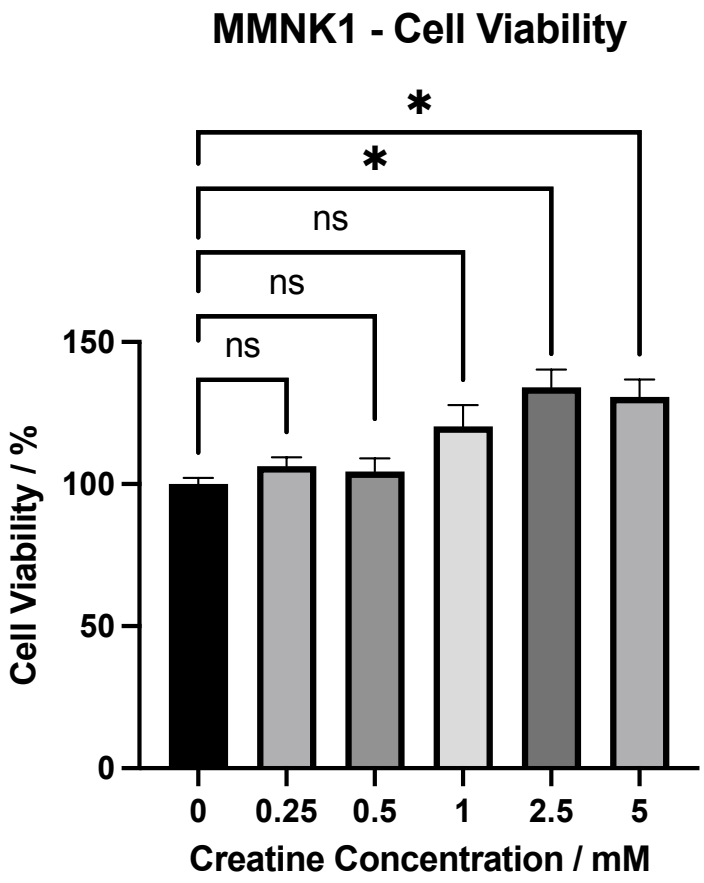


Figure 5:24 – Exogenous creatine increases MMNK1 cell viability*. MMNK1 cells were treated with doses of 0.25, 0.50, 1.00, 2.50, and 5.00 mM exogenous creatine and cultured for 48 hours in low glucose DMEM supplemented with 0.1% BSA. Cell viability was evaluated via CCK8 colorimetric analysis. Exogenous creatine doses of 2.5 and 5.0 mM significantly increased MMNK1 cholangiocyte viability (*P<0.05)(n=6).*

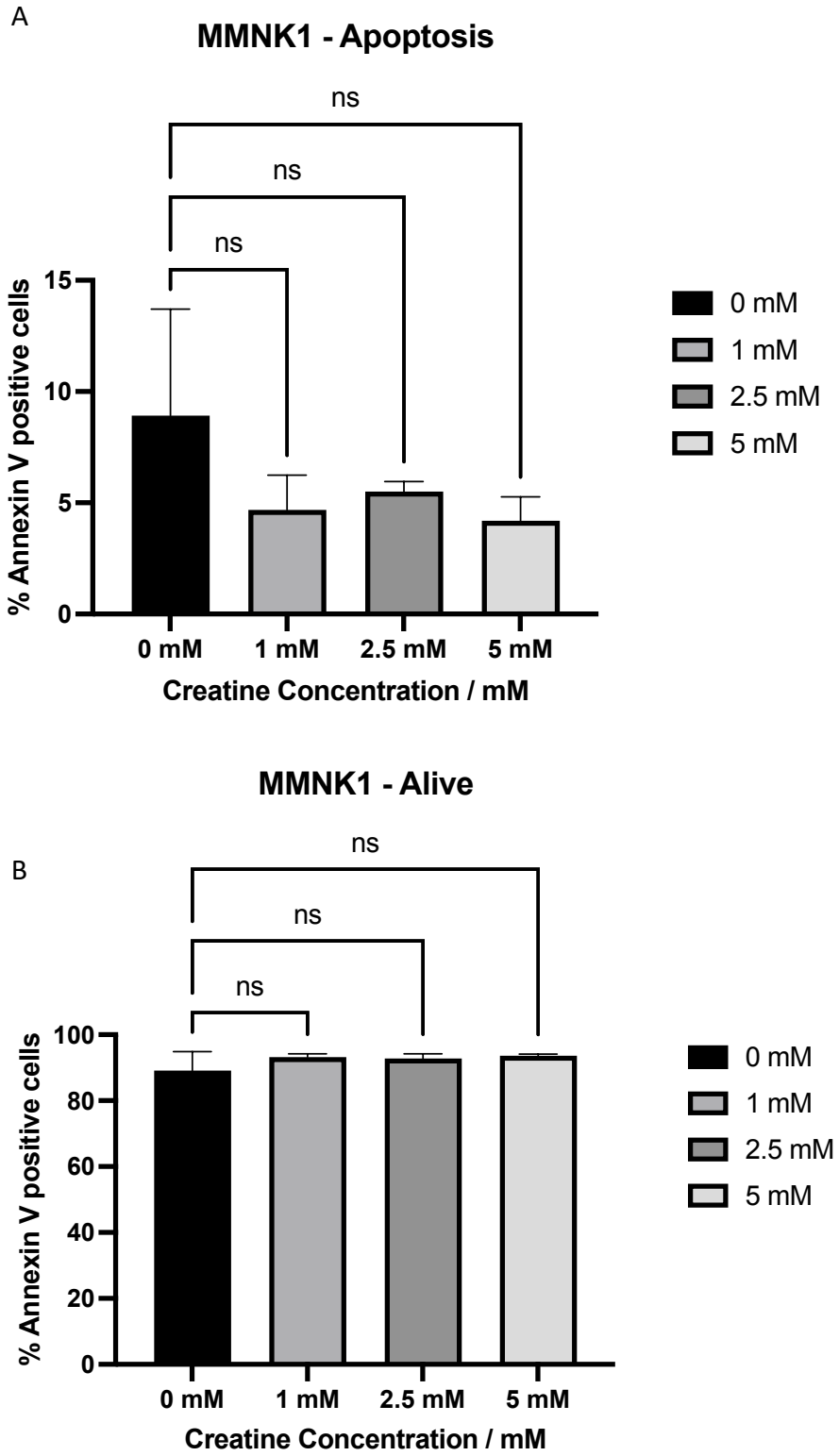
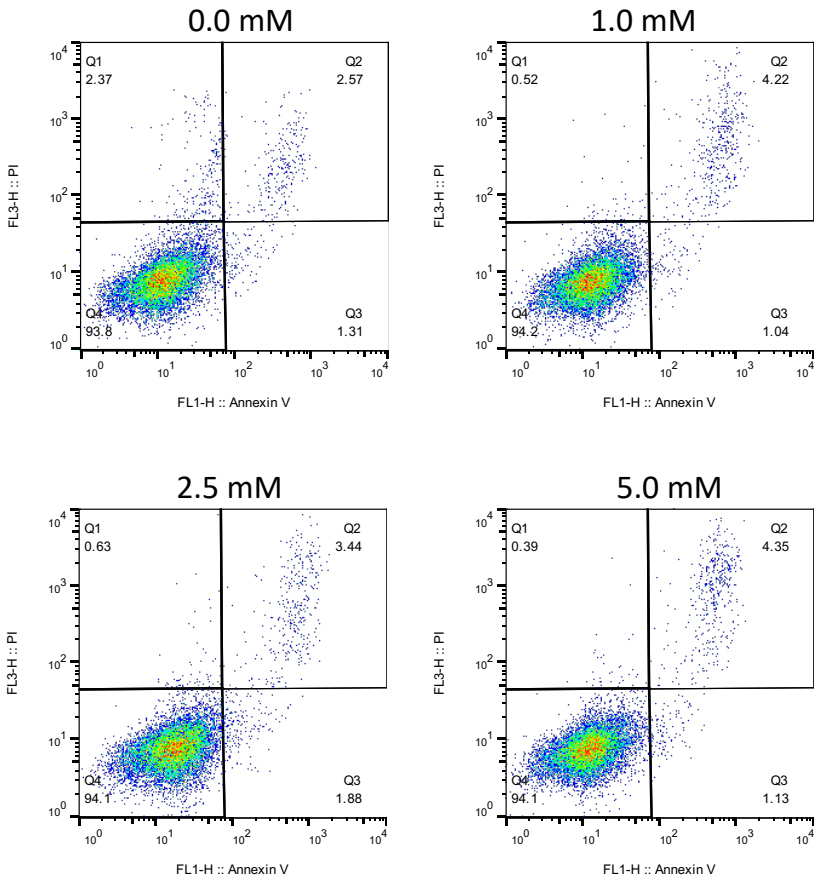


Figure 5:25 - Exogenous creatine has no effect on the proportion of apoptotic or viable MMNK1 cells*. MMNK1 cells were treated with 1.0, 2.5, and 5.0 mM of exogenous creatine and cultured in low glucoses DMEM supplemented with 0.1% BSA for 48 hours. Cells were stained with propidium iodide and annexin V prior to flow cytometry, to evaluate the proportion of A) apoptotic, and B) viable cells, after treatment with exogenous creatine. Quadrants from the flow cytometry analysis are shown in C). Exogenous creatine had no effect on the proportion of apoptotic or viable MMNK1 cholangiocytes.*

C


0.0 mM
Q1
2.37
Q2
2.57
Q4
93.8
Q3
1.31
1.0 mM
Q1
0.52
Q2
4.22
Q4
94.2
Q3
1.04
2.5 mM
Q1
0.63
Q2
3.44
Q4
94.1
Q3
1.88
5.0 mM
Q1
0.39
Q2
4.35
Q4
94.1
Q3
1.13
FL3-H :: PI
FL1-H :: Annexin V

Cyclocreatine is a chemical analogue of creatine that is used to inhibit the creatine system as a direct competitor for both the creatine kinase enzyme and transporter uptake. We also used cyclocreatine at the same concertation values as exogenous creatine, to provide further support for MMNK1 cell reliance on the creatine system for its phenotypic behaviour. An exogenous cyclocreatine dose of 5.00 mM caused a statistically significant decrease in MMNK1 cell viability (P=0.0235)(Figure 5:26), as well as a non-significant increase in the proportion of apoptotic MMNK1 cells (P=0.539)(Figure 5:27A) with no change to the proportion of alive cells (P=0.8380, 0.6138, and 0.4655 respectively)(Figure 5:27B).

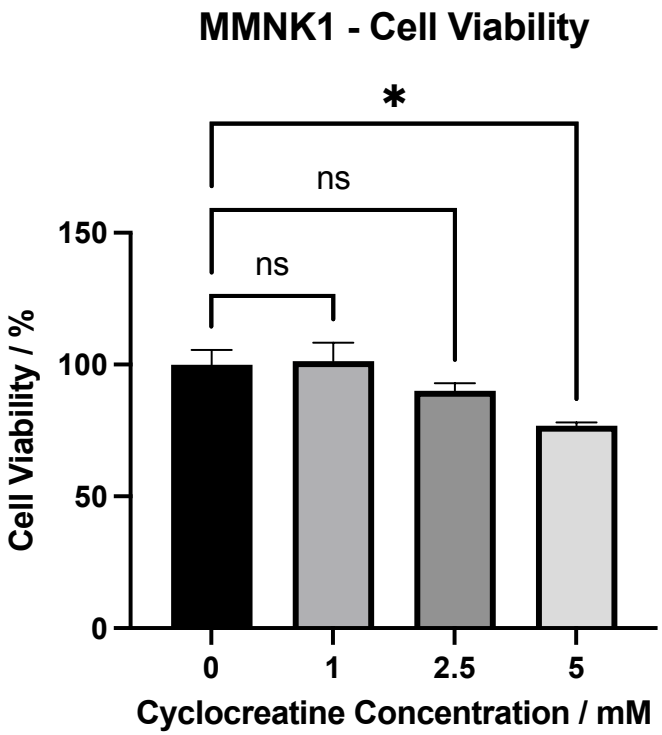


Figure 5:26 - Exogenous cyclocreatine decreases MMNK1 cell viability*. MMNK1 cells were treated with doses of 1.00, 2.50, and 5.00 mM exogenous cyclocreatine and cultured for 48 hours in low glucose DMEM supplemented with 0.1% BSA. Cell viability was evaluated via CCK8 colorimetric analysis. An exogenous cyclocreatine dose of 5.0 mM significantly decreased MMNK1 cholangiocyte viability (*P<0.05)(n=3).*

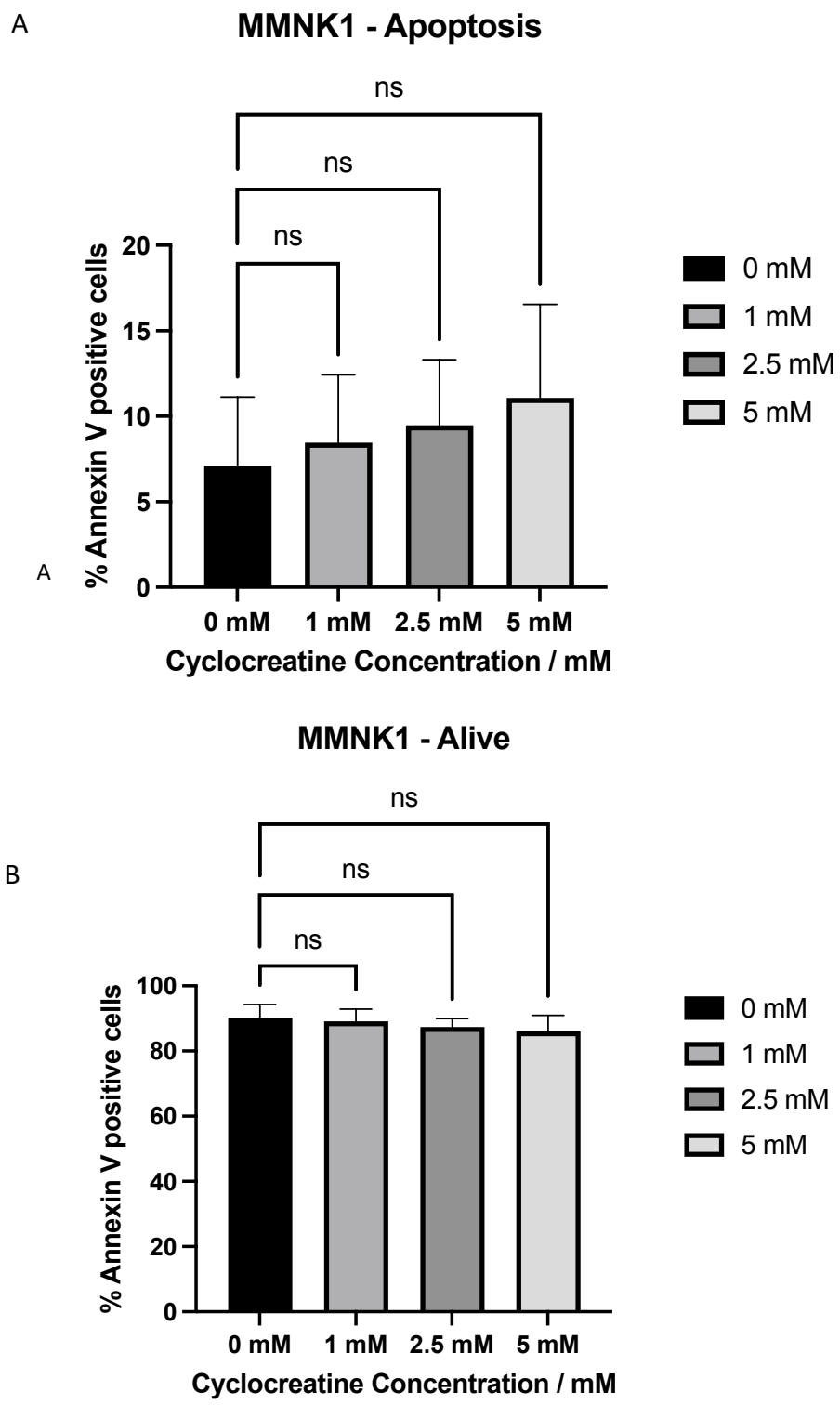
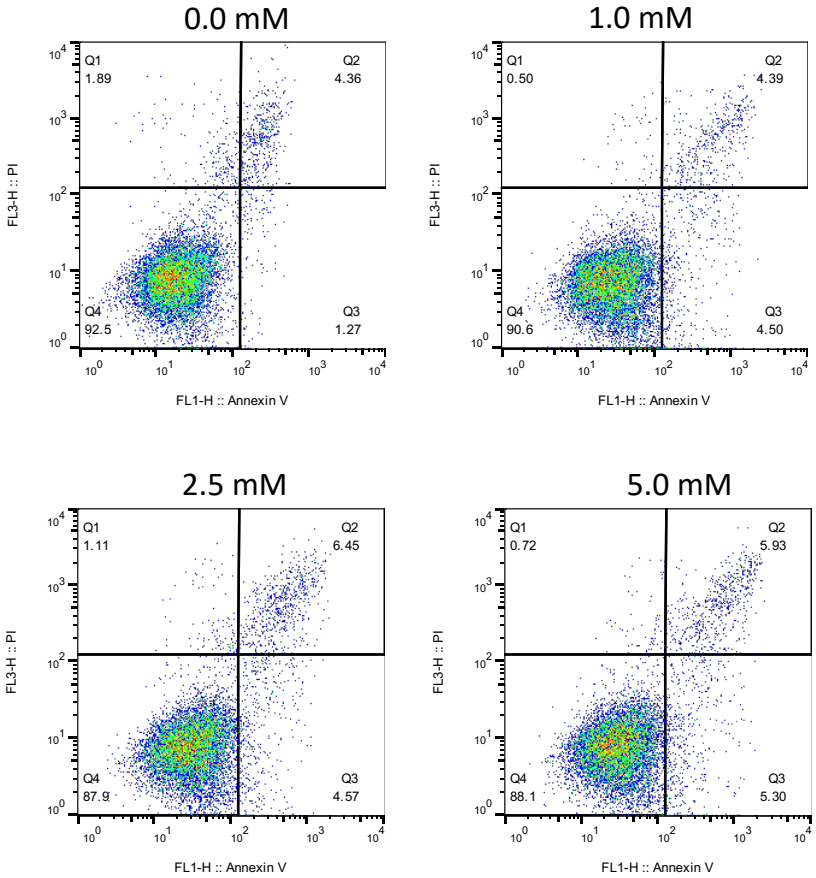


Figure 5:27 – Exogenous cyclocreatine has no effect on the proportion of apoptotic or viable MMNK1 cells*. MMNK1 cells were treated with 1.0, 2.5, and 5.0 mM of exogenous cyclocreatine and cultured in low glucoses DMEM supplemented with 0.1% BSA for 48 hours. Cells were stained with propidium iodide and annexin V prior to flow cytometry, to evaluate the proportion of A) apoptotic, and B) viable cells, after treatment with exogenous cyclocreatine. Quadrants from the flow cytometry analysis are shown in C). Exogenous cyclocreatine had no effect on the proportion of apoptotic or viable MMNK1 cholangiocytes.*

C


0.0 mM
Q1
1.89
Q2
4.36
Q4
92.5
Q3
1.27
1.0 mM
Q1
0.50
Q2
4.39
Q4
90.6
Q3
4.50
2.5 mM
Q1
1.11
Q2
6.45
Q4
87.9
Q3
4.57
5.0 mM
Q1
0.72
Q2
5.93
Q4
88.1
Q3
5.30
FL3-H :: PI
FL1-H :: Annexin V

Likewise, we used a combination of exogenous choline with creatine to assess whether creatine could recover cell viability. 20 µM of choline had no effect on cell viability (P=0.8729)(Figure 5:28) during these rounds of experiments, whilst 5 mM creatine caused a statistically significant increase in cell viability (P=0.0286)(Figure 5:28). However, when the dual combination was applied, there was no change in cell viability (P=0.2992)(Figure 5:28).

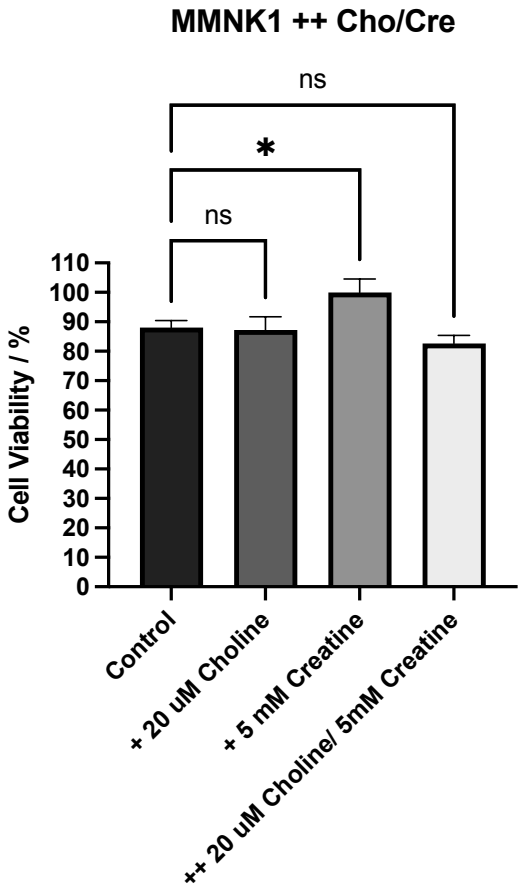


Figure 5:28 – Dual exogenous doses of creatine and choline have no effect on MMNK1 cell viability. *MMNK1 cells were treated with exogenous doses of 20 µM of choline, 5 mM of creatine, or a dual combination, and cultured for 48 hours in low glucose DMEM supplemented with 0.1% BSA. Cell viability was evaluated via CCK8 colorimetric analysis. 5.0 mM of creatine significantly increased MMNK1 cholangiocyte viability, which was ablated by supplementation with 20 µM of choline(*P<0.05) (n=3).*

We hypothesised that the increased concentration of creatine in MMNK1 cells during co-culture, would increase cellular ATP levels. Therefore we used an luminescence-based assay to calculate the concentration of ATP in MMNK1 cells during co-culture. Figure 5:29 shows that co-culturing MMNK1 cells with CC-SW1 cells leads to a significant increase in ATP concentration (P=0.0013). This was also validated for co-culture with SNU-1079, CC-LP1, and SNU-1196 cells (Figure 5:29), where we found a significant increase in ATP concentration during co-culture with all 3 CCA cell lines (P=0.0051, 0.0061, and 0.0034 respectively).

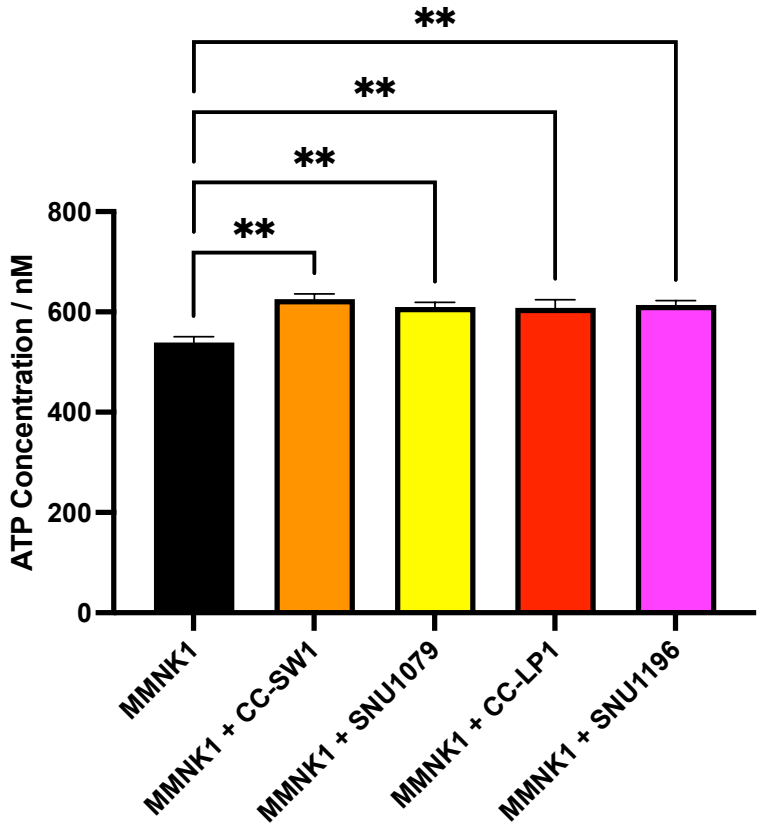


Figure 5:29 – Indirect co-culture with CCA cells increases the concentration of available ATP in MMNK1 cells. *The concentration of ATP in MMNK1 cells when cultured alone, or in indirect co-culture with CC-SW1, SNU-1079, CC-LP1, and SNU-1196 CCA cells was evaluated using luminescence-based CellTiter-Glo Assay. Indirect co-culture with all four CCA lines significantly increased the concentration of available ATP in MMNK1 cholangiocytes (**P<0.01)(n=3).*

We then treated MMNK1 cells with 5 exogenous doses of creatine and assessed ATP concentration. Creatine concentrations of 1, 2.5, and 5 mM caused a significant increase in ATP concentration (P= 0.0007, 0.0158, and 0.0028 respectively) whilst 10 mM creatine had no significant effect on ATP concentration (P=0.2127)(Figure 5:30A). Likewise, we also treated MMNK1 cells with 5 exogenous doses of cyclocreatine and assessed ATP concentration. Cyclocreatine concentrations of 1.0, 2.5, and 5.0 mM creatine had no significant effect on ATP concentration (P=0.8098, 0.1840, and 0.4536 respectively), however a cyclocreatine concentration of 10 mM caused a significant decrease in ATP concentration (P=0.0140)(Figure 5:30B).

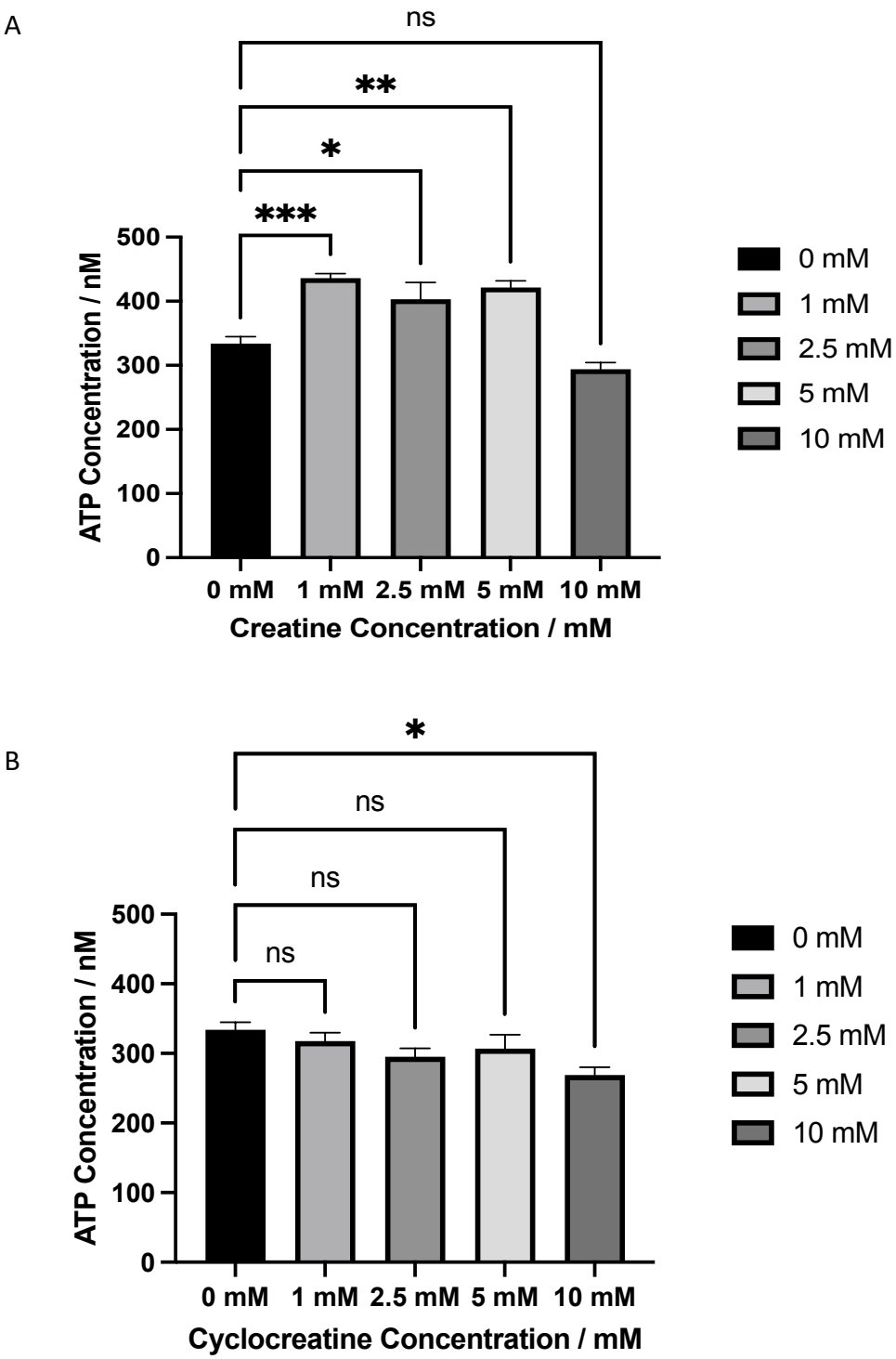


Figure 5:30 – Exogenous creatine increases the concentration of cellular ATP in MMNK1 cells. *The concentration of ATP in MMNK1 cells when treated with 1.0, 2.5, 5.0, and 10.0 mM of A) exogenous creatine, and B) exogenous cyclocreatine, was evaluated using luminescence-based CellTiter-Glo Assay. Exogenous creatine doses of 1.0, 2.5, and 5.0 mM significantly increased ATP concentration in MMNK1 cholangiocytes, whilst 10 mM exogenous cyclocreatine significantly decreased MMNK1 ATP concentration(*P<0.05,**P<0.01, ***P<0.001)(n=3).*

5.3.4 Summary

In summary we used exogenous doses of 3 metabolites to modulate cholangiocyte behaviour. Exogenous asparagine increased cholangiocyte cell viability and migratory behaviour from 1.00 mM, whilst exogenous choline reduced cholangiocyte cell viability from 2 µM, with no effect on migratory behaviour, or apoptosis.

Exogenous creatine from a concentration of 2.5 mM increased cholangiocyte cell viability, and caused a non-significant reduction in the proportion of apoptotic MMNK1 cells. Exogenous creatine caused a significant increase in ATP concentration. Co-culture of cholangiocytes with the iCCA cell lines CC-SW1, CC-LP1, and SNU-1079, as well as the eCCA cell line SNU-1196, caused a significant increase in ATP concentration. A combination of exogenous choline and exogenous creatine demonstrated that creatine could recover a decrease in cell viability due to choline supplementation. The creatine analogue cyclocreatine caused a statistically significant decrease in MMNK1 cell viability, a non-significant increase in the proportion of apoptotic MMNK1 cells, and a significant decrease in ATP concentration.

5.4 Changes to the cholangiocarcinoma metabolome during indirect co-culture

After establishing the individual metabolic profiles of CCA and cholangiocytes, we proceeded to evaluate the concentration of intracellular metabolites in CC-SW1 cells when in co-culture with MMNK1 cells. We extracted intracellular metabolites after several timepoints (6, 24, and 48 hours) and proceeded to evaluate the change in metabolite concentration at every time point, in order to understand both early, intermediate, and late metabolic changes that occurred during coculture. For all timepoints, we performed hierarchical clustering and PCA analysis to understand the biological distances and relevance between the two compartments.

5.4.1 6 hours of co-culture decreased nucleoside mono-, di-, and triphosphate concentration in cholangiocarcinoma cells

It should be noted that during early coculture, there was weak separation between the two compartments. The hierarchical clustering in Figure 5:31A highlights a distinct overlap in monoculture and co-culture samples, suggesting that there were little biological differences to tell them apart mathematically. Likewise, the PCA revealed a small overlap between monoculture and co-culture clusters (Figure 5:31B), and a greater variation along PC1 within clusters (intragroup) as opposed to between mono- and co-culture samples (intergroup). Therefore, 6 hours of co-culture may not be an appropriate time point in order to detect co-culture mediate changes to the CC-SW1 metabolome, due to the poor mathematical segregation of monoculture and co-culture samples.

The metabolite profile as denoted in the heatmap (Figure 5:32) showing relative expression of metabolites (rows) in each sample (columns), illustrates the numerous variations in metabolite concentration occurring within and between samples, thus explaining the inability to separate them clearly at this timepoint.

We subsequently used the expression of each metabolite to conduct statistical analysis, to assess whether any metabolites were significantly differentially expressed after 6 hours, using the threshold of a Fold Change >2/<-2 and $P<0.01$. As shown in the volcano plot in Figure 5:33A, 14 metabolites met our selection criteria. 9 metabolites had a fold change in concentration >2 and $P<0.01$, and 5 metabolites had a fold change in concentration <-2 and $P<0.01$. Figure 5:33B lists the fold changes and P-values for the 14 metabolites.

Using a Metabolic Pathway enrichment analysis, we investigated the weight of each metabolite on its respective metabolic pathway. The volcano plot in Figure 5:34 illustrates the metabolic pathways enriched in CCA cells after 6 hours of co-culture. Phenylalanine/tyrosine/tryptophan biosynthesis had the largest Pathway Impact, followed by alanine/aspartate/glutamate metabolism. The TCA cycle had one of the highest level of significance. The majority of metabolites with a reduction in concentration at 6 hours were triphosphates (ATP, CTP, GTP, and UTP) which contribute to cellular energy production, suggesting an increase in energy demand in CC-SW1 cells during co-culture.

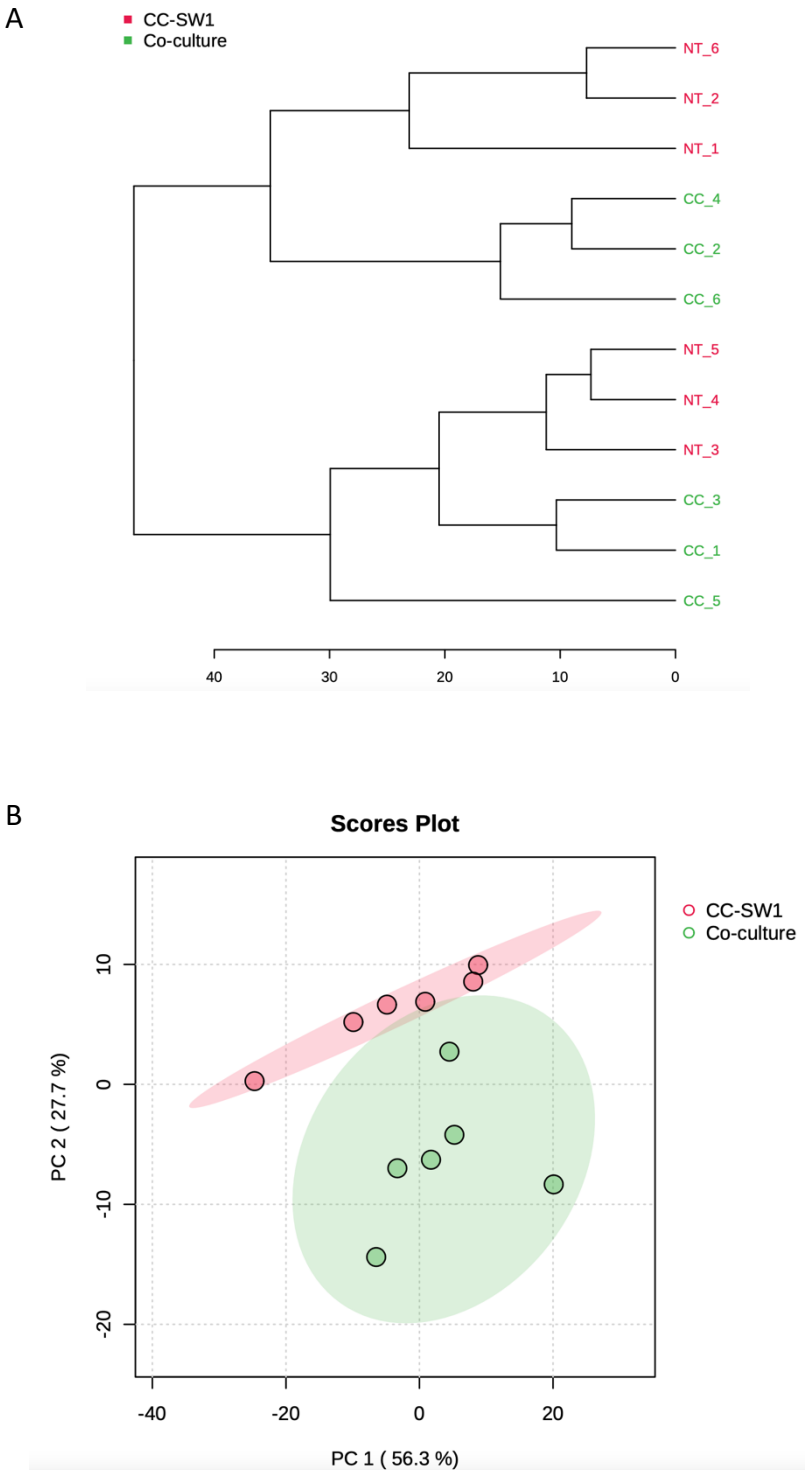


Figure 5:31 - Dendrogram and Scores Plot for the metabolic profiling of CC-SW1 cells after 6 hours of mono- and co-culture. *Normalisation and clustering was conducted on the metabolic profiles of CC-SW1 cells after 6 hours of mono- (green) and co-culture (red) with MMNK1 cells. A) Dendrogram illustrates hierarchical clustering of samples based on Euclidean distances calculated from concentration profiles. Samples with similar profiles are grouped together, as indicated by the branches, whilst vertical lines represent the distance at which clusters merge, identifying sample clusters and subgroups. B) Scores plot represents the complete 6 hour metabolic dataset in a two-dimensional space, generated through the principal component analysis (PCA). Each point on the plot corresponds to a sample. Both mono- and co-culture CC-SW1 samples are spread along PC1, suggesting low levels of co-culture mediated biological variation in metabolite profile after 6 hours.*

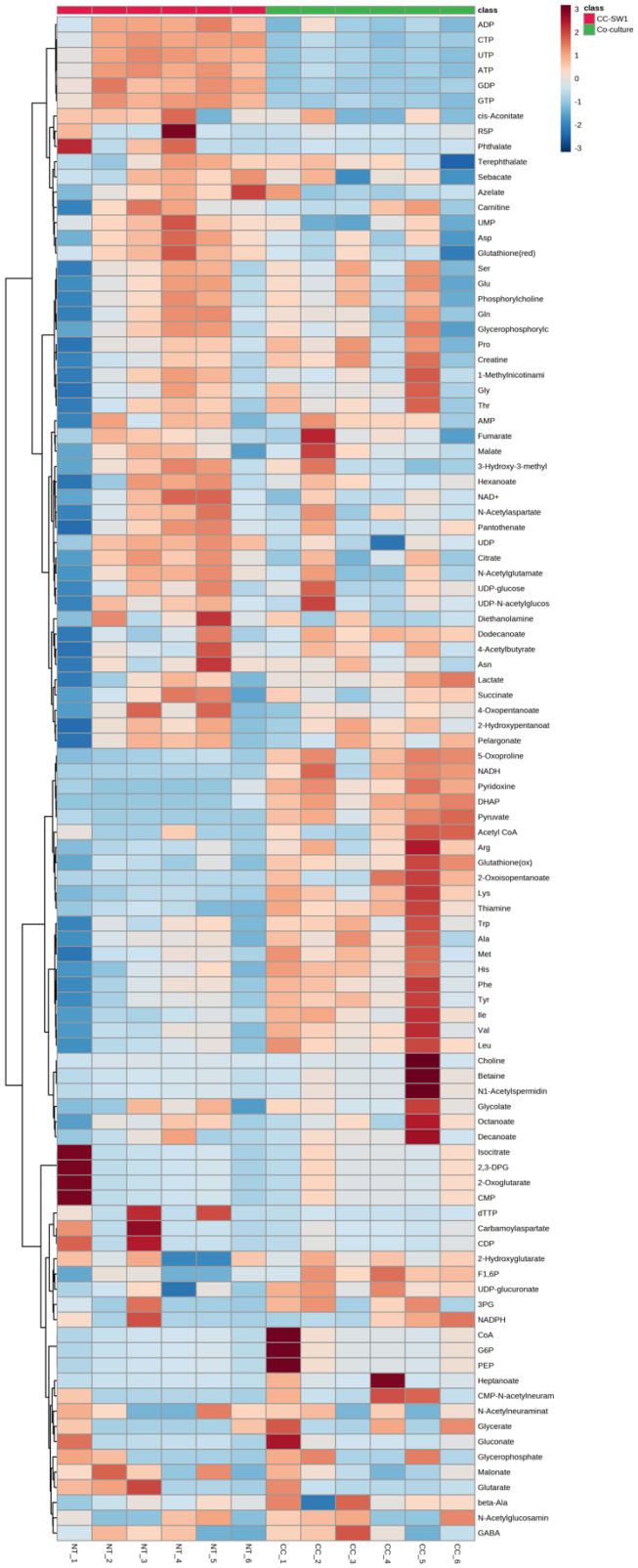
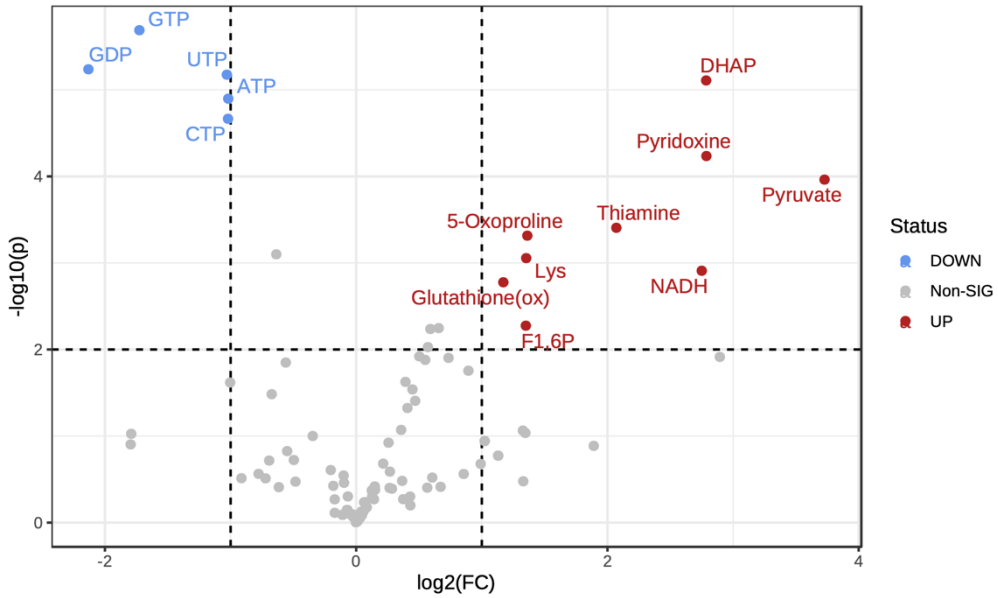


Figure 5:32 – Heatmap of differentially expressed metabolites in CC-SW1 after 6 hours of indirect co-culture*. The relative expression of each metabolite (rows) in CC-SW1 after 6 hours of monoculture, or co-culture with MMNK1 cells. Metabolites which are more highly expressed are shown in red, whilst metabolites which are reduced in concentration are shown in blue. Each column represents a sample, monoculture in red and co-culture in green.*

A



B

Table 4: Important features identified by volcano plot

	Compounds	FC	log2(FC)	raw.pval	-log10(p)
1	GTP	0.3023	-1.726	2.0476e-06	5.6888
2	GDP	0.22819	-2.1317	5.7918e-06	5.2372
3	UTP	0.48966	-1.0301	6.6865e-06	5.1748
4	DHAP	6.8935	2.7852	7.7916e-06	5.1084
5	ATP	0.49354	-1.0188	1.2654e-05	4.8978
6	CTP	0.49287	-1.0207	2.1604e-05	4.6655
7	Pyridoxine	6.9024	2.7871	5.8204e-05	4.235
8	Pyruvate	13.252	3.7281	0.00010894	3.9628
9	Thiamine	4.2002	2.0705	0.00039247	3.4062
10	5-Oxoproline	2.5704	1.362	0.0004838	3.3153
11	Lys	2.5549	1.3532	0.0008799	3.0556
12	NADH	6.7281	2.7502	0.001231	2.9098
13	Glutathione(ox)	2.2516	1.171	0.0016729	2.7765
14	F1,6P	2.5495	1.3502	0.0053065	2.2752

Figure 5:33 - Differentially expressed metabolites in CC-SW1 cells after 6 hours of indirect co-culture with MMNK1 cells. *A) Volcano plot depicting the results of the differential expression analysis for intracellular metabolites in CC-SW1 cholangiocytes after 6 hours of indirect co-culture with MMNK1 cholangiocytes. Each point on the plot represents a metabolite, with its position indicating both statistical significance and fold-change in expression. The dashed horizontal line represents the predefined threshold for significance of -log10(P-value) >2, equating to a raw P-value < 0.01. The dashed vertical lines represents the predefined thresholds for fold change, log_2fold change <1 and log_2fold change >1, equating to a raw fold change <-2 and >2 respectively. Metabolites falling above the upper threshold line (red) are considered significantly upregulated, whilst those below the lower threshold line (blue) are significantly downregulated. B) 14 metabolites are differentially expressed in CC-SW1 cells after 6 hours of co-culture.*

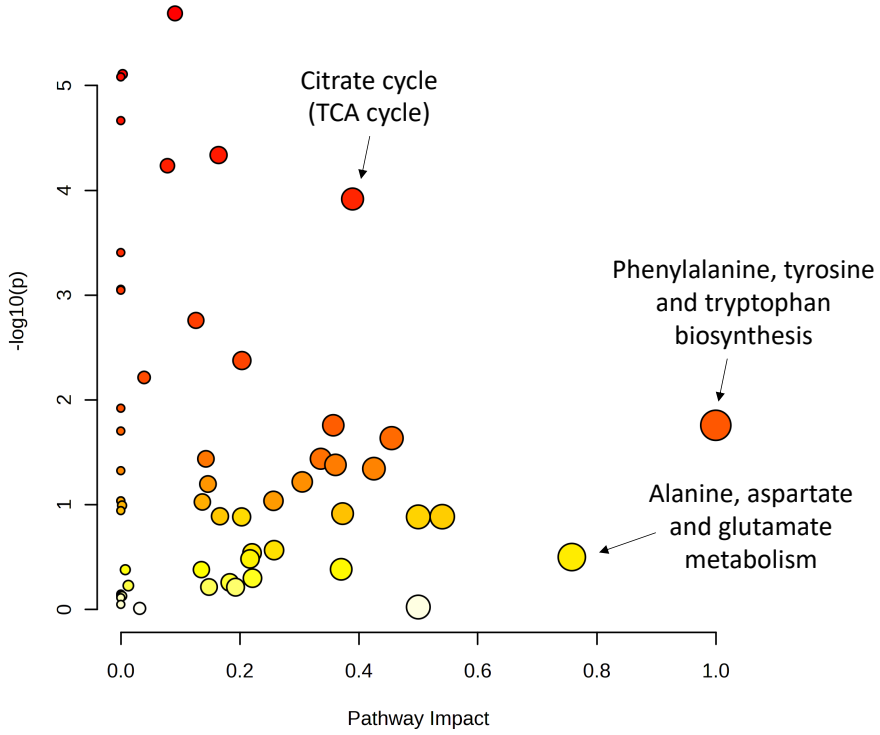


Figure 5:34 - Enriched metabolic pathways in CC-SW1 cells after 6 hours of indirect co-culture with MMNK1 cholangiocytes. *Volcano plot depicting enriched metabolic pathways in CC-SW1 cells after 6 hours of indirect co-culture with MMNK1 cholangiocytes, compared to CC-SW1 cells cultured in monoculture, as identified by metabolic pathway enrichment analysis. Each point on the plot corresponds to a metabolic pathway, and its position conveys both the pathway impact, which reflects the cumulative influence of metabolite changes within each pathway as a measure of biological relevance, and the pathway significance. A subset of enriched metabolic pathways meeting the highest significance, and highest impact criteria are marked with black arrows and labelled, to highlight the most relevant pathways in the analysis. In CC-SW1 cells after 6 hours of indirect co culture, these pathways included alanine/aspartate/glutamate metabolism, phenylalanine/tyrosine/tryptophan biosynthesis, and the TCA cycle.*

5.4.2 24 hours of co-culture increased 2-oxoisopentanote and decreased glutamine concentrations in cholangiocarcinoma cells

The hierarchical clustering of monoculture and co-culture samples was improved after 24 hours (Figure 5:35A). Compared to the hierarchical clustering of samples after 6 hours, 24 hours demonstrates very clear separation between the clusters of monoculture samples and the cluster of co-culture samples. Likewise, the PCA revealed clear separation between monoculture and co-culture clusters (Figure 5:35B) along PC1, which explains 73.9% of the variation in our data. This suggests samples are clustered according to strong biological differences, equating to significant metabolic differences between CC-SW1 cells in mono- and co-culture at 24 hours.

This is further supported by the metabolite profile, as shown in the heatmap (Figure 5:36), which illustrates clear patterns in metabolite expression and decreased intrasample variation.

We subsequently used the expression of each metabolite to conduct statistical analysis, to evaluate which metabolites contributed to this clear mathematical separation. As shown in the volcano plot in Figure 5:37A, 14 metabolites met our selection criteria. 9 metabolites had a fold change in concentration >2 and $P<0.01$, and 5 metabolites had a fold change in concentration <-2 and $P<0.01$. Figure 5:37B lists the fold changes and P-values for the 14 metabolites.

Using a Metabolic Pathway enrichment analysis, we investigated the weight of each metabolite on its respective metabolic pathway. After 24 hours of co-culture there is clear enrichment of the purine and pyrimidine biosynthesis pathways, as well as the emergence

of the glutamine/glutamate metabolic pathway, in agreement with the decrease in glutamine concentration (Figure 5:38).

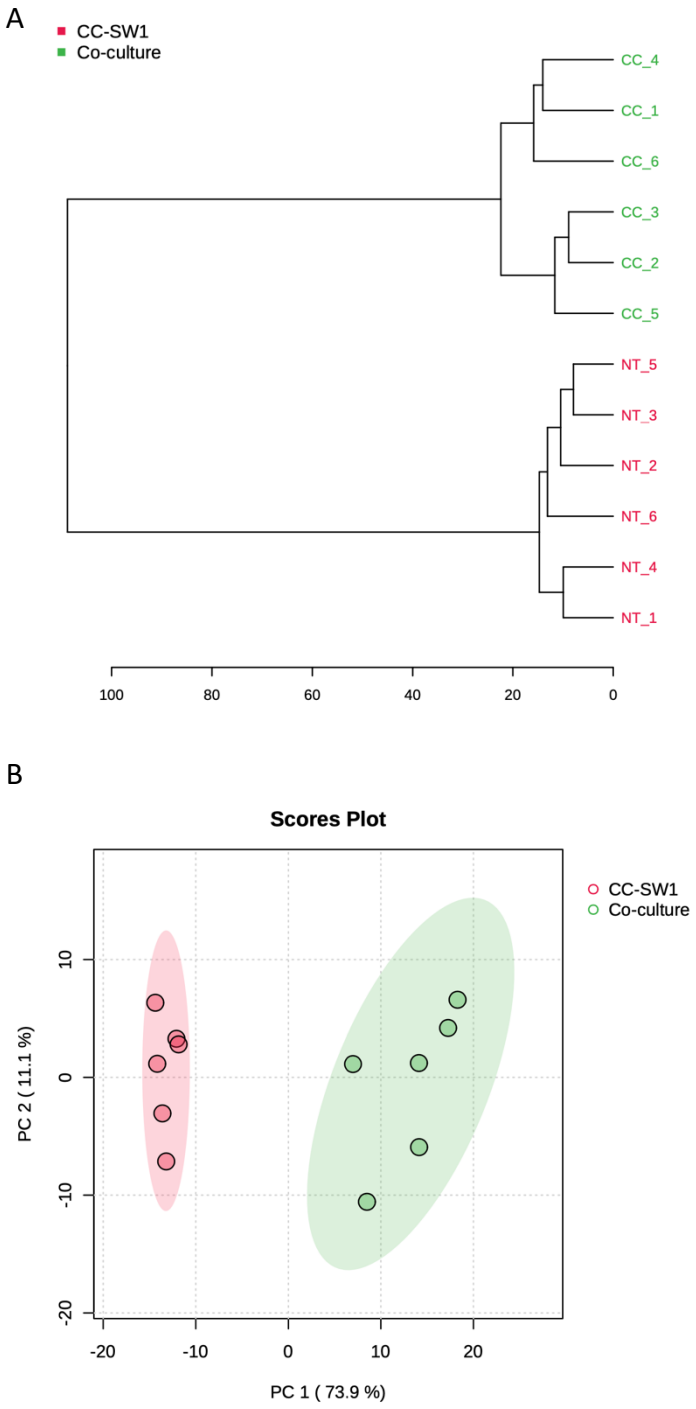


Figure 5:35 - Dendrogram and Scores Plot for the metabolic profiling of CC-SW1 cells after 24 hours of mono- and co-culture. *Normalisation and clustering was conducted on the metabolic profiles of CC-SW1 cells after 24 hours of mono- (green) and co-culture (red) with MMNK1 cells. A) Dendrogram illustrates hierarchical clustering of samples based on Euclidean distances calculated from concentration profiles. Samples with similar profiles are grouped together, as indicated by the branches, whilst vertical lines represent the distance at which clusters merge, identifying sample clusters and subgroups. B) Scores plot represents the complete 24 hour metabolic dataset in a two-dimensional space, generated through the principal component analysis (PCA). Each point on the plot corresponds to a sample. There is clear cluster separation in the mono- and co-culture CC-SW1 samples along PC1, suggesting distinct co-culture mediated biological variation in metabolite profile after 24 hours.*

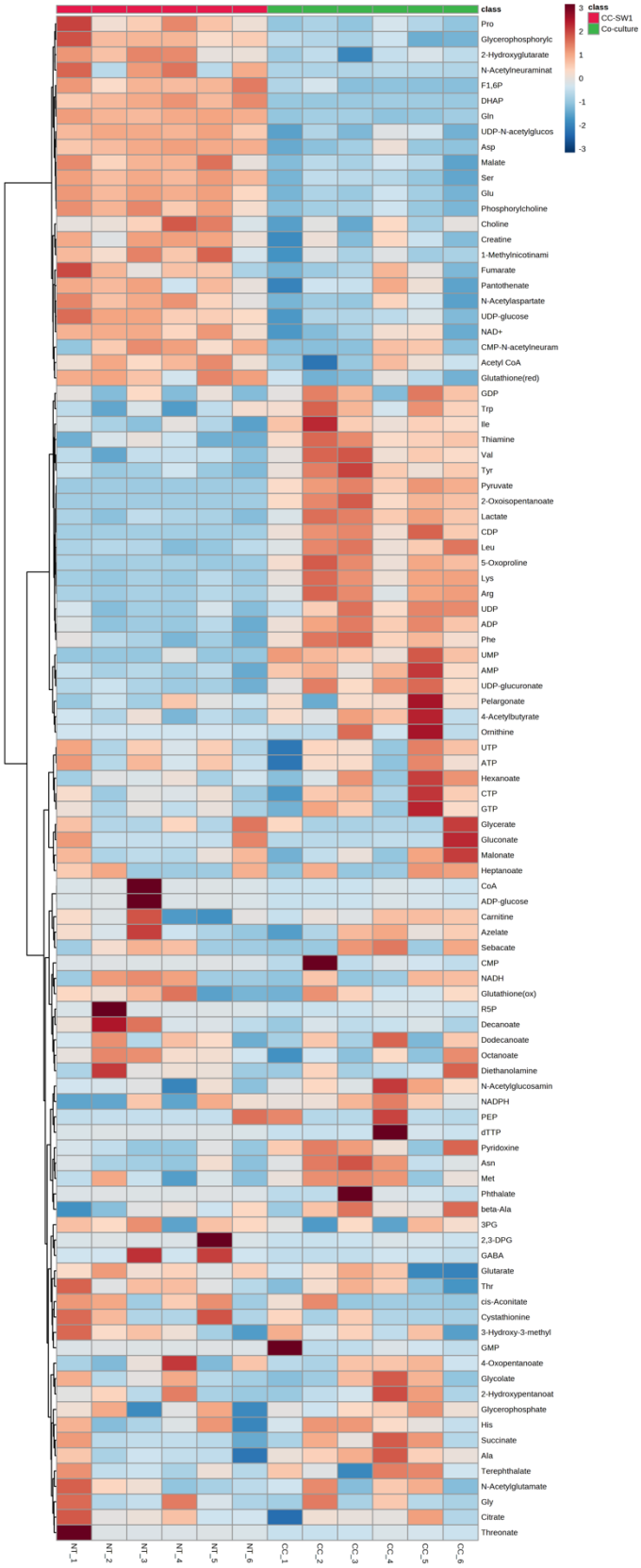
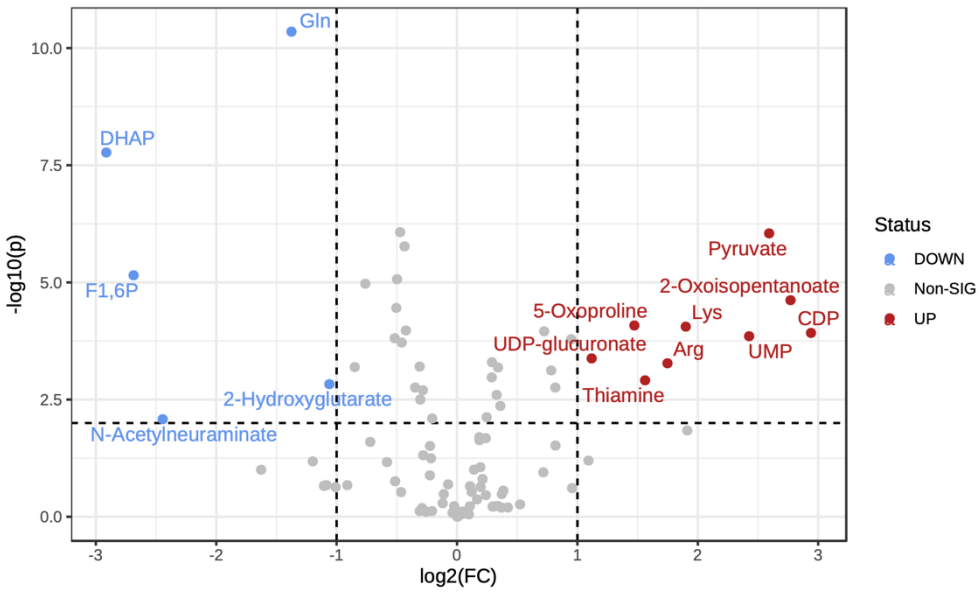


Figure 5:36 - Heatmap of differentially expressed metabolites in CC-SW1 after 24 hours of indirect co-culture. *The relative expression of each metabolite (rows) in CC-SW1 after 24 hours of monoculture, or co-culture with MMNK1 cells. Metabolites which are more highly expressed are shown in red, whilst metabolites which are reduced in concentration are shown in blue. Each column represents a sample, monoculture in red and co-culture in green.*

A



B

Table 4: Important features identified by volcano plot

	Compounds	FC	log2(FC)	raw.pval	-log10(p)
1	Gln	0.38534	-1.3758	4.4602e-11	10.351
2	DHAP	0.13272	-2.9135	1.6887e-08	7.7724
3	Pyruvate	6.0293	2.592	8.989e-07	6.0463
4	F1,6P	0.15533	-2.6866	7.0462e-06	5.152
5	2-Oxoisopentanoate	6.8184	2.7694	2.3931e-05	4.621
6	5-Oxoproline	2.7754	1.4727	8.2876e-05	4.0816
7	Lys	3.7308	1.8995	8.7748e-05	4.0568
8	CDP	7.675	2.9402	0.00011956	3.9224
9	UMP	5.373	2.4257	0.00014059	3.8521
10	UDP-glucuronate	2.1703	1.1179	0.00041813	3.3787
11	Arg	3.3579	1.7476	0.00053124	3.2747
12	Thiamine	2.952	1.5617	0.0012279	2.9108
13	2-Hydroxyglutarate	0.47961	-1.0601	0.0014812	2.8294
14	N-Acetylneuraminate	0.18363	-2.4451	0.0082793	2.082

Figure 5:37 - Differentially expressed metabolites in CC-SW1 cells after 24 hours of indirect co-culture with MMNK1 cells. *A) Volcano plot depicting the results of the differential expression analysis for intracellular metabolites in CC-SW1 cholangiocytes after 24 hours of indirect co-culture with MMNK1 cholangiocytes. Each point on the plot represents a metabolite, with its position indicating both statistical significance and fold-change in expression. The dashed horizontal line represents the predefined threshold for significance of -log10(P-value) >2, equating to a raw P-value < 0.01. The dashed vertical lines represents the predefined thresholds for fold change, log_2fold change <1 and log_2fold change >1, equating to a raw fold change <-2 and >2 respectively. Metabolites falling above the upper threshold line (red) are considered significantly upregulated, whilst those below the lower threshold line (blue) are significantly downregulated. B) 14 metabolites are differentially expressed in CC-SW1 cells after 24 hours of co-culture.*

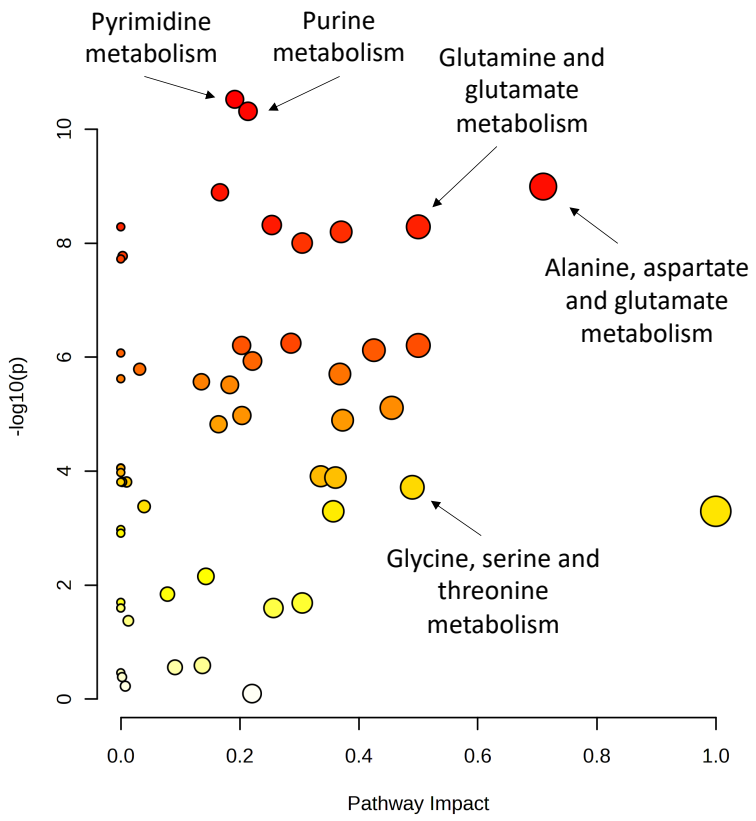


Figure 5:38 - Enriched metabolic pathways in CC-SW1 cells after 24 hours of indirect co-culture with MMNK1 cholangiocytes. *Volcano plot depicting enriched metabolic pathways in CC-SW1 cells after 24 hours of indirect co-culture with MMNK1 cholangiocytes, compared to CC-SW1 cells cultured in monoculture, as identified by metabolic pathway enrichment analysis. Each point on the plot corresponds to a metabolic pathway, and its position conveys both the pathway impact, which reflects the cumulative influence of metabolite changes within each pathway as a measure of biological relevance, and the pathway significance. A subset of enriched metabolic pathways meeting the highest significance, and highest impact criteria are marked with black arrows and labelled, to highlight the most relevant pathways in the analysis. In CC-SW1 cells after 24 hours of indirect co culture, these pathways included alanine/aspartate/glutamate metabolism, glycine/serine/threonine metabolism, glutamine/glutamate metabolism, as well as purine and pyrimidine metabolism.*

5.4.3 48 hours of co-culture increased 2-oxoisopentanote, and decreased glutamine/glutamate concentrations in cholangiocarcinoma cells

As with the trend in improved hierarchical clustering after 24 hours, hierarchical clustering for samples after 48-hours of indirect co-culture showed distinct separation between monoculture and the co-culture samples (Figure 5:39A). This is recapitulated in the PCA (Figure 5:39B) to a greater degree than at 24 hours, as clusters are separated via loading scores ranging from - 40 to +20, as opposed to -10 to +20, along PC1, which accounts for a greater proportion of variation in our data (83.1%). This highlights a greater degree of mathematical separation in clusters after 48 hours, suggesting the samples are clustered according to strong biological differences. Moreover, the metabolite profile, as shown in the heatmap (Figure 5:40), illustrates clear patterns in metabolite expression and decreased intrasample variation. This further supports the notion that metabolite concentration via co-culture is time-dependent, and that analysis of metabolite concentration after 48 hours is the most optimal way of detecting biological changes to the CC-SW1 metabolome during co-culture.

The volcano plot in Figure 5:41A combines the results from the Fold Change Analysis and Student's T-Test to allow us to identify metabolites based on statistical and biological significance. Taken together, 21 metabolites emerge, 5 metabolites with a fold change in concentration >2 and $P<0.01$, and 16 metabolites with a fold change in concentration <-2 and $P<0.01$. Figure 5:41B lists the fold changes and P-values for the 21 metabolites.

The concentration of the amino acids aspartate, serine, proline, glutamate, glutamine, as well as concentrations of the TCA intermediates malate and fumarate, the lysine metabolite carnitine, the serine metabolite choline, and CTP, UTP, UDP-glucose, UDP-glucoronate, 2-hydroxyglutarate, and the reduced form of glutathione (GSH) were decreased at 48 hours. The concentrations of CoA precursor pantothenate, glycolytic intermediates 3PG and PEP, urea metabolite ornithine, and 2-oxoisopentanoate (Figure 5:42), were increased at 48 hours.

After 24 hours, we highlighted enrichment of the glycine/serine/threonine, alanine/aspartate/glutamate, and glutamine/glutamate metabolic pathways. This was recapitulated to a greater extent after 48-hours, with the significance of each pathway increasing (Figure 5:43). This suggest co-culture exerts a disproportion attenuation on these pathways, highlighting a potential mechanism for phenotypic control.

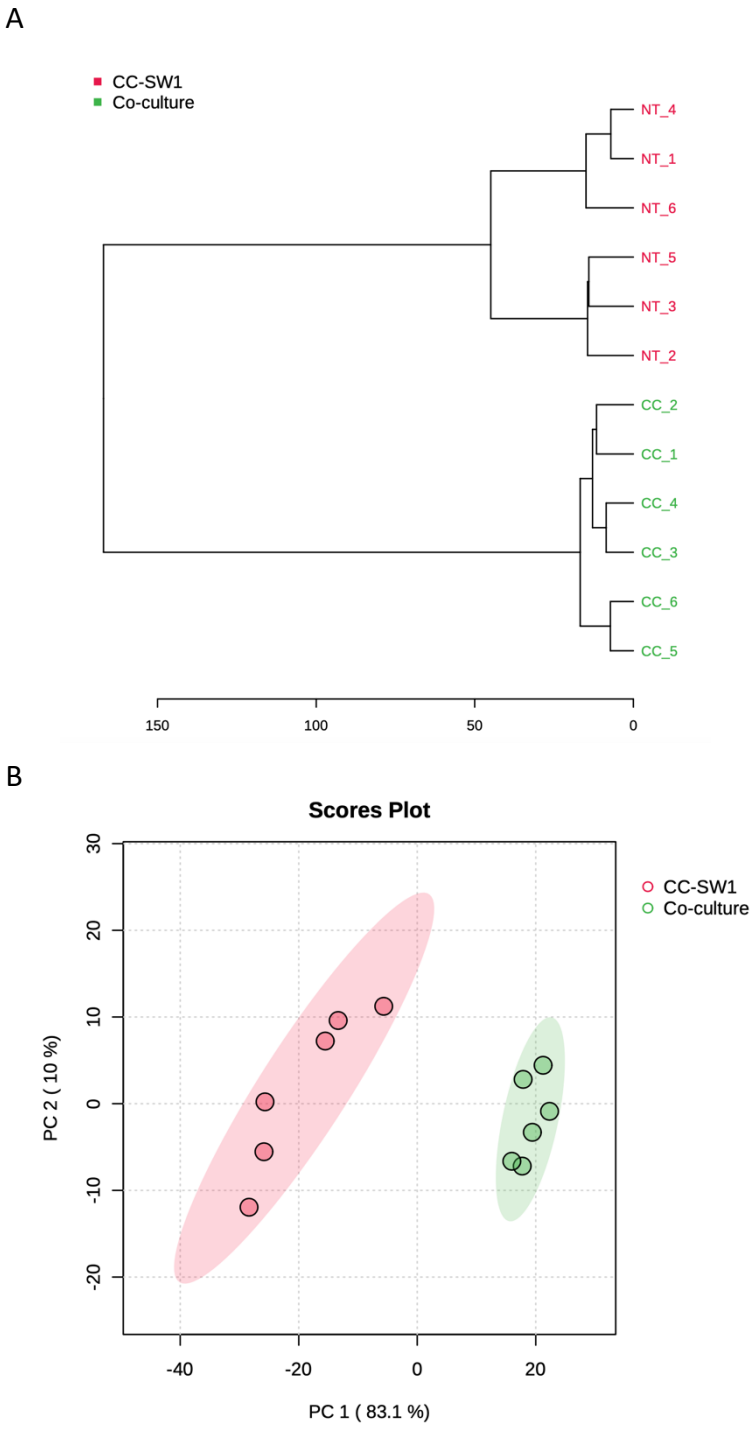


Figure 5:39 - Dendrogram and Scores Plot for the metabolic profiling of CC-SW1 cells after 48 hours of mono- and co-culture. *Normalisation and clustering was conducted on the metabolic profiles of CC-SW1 cells after 48 hours of mono- (green) and co-culture (red) with MMNK1 cells. A) Dendrogram illustrates hierarchical clustering of samples based on Euclidean distances calculated from concentration profiles. Samples with similar profiles are grouped together, as indicated by the branches, whilst vertical lines represent the distance at which clusters merge, identifying sample clusters and subgroups. B) Scores plot represents the complete 48 hour metabolic dataset in a two-dimensional space, generated through the principal component analysis (PCA). Each point on the plot corresponds to a sample. CC-SW1 samples in co-culture are clustered far from CC-SW1 samples in monoculture along PC1, suggesting distinct co-culture mediated biological variation in metabolite profile after 48 hours.*

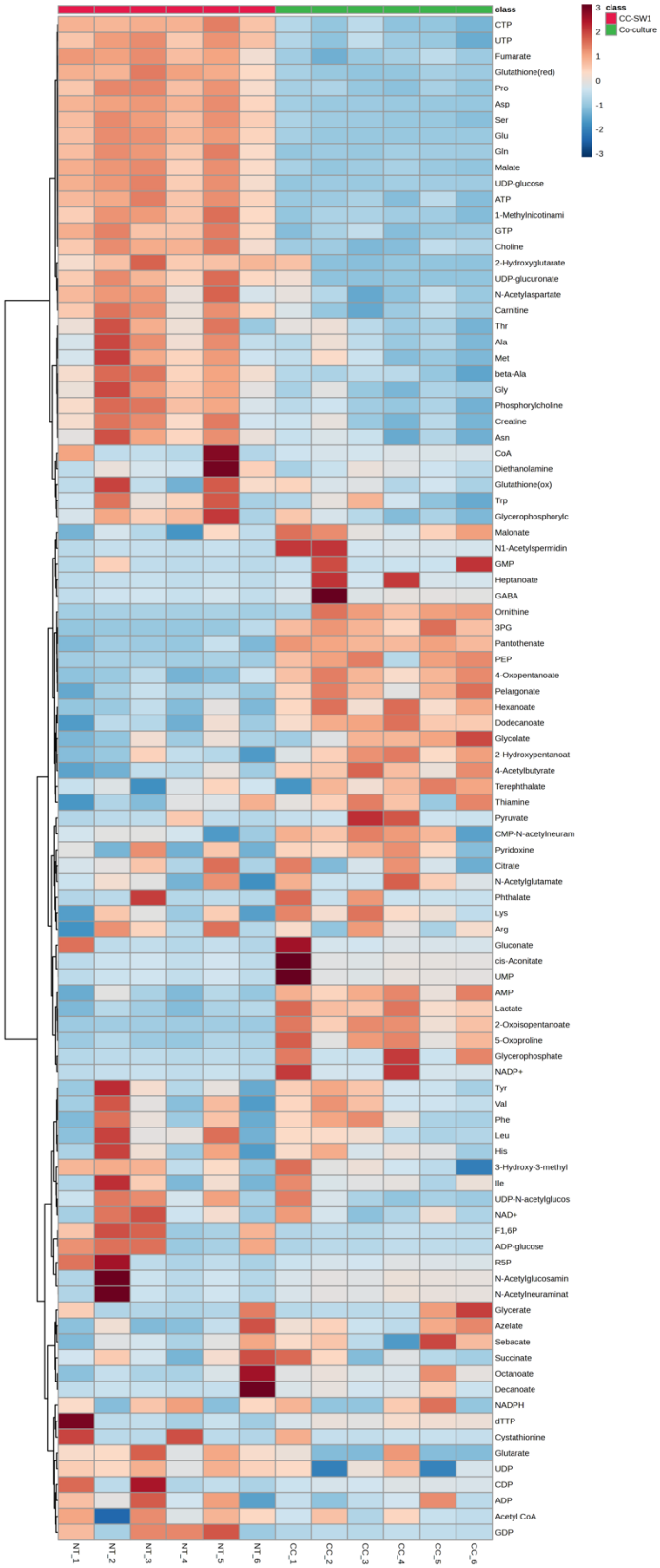
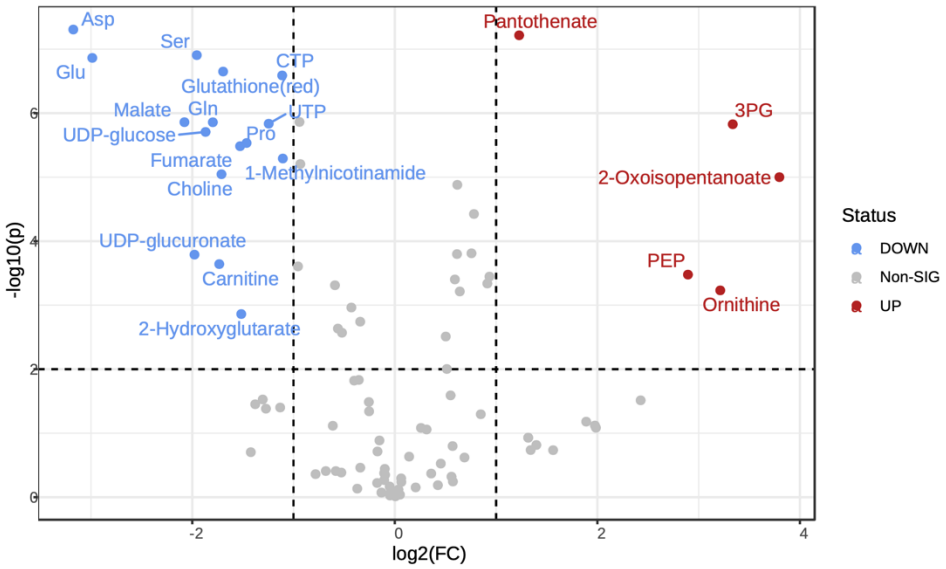


Figure 5:40 - Heatmap of differentially expressed metabolites in CC-SW1 after 48 hours of indirect co-culture*. The relative expression of each metabolite (rows) in CC-SW1 after 48 hours of monoculture, or co-culture with MMNK1 cells. Metabolites which are more highly expressed are shown in red, whilst metabolites which are reduced in concentration are shown in blue. Each column represents a sample, monoculture in red and co-culture in green.*

A



B

Table 4: Important features identified by volcano plot

	Compounds	FC	log2(FC)	raw.pval	-log10(p)
1	Asp	0.11073	-3.1749	4.93e-08	7.3072
2	Pantothenate	2.3417	1.2275	6.0679e-08	7.217
3	Ser	0.25779	-1.9557	1.2395e-07	6.9067
4	Glu	0.1261	-2.9874	1.3686e-07	6.8637
5	Glutathione(red)	0.30866	-1.6959	2.2359e-07	6.6505
6	CTP	0.46243	-1.1127	2.5719e-07	6.5897
7	Malate	0.2369	-2.0777	1.3818e-06	5.8596
8	Gln	0.28768	-1.7975	1.3857e-06	5.8583
9	UTP	0.42171	-1.2457	1.4601e-06	5.8356
10	3PG	10.1	3.3362	1.4893e-06	5.827
11	UDP-glucose	0.27373	-1.8692	1.9629e-06	5.7071
12	Pro	0.36244	-1.4642	2.9221e-06	5.5343
13	Fumarate	0.34668	-1.5283	3.2774e-06	5.4845
14	1-Methylnicotinamide	0.46445	-1.1064	5.1058e-06	5.2919
15	Choline	0.30523	-1.712	8.9912e-06	5.0462
16	2-Oxoisopentanoate	13.902	3.7972	9.9827e-06	5.0008
17	UDP-glucuronate	0.25376	-1.9785	0.00016226	3.7898
18	Carnitine	0.30063	-1.734	0.00022811	3.6419
19	PEP	7.4325	2.8938	0.00033298	3.4776
20	Ornithine	9.2724	3.2129	0.00058679	3.2315
21	2-Hydroxyglutarate	0.34947	-1.5168	0.0013757	2.8615

Figure 5:41 - Differentially expressed metabolites in CC-SW1 cells after 48 hours of indirect co-culture with MMNK1 cells. *A) Volcano plot depicting the results of the differential expression analysis for intracellular metabolites in CC-SW1 cholangiocytes after 48 hours of indirect co-culture with MMNK1 cholangiocytes. Each point on the plot represents a metabolite, with its position indicating both statistical significance and fold-change in expression. The dashed horizontal line represents the predefined threshold for significance of -log10(P-value) >2, equating to a raw P-value < 0.01. The dashed vertical lines represents the predefined thresholds for fold change, log_2fold change <1 and log_2fold change >1, equating to a raw fold change <-2 and >2 respectively. Metabolites falling above the upper threshold line (red) are considered significantly upregulated, whilst those below the lower threshold line (blue) are significantly downregulated. B) 21 metabolites are differentially expressed in CC-SW1 cells after 48 hours of co-culture.*

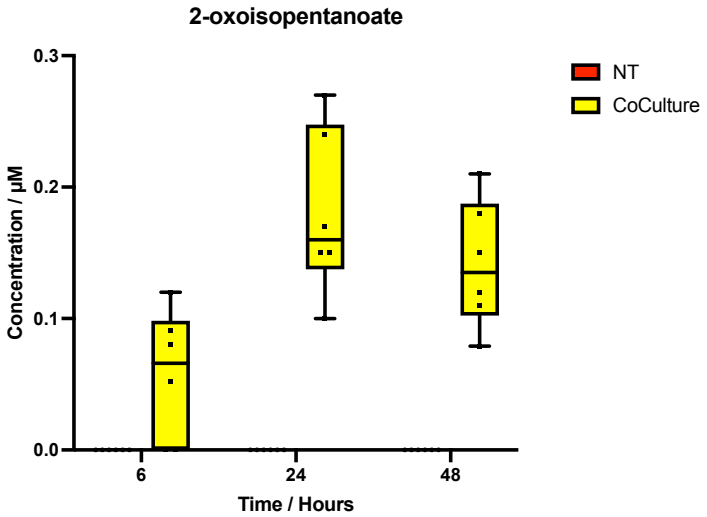


Figure 5:43 - Flux in 2-oxoisopentanoate concentration in CC-SW1 cells during co-culture. *2-oxoisopentanoate concentration was evaluated in CC-SW1 cells after 6, 24, and 48 hours of mono- and co-culture. 2-oxoisopentanoate was not detected in monocultured CC-SW1 cells.*

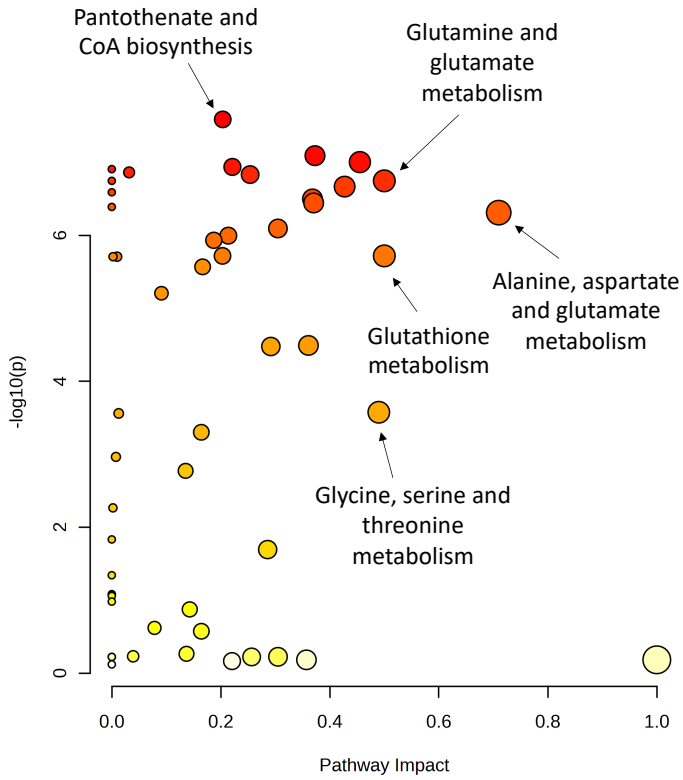


Figure 5:42 - Enriched metabolic pathways in CC-SW1 cells after 48 hours of indirect co-culture with MMNK1 cholangiocytes*. Volcano plot depicting enriched metabolic pathways in CC-SW1 cells after 48 hours of indirect co-culture with MMNK1 cholangiocytes, compared to CC-SW1 cells cultured in monoculture, as identified by metabolic pathway enrichment analysis. Each point on the plot corresponds to a metabolic pathway, and its position conveys both the pathway impact, which reflects the cumulative influence of metabolite changes within each pathway as a measure of biological relevance, and the pathway significance. A subset of enriched metabolic pathways meeting the highest significance, and highest impact criteria are marked with black arrows and labelled, to highlight the most relevant pathways in the analysis. In CC-SW1 cells after 48 hours of indirect co culture, these pathways included alanine/aspartate/glutamate metabolism, glycine/serine/threonine metabolism, glutamine/glutamate metabolism, pantothenate/CoA biosynthesis, and glutathione metabolism.*

5.5 Validation of cholangiocarcinoma metabolite concentration

Through the timepoint metabolomic analysis, we observed many transient changes across the timepoints. However, we focused our investigation on 2-oxoisopentanoate, due to the significant increase and sustained concentration during co-culture, compared to monoculture, where 2-oxoisopentanoate was not detected, at any time point. We hypothesised that 2-oxoisopentanoate may attenuate CC-SW1 migration and cell viability, as identified in Chapter 1.

5.5.1 Exogenous 2-Oxoisopentanoate reduces CCA cell viability

From the metabolomics analysis, we found the intermediate metabolite 2-oxoisopentanoate was expressed highly in CC-SW1 during co-culture at 6, 24, and 48-hours (P=0.0371, 0.0008, and 0.0008 respectively)(Figure 5:42A) but was not expressed at all in CC-SW1 cells in monoculture.

As 2-oxoisopentanoate is a product of valine degradation, we evaluated the concentration of valine in the metabolomics data. There was no significant difference in the concentration of valine in CC-SW1 in monoculture or co-culture after 6 hours (P=0.5047)(Figure 5:42B). At 24-hours there was a significantly higher concentration of valine in co-cultured cells (P=0.0088)(Figure 5:44B), whereas at 48-hours there was a significantly higher concentration of valine (P=0.0005) in monocultured cells, whilst the concentration of valine in co-cultured cells remained consistent with the concentration identified at 24-hours (Figure 5:44B).

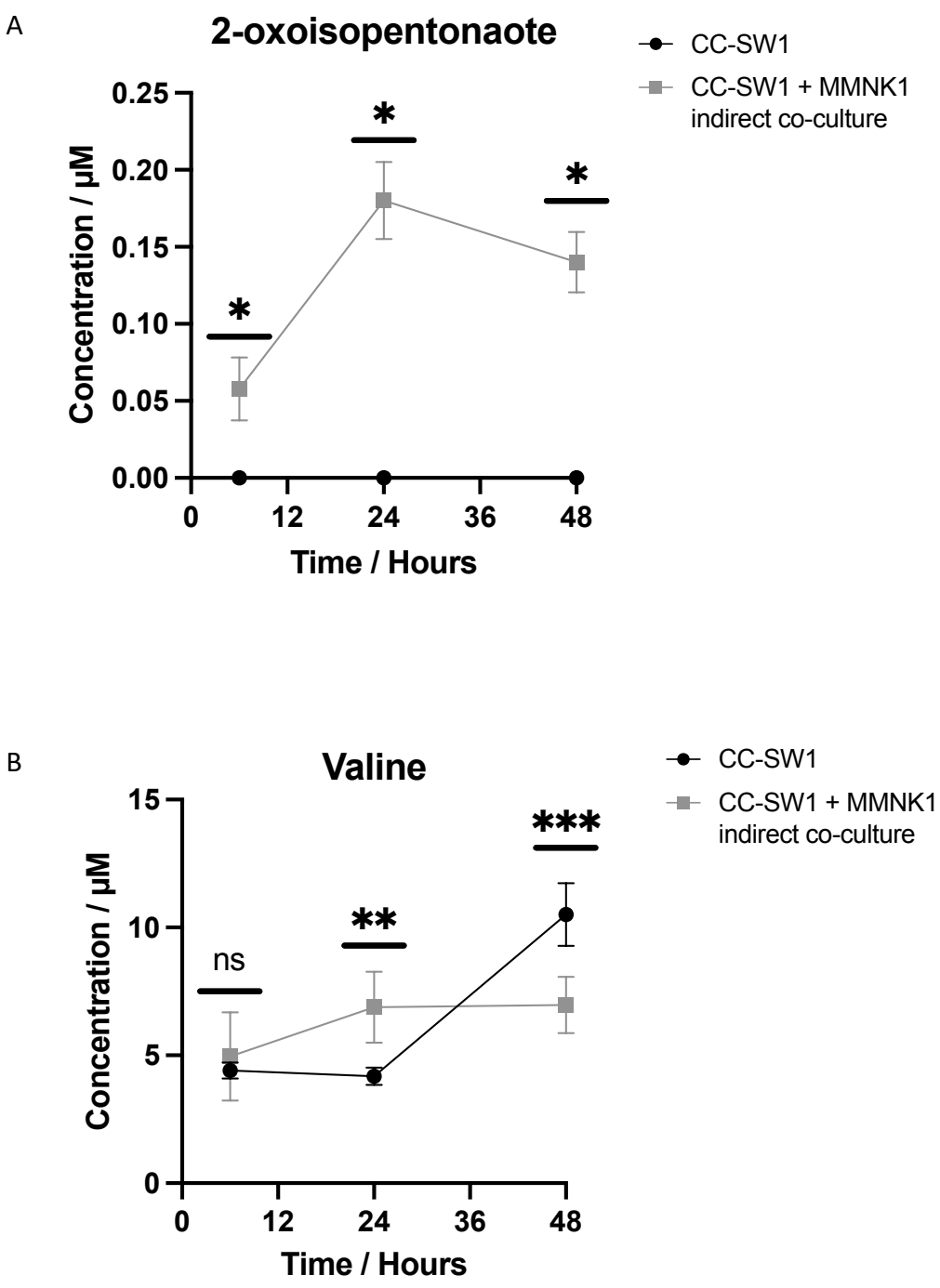


Figure 5:44 - Flux in 2-oxoisopentanoate and valine concentration in CC-SW1 cells over 48 hours*. The concentration of the metabolites A) 2-oxoisopentanoate, and B) valine at 6, 24, and 48 hours, as reported by the metabolomic analysis. Concentrations for CC-SW1 cells in monoculture are shown in black, whilst concentrations for CC-SW1 cells in indirect co-culture with MMNK1 cholangiocytes are shown in grey. 2-oxoisopentanoate concentration was significantly increased in CC-SW1 cells across all time points during co-culture. There was no difference in the concentration of valine after 6 hours of co-culture, however this increased significantly after 24 hours, before decreasing significantly after 48 hours of co-culture (P*<0.05, P**<0.01, P***<0.001)(n=6).*

We chose 4 exogenous doses of 2-oxoisopentanoate; 1.0, 2.5, 5.0, and 10.0 mM to recapitulate the effect of co-culture. CC-SW1 cells were dosed with exogenous 2-oxoisopentanoate and cultured for 48 hours. Exogenous 2-oxoisopentanoate had a negative effect on CC-SW1 cell viability, 1 mM 2-oxoisopentanoate had no effect on cell viability (P=0.9998), and 2.5 mM caused a non-significant decrease in cell viability (P=0.0860)(Figure 5:45A). 5.0 mM and 10.0 mM of 2-oxoisopentanoate caused a statistically significant decrease in CC-SW1 cell viability (P=0.0047 and 0.0012 respectively)(Figure 5:45A). We also assessed the effect of exogenous valine on CC-SW1 viability, with concentrations of 1.0, 2.5, 5.0, and 10.0 mM of valine. Exogenous valine had no effect on CC-SW1 cell viability, at all concentrations tested (P= 0.8957, 0.2670, 0.2806, and 0.6180 respectively)(Figure 5:45B).

We evaluated the effect of exogenous 2-oxoisopentanoate on the proportion of apoptotic and alive cells using flow cytometry. At all concentrations of exogenous 2-oxoisopentanoate tested, there was no significant difference in the proportion of apoptotic (P=0.6255, 0.7470, 0.8382, and 0.5774 respectively)(Figure5:46A) or viable (P=0.7203, 0.6451, 0.7415, and 0.5738 respectively)(Figure 5:46B) CC-SW1 cells.

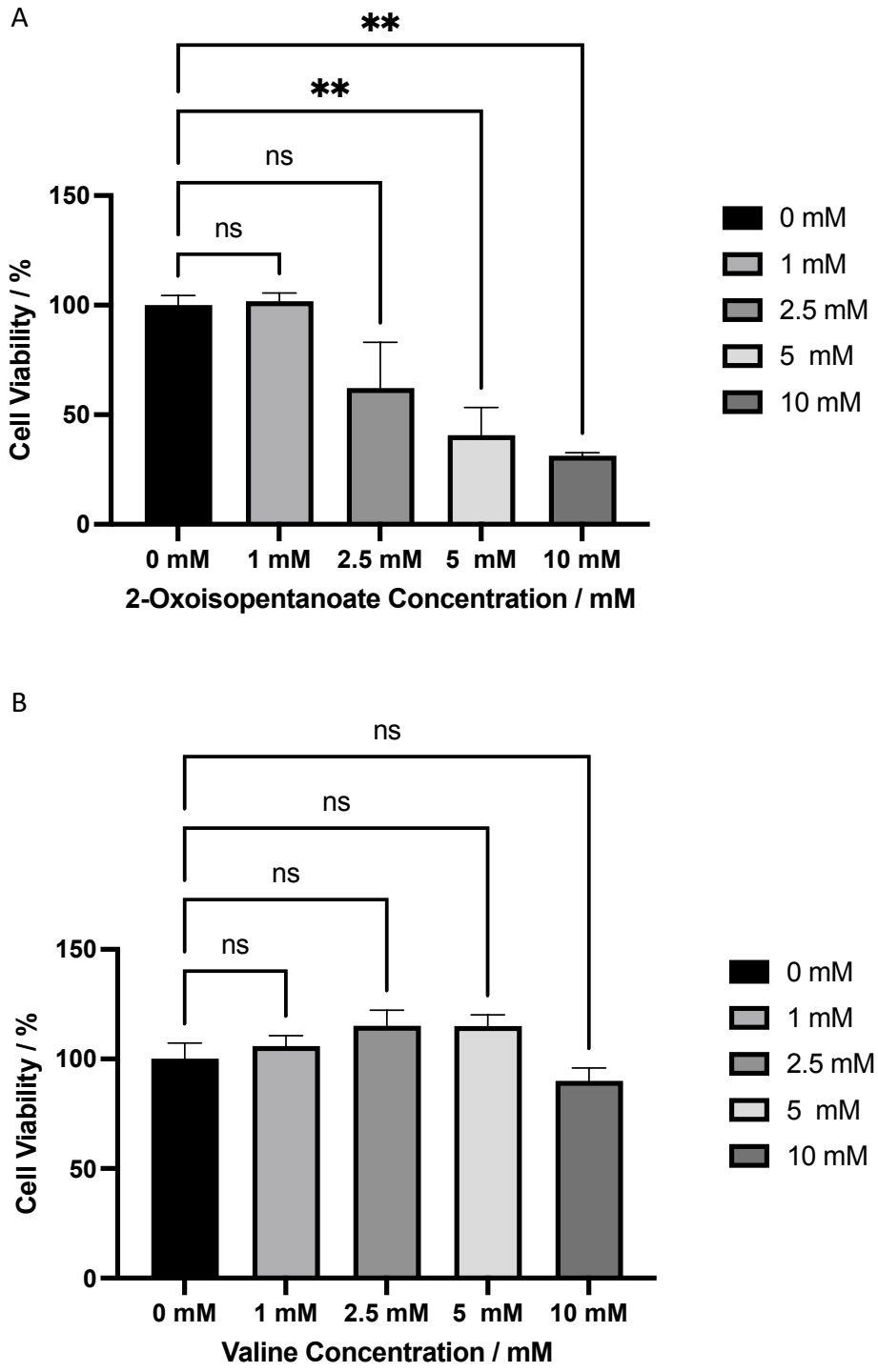


Figure 5:45 - Exogenous 2-oxoisopentanoate reduces CC-SW1 cell viability. *CC-SW1 cells were treated with exogenous doses of 1.00, 2.50, 5.00 and 10.00 mM A) 2-oxoisopentanoate, or B) valine, and cultured for 48 hours in low glucose DMEM supplemented with 0.1% BSA. Cell viability was evaluated via CCK8 colorimetric analysis. Exogenous doses of 5.0 and 10.0 mM of 2-oxoisopentanoate significantly decreased CC-SW1 cell viability, whilst exogenous valine had no significant effect on CC-SW1 cell viability (**P<0.01)(n=6).*

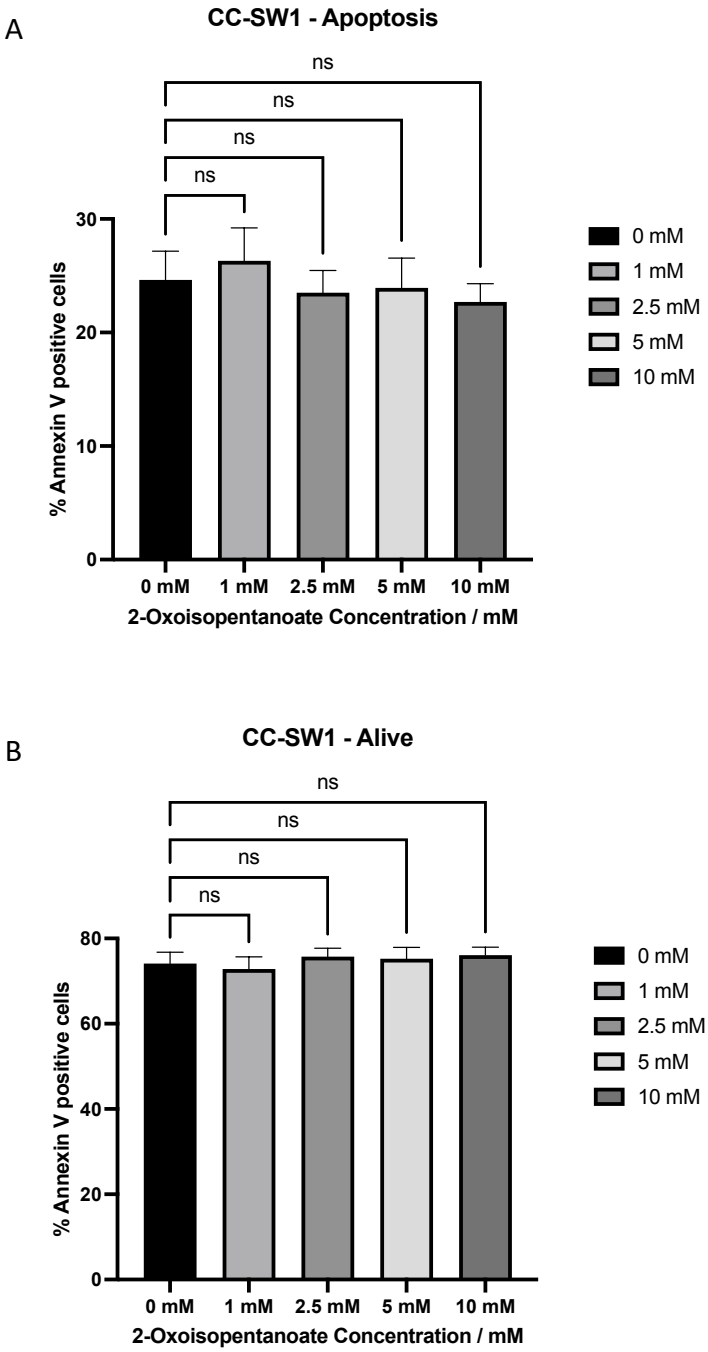
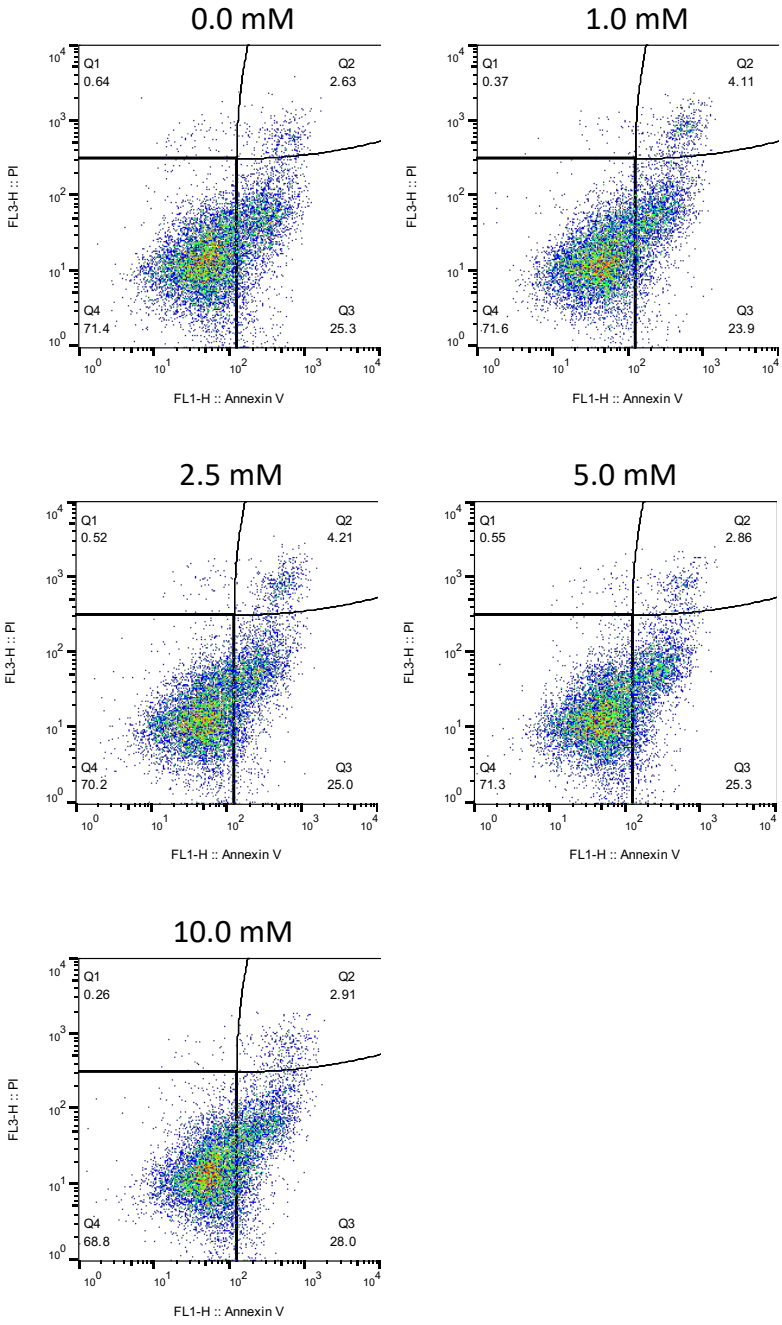


Figure 5:46 - Exogenous 2-oxoisopentanoate has no effect on the proportion of apoptotic or viable CC-SW1 cells*. CC-SW1 cells were treated with 1.0, 2.5, 5.0, and 10.0 mM of exogenous 2-oxoisopentanoate and cultured in low glucoses DMEM supplemented with 0.1% BSA for 48 hours. Cells were stained with propidium iodide and annexin V prior to flow cytometry, to evaluate the proportion of A) apoptotic, and B) viable cells, after treatment with exogenous 2-oxoisopentanoate. Quadrants from the flow cytometry analysis are shown in C). Exogenous 2-oxoisopentanoate had no effect on the proportion of apoptotic or viable CC-SW1 cells (ns, P>0.05)(n=3).*

C


0.0 mM
Q1
0.64
Q2
2.63
Q4
71.4
Q3
25.3
1.0 mM
Q1
0.37
Q2
4.11
Q4
71.6
Q3
23.9
2.5 mM
Q1
0.52
Q2
4.21
Q4
70.2
Q3
25.0
5.0 mM
Q1
0.55
Q2
2.86
Q4
71.3
Q3
25.3
10.0 mM
Q1
0.26
Q2
2.91
Q4
68.8
Q3
28.0
FL3-H :: PI
FL1-H :: Annexin V

We evaluated the effect of exogenous 2-oxoisopentanoate on CC-SW1 cell proliferation over 48 hours, using the IncuCyte imaging system. We then applied the same range of concentrations to the other intrahepatic CCA lines CC-LP1 and SNU-1079, as well as the extrahepatic CCA line SNU-1196, and the cholangiocyte cell line MMNK1.

Conversely to what we expected, 5 mM of 2-oxoisopentanoate increased cell proliferation in MMNK1 cells at 48 hours (P=0.0390)(Figure 5:47A). A 2-oxoisopentanoate concentration of 10 mM significantly reduced CC-SW1 cell proliferation at 40, 44, and 48 hours (P=0.050, 0.0273, and 0.0163 respectively)(Figure 5:47B).

Exogenous 2-oxoisopentanoate had no significant effect (P>0.05) on CC-LP1 (Figure 5:47C) or SNU-1079 (5:47D) cell proliferation at all concentrations of 2-oxoisopentanoate and time points assessed, although a trend of decreasing proliferation with higher concentrations was witnessed.

In SNU-1196 2.5 mM of 2-oxoisopentanoate significant reduced proliferation at 12,16, 24, 28, 32, 36, 40, 44, and 48 hours (P=0.0436, 0.0480, 0.0352, 0.0368, 0.0277, 0.0351, 0.0365, 0.0079, and 0.0285 respectively)(Figure 5:47E). Likewise, 5 mM of 2-oxoisopentanoate significant reduced proliferation at 24, 32, 36, 40, 44, and 48 hours (P=0.0481, 0.0425, 0.0462, 0.0464, 0.0088, and 0.0292 respectively)(Figure 5:47E).

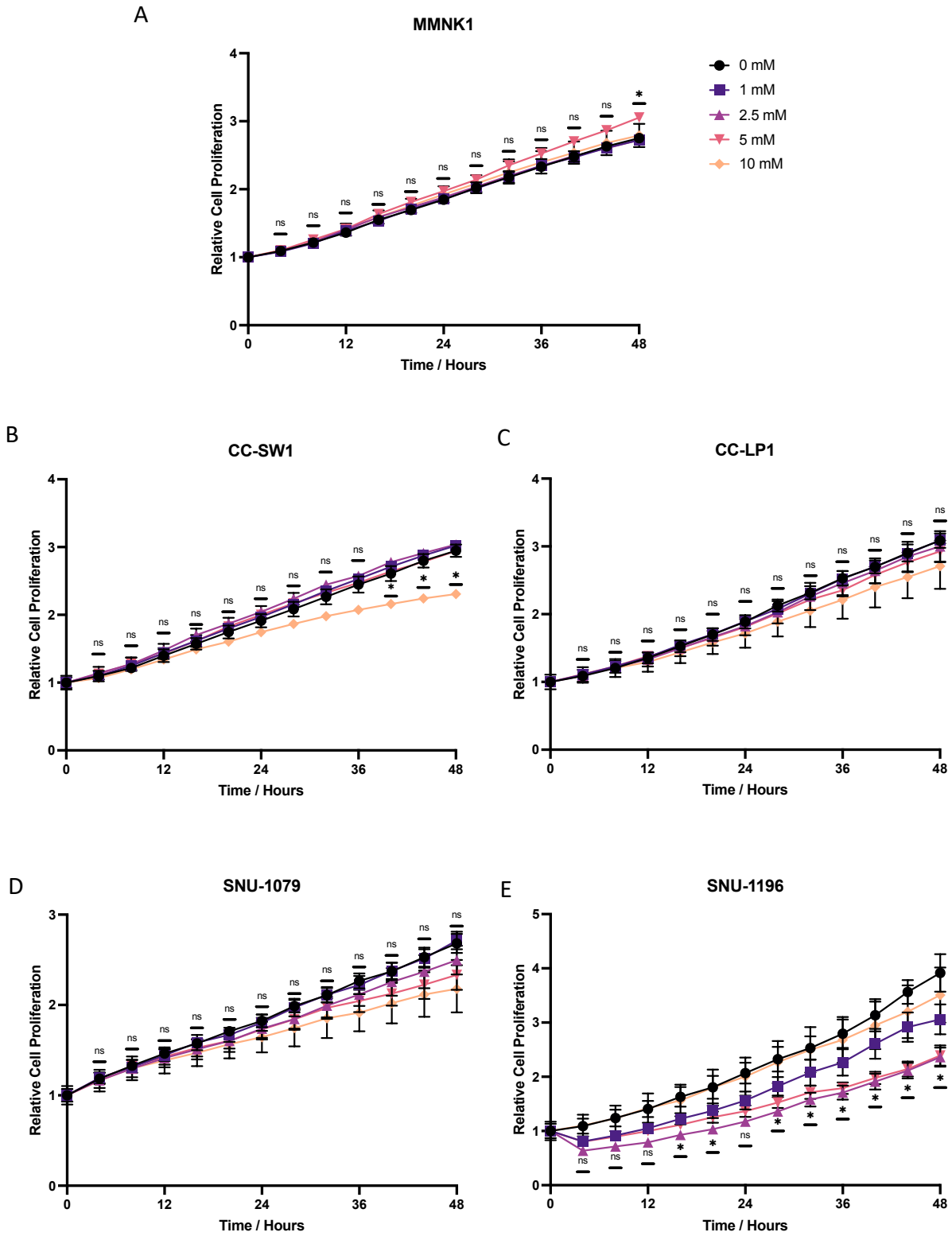


Figure 5:47 - Exogenous 2-oxoisopentanoate has divergent effects on CCA cell proliferation. *A) MMNK1, B) CC-SW1, C) CC-LP1, D) SNU-1079, and E) SNU-1196 cells were treated with 1.0, 2.5, 5.0, and 10.0 mM of exogenous 2-oxoisopentanoate, and the effect on cell proliferation evaluated using the IncuCyte imaging system(*P<0.05)(n=3).*

5.5.2 Summary

Exogenous 2-oxoisopentanoate reduced CC-SW1 cell viability and proliferation, with no significant effect on the proportion of apoptotic or alive CC-SW1 cells, whilst exogenous valine had no effect on CC-SW1 cell viability, at all concentrations tested.

High concentrations of exogenous 2-oxoisopentanoate caused a non-significant decrease in the intrahepatic cell lines CC-LP1 and SNU-1079 proliferation, a significant reduction in the proliferation of the extrahepatic CCA cell line SNU-1196, and a significant increase in MMNK1 cholangiocyte proliferation.

5.6 Cytokine-Mediated Crosstalk

5.6.1 Indirect co-culture triggers a reciprocal shift in cytokine secretion

As alluded to earlier, soluble factors can also take the form of cytokines that have been widely reported to mediate long distance signalling cascades. To evaluate the cytokine secretome, we used the RayBio® C-Series Human Cytokine Antibody Array C3 to simultaneously screen for the relative protein expression and patterns of 42 cytokines and growth factors, with high specificity and sensitivity.

Blots were analysed via densitometry using the Protein Array Analyzer macro in ImageJ (Materials & Methods 3.14). Each blot contained Positive Control Spots, whereby the concentration of biotinylated antibody on each Positive Control Spot was consistent between arrays, which was therefore used for the normalisation. Likewise Negative Control Spots which contained no biotinylated antibody, and were used for background subtraction. This permitted a comparison of cytokines present in each cell line when grown alone, or in indirect co-culture.

5.6.2 Changes to the cholangiocyte secretome during indirect co-culture

Figures 5:48A and B illustrates the characteristics of the ECL array membranes that were developed from the supernatant of 48-hour cultured MMNK1 cells with or without co-culture with CC-SW1 cells. As shown, this methodology was clearly able to detect the presence of MCP-1, CXCL5, IL-6, Angiogenin, IL-8, GRO, IL-10, CCL5, VEGF-A, and CXCL1. Quantification of cytokine secretion via densitometry (Figure 5:49A) revealed a significant increase in the concentration of GRO, CXCL1, and Angiogenin in the media from co-cultured cells, whilst a reduction in concentration was identified for IL-6, MCP-1, and CCL5. The relative fold changes and P-values for these cytokines are shown in Figure 5:49B.

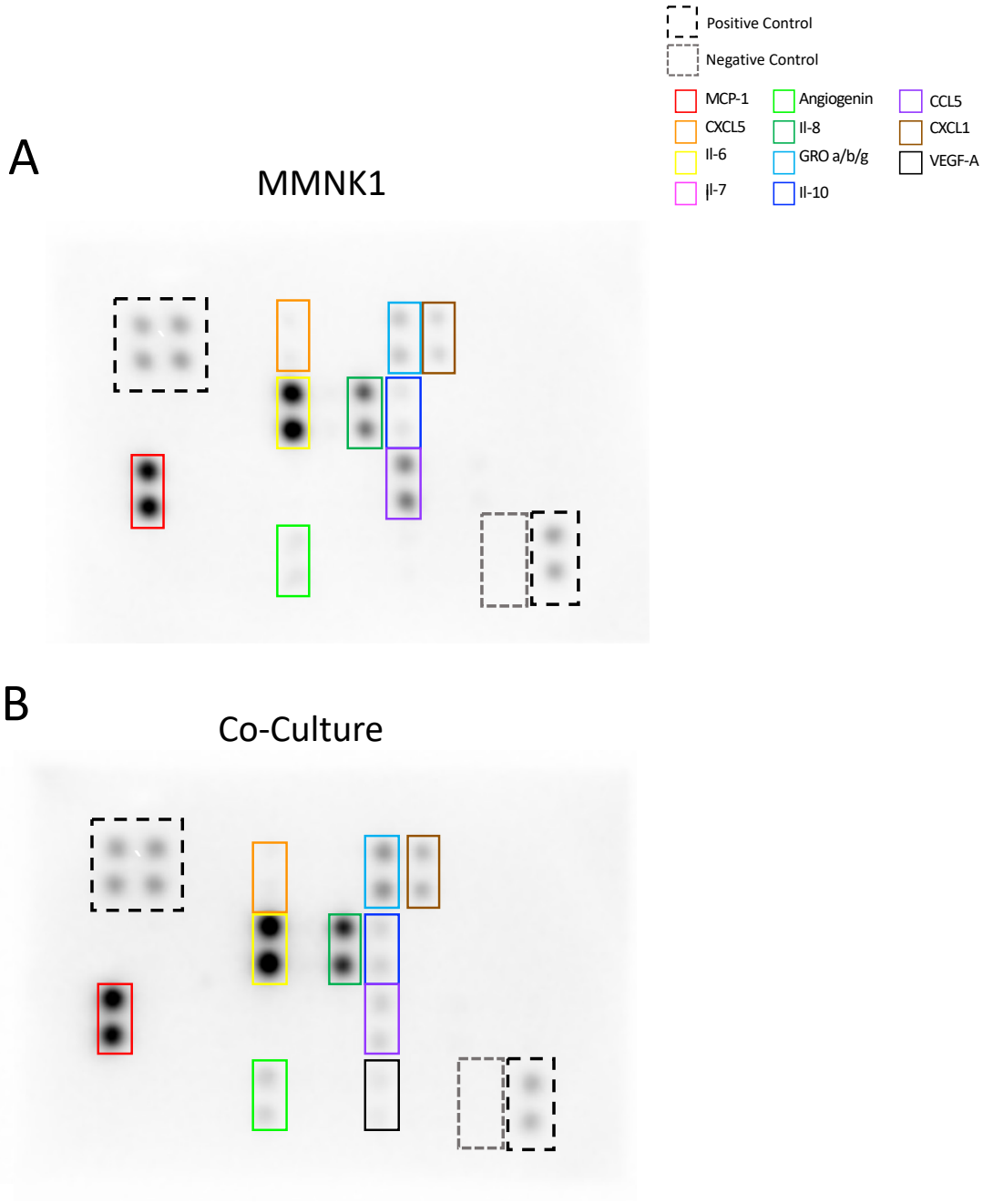
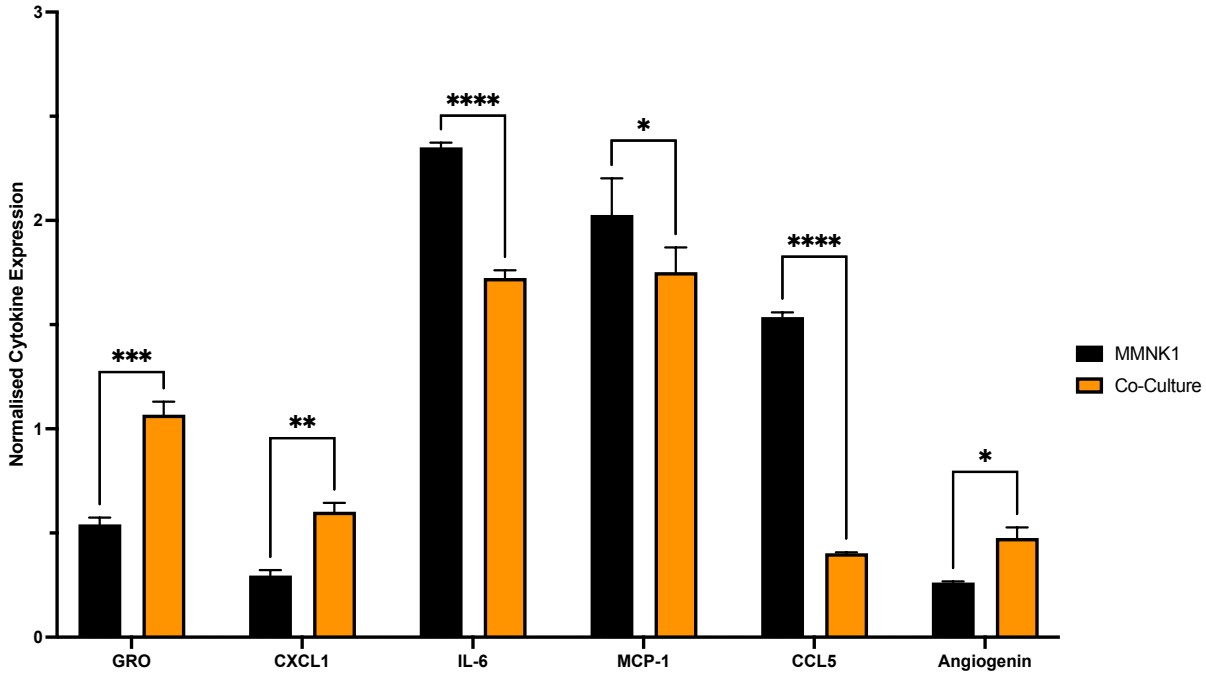


Figure 5:48 - Evaluation of cytokine expression in MMNK1 cells in mono- and co-culture with CC-SW1 cells. *Culture media were harvested from MMNK1 cells in A) monoculture, and B) indirect co-culture with CC-SW1 cells, for cytokine array analysis. Representative expression spots were analysed via densitometry. Sample positive results for MCP-1, CXCL5, IL-6, angiogenin, IL-8, GRO a/b/g, IL-10, CXCL1, and VEGF-A are delineated by coloured rectangles on the cytokine array membrane.*

A



B

Cytokine	FC	P-value
GRO	1.97	0.0002
CXCL1	2.04	0.0087
IL-6	0.73	<0.0001
MCP-1	0.87	0.0159
CCL5	0.26	<0.0001
Angiogenin	1.82	0.0493

Figure 5:49 - Quantification of differentially expressed cytokines in MMNK1 cells after indirect co-culture with CC-SW1 cells. *A) Quantification of cytokine expression in the media extracted from MMNK1 cells cultured alone (black) or in indirect co-culture with CC-SW1 cells (orange) displayed as Normalised Cytokine Expression ± SEM. B) Table of significantly differentially expressed cytokines with Fold Change and P-value. (*P<0.05, **P<0.01, ***P<0.001, ****P<0.0001).*

5.6.3 Changes to the cholangiocarcinoma secretome during indirect co-culture

Figures 5:50A and 5:50B illustrates the characteristics of the ECL array membranes that were developed from the supernatant of 48-hour cultured CC-SW1 cells with or without co-culture with MMNK1 cells. As shown, this methodology was clearly able to detect the presence of MCP-1, Angiogenin, IL-8, GRO, CXCL1, IL-10, VEGF-A, IL-6, IL-7, and CCL5. Quantification of cytokine expression via densitometry (Figure 5:51A) revealed a significant increase in the concentration of GRO, IL-6, IL-7, and CCL5, whilst a reduction in concentration was identified for CXCL1, IL-8, and MCP-1. The relative fold changes and P-values for these cytokines are shown in Figure 5:51B.

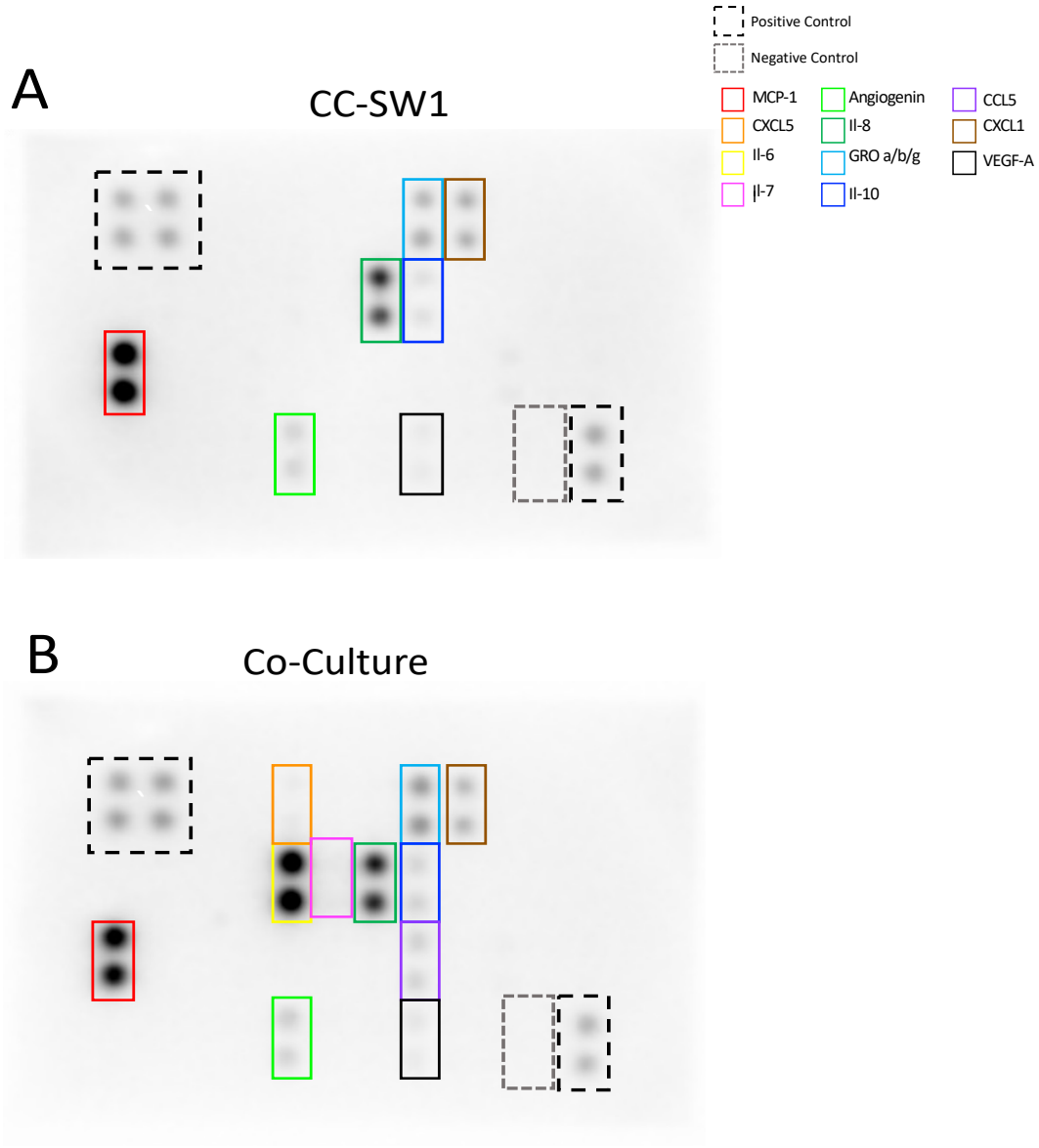
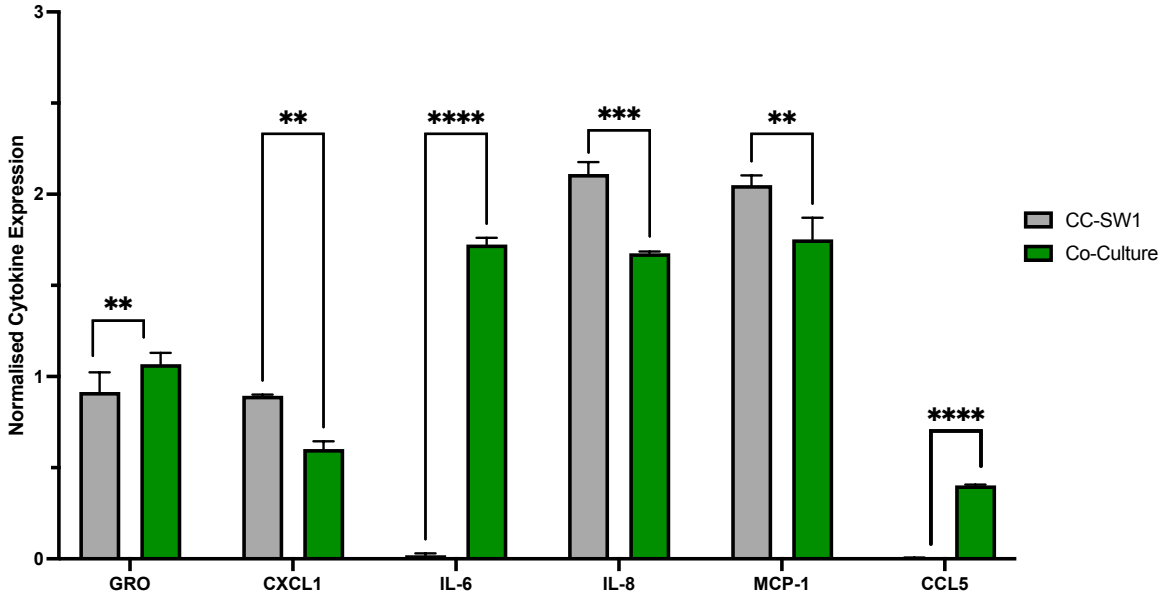


Figure 5:50 - Evaluation of cytokine expression in CC-SW1 cells in mono- and co-culture with MMNK1 cells. *Culture media were harvested from CC-SW1 cells in A) monoculture, and B) indirect co-culture with MMNK1 cells, for cytokine array analysis. Representative expression spots were analysed via densitometry. Sample positive results for MCP-1, CXCL5, IL-6, angiogenin, IL-8, GRO a/b/g, IL-10, CXCL1, and VEGF-A are delineated by coloured rectangles on the cytokine array membrane.*

A



B

Cytokine	Fold Change	P-Value
GRO	1.17	0.0051
CXCL1	0.67	0.0018
IL-6	123.07	<0.0001
IL-8	0.79	<0.0001
MCP-1	0.85	0.0015
CCL5	15.77	<0.0001

Figure 5:51 - Quantification of differentially expressed cytokines in CC-SW1 cells after indirect co-culture with MMNK1 cells. *A) Quantification of cytokine expression in the media extracted from CC-SW1 cells cultured alone (grey) or in indirect co-culture with MMNK1 cholangiocytes (green) displayed as Normalised Cytokine Expression ± SEM. B) Table of significantly differentially expressed cytokines with Fold Change and P-value. (*P<0.05, **P<0.01, ***P<0.001, ****P<0.0001).*

5.6.4 Summary

In summary CCA cells experienced an increase in IL-7 concentration concurrent with a reduction in IL-8 concentration, whilst cholangiocytes experienced an increase in angiogenin concentration. Both cholangiocytes and cholangiocarcinoma cells were exposed to an increase GRO in concentration, as well as a reduction in MCP-1 concentration after 48 hours of co-culture. During co-culture, cholangiocytes experienced an increase in CXCL1 concentration whilst CCA cells experienced a reduction in CXCL1 exposure. CCA cells experienced an increase in IL-6 and CCL5 exposure , whilst cholangiocytes experienced a reduction in IL-6 and CCL5 concentration.

5.7 Discussion

In this study, we sought to parse out the secretome that mediates the indirect crosstalk between cholangiocytes and CCA cells, in terms of both the metabolic compartment, and the growth factor compartment. Specifically, we aimed to identify specific factors responsible for eliciting the time-dependent functional alterations to cellular phenotypes as discussed in the previous chapter (Results Chapter 1). This included changes to cell viability, migration, cell cycle progression, and apoptosis. To this end, we utilized large scale metabolomics to evaluate the change in concentration of intracellular metabolites and a cytokine array to simultaneously screen for the relative expression and pattern of 42 cytokines and growth factors in the supernatant from the co-culture at 48 hours. As the onset and progression of CCA is modulated by deregulated metabolic pathways, we aimed to uncover whether exogenous dosing of these metabolites could imitate co-culture induced phenotype alterations.

In general, we successfully replicated some of the phenotypic behaviours of MMNK1 cholangiocytes in co-culture solely through the supplementation of individual exogenous metabolites identified by the metabolomic analysis. However, not a single metabolite alone could be attributed to the sole control the phenotypic changes seen in cholangiocytes. Further investigation into combinations of multiple metabolites on MMNK1 cholangiocyte behaviour is required. Ultimately, creatine and choline were the only metabolites enriched in cholangiocytes after 48 hours of co-culture, with both concentrations being strongly associated with flux over time. Exogenous choline reduced cholangiocyte viability, suggesting that whilst choline availability as a resource for cellular construction is essential for growth, choline concentration is not driving phenotypic alterations alone. Exogenous

creatine provided the most compelling candidate for the key driver of changes, due to the increase in cholangiocyte cell viability and cell cycle progression, and reduction in apoptosis, we theorise to be due to the identified increase in ATP availability.

The concentration of creatine has been identified as a predictive marker for predicting CCA recurrence, with patients with lower levels of creatine demonstrating significantly shorter recurrence-free survival than patients with higher levels (137). Likewise the concentration of creatine riboside, a urinary metabolite formed from the breakdown of creatine and phosphocreatine into creatinine, has also been shown to corelate with CCA (138). Moreover, in HCC, the activity of mitochondrial creatine kinase (MtCK) is increased (139). Energy metabolism is dysregulated in CCA, (140–142) and taken together, we provide evidence to suggest that creatine metabolism may play a role in this.

In the CCA compartment, we see a considerable increase in the concentration of the branched-chain keto-acid (BCKA) 2-oxoisopentanote during co-culture, which was shown to reduce both iCCA and eCCA cell viability. Interestingly, the basal concentration of 2-oxoisopentanote was significantly higher in MMNK1 cholangiocytes compared to CC-SW1 cells, with virtually no detectable 2-oxoisopentanote detected during monoculture. Amino acid metabolism is used to provide energy to cancer cells, via the production of an α-ketoacid, which is then oxidized by the tricarboxylic acid (TCA) cycle and oxidative phosphorylation, for the production of ATP (143). The degradation of valine results in the production of the BCKA 2-oxoisopentanote, and α-ketoglutarate which proceeds into the TCA cycle to form isocitrate. The branched-chain amino acids (BCAA) valine, leucine, and isoleucine are the major nitrogen source for glutamine and alanine synthesis (144), and the increased conversion of BCAA's to their respective keto analogues, branched-chain keto

acids (BCKA), enhances production glutamine (144). Glutamine functions as a anaplerotic metabolite, fulfilling the TCA cycle in order to maintain mitochondrial ATP production (145). Cancer cells can become dependent of glutamine in order to fuel aberrant growth and survival. Certain leukaemia's generate high concentrations of BCAAs from BCKA's, and increased BCAA-BCKA catabolism has been identified in NSCLC and glioblastoma (146), whilst elevation of circulating BCAAs (leucine, isoleucine, and valine) is an early event during the development of PDAC (147). Likewise, upregulation of BCAT1 and BCAT2, the transaminases responsible for BCAA-BCKA catabolism, are upregulated in iCCA (148). Hence we postulate that cholangiocytes are restricted by BCAA catabolism under normal conditions. We suggest that indirect co-culture leads to glutamine starvation in CCA cells, triggering a shift in BCAA-BCKA metabolism, leading to an accumulation of 2-oxoisopentanote. Taken together, we consider abrogated BCAA-BCKA metabolism to be a contributing factor in CCA development.

As well as altered BCAA metabolism, there was a decrease in the concentration of reduced glutathione (GSH) in CC-SW1 cells. The antioxidant GSH is often reduced to form oxidised glutathione (GSSG) during oxidative stress, and as such the ratio of GSH/GSSG can reflect oxidative stress in cells. Moreover, glutathione biosynthesis had the second most significant impact in the joint transcriptomic-metabolomic pathway analysis for CC-SW1 cells. It would be prudent to measure potential mitochondrial dysfunction using a combined ATP assay (Promega's Mitochondrial ToxGlo Assay), in combination with a ROS assay (Promega's, ROSGlo H_2O_2 assay) to therefore to evaluate mitochondrial activity and oxidative stress in CC-SW1 cells during co-culture.

We found that the profile of cytokines was different when the cells were in mono- to when they were in co-culture. However, to investigate the actual source of the cytokines in the co-culture system, we would need to measure intracellular levels of the cytokines in question, before conducting gene knockdown studies and determining the secretome after the knockdown via ELISA (R&D Systems). Given more time, I would evaluate the effect of exogenous doses of CXCL1/2/3, IL-6, and CCL5 on CCA cell behaviour, in order to recapitulate the effect of indirect co-culture with cholangiocytes, as well as utilising a combinatorial approach of small-molecule inhibition of each of the cytokines in order to identify the key driver in the phenotypic shift. Regardless of which compartment they were secreted from, the indirect co-culture system led to a change in exposure of these cytokines to the cells, including IL-6, MCP-1, CXCL1/2/3, CCL5, and IL-8.

The relationship between cytokines and metabolism are intertwined. Some cytokines play a positive role in metabolism, whilst others have a negative metabolic role, linking to the induction of metabolic dysfunction. Likewise, there is a role for metabolic reprogramming in the secretion of pro-inflammatory cytokines. The chronology in this axis therefore requires further elucidation.

Both genetic and epigenetic changes can confer vital survival advantages to cancer cells in nutrient-deprived environments, triggering metabolic reprograming, and the secretion of pro-survival cytokines. Therefore, the evaluation of gene expression changes is of principal importance to the next stage of our investigation.

6 Results Chapter 3 – Interpreting the Transcriptomic Alterations due to Indirect Cell-Cell Communication

6.1 Introduction

The genetic landscape of iCCA has been revealed via recent progress in genomic and transcriptomic sequencing, with Next-Generation Sequencing (NGS) of CCA patients providing compelling evidence of the significant molecular heterogeneity exhibited by this malignancy at both intra- and inter-tumoral levels.

Extensive evidence has demonstrated substantial variations in the genomic landscape of CCA based on anatomical subtypes and underlying aetiology. Most genetic association studies have been in liver fluke positive CCA (149), as opposed to spontaneous cases, and although there has been little work conducted on the molecular comparison of iCCA and eCCA, some studies have shown a disparity in mutational burden, with *IDH* and *BAP1* mutations as well as *FGFR2* fusions primarily identified in iCCA, whilst *PRKACA* and *PRKACB* fusions and *ELF3* and *ARID1* mutations have been identified in eCCA (150). The activation of the receptor tyrosine kinase (RTK) signalling pathway is a prevalent occurrence in all CCA subtypes, although abnormal expression of *EGFR*, *ERBB2*, and *MET* are identified differentially depending on subtype, overall aberrant expression is associated with a poorer prognosis (37).

Cancer cells often acquire genetic and epigenetic alterations that are specific to their malignant phenotype, and it has been commonly shown that the induction of oncogenes and the loss of tumour suppressors are sufficient to drive metabolic changes in cancer cells. Mutations in classical tumour development pathways have been identified in CCA, such as

genes involved in DNA damage and genomic instability including *CDKN2A*, *CCND1*, *BRCA1* and *BRAC2* (38,151) whilst mutations in *TP53* are frequently observed in CCA, and are associated with poor prognosis (15). Mutations in *KRAS* and *BRAF* are common in many cancers, and CCA is no exception. These mutations activate signalling pathways that promote cell proliferation and survival, and whilst *KRAS* mutations have been identified in all CCA subtypes, *KRAS* mutations are more prevalent in iCCA, with *BRAF* mutations more commonly found in eCCA (150). Moreover, aberrant kinase signalling has been shown to stem from mutations *KRAS, ERBB1–3, BRAF, PIK3CA, PTEN, STK11, SMAD4* and *FGFR1–3* (38,152), whilst immune dysregulation has been attributed to mutations in the JAK–STAT3 signalling pathway (65).

The most important genetic discovery in CCA was the identification of hotspot IDH mutant CCA, impacting both epigenetic regulation and metabolism. Both $IDH1^{R132}$ and $IDH2^{R172}$ lead to the accumulation of the onco-metabolite 2-hydroxyglutarate (2HG)(153). 2-HG acts as an antagonist to α-ketoglutarate (2-oxoglutarate) by binding to the catalytic site and competitively inhibiting the activity of α-KG-dependent dioxygenases. These dioxygenases include α-KG-dependent histone demethylases and the TET family of 5-methylcytosine hydroxylases (154,155), epigenetic regulators that show how genomic mutations to the metabolic IDH1 and IDH2 enzymes induce changes in histone and DNA methylation, highlighting the genomic-metabolic-epigenomic axis of control in CCA.

The absence of sequential genetic and molecular alterations that drive the development of CCA poses a challenge to identifying actionable therapeutic targets, highlighting the need for a deeper comprehension of molecular pathway responsible for driving CCA

development. The best use of metabolomics in research is in combination with other omics approaches, in order to discover functionally and diagnostically relevant alterations in cancer cells. Mutant IDH CCA is prime example of the interconnectivity of the genome, metabolism, and epigenome, further supporting the direction of our investigation.

Therefore, we proceeded to evaluate changes to the CCA transcriptome during co-culture. We conducted bulk RNA-sequencing to identify changes to the transcriptome that could be used to explain the changes we identified in in our functional, metabolic, and cytokine profile. This involved extracting RNA from MMNK1 and CC-SW1 cells in mono- and coculture after 48 hours, and validating the expression via qPCR. We utilised CCA patient gene expression data from The Cancer Genome Atlas (TCGA) to highlight any genetic changes identified in co-culture that have the potential for clinical relevance.

6.2 Genomic differences between cholangiocyte and cholangiocarcinoma cells

Phenotypic changes occur through a variety of mechanisms that can alter the observable characteristics or traits of a cell, influenced by genetic, epigenetic, and tumour microenvironmental factors, with both mutations and transient expression changes contributing to the genetic component.

Given that indirect coculture was able to elicit phenotypic changes to cellular compartments, we reasoned that it is essential to explore the transcriptomic changes to both CCA cells and cholangiocytes. As such, we performed transcriptomic analysis on both cellular compartments to understand their individual gene expression profiles. We used bulk RNA-sequencing to evaluate gene expression in CC-SW1 cells and MMNK1 in monoculture at 48 hours, to illustrate the baseline gene expression differences between our CCA cell line and the cholangiocytes in our model.

6.2.1 Application of the DESeq2 model

Principle Component Analysis (PCA) is commonly used in RNA-seq analysis to visualize and explore the overall patterns of gene expression across samples. RNA-seq data consists of large numbers of gene expression data, resulting in high-dimensional datasets. PCA helps reduce the dimensionality by transforming the data into a smaller set of uncorrelated variables called principal components (PCs). The first principal component (PC1) captures the largest source of variation in the data. It is a linear combination of the original gene expression data that maximizes the variance. In other words, PC1 represents the direction in the data space along which the data points exhibit the most significant variability, which in our case should allow for identification of CC-SW1 and MMNK1 samples, or monoculture and co-culture samples later on, based on differential gene expression alone.

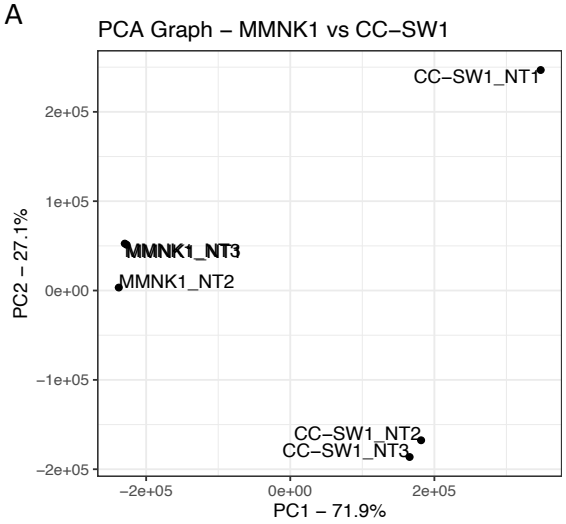
The PCA plot in Figure 6:1A represents a 2D plot using the first 2 Principle Components (PC) PC1 on the X-axis and PC2 on the Y-axis. PC1 accounts for 71.9% of the variation between the samples (Figure 6:1A), denoting a large difference between the CC-SW1 and MMNK1 transcriptomic profiles, as MMNK1 samples are clustered on left, whilst CC-SW1 samples are clustered on the right. The scree plot in Figure 6:1B shows that together, PC1 and PC2 exceed 80% of the variation within the data. Retaining fewer principal components simplifies the analysis and interpretation of results, and the scree plot helps strike a balance between complexity and the amount of information retained, allowing us to decide how many principal components are sufficient to capture the essence of the data without unnecessary redundancy. Simply put, the DESeq2 mathematical model is appropriate to apply to our data due to clear sample separation and explanation of variance.

Loading scores are coefficients that represent the relationships between the original variables and the principal components. Loading scores indicate the contribution of each gene to the composition of the PCs. Therefore, the loading scores provide insights into how strongly each gene influences each PC, whereby positive loading scores push the CC-SW1 samples to the right side of the graph. The magnitude of the loading scores indicates the strength of the relationship between the gene and the PC, and the table in Figure 6:1C shows the names of the top 10 genes with the largest loading score magnitudes. The gene for osteonectin, *SPARC*, has the largest loading score, of 0.305 (Figure 6:1C) which contributes to how far right the CC-SW1 samples are on the graph, overall contributing more to the overall variance explained by PC1.

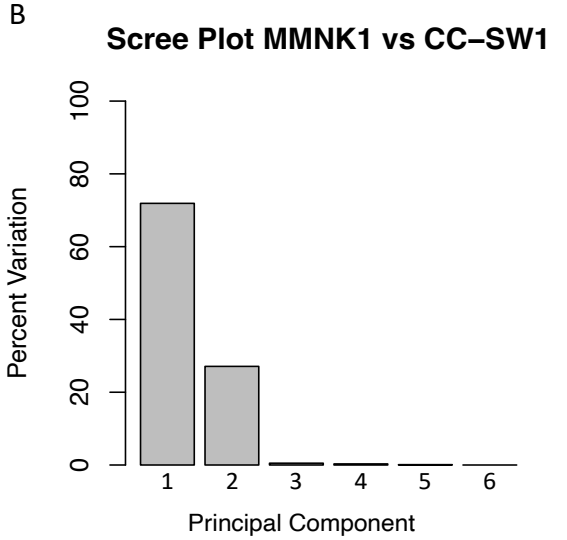
Dispersion is a measure of spread or variability in the data. The DESeq2 dispersion estimates reflect the variance in gene expression for a given mean value, allowing us to predict the variation around the mean across all 3 biological replicates for each samples. Therefore the dispersion for genes with the same mean will only differ based on their variance. In order to accurately model sequencing counts, we must generate accurate estimates of variation between replicates of the same sample group for each gene. DESeq2 uses a 'shrinkage' method to share information across genes, assuming a similar dispersion for genes with similar expression levels. In order to model the dispersion based on mean counts of the replicates, the most likely estimate of dispersion is calculated (the estimated gene-wise dispersions). As in Figure 6:1D, a curve is fitted to dispersion estimates for each gene, assuming a reasonable estimation of dispersion across all genes (shown in red) plotting the expected dispersion for each with a given expression (mean count). This allows differentially expressed genes to more accurately be identified when the sample sizes are small, in our

case 3 monoculture and 3 co-culture. The black dots represent each gene, with mean expression and maximum likelihood estimation (MLE) of the dispersion. In order to reduce the likelihood of false positives, the shrinkage method is used, whereby genes with low dispersion values are shrunken towards the curve and used to finalise the model for differential expression analysis. Genes with high dispersion estimates are not shrunk towards the curve as it is likely these do not follow the model assumptions, and are highlighted in blue (Figure 6:1D). Overall, the plot is used to show our RNAseq data is a good fit for the DESEQ2 model.

A



B



C

Gene	Loading Score
SPARC	0.305418
MTCO1P12	0.297665918
MTCO3P12	0.248387544
ACTG1	0.190422411
FLNA	0.187257969
MTRNR2L12	0.155851407
ANXA2	0.132991517
COL1A1	-0.153364683
CALR	-0.16734768
HSPA5	-0.266418308

D

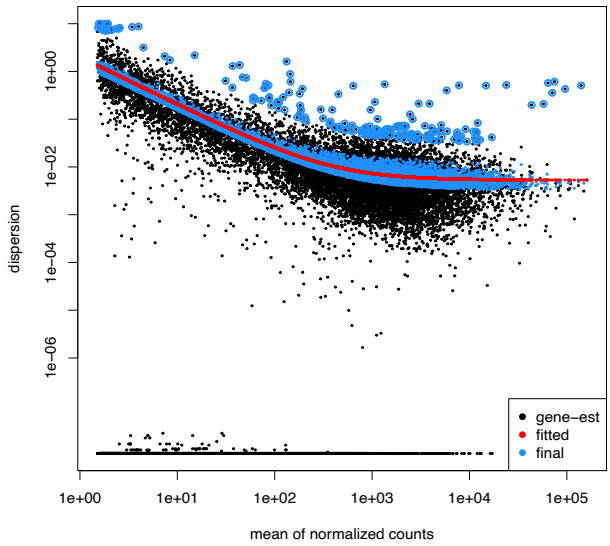


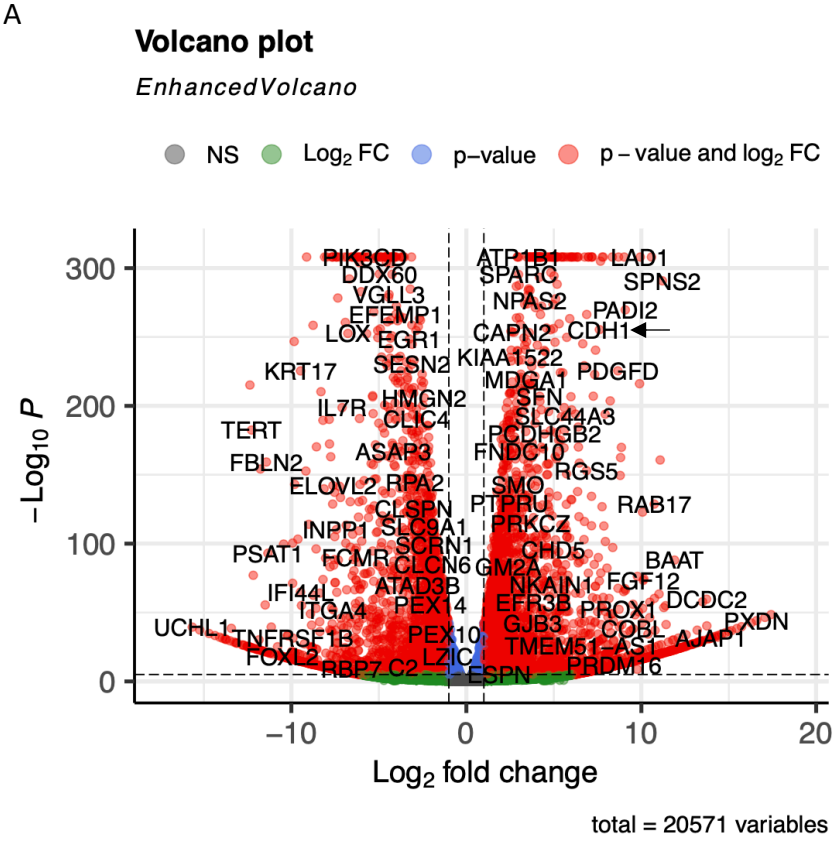
Figure 6:1 – Normalisation of MMNK1 and CC-SW1 gene expression data from RNA-seq. *RNA was extracted from MMNK1 cholangiocytes and CC-SW1 cells after 48 hours of monoculture, for the evaluation of gene expression. A) The PCA plot is a two-dimensional representation of RNA-seq data. Each point represents a sample, with its position reflecting its placement in a lower-dimensional space generated by the PCA. Samples with similar gene expression profiles cluster together, and as such enables visualization of sample relationships. MMNK1 samples are clustered tightly together, whilst CC-SW1 samples are more disperse. The scree plot illustrates the explained variance associated with each principal component in PCA. This plot helps determine the number of principal components that capture the most significant variation in the data, guiding dimensionality reduction. C) Table of the top ten genes and equivalent loading scores associated with Principal Component 1 from the PCA. Loading scores indicate the contribution of individual genes to the variation explained by each component. High loading scores suggest genes that strongly influence the observed separation in the PCA plot. D) The gene dispersion estimation plot depicts the relationship between gene expression dispersion and mean expression level. We use this to model statistical variability in the gene expression data.*

6.2.2 Differential gene expression

20,571 genes were analysed for the differential gene expression (DGE) analysis, a comparison of the gene expression levels in counts per million, between CC-SW1 and MMNK1 samples. 14,448 genes were significantly differentially expressed in our samples ($P<0.05$). Direction of comparison is CC-SW1 vs MMNK1 cells, whereby a positive fold change denoted a higher level of gene expression in CCA cells compared to MMNK1 cells. Of these, 4,108 genes had a $Log_2FC >1$ (equivalent to a Raw Fold Change in gene expression >2) whilst 4,957 genes had a $Log_2FC <-1$ (equivalent to a Raw Fold Change in gene expression <-2). We can visualise the results of the differential gene expression analysis using a volcano plot, (Figure 6:2A), which displays a measure of statistical significance on the Y-axis ($-Log_{10}$P-value) and a measure of magnitude of change on the X-axis (Log_2FoldChange). Genes with a Log_2Fold Change >1 or <- are highlighted in green, genes with a P-value <0.05 are highlighted in blue, whilst genes that have both a Log_2Fold Change >1 or <-1 and a P-value <0.05 are highlighted in red.

For example, the black arrow on Figure 6:2A highlights the location of *CDH1*, the gene encoding E-cadherin. *CDH1* expression is significantly (P=4.09E-256) differentially expressed between our CC-SW1 and MMNK1 samples, with a Log2FoldChange of 7.60299874. Figure 6:2B shows the normalised count data for CDH1 gene expression in both cell lines, and we can see that *CDH1* has considerably more counts in CC-SW1 cells compared to MMNK1 cells, in agreement with the identified Log2FoldChange. Therefore, genes with a large positive Log2FoldChange are expressed to a greater degree in CC-SW1 cells, whilst genes with a large negative Log2FoldChange are expressed to a lower extent in CC-SW1 cells compared to expression in MMNK1 cholangiocytes.

A



B

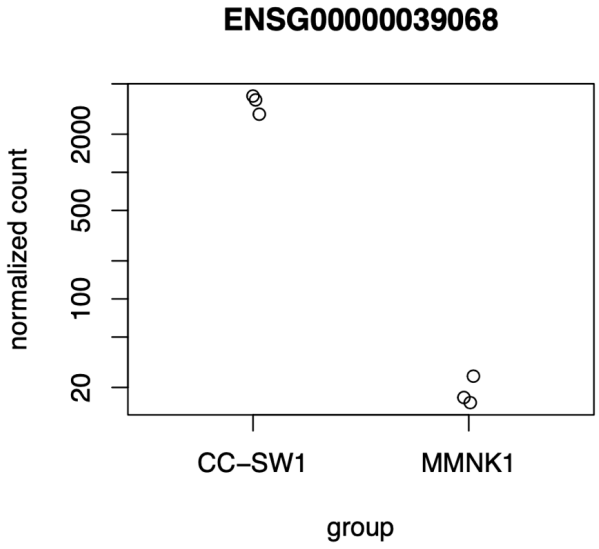


Figure 6:2 – Differential gene expression analysis of MMNK1 and CC-SW1 gene expression at 48 hours. *A) Volcano plot depicting differential gene expression between CC-SW1 and MMNK1 cells. Each point on the plot represents a gene with its position indicating both statistical significance and fold-change in gene expression. The dashed horizontal line represents the predefined threshold for significance, -log10(p-value) > 1.3 (blue), whilst the dashed vertical lines represents the predefined threshold for fold-change, log2 fold-change>1/<-1 (green). Genes which fulfil both significance and fold change criteria are shown in red, with upregulated genes on the right side, and downregulated genes on the left side. The black arrow denotes the position of the CDH1 gene on the volcano plot. B) Dot plot of the normalised gene count for the CDH1 gene (ENSG00000039068) in CC-SW1 and MMNK1 samples.*

6.2.3 Gene Set Enrichment Analysis

Pathway analysis was conducted to help interpret these gene expression changes in a broader biological context, by identifying the pathways or biological processes that are enriched, providing insights into the functional implications of the gene expression changes allowing us understand the underlying difference in biology between CCA and cholangiocytes. The Hallmark database encompasses a comprehensive collection of well-defined biological pathways and processes. It consists of 50 gene sets that capture core biological functions, signalling pathways, and cellular processes that are highly relevant in various biological contexts. We used the Hallmark database to conduct a pathway enrichment analysis to investigate the difference in pathway enrichment in CC-SW1 and MMNK1 cells, and chose to include all pathways assessed in order to evaluate all associated with metabolism, cell cycle, or apoptotic processes. Figure 6:3 shows the Hallmark pathways which are ranked by Normalised Enrichment Score (NES). The bars are colour coded by significance values, with blue denoting 'True' that a pathway has. P-value<0.05 and is therefore significantly enriched, whilst red denotes 'False', meaning that pathway has a P-value>0.05, and is therefore not significantly enriched. Pathways with a positive enrichment score, such as the Reactive Oxygen Species pathway, are highly enriched in CC-SW1 cells. Pathways with a negative enrichment score, such as the Interferon Alpha Response pathway, are under expressed in CC-SW1 cells compared to enrichment in MMNK1 cells. Reactive oxygen species (ROS) are chemically reactive molecules containing oxygen that are naturally produced as by-products of normal cellular metabolism. While ROS are involved in various physiological processes, excessive levels can induce oxidative stress, causing damage to cellular components such as DNA, proteins, and lipids. This oxidative damage can further contribute to tumorigenesis, through mutation, genomic instability, and alterations in

signalling pathways. Moderate levels of ROS are involved in cellular signalling pathways that regulate transcription factor activation and gene expression related to cell growth, proliferation, and survival. Cancer cells often exhibit an imbalance between ROS production and antioxidant defence mechanisms, resulting in increased ROS levels and a state of chronic oxidative stress, whilst some cancers exploit ROS production to their advantage, activating signalling pathways to promote cell survival and proliferation in response to moderate levels of ROS, while simultaneously developing enhanced antioxidant systems to counteract excessive ROS and prevent oxidative stress-induced cell death. We speculate that this basal enrichment of the Reactive Oxygen Species response pathway allows CC-SW1 cells to survive and thrive in the hostile environment caused by elevated ROS levels from increased metabolic activity due to rapid proliferation compared to cholangiocytes.

Likewise, overall gene expression for components in the Interferon Alpha Response pathway were decreased in CC-SW1 cells compared to MMNK1 cells. Interferon alpha (IFN-α) is a cytokine belonging to the interferon family, and is known to exert direct antitumor and immunomodulatory effects. IFN-α triggers activation of STAT1 (signal transducer and activator of transcription 1), resulting in the induction of cell cycle arrest, apoptosis, and inhibition of angiogenesis. This is further supported by the reduction in the Apoptosis pathway compared to MMNK1 cholangiocytes. We postulate that expression of the IFN-α pathway in CC-SW1 is suppressed in order for cells to maintain aberrant rates of proliferation, and apoptosis avoidance.

Expression of genes involved in the Inflammatory Response, as well as IL-6-JAK-STAT3 Signalling pathways are also reduced at a basal level in CC-SW1 cells compared to MMNK1 cholangiocytes. The IL-6 signalling pathway is often triggered in response to inflammation, and specifically, IL-6 has a crucial role in promoting liver regeneration by stimulating

hepatocyte proliferation and survival. This apparent reduction in CCA expression, is actually an enrichment in expression in MMNK1 cholangiocytes. This is potentially due to the ability of cholangiocytes to respond to inflammation and injury as in the ductular reaction, a rapid expansion of cholangiocyte populations. The ductular reaction is an important regenerative mechanism that aims to restore the structural integrity and function of the biliary tree in response to injury (97). Cholangiocytes interact with immune cells and modulate the immune response during the repair process via the secretion of various cytokines, chemokines, and growth factors (156). The increased expression of genes from both the Inflammatory, and IL-6-JAK-STAT3 Signalling pathways highlight the plastic, basal, paracrine response of MMNK1 cholangiocytes.

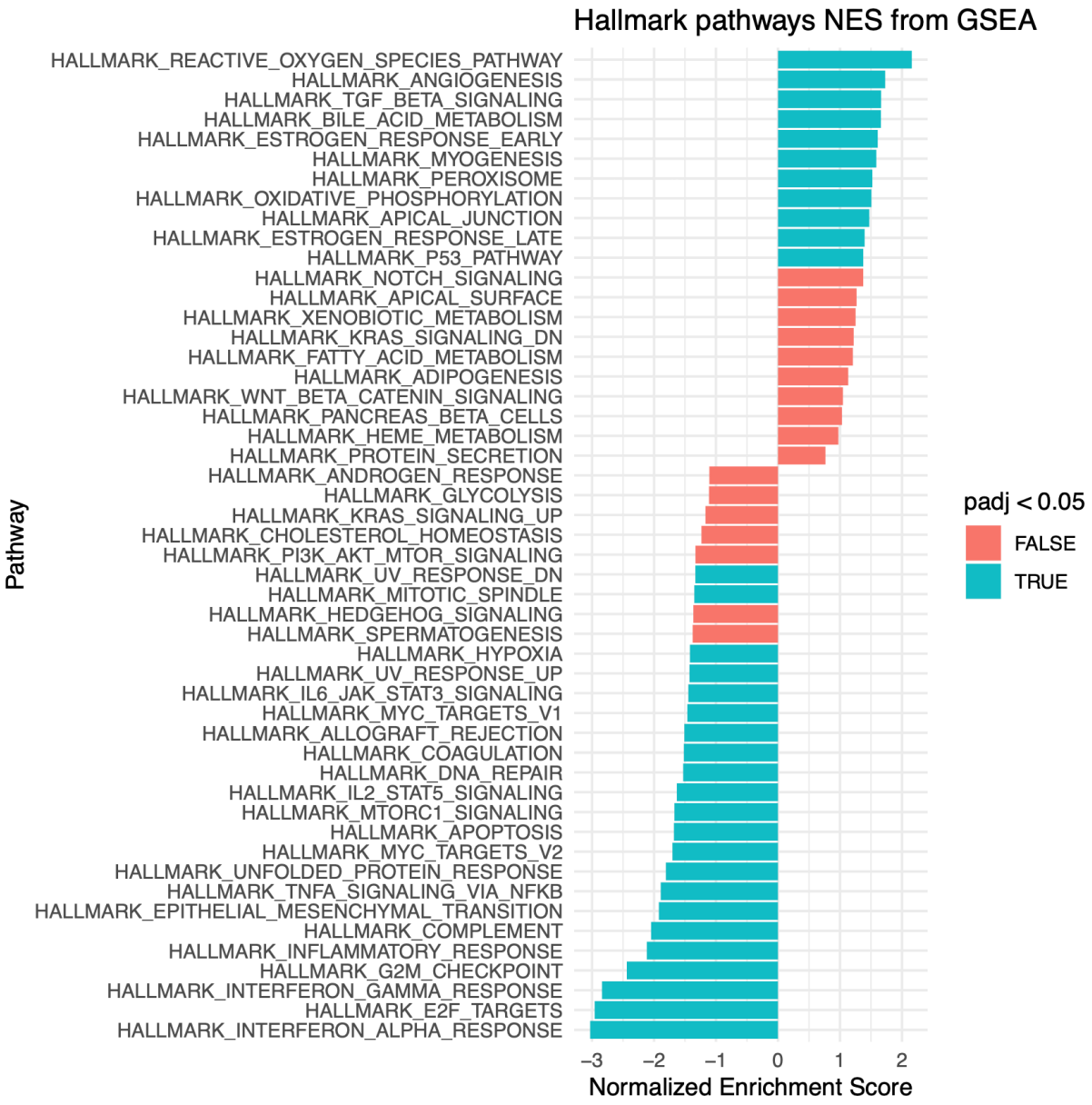


Figure 6:3 - Histogram comparing enriched gene expression pathways in CC-SW1 and MMNK1 cells. *The histogram displays the results of Gene Set Enrichment Analysis (GSEA). Each bar represents a hallmark pathway, with the length corresponding to the Normalized Enrichment Score (NES) for that pathway. Positive scores represent upregulation, whilst negative scores represent downregulation. Each bar is coloured to indicate the significance of enrichment (blue for P<0.05, red for pathways P>0.05). The histogram therefore highlights which hallmark-based gene pathways are significantly upregulated or downregulated in CC-SW1 cells compared to MMNK1 cholangiocytes.*

6.3 Genomic alterations in cholangiocytes due to co-culture

6.3.1 Transcriptomic analysis

Indirect coculture elicited distinct phenotypic changes to MMNK1 cholangiocytes in co-culture, including improved cell viability, and a reduction in apoptosis. Evaluating the transcriptome, which refers to the complete set of RNA transcripts in a cell, can allow for the identification of specific genes and pathways that are differentially expressed, providing clues about the molecular mechanisms responsible for the observed phenotype. Moreover, transcriptomic analysis of the co-culture system has the potential to reveal previously unrecognized genes or pathways that are differentially expressed and associated with the observed co-culture mediated phenotype, which could be used for the identification of potential therapeutic targets or biomarkers in the future. Therefore, we used bulk RNA-sequencing to evaluate the transcriptomic changes to MMNK1 cholangiocytes when grown in monoculture, and co-culture with CC-SW1 cells after 48-hours, highlighting the effect of CC-SW1 cells on MMNK1 cell gene expression profiles.

6.3.2 Application of the DESeq2 model

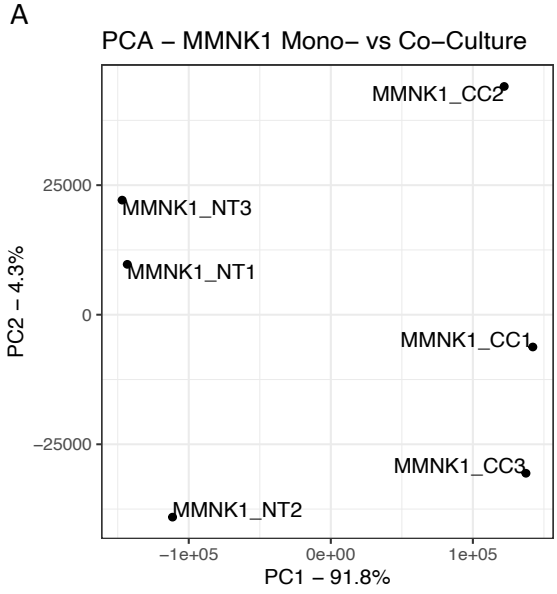
We used a PCA to visualize and explore the overall patterns of gene expression in MMNK1 cells in mono- and co-culture. Figure 6:4 shows a PCA plot using the first 2 Principle Components (PC), PC1 on the X-axis and PC2 on the Y-axis. The MMNK1 samples in monoculture are clustered on the left side of the graph, whilst the co-culture samples are clustered on the right side of the graph. This clear separation in monoculture and co-culture samples shows samples can accurately be mathematically determined as mono- or co-culture. Both Figure 6:4 and the Scree Plot in Figure 6:4 show that PC1 is responsible for 91.8% of the variation between samples. This is considerably above an 80% threshold,

showing this statistical model is a good fit for our data. Likewise, when combined with PC2 which accounts for 4.3% of the variation in the data, we can mathematically represent 95.1% of the variation between our MMNK1 mono- and co-culture samples. Loading scores are coefficients that indicate the contribution of each gene to the composition of the PCs, and as such where samples are plotted on the PCA plot. Overall, loading scores play a crucial role in interpreting the results of PCA by revealing the variable-PC relationships and providing insights into the significance and contributions of variables to the principal components. Positive loading scores push the coculture samples to the right side of the graph, and negative loading scores push the monoculture samples to the left side of the graph. The table in Figure 6:4 shows the names of the top 10 genes with the largest loading score magnitudes. The gene *HSPA5*, a member of the heat shock protein 70 (HSP70) family, had the largest loading score, of -0.515 (Figure 6:4) showing *HSPA5* expression contributes significantly to the variation explained by PC1, which contributes to how far left the monoculture samples are on the PCA plot. The gene *COL1A1*, encoding the pro-alpha1 chain of type I collagen had the second largest loading score, of 0.383 (Figure 6:4) showing *COL1A1* expression contributes significantly to the variation explained by PC1,which contributes to how far right the co-culture samples are on the PCA plot.

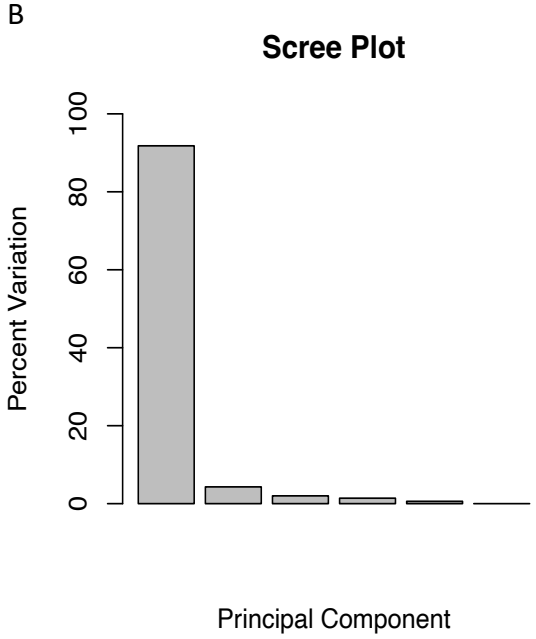
Together, this suggests the gene expression of *HSPA5* and *COL1A1* give a good indication as to whether MMNK1 cells are in monoculture or co-culture. The estimated gene-wise dispersion plot in Figure 6:4 shows a very close alignment of the estimated dispersion across all genes (shown in red) to the mean expression of each gene (shown in black), even more so than the comparison between MMNK1 and CC-SW1 samples (Figure 6:1). This is to be expected, as MMNK1 cells in monoculture and co-culture are much more genetically similar

than MMNK1 and CC-SW1 cells. Overall, the plot in Figure 6:4 shows the MMNK1 mono- and co-culture RNAseq data is a good fit for the DESeq2 model.

A



B



C

Gene	Loading Score
COL1A1	0.38272619
ACTB	0.29548348
GAPDH	0.20206909
ACTG1	0.13851277
TUBB	0.13634341
TUBA1B	0.11583958
HSPA8	0.10464325
HSP90B1	-0.1017179
CALR	-0.2577222
HSPA5	-0.5152372

D

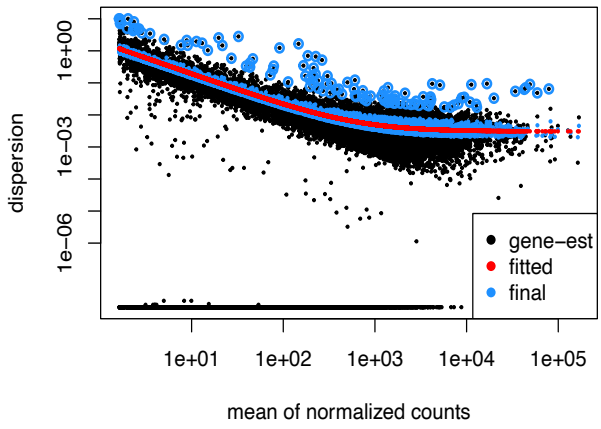


Figure 6:4 - Normalisation of RNA-sequencing expression data from MMNK1 cells. *RNA was extracted from MMNK1 cholangiocytes after 48 hours of monoculture, and indirect co-culture with CC-SW1 cells, for the evaluation of gene expression changes. A) The PCA plot is a two-dimensional representation of RNA-seq data, with each pointing representing a sample. Samples with similar gene expression profiles cluster together, and as such enables visualization of sample relationships. MMNK1 monoculture samples are clustered away from co-cultured samples along PC1. B) The scree plot illustrates the explained variance associated with each principal component in PCA, highlighting only 1 principal component is required to capture the most significant variation in the MMNK1 expression data. C) Table of the top ten genes and equivalent loading scores associated with Principal Component 1 from the PCA. Loading scores indicate the contribution of individual genes to the variation explained by each component. High loading scores suggest genes that strongly influence the observed separation in the PCA plot. D) The gene dispersion estimation plot depicts the relationship between gene expression dispersion and mean expression level. We use this to model statistical variability in the gene expression data.*

6.3.3 Differential Gene Expression

The DGE analysis of MMNK1 cells in co-culture assessed 15,899 genes; 6476 of these genes were significantly differentially expressed (P<0.05). The results from the DGE analysis are illustrated in the volcano plot in Figure 6:5. Genes with a Log_2FC of >1/<-1, equating to a Raw Fold Change in gene expression >2/<-2, are highlighted in green; genes with a P-value <0.05 are highlighted in blue, whilst genes that have both a Log_2FC of >1/<-1 and a P-value <0.05 are highlighted in red. The most significantly differentially expressed gene was identified as ENSG00000044574 (*HSPA5*), which had a Log_2FC of -3.2, equating to a raw fold change in gene expression of 9.2 for MMNK1 cells in coculture (Figure 6:5).

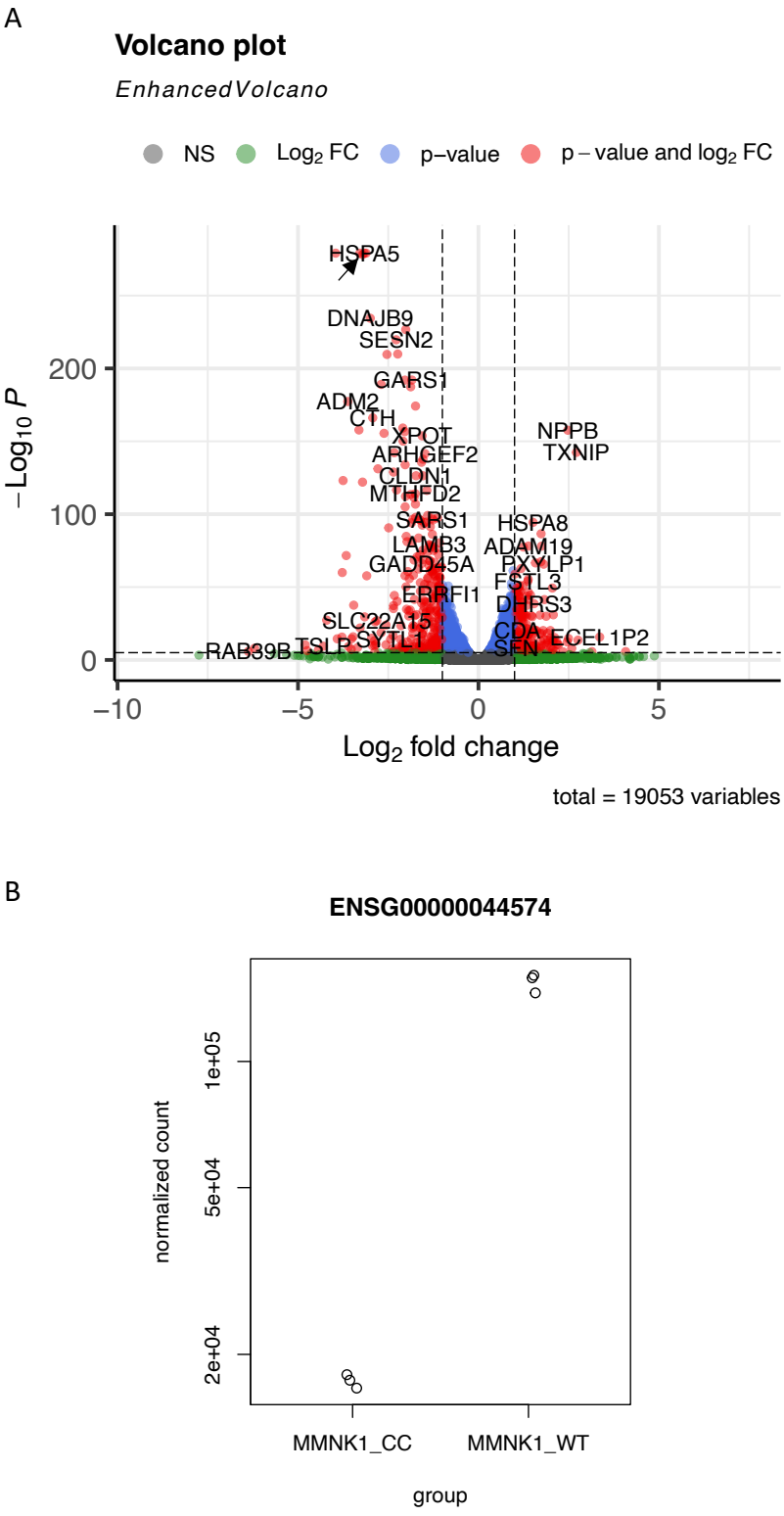


Figure 6:5 - Differential gene expression analysis of MMNK1 cholangiocytes after 48 hours of co-culture with CC-SW1 cells. *A) Volcano plot depicting differential gene expression between MMNK1 cells in monoculture and after 48 hours of co-culture with CC-SW1 cells. Each point on the plot represents a gene with its position indicating both statistical significance and fold-change in gene expression. The dashed horizontal line represents the predefined threshold for significance, -log10(p-value) > 1.3 (blue), whilst the dashed vertical lines represents the predefined threshold for fold-change, log2 fold-change>1/<-1 (green). Genes which fulfil both significance and fold change criteria are shown in red, with upregulated genes on the right side, and downregulated genes on the left side. The most significantly differentially expressed gene was HSPA5, denoted by the black arrow. B) Dot plot of the normalised gene count for the HSPA5 gene (ENSG00000044574) in MMNK1 mono- and co-culture samples.*

6.3.4 Gene Set Enrichment Analysis

Pathway analysis was conducted to help interpret MMNK1 gene expression changes in a broader biological context, by identifying the pathways or biological processes that are enriched as a result of co-culture. We used the Hallmark database to conduct a pathway enrichment analysis, with results shown in Figure 6:6. Pathways are ranked by Normalised Enrichment Score (NES) and colour coded by significance (blue $P<0.05$, red $P>0.05$). The pathway analysis was used to assist in prioritizing genes for further experimental validation. Genes that are differentially expressed and also involved in enriched pathways are more likely to be functionally relevant and play a significant role in the phenotypic changes identified in co-culture. The G2M Checkpoint pathway was the most significantly enriched pathway in our co-culture samples, and as such we nominated the G2M checkpoint for further analysis (Padj=0.007). The top 10 differentially expressed genes in the G2M checkpoint pathway are as shown in Figure 6:6B.

No single database can capture the entire complexity of biological pathways, databases may have varying gene sets, annotations, or definitions of pathways and as such each database has its own limitations, biases, and focuses. For example, the KEGG database focuses on metabolic pathways, while the Hallmark database emphasizes well-defined biological functions. By using multiple databases, we can overcome some of these limitations and biases. As such, we also conducted a pathway analysis using the KEGG database. This assessed 18,738 genes, 47.6% of which (8,926 genes) correlated with our co-culture phenotype, whilst 52.4% (9,812 genes) correlated with our monoculture phenotype (Figure 6:7). The top 50 DEG associated with each phenotype is shown in the heatmap in Figure 6:7.

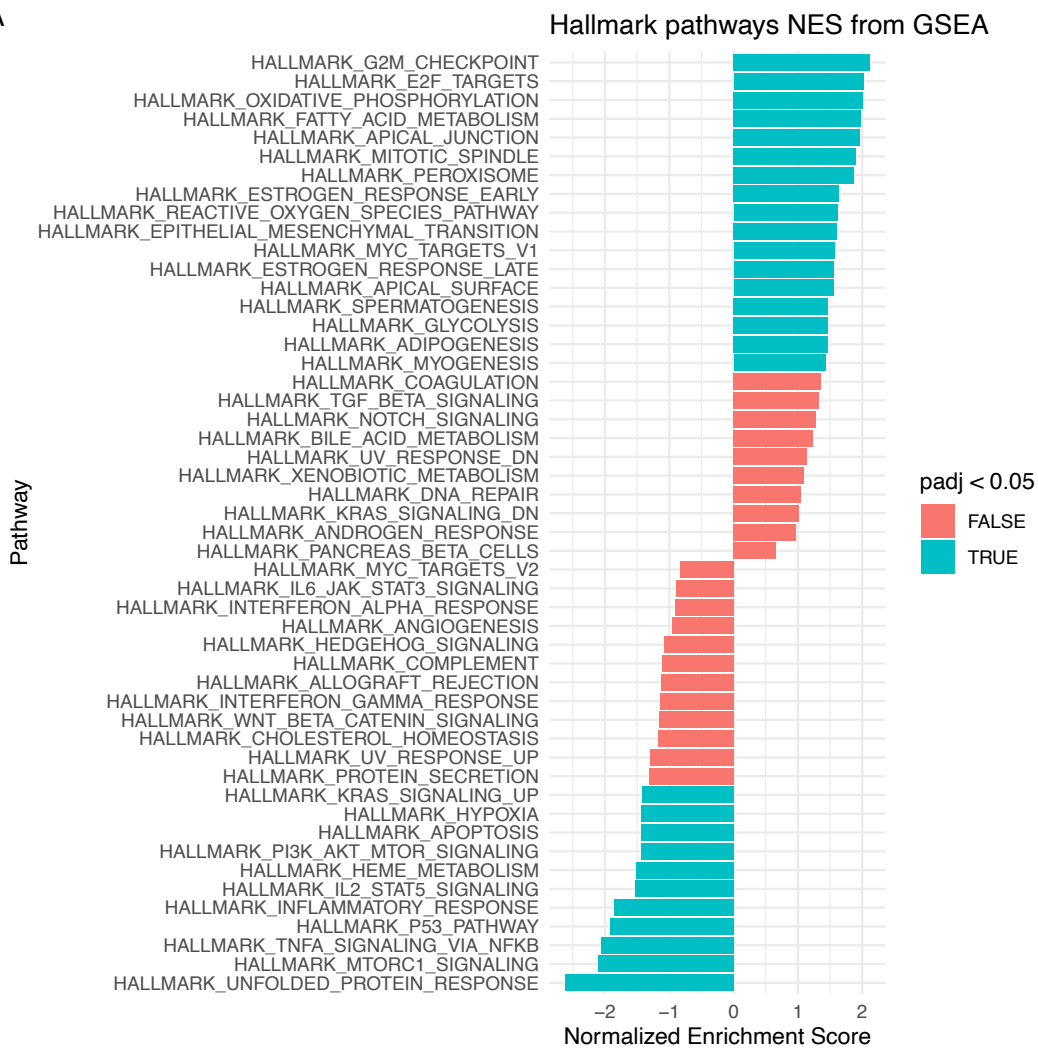
SOAT2, an Acyl Co-A Cholesterol Acyltransferase, was the top gene associated with co-culture in MMNK1 cells, whilst the transcription factor *HMX3* was the top gene associated with MMNK1 in monoculture (Figure 6:7). High levels of *SOAT2* expression have been shown to correlate with poor prognosis in HCC (157) as well as PCa (158), whilst low expression of *HMX3* has been identified in CRC tissues and cell lines, consistent with lower *HMX3* expression associated with poor prognosis in CRC patients (159). These two gene expression changes are indicative of a pro-tumour response in MMNK1 cholangiocytes during co-culture.

The KEGG dataset is comprised of 186 gene sets, which after filtering, resulted in 161 gene sets for analysis. Figure 6:8 shows the KEGG Pathways, ranked by Normalised Enrichment Score (NES) and colour coded by significance (blue $P<0.05$, red $P>0.05$).

44 gene sets were significantly upregulated during co-culture, whilst 11 gene sets were significantly downregulated.

The Oxidative-Phosphorylation, Glycolysis, Cell Cycle, and Fatty Acid Metabolism gene sets were significantly enriched in both the KEGG and Hallmark analysis (Figure 6:9). Likewise, the JAK-STAT, and p53 gene sets were significantly reduced both the KEGG and Hallmark analysis (Figure 6:10). This suggests these pathways have the most significant alterations to gene expression during co-culture. Two of the most significantly downregulated KEGG gene sets were the Glycine-Serine-Threonine, and the Alanine-Aspartate-Glutamate metabolic pathways (Figure 6:10), further implicating aberrant metabolism as a result of co-culture, and supporting our earlier identification of aspartate/asparagine, choline, and creatine as metabolites of interest.

A



B

Gene	Log_2FoldChange	Padj	Name
HSPA8	1.512243491	1.15E-92	Heat Shock Protein Family A Member 8
AURKA	1.015613539	1.63E-57	Aurora Kinase A
PLK1	0.915090343	2.82E-51	Polo Like Kinase 1
BCL3	1.234485463	1.46E-49	BCL3 Transcription Coactivator
KPNA2	0.893002096	2.6E-42	Karyopherin Subunit Alpha 2
CCND1	0.933736979	3.94E-39	Cyclin D1
INCENP	0.856440446	8.44E-38	Inner Centromere Protein
CDC20	0.826889694	4.78E-32	Cell Division Cycle 20
CCNF	0.815601811	7.98E-32	Cyclin F
UBE2C	0.784663435	1.53E-28	Ubiquitin Conjugating Enzyme E2 C

Figure 6:6 - Histogram comparing enriched gene expression pathways in MMNK1 cholangiocytes after 48 hours of co-culture. *The histogram displays the results of Gene Set Enrichment Analysis (GSEA). Each bar represents a hallmark pathway, with the length corresponding to the Normalized Enrichment Score (NES) for that pathway. Positive scores represent upregulation, whilst negative scores represent downregulation. Each bar is coloured to indicate the significance of enrichment (blue for P<0.05, red for pathways P>0.05). The histogram therefore highlights which hallmark-based gene pathways are significantly upregulated or downregulated in MMNK1 cholangiocytes after 48-hours of indirect co-culture with CC-SW1 cells. B) Table of the top ten genes in the Hallmark G2M checkpoint pathway, with respective significance and fold change values.*

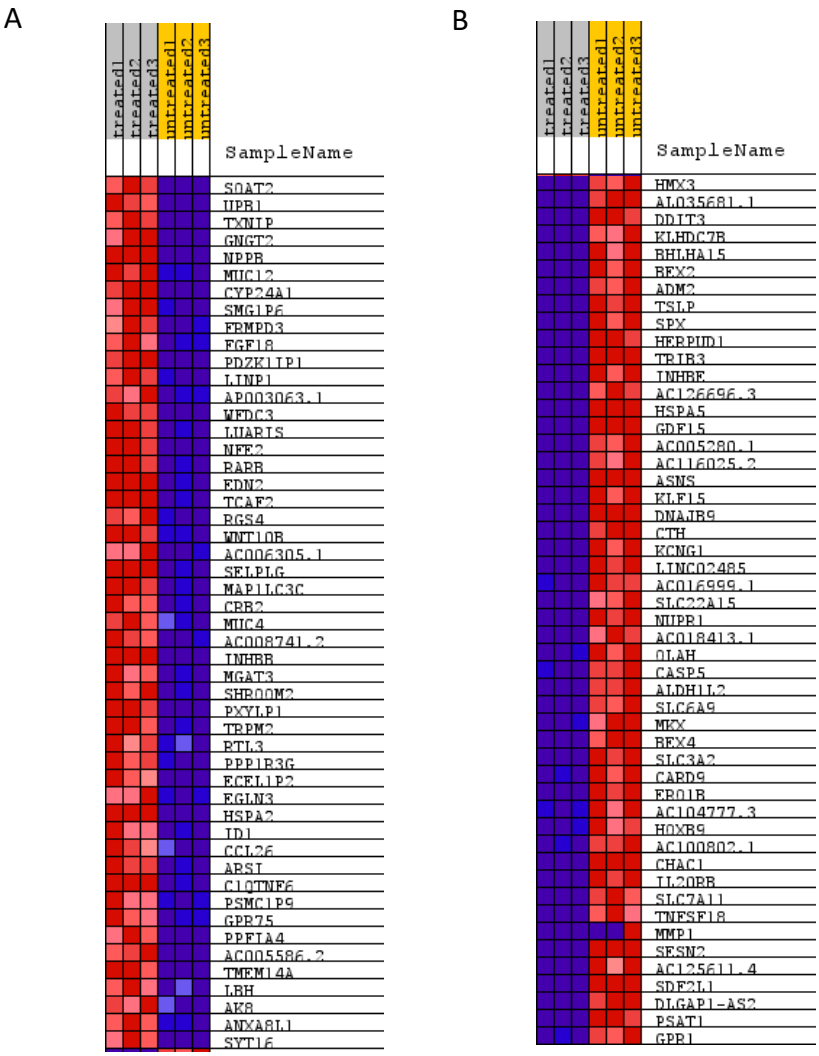


Figure 6:7 - Heat Map depicting the top 100 most differentially expressed genes in MMNK1 cholangiocytes. *The heatmap visually represents the expression patters of the 50 most influential genes as identified by the RNA-seq analysis, with their functional annotations based on the Kyoto Encyclopaedia of Genes and Genomes (KEGG) database. Each row corresponds to a specific gene, each column represents a sample, and the colour represents either increased (red) or decreased (blue) expression. Genes upregulated in MMNK1 cells during co-culture are highlighted in (A), whilst genes downregulated during co-culture are highlighted in (B).*

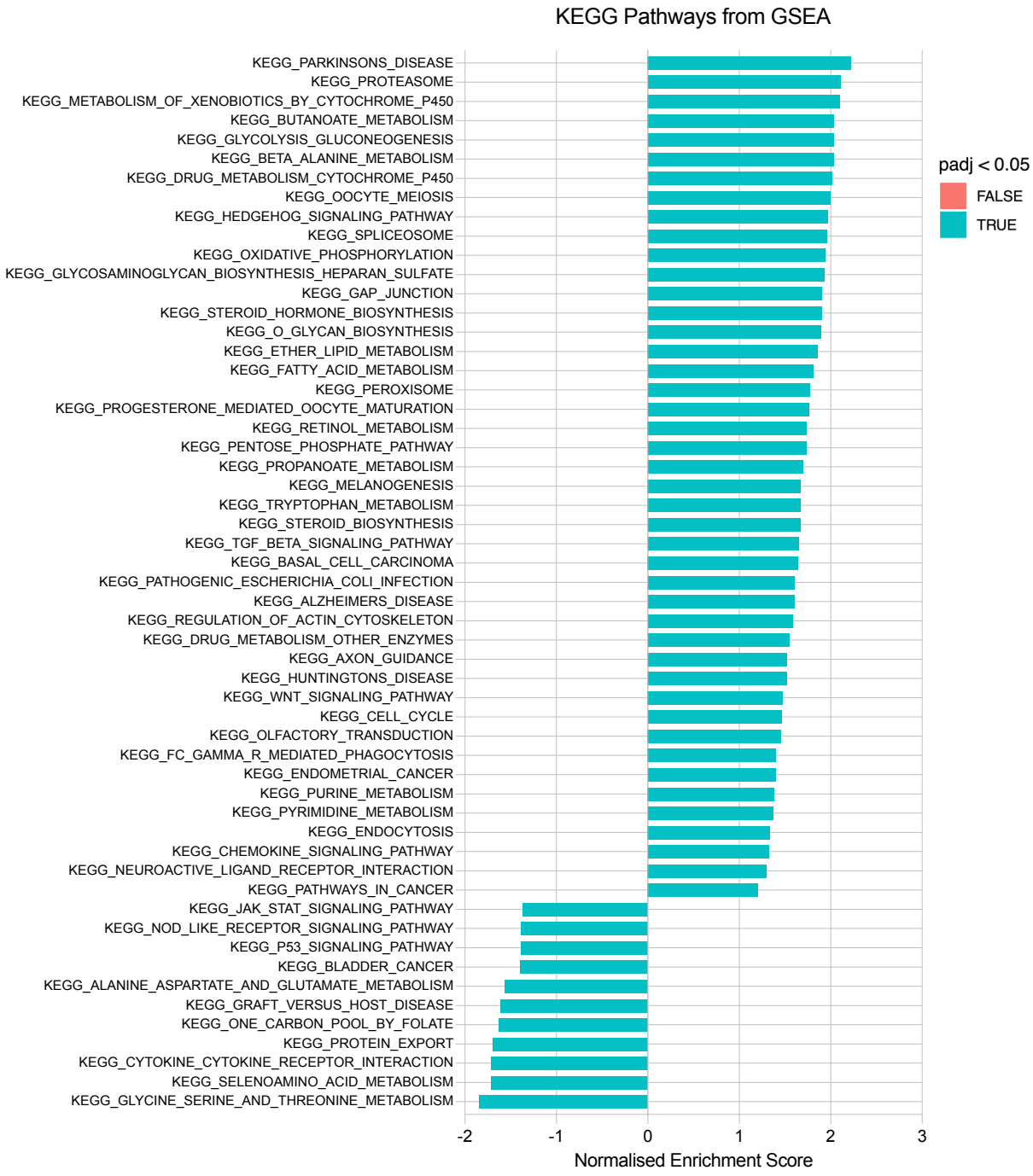
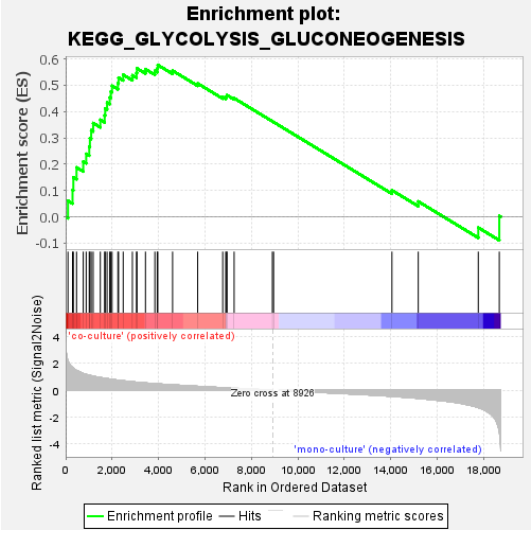
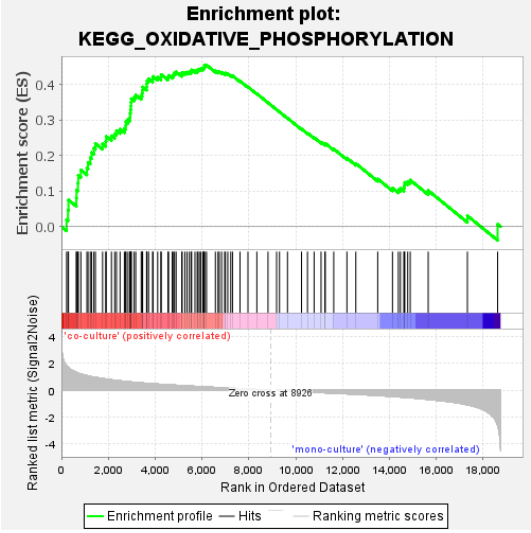


Figure 6:8 - Histogram of KEGG pathways differentially expressed in MMNK1 cells after 48 hours of co-culture. *The histogram displays the results of Gene Set Enrichment Analysis (GSEA). Each bar represents a KEGG pathway, with the length corresponding to the Normalized Enrichment Score (NES) for that pathway. Positive scores represent upregulation, whilst negative scores represent downregulation. Each bar is coloured to indicate the significance of enrichment (blue for P<0.05, red for pathways P>0.05). The histogram therefore highlights which KEGG-based gene pathways are significantly upregulated or downregulated in MMNK1 cholangiocytes after 48-hours of indirect co-culture with CC-SW1 cells.*

A



B



C

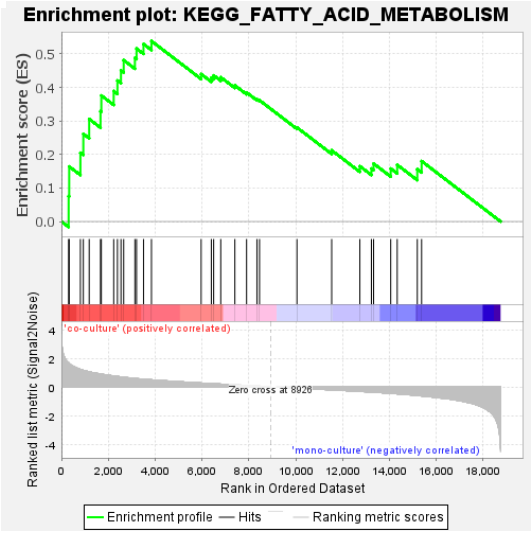


Figure 6:9 - Enrichment plots demonstrating positive gene set correlations in MMNK1 cholangiocytes. *This figure presents a set of enrichment plots, each representing the correlation between specific gene sets from A) Glycolysis, B) Oxidative Phosphorylation, and C) Fatty Acid metabolism, in MMNK1 cholangiocytes after indirect co-culture with CC-SW1 cells. Each plot illustrates the enrichment scores for a particular gene set against expression levels in co-culture and monoculture, which reflect the extent to which genes in the set are associated with either condition. The position of genes in the ranked list based on differential expression are denoted by vertical lines.*

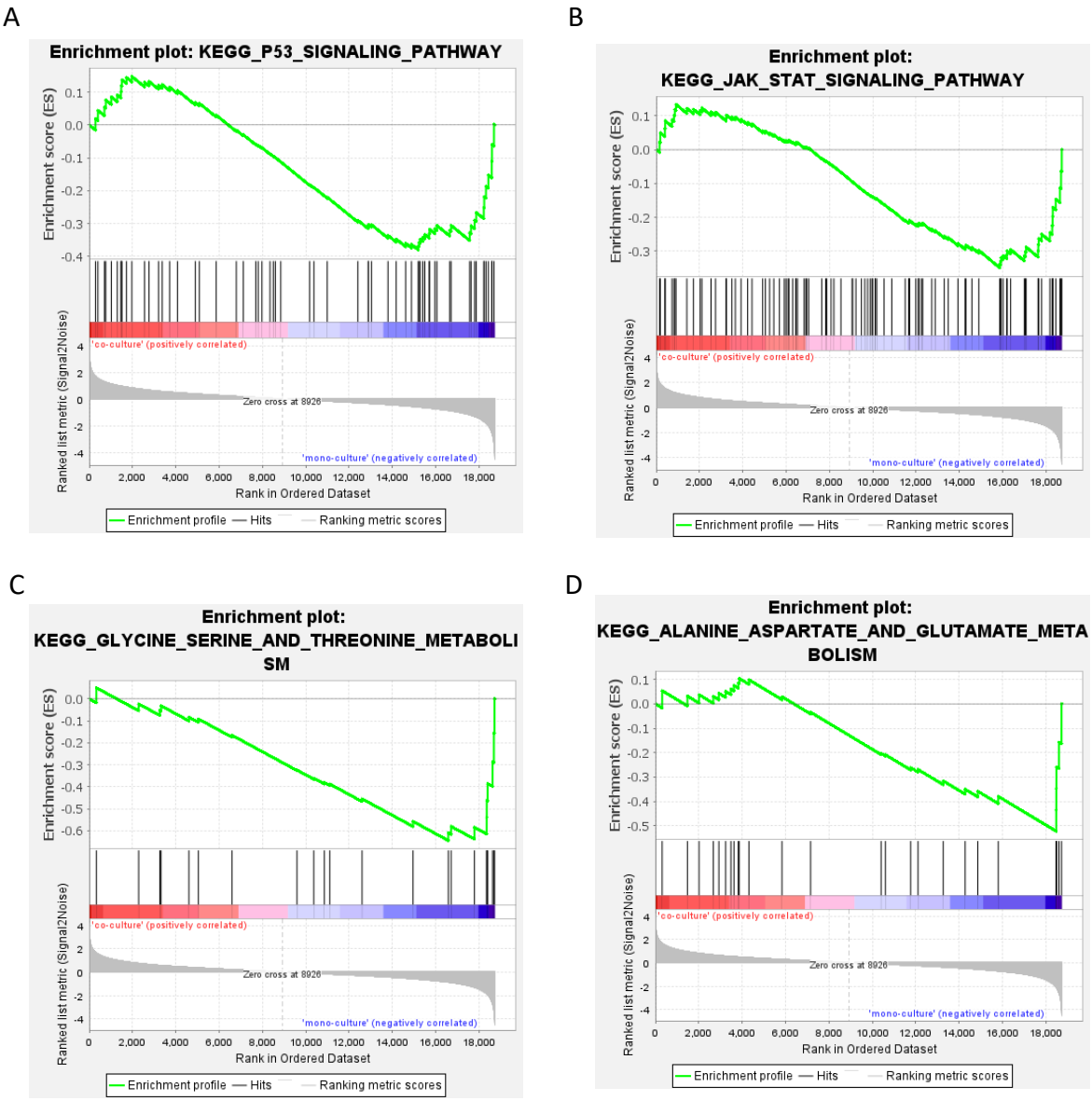


Figure 6:10 - Enrichment plots demonstrating negative gene set correlations in MMNK1 cholangiocytes. *This figure presents a set of enrichment plots, each representing the correlation between specific gene sets from A) p53 Pathway, B) JAK-STA Signalling, C) Glycine-Serine-Threonine metabolism, and D) Alanine-Aspartate-Glutamate metabolism, in MMNK1 cholangiocytes after indirect co-culture with CC-SW1 cells. Each plot illustrates the enrichment scores for a particular gene set against expression levels in co-culture and monoculture, which reflect the extent to which genes in the set are associated with either condition. The position of genes in the ranked list based on differential expression are denoted by vertical lines.*

6.4 Validation of cholangiocyte genomic alterations

6.4.1 Validation of RNAseq data

We selected 2 panels of genes from the RNA sequencing for validation. For the first panel, we selected 5 of the most differentially expressed genes from MMNK1 cells in co-culture (Log2Fold Change>1, p<0.05) for further evaluation: *HSPA8* (Heat Shock Protein Family A [Hsp70] Member 8), *TXNIP* (Thioredoxin Interacting Protein), *TXN* (Thioredoxin), AURKA (Aurora Kinase A), and *NPPB* (Natriuretic Peptide B). The gene expression of *AURKA, HSPA8, NPPB, TXNIP,* and *TXN* in MMNK1 cells after 48 hours of indirect co-culture with CC-SW1 compared to MMNK1 cells grown in monoculture, was validated by qPCR where we saw a clear trend in increasing gene expression during co-culture (P=0.014, 0.09,0.03, 0.1, and 0.02 respectively)(Figure 6:11).

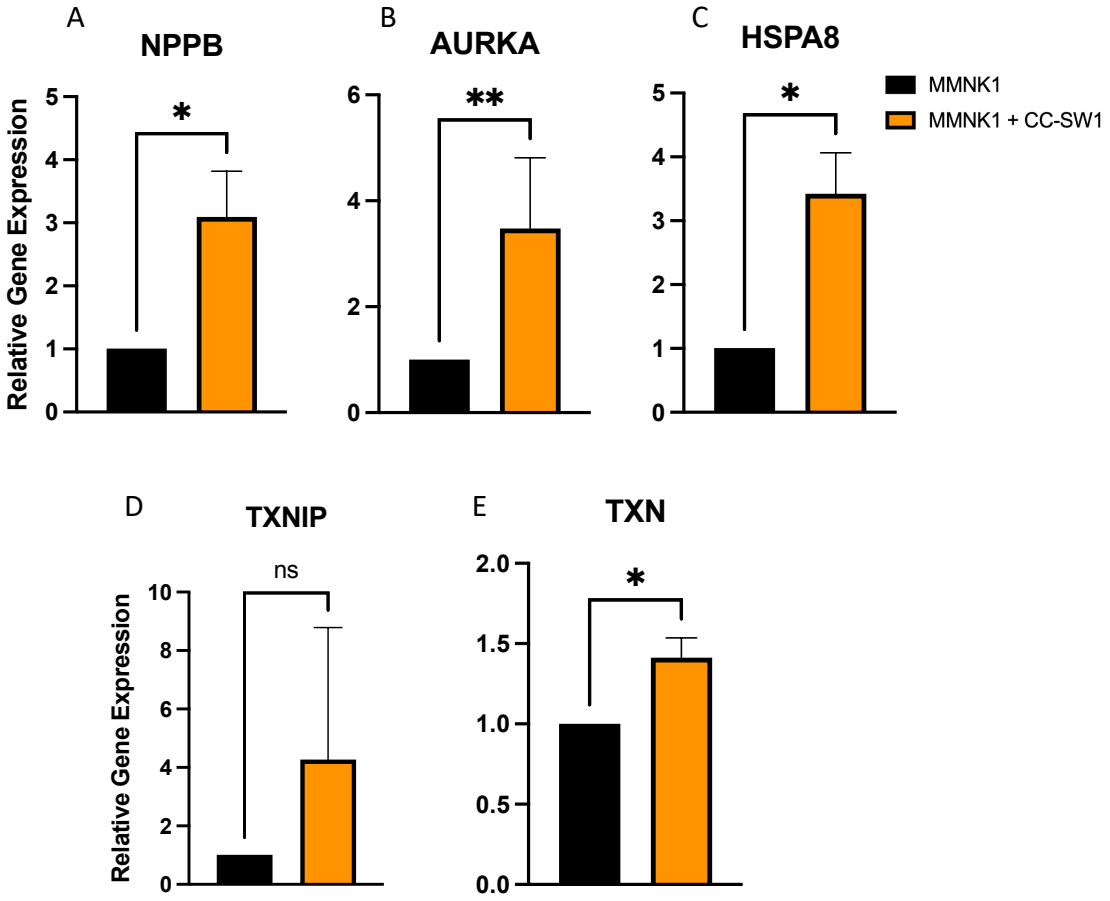


Figure 6:11 - qPCR validation of RNAseq gene expression in MMNK1 cholangiocytes. *MMNK1 cholangiocytes were cultured for 48 hours alone, or in indirect co-culture with CC-SW1 cells prior to RNA extraction. qPCR was used to evaluate gene expression levels of the target genes identified from the RNA-sequencing analysis in Panel 1, A)* NPPB*, B)* AURKA*, C)* HSPA8*, D)* TXNIP*, and E)* TXN*, enabling the comparison of gene expression changes in MMNK1 cells in monoculture and co-culture (*P<0.05,**P<0.01)(n=6).*

For the second panel, we selected 5 of the most differentially expressed genes from MMNK1 cells in co-culture (Log2Fold Change>1, p<0.05) that were not detected in CC-SW1 cells, for further evaluation: *KCNK3* (Potassium Two Pore Domain Channel Subfamily K Member 3), *EXTL1* (Exostosin Like Glycosyltransferase 1), *MGAT3* (Beta-1,4-Mannosyl-Glycoprotein 4-Beta-N-Acetylglucosaminyltransferase), *FAP* (Fibroblast Activation Protein Alpha), and *IDO1* (Indoleamine 2,3-Dioxygenase 1). The expression levels were validated by qPCR, where we saw a trend in increasing gene expression during co-culture in agreement with the RNAseq. (P=0.0971, 0.0371, 0.0382, 0.1402, and 0.0755 respectively)(Figure 6:12).

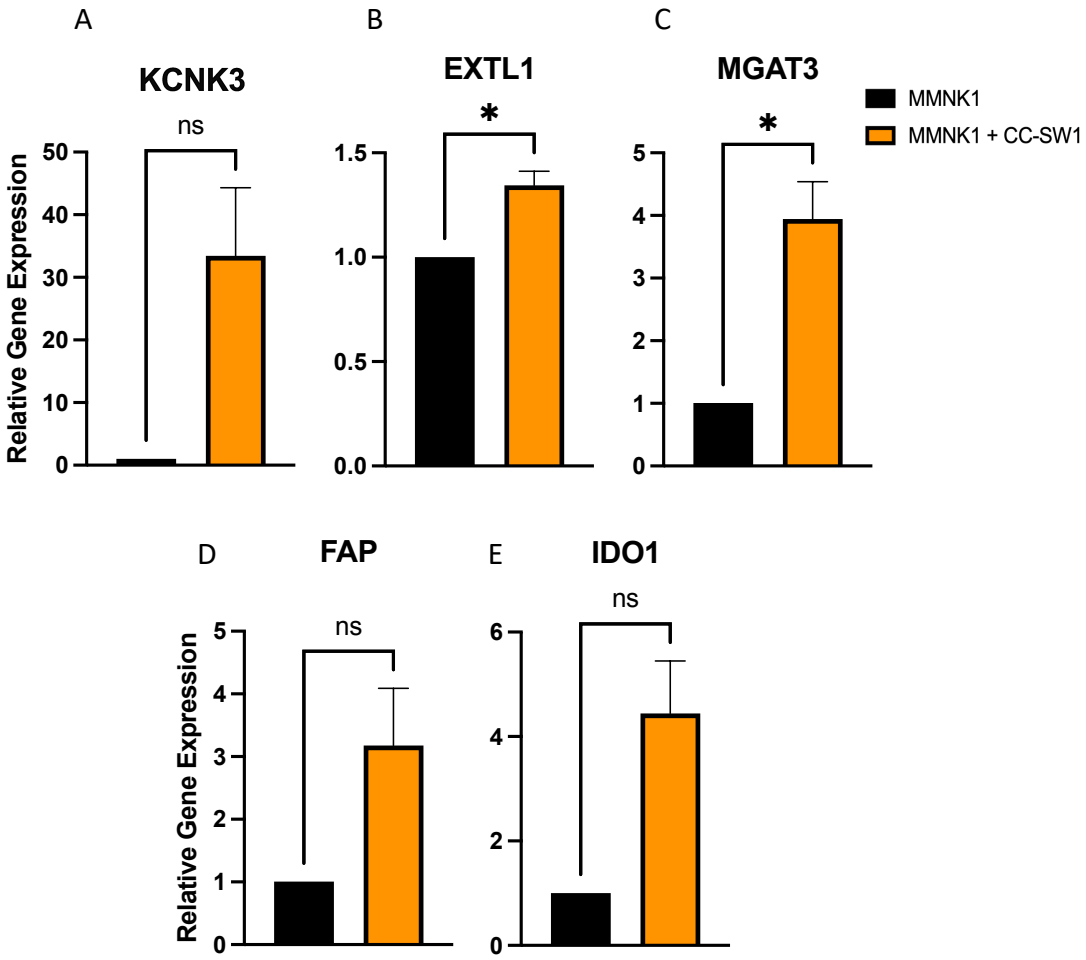


Figure 6:12 - qPCR validation of RNAseq gene expression exclusive to MMNK1 cholangiocytes. *MMNK1 cholangiocytes were cultured for 48 hours alone, or in indirect co-culture with CC-SW1 cells prior to RNA extraction. qPCR was used to evaluate gene expression levels of the target genes only expressed in MMNK1 cholangiocytes in the RNA-sequencing analysis, Panel 2, A) KCNK3, B) EXTL1, C) MGAT3, D) FAP, and E) IDO1, enabling the comparison of gene expression changes in MMNK1 cholangiocytes in monoculture and co-culture for genes exclusively expressed in MMNK1 cholangiocytes (*P<0.05)(n=3).*

We used Western Blotting to assess whether the change in gene expression in Panel 1 was reflected in the protein expression of our genes of interest. Evaluation of protein expression via Western Blotting showed signifcant global downregulation of protein expression for HSPA8, TXNIP, and TXN in co-culture (Figure 6:13).

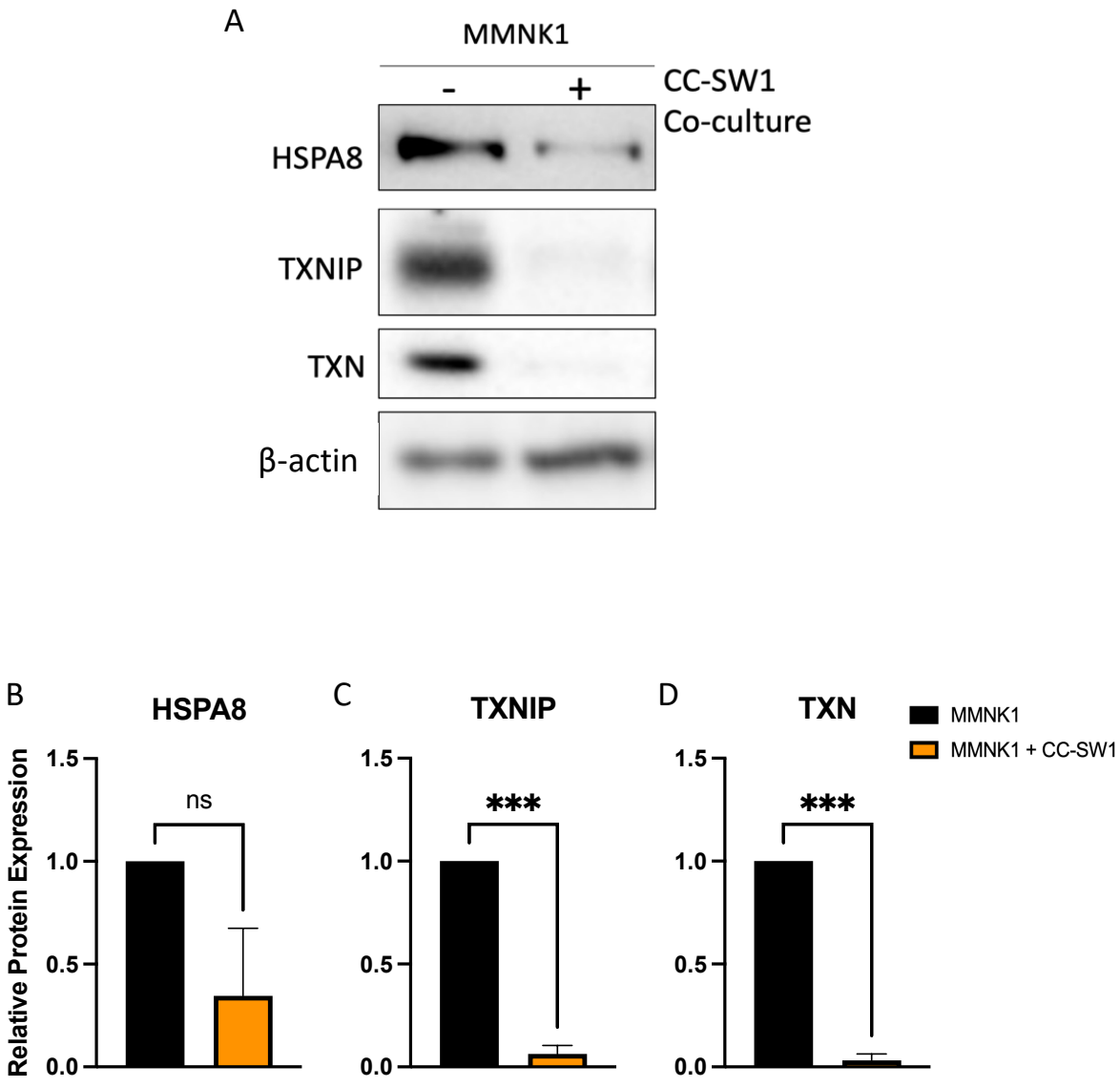


Figure 6:13 - Validation of HSPA8, TXNIP, and TXN protein expression*. MMNK1 cholangiocytes were cultured for 48 hours alone, and in indirect co-culture with CC-SW1 cells, prior to protein extraction. A) Evaluation of the protein expression of B) HSPA8, C) TXNIP, and D) TXN, relative to β-actin control, was conducted using Western Blotting. Quantification revealed a significant decrease in TXNIP and TXN protein expression during co-culture (P***<0.001)(n=3).*

6.4.2 siRNA knockdown of HSPA8

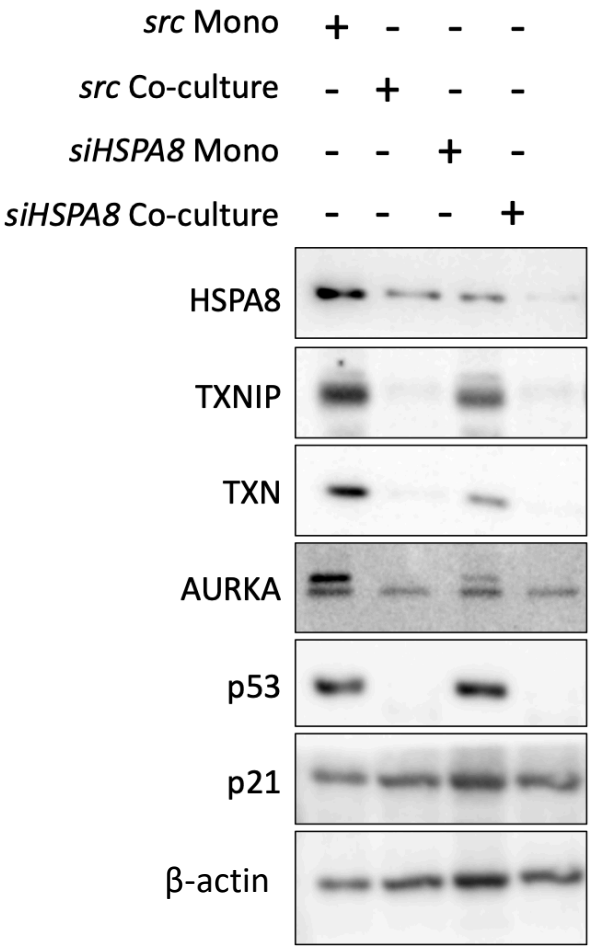
As the most differentially expressed gene in the G2M pathway in MMNK1 cells during co-culture as identified by the RNA-sequencing and validated by qPCR, we selected HSPA8 as our target of interest to knockdown using siRNA.

The knockdown of *HSPA8* was achieved using siRNA reversed transfection. Specifically, a pool of siRNAs targeting *HSPA8* mRNA was employed, ensuring robust and efficient gene silencing. The siRNAs were delivered into the MMNK1 cells using Lipofectamine™ RNAiMAX Transfection Reagent, allowing for effective cellular uptake. To maintain consistent knockdown levels, the siRNA was present for 12 hours, before the culture media refreshed. This duration was chosen to allow for sufficient time to observe the downstream effects of HSPA8 depletion on cellular processes. To control for non-specific effects of siRNA transfection, a scrambled siRNA (scr control) was used in parallel, ensuring that any observed changes were specifically attributed to the knockdown of HSPA8 and not a result of off-target effects or transfection-related artifacts.

siRNA knockdown of *HSPA8* in MMNK1 cells, led to responsive downregulation of HSPA8, TXNIP, TXN, AURKA, and p53 protein expression during monoculture, with no effect on p21 protein expression. The same pattern in downregulated protein expression was elicited when the siHSPA8 MMNK1 cells were grown in co-culture for HSPA8, TXNIP, TXN and p53, but with no effect on the protein expression of AURKA or p21 (Figure 6:14).

It is important to note however, that RNA turnover does not necessarily correlate with protein turnover, and as such our investigation into the function of HSPA8 requires more than just the transcriptional or protein level.

A


src Mono + - - -
src Co-culture - + - -
siHSPA8 Mono - - + -
siHSPA8 Co-culture - - - +
HSPA8
TXNIP
TXN
AURKA
p53
p21
β-actin

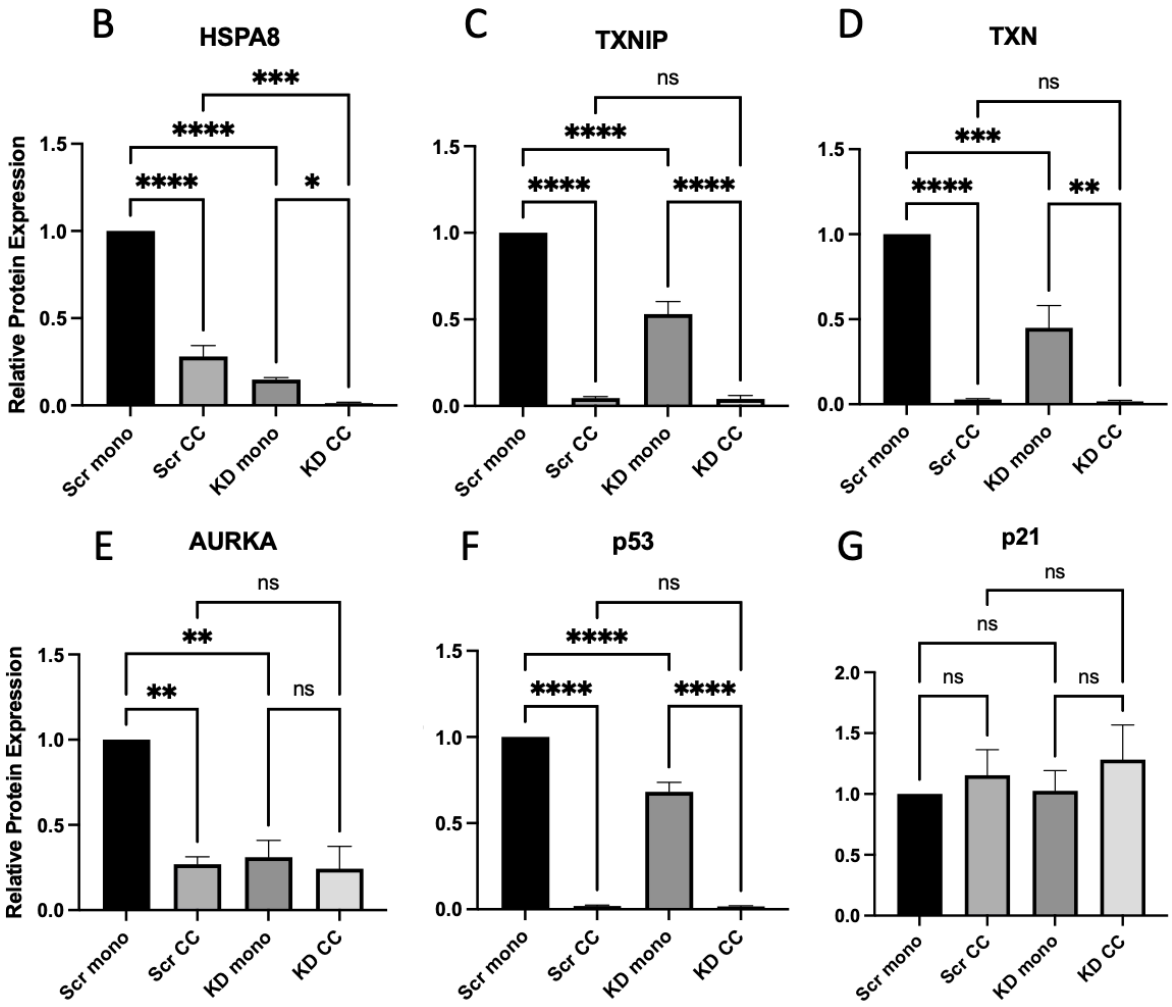


Figure 6:14 – Impact of HSPA8 knockdown on target protein expression in MMNK1 cholangiocytes. *A) Western blot analysis of MMNK1 lysates following HSPA8 knockdown (*siHSPA8*) compared to control (*Scr*) for cells in monoculture and indirect co-culture with CC-SW1 cells. Blotting was performed using antibodies against the target protein(s) of interest B) HSPA8, C) TXNIP, D) TXN, E) AURKA, F) p53, and G) p21. β-actin was used as a loading control. Quantification of protein expression levels are relative to protein expression levels for the monocultured control cells (Scr). Knockdown of HSPA8 led to a significant decrease in HSPA8, TXNIP, TXN, AURKA, and p53 in monocultured MMNK1 cholangiocytes. Data are presented as mean ± (SEM)(*P < 0.05, **P < 0.01,***P < 0.001,****P<0.0001)*

As demonstrated in Chapter 1 in our FACS cell cycle functional study, co-culture with CC-SW1 cells led to an increase in the proportion of MMNK1 cells in the G2M phase of the cell cycle, with no effect on the proportion of cells in the G1 or S phase. The RNA-sequencing data also demonstrated an enrichment in the gene expression for genes in the G2M checkpoint pathway. Therefore, we proceeded to recapitulate the role of HSP8A in governing the cell cycle in our co-culture model (Figure 6:15).

We see no difference (P=0.885) in the proportion of cells in the G1 phase between our control cells in monoculture *(scr Mono)* or in co-culture *(scr Co-Culture)*. We see a significant increase in the number of cells in the G1 phase in our knockdown cells during monoculture (*siHSPA8 Mono*) compared to our control cells in monoculture *(scr Mono)*(P<0.0001). Likewise, we see an increase in the number of cells in the G1 phase when comparing our knockdown cells in monoculture (*siHSPA8 Mono*) to those grown in co-culture (*siHSPA8 Co-Culture*)(P<0.0001). Co-culture of the knockdown cells (*siHSPA8 Co-Culture*) had a greater proportion of cells in the G1 phase than co-culture of our control cells *(scr Co-Culture)* (P<0.0001).

We see no difference (P=0.079) in the proportion of cells in the S phase between our control cells in monoculture *(scr Mono)* or in co-culture *(scr Co-Culture)*. We see a significant decrease in the number of cells in the S phase in our knockdown cells during monoculture (*siHSPA8 Mono*) compared to our control cells in monoculture *(src Mono)*(P<0.0001). Likewise, we see no difference (P=0.356) in the number of cells in the S phase when comparing our knockdown cells in monoculture (*siHSPA8 Mono*) to those grown in co-culture (*siHSPA8 Co-Culture*). Co-culture of the knockdown cells (*siHSPA8 Co-Culture*) had less cells in the S phase than co-culture of our control cells *(scr Co-Culture)* (P<0.0001).

We see a significant increase (P<0.0001) in the proportion of cells in the G2M phase comparing the control cells in monoculture *(scr Mono)* to co-culture *(scr Co-Culture)* as we would expect from our previous studies. We see a significant decrease in the number of cells in the G2M phase comparing our knockdown cells in monoculture (*siHSPA8 Mono*) to the control cells in monoculture *(scr Mono)*(P=0.0087). Unlike our usual co-culture system however, we see no significant difference (P=0.778) in the number of cells in the G2M phase comparing the knockdown cells in monoculture (*siHSPA8 Mono*) to those grown in co-culture (*siHSPA8 Co-Culture*). The co-cultured knockdown cells (*siHSPA8 Co-Culture*) had less cells in the G2M phase than the co-cultured our control cells *(scr Co-Culture)* (P=0.087).

In summary, knockdown of HSPA8 led to a reduction in the proportion of cells in the S and G2M phase of the cell cycle, and an increase the proportion of cells in the G1 phase. This effect was not recovered by co-culture, in-fact, co-culture contributed to a further reduction of the proportion of cells in the S and G2M phase of the cell cycle, and an increase in the proportion of cells in the G1 phase. We postulate this is due to the function of HSPA8 as a cyclin D1 binding protein. Cyclin D1-CDK4 is required for cell cycle G1/S transition via Rb inhibition, and HSPA8 has been shown to promote the stabilization of newly synthesized cyclin D1 and thereby increases its availability for association with CDK4, contributing to cell cycle progression (160). As such, knockdown of HSPA8 leads to a reduction in Cyclin D1-CDK4 complex formation, and the abrogation of cell cycle progression at the G1/S checkpoint.

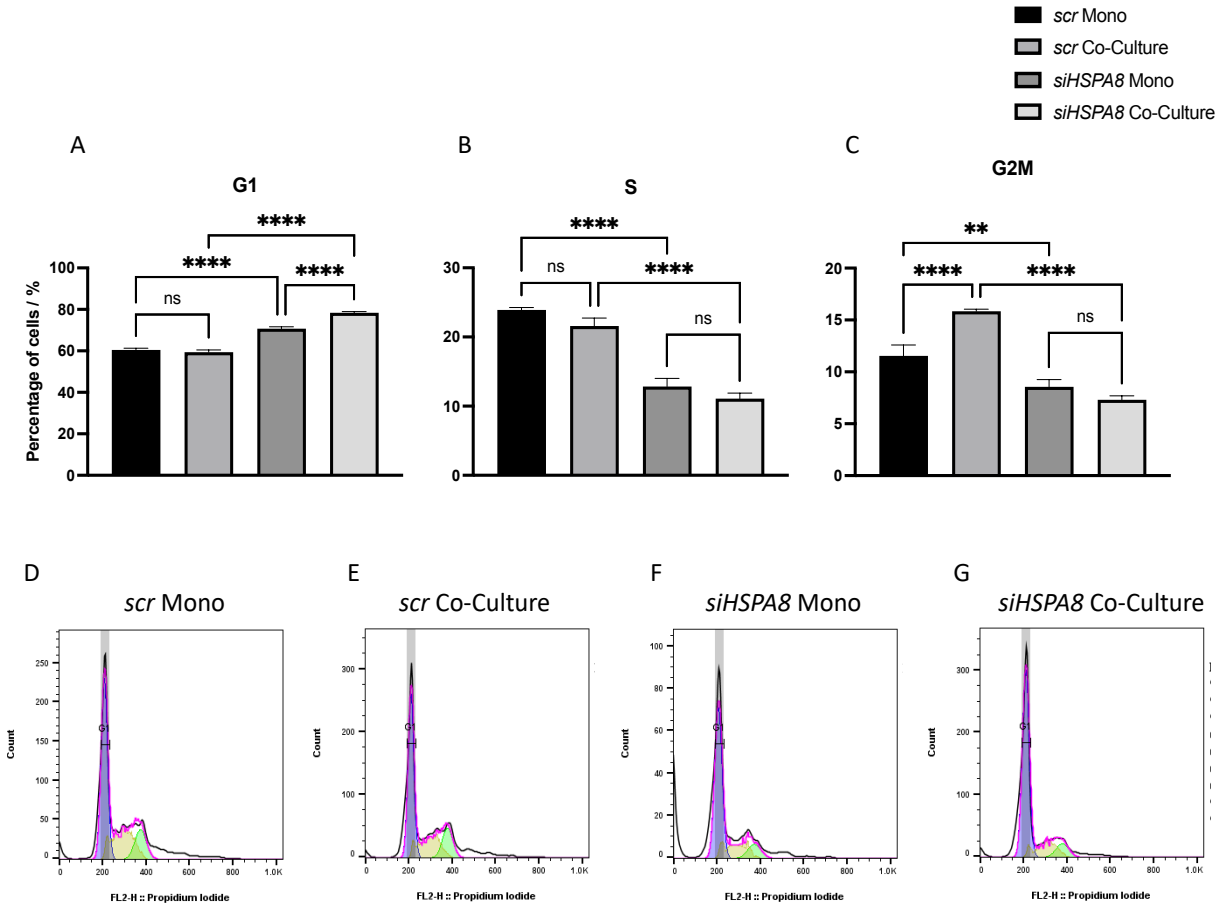


Figure 6:15 – Knockdown of HSPA8 leads to a reduction in cell cycle progression, irrecoverable by co-culture. *Quantitative analysis of the proportion of MMNK1 cholangiocytes in A) G1, B) S, and C) G2/M phases of the cell cycle, following HSPA8 knockdown and co-culture with CC-SW1 cells. Representative flow cytometry histograms depicting the distribution of MMNK1 cells in each cell cycle stage following D) control treatment (scr Mono), E) control co-culture (scr Co-Culture), F) HSPA8 knockdown in monoculture (siHSPA8 Mono) and G) HSPA8 knockdown during co-culture with CC-SW1 cells. The x-axis represents DNA content (propidium iodide staining), while the y-axis indicates cell count. FlowJo analysis colours cells in the G1 phase in purple, S phase in yellow, and G2M in green. Data are presented as mean ± (SEM)(**P < 0.01,****P<0.0001).*

Furthermore, as demonstrated in Chapter 1, MMNK1 cells co-cultured with CC-SW1 cells led to a decrease in the proportion of apoptotic MMNK1 cells, and an increase in the proportion of alive cells. The RNA-sequencing data also demonstrated a reduction in the gene expression for genes in the intrinsic apoptosis pathway. Therefore, we proceeded to investigate the role of HSP8A in governing apoptosis in our co-culture model (Figure 6:16).

There was no change in the proportion of necrotic cells in monoculture and co-culture for our control *(scr Mono* and *scr Co-Culture)* and knockdown *(siHSPA8 mono* and *scr Co-Culture)* cells.

There was a significant increase in the proportion of alive cells (Annexin V negative, PI negative) in co-culture of our control cells *(scr Mono* vs *scr Co-Culture)*(P=0.027). Likewise, there was also a significant increase in the proportion of alive cells in co-culture of our knockdown cells *(siHSPA8 mono* vs *siHSPA8 Co-Culture)*(P=0.027). Knockdown of *HSPA8* led to a decreased in the proportion of alive cells compared to the control cells *(scr mono* vs *siHSPA8 mono)*(P=0.0175). Interestingly, there was no signficant difference in the proportion of alive cells between our control cells and our knockdown cells during co-culture *(scr Co-Culture* vs *siHSPA8 Co-Culture)*(P=0.437).

There was a significant decrease in the proportion of cells undergoing early apoptosis in co-culture of our control cells *(scr Mono* vs *scr Co-Culture)*(P=0.0184). This decrease was not recapitulated during co-culture of the knockdown cells *(siHSPA8 mono* vs *siHSPA8 Co-Culture)*(P=0.663). Likewise, there was no signficant difference in the proportion of cells

undergoing early apoptosis between our control cells and our knockdown cells during monoculture *(scr mono* vs *siHSPA8 mono)*(P=0.373), as well as a non-signficant increase during co-culture *(scr Co-Culture* vs *siHSPA8 Co-Culture)*(P=0.0518).

There was a non-significant decrease in the proportion of cells undergoing late apoptosis in co-culture of our control cells *(scr Mono* vs *scr Co-Culture)*(P=0.465). Interestingly, this decrease was markedly greater during co-culture of the knockdown cells *(siHSPA8 mono* vs *siHSPA8 Co-Culture)*(P<0.0001). There was significantly more knockdown cells undergoing late apoptosis during monoculture than the control cells in monoculture *(scr mono* vs *siHSPA8 mono)*(P=0.0018), whilst there was no signficant difference between knockdown and control cells in co-culture *(scr Co-Culture* vs *siHSPA8 Co-Culture)*(P=0.267).

In summary, knockdown of *HSPA8* lead to a reduction in the proportion of alive cells, and an increase in the proportion of cells undergoing late apoptosis, which could be recovered by co-culture with CC-SW1 cells. This suggests that HSPA8 does not mediate the the apoptosis inhibition seen during co-culture.

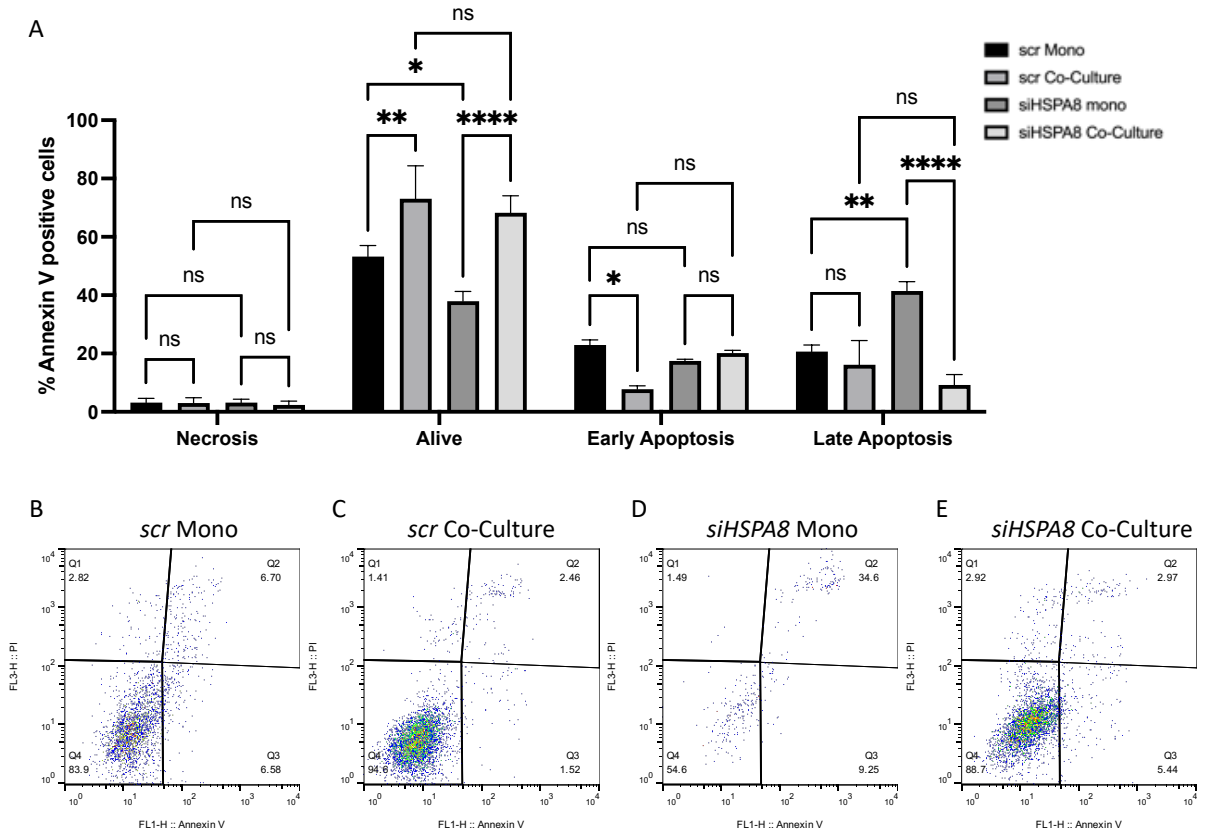


Figure 6:16 – Knockdown of HSPA8 leads to an increase in apoptosis, recoverable by co-culture. *A) Quantitative analysis of the percentage of early apoptotic, late apoptotic, viable, and necrotic MMNK1 cholangiocytes following HSPA8 knockdown and co-culture with CC-SW1 cells. Representative flow cytometry dot plots depicting the distribution of MMNK1 cells in each apoptotic stage following D) control treatment (scr Mono), E) control co-culture (scr Co-Culture), F) HSPA8 knockdown in monoculture (siHSPA8 Mono) and G) HSPA8 knockdown during co-culture with CC-SW1 cells. The x-axis represents Annexin V staining, while the y-axis indicates Propidium Iodide staining. Each cell is indicated by a dot. The data revealed that knockdown of HSPA8 leads to an increase MMNK1 cholangiocyte apoptosis, which recoverable by indirect co-culture with CC-SW1 cells. Data are presented as mean ± (SEM)(*P<0.05,**P < 0.01,****P<0.0001)(n=3).*

6.5 Validation of Cytokine Secretion

As demonstrated previously, (Chapter 2, Figure 5:47), co-culture resulted in a significant change to the concentration of cytokines MMNK1 cholangiocytes were exposed to. We selected to evaluate whether the change in cytokine expression was due to a co-culture mediated change to cytokine gene expression and as such whether it could be recapitulated at the gene level, or whether it could be attributed to secretion by CC-SW1 CCA cells. As such, we used the RNA-sequencing gene expression data to investigate the gene expression of cytokines detected in the cytokine assay in MMNK1 cells during co-culture. Figure 6:17 shows a table of relative cytokine gene expression for MMNK1 cells in co-culture, as detected by RNA-sequencing. There was a significant increase in the gene expression of *IL-6R, MCP-1,* and *CCL5* in MMNK1 cells during co-culture, with a concurrent decrease in the gene expression of *CXCL2, CXCL3, IL-6, IL-8,* and *VEGF* (Figure 6:17). There was no change in the expression of *CXCL1, IL-7R,* and *HIF1A* in CC-SW1 cells during co-culture as detected by RNA-sequencing. The gene expression of *IL-7* was not detected.

The gene expression of *CXCL1, CXCL2, CXCL3, IL-6, VEGFA,* and *HIF1A* was then validated by qPCR; Figure 6:17 shows qPCR data for 6 selected cytokines genes. In agreement with the RNA-seq data, there was a statistically significant decrease in *CXCL3* (P=0.0016) and *VEGF-A* (P= 0.0114). Likewise, there was no significant change in *CXCL1* and *HIF1A* expression (P=0.1042, and 0.2635 respectively). There was a decrease in trend in *CXCL2* (P=0.0510) and *IL-6* (P= 0.0612) expression, in agreement with the RNA-seq.

As show in Figure 5:47, MMNK1 cells were exposed to a greater concentration of CXCL1 and GRO a/b/g during co-culture. Both RNA-sequencing and PCR validation confirmed no

significant change in *CXCL1* gene expression in MMNK1 cells, with a significant decrease in *CXCL2* and *CXCL3* gene expression. This further supports our hypothesis that the increased exposure of MMNK1 cells to these 3 cytokines is due to secretion by the CC-SW1 compartment.

The RNA-sequencing identified a significant decrease in *IL-6* expression, and this trend was echoed in the qPCR validation. As show in Figure 5:47, MMNK1 cells were exposed to a reduction in IL-6 protein concentration, likely in part due to the reduction in gene expression seen here.

Whilst *MCP-1* and *CCL5* gene expression was not validated by qPCR, RNA-seq analysis revealed a significant increase in expression (Figure 6:17), contradictory to the decrease in both MCP-1 and CCL5 protein expression seen in Figure 5:47. This is potentially the mark of a compensatory mechanism to recover protein expression levels, potentially due to sequestering by CC-SW1 cells, and therefore requires the evaluation of the CC-SW1 gene expression.

There was no significant change in protein concentration of *VEGF* in MMNK1 cells, however RNA-sequencing and qPCR validation confirmed a significant decrease in *VEGF* gene expression. It perhaps stands that this alteration to gene expression is early enough to be detected without a knock-on effect on cellular protein levels, or this protein component is supplemented by CC-SW1 secretion.

A

Cytokine	Log_2FoldChange	Padj	Name
CXCL1	0.77279602	0.62978071	No change
CXCL2	-1.637168043	2.34E-09	Decrease
CXCL3	-1.157998473	5.35E-06	Decrease
IL-6	-0.551895715	0.00846325	Decrease
IL-6R	0.394309044	0.00206331	**Increase**
IL-7	ND	ND	Not Detected
IL-7R	0.144810663	0.08017954	No change
MCP-1	1.499213666	3.43E-09	**Increase**
IL-8	-0.933541286	4.17E-06	Decrease
CCL5	0.404642297	3.20E-05	**Increase**
HIF1A	-0.100690794	0.24906602	No change
VEGF	-2.031020946	6.30E-132	Decrease

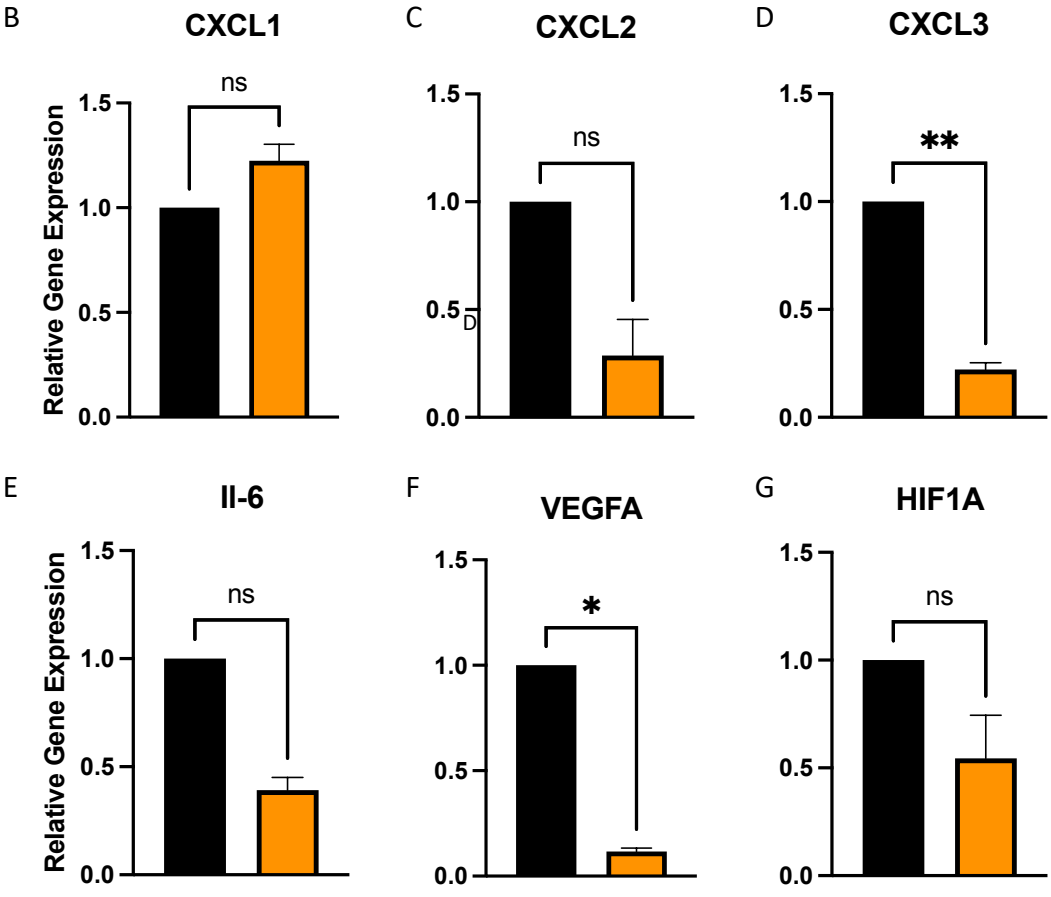


Figure 6:17 - RNA-based validation of co-culture mediated alterations to MMNK1 cytokine expression during co-culture. *A) We evaluated the RNA-sequencing data MMNK1 cholangiocytes in co-culture with CC-SW1 cells for the gene expression of our cytokines of interest. The table lists the significance value, Log_2FC, and the direction of expression change during co-culture. qPCR validation of a panel of six cytokines: B) CXCL1, C) CXCL2, D) CXCL3, E) Interleukin-6, F) VEGF-A, and G) HIF1A, was conducted. Gene expression is displayed relative to the gene expression of the β-actin control.(P*<0.05, P**<0.01).*

6.6 Integrating cholangiocyte metabolomic and genomic data

We chose to utilise the RNA-sequencing data to evaluate firstly, changes to the gene expression responsible for metabolism, and secondly the reciprocity of metabolome changes on genomic changes. As we highlighted earlier in the evaluation of KEGG gene sets (Figure 6:10), co-culture triggered a significant downregulation in the gene expression of genes in the Glycine-Serine-Threonine, and the Alanine-Aspartate-Glutamate metabolic pathways. Therefore, we integrated the 2 -omics datasets, transcriptomics and metabolomics, to elucidate metabolic pathway alterations likely due to genomic expression changes.

6.6.1 Joint-Pathway Analysis highlights increased TCA cycle

The joint pathway analysis tool from MetaboAnalyst integrates information from gene expression profiles (transcriptomic data) and metabolite profiles (metabolomic data) simultaneously, to identify coordinated changes and interactions between genes and metabolites. Specifically, we utilised the fold changes in metabolite concentration in combination with the fold changes in gene expression, and selected to evaluate only metabolic pathways. This method takes into account the interconnected nature of metabolic pathways, and identifies significant perturbations that may not be apparent when considering individual metabolites in isolation. Each pathway is ranked top to bottom according to significance ($-Log_{10}P$) and listed in Figure 6:18, with the relative pathway impact indicated by the size of the bar. The TCA cycle metabolic pathway had the greatest Pathway Impact, followed by purine and pyrimidine metabolism, whilst arginine biosynthesis followed by glycolipid biosynthesis had the most significant impact. The Pantothenate and CoA biosynthesis, Taurine and hypotaurine metabolism, and Neomycin,

kanamycin and gentamicin biosynthesis pathways were identified in MMNK1 samples, not CC-SW1 samples.

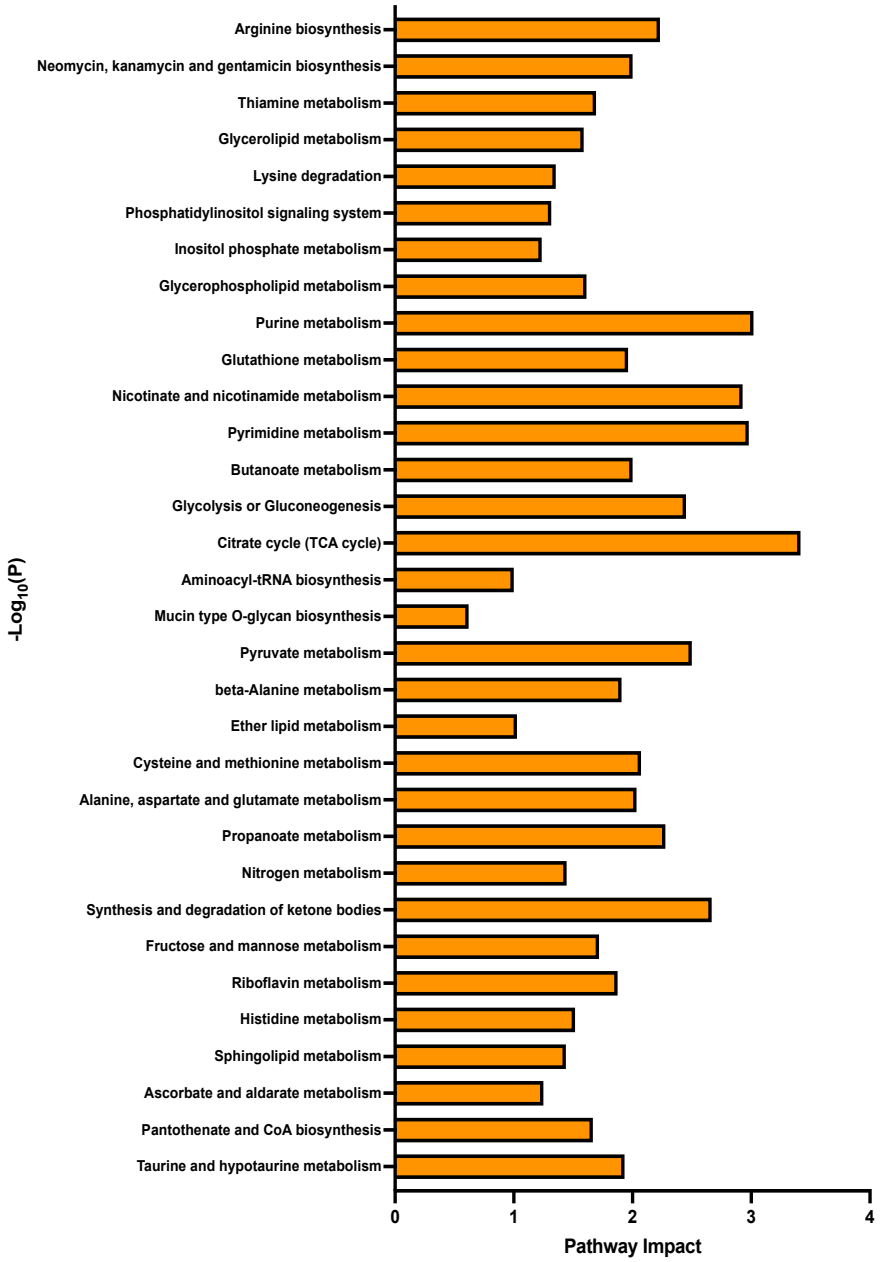


Figure 6:18 – Integrating MMNK1 metabolomic and RNAseq data. The histogram displays the metabolic pathways based on the KEGG database, enriched in MMNK1 cholangiocytes after 48 hours of co-culture with CC-SW1. The integration involved combining the metabolite concentrations from the metabolomic analysis, with the gene expression data from the RNA-sequencing analysis. Each row represents a KEGG metabolic pathway, with the length of the bar equivalent to the pathway impact. Pathways are ranked by signficance ($-Log_{10}P$); the most most signifcantly enriched pathway was arginine biosynthesis.

6.6.2 Evaluation of metabolic-associated genes

During the metabolomic analysis, we identified changes to the concentration of metabolites in MMNK1 cells during co-culture, and in the transcriptomic analysis we identified changes to gene expression in MMNK1 cells during co-culture. We then proceeded to use the transcriptomic data to evaluate the changes in the gene expression of genes linked to specific metabolites identified via metabolomic analysis.

6.6.2.1 Asparagine metabolism related Gene Expression

As highlighted previously, aspartate concertation was significantly reduced in MMNK1 cells during co-culture (Figure 5:15), and exogenous supplementation of asparagine could increase MMNK1 cell viability and migration (Figures 5:18 and 5:19). We hypothesised that the decrease in aspartate concentration was due to increased demand for asparagine, leading to improved cholangiocyte viability. Therefore, we chose to investigate whether the change in aspartate/asparagine metabolism was due to co-culture induced gene expression changes of genes in the aspartate/asparagine metabolic pathway (see Figure 6:19).

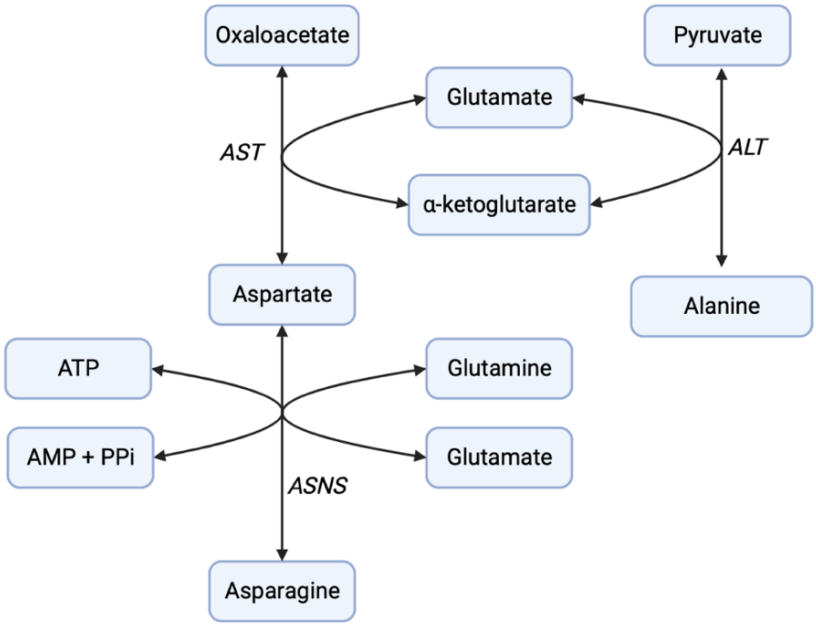


Figure 6:19 – Schematic of the asparagine metabolic pathways. *Asparagine can be synthesized de novo within cells, in an ATP-dependent process catalysed by the enzyme ASNS. This pathway starts with the conversion of oxaloacetate to aspartate by AST, which uses glutamate as an amino group donor. Glutamate can be produced during the reversible transamination of alanine to pyruvate by the enzyme ALT. In the final ATP-dependent step, aspartate amidated to asparagine by ASNS, using glutamine as an amine donor. AST = Aspartate Aminotransferase, ALT= Alanine Aminotransferase, ASNS = Asparagine Synthetase.*

Asparagine Synthetase (*ASNS*) encodes the enzyme responsible for the conversion of cellular aspartate to asparagine (Figure 6:19). The RNA-sequencing data demonstrated co-culture caused a reduction in *ASNS* gene expression with a Log2FoldChange of -3.1 and a P-value of 1.88E-58 (Figure 6:20A). We validated this using qPCR and found a significant decrease in the gene expression of *ASNS* (P=0.0112)(Figure 6:20B).

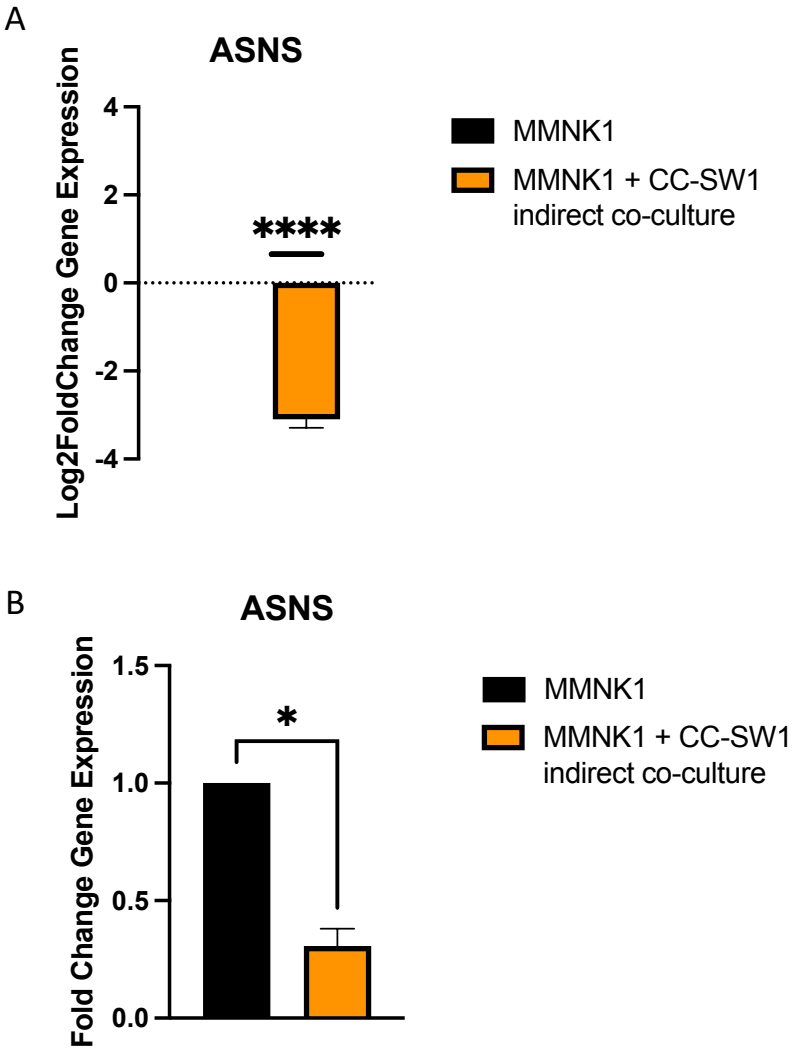


Figure 6:20 - Gene expression of ASNS in co-culture**. MMNK1 cholangiocytes were cultured for 48 hours alone, or in indirect co-culture with CC-SW1 cells prior to RNA extraction. A) Evaluation of ASNS gene expression in MMNK1 cells during co-culture using the RNA-seq data revealed a significant decrease in gene expression. B) qPCR was use to validate the gene expression of ASNS, which revealed a significant decrease in gene expression(*P<0.05,*P<0.0001)(n=3).*

We employed immunoblotting to assess whether the change in *ASNS* gene expression during co-culture had an impact on the corresponding protein levels. As shown by the blot in Figure 6:21A, co-culture resulted in a significant (P<0.05) decrease in ASNS protein expression (Figure 6:21B).

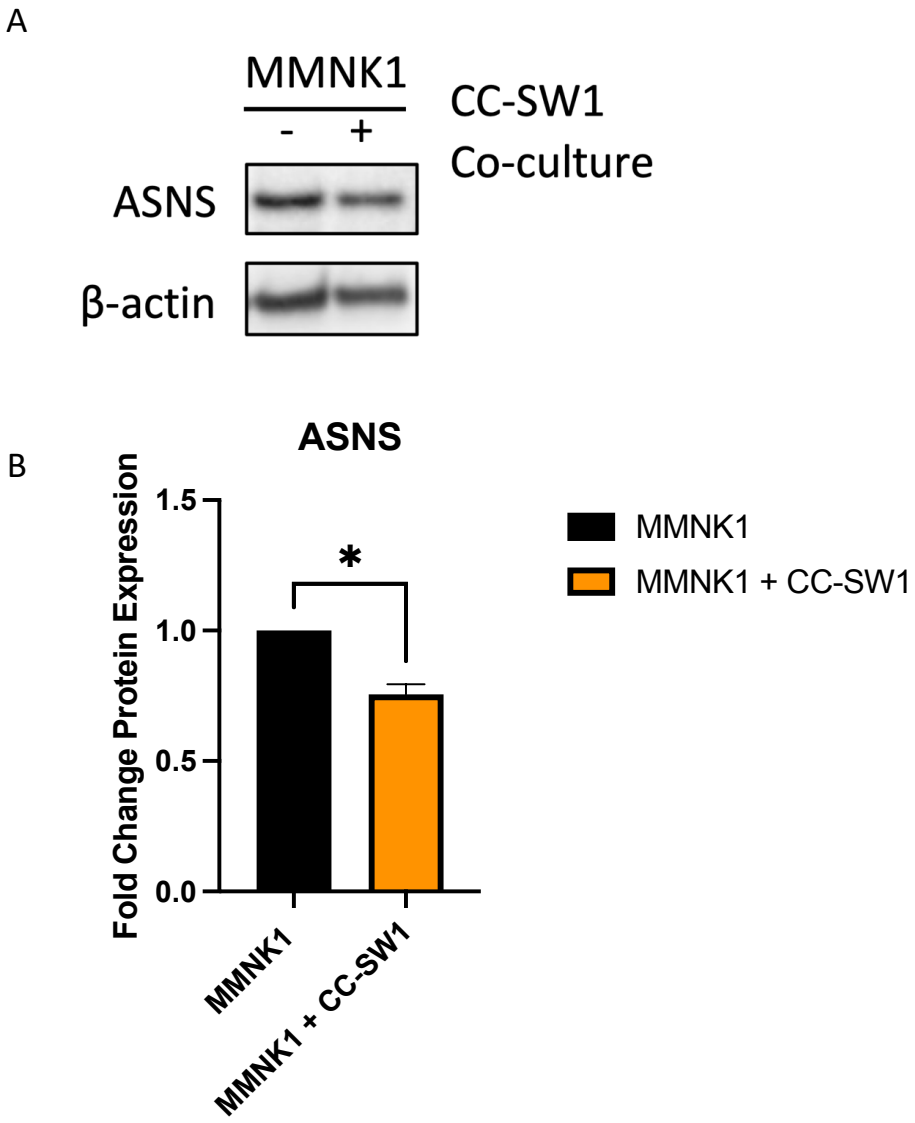


Figure 6:21 - Protein expression of ASNS in co-culture. *MMNK1 cholangiocytes were cultured for 48 hours alone, and in indirect co-culture with CC-SW1 cells, prior to protein extraction. Evaluation of the protein expression of ASNS relative to β-actin control, was conducted using A) Western Blot, and B) quantification revealed a significant decrease in ASNS protein during co-culture(P*<0.05)(n=3).*

We proceeded to investigate whether the dose-dependent improvement in cholangiocyte viability by exogenous asparagine was due to a dose-dependent increase in ASNS protein expression. As such, we used immunoblotting to evaluate ASNS protein expression after treatment with various doses of exogenous asparagine (Figure 6:22A). Exogenous doses of asparagine caused a statistically significant decrease in ASNS protein expression at 0.01 mM (P=0.0010), 0.10 mM (P=0.0003), and 1.00mM (P=0.0005)(Figure 6:22B).

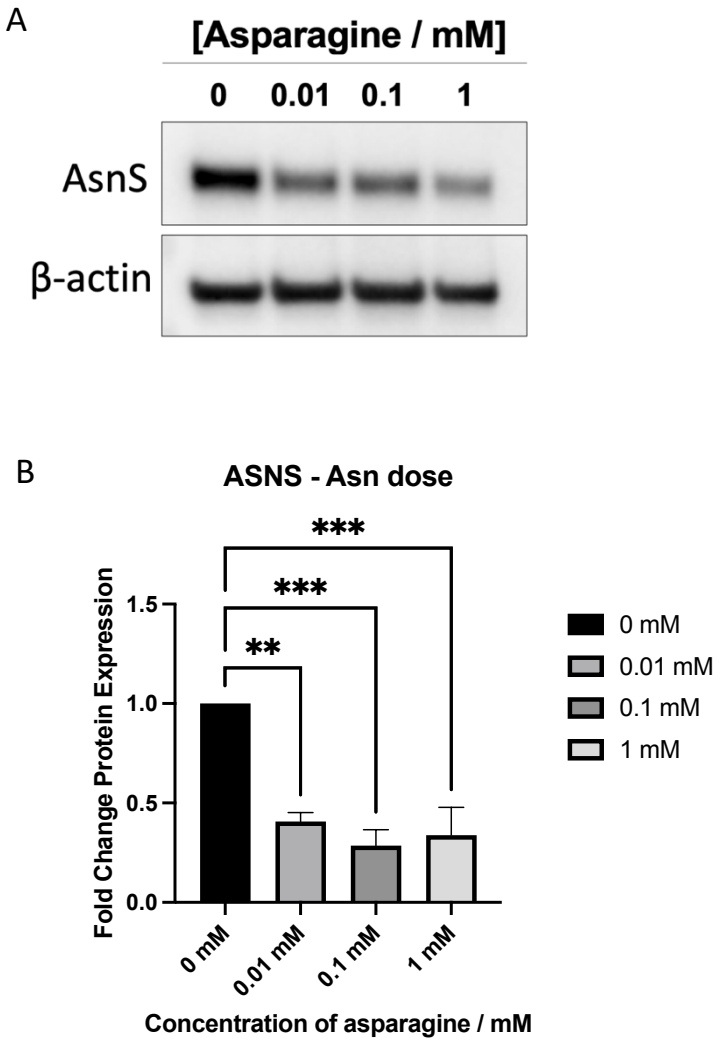


Figure 6:22 - Exogenous asparagine reduces ASNS protein expression*. MMNK1 cholangiocytes were cultured for 48 hours with 0, 0.01, 0.10, and 1.00 mM of exogenous asparagine, prior to protein extraction. Evaluation of the protein expression of ASNS, relative to β-actin control, was conducted using A) Western Blot, and B) quantification revealed a significant decrease in ASNS protein expression after treatment with 0.01, 0.10, and 1.00 mM of exogenous asparagine (*P<0.05,**P<0.01)(n=3).*

6.6.2.2 Choline metabolism related Gene Expression

As highlighted previously, choline concentration was significantly increased in MMNK1 cells during co-culture (Figure 5:15), and exogenous supplementation of choline could decrease MMNK1 cell viability (Figure 5:20). We chose to investigate whether the change in choline concentration was due to changes in the expression of genes in the choline metabolic pathways (see Figure 6:23).

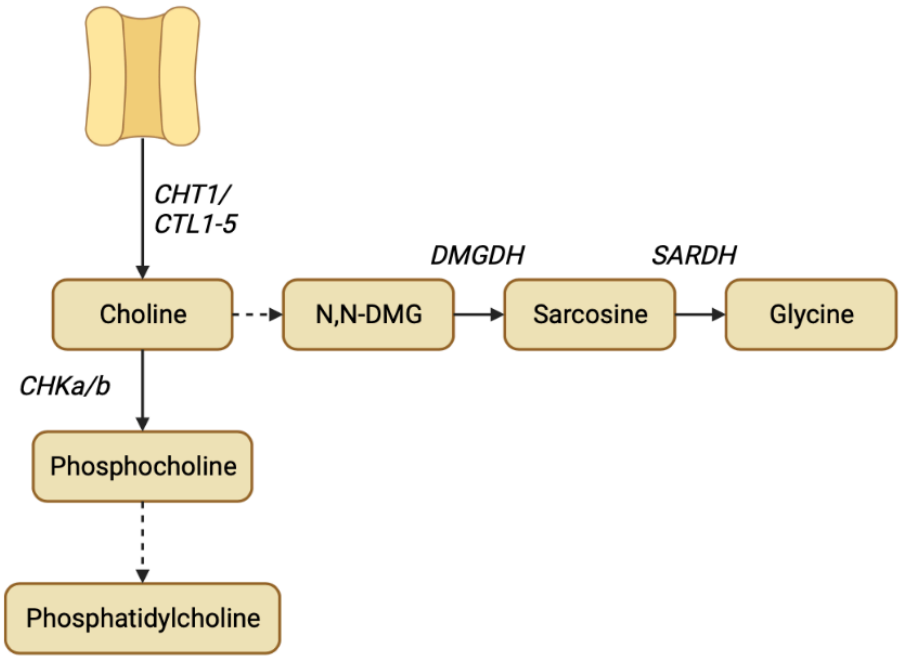


Figure 6:23 – Schematic of the choline metabolism. *Choline enters the cell via various choline transporters such as CHT1, and CTL1-5. Inside the cell, choline is first phosphorylated to form phosphocholine by CHKα/β phosphorylates. Phosphatidylcholine is formed from phosphocholine through a series of biochemical reactions known as the Kennedy pathway. Choline also acts as the precursor to glycine, via conversion to, DMG, and sarcosine via DMGDH and SARDH. CHT1= High-affinity Choline Transporter, CTL1-5= Choline Transporter-Like Protein 1-5, CHKα/β= Choline Kinase Alpha/Beta, DMG=Dimethylglycine, DMGDH= Dimethylglycine Dehydrogenase, SARDH= Sarcosine Dehydrogenase.*

The expression of the genes *CHKA* (CHKα) and *CHKB* (CHKβ), from the phosphatidylcholine biosynthesis pathway (Figure 6:23), as well as the choline uptake transporters (Figure 6:23) *SLC44A1* (CTL1), *SLC44A2* (CTL2), *SLC44A3* (CTL3), and *SLC44A4* (CTL4) were assessed in our RNA-sequencing data. There was a statistically significant increase in gene expression of *CTL1* (SLC44A1) P=0.00013, and *CTL3* (SLC44A3) P=0.0073 during co-culture (Figure 6:24).

We validated the expression of these genes, in addition to *CHT1* (SLC5A7) and *CTL5* (SLC44A5), using qPCR. Co-culture caused a significant increase in the gene expression of *CHK*α (P=0.0006), *CHK*β (P=0.0001), *CTL3* (P<0.0001), *CTL4* (P=0.0171), and *CTL5* (P<0.0001)(Figure 6:25). The profile of gene expression as detected by qPCR was only the same for *CTL3* (SLC44A3).

A

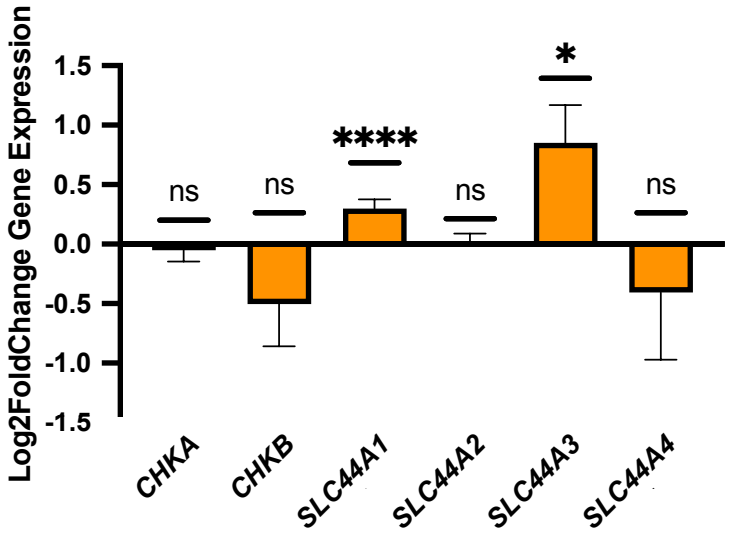


Figure 6:24 - Evaluation of choline metabolism gene expression via RNA-seq*. MMNK1 cholangiocytes were cultured for 48 hours alone, or in indirect co-culture with CC-SW1 cells prior to RNA extraction. Evaluation of the RNA-seq data for the gene expression of genes pertaining to choline metabolism revealed a significant increase in* SLC44A41 *and* SLC44A3 *gene expression (*P<0.05,****P<0.0001).*

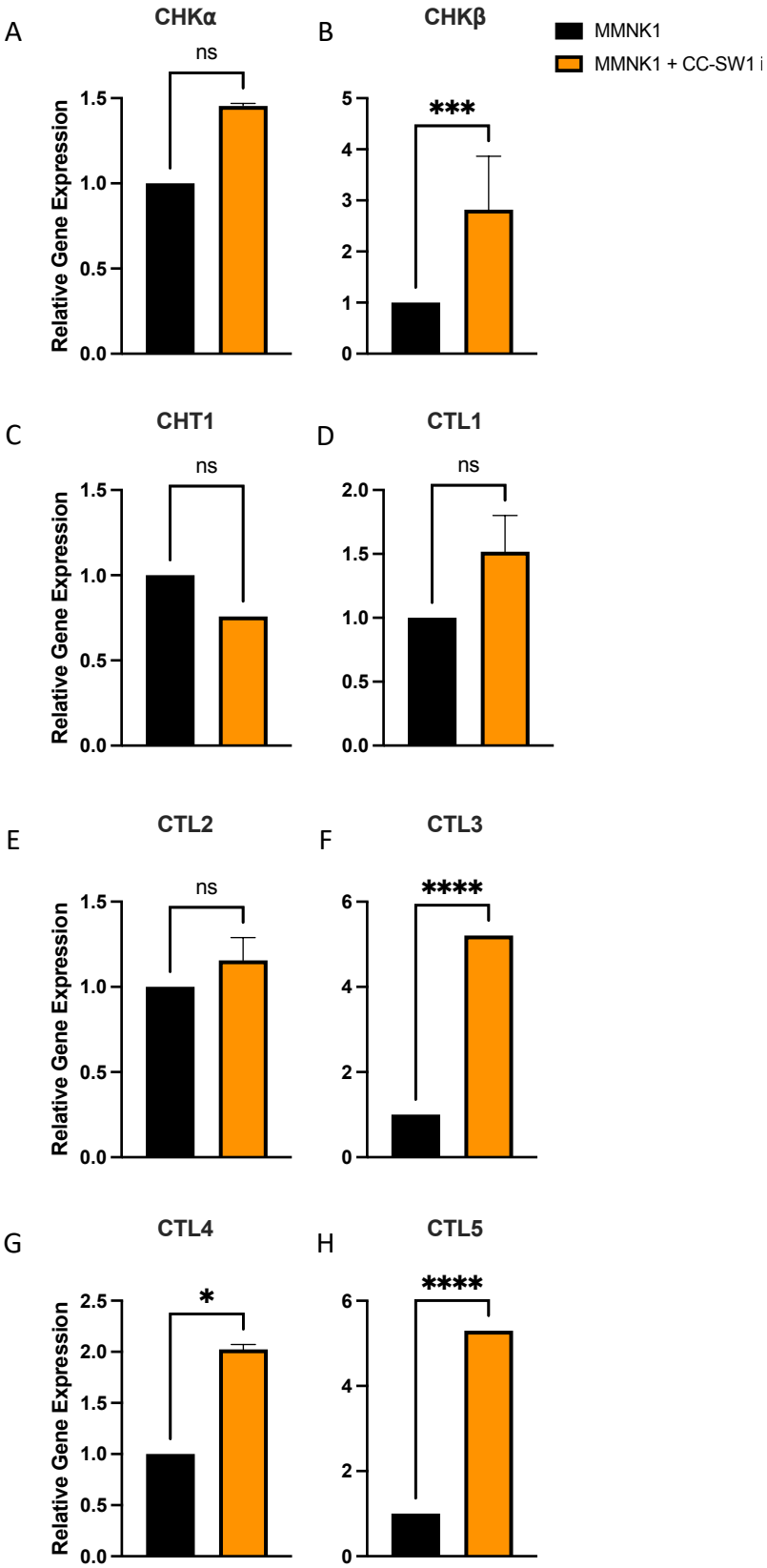


Figure 6:25 - Co-culture increases gene expression for choline metabolism*. MMNK1 cholangiocytes were cultured for 48 hours alone, or in indirect co-culture with CC-SW1 cells prior to RNA extraction. qPCR was used to validate the gene expression of A)* CHKα, *B)* CHKβ, *C)* CHT1, *D)* CTL1, *E)* CTL2, *F)* CTL3, *G)* CTL4, and *H)* CTL5*. Analysis of the qPCR revealed a significant increase in* CHKβ, CTL3, CTL4, *and* CTL5 *gene expression in MMNK1 cholangiocytes during co-culture(*P<0.05,***P<0.001,****P<0.0001)(n=3).*

We employed immunoblotting to assess whether the change in *CHKα* gene expression during co-culture had an impact on the corresponding protein level. As shown by the blot in Figure 6:26A, co-culture resulted in a significant (P=0.0230) decrease in CHKα protein expression (Figure 6:26B).

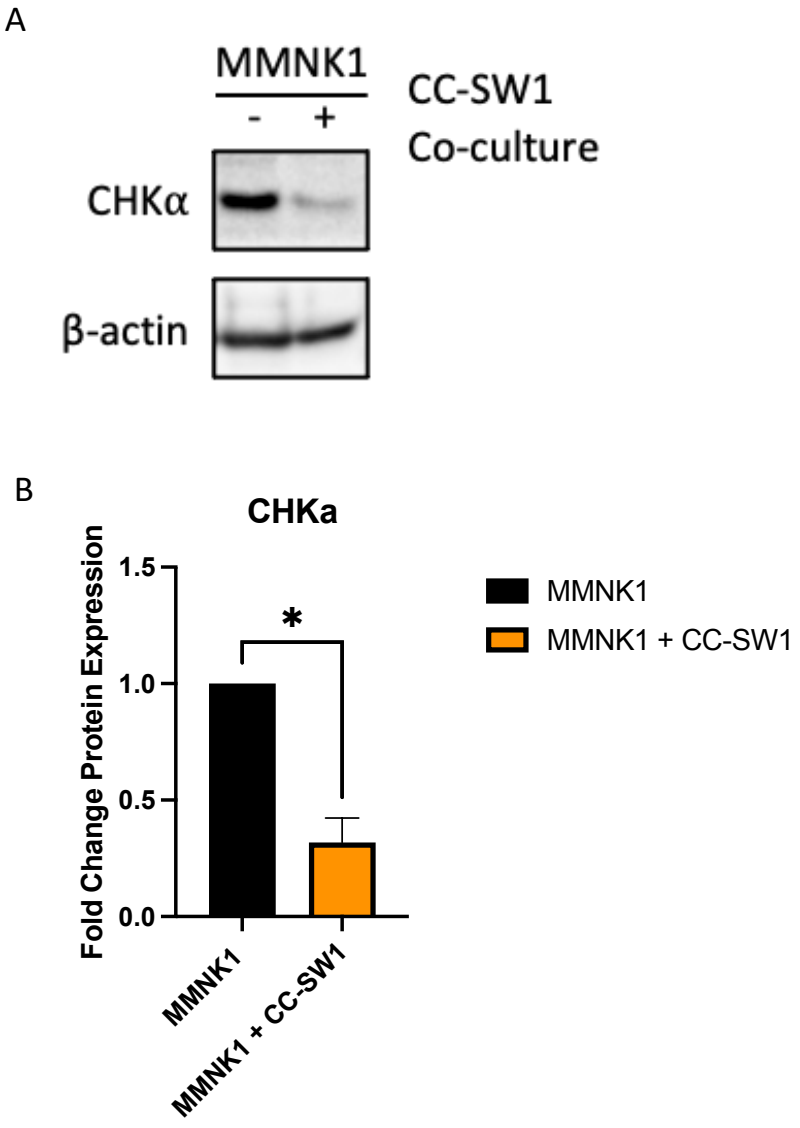


Figure 6:26 - Co-culture decreases CHKα protein expression*. MMNK1 cholangiocytes were cultured for 48 hours alone, and in indirect co-culture with CC-SW1 cells, prior to protein extraction. Evaluation of the protein expression of CHKAα, relative to β-actin control, was conducted using A) Western Blot, and B) quantification revealed a significant decrease in CHKAα, protein expression during co-culture(P*<0.05)(n=3).*

We proceeded to investigate whether the dose-dependent reduction in cholangiocyte viability by exogenous choline was due to a dose-dependent decrease in CHKα protein expression. As such, we used immunoblotting to evaluate CHKα protein expression after treatment with various doses of exogenous choline (Figure 6:27A). Exogenous doses of 2, 20, and 40 µM of choline caused a non-significant increase in CHKα protein expression (P=0.7041, 0.3543, and 0.3408 respectively)(Figure 6:27B).

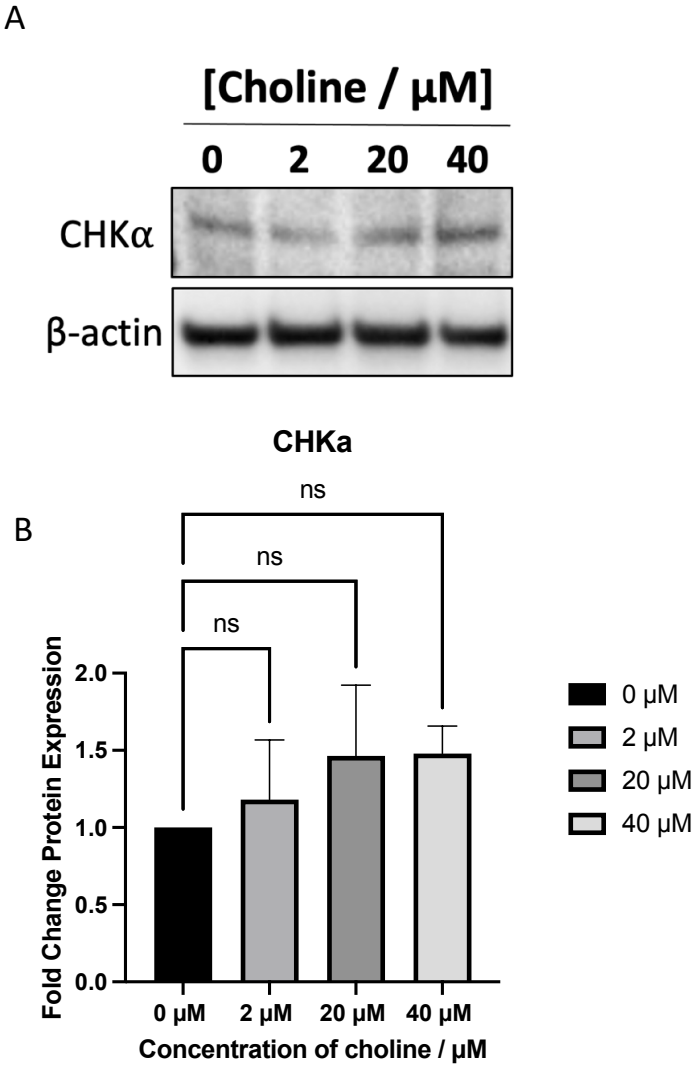


Figure 6:27 - Exogenous choline decreases CHKα protein expression. *MMNK1 cholangiocytes were cultured for 48 hours with 0, 2, 20, and 40 µM of exogenous choline, prior to protein extraction. Evaluation of the protein expression of CHKAα, relative to β-actin control, was conducted using A) Western Blot, and B) quantification revealed no significant difference in CHKAα protein expression after treatment with exogenous choline(ns, P>0.05)(n=3).*

6.6.2.3 Creatine metabolism related Gene Expression

As highlighted previously, creatine concentration was significantly increased in MMNK1 cells during co-culture (Figure 5:15), and exogenous supplementation of creatine could improve MMNK1 cell viability and ATP availability (Figures 5:24 and 5:28). We hypothesised that the increase in creatine concentration was due to increased *de novo* synthesis, and this promoted the creation of phosphocreatine as an energy store, permitting an increase availability of ATP and thereby improving cholangiocyte viability. Therefore we chose to investigate whether the change in creatine metabolism was due to a co-culture induced change in the gene expression of genes in the creatine metabolic pathways (see Figure 6:28).

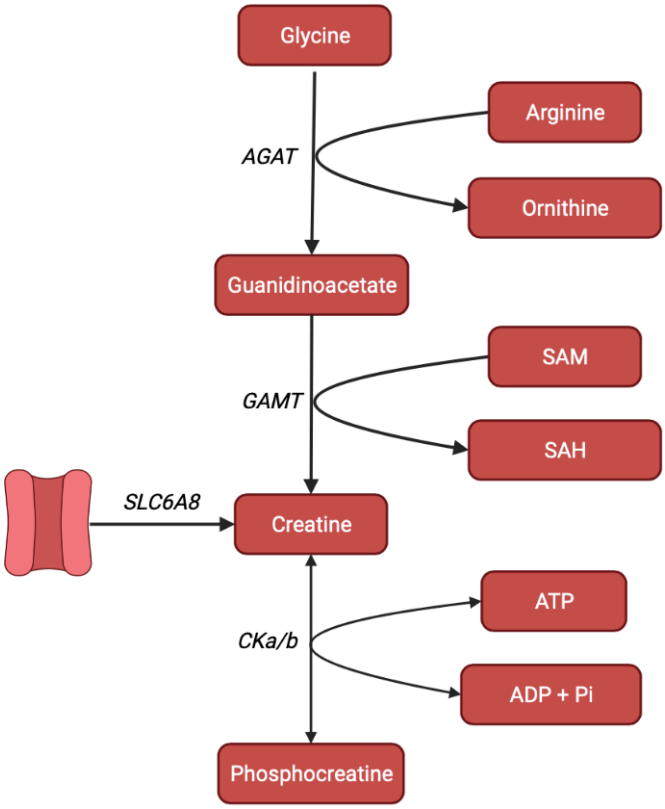


***Figure 6:28 – Schematic of the creatine metabolic pathway**. The first step in de novo creatine synthesis occurs in the liver and kidneys. GAMT catalyses the transfer of a methyl group from S-adenosylmethionine (SAM) to guanidinoacetate. This enzyme reaction forms creatine and S-adenosylhomocysteine (SAH). Guanidinoacetate can be formed from glycine via AGAT. Creatine can also be transported into cells via SLC6A8. Creatine is phosphorylated by creatine kinase using ATP to form creatine phosphate (PCr). This reaction is reversible, and PCr serves as a high-energy phosphate reservoir. SLC6A8 = Sodium-And Chloride-Dependent Creatine Transporter 1, SAM= S-adenosylmethionine, SAH = S-adenosylhomocysteine, AGAT = Arginine:glycine amidinotransferase, GAMT = Guanidinoacetate methyltransferase,CK$\alpha\beta$ = Creatine kinase alpha/beta.*

The expression of *GAMT*, the final enzyme in the *de novo* synthesis of creatine from glycine, *SLC6A8*, the extracellular creatine transporter, and Creatine Kinase B (*CKB*), the enzyme responsible for phosphorylation of creatine forming the phosphorous store used for the production of ATP phosphocreatine, was significantly increased during co-culture, as detected by RNA-sequencing (Figures 6:29)

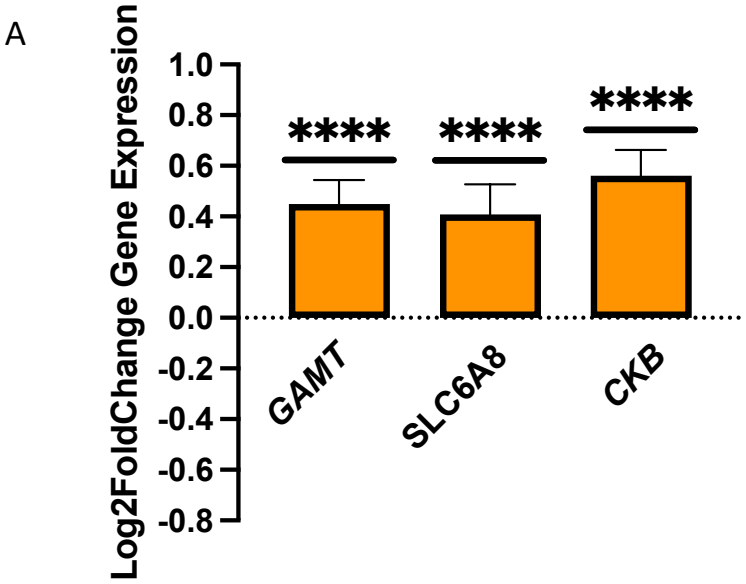


Figure 6:29 - RNAseq evaluation of creatine metabolism gene expression. *MMNK1 cholangiocytes were cultured for 48 hours alone, or in indirect co-culture with CC-SW1 cells prior to RNA extraction. Evaluation of the expression of the creatine metabolism genes* GAMT, SLC6A8, *and* CKβ *in MMNK1 cells during co-culture using the RNA-seq data revealed a significant increase in gene expression expression(****P<0.0001).*

6.6.2.4 Exogenous Creatine Modulated MMNK1 Gene Expression

In order to evaluate the metabolome-genome reciprocal axis, we then chose to investigate whether exogenous creatine could modulate MMNK1 gene expression in a dose-dependent manner. We therefore dosed MMNK1 cholangiocytes with 1, 2.5, and 5 mM of exogenous creatine, and evaluated the change in gene expressoin in our gene panel of interest (*KCNK3, EXTL1, IDO1, MGAT3,* and *FAP*) identifed by RNA-sequencing (see Figure 6:30). Exogenous creatine had no significant effect on the gene expression of *KCNK3* (P=0.9914, 0.7514, and 0.4039 respectively). Creatine concentrations of 1 mM and 2.5 mM caused a significant decrease in *EXTL1* gene expression (P=0.0030, and 0.0151 respectively) whilst a concentration of 10 mM had no significant effect on the gene expression of *EXTL1* (P=0.5859). Similarly, a creatine concentration of 1 mM caused a significant decrease in *IDO1* gene expression (P=0.0028) whilst 2.5 and 5.0 mM had no significant effect on gene expression (P=0.3853 and 0.3429 respectively. Exogenous concentrations of creatine had no significant effect on the gene expression of *MGAT3* (P=0.7016, 0.1021, and 0.3419 respectively) or *FAP* (P=0.6887, 0.4466, and 0.3567 respectively).

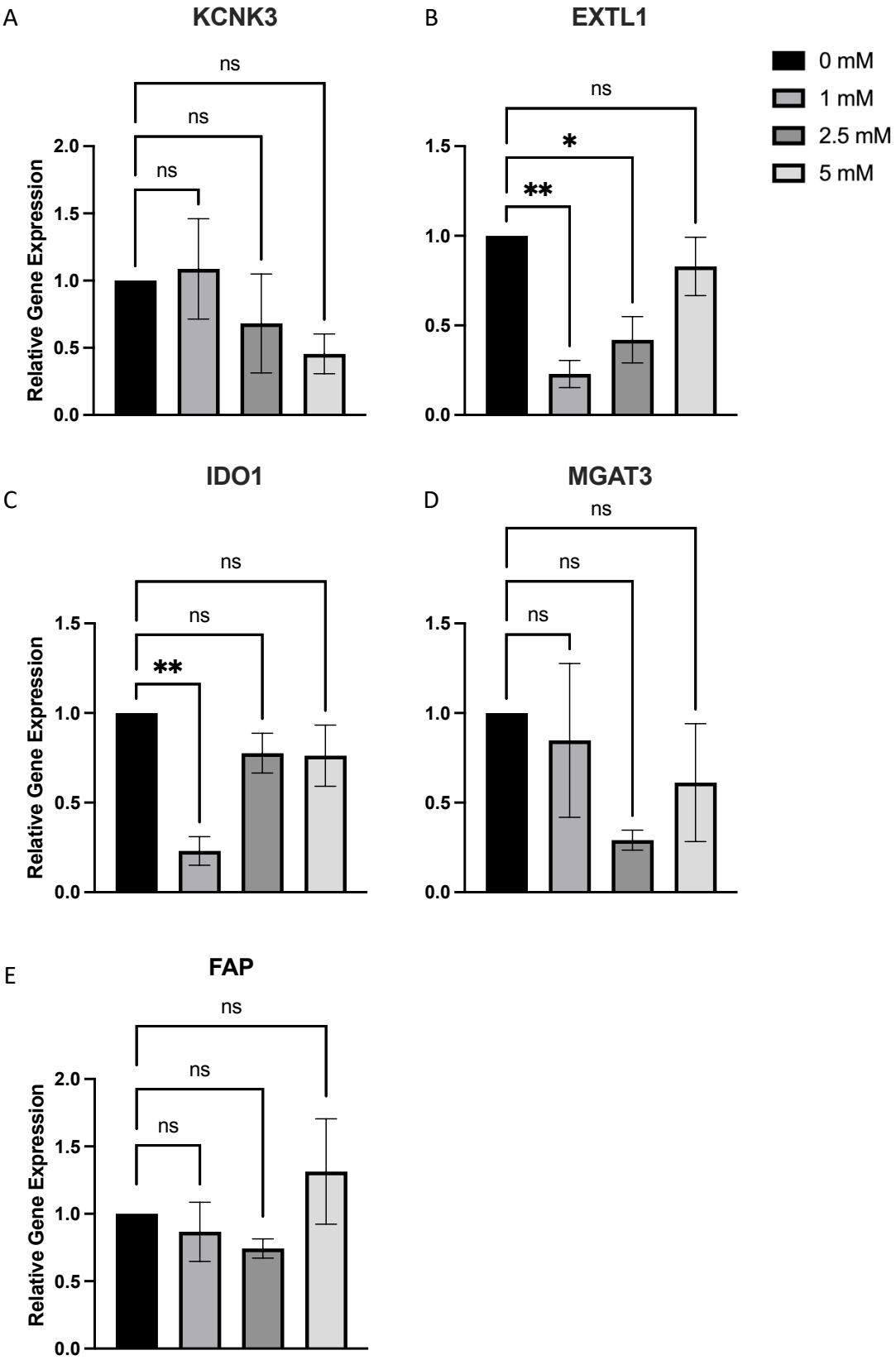


Figure 6:30 - Exogenous creatine reduces EXTL1 and IDO1 gene expression*. MMNK1 cholangiocytes were treated with 0.0, 1.0, 2.5, and 5.0 mM of exogenous creatine and cultured for 48 hours prior to RNA extraction. The gene expression levels of A)* KCNK3*, B)* EXTL1*, C)* IDO1*, D)* MGAT3*, and E)* FAP *were evaluated by qPCR after creatine treatment. Low concentrations of creatine (1 mM) reduced* EXTL1 *and* IDO1 *target expression in MMNK1 cholangiocytes. Exogenous creatine had no statistically significant effect on the expression of* KCNK3, MGAT3, *or* FAP *in MMNK1 cholangiocytes (*P<0.05,**P<0.01)(n=3).*

6.7 Genomic alterations in cholangiocarcinoma cells due to co-culture

6.7.1 Transcriptomic analysis

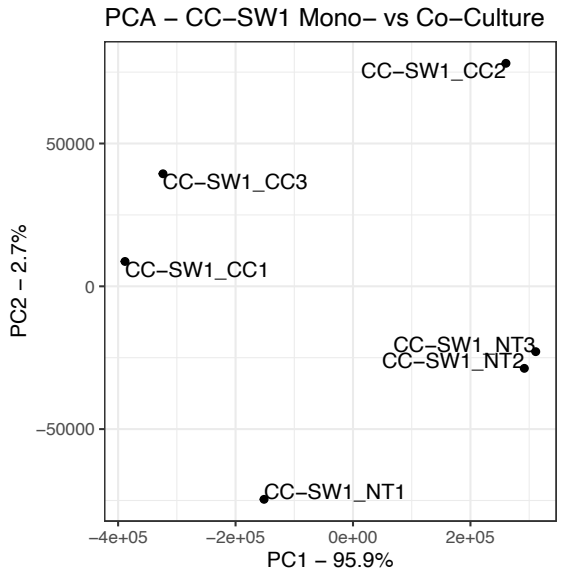
Indirect coculture elicited distinct phenotypic changes CC-SW1 cells in co-culture, including reduced cell viability, migration, and cell cycle progression. Evaluating the transcriptome can allow for the identification of specific genes and pathways that are differentially expressed, providing clues about the molecular mechanisms responsible for the observed changes to the CC-SW1 functional phenotype. Moreover, transcriptomic analysis of the co-culture system has the potential to reveal previously unrecognized genes or pathways that are differentially expressed during co-culture, and therefore possibly linked to CCA tumorigenesis, which could be used for the identification of potential therapeutic targets or biomarkers in the future. Therefore, we used bulk RNA-sequencing to evaluate the transcriptomic changes to CC-SW1 cells when grown in monoculture, and co-culture with MMNK1 cells after 48-hours, highlighting the effect of cholangiocyte cells on CCA gene expression profiles.

6.7.2 Application of the DESeq2 model

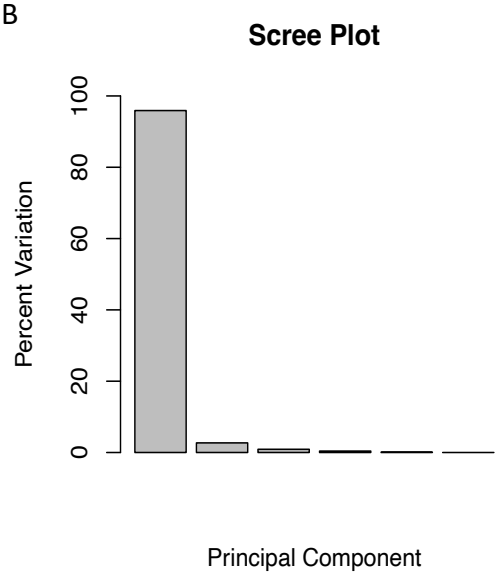
We used a PCA to visualize and explore the overall patterns of gene expression in CC-SW1 cells in mono- and co-culture. Figure 6:31 shows a PCA plot using the first 2 Principal Components (PC), PC1 on the X-axis and PC2 on the Y-axis. The CC-SW1 monoculture samples are clustered on the bottom right side of the graph, whilst the co-culture samples are clustered on the top left side of the graph. Using the Scree Plot in Figure 6:31, we can see that PC1 accounts for 95.9% of the variation between samples, and this in combination with the clear separation in monoculture and co-culture samples shows samples can accurately be mathematically determined as mono- or co-culture. Loading scores are

coefficients that indicate the contribution of each gene to the composition of the PCs, and as such where samples are plotted on the PCA plot. The loading scores determine which genes have the largest effect on where samples are plotted on the PCA plot, as such positive loading scores push the monoculture samples to the right side of the graph, and negative loading scores push the co-culture samples to the left side of the graph. The table in Figure 6:31C shows the names of the top 10 genes with the largest loading score magnitudes. The gene *MTCO1P12*, a pseudogene of a Mitochondrially Encoded Cytochrome C Oxidase I member, had the largest loading score, of -0.665 (Figure 6:31C) which contributes to how far left the coculture samples are on the PCA plot. Likewise the gene *FLNA*, which encodes Filamin A, had a loading score of 0.00648, which contributes to how far right the monoculture samples are on the graph. The estimated gene-wise dispersion plot in Figure 6:31D shows a close alignment of the estimated dispersion across all genes (shown in red) to the mean expression of each gene (shown in black). This is better than the comparison between MMNK1 and CC-SW1 samples in Figure 6:1, which is to be expected, as CC-SW1 cells in monoculture and co-culture are much more genetically similar than MMNK1 and CC-SW1 cells. Overall, the plot in Figure 6:31 shows the CC-SW1 mono- and co-culture RNAseq data is a good fit for the DESeq2 model.

A



B



C

Gene	Loading Score
FLNA	0.06482775
MTND5P11	-0.0579801
MTND1P23	-0.0944865
MTND2P28	-0.144905
MTRNR2L12	-0.1915387
MTCO2P12	-0.2333034
MTATP6P1	-0.2897915
MTND4P12	-0.312513
MTCO3P12	-0.4733148
MTCO1P12	-0.66481117

D

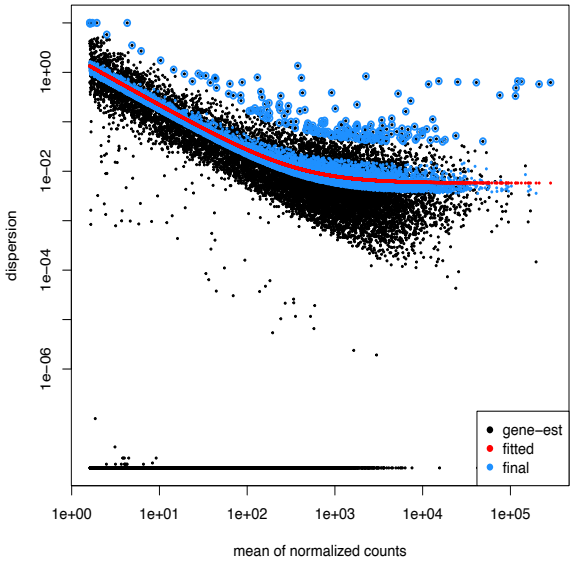


Figure 6:31 - Normalisation of CC-SW1 gene expression data from RNA-sequencing. *RNA was extracted from CC-SW1 cells after 48 hours of monoculture, and co-culture with MMNK1 cholangiocytes, for the evaluation of gene expression. A) The PCA plot is a two-dimensional representation of RNA-seq data. Each point represents a sample, with its position reflecting its placement in a lower-dimensional space generated by the PCA. Samples with similar gene expression profiles cluster together, and as such enables visualization of sample relationships. B) The scree plot illustrates the explained variance associated with each principal component in PCA. This plot helps determine the number of principal components that capture the most significant variation in the data, guiding dimensionality reduction. C) Table of the top ten genes and equivalent loading scores associated with Principal Component 1 from the PCA. Loading scores indicate the contribution of individual genes to the variation explained by each component. High loading scores suggest genes that strongly influence the observed separation in the PCA plot. D) The gene dispersion estimation plot depicts the relationship between gene expression dispersion and mean expression level. We use this to model statistical variability in the gene expression data.*

6.7.3 Differential Gene Expression

Using DESeq2, we conducted a DGE analysis of CC-SW1 cells in co-culture, where a total of 19,824 genes were analysed. Of these, 2325 genes were significantly differentially expressed (P<0.05). The results from the DGE analysis are illustrated in the volcano plot in Figure 6:32A. Genes with a Log2FC of >1/<-1 (equating to a Raw Fold Change in gene expression >2/<-2) are highlighted in green; genes with a P-value <0.05 are highlighted in blue, whilst genes that have both a Log2FC of >1/<-1 and a P-value <0.05 are highlighted in red. The black arrow in Figure 6:32A denotes the location of *STC2*, the most significantly (P= 1.035E-63) differentially expressed gene between CC-SW1 mono- and co-culture samples. *STC2* encodes Stanniocalcin 2 (ENSG00000113739), a secreted glycoprotein hormone that is broadly upregulated in human tumours (161). CC-SW1 cells experienced a Log2FC of 1.7 during co-culture, equating to a raw fold change reduction in gene expression of 3.2, which is further highlighted by the normalised count data for *STC2* in mono- and co-culture (Figure 6:32B).

Genes with a large positive Log2FoldChange are expressed to a greater degree in CC-SW1 cells during co-culture, whilst genes with a large negative Log2FoldChange are expressed to a lower extent compared to CC-SW1 cells in monoculture..

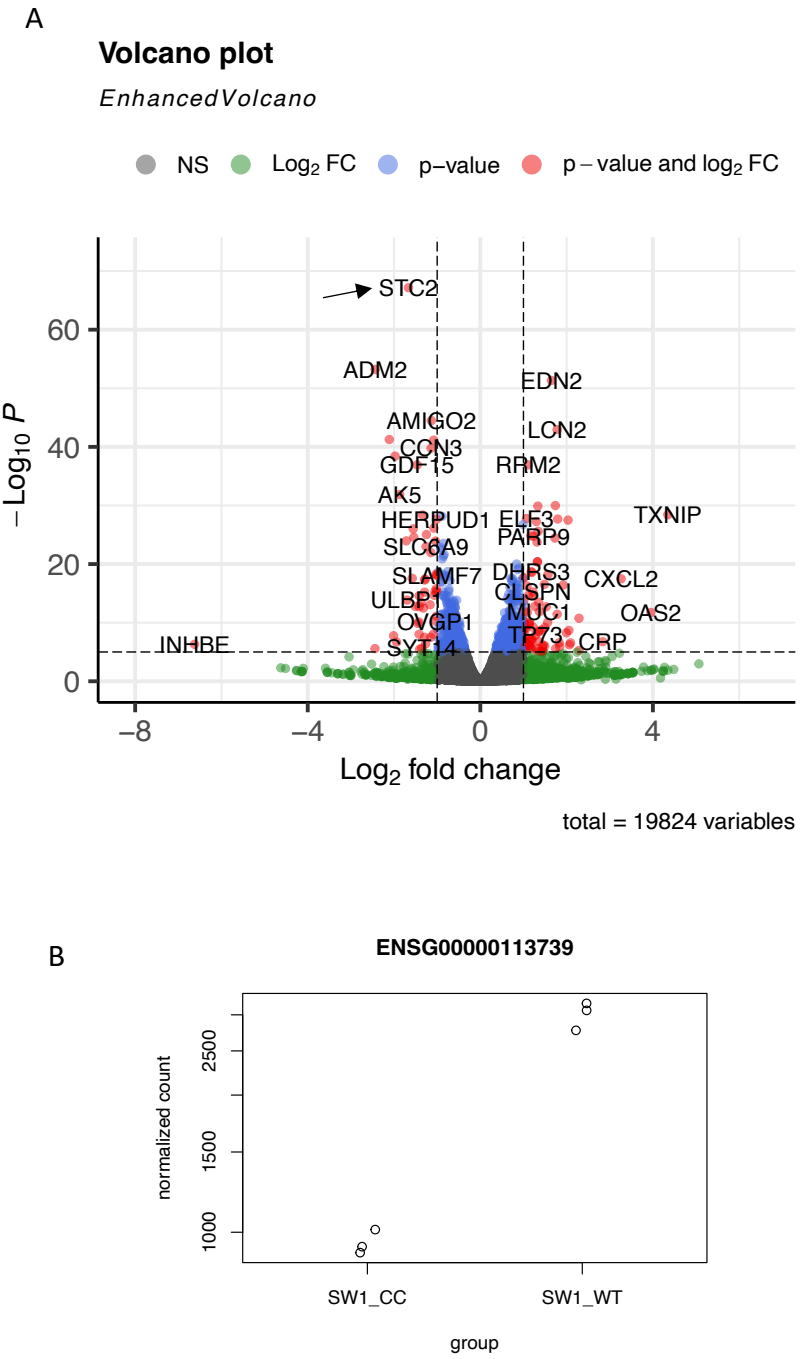


Figure 6:32 - Differential gene expression analysis of CC-SW1 cells after 48 hours of co-culture with MMNK1 cholangiocytes. *A) Volcano plot depicting differential gene expression between CC-SW1 cells in monoculture and after 48 hours of co-culture with MMNK1 cholangiocytes. Each point on the plot represents a gene with its position indicating both statistical significance and fold-change in gene expression. The dashed horizontal line represents the predefined threshold for significance, -log10(p-value) > 1.3 (blue), whilst the dashed vertical lines represents the predefined threshold for fold-change, log2 fold-change>1/<-1 (green). Genes which fulfil both significance and fold change criteria are shown in red, with upregulated genes on the right side, and downregulated genes on the left side. The most significantly differentially expressed gene was* STC2*, denoted by the black arrow. B) Dot plot of the normalised gene count for the* STC2 *gene (ENSG00000113739) in CC-SW1 mono- and co-culture samples.*

6.7.4 Gene Set Enrichment Analysis

We conducted two Gene Set Enrichment Analyses in parallel, one utilising the Hallmark Pathway database and one utilising the KEGG database. This resulted in 2 sets of DEGs and 2 sets of pathway analyses. We used this to identify concordant pathways and genes. The pathway analyses were conducted to help interpret CC-SW1 gene expression changes in a broader biological context, by identifying the pathways or biological processes that are enriched as a result of co-culture. The first analysis utilised the Hallmark database in order to conduct a pathway enrichment analysis, with results shown in Figure 6:33. Pathways are ranked by Normalised Enrichment Score (NES) and colour coded by significance (blue $P<0.05$, red $P>0.05$). Genes that are differentially expressed and also involved in enriched pathways are more likely to be functionally relevant and play a significant role in phenotypic changes identified in co-culture. Of the 15 significantly enriched Hallmark pathways highlighted in CC-SW1 cells during co-culture, four were linked to cytokine signalling, including the Interferon-α (IFN-α) Response, Interferon-γ (IFN-γ) response, IL-6-JAK-STAT3 signalling, and TNFα signalling via NFKB. Cytokine signalling is known as a driving factor in cancer-related inflammation, and specifically increased IL-6 has been identified in CCA, as a cholangiocyte mitogenic factor, suggesting co-culture is driving CCA development through increase cytokine signalling activation.

As highlighted previously (3.1.3) no one single database can capture the entire complexity of biological pathways. As such we used both the Hallmark database, which emphasizes well-defined biological functions, in combination with the KEGG database, which emphasizes metabolic pathways. The pathway analysis using the KEGG database assessed 19,469 genes, 44.2% of which (8,610 genes) correlated with our co-culture phenotype, whilst 55.8% (10,859 genes) correlated with our monoculture phenotype (Figure 6:34). The top 50 DEG

associated with each phenotype (either monoculture of co-culture) is shown in the heatmap in Figure 6:34. The expression values are represented as colours, where the range of colours (red, pink, light blue, dark blue) shows the range of expression values (respectively high, moderate, low, lowest).

TXNIP (Thioredoxin Interacting Protein), a thiol-oxidoreductase that functions as an inhibitor of the antioxidative function of thioredoxin, was the top gene associated with co-culture in CC-SW1, whilst *H3.Y,* a primate-specific variant of Histone H3, was the top gene associated with CC-SW1 in monoculture (Figure 6:34). As well as the modulation of the antioxidant system, TXNIP is also known to trigger metabolic reprogramming, leading to inhibition of proliferation, invasion, and migration of breast cancer cells, through the TXNIP-HIF1α-TWIST signalling axis (162). Given the extensive function of TXNIP, we postulate that upregulation of TXNIP in CC-SW1 cells as a result of co-culture may have implication on the observations we made previously on the reduction in cell viability and migration.

The KEGG dataset is comprised of 186 gene sets, which after filtering, resulted in 162 for analysis. Figure 6:35 shows the KEGG Pathways, ranked by Normalised Enrichment Score (NES) and colour coded by significance (blue $P<0.05$, red $P>0.05$). 15 gene sets were significantly upregulated during co-culture, whilst 10 gene sets were significantly downregulated.

Pathways associated with DNA repair and division, including DNA replication, E2F targets, base excision repair, and mitotic spindle pathways, as well as Cytokine and Chemokine signalling pathways, were significantly enriched in both the KEGG and Hallmark analysis (Figure 6:36).

There was a discord in the expression of the p53 pathway, with a significant reduction in pathway expression highlighted using the Hallmark database, and a non-significant increase

in pathway expression highlighted using the KEGG database. The most concurrent pathway reduction were pathways associated with the protein response, including protein secretion, unfolded protein response, lysosome, and ribosome pathways. This might be interpreted as a cellular stress response, wherein the cell undergoes a deliberate adjustment period to discern which proteins to prioritize for synthesis. Consequently, it may slow down the translocation process to the endoplasmic reticulum (ER) and the subsequent processing and secretion pathways. Protein synthesis relies on the availability of essential raw materials for generating new proteins, and consequently it is reasonable to expect a reduction in protein synthesis when amino acid metabolism is disrupted. Notably, co-culture conditions led to the identification of abnormal metabolic patterns, including a significant downregulation in Arginine-Proline metabolism along with modest, non-significant alterations in the Valine-Leucine-Isoleucine degradation pathway. Additionally, there was a non-significant increase in metabolic activity within the Alanine-Aspartate-Glutamate pathways, as depicted in Figure 6:37.

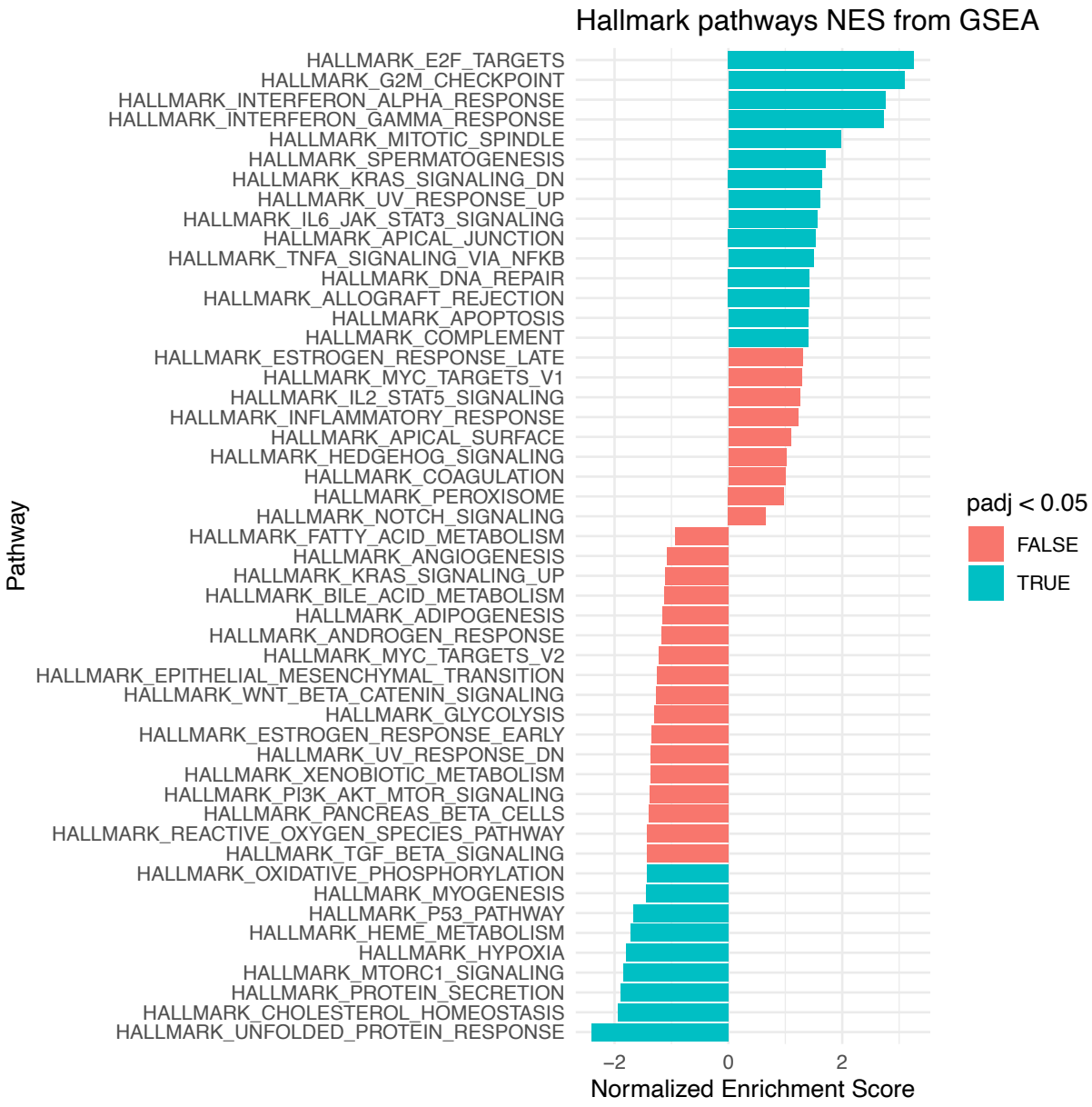


***Figure 6:33** - **Histogram of enriched Hallmark gene pathways in CC-SW1 cells after 48 hours of co-culture.** The histogram displays the results of Gene Set Enrichment Analysis (GSEA). Each bar represents a hallmark pathway, with the length corresponding to the Normalized Enrichment Score (NES) for that pathway. Positive scores represent upregulation, whilst negative scores represent downregulation. Each bar is coloured to indicate the significance of enrichment (blue for P<0.05, red for pathways P>0.05). The histogram therefore highlights which hallmark-based gene pathways are significantly upregulated or downregulated in CC-SW1 cells after 48-hours of indirect co-culture with MMNK1 cholangiocytes.*

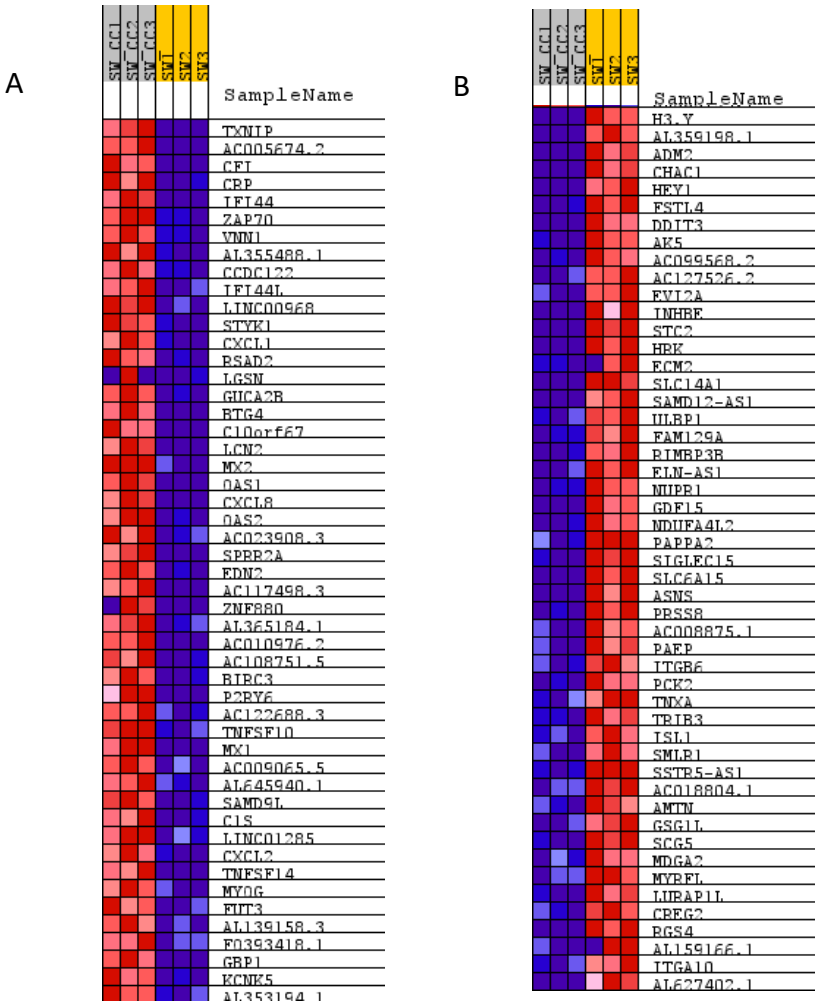


Figure 6:34 – Heat Map depicting the top 100 most differentially expressed genes in CC-SW1 cells. *The heatmap visually represents the expression patters of the 50 most influential genes as identified by the RNA-seq analysis, with their functional annotations based on the Kyoto Encyclopaedia of Genes and Genomes (KEGG) database. Each row corresponds to a specific gene, each column represents a sample, and the colour represents either increased (red) or decreased (blue) expression. Genes upregulated in CC-SW1 cells during co-culture are highlighted in (A), whilst genes downregulated during co-culture are highlighted in (B).*



Figure 6:35 - Histogram of enriched KEGG pathways in CC-SW1 cells after 48 hours of co-culture. *The histogram displays the results of Gene Set Enrichment Analysis (GSEA). Each bar represents a KEGG pathway, with the length corresponding to the Normalized Enrichment Score (NES) for that pathway. Positive scores represent upregulation, whilst negative scores represent downregulation. Each bar is coloured to indicate the significance of enrichment (blue for P<0.05, red for pathways P>0.05). The histogram therefore highlights which KEGG-based gene pathways are significantly upregulated or downregulated in CC-SW1 cells after 48-hours of indirect co-culture with MMNK1 cholangiocytes.*

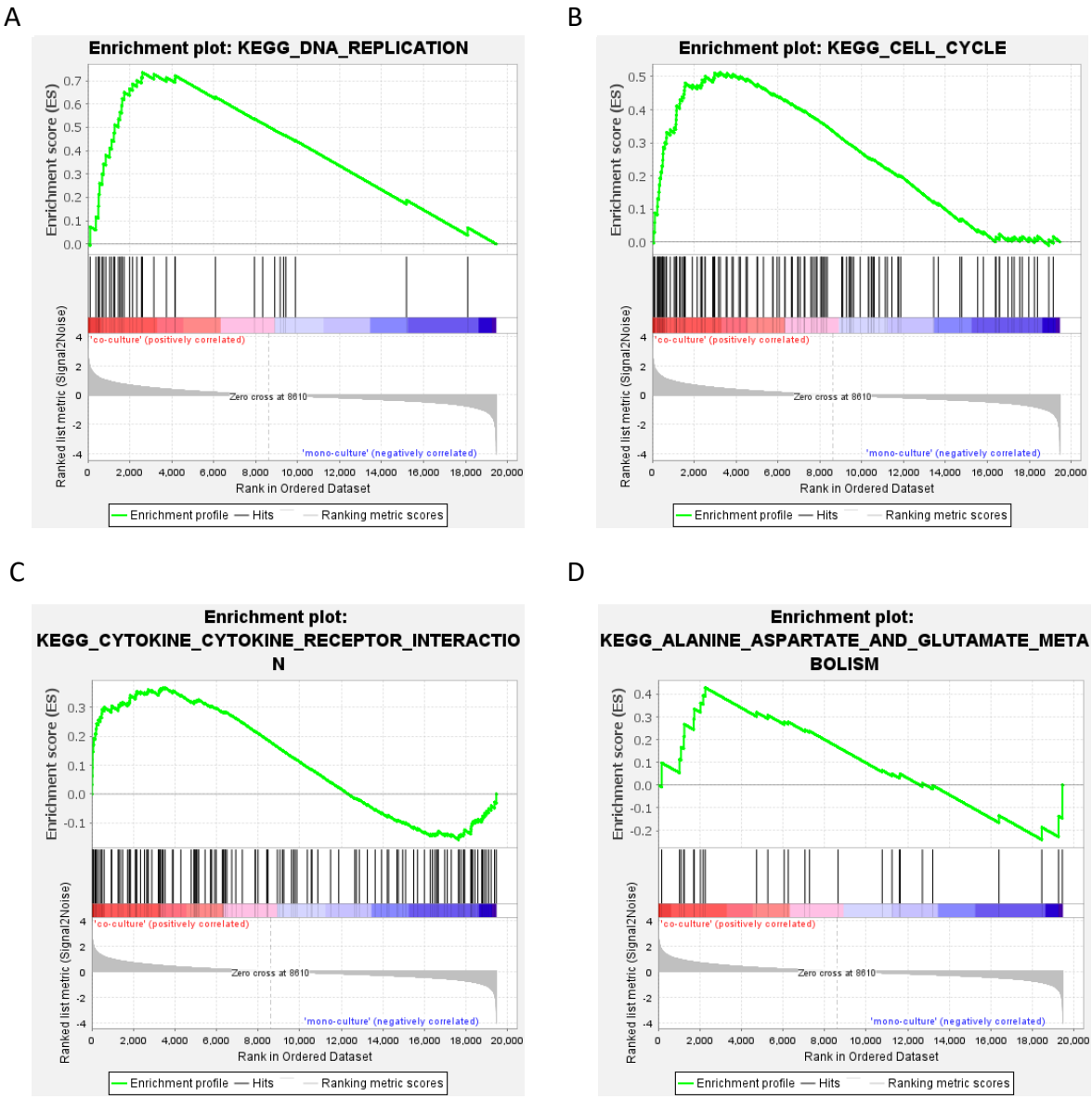


Figure 6:36 – Enrichment plots demonstrating positive gene set correlations in CC-SW1 cells. *This figure presents a set of enrichment plots, each representing the correlation between specific gene sets from A) DNA replication, B) Cell cycle, C) Cytokine-cytokine receptor interactions, and D) Alanine-aspartate-glutamate metabolism, in CC-SW1 cells after indirect co-culture with MMNK1 cholangiocytes. Each plot illustrates the enrichment scores for a particular gene set against expression levels in co-culture and monoculture, which reflect the extent to which genes in the set are associated with either condition. The position of genes in the ranked list based on differential expression are denoted by vertical lines.*

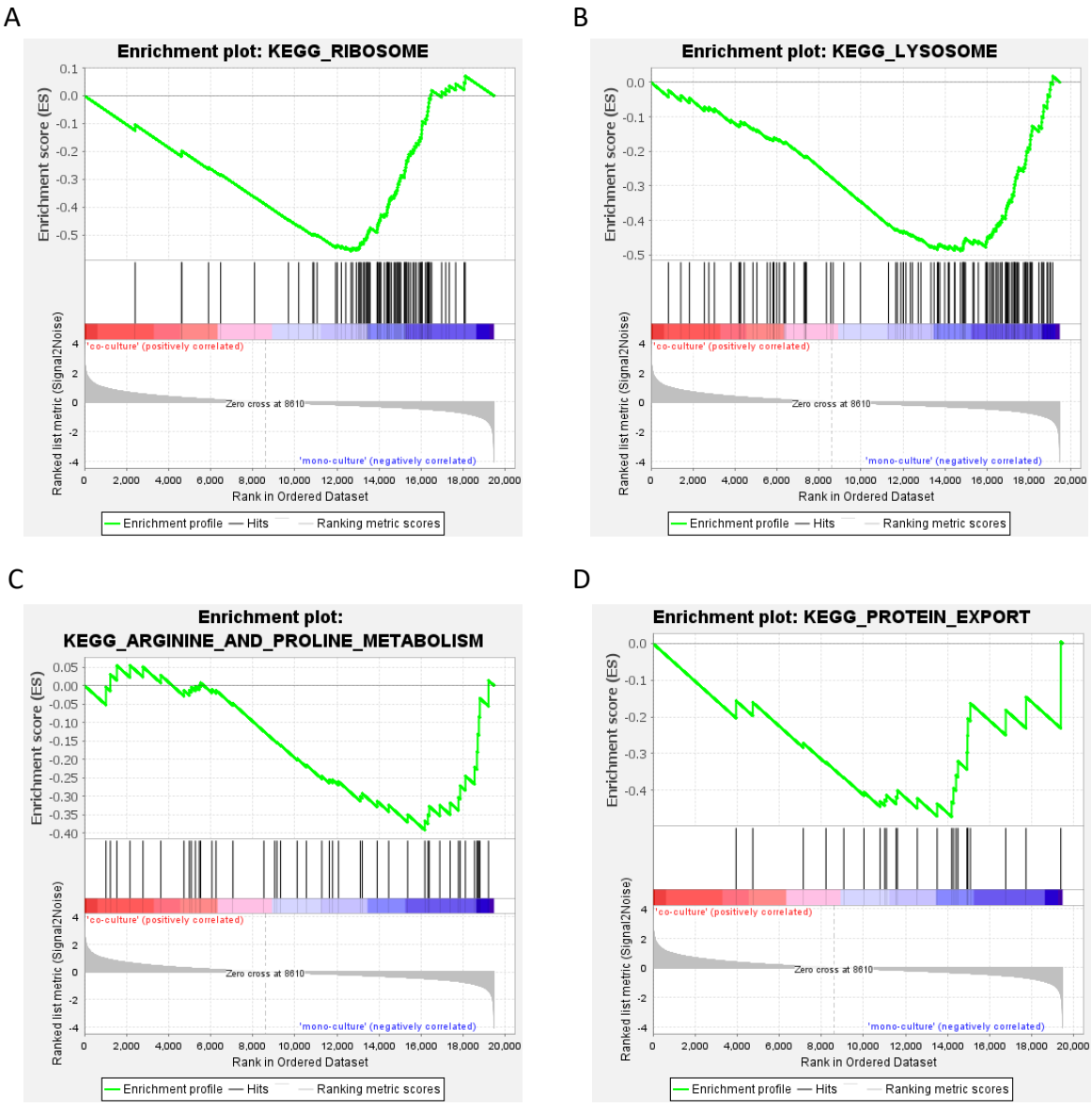


Figure 6:37 - Enrichment plots demonstrating negative gene set correlations in CC-SW1 cells. *This figure presents a set of enrichment plots, each representing the correlation between specific gene sets including A) Ribosome, B) Lysosome, C) Arginine-proline metabolism, and D) protein export, in CC-SW1 cells after indirect co-culture with MMNK1 cholangiocytes. Each plot illustrates the enrichment scores for a particular gene set against expression levels in co-culture and monoculture, which reflect the extent to which genes in the set are associated with either condition. The position of genes in the ranked list based on differential expression are denoted by vertical lines.*

6.8 Validation of cholangiocarcinoma genomic alterations

6.8.1 Validation of RNAseq

We went on to validate the CCA co-culture gene expression data from RNA-sequencing, by selecting a panel of the most differentially expressed genes (Log2Fold Change>1, p<0.05) solely expressed in CC-SW1 cells for validation. The expression of *LBP* (Lipopolysaccharide Binding Protein), *CFI* (Complement Factor I), *SPRR2A* (Small Proline Rich Protein 2A), and *KL* (Klotho), were then validated by qPCR. Data are displayed as relative gene expression, relative to the normalised *β-actin* control level. There is a clear trend in increasing target gene expression in CC-SW1 cells during co-culture (P=0.0143, 0.0452, 0.4474, and 0.3719 respectively)(Figure 6:38).

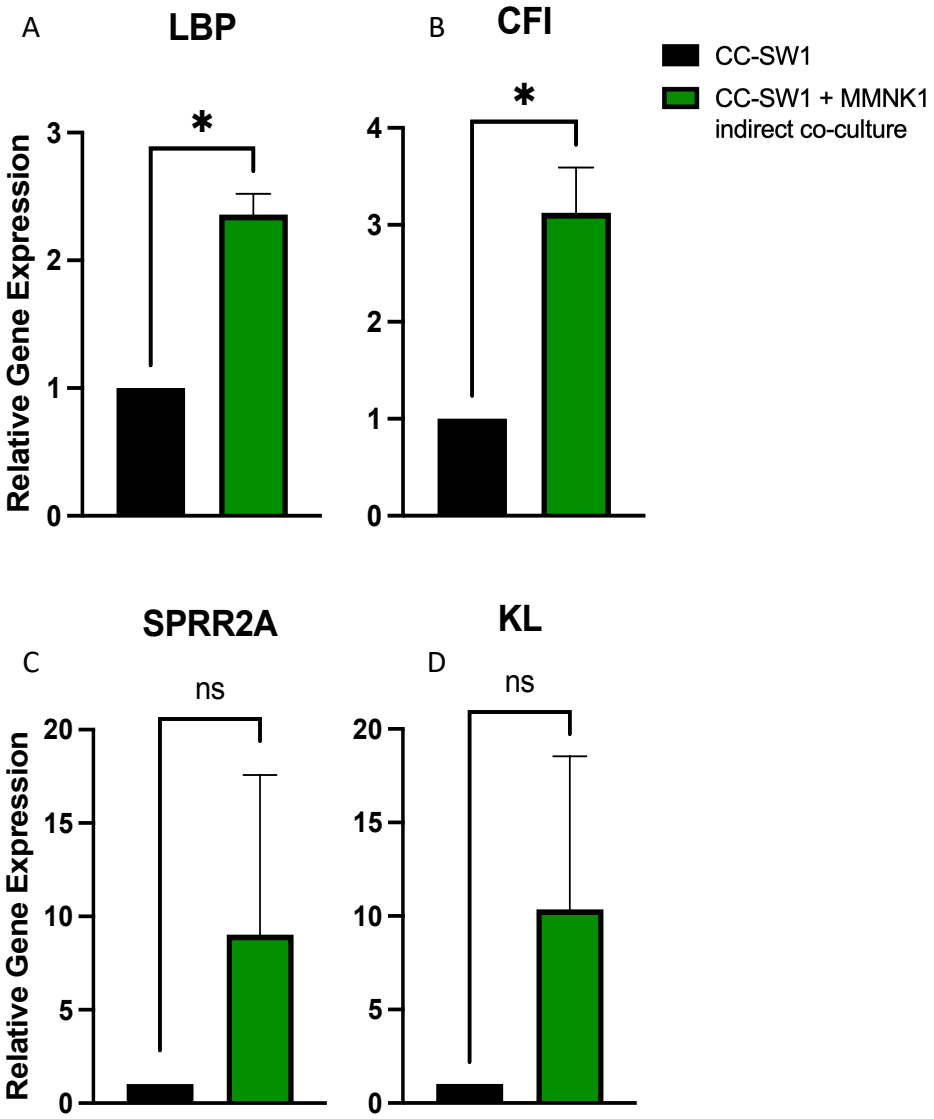


Figure 6:38 - qPCR validation of RNAseq gene expression in CC-SW1 cells*. CC-SW1 cells were cultured for 48 hours alone, or in indirect co-culture with MMNK1 cholangiocytes prior to RNA extraction. qPCR was used to evaluate gene expression levels of the target genes identified from the RNA-sequencing analysis, A)* LBP*, B)* CF1*, C)* SPRR2A*, and D)* KL*, enabling the comparison of gene expression changes in CC-SW1 cells between monoculture and co-culture (*P<0.05)(n=5).*

6.8.2 Validation of Cytokine Expression

As demonstrated previously, (Figure 5:49), co-culture resulted in a significant change in the cytokine protein concentration CC-SW1 cells were exposed to. We selected to evaluate whether the change in cytokine expression was due to a co-culture mediated change to cytokine gene expression and as such whether the changes were recapitulated at the gene level, or whether it could be attributed to secretion by MMNK1 cholangiocytes. As such, we used the RNA-sequencing gene expression data to investigate the gene expression of cytokines detected in the cytokine assay. Figure 6:39A shows a table of relative cytokine gene expression for MMNK1 cells in co-culture, as detected by RNA-sequencing.
Figure 6:39A shows a table of relative cytokine gene expression for CC-SW1 cells in co-culture, as detected by RNA-sequencing. There was a significant increase in the gene expression of *CXCL1/2/3, IL-8*, and *MCP-1* in CC-SW1 cells during co-culture, with a concurrent decrease in the gene expression *of IL-6R,* and *VEGF* (Figure 6:39A). There was no change in the expression of *CCL5,* and *HIF1A* in CC-SW1 cells during co-culture as detected by RNA-sequencing. The gene expression of *IL-6* was not detected.

The gene expression of *CXCL1, CXCL2, CXCL3, IL-6, VEGFA,* and *HIF1A* was then validated by qPCR; Figure 6:39B shows qPCR data for six selected cytokine genes. There was an increase in the trend of *CXCL1, CXCL2, CXCL3,* and *HIF1A* gene expression (P= 0.1879, 0.2248, 0.0718, and 0.0551 respectively)(Figures 6:29B, C, D, and G). As show in Figure 5:49, CC-SW1 cells were exposed to a greater concentration of GRO (a/b/g) but a reduction in CXCL1 concentration, during co-culture. RNA-sequencing confirmed a significant increase in *CXCL1, CXCL2,* and *CXCL3* gene expression, a trend that was recapitulated in qPCR validation. This suggests that co-coculture triggered an increase in gene expression, and subsequent

secretion of these 3 cytokines, which contributed to the cholangiocyte compartment and sequestering of CXCL1.

Although not detected via RNA-sequencing, *IL-6* gene expression was increased during co-culture as assessed by qPCR (P=0.3897)(Figure 6:39). We see a tremendous increase in IL-6 protein concentration during co-culture, with a Fold Change in expression of 123.07 (Figure 5:49), suggesting it is the cholangiocyte compartment that contributes to the IL-6 concentration during co-culture, potentially triggering the IL-6-STAT3 signalling pathway and thereby increasing CC-SW1 production of IL-6.

There was no significant change in protein concentration of VEGF in CC-SW1 cells, however RNA-sequencing and qPCR validation confirmed a decrease in *VEGF* gene expression.

Whilst *MCP-1* gene expression was not validated by qPCR, RNA-seq analysis revealed a significant increase in expression (Figure 6:39), contradictory to the decrease in protein expression seen in Figure 5:49. Likewise whilst RNA-seq analysis revealed no significant change in *CCL5* gene expression, CC-SW1 experienced an increase in CCL5 protein concentration during co-culture, likely due to secretion by MMNK1 cholangiocytes.

A

Cytokine	Log_2FoldChange	Padj	Direction of Change
CXCL1	2.03417041	2.22E-25	**Increase**
CXCL2	57.3996952	7.47E-16	**Increase**
CXCL3	14.6765296	0.00094572	**Increase**
IL-6	ND	ND	Not Detected
IL-6R	-1.0231608	1.39E-16	Decrease
IL-8	1.73079395	1.76E-22	**Increase**
MCP-1	0.36470299	6.69E-05	**Increase**
CCL5	0.48737975	0.67871888	No Change
HIF1A	-0.0267972	0.89337211	No Change
VEGF	-0.4806423	4.61E-05	Decrease

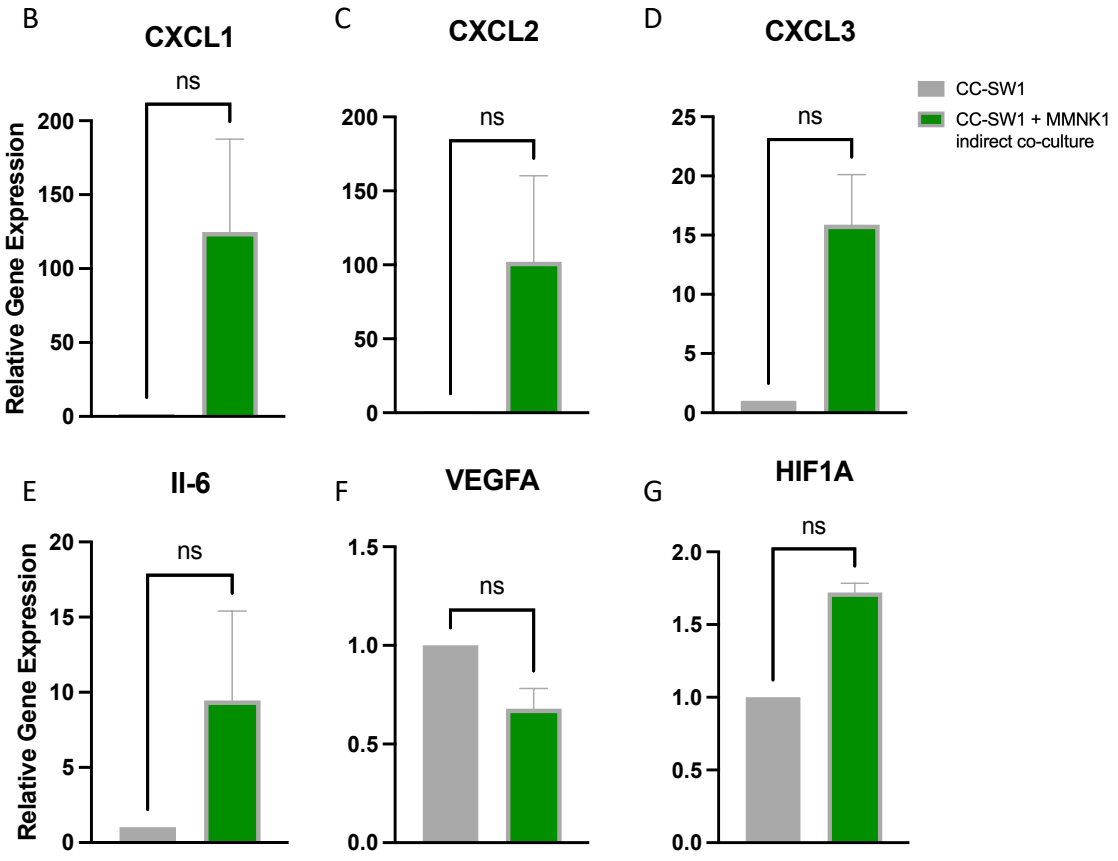


Figure 6:39 – RNA-based validation of co-culture mediated alterations to CC-SW1 cytokine expression during co-culture. *A) We evaluated the RNA-sequencing data for CC-SW1 cells in co-culture with MMNK1 cholangiocytes for the gene expression of our cytokines of interest. The table lists the significance value, Log_2FC, and the direction of expression change during co-culture. qPCR validation of a panel of six cytokines: B)* CXCL1*, C)* CXCL2*, D)* CXCL3*, E)* Interleukin-6*, F)* VEGF-A*, and G)* HIF1A*, was conducted. Gene expression is displayed relative to the gene expression of the* β-actin *control. There is a trend in increasing in cytokine expression in CC-SW1 cells after co-culture.*

6.9 Integrating cholangiocyte metabolomic and genomic data

We chose to implement the RNA-sequencing data to evaluate firstly, changes to the gene expression responsible for metabolism, and secondly the reciprocity of metabolome changes on genomic changes. Firstly, we integrated the two -omics datasets, transcriptomics and metabolomics, to elucidate metabolic pathway alterations likely due to genomic expression changes.

6.9.1 Joint-Pathway Analysis highlights increased TCA cycle

We conducted a Joint-Pathway Analysis using metabolite concentration data and RNA expression data from CC-SW1 cells in co-culture for 48 hours. Each pathway is ranked top to bottom according to significance ($-Log_{10}P$) and listed in Figure 6:40 with the relative pathway impact indicated by the size of the bar. The TCA cycle metabolic pathway had the greatest Pathway Impact, followed by purine and pyrimidine metabolism. Arginine biosynthesis followed by glutathione biosynthesis had the most significant impact. Moreover, the pathways for Glyoxylate and dicarboxylate metabolism, Pentose and glucuronate interconversions, Retinol metabolism, Drug metabolism, Phenylalanine metabolism, and most crucially, Glycine, serine and threonine metabolism were only enriched in CC-SW1 cells, not MMNK1 cholangiocytes.

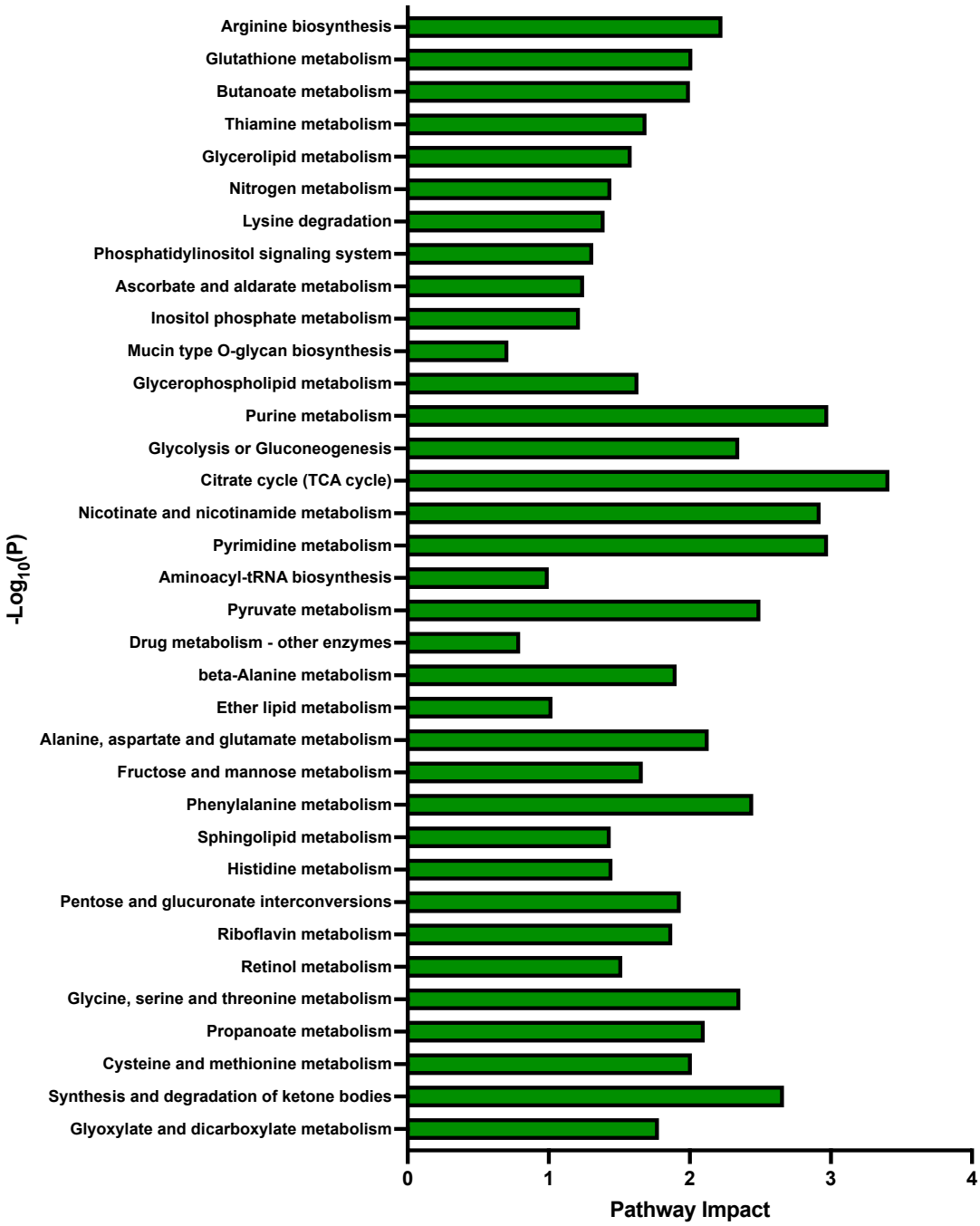


Figure 6:40 – Integrating CC-SW1 metabolomic and RNAseq data. The histogram displays the metabolic pathways based on the KEGG database, enriched in CC-SW1 cells after 48 hours of co-culture with MMNK1. The integration involved combining the metabolite concentrations from the metabolomic analysis, with the gene expression data from the RNA-sequencing analysis. Each row represents a KEGG metabolic pathway, with the length of the bar equivalent to the pathway impact. Pathways are ranked by signficance ($-Log_{10}P$); the most most signifcantly enriched pathway was arginine biosynthesis.

6.9.2 Evaluation of metabolic-associated genes

During the metabolomic analysis, we identified changes to the concentration of metabolites in CC-SW1 cells during co-culture, and in the transcriptomic analysis we identified changes to gene expression in CC-SW1 cells during co-culture. We then proceeded to use the transcriptomic data to evaluate the changes in the gene expression of genes linked to specific metabolites identified via metabolomic analysis.

6.9.2.1 2-Oxoisopentanoate metabolism related Gene Expression

As highlighted previously, 2-oxoisopentanoate concertation was significantly increased in CC-SW1 cells during co-culture (Figure 5:40), and exogenous supplementation of 2-oxoisopentanoate could reduce CC-SW1 cell viability and proliferation (Figures 5:43 and 5:45). We hypothesised that the increase in 2-oxoisopentanoate concentration was due to increased BCAA catabolism, as a cellular stress response method to supply glutamine for the glutamine-starved CCA cells. Therefore we chose to investigate whether the increase in 2-oxoisopentanoate concentration was due to changes in the gene expression of genes in the 2-oxoisopentanoate metabolic pathways. As 2-oxoisopentanoate typically exists as a transient intermediate, we chose to evaluate two related KEGG pathways: Valine, leucine and isoleucine degradation, and Pantothenate and CoA biosynthesis (see Figure 6:41).
The gene expression data for all genes in the valine, leucine and isoleucine degradation, and pantothenate and CoA biosynthesis pathways are shown in Figure 6:42, whilst the top 15 differentially expressed genes in either pathway are shown in Figure 6:42. *MCCC1* was the most differentially expressed ($P=8.07859x10^{-8}$) with the greatest reduction in expression (Log2FC= -0.618943255) during co-culture. We also see a significant reduction in the expression of *BCAT1, BCAT2, ALDH3A2, PCCA, ACAR1, HADHB, HIBADH, HMGCL,* and a non-

significant reduction in *ALDH1B1* expression. *VNN1* had the greatest increase in expression (Log2FC = 2.041838566, P=9.30732x10^{-5}). We also saw a significant increase in *AOXI, ABAT, UPB1,* and *VNN2* expression.

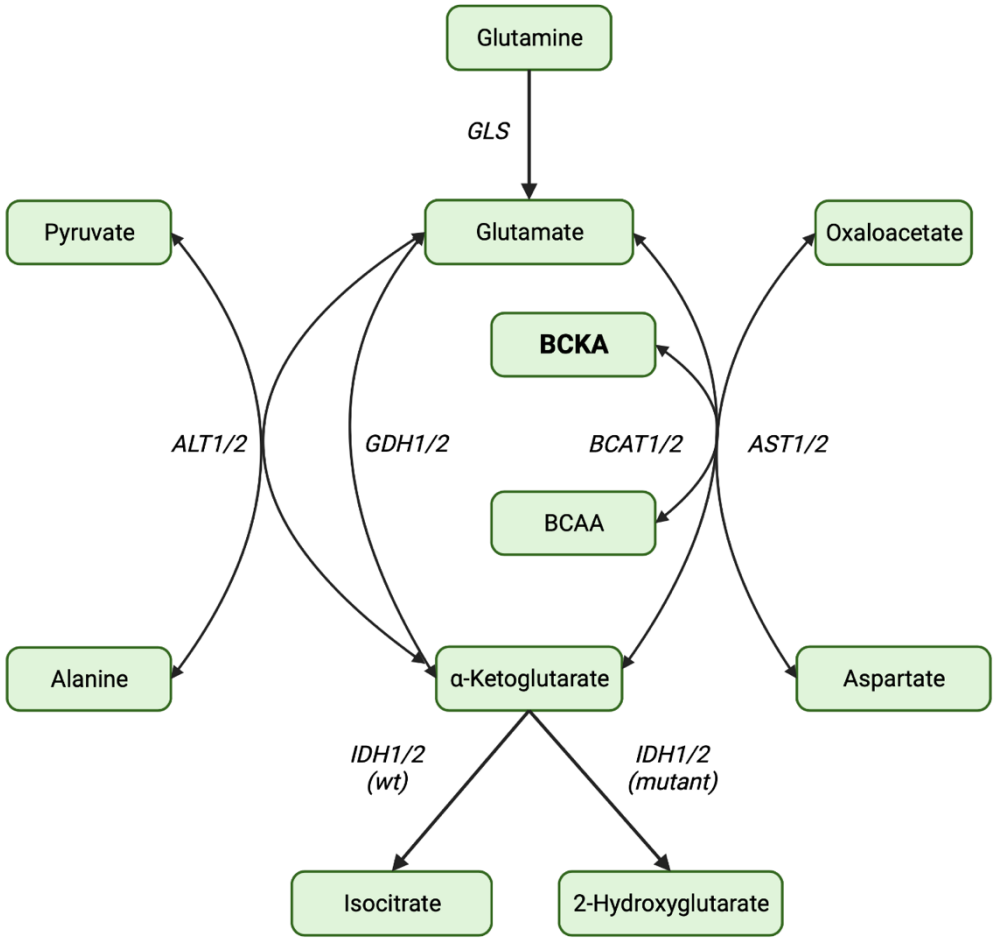


Figure 6:41 - Schematic of 2-oxoisopentanoate metabolic pathways. *Branched-chain keto acids (BCKAs) are intermediates in the metabolism of branched-chain amino acids (BCAAs) leucine, isoleucine, and valine. These amino acids are essential, and their catabolism involves several enzymatic reactions. BCAAs are initially transaminated by the enzyme BCAT. BCAA = Branched-chain amino acids, BCKA = Branched-chain keto acids, GLS = Glutaminase, ALT1/2 = Alanine aminotransferase, GDH1/2 = Glutamate dehydrogenase, BCAT1/2 = Branched-Chain Aminotransferase, AST1/2 = Aspartate transaminase, IDH1/2 = Isocitrate dehydrogenase.*

A

Gene	$Log_2FoldChange$	Padj	Name
MCCC1	-0.618943255	2.91419E-06	methylcrotonyl-CoA carboxylase subunit 1
AOX1	0.815929237	0.004553621	aldehyde oxidase 1
BCAT1	-0.46278999	0.006825136	branched chain amino acid transaminase 1
ABAT	0.469662864	0.018330493	4-aminobutyrate aminotransferase
ALDH3A2	-0.235453286	0.024402688	aldehyde dehydrogenase 3 family member A2
PCCA	-0.420492852	0.025678839	propionyl-CoA carboxylase subunit alpha
ACAT1	-0.304395627	0.037000322	acetyl-CoA acetyltransferase 1
HADHB	-0.237112455	0.043893876	hydroxyacyl-CoA dehydrogenase trifunctional multienzyme complex subunit beta
HIBADH	-0.256092225	0.062784497	3-hydroxyisobutyrate dehydrogenase
HMGCL	-0.303421966	0.139789535	3-hydroxy-3-methylglutaryl-CoA lyase
ALDH1B1	-0.147044555	0.188879165	aldehyde dehydrogenase 1 family member B1
ALDH6A1	-0.26668421	0.262728627	aldehyde dehydrogenase 6 family member A1
AUH	-0.297462529	0.317806716	AU RNA binding methylglutaconyl-CoA hydratase
OXCT1	-0.402364131	0.347952087	3-oxoacid CoA-transferase 1
EHHADH	0.328490104	0.436215076	enoyl-CoA hydratase and 3-hydroxyacyl CoA dehydrogenase
ACAA2	-0.114236833	0.466630938	acetyl-CoA acyltransferase 2
IL4I1	2.02792974	NA	interleukin 4 induced 1
PCCB	-0.111084008	0.519739033	propionyl-CoA carboxylase subunit beta
ACAD8	0.158221203	0.570368619	acyl-CoA dehydrogenase family member 8
HIBCH	0.139913787	0.656729627	3-hydroxyisobutyryl-CoA hydrolase
ALDH2	-0.097369989	0.68839281	aldehyde dehydrogenase 2 family member
MMUT	-0.083228641	0.700951138	methylmalonyl-CoA mutase
HSD17B10	0.080008071	0.719292496	hydroxysteroid 17-beta dehydrogenase 10
ALDH9A1	-0.059284975	0.741071466	aldehyde dehydrogenase 9 family member A1
ACAA1	0.091065483	0.755162688	acetyl-CoA acyltransferase 1
MCEE	-0.191780872	0.759134339	methylmalonyl-CoA epimerase
HMGCS1	0.0592831	0.777206687	3-hydroxy-3-methylglutaryl-CoA synthase 1
DBT	-0.065568274	0.789334078	dihydrolipoamide branched chain transacylase E2
ACADS	0.083318702	0.802171015	acyl-CoA dehydrogenase short chain
ECHS1	0.049911872	0.804642631	enoyl-CoA hydratase, short chain 1
HADH	0.046499536	0.810528845	hydroxyacyl-CoA dehydrogenase
ACAT2	0.050120199	0.826800818	acetyl-CoA acetyltransferase 2
ACADM	0.056838053	0.833447057	acyl-CoA dehydrogenase medium chain
BCKDHA	-0.183001641	0.84890195	branched chain keto acid dehydrogenase E1 subunit alpha
ALDH7A1	-0.034128268	0.851144621	aldehyde dehydrogenase 7 family member A1
IVD	-0.030725166	0.869184148	isovaleryl-CoA dehydrogenase
BCAT2	-0.01784577	0.946122089	branched chain amino acid transaminase 2
ACADSB	0.02058533	0.949593026	acyl-CoA dehydrogenase short/branched chain
HADHA	-0.00519279	0.980554464	hydroxyacyl-CoA dehydrogenase trifunctional multienzyme complex subunit alpha
BCKDHB	0.010835326	0.982270678	branched chain keto acid dehydrogenase E1 subunit beta
MCCC2	0.003508434	0.989380058	methylcrotonyl-CoA carboxylase subunit 2
DLD	0.003664382	0.990882503	dihydrolipoamide dehydrogenase

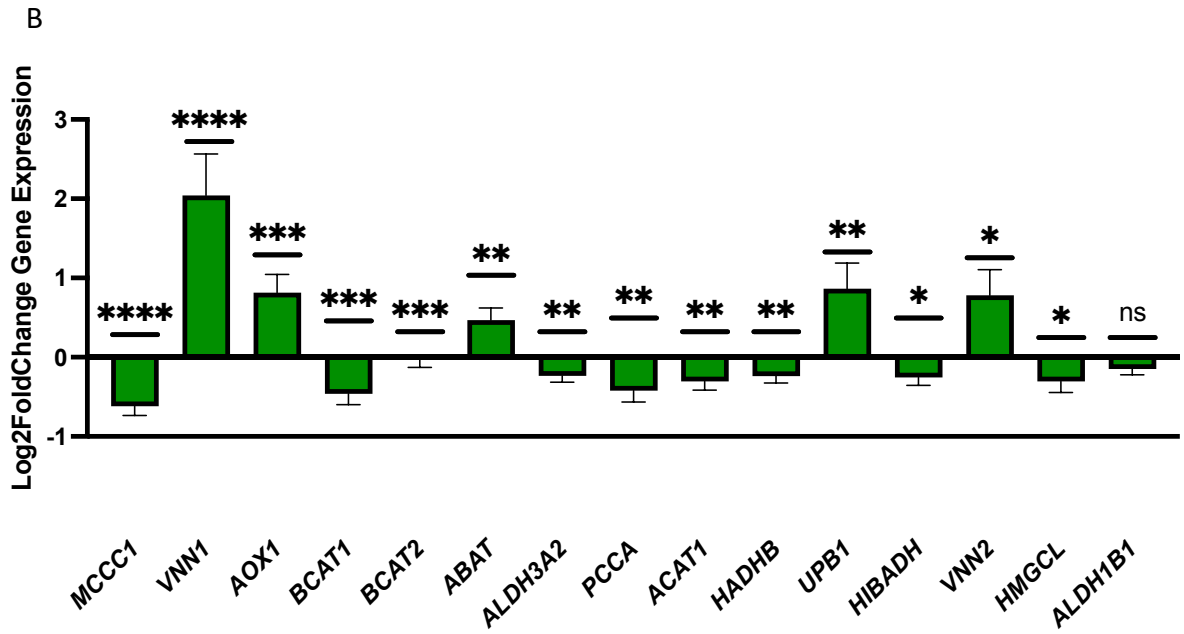


Figure 6:42 – Evaluation of 2-oxoisopentanoate metabolism using gene expression data from RNAseq. *A) The table lists the Log_2FoldChange and significance values for all the genes relating to 2-oxoisopenatanoate metabolism, identified in the RNA-sequencing data for CC-SW1 cells during indirect co-culture with MMNK1 cholangiocytes. This primarily includes genes in the valine/leucin/isoleucine degradation pathway, and the Pantothenate and CoA biosynthesis pathways, as denoted by the KEGG database. B) The histogram displays the top 15 of these genes associated 2-oxoisopenatanoate metabolism. The height of the bar represents the direction and magnitude of the Log_2FoldChange in gene expression in CC-SW1 during co-culture (P*<0.05, P**<0.01, P***<0.001, P****<0.0001).*

6.9.3 Exogenous 2-Oxoisopentanoate Modulated CC-SW1 Gene Expression

In order to evaluate the metabolome-genome reciprocal axis, we subsequently chose to investigate whether 2-oxoisopentanoate could modulate CC-SW1 gene expression. Therefore, we evaluated the effect of 4 exogenous 2-oxoisopentanoate concentrations on the gene expression of our gene panel of interest, used during RNA-sequencing validation. Exogenous 2-oxoisopentanoate had no significant effect on the gene expression of *LBP* at 1.0 and 2.5 mM (P=0.2053 and 0.0720 respectively) but caused a significant increase in gene expression at 5 mM (P=0.0051) which was not continued at 10 mM (P=0.0890)(Figure 6:43). Exogenous 2-oxoisopentanoate had no significant effect on the gene expression of *CFI* at 1.0 and 2.5 mM (P=0. 9502 and 0.9747 respectively) but caused a significant increase in gene expression at 5.0 and 10.0 mM (P=0. 0294 and <0.0001 respectively). A similar pattern was

seen in *SPRR2A* expression, whereby 1.0, 2.5, and 5.0 mM of 2-oxoisopentanoate had no significant effect on the gene expression (P=0.9858, 0.9781, and 0.4263) but 10.0 mM 2-oxoisopentanoate caused a significant increase in *SPRR2A* gene expression (P=0.0184). Exogenous 2-oxoisopentanoate led to a significant increase in *KL* gene expression (P=0.0258, 0.2357, 0.0087, and <0.0001)(Figure 6:43).

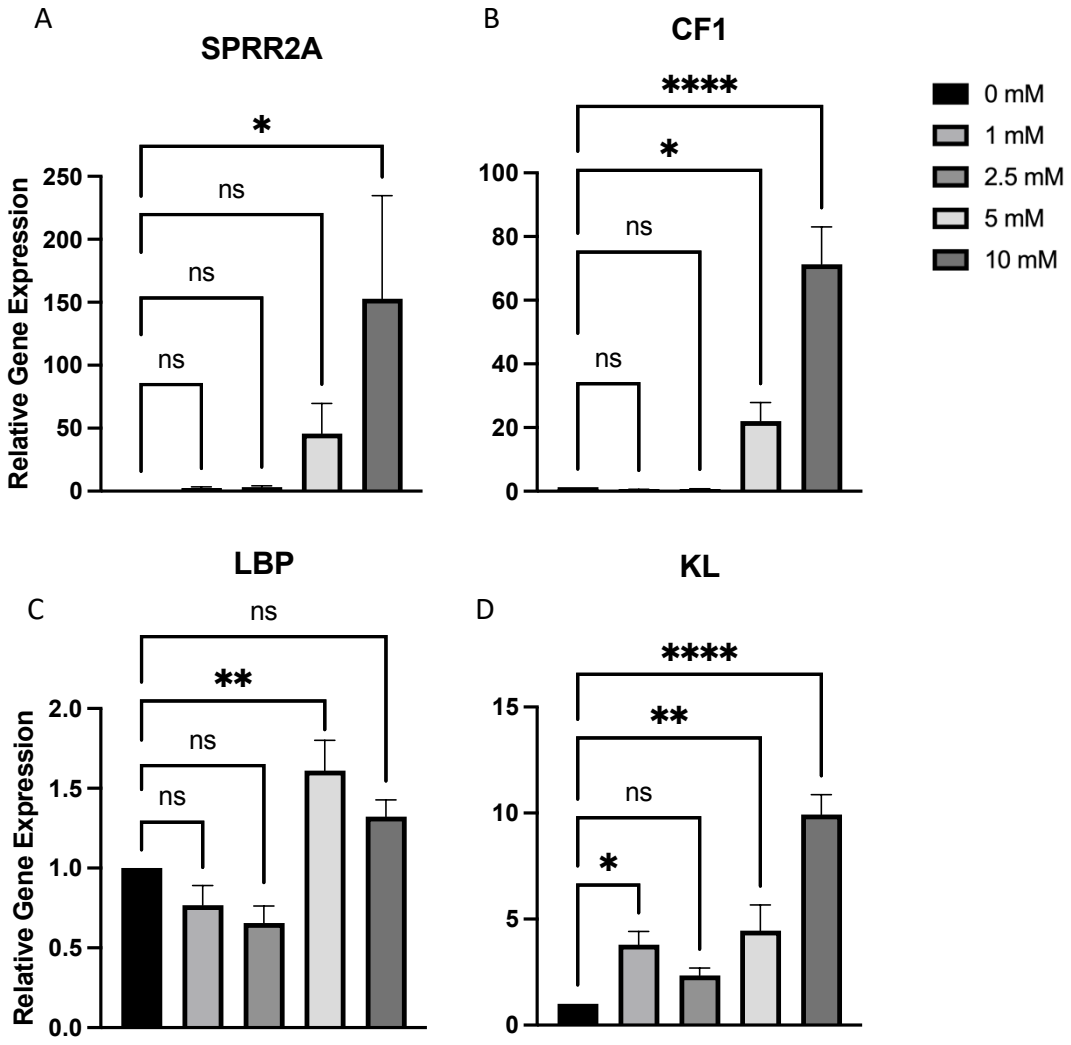


Figure 6:43 – Exogenous 2-oxoisopetanoate increases target gene expression in CC-SW1 cells. *CC-SW1 cells were treated with 0.0, 1.0, 2.5, 5.0, and 10.0 mM of exogenous 2-oxoisopentanoate and cultured for 48 hours prior to RNA extraction. The gene expression levels of A)* SPRR2A*, B)* CF1*, C)* LBP*, and D)* KL *were evaluated by qPCR after 2-oxoisopentanoate treatment. High concentrations of exogenous 2-oxoisopetanoate increased target gene expression in CC-SW1 cells (*P<0.05, **P<0.01, ***P<0.001, ****P<0.0001)(n=3).*

6.10 TCGA Genomic Validation

6.10.1 Introduction

The Cancer Genome Atlas (TCGA) was used to extract a public CCA dataset, which we used to determine differential expression of mRNAs between CCA and normal tissue, in order to provide further support for the genomic alterations identified during co-culture. This included pan-gene expression and the identification of metabolic gene sets.

6.10.2 CCA vs Normal Tissue Differential Gene Analysis

The PCA plot in Figure 6:44 shows robust separation between the 36 tumour samples (left) and the 9 normal samples (right), with a large range in variance from -100 to +200. We can see that PC1 accounts for 90% of the variation between the samples, showing the data is a good fit for the DESEQ2 model. Using DESEQ2, 11 genes (0.057%) were filtered out due to low counts, whilst 19223 genes were successfully processed. 42% of genes exhibited a Log2FC>0 (up) (7980 genes) and 37% a Log2FC<0 (down) (7158 genes). 15138 genes had a Log2FC of either direction P<0.05, whilst 14140 genes had a Log2FC of either direction P<0.01.

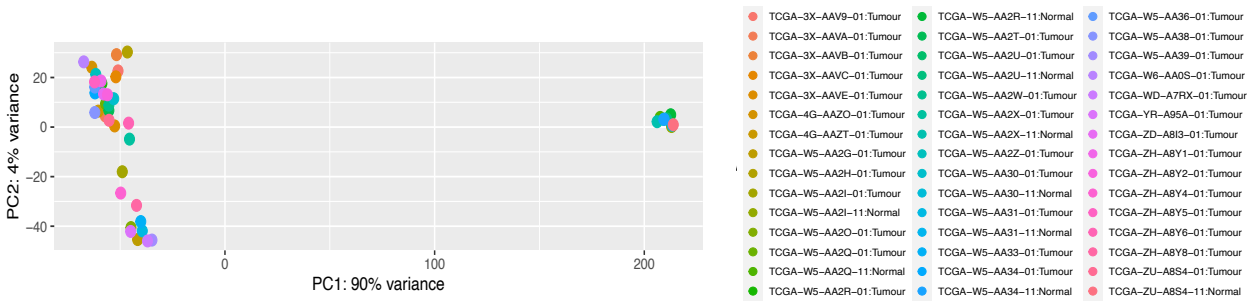


***Figure 6:44 - Principle Component Analysis of TCGA data**. A) PCA plot of CCA Tumour (n=36) vs Normal (n=9) mRNA expression data samples from TCGA Pan Cancer Atlas dataset analysis. Each point represents a sample, with its position reflecting its placement in a lower-dimensional space generated by the PCA. Samples with similar gene expression profiles cluster together. There is robust separation and clustering of the tumour samples from the normal samples in the analysis.*

The volcano plot in Figure 6:45A shows the differentially expressed genes between tumour and normal samples. Genes with a Log2FC >2 or <-2 are shown in green, genes with a P-value <0.05 are shown in blue, and genes with both a Log2FC >2 or <-2 and a P-value <0.05 are shown in red.

Figure 6:45B represents the gene with the most significant differential expression (P<0.0001) *ATP4B* (Entrez ID 496), a H+/K+ coupled ATPase, was significantly reduced in tumour samples.

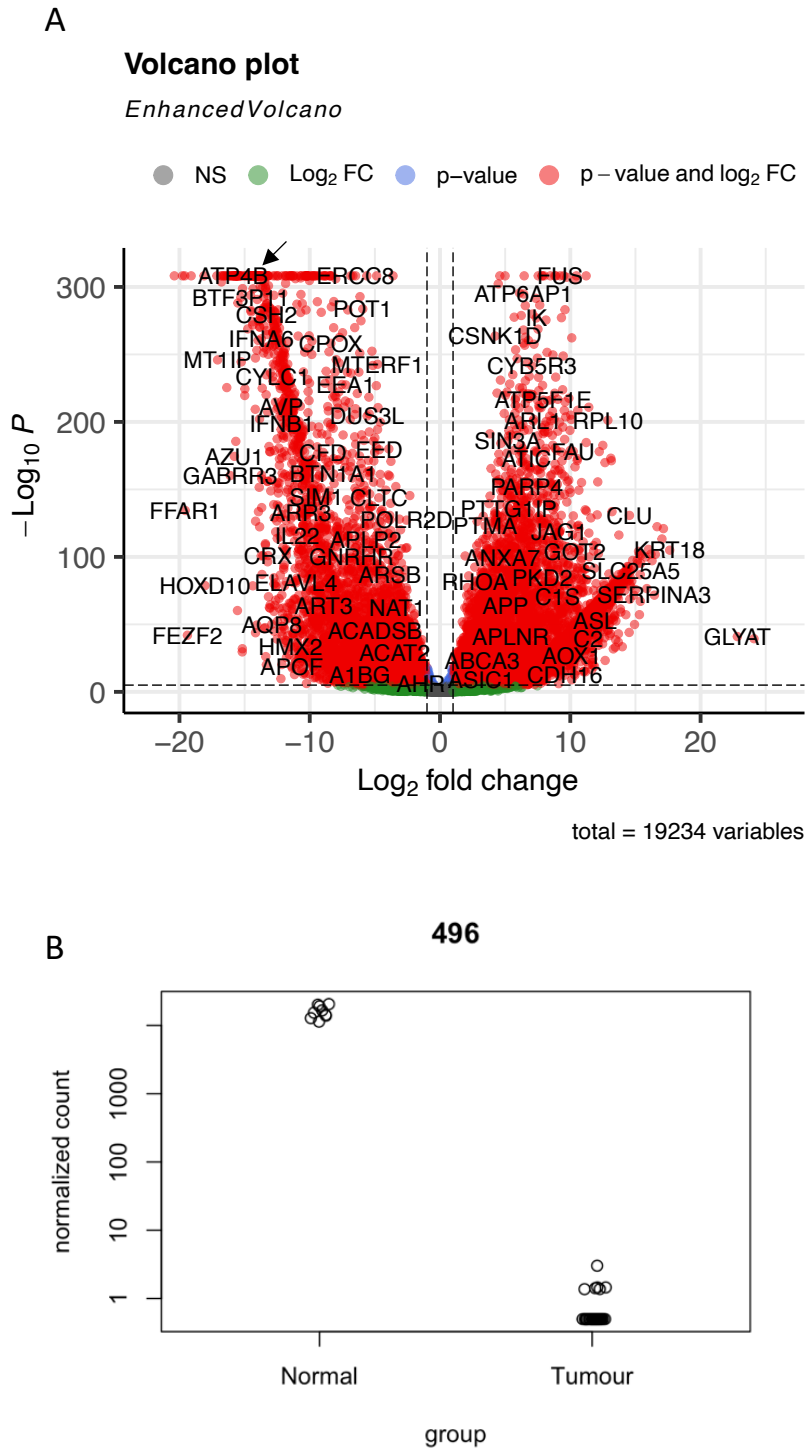


Figure 6:45 - Differential gene expression analysis of CCA vs normal tissue. *A) Volcano plot depicting the differential gene expression in CCA tumour against non-tumour tissue, extracted from the PanCancerAtlas mRNA-seq data from The Cancer Genome Atlas (TCGA). Each point on the plot represents a gene with its position indicating both statistical significance and fold-change in gene expression. The dashed horizontal line represents the predefined threshold for significance, -log10(p-value) > 1.3 (blue), whilst the dashed vertical lines represents the predefined threshold for fold-change, log2 fold-change>1/<-1. whilst the dashed vertical lines represents the predefined threshold for fold-change, log2 fold-change>1/<-1 (green). Genes which fulfil both significance and fold change criteria are shown in red, with upregulated genes on the right side, and downregulated genes on the left side. The black arrow denotes the position of the most differentially expressed gene,* ATPB4*, on the volcano plot. B) Dot plot of normalized gene count for* ATPB4 *(496) in CCA vs normal samples from TCGA.*

6.10.3 Metabolic Gene Set Enrichment Analysis

For the TCGA analysis, differentially expressed genes were stratified according to 75 metabolic gene sets. These metabolic gene sets were obtained from established GSEA cancer analyses (80–82), and comprised of 2,752 genes encoding all known human metabolic enzymes and transporters classified according to the Kyoto Encyclopaedia of Genes and Genomes (KEGG) (80,82,83). These metabolic gene sets were then ranked based on median fold expression changes in CCA tumours vs normal tissue, as shown in Figure 6:46.

We applied the same threshold used during the RNA-sequencing analysis: a Log2FC threshold of 1, and P-value of 0.05. In this instance, 26 metabolic gene sets were over-expressed in CCA tumours: BCAAs, Glyoxylate, Creatine, Urea, Bile Acid, Polyamine, Tyrosine, NAD, ATPase, BH4, Cholesterol, Mevalonate, Glutathione, Serine, Methionine, Aminosugar, Pentose Phosphate, Glycolysis, Sulphate, Other Transport, Hormone, Glycan, Glycan Sulphate, Signalling, Ketone Bodies, and Ion Transport.

Likewise, 27 metabolic gene sets were under-expressed in CCA tumours: CoA, Small Molecule Transport, Porphyrin, ABC Transporter, Nucleotide, Ubiquinone, Other, Sphingolipid, Nucleotide Sugar, Multipurpose, Glutamate, Heparin Sulphate, Amino Acid, Fatty Acid, Tryptophan, Neurotransmitter, Carbohydrate Storage, Xylulose, Reactive Oxygen, Detox, Vitamin A, Propanoate, Steroid, Vitamin B6, Anaerobic Glycolysis, B12, and Histidine. The most over-expressed metabolic gene set in the TCGA data was that of Branched Chain Amino Acids (BCAAs) (median Log2FoldChange = 8.271082933). Likewise,

the third over-expressed metabolic gene set was that of creatine (median Log2FoldChange = 7.6138020295).

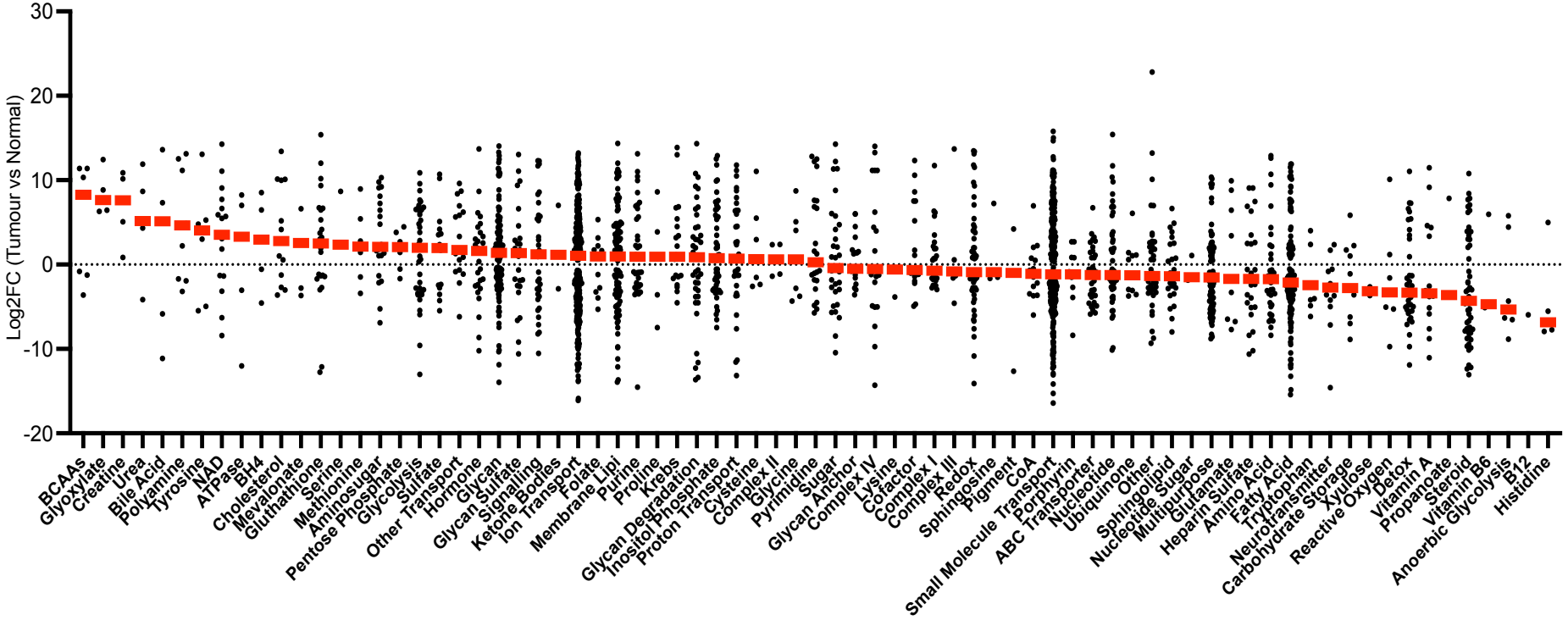


Figure 6:46 - Metabolic Gene Set Analysis of TCGA RNA-seq data classified by KEGG pathways. *This figure presents the results of a comprehensive analysis of the PanCancerAtlas RNA-seq data sourced from The Cancer Genome Atlas (TCGA) dataset. Genes classified and stratified into 75 metabolic gene sets according to the Kyoto Encyclopaedia of Genes and Genomes (KEGG) metabolic pathways. A ranked list of metabolic gene sets was generated based on Log2FoldChange expression in CCA tumours (n = 36) and normal bile duct (n = 9). The median Log2FoldChange in gene expression for each metabolic gene set is denoted by a red rectangle. The Log2FoldChange in expression for each gene within the respective metabolic gene set is denoted by a black circle. Metabolic gene sets are ranked from largest increase in Log2FoldChange in gene expression in tumour samples, to largest decrease in gene expression in tumour samples compared to normal tissue. The same threshold for significance and biological relevance was applied, a Log2FC of >1/>-1, and P-value of 0.05, resulting in 26 KEGG metabolic gene sets upregulated in CCA tumour samples, and 27 KEGG metabolic gene sets downregulated in CCA tumour samples. The most over-expressed metabolic gene set in the TCGA data was that of Branched Chain Amino Acid metabolism(BCAAs) (median Log2FoldChange = 8.271082933), whilst the Histidine metabolism gene set had the largest reduction in expression (median Log2FoldChange = -6.843533438).*

6.10.4 TCGA validation of target genes

We used the TCGA gene expression data to compare the pattern of gene expression changes in tumour vs normal tissue against our mono- vs co-culture RNA-seq gene expression validation data.

Figure 6:47 lists the genes significantly upregulated in MMNK1 (top) cells, as identified by RNA-sequencing. In tumour samples, only *HSPA8, MGAT3,* and *KCNK3* gene expression was significantly upregulated. The expression of *TXNIP,FAP, IDO1, EXTL1,* and *AURKA* was significantly decreased in tumour samples, whilst there was no significant change in *TXN* and *NPPB* gene expression.

Figure 6:47 lists the genes significantly upregulated in CC-SW1 (middle) cells, as identified by RNA-sequencing. In tumour samples, none of these genes experienced a significant upregulation in gene expression, and there was no significant difference in *SPRR2A* and *CFI* gene expression. Tumour samples displayed a significant reduction in *LBP* and *Klotho* gene expression, contrary to the trend in expression seen in our co-culture system.

Figure 6:47 (bottom) lists cytokines differentially expressed in our indirect co-culture assay. In tumour samples, the expression of *CXCL1* and *2* was significantly increased, whilst the expression of *CXCL3* was significantly reduced. There was no significant difference in the gene expression of *IL-6* or *MCP-1*.

Gene	Log_2FoldChange	Padj	Name
HSPA8	9.037889503	8.12E-216	Heat Shock Protein Family A (Hsp70) Member 8
AURKA	-3.725266584	1.27E-30	Aurora Kinase A
EXTL1	-3.594885844	1.51E-12	Exostosin Like Glycosyltransferase 1
MGAT3	4.411957082	8.66E-08	Beta-1,4-mannosyl-glycoprotein 4-beta-N-acetylglucosaminyltransferase
KCNK3	2.177450437	0.000986674	Potassium Two Pore Domain Channel Subfamily K Member 3
IDO1	-2.226277377	0.005934298	Indoleamine 2,3-Dioxygenase 1
FAP	-1.212927985	0.009938606	Fibroblast Activation Protein Alpha
TXNIP	-1.136782569	0.021502768	Thioredoxin Interacting Protein
TXN	-0.554502879	0.076437205	Thioredoxin
NPPB	-2.22005408	0.097173772	Natriuretic Peptide B

Gene	Log_2FoldChange	Padj	Name
KL	-6.299670054	9.02E-25	Klotho
LBP	-2.049665437	0.017703944	Lipopolysaccharide Binding Protein
CFI	-0.650204235	0.10783487	Complement Factor I
SPRR2A	1.482413483	0.243942116	Small Proline Rich Protein 2A

Gene	Log_2FoldChange	Padj	Name
CXCL1	5.59031989	9.50E-21	Chemokine Ligand 1
CXCL2	4.36374746	1.27E-14	Chemokine Ligand 2
CXCL3	-2.517626419	0.000265179	Chemokine Ligand 3
IL-6	1.4237768	0.11642	Interleukin 6
MCP-1	-0.819345905	0.207794961	Monocyte Chemoattractant Protein 1

Figure 6:47 - Table of gene expression data from The Cancer Genome Atlas (TCGA) in CCA tumour samples for our genes of interest*. We conducted differential gene analysis on the PanCancerAtlas RNA-seq data sourced from The Cancer Genome Atlas (TCGA) dataset. We extracted the expression data for our genes of interest identified in our RNA-sequencing analysis: MMNK1 cells (top), CC-SW1 cells (middle), and cytokines of interest (bottom.)*

As previously discussed, we used our metabolomics analysis to select specific metabolites for investigation, highlighting asparagine, choline, and creatine in MMNK1 cells, and 2-oxoisopentanoate in CC-SW1 cells. Using our transcriptomic data we also evaluated gene expression changes in the genes relating to the metabolism of each of these metabolites. Here we use the TCGA CCA dataset PanCancerAtlas to compare the pattern of gene expression changes in tumour vs normal tissue against our mono- vs co-culture RNA-seq gene expression data for these metabolic genes.

For asparagine, we identified a significant decrease in *ASNS* expression in MMNK1 cells through RNA-sequencing, which was validated via qPCR. This decrease was replicated in tumour samples (Log2FoldChange= -0.6312216, Padj=0.04908)(Figure 6:48, top).

For choline, RNA-sequencing identified no significant difference in the expression of Choline Kinases A (*CHKA*) or B (*CHKB*). However, when validating by qPCR, we found a significant increase in both *CHKA* (P=0.0006) and *CHKB* (P=0.0001) gene expression. Likewise, there was a significant increase in *CHKA* (Log2FoldChange=1.189540264, Padj=0.000396721) and a dramatic increase in *CHKB* expression (Log2FoldChange=5.002219508, Padj=9.85226E-78) in tumour samples (Figure 6:48). The choline transporters *SLC44A1* (CTL1), *SLC44A2* (CTL2), *SLC44A3* (CTL3), *SLC44A4* (CTL4), *CTL5* (SLC44A5) and *CHT1* (SLC5A7) were also assessed. RNA-sequencing identified a significant increase in *SLC44A1* expression, which was not replicated by qPCR (P= 0.2114). Contrary to this, a significant decrease in *SLC44A1* expression was identified in tumour samples (Log2FoldChange=-1.4026, Padj=1.88759E-05).

RNA-sequencing identified no significant difference in *SLC44A2* expression, which was validated by qPCR (P= 0.7041). Contrary to this, a significant increase in *SLC44A2* expression was identified in tumour samples (Log2FoldChange=1.18954, Padj=3.3134E-06).
RNA-sequencing identified a significant increase in *SLC44A3* expression, which was validated by qPCR (P<0.0001). However, no significant change in expression was detected in tumour samples (Padj=0.11639).
RNA-sequencing identified no significant difference in *SLC44A4* expression, contrary to qPCR which identified a significant increase in expression (P= 0.0171). No significant change in expression was identified in tumour samples (Padj=0.334968).
SLC44A5 expression was not detected during RNA-sequencing, however qPCR identified a significant increase in expression (P<0.0001). A significant increase was also identified in tumour samples (Log2FoldChange=1.6793, Padj=0.0480).
SLC5A7 expression was not detected during RNA-sequencing, and qPCR identified no significant change in expression (P= 0.5982). In tumour samples however, there was a significant decrease in expression (Log2FoldChange=-11.7522, Padj=2.2923E-147).
Taken together, the pattern of choline transporter gene expression in our co-culture system was contradictory to the profile in TCGA tumour samples, whilst the expression of choline kinases was consistent.

The third over-expressed metabolic gene set in the TCGA data was that of creatine, and the genes corresponding to creatine metabolism are shown in Figure 6:48 (middle). Consistent with our RNA-sequencing data for MMNK1 cells in co-culture, there was a significant increase in the gene expression of *GAMT* (Log2FoldChange=10.15674, Padj= 3.6477E-44) and *CKB* (Log2FoldChange=10.87919, Padj= 5.18997E-49). Taken together, the gene

expression for creatine metabolism in our co-culture system was consistent with the gene expression profile in TCGA tumour samples.

2-oxoisopentanote was identified as our metabolite of interest in CC-SW1 cells from our metabolomic analysis. The genes corresponding to 2-oxoisopentanote metabolism fall within the Branched Chain Amino Acid metabolism gene set, the most over-expressed metabolic gene set in the TCGA data, and are shown in Figure 6:48 (bottom).
The expression of MCCC1, *DBT, HIBCH, MCCC2,* and *HIBADH* was significantly increased in tumour samples, whilst the expression of *BCKDHA, BCAT2,* and *BCKDHB* was significantly decreased.

When comparing the trend in tumour expression to co-culture expression, we see very little consistency. There was a significant increase *in MCCC1* and *HIBADH* gene expression in tumour samples, but a reduction during co-culture, whilst a significant increase in *DBT, HIBCH, MCC2* gene expression was observed in tumour samples, but these had no change during co-culture. There was no significant difference in *BCAT1* gene expression in tumour samples, but a significant decrease in *BCAT2* gene expression, whilst the reverse was true in co-culture.
Likewise, *BCKDHA* and *BCKDHB* expression was significantly reduced in tumour samples, with no change during co-culture.

Gene	Log_2FoldChange	Padj	Name
ASNS	-0.6312216	0.049084292	Asparagine Synthetase
CHKA	1.189540264	0.000396721	Choline Kinase Alpha
CHKB	5.002219508	9.85226E-78	Choline Kinase Beta
SLC5A7	-11.7522229	2.2923E-147	Solute Carrier Family 5 Member 7
SLC44A1	-1.402620361	1.88759E-05	Solute Carrier Family 44 Member 1
SLC44A2	1.189264617	3.3134E-06	Solute Carrier Family 44 Member 2
SLC44A3	0.714020629	0.116394203	Solute Carrier Family 44 Member 3
SLC44A4	1.092702195	0.334968466	Solute Carrier Family 44 Member 4
SLC44A5	1.679246613	0.048001131	Solute Carrier Family 44 Member 5

Gene	Log_2FoldChange	Padj	Name
CKB	10.87791925	5.18997E-49	Creatine Kinase B
GAMT	10.15674335	3.6477E-44	Guanidinoacetate N-Methyltransferase
GATM	5.070860709	1.53964E-21	Glycine Amidinotransferase
CKBE	0.851591791	1.40627E-05	Tubulin Folding Cofactor B
CKMT1B	1.592691552	0.075736736	Creatine Kinase, Mitochondrial 1A
CKMT1A	-1.003804475	0.216822226	Creatine Kinase, Mitochondrial 1B
CKM	-0.801564389	0.248855453	Creatine Kinase, M-type
CKMT2	-0.540434312	0.506084209	Creatine Kinase, Mitochondrial 2

Gene	Log_2FoldChange	Padj	Name
MCCC2	8.404198564	8.0088E-122	Methylcrotonyl-CoA Carboxylase Subunit 2
HIBADH	8.137967302	1.39753E-93	3-Hydroxyisobutyrate Dehydrogenase
DBT	11.37174332	3.92278E-57	Dihydrolipoamide Branched Chain Transacylase E2
MCCC1	11.38617252	7.45681E-48	Methylcrotonyl-CoA Carboxylase Subunit 1
HIBCH	10.33721016	3.3078E-46	3-Hydroxyisobutyryl-CoA Hydrolase
BCKDHB	-3.622890957	7.83017E-30	Branched Chain Keto Acid Dehydrogenase E1 Subunit Beta
BCAT2	-1.229493519	6.32755E-09	Branched Chain Amino Acid Transaminase 2
BCKDHA	-0.809940256	0.002535947	Branched Chain Keto Acid Dehydrogenase E1 Subunit Alpha
IVD	0.278968582	0.189929679	Isovaleryl-CoA Dehydrogenase
BCAT1	-0.512659952	0.265108135	Branched Chain Amino Acid Transaminase 1

Figure 6:48 - Table of gene expression data from The Cancer Genome Atlas (TCGA) in CCA tumour samples for our metabolic genes of interest*. We conducted differential gene analysis on the PanCancerAtlas RNA-seq data sourced from The Cancer Genome Atlas (TCGA) dataset. We extracted the expression data for our genes of interest identified in our metabolomic analysis: Asparagine and choline metabolism (top), creatine metabolism (middle), and Branched Chain Amino Acid metabolism(bottom).*

6.11 Discussion

In this study, we sought to parse out the gene expression changes that mediate the alterations to cellular phenotypes as discussed in the previous chapter (Results Chapter 1), comprising of the time-dependent decrease in apoptosis in MMNK1 cholangiocytes, and decrease in EMT in CC-SW1 cells. Specifically, we aimed to identify differential gene expression responsible for eliciting alterations to metabolism and cytokine expression during indirect co-culture, and whether these alterations were replicated in CCA tumour samples. To this end, we utilized large scale transcriptomics to evaluate the change in gene expression for each cell line during co-culture at 48 hours, with selected targets subsequently validated by qPCR, and genes of interest evaluated in a database from TCGA.

We successfully validated the gene expression of two panels of genes as identified by RNA-sequencing from MMNK1 cells during co-culture. We also evaluated the expression of metabolism-related genes. The gene expression of *AURKA, HSPA8, NPPB,TXNIP,* and *TXN* was increased in MMNK1 cells during co-culture as identified by RNA-sequencing, and validated by qPCR. Evaluation of protein expression via Western Blotting showed global downregulation of protein expression for *HSPA8, TXNIP,* and *TXN* in co-culture. Likewise, the expression of genes only identified in MMNK1 cells *KCNK3, EXTL1, MGAT3, FAP,* and *IDO1*, were validated by qPCR, where we saw a trend in increasing gene expression during co-culture in agreement with the RNAseq. It was interesting to note that the mRNA and protein levels for our first target panel of interest did not correlate. Gene expression levels do not always perfectly reflect protein levels for many reasons, including post-transcriptional processes such as alternative splicing, and RNA stability regulation, which can lead to differences in mRNA isoforms and stability, thereby impacting protein

abundance. Likewise, translation efficiency, influenced by factors like ribosome availability, mRNA secondary structure and even alternative initiation codon selection can also vary, affecting the correlation between mRNA and protein levels. Additionally, proteins undergo post-translational modifications and have different degradation rates, which are not reflected in gene expression data. Due to the modification to genes in the unfolded protein response (Figure 6:33) and a generalised reduction in the gene expression of translation machinery, in combination with the global downregulation of protein expression, the discordance in our results may be due to both abrogated protein degradation and decrease in translation.

Creatine concertation was significantly increased in MMNK1 cells during co-culture, and evaluation of creatine metabolism-related gene expression via transcriptomic analysis revealed a significant increase in *GAMT, SLC6A8,* and *CKB* expression. Exogenous creatine had no significant effect on the gene expression of *KCNK3, MGAT,* or *FAP*, whilst low concentrations of creatine caused a significant decrease in *EXTL1* and *IDO1* gene expression. Creatine was not responsible for the increase in *KCNK3*, *EXTL1, IDO1, MGAT3,* and *FAP* gene expression during co-culture, in fact exogenous creatine actually triggered a significant decrease in *EXTL1* and *IDO1* gene expression.

Exogenous asparagine led to a dose-dependent reduction of ASNS protein expression. ASNS protein level is controlled in a negative feedback mechanism via the direct binding of asparagine to LKB1 proceeding to inhibit AMPK, releasing p53 which proceeds to transcriptionally repress ASNS expression (163)

Furthermore, we successfully validated the gene expression of a panel of genes as identified by RNA-sequencing from CC-SW1 cells during co-culture. We also evaluated the expression of metabolism-related genes. Exogenous 2-oxoisopentanoate reduced gene expression of KL at 1mM, *LBP* ad *CF1* at 5mM, *SPRR2A* at 10mM. We see a significant decrease in the expression of *BCAT1* and *BCAT2*, the cytosolic and mitochondrial form of the Branched-Chain amino Acid Transaminase enzymes, which are responsible for the reversible transamination of branched-chain alpha-keto acids to branched-chain L-amino acids.

As shown previously, indirect co-culture altered the constituent cytokines that MMNK1 cholangiocytes and CC-SW1 cells were exposed to. To begin to shine a light on the respective secretion from each compartment, we evaluated the change in cytokine gene expression in each cell line during co-culture.

We witnessed a positive enrichment of cytokine-related pathways in CC-SW1 cells during co-culture and, however at an individual gene level, RNA-sequencing showed no significant change in *CXCL1* gene expression in MMNK1 cells during co-culture, with a significant decrease in *CXCL2* and *CXCL3* gene expression, where all three trends were was mirrored by qPCR validation. CC-SW1 cells on the other hand exhibited an increase in *CXCL1/2* and *3* gene expression as detected by RNA-seq, which was supported by the trend seen in the qPCR validation. Whilst the qPCR plots for CC-SW1 in Figures 6:39 highlight an increase in mRNA expression of *CXCL1*, *CXCL2* and *CXCL3*, this increase in not significant. However, due to the mirrored trends in the RNA-sequencing, we believe this increase in *CXCL1/2/* and *3* expression may be true. It would be crucial to validate the protein level of these cytokines using Human Quantikine ELISA Kits moving forwards, and PCR data repeated using an

additional housekeeping gene after careful consideration of the endogenous RNA control for normalisation.

Using a retrospective analysis of the PanCancerAtlas TCGA data, we also identified a significant increase in *CXCL1* and *CXCL2* gene expression in tumour samples, which was comparable to CC-SW1 gene expression during co-culture. Taken together, the data shown here suggests that CCA cells contribute to the majority of the secreted *CXCL1/2/* and *3* protein during co-culture and tumour development. Whilst the implications of *CXCL1/2/3* overexpression ought to be further delineated, the concordance shared between coculture and TCGA analysis potentially suggests that we have identified a cellular compartment that recapitulated, at least in part, *in vivo* observations in patient tumour samples.

RNA-sequencing identified a decrease in *IL-6* gene expression, which was replicated in qPCR validation in MMNK1 cells during co-culture. Interestingly *IL-6* was not detected in CC-SW1 cells during RNA-sequencing, but qPCR demonstrated a non-significant increase in expression. There was no significant change in *IL-6* gene expression in TCGA tumour samples. Taken together, we suggest that MMNK1 cells contribute the majority of the secreted IL-6 protein during in-direct co-culture, and alongside CAFs, contribute to IL-6 concentrations during tumour development.

Further work to support our hypothesis is required, including the knockdown of cytokines highlighted here, and the evaluation of intracellular cytokine concentrations, in order to work out which compartment they were secreted from during co-culture.

Investigating changes to gene expression is a crucial step in understanding how co-culture modulates CCA cell behaviour. However, the complexity of gene regulation goes beyond the mere expression or repression of genes. Epigenetic modifications can alter the accessibility

of genes for transcription, without changing the underlying DNA sequence, and play a pivotal role in gene expression regulation. Therefore, it is imperative to evaluate the response to epigenetic inhibition alongside gene expression studies. In doing so, we can begin to unravel the intricate interplay between genetic and epigenetic factors, providing insights into the mechanisms underlying co-culture, as a measure of CCA development. In order to take this integrated approach, we therefore need to evaluate the response of CCA cells in co-culture to epigenetic inhibition.

7 Results Chapter 4 – Evaluation and Inhibition of the Epigenome during Co-Culture

7.1 Introduction

Classically, CCA is very chemoresistant, and is commonly reported to be resistant to standard chemotherapeutic regimes (164). CCA cell lines replicate this behaviour, and as such are resistant to established does of 5-Fluorouracil (5-FU)(Figure 7:1A-C). 5-FU is a common chemotherapeutic drug that inhibits thymidylate synthase, a key enzyme in thymidine synthesis, resulting in reduced thymidine availability for DNA synthesis and thereby inhibiting cancer cell growth and division. Of the molecular targeted therapies in development, epigenetic modifies display one of the greatest untapped benefit, especially as the predominant genomic alterations in CCA are associated with epigenetic processes (153).

There are 3 canonical programs of epigenetic regulation: DNA methylation, non-coding RNAs, and histone modification, all of which have been identified as essential for the onset and progression of CCA(1). Hypermethylation of the *p16INK4a* gene disrupts cell cycle control, as under normal conditions, *p16INK4a* acts to regulate the cell cycle by preventing the formation of the Cyclin D1-CDK4 complex. However when the p16INK4a gene is hypermethylated, the Cyclin D1-CDK4 complex is formed and the cell progresses through the S phase. This hypermethylation of *p16INK4a* is thought to occur in around 83% of CCA cases(165). Moreover, the transcriptional partner of p16INK4a, *p14ARF*, is also hypermethylated in CCA, preventing p14ARF from protecting p53 from degradation(166), a loss of control commonly seen in CCA.

Histone deacetylase 6 (HDAC6) overexpression has also been reported in CCA, with consequential pharmacological interruption diminishing CCA proliferation (167), whilst recurrent, inactivating mutations in chromatin regulators, such as *BAP1, ARID1A, PBRM1, SMARCA2, SMARCA4,* and *SMARCAD1* (150,153,168), demonstrate that CCA has an epigenetically-inclined mutational spectrum, further providing support for the use of epigenetic modifiers in CCA.

Moreover, it is well established that the inflammatory response is critical to the development of CCA. The continuous overexpression of interleukin-6 (Il-6), via the epigenetic silencing of the cytokine 3 signalling (*SOCS-3*) repressor (65) has been identified in CCA, whilst the use of Histone Deacetylase Inhibitors (HDACis) have been shown to play a role in the suppression of proinflammatory cytokine production (169,170). Likewise, IL-6 has been shown to upregulate miRNA expression (171) and increased microRNA expression of *miR-222, miR-483-5p,* and *miR-221* have been identified in CCA patients, where *miR-221* has been found to strongly associate with increased EMT and metastasis in eCCA patients (172). The acetylation and methylation of histones and non-histone substrates play a crucial role in CCA development and progression. Important for the regulation of chromatin structure and function, as well as the control of gene expression, the balance between histone acetylation and deacetylation acts as a switch for the transcriptional repression of genes responsible for migration and proliferation (173). The methylation of lysine 27 on histone 3 by Enhance of zeste homolog 2 (*EZH2*) is associated with gene repression in CCA (153), and the overexpression of *EZH2* is typified by poor prognosis in iCCA as well as eCCA (153). Taken together, there are distinct epigenetic controls of CCA that have the potential for targeting.

In order to evaluate the epigenetic vulnerability of CCA cells in vitro, we conducted a drug screen using the SGC Epigenetic Chemical Probes library, comprising of 63 epigenetic inhibitors including methyltransferase inhibitors (MT), lysine demethylase inhibitors (KDM), and bromodomain inhibitors (BRD). From this panel, we selected epigenetic compounds of interest for further investigation into the modulation of chemosensitivity by cholangiocyte cells.

7.2 5-Fluorouracil Resistance in CCA cell lines

We evaluated the response of the CCA cell lines CC-LP1, SNU-1079, and SNU-1196 to varying concentrations of the chemotherapeutic 5-Fluorouracil (5FU). The dose-response curves in Figure 7:1A-C show the cell viability of each these cell lines over 10 µM of 5FU. Cell viability did not drop below 100% for CC-LP1 cells (Figure 7:1A), whilst SNU-1079 and SNU-1196 cells experienced a cell viability of 62% and 73% respectively (Figures 7:1B &C) following treatment with 10 µM of 5FU.

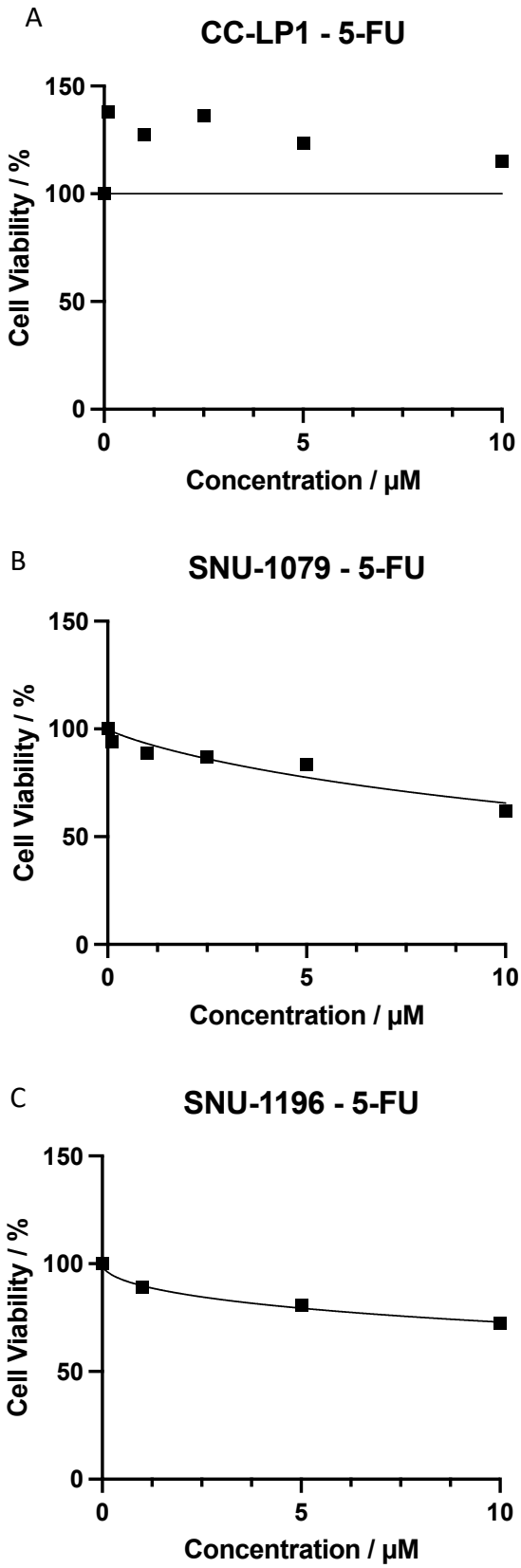


Figure 7:1 – CCA cell resistance to 5-fluroruacil. *A) Dose-response curve showing CC-LP1 cell viability when treated with various concentrations of 5-FU. B) Dose-response curve showing SNU-1079 cell viability when treated with various concentrations of 5-FU. C) Dose-response curve showing SNU-1196 cell viability when treated with various concentrations of 5-FU.*

7.3 Epigenetic Inhibitor Panel

A CCA cell viability of <60% was chosen as the threshold for compound efficacy, whilst an additional threshold of MMNK1 cell viability of >80% was chosen as compound selectivity. These thresholds were chosen in order to identify compounds that selectively killed CCA cells, but not the non-tumour MMNK1 cholangiocyte cells. Cancer cells often acquire genetic and epigenetic alterations that are specific to their malignant phenotype. Targeting these alterations selectively in cancer cells while sparing normal cells can improve the efficacy and reduce the toxicity of cancer treatments.

We can see from the heatmap in Figure 7:2A, the response pattern of the intrahepatic CCA cell lines are broadly similar. The response of the extrahepatic cell line SNU-1196 is markedly different to the iCCA cell lines, whilst the response of the cholangiocyte cell line MMNK1 appears a midway point between the two sets. As we required a compound selective for the tumour cells, five compounds were excluded from further analysis for causing a reduction in MMNK1 cell viability <80%: LLY-507, BAY-850, UNC0638, UNC 1999 and JQ1.

Figure 7:2B shows 11 compounds which significantly reduced cell viability of at least one CCA cell line. Based on our criteria, all intrahepatic CCA lines (CC-SW1, CC-LP1, and SNU1079) were sensitive to GSK-J4 at 10 µM (P=0.02204, 0.00352, and 0.00063 respectively). Likewise, CC-SW1 and SNU1079 cells were sensitive to UNC0642 at 10 µM (P=0.0114 and 0.00029). The perihilar CCA cell line SNU1196 was only sensitive to SGC 3027 at 10 µM (P=0.04688), as well as the intrahepatic cell line CC-LP1 (P=0.00567).

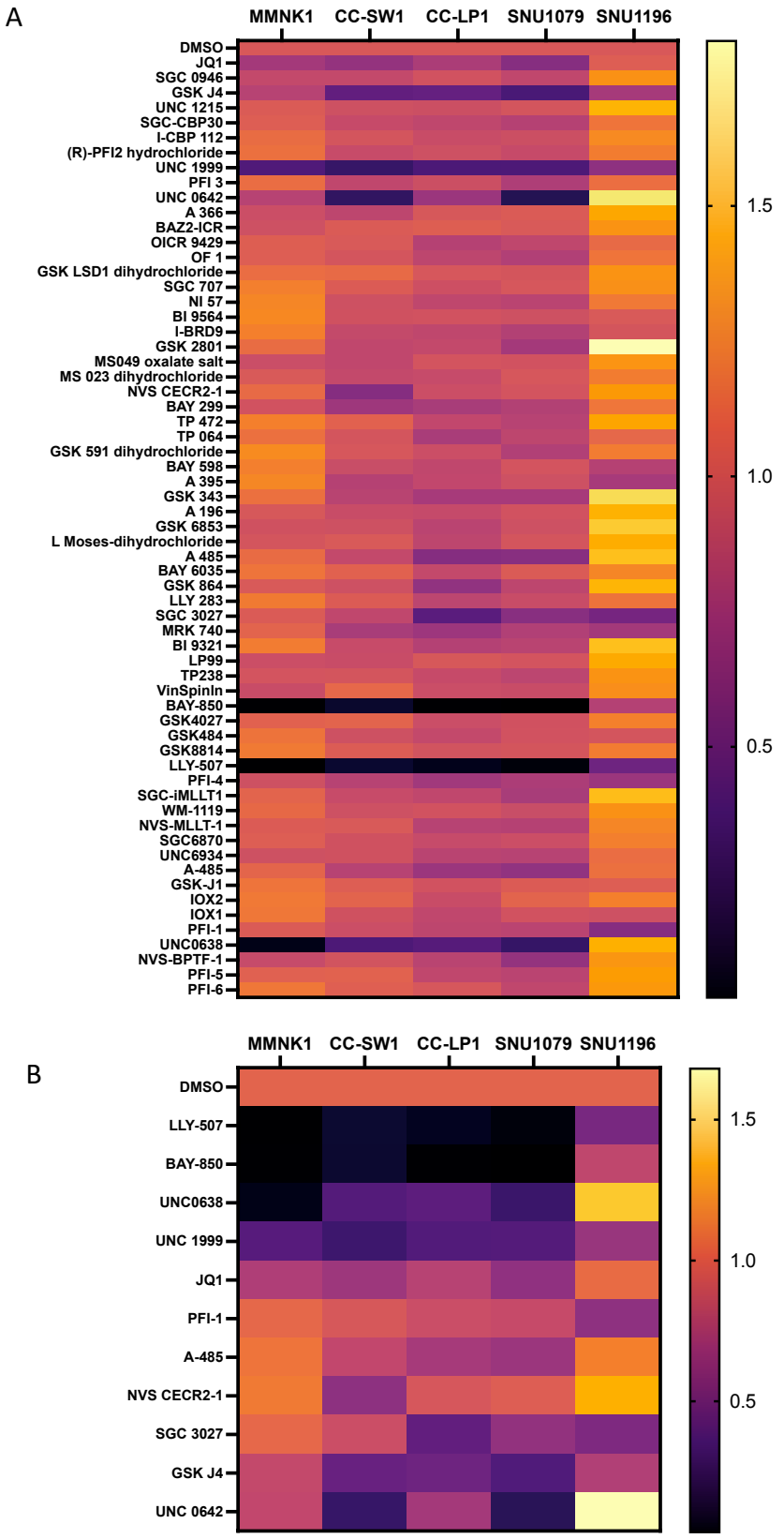
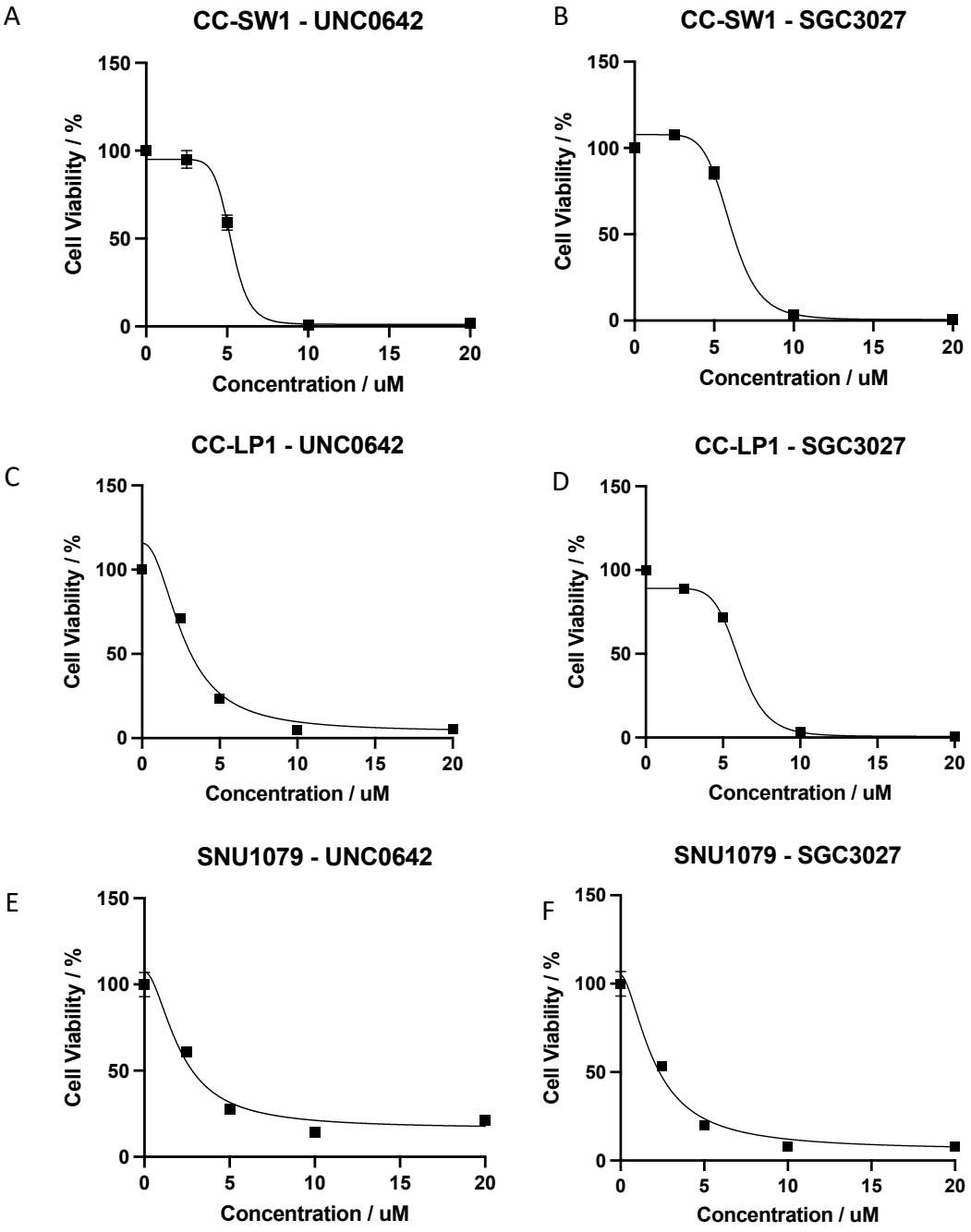


Figure 7:2 – Epigenetic inhibitor screen in CCA cells. *A) Heatmap showing the viability of MMNK1 cholangiocytes, CC-SW1, CC-LP1, SNU-1079, and SNU-1196 CCA cells after treatment with 63 epigenetic compounds from the SGC epigenetic inhibitor panel. B) Heatmap highlighting the top 11 epigenetic inhibitors that reduced CC-SW1, CC-LP1, SNU-1079, or SNU-1196 cell viability by at least 60%, whilst maintaining MMNK1 cholangiocyte cell viability at 80%. DMSO used as a control. The darker colour (purple/black) equates to a lower cell viability (%), whilst the brighter colour (orange/yellow) indicates higher cell viability, 100% viability is indicated by 1.0 (%)(n=3).*

7.4 Analysis of UNC0642 and SGC-3027

We selected two compounds for further investigation: UNC0642 an inhibitor of the methyltransferases G9a/GLP; and SGC-3027, an inhibitor of the arginine methyltransferase PRMT7. Cell survival analyses were conducted for both compounds (Figure 7:3A-F)

The IC50 values for UNC0642 was 5.253, 2.673, and 2.096 µM in CC-SW1, CC-LP1, and SNU-1079 cells respectively (Figure 7:3A, C, & E). Likewise, the IC50 values for SGC-3027 was 6.049, 6.090, and 2.038 µM in CC-SW1, CC-LP1, and SNU-1079 cells respectively (Figure 7:3B, D, & F).



G

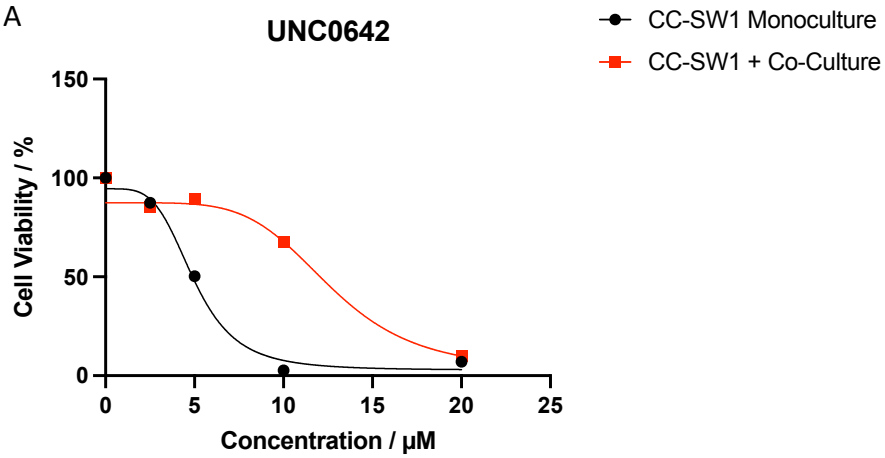
Cell Line	IC50 Value / µM	
	UNC0642	SGC3027
CC-SW1	5.253	6.049
CC-LP1	2.673	6.090
SNU-1079	2.096	2.038

Figure 7:3 - The effect of the epigenetic inhibitors UNC0642 and SGC3027 on iCCA cell viability*. A) Dose-response curve showing CC-SW1 cell viability when treated with various concentrations of UNC0642. B) Dose-response curve showing CC-SW1 cell viability when treated with various concentrations of SGC3027. C) Dose-response curve showing CC-LP1 cell viability when treated with various concentrations of UNC0642. D) Dose-response curve showing CC-LP1 cell viability when treated with various concentrations of SGC3027. E) Dose-response curve showing SNU-1079 cell viability when treated with various concentrations of UNC0642. F) Dose-response curve showing SNU-1079 cell viability when treated with various concentrations of SGC3027. G) Table of IC50 values for UNC0642 and SGC3027 in CC-SW1, CC-LP1, and SNU-1079 cells.*

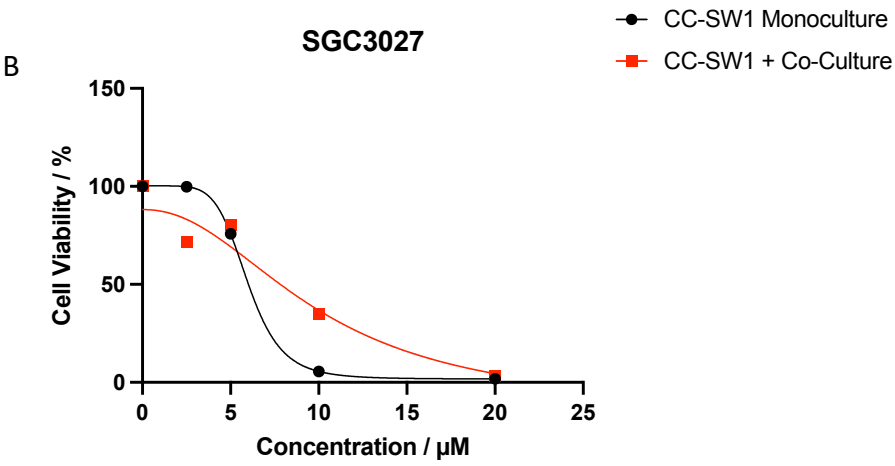
7.5 Effect of Co-Culture on UNC0642 and SGC-3027 Efficacy

To investigate the impact of indirect co-culture with MMNK1 cholangiocytes on CC-SW1 cell drug sensitivity, we applied our transwell model, and co-cultured cholangiocytes in transwell inserts which were removed prior to the evaluation of CC-SW1 cell viability via CCK8 colorimetric analysis. After co-culture, the IC50 of UNC0642 increased to 12.63 µM (Figure 7:4A & C). Likewise, after co-culture, the IC50 of SGC3027 increased to 9.967 µM (Figure 7:4B &C).

A



B



C

Drug	IC50 Value / µM	
	Monoculture	Co-Culture
UNC0642	5.253	12.630
SGC3027	6.049	9.967

***Figure 7:4 - The effect of co-culturing CC-SW1 cells with MMNK1 cells on epigenetic inhibitor efficacy**. A) Dose-response curve showing CC-SW1 cell viability when treated with various concentrations of UNC0642 in mono- (black) and co-culture with MMNK1 cells (red). B) Dose-response curve showing CC-SW1 cell viability when treated with various concentrations of SGC3027 in mono- (black) and co-culture with MMNK1 cells (red). C) Table of IC50 values for UNC0642 and SGC3027 in CC-SW1 cells when in mono and co-culture with MMNK1 cells.*

7.6 Evaluation of Epigenome-Associated Genes

We used the transcriptomic data from our RNA-sequencing to evaluate differences in the expression of the epigenetic inhibitor targets, in order to evaluate whether differences in drug sensitivity were due to differences in basal gene expression. Furthermore, we used the co-culture transcriptomic data to explore whether co-culture mediated epigenetic inhibitor target gene changes, to explain co-culture induced sensitivity differences. We then proceeded to validate whether these gene expression changes were recapitulated in CCA patients, using TCGA transcriptomic data.

7.6.1 *EHMT1*, *EHMT2*, and *PRMT7* transcriptomic data

From our RNA-sequencing experiments, we can see that G9a (gene name *EHMT2*) and GLP (gene name *EHMT1*) were expressed to a greater degree in our CC-SW1 cells compared to MMNK1 cells (Log2FoldChange =1.9466491, Padj=1.58E-128 and Log2FoldChange =0.5117206, Padj=9.32E-10 respectively). Likewise, *PRMT7* expression was significantly greater in CC-SW1 CCA cells than MMNK1 cholangiocyte cells (Log2FoldChange = 1.645939664, Padj= 5.49E-60) (Figure 7:5A).

We see in Figure 7:5B that co-culture of MMNK1 cells with CC-SW1 cells increases the gene expression of *EHMT1, EHMT2,* and *PRMT7* (Log2FoldChange =0.160763855, Padj=0.04765513, Log2FoldChange =0.458740966, Padj=1.01E-08, and Log2FoldChange =0.831582697, Padj= 5.25E-16 respectively). Figure 7:5C shows co-culture of CC-SW1 cells with MMNK1 cells had no effect on the gene expression of *EHMT1, EHMT2,* or *PRMT7* (Padj=0.99728019, 0.56208527, and 0.7766911 respectively).

7.6.2 EHMT1, EHMT2, and PRMT7 TCGA data

The TCGA analysis showed that whilst *EHMT2* was significantly overexpressed in tumour tissue samples (Log2FoldChange =2.68943178, Padj=1.12E-38), *EHMT1* expression was reduced (Log2FoldChange =-2.0189534, Padj=7.15E-39) (Figure 7:6). There was a non-significant, marginal reduction in *PRMT7* expression in CCA tumour samples in our TCGA analysis (Log2FoldChange = -0.3927387, Padj= 0.06886911) (Figure 7:6).

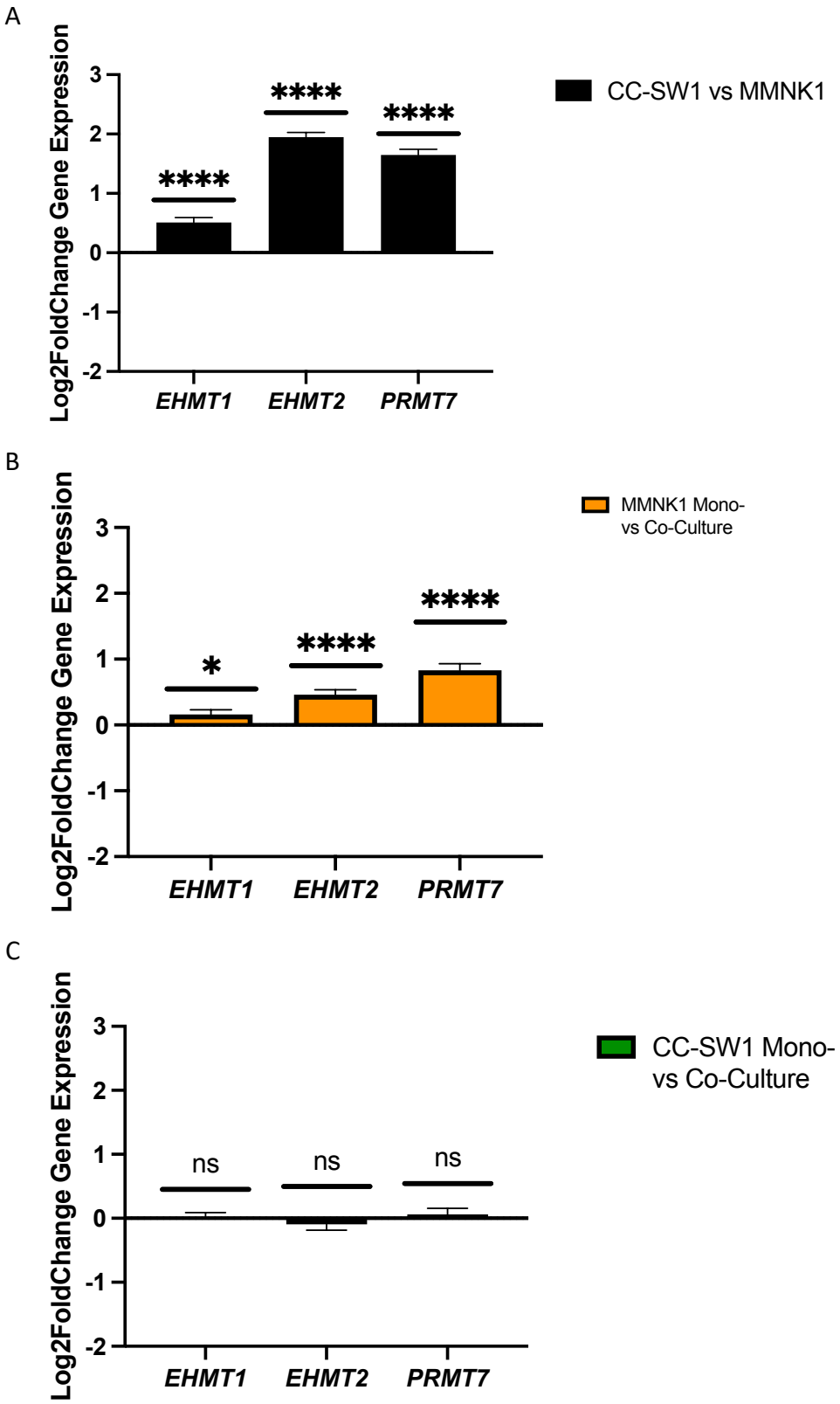


Figure 7:5 – Relative mRNA gene expression of* EHMT1, EHMT2, *and* PRTM7 *in CC-SW1 and MMNK1 cells. *A) Relative basal gene expression of* EHMT1, EHMT2, *and* PRTM7 *in CC-SW1 cells, compared to MMNK1 cells. B) Comparison of* EHMT1, EHMT2, *and* PRTM7 *gene expression in MMNK1 cholangiocytes cells in co-culture compared to MMNK1 cholangiocytes in monoculture. C) The comparison of* EHMT1, EHMT2, *and* PRTM7 *gene expression in CC-SW1 cells in co-culture compared to CC-SW1 cells in monoculture. Values represent Log2FoldChange ± Standard Error. *P≤ 0.05, **P≤ 0.01, ***P≤ 0.001, ****P≤ 0.0001.*

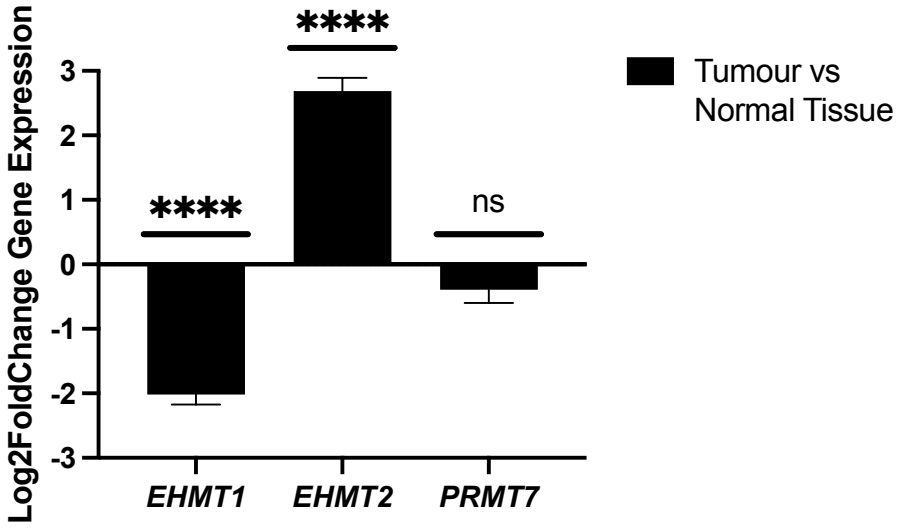


Figure 7:6 - Relative mRNA gene expression of* EHMT1, EHMT2, *and* PRTM7 *in TCGA tumour samples. *Evaluation of* EHMT1, EHMT2, *and* PRMT7 *gene expression in CCA and adjacent normal tissue, from the TCGA PanCancerAtlas dataset. Values represent Log2FoldChange ± Standard Error. *P≤ 0.05, **P≤ 0.01, ***P≤ 0.001, ****P≤ 0.0001.*

7.7 Summary

The SGC epigenetic inhibitor panel screen revealed two targets of interest, UNC0642 and SGC-3027, which selectively inhibited CC-SW1 viability, with little effect on MMNK1 viability. The IC50 values for UNC0642 were 5.253, 2.673, and 2.096 µM in CC-SW1, CC-LP1, and SNU-1079 cells respectively. Likewise, the IC50 values for SGC-3027 were 6.049, 6.090, and 2.038 µM in CC-SW1, CC-LP1, and SNU-1079 cells respectively. Co-culture of CC-SW1 with MMNK1 cholangiocytes led to an increase in the IC50 value for both UNC0642 and SGC3027 (12.63 µM, and 9.967 µM respectively) in CC-SW1 cells. Evaluation of our transcriptomic data revealed significantly greater basal gene expression of the UNC0642 targets G9a/GLP (*EHMT1*/*EHMT2*); as well as the SGC-3027 target PRMT7, in CC-SW1 cells compared to MMNK1 cholangiocytes. Evaluating the co-culture transcriptomic data demonstrated a significant increase in gene expression of EHMT1, EHMT2, and PRTM7 in MMNK1 cells when in co-culture, whilst co-culture of CC-SW1 cells with MMNK1 cholangiocytes had no effect

on *EHMT1, EHMT2,* or *PRTM7* gene expression in CC-SW1 cells. Expression data from the TCGA PanCancerAtlas database revealed a significant decrease in *EHMT1* expression, and a significant increase in *EHMT2* expression, in tumour samples compared to normal tissue. There was no significant difference in *PRTM7* expression in tumour tissue.

7.8 Discussion

What was quite striking from our experiments, was the marked increase in IC50 value for both UNC0642 and SGC3027 during co-culture with MMNK1 cholangiocyte cells. A previous study reported that co-culture of the CCA cell lines KKU-055 and KKU-213A with CAFs caused a 0.5- and 0.8-fold increase in cell viability compared to those in monoculture after treatment with gemcitabine, suggesting co-culture with CAFs could increase gemcitabine resistance in CCA cells (107). Therefore it is prudent to consider that not only CAFs, but also cholangiocyte cells can contribute towards CCA insensitivity to drug targeting.

The lysine methyltransferases G9a and GLP, catalyse the mono and di-methylation of lysine 9 of histone 3 (H3K9), as well as non-histone substrates like p53. Overexpression of G9a has been identified in multiple tumour types, including gastric (174), ovarian (175), oesophageal (176), and HCC (177). The inhibitor UNC0642 has been reported to trigger a potent reduction of H3K9me2 in MDA-MB231 cells with an IC50 = 106 nM (178), whilst it has been shown that in urinary bladder cancer, targeting of G9a overexpression by UNC0642 not only reduced cell viability of UBC cells in vitro, but also suppressed tumour growth in mouse xenograft models (179). In our intrahepatic CCA cell lines, UNC0642 had an IC50 value of ~<5 µM, which is within the recommended compound potency of 100 nM–5 µM for early drug discovery (180). G9a overexpression has been identified in mouse models of CCA (126)

and is also associated with poor prognosis in CCA patients (181). The mechanism for G9a as a driver of cholangiocarcinogenesis centres on the Hippo pathway. Specifically, H3K9me2 originating from G9a has been shown to suppress the tumour suppressor LATS2, leading to a subsequent reduction in YAP phosphorylation, and the activation of oncogenic YAP (181). Knockdown of G9a by siRNA or shRNA has also been shown to inhibit CCA tumour growth in SCID mice, consistent with the action of UNC0642 (181).

G9a overexpression is also correlated with Phosphoglycerate Dehydrogenase (PHGDH) overexpression in human iCCA (126), the rate-limiting enzyme in the serine-glycine pathway, also identified in our RNA-sequencing and metabolomic analyses, and G9a overexpression is thought to activate the serine-glycine synthesis pathway (182) suggesting a link with metabolic regulation of epigenetic mechanisms in CCA development.

From our RNA-sequencing experiments, we can see that G9a (gene name *EHMT2*) and GLP (gene name *EHMT1*) were expressed to a greater degree in our CC-SW1 cells compared to MMNK1 cells (Log2FoldChange =1.9466491, Padj=1.58E-128 and Log2FoldChange =0.5117206, Padj=9.32E-10 respectively), suggesting that basal expression levels could be responsible for the selective effect on CC-SW1 cell viability. Interestingly, whilst co-culture reduced CC-SW1 sensitivity to UNC0642, we saw no change in gene expression in CC-SW1 cells, suggesting the existence of alternative mechanisms that confer resistance to the inhibitor when CC-SW1 cells are in coculture with MMNK1 cells. The TCGA analysis demonstrated that whilst *EHMT2* was significantly overexpressed in tumour samples (Log2FoldChange =2.68943178, Padj=1.12E-38), *EHMT1* expression was actually reduced

(Log2FoldChange =-2.0189534, Padj=7.15E-39), potentially indicating that EHMT2 inhibition may have a more significant effect when tested in vivo.

Taken together, the data provides further support to the notion that UNC0642 and the development of secondary inhibitors of G9a/GLP could form a viable therapeutic direction for the treatment of CCA.

The arginine methyltransferase PRMT7 catalyses the irreversible monomethylation of arginine residues on histone proteins such as H2B, as well as non-histone substrates like HSPA8 of the HSP70 family, using SAM (S-Adenosyl Methionine) as a methyl donor. Not only has PRMT7 overexpression been identified in breast cancer cell lines, but it has also been shown to increase the expression of matrix metalloproteinase 9 (MMP9), as well as inhibiting E-cadherin expression via promoter binding to mediate tumour EMT and metastasis (183,184).

SGC3027 is a pro-drug, which when acted upon by cell reductases, produces the active drug SGC8158 (185) a SAM-competitive PRMT7 inhibitor, which has been shown to inhibit PRMT7 with an IC50 < 2.5 nM. In the myoblast cell line C2C12, SGC3027 has been shown in inhibit the methylation of HSP70 with an IC50 value of 2.4 µM (185). Inhibition of HSP70 methylation via SGC3027 has been shown to sensitise cells to heat shock and proteasomal stresses, implicating PRMT7 in the stress response (185). From our RNA-sequencing experiments, we can see that PRMT7 expression was significantly greater in CC-SW1 CCA cells than MMNK1 cholangiocyte cells (Log2FoldChange = 1.645939664, Padj= 5.49E-60), further suggesting that basal gene expression levels could be responsible for the selective effect on CC-SW1 cell viability. Interestingly, whilst co-culture reduced CC-SW1 sensitivity to SGC3027, we saw no change in *PRMT7* gene expression in CC-SW1 cells during co-culture, suggesting an alternate mechanism was responsible for decreased sensitivity during

co-culture. There was a non-significant, marginal reduction in PRMT7 expression in CCA tumour samples in our TCGA analysis (Log2FoldChange = -0.3927387, Padj= 0.06886911), which could be explained by redundancy in the PRMT family, and the action of PRMT5 (186) which has been implicated in HCC (187).

One of the limitations of this study was the lack of validation for the extrahepatic cell line SNU-1196.The striking profile difference in the response of extrahepatic CCA to epigenetic inhibition warrants a deeper delve, and with more time, IC50 values in monoculture and co-culture with MMNK1 cells would have been evaluated. As well as a markedly different genomic profile, eCCA has been shown to exhibit a separate epigenetic profile to iCCA (153), despite little work being published on eCCA epigenome modifications due to iCCA being the primary focus of the field. Likewise, one particular limitation to the TCGA data is the inability to separate the iCCA and eCCA expression data, as the evaluation of *EHMT1/2* and *PRMT7* expression in iCCA vs eCCA would provide further evidence for drug/cell selectivity.

Likewise, although 5-FU has been established for use in CCA research (102), it would be necessary to evaluate the effect of gemcitabine with/without cisplatin in the cell lines. As a nucleoside analogue, 5-FU has the potential to function in a similar manner to gemcitabine, and due to access and cost limitations, 5-FU was chosen for the present study. However, as Gem/Cis is the first line therapy for CCA it would be necessary to establish the response of the cell lines and the indirect co-culture system moving forwards.

With more time, this finding would have been validated in the other intrahepatic cell lines CC-LP1 and SNU-1079, however, it will be important for further research to be focused on xenograft models rather than 2D cell line models, due to the integration with surrounding cellular and organ systems, to fully understand the impact of the tumour niche on CCA sensitivity to epigenetic inhibition. Moreover, it is important to consider the implications of the co-culture system on the microenvironment as the cause of the increased insensitivity. We have shown previously that co-culture effects both metabolite and cytokine availability, and also that co-culture increases P450 cytochrome and xenobiotic activity in cholangiocytes. Whether the result is caused by innate cholangiocyte behaviour from increased xenobiotic activity, or indirect via metabolic and secretory modulation requires further investigation, as it is well established that a vital component of genome regulation is metabolic state (188). As such, it would be prudent to test the combination of SGC-3027 and UNC0642 with Gem/Cis, as a way of evaluating the potential for overcoming chemotherapeutic resistance or increasing response to conventional therapies.
Validation of UNC0642 and SGC-3027 through siRNA knockdown of both molecular targets (EHMT1/2 and PRMT7) in CC-SW1 cells would be performed next to confirm CCA targeted efficacy, as well as validation that the gene expression changes are replicated at the protein level. Likewise, it would be interesting to assess the efficacy of these compounds in the Human Primary Cholangiocyte cell line NHC3 to replicate the selectivity identified from MMNK1 cells. Moreover dose-escalation and toxicity experiments must be conducted in mouse xenograft models in order to validate these findings in vivo.

In summary, we hypothesis that higher basal levels of *EHMT1/2* and *PRMT7* gene expression contributes to increased protein expression of G9a/GLP and PRMT7, which is responsible for

the increased sensitivity of CC-SW1 to the inhibitors SGC-3027 and UNC0642. We further suggest that co-culture induced resistance is due to the activation of an alternate mechanism. Although a considerable amount of work is still required, there is a clear molecular basis for further evaluation of SGC-3027 and UNC0642 in CCA, and more broadly how epigenetic inhibition of CCA could provide a promising avenue for novel treatment.

8 Overall Discussion

8.1 Conclusion

This study aimed to gain insight into the molecular mechanisms underpinning the early development of CCA via a model of paracrine interactions between CCA and cholangiocyte cells utilising an indirect co-culture system. A firm sequence of molecular alterations during the pathogenesis of CCA is yet to be elucidated, and the contribution of neighbouring cholangiocyte cells is often overlooked in cholangiocarcinogenesis. Deciphering the aberrant paracrine signalling during the onset of CCA has the potential for the development of interventions to modulate these signal changes, and restore normal tissue function.

The overall objective of this study was to investigation the paracrine-driven molecular control cholangiocytes exude over CCA cells, and vice versa, during tumour development. Specifically, the studies presented here dissected the cholangiocyte-CCA cell indirect interaction from three primary angles. Firstly, we shed light on the phenotypic and behavioural changes to CCA cells during the early onset of tumour development, which we demonstrate to provide cholangiocyte cells with a growth advantage. We then proceeded to highlight the cascade of multi-step molecular changes between the two components triggered by the paracrine signalling, comprising of both metabolomic and transcriptomic adaptations. It is crucial to understand these changes during the early onset of the interactions between these two compartments, and hence CCA development, in order to identify the switch point, which ultimately gives rise to a microenvironment conducive to CCA progression. Therefore, a comprehensive understanding of the complex, multifaceted paracrine communications between cancer and reactive cholangiocyte cells in CCA will help

identify prognostically relevant molecular signatures, leading to novel diagnostic and therapeutic targets, with the ultimate goal to improve the diagnosis, detection and treatment of CCA.

Although a significant amount of research into this interaction is still needed, it is possible to identify numerous novel observations from our results, which are primarily how indirect co-culture elicits divergent responses in cholangiocyte and CCA cell behaviour, metabolic and cytokine profile, gene expression, and sensitivity to epigenetic inhibition.

We hypothesise that indirect co-culture instigates a metabolic shift due to metabolic competition, attenuated metabolite concentrations, and altered cytokine exposure. This results in the modulation of gene expression for various cell growth and survival pathways in each cell line. In turn, aberrations in gene expression translates to a reduction in apoptosis, cell cycle progression, and increased cell proliferation in cholangiocytes, and a reduction in migration, viability, and proliferation in CCA cells.

After experiencing biliary or liver insults, the secretion of proinflammatory cytokines such as IL-6, activates cholangiocytes and recruits immune cells. These proliferating cholangiocytes counteract the cell loss and repair the injury (47), and in this case, the pro-inflammatory response is transient and resolved quickly (36). Whilst PSC is inherently different from CCA, both diseases share a chronic inflammatory phenotype (189) typified by aberrant cholangiocyte proliferation. In the literature surrounding the development of PSC, it is noted that cholangiocyte cells take divergent pathways in response to molecular cues. In particular, cholangiocyte cells can exhibit either a ‘reactive’ phenotype, characterised by increased proliferation, migration, and fibrotic secretions, or a senescence-associated-

secretory phenotype (SASP), characterised by an increase in the expression of pro-inflammatory cytokines, and cell cycle inhibition. We show evidence here for the contribution of cholangiocytes to the persistent inflammatory response in CCA. Ultimately, this chronic activation causes the reparative process to become ineffective, which can trigger further aberrant bile duct proliferation, and the progression of CCA. Interestingly, one study demonstrated a hypersecretory state in cholangiocyte cells isolated from PSC patients, from which transcriptomic analysis indicated increased expression of numerous cytokines, chemokines, and growth factors (94). Likewise the secretory profile of our co-culture cells is similar to PSC cholangiocytes, which express components of the SASP, including cytokines and chemokines (IL-6, IL-8, MCP1, plasminogen activator inhibitor-1), growth factors (PDGF, EGF), and extracellular matrix proteins (fibronectin)(50). In addition, a previous 2D and 3D in vitro study demonstrated how the co-culture of senescent cholangiocytes could trigger the activation and migration of the monocytic cell line THP-1, which was not achieved by normal cholangiocytes (56). Likewise, blocking key cholangiocyte SASP cytokines such as IL-6, IL-8, and MCP1 inhibited this process (94). It would therefore be prudent to evaluate whether our indirect co-culture-primed CCA cells could elicit the same effect, indicative of this cholangiocyte co-culture induced SASP-like CCA transformation. We hypothesise that CCA cells trigger the remodelling of the tumour stroma through the recruitment and activation of surrounding cholangiocytes, resulting in a 'reactive cholangiocyte' status in the non-transformed cells, and a SASP phenotype in the CCA cells. This in turns leads to further chronic inflammation and the recruitment of other inflammatory and mesenchymal cell types to promote the long-term survival of the tumour.

We suggest indirect co-culture triggers this 'reactive cholangiocyte' phenotype in MMNK1 cells, as indicated by rapid proliferation, cell cycle progression, reduction in apoptosis, and energetic rearrangements as indicated by upregulation in the gene expression of glycolysis, TCA, and oxidative phosphorylation, in addition to increased creatine availability and metabolism, and ATP availability.

We hypothesise this anti-tumoral effect is aligned with the cholangiocyte inclination to maintain tissue homeostasis, as epithelial cells expressing oncogenic tendencies competing for space and nutrients and are often eliminated via processes that require surrounding normal cells (190), such as during the very early onset of tumour development. Similar to Darwinian selection, this continues until the point at which the cancer cells outcompete normal cells (denoted as the 'switch point')(191). Cell-cell competition is not triggered by differences in growth and proliferation rates alone (192), and crucially, our experiments were only conducted over 48 hours, unlike the weeks and months it takes for a tumour to develop, and as such we hypothesise this 'switch point' is significantly after the duration used in our model system. Moreover, our model used a finite supply of starting resource (e.g. glutamine, and glucose) whereas *in vivo*, tumours have access to a continued supply of nutrients. Strong competition exists between neighbouring cells, and to the tumour microenvironment, as demand for resources in the cancer niche is high (193) modulating which cells can survive and outcompete others, ergo modulating the anti-tumoral or pro-tumoral effect. Delineating the molecular mechanisms behind this homeostatic control by 'reactive cholangiocytes' will provide essential novel pathways to circumvent CCA growth and progression.

As the flow of bile in the intrahepatic bile duct is regulated by ATP, ATP concentration is tightly regulated in cholangiocytes in both an autocrine and a paracrine fashion (194). To maintain ATP levels, cells utilize phosphocreatine as a reservoir of high-energy phosphate groups, and as such it is logical to investigate the non-canonical, off-target effects of increased creatine concentration. Our study demonstrated that increased creatine was not responsible for the increase in target gene expression, and actually demonstrated small increases in creatine concentration could reduce the gene of expression of IDO1, involved in tryptophan metabolism, and EXTL1, involved in glycosaminoglycan biosynthesis. The RNA-seq analysis revealed an upregulation in the expression of genes related to creatine metabolism during co-culture, which we suggest generates the increased creatine concentration in the cholangiocytes after co-culture. This is corroborated by the TCGA data analysis, which indicated that the third most highly overexpressed metabolic gene set in tumour samples from CCA patients was associated with creatine metabolism. This included upregulation of the rate-limiting enzyme in creatine synthesis, GATM. GATM is also highly expressed in colorectal cancer (CRC) liver metastases, and is associated with poorer prognosis in CRC patients, whilst creatine concentration significantly correlates with the clinical stage of HCC (195). Taken together, this suggests a mechanism for creatine metabolism as an energy source for CCA development. Whilst the evaluation of creatine concentration on the expression of HSPA8 was not conducted, it would be beneficial to conduct such an evaluation in order to investigate the potential effects of HSPA8 on cell cycle regulation in addition to cholangiocyte ATP availability.

Co-culture resulted in multiple changes to cell cycle regulation in MMNK1 cholangiocytes, indicated by increased cell cycle progression and cell proliferation, in addition to

upregulation in the expression of genes in the G2M pathway. Knockdown of the most differentially expressed gene in this pathway, *HSPA8*, led to a responsive decrease in cell-cycle progression, as well as a decrease in target gene expression, including *AURKA*, *TXN* and its regulator *TXNIP*, which acts as an antioxidant to reduce ROS-induced damage. Likewise, HSPA8 has been shown to bind to TXNIP, as well being an inhibitor of AURKA, which in turn is an inhibitor of p53, a controller of cellular apoptosis (196). Previously publications have demonstrated HSPA8 to be crucial to cell survival during mild oxidative stress (197), and it is also involved in progression of the cell cycle from G1/S as a binding partner of cyclin D1 (160). Moreover, HSPA8 has been shown to partake in cellular metabolism via the inhibition of oxidative phosphorylation, enhancing glycolytic activity in HeLa cells to restore ATP balance (198). Increased *HSPA8* expression has also been identified as a hallmark of poor prognosis in several human cancers including uterine corpus endometrial carcinoma, cervical squamous cell carcinoma, and lung adenocarcinoma (199,200). The TCGA data revealed a significant increase ($Log_2FC = 9.04$) in HSPA8 gene expression in CCA patient tumour samples, supporting the notion of HSPA8 as a contributor to CCA development.

The indirect co-culture experiments have unveiled a complex interplay of multiple mechanisms between cholangiocytes and CCA cells. It is likely both mechanisms, creatine metabolism and HSPA8 overexpression are triggered simultaneously, both contributing to the observed outcomes independently within their respective pathways, rather than directly interacting with each other. Their collective influence during indirect co-culture experiments underscores the intricate nature of cellular responses, highlighting the need for further comprehensive investigation to unravel the intricate network of interconnected

pathways that drive this reactive cholangiocyte state in MMNK1 cholangiocytes behaviour during co-culture.

As many cell types exist concurrently within the TME, it is reasonable to explore how cholangiocyte paracrine signalling impacts not only malignant CCA cells, but also surrounding CAFs, TAMs, TILs, endothelial cells, and hepatocytes. The activation of hepatic stellate cells (HSCs) is induced by activated cholangiocytes secreting factors such as TGF-α, PDGF-BB, TGF-β2, and NO (201). Likewise, cholangiocyte activation stimulates myofibroblasts, which are responsible for collagen deposition within the liver (201), and thereby contributes to the highly desmoplastic nature of cholangiocarcinoma (CCA). Paracrine signalling by cholangiocytes is also thought to modulate the immune response (202), as the secretion of IL-6 promotes differentiation of B cells and the secretion of immunoglobulins (203), and the secretion of IL-8, epithelial cell derived neutrophil activating protein (ENA-78), and growth-related oncogene (GRO) determines neutrophil recruitment (204). Cholangiocytes are dynamic cells, which undergo extensive phenotypic modifications in response to liver inflammatory injury, and this phenotype is heavily modulated during cholangiocarcinogenesis. This extensive paracrine signalling contributes significantly to the overall complexity of the tumour stroma, and more research is required to fully delineate cholangiocyte interactions in the TME.

In regards to the CCA cells, we suggest indirect co-culture triggers a SASP-like state in CC-SW1 CCA cells, indicated by the reduction in cell cycle progression, reduced EMT protein expression and migration, increase in cytokine gene expression, and shift in BCAA metabolism. We demonstrate a co-culture mediated downregulation in BCAA gene

expression, which we suggest to be responsible for the increase in BCAA catabolism, resulting in the increased concentration of the BCKA 2-oxoisopentanoate. We further demonstrate that high concentrations of 2-oxoisopentanoate can reduce CCA cell proliferation and target gene expression (*KL, SPRR2A, LPS,* and *CFI*).

BCAT1 and BCAT2, the cytosolic and mitochondrial form of the Branched-Chain Amino Acid Transaminase enzymes, are responsible for the reversible conversion of the branched chain amino acids valine, leucine, and isoleucine to their respective keto-acids. As highlighted previously, RNA-seq data demonstrated a co-culture induced reduction in BCAT expression.

BCAT1 expression has been shown to be inhibited by the oncometabolite 2HG in IDH1 mutant cells, resulting in the decreased level of glutamate and increasing the cells dependence on glutaminase (GLS) for the biosynthesis of glutamate, with glutamine as the primary nitrogen donor, as well as the redox protein glutathione (205). Inhibition of BCAT can therefore induce a compensatory glutamine metabolism pathway (205). We saw and upregulation in the gene expression signatures for reactive oxygen species, suggesting an increase in redox stress in CC-SW1 cells, as well as observing decreased glutamine and increased 2-oxoisopentanoate. Therefore, we postulate co-culture triggers cells to switch to a glutamine scavenging mechanism. The inhibition of BCAT is forcing cells to divert metabolism from α-KG formation to the formation of glutamate, making more pyruvate, possibly potentiating CCA survival at a later time point. This is supported by the TCGA data analysis, in which the most over-expressed metabolic gene set was that of Branched Chain Amino Acids (BCAAs) in CCA patient tumour samples. Taken together, our data suggests glutamate-BCKA metabolism as a controlling factor in CC-SW1. Although high

concentrations of 2-oxoisopetanoate are toxic to the cells, we hypothesise the accumulation is due to the necessary rapid production of glutamate from α-KG and BCAAs, in order to sustain cell viability, combined with the lack of glutamate production from asparagine as the cell attempts to recover aspartate levels in addition to glutamate levels.

Aberrant metabolism in cancer is not only involved in maintaining a high proliferative rate and survival, but also impacts epigenetic mechanisms. Moreover epigenetic changes, not just genetic changes, can confer vital survival advantages to cancer cells, particularly in nutrient-deprived environments. To this end, we evaluated the response of CCA cells to epigenetic inhibition, and evaluated the respective target gene expression. We hypothesise that higher basal levels of EHMT1/2 and PRMT7 are responsible for the increased sensitivity of CC-SW1 to the epigenetic inhibitors SGC-3027 and UNC0642. Indirect co-culture attenuates CCA cell sensitivity to the epigenetic inhibitors SGC-3027 and UNC0642, and we suggest that this co-culture induced resistance is due to the activation of an alternate mechanism, not reliant on changes to the target gene expression.

Not only has the effort to develop effective pharmacological strategies for CCA been hindered by significant inter-tumour heterogeneity (1) but also due to the fact that traditional anti-cancer treatments have primarily focused on targeting inherent characteristics and mutations of cancer cells, neglecting the crucial role of the surrounding microenvironment in both cancer development and treatment efficacy. Epigenetic inhibitors show promise as a way to specifically target and modulate epigenetic changes that control gene expression and drive tumorigenesis, in order to restore normal gene expression patterns and reduce disease progression. We demonstrate here that reactive cholangiocytes

may play a key role in modulating the permissive or intolerant state of CCA tumour growth, and that the addition of indirect cholangiocyte interactions reduces CCA sensitivity to epigenetic inhibition. Further understanding of the mechanism behind these interactions will shed light on CCA epigenetic regulation, and allow researchers to further explore alternative epigenetic strategies or combination therapies that can overcome resistance and improve treatment outcomes.

8.2 Study Limitations

As with all scientific investigations, there were inevitable limitations during this project. As highlighted in the COVID-19 Discrepancy, it was the intention to complete the study utilising three intrahepatic CCA cell lines (CC-SW1, CC-LP1, and SNU-1079), and contrast these with the extrahepatic CCA line (CC-SNU-1196), however this validation was not completed due to COVID-19 pandemic aggregated time pressures. A singular iCCA cell line is not enough to extrapolate for iCCA tumours, and cannot be used for eCCA's, and as such the need for validation in multiple CCA lines, and the addition of other models listed below, is crucial.

Another limitation of the project is the use of the MMNK1 cell line as our 'normal' cholangiocyte line. As highlighted in 4.2.1 Cholangiocyte Phenotype, MMNK1 is an immortalised cell line, having been transfected with SV40-T and hTERT. The precursor line OUMS-21 was generated from epithelial-like cells extracted from human foetal liver tissue, and immortalised using the SV40 T-Antigen (85). SV40-induced immortalization permits cells to proliferate for a limited number of population doublings beyond the point at which cells would normally undergo senescence. This is primarily due to the SV40 large T antigen binding and inhibiting the tumour suppressor genes p53 and retinoblastoma (Rb) (206) blocking p53-dependent gene expression, and blocking the growth-suppressive functions on the Rb family of proteins, pRb, p107 and p130(207). In the case of MMNK1, the OUMS-21 cells displayed delayed senescence, but not immortality (85), and as such was transduced with a retroviral vector expressing human telomerase reverse transcriptase (hTERT) in order to reconstitute telomerase activity and thereby induce immortality (74) creating the MMNK1 cell line. It is important to consider the effect of the SV40 on MMNK1 in terms of cell cycle progression and inhibition of apoptosis (208), however, whilst the inactivation of

Rb proteins and of p53 has been identified during malignant transformation, numerous studies indicate that these actions alone not sufficient to drive transformation (209,210), suggesting cell lines transfected with SV40 are not inherently transformed.
Moreover, the MMNK1 cell line was shown to express cholangiocyte markers such as CK-7 and CK-19, produced IL-6, and formed bile duct-like structures in immunodeficient mice, leading to the immortalized cholangiocyte nomenclature (74). Likewise, MMNK-1 cells did not express secretin receptors, suggesting that MMNK-1 cells were derived from small cholangiocytes, as secretin receptors are only found on large cholangiocytes (211). Taken together, the MMNK1 cell line acts as cholangiocyte with unlimited replicative potential, rather than as a malignant CCA cell, and is therefore valuable to this study. We recognise the immense benefit of using a primary cholangiocyte cell line for this study, without modulation of the innate p53 and Rb pathways, and providing a more biologically relevant model system. However, due to the significant cost, difficult maintenance, limited availability, and limited proliferation time of primary cell lines, the decision was made to use the immortalised cell line for the present study. Further validation in primary cell lines (such as NHC3 used here) should be conducted.

We successfully implemented a 2D indirect co-culture system to investigate paracrine cholangiocyte-CCA cell interactions. There are several benefits to using this system, including the relative simplicity and ease of setting up 2D models compared to more complex 3D culture models. Additionally, as cells were grown in a single monolayer, this meant they could be readily analysed using standard biochemical and molecular biology techniques such as western blot and qPCR, and as cells were adherent, we were able to investigate migratory and proliferative behaviour changes which would have been more

challenging in 3D models. Moreover, this model also proved valuable for high-throughput screening of the 63 epigenetic inhibitors tested. Likewise, this system allowed for a tightly controlled environment to study CCA-cholangiocyte cell interactions, permitting the precise control over the ratio and arrangement of different cell types, as well as targeted investigations into specific media and metabolite compositions. The 2D co-culture system also provided a well-defined and reproducible experimental platform, for establishing standardized protocols and optimal conditions for CCA and cholangiocyte cell types, enabling easier comparison of results between different studies. One considerable benefit of the 2D indirect co-culture system compared to 3D/organoid and in vivo models is reduced cost, due to the high expense of set-up, validation, and investigation in in vivo models in particular. However, there are considerable limitations to using a 2D co-culture system. This is primarily due to the fact that 2D systems are an oversimplification of cell-cell interactions within the TME, and do not fully replicate the complexity of the in vivo cellular microenvironment. This means there may well be significant altered cell behaviours and responses. Therefore, it is necessary to complement 2D co-culture studies with more physiologically relevant 3D co-culture models, including the use of spheroid and organoid models, as well as in vivo xenograft and mouse models to obtain a comprehensive understanding of cell-cell interactions in a biological setting.

Another limitation to the study was the singular time point transcriptomics, and the selected gene panels of interest. It would be prudent to evaluate transcriptional changes at 6 and 24 hours in order to combine with the metabolomics data, for a more representative evaluation in gene expression flux, and then to validate genes in metabolic pathways only, as opposed to the most differentially expressed genes in a single compartment.

One of the well-recognized limitations of transcriptomics is the fact that changes in RNA levels don't always directly correlate with changes in protein levels, or with signalling events that ultimately affect cellular activity, such as activation of the kinase pathways rather than the expression of a single component. Therefore, it is important to acknowledge there are several other ways by which metabolite concentrations may be altered including post-translational modifications of proteins, protein-protein interactions, protein degradation rates, subcellular localization changes, alterations in metabolic enzyme activity, and substrate availability. These factors can play a significant role in shaping the cellular metabolome, even when gene expression patterns do not exhibit a direct one-to-one relationship with observed metabolic changes.

Moreover, it is imperative to evaluate both in vitro and in vivo work in patient samples, in order to bridge the gap between laboratory research and clinical practice to ensure that scientific findings are relevant, safe, and effective in real-world healthcare settings. Due to time constraints, we were unable to validate our findings in our patient samples, however we utilised TCGA gene expression data to mitigate this. One limitation of this was lack of high-quality gene expression data from TCGA. CCA is still seen as a rare cancer, although there is a shift in the literature which identifies iCCA as commonly as HCC. As such there are very few large-scale transcriptomic data for CCA and corresponding non-cancerous cholangiocyte cells, hindering the power of differential gene expression and GSEA analyses. In our analysis, we utilised 36 CCA samples and 9 normal tissue samples from the PanCancerAtlas, which is a very small sample size. Moreover, the TCGA data does not differentiate between iCCA and eCCA tissue, or between CCA tissue and tumour stromal cells, impacting the genetic evaluation. In summary, whilst we acknowledge the limitations

of our model, the indirect co-culture system offers a highly controlled and versatile approach for investigating the development of CCA, allowing us to precisely dissect the complex paracrine interactions that occur within the tumour microenvironment whilst maintaining a controlled and reproducible experimental environment.

8.3 Potential Future Work

Due to the time and budget constraints associated with conducting a DPhil project, there are still outstanding investigations that could be completed to give us a more complete picture.

In addition to the iCCA and eCCA cell line validation listed above, there are a number of validation experiments that could be conducted, including validation of intracellular metabolite concentrations of creatine and 2-oxoisopentanoate, using high-performance liquid chromatography (HPLC). Likewise, the level of the cytokine secretion of IL-6, IL-7, and IL-8 could be validated using the Human Quantikine ELISA Kits from R&D Systems. Furthermore, we could utilise the Caspase-Glo 3/7 assay from Promega to evaluate caspase activity to validate the impact of co-culture on apoptotic behaviour. Similarly, the evaluation of exogenous doses of 2-oxoisopentanoate on both cytokine expression, and CCA cell migration would provide further evidence to the inhibitory effect of abrogated BCAA metabolism in CCA cells.

As mentioned previously, gene expression levels as measured by transcriptomics, do not always perfectly reflect protein levels. Post-transcriptional processes such as alternative splicing and RNA stability regulation can lead to differences in mRNA isoforms and stability, impacting protein abundance. Translation efficiency, influenced by factors like ribosome availability, mRNA secondary structure and even alternative initiation codon selection can also vary, affecting the correlation between mRNA and protein levels (212). Additionally, proteins undergo post-translational modifications and have different degradation rates, which are not reflected in gene expression data (213). We see increased proliferation and cell cycle progression in cholangiocytes during co culture, in combination with a generalised

reduction in the gene expression of translation machinery and unfolded protein response as per the RNA-seq data, in combination with the global downregulation of protein expression, which could, in part, explain the discord between protein and gene expression levels.

Proteomics focuses on the comprehensive analysis of proteins within a biological system. Evaluation of the proteome of each cell line during indirect co-culture would allow for integration with our transcriptomic and metabolomic data, providing evidence to support metabolite changes as a result of gene expression changes. Likewise, proteomic profiling would provide clues as to the level of pathway control in our system.

Likewise, the in vivo evaluation of metabolic crosstalk would be crucial moving forwards. Stable isotopically labelled tracers, comprising of any organic molecule containing ^{13}C, ^{2}H, or ^{15}N isotopes, can be used via dilution or incorporation to calculate metabolite turnover. The use of ^{15}N-labeled amino acids to investigate *in vivo* kinetics of protein turnover has been used since the 1930's (214), and as such could be applied here with ^{15}N-labeled valine to trace 2-oxoisopentanoate metabolism *in vivo*. The D3-creatine dilution method is already established as a way to determine functional muscle mass, and as such could be applied to our model system to trace creatine metabolism (215). Moreover, the use of PET or MRI could be used for *in vivo* cell tracking; monitoring the localization, survival, migration, and growth of CCA cells in a live subject (216,217).

During this study, we had initiated the optimisation of 3D co-culture spheroid models in order to provide a more physiologically relevant system. However due to time constraints

we were unable to evaluate our genes and metabolites of interest in this system, therefore validation in 3D co-cultures are required.

Moving forwards, it would be imperative to conduct validation of our studies in vivo. Firstly, this would be conducted using Xenograft Models via the implantation of our CCA cell lines and cholangiocyte cells into immunocompromised mice to generate xenograft models. This would allow for the monitoring of tumour growth, invasion, and metastasis for the analysis of the interactions within a living organism. This would be first conducted subcutaneously, then moving towards orthotopic implantation of CCA cells and cholangiocyte cells directly into the bile duct the of mice, for an increasingly relevant physiological evaluation of cell-cell interactions. Validation of our transcriptomic analysis would be completed via RNA sequencing of tumour tissue isolated from the in vivo models.

The results gained would be validated using Patient-Derived Xenograft (PDX) Models; the implantation of patient derived tumour cells into immunocompromised mice. Consequently, we would implement the use of genetically engineered mouse models (GEMMs) to study the CCA-cholangiocyte cell interactions, which would allow for the conditional knockout or overexpression of our target gene of interest.

The GEMMs can also be used to overexpress G9a and PRMT7 to evaluate how critical these genes are in CCA development and progression, and hence how effective our chosen inhibitors UNC0642 and SGC3027 would be against CCA development. The Promega NanoBiT assay would be utilised to interpret the efficacy of our epigenetic inhibitors in vitro, using a light-based luciferase assay to evaluate the protein binding of the targets of each.

Moreover, it is imperative to evaluate the effect of UNC0642 and SGC3027 on in vivo models to establish the CCA killing efficacy, alone and in combination with standard chemotherapeutics, before these drugs could be moved towards clinical trials.

We had been granted access to 12 patient samples, for which we were preparing to use immunohistochemistry (IHC), immunofluorescence staining, and flow cytometry to assess protein and gene expression, as well as cell population interactions, to support our in vitro work but due to time constraints, this work will require investigation in the future. Moreover, we had intended to complete a whole transcriptome spatial profiling of these patient samples using NanoString Technologies's GeoMx Human Whole Transcriptome Atlas (WTA), to validate the spatial, and therefore compartmental, separation in the gene expression between CCA cells and cholangiocyte cells.

8.4 Closing Remarks

It is almost inevitable that CCA will become not only a burden to the NHS in the UK, but a burden to all healthcare provisions across the globe. Both incidence and mortality of CCA is increasing worldwide, with no simple explanation. It is imperative further research into the pathogenesis of CCA is conducted, and we have demonstrated here why it is critical to include the evaluation of surrounding cholangiocyte cells when evaluating the modulation of CCA development and progression. Understanding the delicate and dynamic interaction between CCA cells and neighbouring cholangiocytes also constitutes great translational importance, to allow for the development of future diagnostics and novel therapeutics.

In summary, investigating the interactions between CCA and cholangiocyte cells is critical for advancing our understanding of CCA, identifying potential biomarkers and therapeutic targets, addressing treatment resistance, and ultimately improving the outcome for CCA patients.

References

1. Banales JM, Marin JJG, Lamarca A, Rodrigues PM, Khan SA, Roberts LR, et al. Cholangiocarcinoma 2020: the next horizon in mechanisms and management. Nat Rev Gastroenterol Hepatol [Internet]. 2020;17(9):557–88. Available from: http://dx.doi.org/10.1038/s41575-020-0310-z
2. Yoo KS, Lim WT, Choi HS. Biology of cholangiocytes: From bench to bedside. Gut Liver. 2016;10(5):687–98.
3. Brindley PJ, Bachini M, Ilyas SI, Khan SA, Loukas A, Sirica AE, et al. Cholangiocarcinoma. Nat Rev Dis Primers. 2021;7(1).
4. UK CR. Cancer Stats: Cancer Statistics for the UK. Cancer Research UK. 2014.
5. Banales JM, Cardinale V, Carpino G, Marzioni M, Andersen JB, Invernizzi P, et al. Expert consensus document: Cholangiocarcinoma: current knowledge and future perspectives consensus statement from the European Network for the Study of Cholangiocarcinoma (ENS-CCA). Nat Rev Gastroenterol Hepatol. 2016;13(5):261–80.
6. Yasser Shaib. The Epidemiology of Cholangiocarcinoma. Semin Liver Dis. 2004;24(2).
7. Shin HR, Oh JK, Masuyer E, Curado MP, Bouvard V, Fang YY, et al. Epidemiology of cholangiocarcinoma: An update focusing on risk factors. Vol. 101, Cancer Science. 2010. p. 579–85.
8. Yao J, Liang X, Liu Y, Li S, Zheng M. Trends in Incidence and Prognostic Factors of Two Subtypes of Primary Liver Cancers: A Surveillance, Epidemiology, and End Results-Based Population Study. Cancer Control. 2022;29:1–14.
9. Valle JW, Borbath I, Khan SA, Huguet F, Gruenberger T, Arnold D, et al. Biliary cancer: ESMO clinical practice guidelines for diagnosis, treatment and follow-up. Annals of Oncology [Internet]. 2016;27(August):v28–37. Available from: http://dx.doi.org/10.1093/annonc/mdw324
10. Bertuccio P, Malvezzi M, Carioli G, Hashim D, Boffetta P, El-Serag HB, et al. Global trends in mortality from intrahepatic and extrahepatic cholangiocarcinoma. J Hepatol. 2019 Jul 1;71(1):104–14.
11. Elvevi A, Laffusa A, Scaravaglio M, Rossi RE, Longarini R, Stagno AM, et al. Clinical treatment of cholangiocarcinoma: an updated comprehensive review. Ann Hepatol [Internet]. 2022;27(5):100737. Available from: https://doi.org/10.1016/j.aohep.2022.100737
12. Kurathong S, Lerdverasirikul P, Wongpaitoon V, Pramoolsinsap C, Kanjanapitak A, Varavithya W, et al. Opisthorchis viverrini Infection and Cholangiocarcinoma A Prospective, Case-Controlled Study.
13. IARC Working Group on the Evaluation of Carcinogenic Risks to Humans. Biological agents. Volume 100 B. A review of human carcinogens. IARC Monogr Eval Carcinog Risks Hum. 2012;100.
14. Dodson RM. Intrahepatic Cholangiocarcinoma: Management Options and Emerging Therapies. J Am Coll Surg. 2013;217(4).
15. Jusakul A, Cutcutache I, Yong CH, Lim JQ, Huang MN, Padmanabhan N, et al. Whole-genome and epigenomic landscapes of etiologically distinct subtypes of cholangiocarcinoma. Cancer Discov. 2017;7(10):1116–35.
16. Khan SA, Davidson BR, Goldin R, Pereira SP, Rosenberg WMC, Thillainayagam A V, et al. Guidelines for the diagnosis and treatment of cholangiocarcinoma. 2009;1–9. Available from: papers://d55905fe-9b37-4a1d-b1da-1e391d512486/Paper/p323

17. Khan SA, Davidson BR, Goldin RD, Heaton N, Karani J, Pereira SP, et al. Guidelines for the diagnosis and treatment of cholangiocarcinoma: An update. Gut. 2012;61(12):1657–69.
18. Razumilava N, Gores GJ. Cholangiocarcinoma. The Lancet. 2014;383(9935):2168–79.
19. Valle JW, Furuse J, Jitlal M, Beare S, Mizuno N, Wasan H, et al. Cisplatin and gemcitabine for advanced biliary tract cancer: A meta-analysis of two randomised trials. Annals of Oncology. 2014;
20. Furuse J, Okusaka T, Boku N, Ohkawa S, Sawaki A, Masumoto T, et al. S-1 monotherapy as first-line treatment in patients with advanced biliary tract cancer: A multicenter phase II study. Cancer Chemother Pharmacol. 2008;62(5):849–55.
21. UK CR. First treatment approved in England for advanced bile duct cancer [Internet]. Available from: https://news.cancerresearchuk.org/2021/07/22/first-treatment-approved-in-england-for-advanced-bile-duct-cancer/
22. Abou-Alfa GK, Sahai V, Hollebecque A, Vaccaro G, Melisi D, Al-Rajabi R, et al. Pemigatinib for previously treated, locally advanced or metastatic cholangiocarcinoma: a multicentre, open-label, phase 2 study. Lancet Oncol. 2020 May 1;21(5):671–84.
23. Moasser MM. The oncogene HER2: Its signaling and transforming functions and its role in human cancer pathogenesis. Vol. 26, Oncogene. 2007. p. 6469–87.
24. Meric-Bernstam F, Beeram M, Hamilton E, Oh DY, Hanna DL, Kang YK, et al. Zanidatamab, a novel bispecific antibody, for the treatment of locally advanced or metastatic HER2-expressing or HER2-amplified cancers: a phase 1, dose-escalation and expansion study. Lancet Oncol. 2022 Dec 1;23(12):1558–70.
25. Zou S, Li J, Zhou H, Frech C, Jiang X, Chu JSC, et al. Mutational landscape of intrahepatic cholangiocarcinoma. Nat Commun. 2014 Dec 15;5.
26. Goeppert B, Stichel D, Toth R, Fritzsche S, Loeffler MA, Schlitter AM, et al. Integrative analysis reveals early and distinct genetic and epigenetic changes in intraductal papillary and tubulopapillary cholangiocarcinogenesis. Gut. 2022;71(2):391–401.
27. Lavingia V, Fakih M. Impressive response to dual BRAF and MEK inhibition in patients with BRAF mutant intrahepatic cholangiocarcinoma-2 case reports and a brief review. J Gastrointest Oncol. 2016;7(6):E98–102.
28. O'Rourke CJ, Munoz-Garrido P, Andersen JB. Molecular Targets in Cholangiocarcinoma. Hepatology. 2021;73(S1):62–74.
29. Brivio S, Cadamuro M, Fabris L, Strazzabosco M. Molecular mechanisms driving cholangiocarcinoma invasiveness: An overview. Gene Expr. 2018;18(1):31–50.
30. Brivio S, Cadamuro M, Strazzabosco M, Fabris L. Tumor reactive stroma in cholangiocarcinoma: The fuel behind cancer aggressiveness. World Journal of Hepatology. 2017.
31. Sulpice L, Rayar M, Desille M, Turlin B, Fautrel A, Boucher E, et al. Molecular profiling of stroma identifies osteopontin as an independent predictor of poor prognosis in intrahepatic cholangiocarcinoma. Hepatology. 2013;58(6):1992–2000.
32. Coulouarn C, Clément B. Stellate cells and the development of liver cancer: Therapeutic potential of targeting the stroma. Vol. 60, Journal of Hepatology. Elsevier B.V.; 2014. p. 1306–9.
33. Haga H, Patel T. Molecular diagnosis of intrahepatic cholangiocarcinoma. J Hepatobiliary Pancreat Sci. 2015 Feb 1;22(2):114–23.

34. Techasen A, Loilome W, Namwat N, Khuntikeo N, Puapairoj A, Jearanaikoon P, et al. Loss of E-cadherin promotes migration and invasion of cholangiocarcinoma cells and serves as a potential marker of metastasis. Tumor Biology. 2014;35(9):8645–52.
35. Lindemans CA, Calafiore M, Mertelsmann AM, O'Connor MH, Dudakov JA, Jenq RR, et al. Interleukin-22 promotes intestinal-stem-cell-mediated epithelial regeneration. Nature. 2015 Dec 24;528(7583):560–4.
36. Roy S, Glaser S, Chakraborty S. Inflammation and Progression of Cholangiocarcinoma: Role of Angiogenic and Lymphangiogenic Mechanisms. Front Med (Lausanne). 2019;6(December):1–12.
37. Andersen JB, Spee B, Blechacz BR, Avital I, Komuta M, Barbour A, et al. Genomic and genetic characterization of cholangiocarcinoma identifies therapeutic targets for tyrosine kinase inhibitors. Gastroenterology. 2012;142(4).
38. Zou S et al. Mutational landscape of intrahepatic cholangiocarcinoma. . Nat Commun. 2014;5.
39. Yokomuro S, Tsuji H, Lunz JG, Sakamoto T, Ezure T, Murase N, et al. Growth control of human biliary epithelial cells by interleukin 6, hepatocyte growth factor, transforming growth factor β1, and activin A: Comparison of a cholangiocarcinoma cell line with primary cultures of non- neoplastic biliary epithelial cells. Hepatology. 2000;32(1):26–35.
40. Li J. Hormonal Carcinogenesis. Vol. 617. 2008. 547–555 p.
41. Affo S, Nair A, Brundu F, Ravichandra A, Bhattacharjee S, Matsuda M, et al. Promotion of cholangiocarcinoma growth by diverse cancer-associated fibroblast subpopulations. Cancer Cell [Internet]. 2021;39(6):866-882.e11. Available from: https://doi.org/10.1016/j.ccell.2021.03.012
42. Zhou M, Wang C, Lu S, Xu Y, Li Z, Jiang H, et al. Tumor-associated macrophages in cholangiocarcinoma: complex interplay and potential therapeutic target. EBioMedicine [Internet]. 2021;67:103375. Available from: https://doi.org/10.1016/j.ebiom.2021.103375
43. Plava J, Cihova M, Burikova M, Matuskova M, Kucerova L, Miklikova S. Recent advances in understanding tumor stroma-mediated chemoresistance in breast cancer. Mol Cancer. 2019;18(1):1–10.
44. Vaquero J, Guedj N, Clapéron A, Nguyen Ho-Bouldoires TH, Paradis V, Fouassier L. Epithelial-mesenchymal transition in cholangiocarcinoma: From clinical evidence to regulatory networks. J Hepatol [Internet]. 2017;66(2):424–41. Available from: http://dx.doi.org/10.1016/j.jhep.2016.09.010
45. Kilanczyk E, Ruminkiewicz D, Banales JM, Milkiewicz P, Milkiewicz M. DHEA Protects Human Cholangiocytes and Hepatocytes against Apoptosis and Oxidative Stress. Cells. 2022;11(6):1–13.
46. Banales JM, Huebert RC, Karlsen T, Strazzabosco M, LaRusso NF, Gores GJ. Cholangiocyte pathobiology. Nat Rev Gastroenterol Hepatol [Internet]. 2019;16(5):269–81. Available from: http://dx.doi.org/10.1038/s41575-019-0125-y
47. Manco R, Clerbaux LA, Verhulst S, Bou Nader M, Sempoux C, Ambroise J, et al. Reactive cholangiocytes differentiate into proliferative hepatocytes with efficient DNA repair in mice with chronic liver injury. J Hepatol [Internet]. 2019;70(6):1180–91. Available from: https://doi.org/10.1016/j.jhep.2019.02.003
48. Raven A. Cholangiocytes act as facultative liver stem cells during impaired hepatocyte regeneration. Nature. 2017;547:350–4.

49. Guicciardi ME, Trussoni CE, LaRusso NF, Gores GJ. The Spectrum of Reactive Cholangiocytes in Primary Sclerosing Cholangitis. Hepatology. 2020;71(2):741–8.
50. Tabibian JH, Masyuk AI, Masyuk T V., O'Hara SP, LaRusso NF. Physiology of cholangiocytes. Compr Physiol. 2013;3(1):541–65.
51. Planas-Paz L. AP, but Not RSPO-LGR4/5, signaling in biliary epithelial cells promotes a ductular reaction in response to liver injury. Cell Stem Cell. 2019;25:39–53.
52. Glaser SS, Gaudio E, Miller T, Alvaro D, Alpini G. Cholangiocyte proliferation and liver fibrosis. Expert Rev Mol Med. 2009;11:1–22.
53. Guicciardi ME, Krishnan A, Bronk SF, Hirsova P, Griffith TS, Gores GJ. Biliary tract instillation of a SMAC mimetic induces TRAIL-dependent acute sclerosing cholangitis-like injury in mice. Cell Death Dis. 2017 Jan 5;8(1).
54. Vince JE, Chau D, Callus B, Wong WWL, Hawkins CJ, Schneider P, et al. TWEAK-FN14 signaling induces lysosomal degradation of a cIAP1-TRAF2 complex to sensitize tumor cells to TNFα. Journal of Cell Biology. 2008 Jul 14;182(1):171–84.
55. Kirkland J. Cellular Senescence: A Translational Perspective. EBioMedicine. 2017;21:21–8.
56. Guicciardi ME, Trussoni CE, Krishnan A, Bronk SF, Lorenzo Pisarello MJ, O'Hara SP, et al. Macrophages contribute to the pathogenesis of sclerosing cholangitis in mice. J Hepatol. 2018 Sep 1;69(3):676–86.
57. Meadows V, Baiocchi L, Kundu D, Sato K, Fuentes Y, Wu C, et al. Biliary Epithelial Senescence in Liver Disease: There Will Be SASP. Front Mol Biosci. 2021;8(December):1–15.
58. Luca F, Strazzabosco M. Epithelial–Mesenchymal Interactions in Biliary Diseases. Semin Liver Dis. 2011;31(1):11–32.
59. Rizvi S, Khan SA, Hallemeier CL, Kelley RK, Gores GJ. Cholangiocarcinoma-evolving concepts and therapeutic strategies. Nat Rev Clin Oncol [Internet]. 2018;15(2):95–111. Available from: http://dx.doi.org/10.1038/nrclinonc.2017.157
60. Chong DQ, Zhu AX. The landscape of targeted therapies for cholangiocarcinoma: Current status and emerging targets. Oncotarget. 2016;7(29):46750–67.
61. Chan-On W, Nairismägi ML, Ong CK, Lim WK, Dima S, Pairojkul C, et al. Exome sequencing identifies distinct mutational patterns in liver fluke-related and non-infection-related bile duct cancers. Nat Genet. 2013;
62. Saborowski A, Lehmann U, Vogel A. FGFR inhibitors in cholangiocarcinoma: what's now and what's next? Vol. 12, Therapeutic Advances in Medical Oncology. SAGE Publications Inc.; 2020.
63. Kurashige J, Mima K, Sawada G, Takahashi Y, Eguchi H, Sugimachi K, et al. Epigenetic modulation and repression of miR-200b by cancer-associated fibroblasts contribute to cancer invasion and peritoneal dissemination in gastric cancer. Carcinogenesis. 2015 Jan 1;36(1):133–41.
64. Rizvi S, Khan SA, Hallemeier CL, Kelley RK, Gores GJ. Cholangiocarcinoma-evolving concepts and therapeutic strategies. Vol. 15, Nature Reviews Clinical Oncology. Nature Publishing Group; 2018. p. 95–111.
65. Isomoto H, Mott JL, Kobayashi S, Werneburg NW, Bronk SF, Haan S, et al. Sustained IL-6/STAT-3 Signaling in Cholangiocarcinoma Cells Due to SOCS-3 Epigenetic Silencing. Gastroenterology. 2007;132(1):384–96.

66. Carbone M, Harbour JW, Brugarolas J, Bononi A, Pagano I, Dey A, et al. Biological mechanisms and clinical signifi cance of BAP1 mutations in human cancer. Cancer Discov. 2020;10(8):1103–20.
67. Saha SK, Parachoniak CA, Ghanta KS, Fitamant J, Ross KN, Najem MS, et al. Mutant IDH inhibits HNF-4α to block hepatocyte differentiation and promote biliary cancer. Nature. 2014 Sep 1;513(7516):110–52.
68. Zheng J. Energy metabolism of cancer: Glycolysis versus oxidative phosphorylation (review). Vol. 4, Oncology Letters. 2012. p. 1151–7.
69. Ruiz de Gauna M, Biancaniello F, González-Romero F, Rodrigues PM, Lapitz A, Gómez-Santos B, et al. Cholangiocarcinoma progression depends on the uptake and metabolization of extracellular lipids. Hepatology. 2022 Dec 1;76(6):1617–33.
70. Tomacha J, Dokduang H, Padthaisong S, Namwat N, Klanrit P, Phetcharaburanin J, et al. Targeting Fatty Acid Synthase Modulates Metabolic Pathways and Inhibits Cholangiocarcinoma Cell Progression. Front Pharmacol. 2021;12(August):1–13.
71. Satriano L, Lewinska M, Rodrigues PM, Banales JM, Andersen JB. Metabolic rearrangements in primary liver cancers: cause and consequences. Nat Rev Gastroenterol Hepatol [Internet]. 2019;16(12):748–66. Available from: http://dx.doi.org/10.1038/s41575-019-0217-8
72. Shimizu Y, Demetris AJ, Gollin SM, Storto PD, Bedford HM, Altarac S, et al. Two new human cholangiocarcinoma cell lines and their cytogenetics and responses to growth factors, hormones, cytokines or immunologic effector cells. Int J Cancer. 1992;52(2):252–60.
73. Ku JL, Yoon KA, Kim IJ, Kim WH, Jang JY, Suh KS, et al. Establishment and characterisation of six human biliary tract cancer cell lines. Br J Cancer. 2002;87(2):187–93.
74. Maruyama M, Kobayashi N, Westerman KA, Sakaguchi M, Allain JE, Totsugawa T, et al. Establishment of a highly differentiated immortalized human cholangiocyte cell line with SV40T and hTERT. Transplantation. 2004;77(3):446–51.
75. Banales JM, Sáez E, Úriz M, Sarvide S, Urribarri AD, Splinter P, et al. Up-regulation of microRNA 506 leads to decreased Cl -/HCO 3- anion exchanger 2 expression in biliary epithelium of patients with primary biliary cirrhosis. Hepatology. 2012 Aug;56(2):687–97.
76. Soga T, Ohashi Y, Ueno Y, Naraoka H, Tomita M, Nishioka T. Quantitative Metabolome Analysis Using Capillary Electrophoresis Mass Spectrometry. J Proteome Res. 2003;2(5):488–94.
77. Fan S, Shahid M, Jin P, Asher A, Kim J. Identification of metabolic alterations in breast cancer using mass spectrometry-based metabolomic analysis. Metabolites. 2020 Apr 1;10(4).
78. Zhou H, Chen Y, Xiao Y, Wu Q, Li H, Li Y, et al. Evaluation of the ability of fatty acid metabolism signature to predict response to neoadjuvant chemoradiotherapy and prognosis of patients with locally advanced rectal cancer. Front Immunol. 2022 Nov 24;13.
79. Tietz-Bogert PS, Kim M, Cheung A, Tabibian JH, Heimbach JK, Rosen CB, et al. Metabolomic profiling of portal blood and bile reveals metabolic signatures of primary sclerosing cholangitis. Int J Mol Sci. 2018 Oct 16;19(10).

80. Missiaen R, Anderson NM, Kim LC, Nance B, Burrows M, Skuli N, et al. GCN2 inhibition sensitizes arginine-deprived hepatocellular carcinoma cells to senolytic treatment. Cell Metab. 2022 Aug 2;34(8):1151-1167.e7.
81. Li B, Qiu B, Lee DSM, Walton ZE, Ochocki JD, Mathew LK, et al. Fructose-1,6-bisphosphatase opposes renal carcinoma progression. Nature. 2014 Sep 11;513(7517):251–5.
82. Ochocki JD, Khare S, Hess M, Ackerman D, Qiu B, Daisak JI, et al. Arginase 2 Suppresses Renal Carcinoma Progression via Biosynthetic Cofactor Pyridoxal Phosphate Depletion and Increased Polyamine Toxicity. Cell Metab. 2018 Jun 5;27(6):1263-1280.e6.
83. Riscal R, Bull CJ, Mesaros C, Finan JM, Carens M, Ho ES, et al. Cholesterol Auxotrophy as a Targetable Vulnerability in Clear Cell Renal Cell Carcinoma. Cancer Discov. 2021 Dec 1;11(12):3106–25.
84. Carpentier G. http://rsb.info.nih.gov/ij/macros/toolsets/ProteinArrayAnalyzer.txt. 2010. Protein Array Analyzer for ImageJ.
85. Miyazaki M, Namba M. Immortalization of Epithelial-like Cells from Human Liver Tissue with SV40 T-Antigen Gene. Exp Cell Res. 1993;206(1):27–35.
86. Obchoei S, Weakley SM, Wongkham S, Wongkham C, Sawanyawisuth K, Yao Q, et al. Cyclophilin A enhances cell proliferation and tumor growth of liver fluke-associated cholangiocarcinoma. Mol Cancer. 2011 Aug 26;10.
87. Armartmuntree N, Murata M, Techasen A, Yongvanit P, Loilome W, Namwat N, et al. Prolonged oxidative stress down-regulates Early B cell factor 1 with inhibition of its tumor suppressive function against cholangiocarcinoma genesis. Redox Biol. 2018 Apr 1;14:637–44.
88. Suwannakul N, Ma N, Midorikawa K, Oikawa S, Kobayashi H, He F, et al. CD44v9 Induces Stem Cell-Like Phenotypes in Human Cholangiocarcinoma. Front Cell Dev Biol. 2020;8(June):1–15.
89. The Christie N. Bile Duct Cancer [Internet]. Available from: https://www.christie.nhs.uk/patients-and-visitors/your-treatment-and-care/types-of-cancer/bile-duct-cancer#:~:text=Bile duct cancer (cholangiocarcinoma) is,every year in the UK.
90. Shen S, Shao Y, Li C. Different types of cell death and their shift in shaping disease. Vol. 9, Cell Death Discovery. Springer Nature; 2023.
91. Francis GL. Albumin and mammalian cell culture: Implications for biotechnology applications. Vol. 62, Cytotechnology. 2010. p. 1–16.
92. Matsarskaia O, Bühl L, Beck C, Grimaldo M, Schweins R, Zhang F, et al. Evolution of the structure and dynamics of bovine serum albumin induced by thermal denaturation. Physical Chemistry Chemical Physics. 2020 Sep 7;22(33):18507–17.
93. Park J, Gores GJ, Patel T. Lipopolysaccharide induces cholangiocyte proliferation via an interleukin-6-mediated activation of p44/p42 mitogen-activated protein kinase. Hepatology. 1999;29(4):1037–43.
94. Tabibian JH, Trussoni CE, O'Hara SP, Splinter PL, Heimbach JK, LaRusso NF. Characterization of cultured cholangiocytes isolated from livers of patients with primary sclerosing cholangitis. Laboratory Investigation. 2014 Jan 1;94(10):1126–33.
95. Pinto C, Giordano DM, Maroni L, Marzioni M. Role of inflammation and proinflammatory cytokines in cholangiocyte pathophysiology. Biochim Biophys Acta Mol Basis Dis. 2018;1864(4):1270–8.

96. Phukhum P, Phetcharaburanin J, Chaleekarn K, Kittirat Y, Kulthawatsiri T, Namwat N, et al. The impact of hypoxia and oxidative stress on proteo-metabolomic alterations of 3D cholangiocarcinoma models. Sci Rep [Internet]. 2023;13(1):1–16. Available from: https://doi.org/10.1038/s41598-023-30204-y
97. Park SM. The crucial role of cholangiocytes in cholangiopathies. Gut Liver. 2012;6(3):295–304.
98. Omenetti A, Diehl AM. Hedgehog signaling in cholangiocytes. Curr Opin Gastroenterol. 2011 May;27(3):268–75.
99. Omenetti A, Yang L, Li YX, McCall SJ, Jung Y, Sicklick JK, et al. Hedgehog-mediated mesenchymal-epithelial interactions modulate hepatic response to bile duct ligation. Laboratory Investigation. 2007 May 5;87(5):499–514.
100. Peinado H, Olmeda D, Cano A. Snail, ZEB and bHLH factors in tumour progression: An alliance against the epithelial phenotype? Vol. 7, Nature Reviews Cancer. 2007. p. 415–28.
101. Mani SA, Guo W, Liao MJ, Eaton EN, Ayyanan A, Zhou AY, et al. The Epithelial-Mesenchymal Transition Generates Cells with Properties of Stem Cells. Cell. 2008 May 16;133(4):704–15.
102. Thongchot S, Vidoni C, Ferraresi A, Loilome W, Khuntikeo N, Sangkhamanon S, et al. Cancer-associated fibroblast-derived il-6 determines unfavorable prognosis in cholangiocarcinoma by affecting autophagy-associated chemoresponse. Cancers (Basel). 2021 May 1;13(9).
103. Wells RG. The epithelial-to-mesenchymal transition in liver fibrosis: Here today, gone tomorrow? Vol. 51, Hepatology. 2010. p. 737–40.
104. Cassiman D, Libbrecht L, Desmet V, Denef C, Roskams T. Hepatic stellate cell/myofibroblast subpopulations in fibrotic human and rat livers [Internet]. Available from: www.elsevier.com/locate/jhep
105. Guicciardi ME, Malhi H, Mott JL, Gores GJ. Apoptosis and necrosis in the liver. Compr Physiol. 2013;3(2):977–1010.
106. Tchkonia T, Zhu Y, Van Deursen J, Campisi J, Kirkland JL. Cellular senescence and the senescent secretory phenotype: Therapeutic opportunities. Vol. 123, Journal of Clinical Investigation. 2013. p. 966–72.
107. Kittirat Y, Suksawat M, Thongchot S, Padthaisong S, Phetcharaburanin J, Wangwiwatsin A, et al. Interleukin-6-derived cancer-associated fibroblasts activate STAT3 pathway contributing to gemcitabine resistance in cholangiocarcinoma. Front Pharmacol. 2022;13(August):1–16.
108. Warburg Effect. Definitions. 2020;2016.
109. Lunt SY, Vander Heiden MG. Aerobic glycolysis: Meeting the metabolic requirements of cell proliferation. Annu Rev Cell Dev Biol. 2011;27.
110. Hanahan D, Weinberg RA. Hallmarks of cancer: The next generation. Vol. 144, Cell. 2011. p. 646–74.
111. Rizzo A, Ricci AD, Brandi G. IDH inhibitors in advanced cholangiocarcinoma: Another arrow in the quiver? Vol. 27, Cancer Treatment and Research Communications. Elsevier Ltd; 2021.
112. Fathi AT, Sadrzadeh H, Borger DR, Ballen KK, Amrein PC, Attar EC, et al. Prospective serial evaluation of 2-hydroxyglutarate, during treatment of newly diagnosed acute myeloid leukemia, to assess disease activity and therapeutic response. Blood. 2012 Nov 29;120(23):4649–52.

113. Ruiz de Gauna M, Biancaniello F, González-Romero F, Rodrigues PM, Lapitz A, Gómez-Santos B, et al. Cholangiocarcinoma progression depends on the uptake and metabolization of extracellular lipids. Hepatology. 2022 Dec 1;76(6):1617–33.
114. Cairns RA, Harris IS, Mak TW. Regulation of cancer cell metabolism. Vol. 11, Nature Reviews Cancer. 2011. p. 85–95.
115. Heiden MGV, Cantley LC, Thompson CB. Understanding the warburg effect: The metabolic requirements of cell proliferation. Vol. 324, Science. 2009. p. 1029–33.
116. Witsch E, Sela M, Yarden Y. Roles for Growth Factors in Cancer Progression. Vol. 25, Physiology. American Physiological Society; 2010. p. 85–101.
117. Xu L, Hausmann M, Dietmaier W, Kellermeier S, Pesch T, Stieber-Gunckel M, et al. Expression of growth factor receptors and targeting of EGFR in cholangiocarcinoma cell lines [Internet]. 2010. Available from: http://www.biomedcentral.com/1471-2407/10/302
118. J V. Unveiling resistance mechanisms to EGFR inhibitors in cholangiocarcinoma. Oncotarget. 2018;9(99):37274–5.
119. Graham RP, Barr Fritcher EG, Pestova E, Schulz J, Sitailo LA, Vasmatzis G, et al. Fibroblast growth factor receptor 2 translocations in intrahepatic cholangiocarcinoma. Hum Pathol. 2014;45(8):1630–8.
120. Wang J, Xing X, Li Q, Zhang G, Wang T, Pan H, et al. Targeting the FGFR signaling pathway in cholangiocarcinoma: promise or delusion? Vol. 12, Therapeutic Advances in Medical Oncology. SAGE Publications Inc.; 2020.
121. Simons M, Gordon E, Claesson-Welsh L. Mechanisms and regulation of endothelial VEGF receptor signalling. Vol. 17, Nature Reviews Molecular Cell Biology. Nature Publishing Group; 2016. p. 611–25.
122. Heindryckx F, Coulon S, Terrie E, Casteleyn C, Stassen JM, Geerts A, et al. The placental growth factor as a target against hepatocellular carcinoma in a diethylnitrosamine-induced mouse model.
123. Matkar PN, Jong ED, Ariyagunarajah R, Prud'homme GJ, Singh KK, Leong-Poi H. Jack of many trades: Multifaceted role of neuropilins in pancreatic cancer. Vol. 7, Cancer Medicine. Blackwell Publishing Ltd; 2018. p. 5036–46.
124. Aoki S, Inoue K, Klein S, Halvorsen S, Chen J, Matsui A, et al. Placental growth factor promotes tumour desmoplasia and treatment resistance in intrahepatic cholangiocarcinoma. Gut. 2022 Jan 1;71(1):185–93.
125. Goydos JS, Brumfield AM, Frezza E, Booth A, Lotze MT, Carty SE, et al. Marked Elevation of Serum Interleukin-6 in Patients With Cholangiocarcinoma Validation of Utility as a Clinical Marker. Vol. 227, ANNALS OF SURGERY. Lippincott-Raven Publishers; 1998.
126. Colyn L, Alvarez-Sola G, Latasa MU, Uriarte I, Herranz JM, Arechederra M, et al. New molecular mechanisms in cholangiocarcinoma: signals triggering interleukin-6 production in tumor cells and KRAS co-opted epigenetic mediators driving metabolic reprogramming. Journal of Experimental and Clinical Cancer Research [Internet]. 2022;41(1):1–18. Available from: https://doi.org/10.1186/s13046-022-02386-2
127. Wehbe H, Henson R, Meng F, Mize-Berge J, Patel T. Interleukin-6 contributes to growth in cholangiocarcinoma cells by aberrant promoter methylation and gene expression. Cancer Res. 2006;66(21):10517–24.

128. Gorgoglione R, Impedovo V, Riley CL, Fratantonio D, Tiziani S, Palmieri L, et al. Glutamine-Derived Aspartate Biosynthesis in Cancer Cells: Role of Mitochondrial Transporters and New Therapeutic Perspectives. Vol. 14, Cancers. MDPI; 2022.
129. Garcia-Bermudez J, Baudrier L, La K, Zhu XG, Fidelin J, Sviderskiy VO, et al. Aspartate is a limiting metabolite for cancer cell proliferation under hypoxia and in tumours. Nat Cell Biol. 2018 Jul 1;20(7):775–81.
130. Zhang J, Fan J, Venneti S, Cross JR, Takagi T, Bhinder B, et al. Asparagine plays a critical role in regulating cellular adaptation to glutamine depletion. Mol Cell. 2014;56(2):205–18.
131. Gwinn DM, Lee AG, Briones-Martin-del-Campo M, Conn CS, Simpson DR, Scott AI, et al. Oncogenic KRAS Regulates Amino Acid Homeostasis and Asparagine Biosynthesis via ATF4 and Alters Sensitivity to L-Asparaginase. Cancer Cell. 2018 Jan 8;33(1):91-107.e6.
132. Krall AS, Xu S, Graeber TG, Braas D, Christofk HR. Asparagine promotes cancer cell proliferation through use as an amino acid exchange factor. Nat Commun. 2016 Apr 29;7.
133. Glunde K, Bhujwalla ZM, Ronen SM. Choline metabolism in malignant transformation. Nat Rev Cancer. 2011;11(12):835–48.
134. Mori N, Wildes F, Takagi T, Glunde K, Bhujwalla ZM. The tumor microenvironment modulates choline and lipid metabolism. Front Oncol. 2016;6(DEC).
135. Bonilla DA, Kreider RB, Stout JR, Forero DA, Kerksick CM, Roberts MD, et al. Metabolic basis of creatine in health and disease: A bioinformatics-assisted review. Vol. 13, Nutrients. MDPI AG; 2021.
136. Wyss M, Kaddurah-Daouk R. Creatine and creatinine metabolism. Physiol Rev. 2000;80(3):1107–213.
137. Padthaisong S, Phetcharaburanin J, Klanrit P, Li J V., Namwat N, Khuntikeo N, et al. Integration of global metabolomics and lipidomics approaches reveals the molecular mechanisms and the potential biomarkers for postoperative recurrence in early-stage cholangiocarcinoma. Cancer Metab. 2021 Dec;9(1).
138. Parker AL, Toulabi L, Oike T, Kanke Y, Patel D, Tada T, et al. Creatine riboside is a cancer cell–derived metabolite associated with arginine auxotrophy. Journal of Clinical Investigation. 2022 Jul 15;132(14).
139. Uranbileg B, Enooku K, Soroida Y, Ohkawa R, Kudo Y, Nakagawa H, et al. High ubiquitous mitochondrial creatine kinase expression in hepatocellular carcinoma denotes a poor prognosis with highly malignant potential. Int J Cancer. 2014 May 31;134(9):2189–98.
140. Pant K, Richard S, Peixoto E, Gradilone SA. Role of Glucose Metabolism Reprogramming in the Pathogenesis of Cholangiocarcinoma. Vol. 7, Frontiers in Medicine. Frontiers Media S.A.; 2020.
141. Pastore M, Lori G, Gentilini A, Taddei ML, Di Maira G, Campani C, et al. Multifaceted Aspects of Metabolic Plasticity in Human Cholangiocarcinoma: An Overview of Current Perspectives. Cells. 2020;9(3).
142. Raggi C, Taddei ML, Rae C, Braconi C, Marra F. Metabolic reprogramming in cholangiocarcinoma. Vol. 77, Journal of Hepatology. Elsevier B.V.; 2022. p. 849–64.
143. Wei Z, Liu X, Cheng C, Yu W, Yi P. Metabolism of Amino Acids in Cancer. Front Cell Dev Biol. 2021 Jan 12;8.

144. Holeček M. Relation Between Glutamine, Branched-Chain Amino Acids, and Protein Metabolism.
145. Lieu EL, Nguyen T, Rhyne S, Kim J. Amino acids in cancer. Exp Mol Med [Internet]. 2020;52(1):15–30. Available from: http://dx.doi.org/10.1038/s12276-020-0375-3
146. Suh EH, Hackett EP, Wynn RM, Chuang DT, Zhang B, Luo W, et al. In vivo assessment of increased oxidation of branched-chain amino acids in glioblastoma. Sci Rep. 2019 Dec 1;9(1).
147. Mayers JR, Torrence ME, Danai L V., Papagiannakopoulos T, Davidson SM, Bauer MR, et al. Tissue of origin dictates branched-chain amino acid metabolism in mutant Kras-driven cancers. Science (1979). 2016 Sep 9;353(6304):1161–5.
148. Kitagawa A, Osawa T, Noda M, Kobayashi Y, Aki S, Nakano Y, et al. Convergent genomic diversity and novel BCAA metabolism in intrahepatic cholangiocarcinoma. Br J Cancer. 2023 Jun 29;128(12):2206–17.
149. Ong CK, Subimerb C, Pairojkul C, Wongkham S, Cutcutache I, Yu W, et al. Exome sequencing of liver flukeg-associated cholangiocarcinoma. Nat Genet. 2012 Jun;44(6):690–3.
150. Nakamura H, Arai Y, Totoki Y, Shirota T, Elzawahry A, Kato M, et al. Genomic spectra of biliary tract cancer. Nat Genet. 2015;
151. Nepal C et al. Genomic perturbations reveal distinct regulatory networks in intrahepatic cholangiocarcinoma. . Hepatology. 2018;68:949–63.
152. Wu YM et al 3, 636–647 (2013). Identification of targetable FGFR gene fusions in diverse cancers. Cancer Discov. 2013;3:636–47.
153. O'Rourke CJ, Munoz-Garrido P, Aguayo EL, Andersen JB. Epigenome dysregulation in cholangiocarcinoma. Biochim Biophys Acta Mol Basis Dis [Internet]. 2018;1864(4):1423–34. Available from: https://doi.org/10.1016/j.bbadis.2017.06.014
154. Reitman ZJ, Jin G, Karoly ED, Spasojevic I, Yang J, Kinzler KW, et al. Profiling the effects of isocitrate dehydrogenase 1 and 2 mutations on the cellular metabolome. Proc Natl Acad Sci U S A. 2011;108(8):3270–5.
155. Wang P et al. Mutations in isocitrate dehydrogenase 1 and 2 occur frequently in intrahepatic cholangio carcinomas and share hypermethylation targets with glioblastomas. Oncogene. 2013;32:3091–100.
156. Alvaro D, Gigliozzi A, Attili AF. Regulation and deregulation of cholangiocyte proliferation. J Hepatol. 2000;33(2):333–40.
157. Chen Y, Yang X, Chen Y, Chen G, Winkler CA, An P, et al. Impacts of the SOAT1 genetic variants and protein expression on HBV-related hepatocellular carcinoma. BMC Cancer. 2021 Dec 1;21(1).
158. Eckhardt C, Sbiera I, Krebs M, Sbiera S, Spahn M, Kneitz B, et al. High expression of Sterol-O-Acyl transferase 1 (SOAT1), an enzyme involved in cholesterol metabolism, is associated with earlier biochemical recurrence in high risk prostate cancer. Prostate Cancer Prostatic Dis. 2022;25(3):484–90.
159. Wang J, Gu Y, Yan X, Zhang J, Wang J, Ding Y. USP38 inhibits colorectal cancer cell proliferation and migration via downregulating HMX3 ubiquitylation. Cell Cycle [Internet]. 2023;22(10):1169–81. Available from: https://doi.org/10.1080/15384101.2022.2042776
160. Diehl JA, Yang W, Rimerman RA, Xiao H, Emili A. Hsc70 Regulates Accumulation of Cyclin D1 and Cyclin D1-Dependent Protein Kinase. Mol Cell Biol. 2003;23(5):1764–74.

161. Qie S, Sang N. Stanniocalcin 2 (STC2): a universal tumour biomarker and a potential therapeutical target. Journal of Experimental and Clinical Cancer Research [Internet]. 2022;41(1):1–19. Available from: https://doi.org/10.1186/s13046-022-02370-w
162. Chen Y, Ning J, Cao W, Wang S, Du T, Jiang J, et al. Research Progress of TXNIP as a Tumor Suppressor Gene Participating in the Metabolic Reprogramming and Oxidative Stress of Cancer Cells in Various Cancers. Front Oncol. 2020;10(October):1–12.
163. Deng L, Yao P, Li L, Ji F, Zhao S, Xu C, et al. p53-mediated control of aspartate-asparagine homeostasis dictates LKB1 activity and modulates cell survival. Nat Commun. 2020 Dec 1;11(1).
164. Zheng Q, Zhang B, Li C, Zhang X. Overcome Drug Resistance in Cholangiocarcinoma: New Insight Into Mechanisms and Refining the Preclinical Experiment Models. Vol. 12, Frontiers in Oncology. Frontiers Media S.A.; 2022.
165. Sarantis P, Tzanetatou ED, Ioakeimidou E, Vallilas C, Androutsakos T, Damaskos C, et al. Cholangiocarcinoma: the role of genetic and epigenetic factors; current and prospective treatment with checkpoint inhibitors and immunotherapy. Am J Transl Res [Internet]. 2021;13(12):13246–60. Available from: http://www.ncbi.nlm.nih.gov/pubmed/35035673%0Ahttp://www.pubmedcentral.nih.gov/articlerender.fcgi?artid=PMC8748131
166. Morris JP, Yashinskie JJ, Koche R, Chandwani R, Tian S, Chen CC, et al. α-Ketoglutarate links p53 to cell fate during tumour suppression. Nature [Internet]. 2019;573(7775):595–9. Available from: http://dx.doi.org/10.1038/s41586-019-1577-5
167. Gradilone SA, Radtke BN, Bogert PS, Huang BQ, Gajdos GB, LaRusso NF. HDAC6 inhibition restores ciliary expression and decreases tumor growth. Cancer Res. 2013;
168. Jiao Y, Pawlik TM, Anders RA, Selaru FM, Streppel MM, Lucas DJ, et al. Exome sequencing identifies frequent inactivating mutations in BAP1, ARID1A and PBRM1 in intrahepatic cholangiocarcinomas. Nat Genet. 2013;
169. Gatla HR, Muniraj N, Thevkar P, Yavvari S, Sukhavasi S, Makena MR. Regulation of chemokines and cytokines by histone deacetylases and an update on histone decetylase inhibitors in human diseases. Vol. 20, International Journal of Molecular Sciences. MDPI AG; 2019.
170. Akimova T, Beier UH, Liu Y, Wang L, Hancock WW. Histone/protein deacetylases and T-cell immune responses. Vol. 119, Blood. American Society of Hematology; 2012. p. 2443–51.
171. Zhong W, Dai L, Liu J, Zhou S. Cholangiocarcinoma-associated genes identified by integrative analysis of gene expression data. Mol Med Rep. 2018;17(4):5744–53.
172. Li J, Yao L, Li G, Ma D, Sun C, Gao S, et al. MiR-221 promotes epithelial-mesenchymal transition through targeting PTEN and forms a positive feedback loop with β-catenin/c-Jun signaling pathway in extra-hepatic cholangiocarcinoma. PLoS One. 2015 Oct 26;10(10).
173. Mastoraki A, Schizas D, Charalampakis N, Naar L, Ioannidi M, Tsilimigras D, et al. Contribution of Histone Deacetylases in Prognosis and Therapeutic Management of Cholangiocarcinoma. Mol Diagn Ther [Internet]. 2020;24(2):175–84. Available from: https://doi.org/10.1007/s40291-020-00454-x
174. Hu L, Zang M De, Wang HX, Zhang BG, Wang ZQ, Fan ZY, et al. G9A promotes gastric cancer metastasis by upregulating ITGB3 in a SET domain-independent manner article. Cell Death Dis. 2018 Mar 1;9(3).

175. Hua KT, Wang MY, Chen MW, Wei LH, Chen CK, Ko CH, et al. The H3K9 methyltransferase G9a is a marker of aggressive ovarian cancer that promotes peritoneal metastasis. Mol Cancer. 2014 Aug 9;13(1).
176. Zhong X, Chen X, Guan X, Zhang H, Ma Y, Zhang S, et al. Overexpression of G9a and MCM7 in oesophageal squamous cell carcinoma is associated with poor prognosis. Histopathology. 2015;66(2):192–200.
177. Yuan LT, Lee WJ, Yang YC, Chen BR, Yang CY, Chen MW, et al. Histone methyltransferase g9a-promoted progression of hepatocellular carcinoma is targeted by liver-specific hsa-mir-122. Cancers (Basel). 2021 May 2;13(10).
178. SGC. UNC0642 A potent, selective inhibitor of G9a/GLP with improved PK properties.
179. Cao Y peng, Sun J ya, Li M qian, Dong Y, Zhang Y heng, Yan J, et al. Inhibition of G9a by a small molecule inhibitor, UNC0642, induces apoptosis of human bladder cancer cells. Acta Pharmacol Sin [Internet]. 2019;40(8):1076–84. Available from: http://dx.doi.org/10.1038/s41401-018-0205-5
180. Hughes JP, Rees SS, Kalindjian SB, Philpott KL. Principles of early drug discovery. Br J Pharmacol. 2011;162(6):1239–49.
181. Ma W, Han C, Zhang J, Song K, Chen W, Kwon H, et al. The Histone Methyltransferase G9a Promotes Cholangiocarcinogenesis Through Regulation of the Hippo Pathway Kinase LATS2 and YAP Signaling Pathway. Hepatology. 2020 Oct 1;72(4):1283–97.
182. Ding J, Li T, Wang X, Zhao E, Choi JH, Yang L, et al. The histone H3 methyltransferase G9A epigenetically activates the serine-glycine synthesis pathway to sustain cancer cell survival and proliferation. Cell Metab. 2013 Dec 3;18(6):896–907.
183. Baldwin RM, Haghandish N, Daneshmand M, Amin S, Paris G, Falls TJ, et al. Protein arginine methyltransferase 7 promotes breast cancer cell invasion through the induction of MMP9 expression. Oncotarget [Internet]. 2015;6(5). Available from: www.impactjournals.com/oncotarget/
184. Yao R, Jiang H, Ma Y, Wang L, Wang L, Du J, et al. PRMT7 induces epithelial-to-mesenchymal transition and promotes metastasis in breast cancer. Cancer Res. 2014 Oct 1;74(19):5656–67.
185. Szewczyk MM, Ishikawa Y, Organ S, Sakai N, Li F, Halabelian L, et al. Pharmacological inhibition of PRMT7 links arginine monomethylation to the cellular stress response. Nat Commun. 2020 Dec 1;11(1).
186. Wang YC, Li C. Evolutionarily conserved protein arginine methyltransferases in non-mammalian animal systems. Vol. 279, FEBS Journal. 2012. p. 932–45.
187. Wright T, Wang Y, Bedford MT. The role of the PRMT5-SND1 axis in hepatocellular carcinoma. Epigenomes. 2021;5(1).
188. Reid MA, Dai Z, Locasale JW. The impact of cellular metabolism on chromatin dynamics and epigenetics. Vol. 19, Nature Cell Biology. Nature Publishing Group; 2017. p. 1298–306.
189. Banales JM, Huebert RC, Karlsen T, Strazzabosco M, LaRusso NF, Gores GJ. Cholangiocyte pathobiology. Vol. 16, Nature Reviews Gastroenterology and Hepatology. Nature Publishing Group; 2019. p. 269–81.
190. Hill W, Zaragkoulias A, Salvador-Barbero B, Parfitt GJ, Alatsatianos M, Padilha A, et al. EPHA2-dependent outcompetition of KRASG12D mutant cells by wild-type neighbors in the adult pancreas. Current Biology. 2021 Jun 21;31(12):2550-2560.e5.

191. Colom B, Herms A, Hall MWJ, Dentro SC, King C, Sood RK, et al. Mutant clones in normal epithelium outcompete and eliminate emerging tumours. Nature. 2021 Oct 21;598(7881):510–4.
192. Madan E, Palma AM, Vudatha V, Trevino JG, Natarajan KN, Winn RA, et al. Cell Competition in Carcinogenesis. Vol. 82, Cancer Research. American Association for Cancer Research Inc.; 2022. p. 4487–96.
193. Chang CH, Qiu J, O'Sullivan D, Buck MD, Noguchi T, Curtis JD, et al. Metabolic Competition in the Tumor Microenvironment Is a Driver of Cancer Progression. Cell. 2015 Sep 10;162(6):1229–41.
194. Feranchak AP FJG. Adenosine triphosphate release and purinergic regulation of cholangiocyte transport. Semin Liver Dis. 2022;22:251–62.
195. Zhang L, Bu P. The two sides of creatine in cancer. Trends Cell Biol [Internet]. 2022;32(5):380–90. Available from: https://doi.org/10.1016/j.tcb.2021.11.004
196. Li L, Yang G, Ren C, Tanimoto R, Hirayama T, Wang J, et al. Glioma pathogenesis-related protein 1 induces prostate cancer cell death through Hsc70-mediated suppression of AURKA and TPX2. Mol Oncol. 2013;7(3):484–96.
197. Valek L, Heidler J, Scheving R, Wittig I, Tegeder I. Nitric oxide contributes to protein homeostasis by S-nitrosylations of the chaperone HSPA8 and the ubiquitin ligase UBE2D. Redox Biol [Internet]. 2019;20(September 2018):217–35. Available from: https://doi.org/10.1016/j.redox.2018.10.002
198. Wang L, Schumann U, Liu Y, Prokopchuk O, Steinacker JM. Heat shock protein 70 (Hsp70) inhibits oxidative phosphorylation and compensates ATP balance through enhanced glycolytic activity. J Appl Physiol [Internet]. 2012;113:1669–76. Available from: http://www.jappl.org
199. Liu Z, Zheng W, Liu Y, Zhou B, Zhang Y, Wang F. Targeting HSPA8 inhibits proliferation via downregulating BCR-ABL and enhances chemosensitivity in imatinib-resistant chronic myeloid leukemia cells. Exp Cell Res [Internet]. 2021;405(2):112708. Available from: https://doi.org/10.1016/j.yexcr.2021.112708
200. Yan LR, Shen SX, Wang A, Ding HX, Liu YN, Yuan Y, et al. Comprehensive Pan-Cancer Analysis of Heat Shock Protein 110, 90, 70, and 60 Families. Front Mol Biosci. 2021;8(October):1–19.
201. Lazaridis KN, Strazzabosco M, Larusso NF. The cholangiopathies: Disorders of biliary epithelia. Gastroenterology. 2004;127(5):1565–77.
202. Vita F, Olaizola I, Amato F, Rae C, Marco S, Banales JM, et al. Heterogeneity of Cholangiocarcinoma Immune Biology. Cells. 2023;12(6).
203. Wu CT, Davis PA, Luketic VA, Gershwin ME. A Review of the Physiological and Immunological Functions of Biliary Epithelial Cells: Targets for Primary Biliary Cirrhosis, Primary Sclerosing Cholangitis and Drug-induced Ductopenias. Clin Dev Immunol. 2004;11(3–4):205–13.
204. Afford SC. The role of cholangiocytes in the development of chronic inflammatory liver disease. Frontiers in Bioscience. 2002;7(5):A923.
205. McBrayer SK, Mayers JR, DiNatale GJ, Shi DD, Khanal J, Chakraborty AA, et al. Transaminase Inhibition by 2-Hydroxyglutarate Impairs Glutamate Biosynthesis and Redox Homeostasis in Glioma. Cell [Internet]. 2018;175(1):101-116.e25. Available from: https://doi.org/10.1016/j.cell.2018.08.038
206. Bryan T, Redder RR. SV40-Induced Immortalization of Human Cells. Crit Rev Oncog. 1994;5(4):331–57.

207. Pipas JM. SV40: Cell transformation and tumorigenesis. Vol. 384, Virology. 2009. p. 294–303.
208. Sheppard HM, Corneillie SI, Espiritu C, Gatti A, Liu X. New Insights into the Mechanism of Inhibition of p53 by Simian Virus 40 Large T Antigen. Mol Cell Biol. 1999 Apr 1;19(4):2746–53.
209. Manfredi JJ, Prives C. Binding of p53 and p105-RB is not sufficient for oncogenic transformation by a hybrid polyomavirus-simian virus 40 large T antigen. J Virol. 1990 Nov;64(11):5250–9.
210. Sachsenmeier KF, Pipas JM. Inhibition of Rb and p53 Is Insufficient for SV40 T-Antigen Transformation. Virology. 2001 Apr;283(1):40–8.
211. Alpini G, Glaser S, Robertson W, Rodgers RE, Phinizy JL, Lasater J, et al. Large but not small intrahepatic bile ducts are involved in secretin-regulated ductal bile secretion. American Journal of Physiology-Gastrointestinal and Liver Physiology. 1997 May 1;272(5):G1064–74.
212. Liu Y, Beyer A, Aebersold R. On the Dependency of Cellular Protein Levels on mRNA Abundance. Cell. 2016 Apr;165(3):535–50.
213. Kristensen AR, Gsponer J, Foster LJ. Protein synthesis rate is the predominant regulator of protein expression during differentiation. Mol Syst Biol. 2013 Jan 17;9(1).
214. Schoenheimer R, Ratner S, Rittenberg D. STUDIES IN PROTEIN METABOLISM. Journal of Biological Chemistry. 1939 Jan;127(1):333–44.
215. Kim IY, Park S, Kim Y, Kim HJ, Wolfe RR. Tracing metabolic flux in vivo: basic model structures of tracer methodology. Vol. 54, Experimental and Molecular Medicine. Springer Nature; 2022. p. 1311–22.
216. Cheng HLM. A primer on in vivo cell tracking using MRI. Vol. 10, Frontiers in Medicine. Frontiers Media SA; 2023.
217. Lechermann LM, Lau D, Attili B, Aloj L, Gallagher FA. In vivo cell tracking using pet: Opportunities and challenges for clinical translation in oncology. Vol. 13, Cancers. MDPI; 2021.